

JULY 2019

AJNR

VOLUME 40 • PP 1083-1250

AJNR

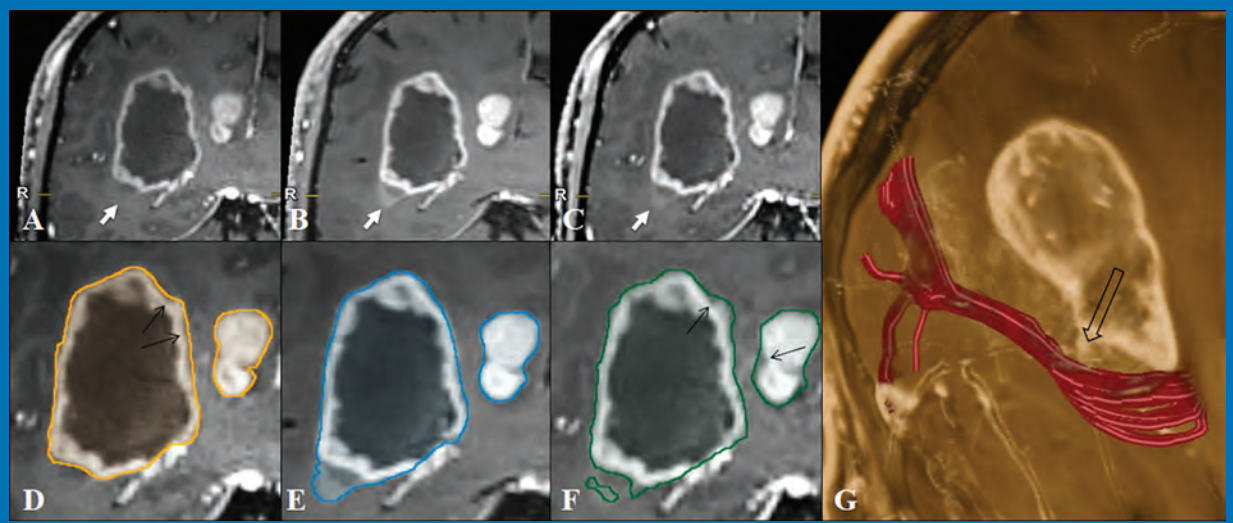
AMERICAN JOURNAL OF NEURORADIOLOGY

JULY 2019
VOLUME 40
NUMBER 7
WWW.AJNR.ORG

THE JOURNAL OF DIAGNOSTIC AND
INTERVENTIONAL NEURORADIOLOGY

3T whole brain MRI microscopy anatomy of basal forebrain
Aneurysm wall enhancement at 7T
Brain tumor enhancement with MPAGE, SPACE, and
VIBE MRI

Official Journal ASNR • ASFNR • ASHNR • ASPNR • ASSR





ONE AND DONE

INDICATIONS FOR USE:

The WEB Aneurysm Embolization System is indicated for use at the middle cerebral artery (MCA) bifurcation, internal carotid artery (ICA) terminus, anterior communicating artery (AComm) complex, or basilar artery apex for the endovascular treatment of adult patients with saccular, wide neck bifurcation intracranial aneurysms with dome diameter from 3 mm to 10 mm and either neck size 4 mm or greater or the dome-to-neck ratio is greater than 1 and less than 2.

The WEB Aneurysm Embolization System is contraindicated for patients with known bacterial infection that may interfere with or negatively affect the implantation procedure and patients with known hypersensitivity to nickel. For complete indications, contraindications, potential complications, warnings, precautions, and instructions, see instructions for use (IFU provided with the device).

The VIA® Catheter is intended for the introduction of non-liquid interventional devices (such as stents/_ow diverters) and infusion of diagnostic (such as contrast media) or non-liquid therapeutic agents into the neuro, peripheral, and coronary vasculature. The VIA Catheter is contraindicated for use with liquid embolic materials, such as n-butyl 2-cyanoacrylate or ethylene vinyl alcohol & DMSO (dimethyl sulfoxide). The VIA Catheter is contraindicated for use in the pediatric population (<22 yrs of age).

Caution: Federal law restricts these devices to sale by or on the order of a physician.

WEB[®]

Aneurysm Embolization System

MicroVention[®] delivers the first intrasaccular solution for wide neck bifurcation aneurysms.

The **world leader**
and **first**
PMA - approved
device in an
important new
category of
intrasaccular
flow disruptors.

The WEB[®] System is a safe
and effective single-device
solution for treating wide
neck bifurcation aneurysms.



SL Device



SLS Device

Contact a MicroVention sales associate to learn more about integrating the WEB[®] device into your practice.



**MicroVention Worldwide
Innovation Center**

35 Enterprise
Aliso Viejo, CA 92656 USA

MicroVention UK Limited

MicroVention Europe, S.A.R.L.

MicroVention Deutschland GmbH

microvention.com

PH +1.714.247.8000

PH +44 (0) 191 258 6777

PH +33 (1) 39 21 77 46

PH +49 211 210 798-0



CERENOVUS

#THINKCERENOVUS

Important information: Prior to use, refer to the instructions for use supplied with this device for indications, contraindications, side effects, warnings, and precautions.
Caution: US Law restricts this device to sale by or on the order of a physician
©CERENOVUS 2019. All rights reserved. 114983-190418



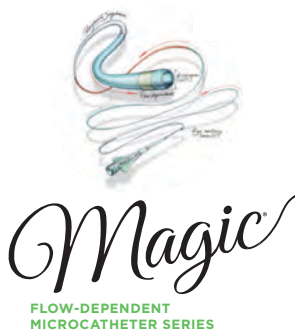
CERENOVUS

PART OF THE *Johnson & Johnson* FAMILY OF COMPANIES

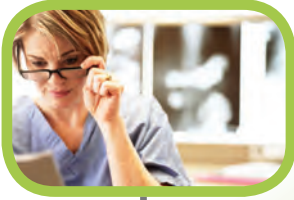
Introducing
Eclipse 2L
DUAL LUMEN BALLOON CATHETER



Balt's Access Portfolio Delivers Unique Solutions



Visit www.balt-usa.com to learn more



Simplify the MOC Process



Manage your CME Credits Online

CMEgateway.org

Available to Members of Participating Societies

American Board of Radiology (ABR)
American College of Radiology (ACR)
American Roentgen Ray Society (ARRS)
American Society of Neuroradiology (ASNR)
Commission on Accreditation of Medical
Physics Educational Programs, Inc. (CAMPEP)
Radiological Society of North America (RSNA)
Society of Interventional Radiology (SIR)
SNM
The Society for Pediatric Radiology (SPR)

It's Easy and Free!

Log on to CME Gateway to:

- View or print reports of your CME credits from multiple societies from a single access point.
- Print an aggregated report or certificate from each participating organization.
- Link to SAMs and other tools to help with maintenance of certification.

American Board of Radiology (ABR) participation!

By activating ABR in your organizational profile, your MOC-fulfilling CME and SAM credits can be transferred to your own personalized database on the ABR Web site.

Sign Up Today!

go to CMEgateway.org

Neuroform Atlas® Stent System

RX ONLY

See package insert for complete indications, contraindications, warnings and instructions for use.

Indications for use

The Neuroform Atlas Stent System is indicated for use with neurovascular embolization coils in the anterior circulation of the neurovasculature for the endovascular treatment of patients ≥ 18 years of age with saccular wide-necked (neck width ≥ 4 mm or a dome-to-neck ratio of < 2) intracranial aneurysms arising from a parent vessel with a diameter of ≥ 2.0 mm and ≤ 4.5 mm.

Contraindications

- Patients in whom the parent vessel size does not fall within the indicated range.
- Patients in whom antiplatelet and/or anticoagulation therapy (e.g., aspirin and clopidogrel) is contraindicated.
- Patients who have not received anti-platelet agents prior to stent implantation.
- Patients with an active bacterial infection.
- Patients in whom angiography demonstrates the anatomy is not appropriate for endovascular treatment due to conditions such as:
 - Severe intracranial vessel tortuosity or stenosis;
 - Intracranial vasospasm not responsive to medical therapy.
- Patients in whom a pre-existing stent is in place in the parent artery at the target intracranial aneurysm location.

Potential adverse events

The potential adverse events listed below, as well as others, may be associated with the use of the Neuroform Atlas Stent System or with the procedure:

- Aphasia
- Allergic reaction to Nitinol metal and medications
- Aneurysm perforation/rupture, leak or contrast extravasation
- Blindness
- Cardiac arrhythmia
- Coil herniation through stent into parent vessel
- Cranial neuropathy
- Death
- Embolus
- Headache
- Hemiplegia
- Hemorrhage (i.e., intracerebral, subarachnoid, retroperitoneal, or in other locations)
- Hydrocephalus
- In-stent stenosis
- Infection
- Ischemia

Stryker or its affiliated entities own, use, or have applied for the following trademarks or service marks: Neuroform Atlas, Stryker. All other trademarks are trademarks of their respective owners or holders.

The absence of a product, feature, or service name, or logo from this list does not constitute a waiver of Stryker's trademark or other intellectual property rights concerning that name or logo.

Copyright © 2019 Stryker

AP002547 v2.0 | Page 2 of 2

AXS Vecta™ Aspiration Catheter

RX ONLY

See package insert for complete indications, contraindications, warnings and instructions for use.

Intended use/indications for use

The AXS Vecta Aspiration System, including the AXS Vecta Aspiration Catheter, Aspiration Tubing Set, and VC-701 Clqi Aspirator Pump, is indicated in the revascularization of patients with acute ischemic stroke secondary to intracranial large vessel occlusive disease (within the internal carotid, middle cerebral – M1 and M2 segments, basilar, and vertebral arteries) within 8 hours of symptom onset. Patients who are ineligible for intravenous tissue plasminogen activator (IV t-PA) or who failed IV t-PA therapy are candidates for treatment.

Device description

The AXS Vecta Aspiration System consist of the AXS Vecta Aspiration Catheter, the Aspiration Tubing Set, and the VC-701 Clqi Aspirator Pump. The AXS Vecta Aspiration Catheter is a single lumen, flexible, variable stiffness catheter. It has a radiopaque marker band on the distal end and a Luer hub at the proximal end. The AXS Vecta Aspiration Catheter shaft has a lubricious hydrophilic coating at the distal end (distal 25 cm) to reduce friction during use. The Scout Introducer may be used in conjunction with the AXS Vecta Aspiration Catheter to facilitate in the introduction of the AXS Vecta Aspiration Catheter into distal vasculature and aid in navigation to distal anatomy. The Scout Introducer has a lubricious hydrophilic coating at the distal end to reduce friction during use. The inner lumen of the AXS Vecta Aspiration Catheters is compatible with the Scout Introducer, guide wires and micro catheters. The inner lumen of the Scout Introducer is compatible with guide wires and micro catheters of an outer diameter of less than 0.044in.

Each package includes one AXS Vecta Aspiration Catheter, one Scout Introducer, one hemostasis valve, and two peel-away introducers. Dimensions of the AXS Vecta Aspiration Catheter and Scout Introducer are included on the individual device label. The AXS Vecta Aspiration Catheters are available in 3 different lengths, the device configurations including the length of the Scout packaged with each catheter and the recommended Microcatheter length is presented in the table 1.0 below.

Catheter part number	INC-11129-115	INC-11129-125	INC-11129-132	INC-11597-115	INC-11597-125	INC-11597-132
Catheter inner diameter (in)	0.071	0.071	0.071	0.074	0.074	0.074
Distal catheter outer diameter (in)	0.082	0.082	0.082	0.083	0.083	0.083
Catheter working length (cm)	115	125	132	115	125	132
Scout Introducer length (cm)	133	143	150	133	143	150
Recommended compatible microcatheter length (cm)	150	160	160	150	160	160
Recommended compatible microcatheter outer diameter (in)	0.044 max					
Recommended compatible guidewire outer diameter (in)	0.038 max					

Stryker or its affiliated entities own, use, or have applied for the following trademarks or service marks: AXS Vecta, Stryker. Scout is a registered trademark of InNeuroCo, Inc. All other trademarks are trademarks of their respective owners or holders.

The absence of a product, feature, or service name, or logo from this list does not constitute a waiver of Stryker's trademark or other intellectual property rights concerning that name or logo.

Copyright © 2019 Stryker

AP002595 v1.0 | Page 2 of 2

- Mass effect
- Myocardial infarction
- Neurological deficit/intracranial sequelae
- Pseudoaneurysm
- Reaction to radiation exposure (i.e., alopecia, burns ranging in severity from skin reddening to ulcers, cataracts, and delayed neoplasia)
- Reactions to anti-platelet/anti-coagulant agents
- Renal failure
- Seizure
- Stent fracture, migration/embolization, or misplacement
- Stent thrombosis
- Stroke
- Transient ischemic attack
- Vasospasm
- Vessel occlusion or closure including parent vessel or non-target side-branches
- Vessel perforation/rupture, dissection, trauma or damage
- Vessel thrombosis
- Visual impairment
- Other procedural complications including but not limited to anesthetic and contrast media risks, hypotension, hypertension, access site complications (including pain, hematoma, local bleeding, local infection, and injury to the artery (i.e. dissection, vein, or adjacent nerves)
- Unplanned intervention

Warnings

Contents supplied STERILE using an ethylene oxide (EO) process. Do not use if sterile barrier is damaged. If damage is found, call your Stryker Neurovascular representative.

For single use only. Do not reuse, reprocess or resterilize. Reuse, reprocessing or resterilization may compromise the structural integrity of the device and/or lead to device failure which, in turn, may result in patient injury, illness or death. Reuse, reprocessing or resterilization may also create a risk of contamination of the device and/or cause patient infection or cross-infection, including, but not limited to, the transmission of infectious diseases) from one patient to another. Contamination of the device may lead to injury, illness or death of the patient.

- After use, dispose of product and packaging in accordance with hospital, administrative and/or local government policy.
- This device should only be used by physicians who have received appropriate training in interventional neuroradiology or interventional radiology and preclinical training on the use of this device as established by Stryker Neurovascular.
- Persons allergic to nickel titanium (Nitinol) may suffer an allergic response to this stent implant.
- Higher adverse event rates may be experienced for distal aneurysms located in the anterior and middle cerebral arteries.
- Do not use device to treat patients with ruptured intracranial aneurysms within a minimum of 30 days from the aneurysm rupture.

Cautions / precautions

- Take all necessary precautions to limit X-ray radiation doses to clinical operators by using sufficient shielding, reducing fluoroscopy times, and modifying X-ray technical factors whenever possible.
- The Neuroform Atlas stent may create local field inhomogeneity and susceptibility artifacts during magnetic resonance angiography (MRA), which may degrade the diagnostic quality to assess effective intracranial aneurysm occlusion.
- Safety and effectiveness of the Neuroform Atlas Stent System in patients below the age of 18 has not been established.
- The benefits may not outweigh the risks of device use in patients with small and medium asymptomatic extracranial intracranial aneurysms, including those located in the cavernous internal carotid artery.
- Carefully weigh the benefits vs. risks of device treatment for each individual patient based on their medical health status and risk factors for intracranial aneurysm rupture during their expected life time such as age, comorbidities, history of smoking, intracranial aneurysm size, location, and morphology, family history, history of prior asymptomatic subarachnoid hemorrhage (sAAH), documented growth of intracranial aneurysm on serial imaging, presence of multiple intracranial aneurysms, and presence of concurrent pathology. The benefits may not outweigh the risks associated with device use in certain patients; therefore, judicious patient selection is recommended based on clinical practice guidelines or tools to assess the life time risk of intracranial aneurysm rupture.

Safety Information Magnetic Resonance Conditional

Non-clinical testing and analysis have demonstrated that the Neuroform Atlas Stent is MR Conditional alone, or when overlapped with a second stent, and adjacent to a Stryker Neurovascular coil mass. A patient with the Neuroform Atlas Stent can be safely scanned immediately after placement of this implant, under the following conditions:

- Static magnetic field of 1.5 and 3.0 Tesla
- Maximum spatial gradient field up to 2500 Gauss/cm (25 Tesla/m)
- Maximum MR system reported whole body averaged specific absorption rate of 2 W/kg (Normal Operating Mode) and head averaged specific absorption rate of 3.2 W/kg.

Under the scan conditions defined above, the Neuroform Atlas Stent is expected to produce a maximum temperature rise of 4 °C after 15 minutes of continuous scanning. The Neuroform Atlas Stent should not migrate in this MRI environment.

In non-clinical testing, the image artifact caused by the device extends approximately 2 mm from the Neuroform Atlas Stent when imaged with a spin echo pulse sequence and 3 Tesla MRI system. The artifact may obscure the device lumen. It may be necessary to optimize MR imaging parameters for the presence of this implant. See additional precaution related to the image artifact from the implant in the "Precautions" section of this labeling.



Stryker Neurovascular

47900 Bayside Parkway

Fremont, CA 94538

strykerneurovascular.com

Date of Release: MAY/2019

EX_EN_US

The AXS Vecta Aspiration System is recommended for use in the following vessel size ranges based on non-clinical testing. Refer to Table 2.0 below.

AXS Vecta Aspiration Catheter	Catheter part number	Vessel size in mm (Vessel size in inches)
AXS Vecta 71	INC-11129-115	2.1-4mm (0.083in – 0.157in)
	INC-11129-125	2.1-4 mm (0.083in – 0.157in)
	INC-11129-132	2.1-4 mm (0.083in – 0.157in)
AXS Vecta 74	INC-11597-115	2.2-4 mm (0.087in – 0.157in)
	INC-11597-125	2.2-4 mm (0.087in – 0.157in)
	INC-11597-132	2.2-4 mm (0.087in – 0.157in)

Contraindications

The AXS Vecta Aspiration Catheter has not been evaluated for use in the coronary vasculature. Do not use automated high-pressure contrast injection equipment with the AXS Vecta Aspiration Catheter because it may damage the device.

Adverse events

- Acute vessel occlusion
- Air embolism
- Allergic reaction and anaphylaxis from contrast media
- Arteriovenous fistula
- Death
- Device malfunction
- Distal embolization
- Emboli
- False aneurysm formation
- Hematoma or hemorrhage at the puncture site
- Inability to completely remove thrombus
- Infection
- Intracranial hemorrhage
- Ischemia
- Kidney damage from contrast media
- Neurological deficit including stroke
- Risks associated with angiographic and fluoroscopic radiation including but not limited to: alopecia, burns ranging in severity from skin reddening to ulcers, cataracts, and delayed neoplasia
- Sterile inflammation or granulomas at the access site
- Tissue necrosis
- Vessel spasm, thrombosis, dissection or perforation

Warning

Contents supplied STERILE using an ethylene oxide (EO) process. Do not use if sterile barrier is damaged. If damage is found, call your Stryker Neurovascular representative. For single use only. Do not reuse, reprocess or resterilize. Reuse, reprocessing or resterilization may compromise the structural integrity of the device and/or lead to device failure which, in turn, may result in patient injury, illness or death. Reuse, reprocessing or resterilization may also create a risk of contamination of the device and/or cause patient infection or cross-infection, including, but not limited to, the transmission of infectious diseases) from one patient to another. Contamination of the device may lead to injury, illness or death of the patient. After use, dispose of product and packaging in accordance with hospital, administrative and/or local government policy.

Warnings

- The AXS Vecta Aspiration Catheter has not been evaluated for more than one (1) clot retrieval attempt.
- The AXS Vecta Aspiration Catheter was evaluated for an average duration of direct aspiration of 4 minutes.
- This product is intended for single use only, do not re-sterilize or reuse. Re-sterilization and/or reuse may result in cross contamination and/or reduced performance.
- When the catheter is exposed to the vascular system, it should be manipulated while under high-quality fluoroscopic observation. Do not advance or retract the catheter if resistance is met during manipulation; determine the cause of the resistance before proceeding.
- Operators should take all necessary precautions to limit X-Radiation doses to patients and themselves by using sufficient shielding, reducing fluoroscopy times, and modifying X-Ray technical factors where possible.
- This device is coated with a hydrophilic coating at the proximal end of the device for a length of 25 cm. Please refer to the Device Preparation Section for further information on how to prepare and use this device to ensure it performs as intended. Failure to abide by the warnings in this labeling might result in damage to the device coating, which may necessitate intervention or result in serious adverse events.

Precautions

- Store in a cool, dry, dark place.
- Do not use kinked, damaged, or opened devices.
- Use the device prior to the "Use By" date specified on the package.
- Exposure to temperatures above 54°C (130°F) may damage device. Do not autoclave.
- Torqueing or moving the device against resistance may result in damage to the vessel or device.
- Maintain a constant infusion of appropriate flush solution.
- If flow through the device becomes restricted, do not attempt to clear the lumen by infusion. Remove and replace the device.
- Examine the device to verify functionality and to ensure that its size and shape are suitable for the specific procedure for which it is to be used.
- The AXS Vecta Aspiration Catheter should be used only by physicians trained in percutaneous procedures and/or interventional techniques.
- The Scout Introducer should be used with a guidewire and microcatheter inserted when in vasculature.
- If using the AXS Vecta Aspiration Catheter for thrombectomy, monitor the canister fluid level and replace the canister if the fill level reaches 75% of the canister volume.
- Administration of anticoagulants and antiplatelets should be suspended until 24 hours post-treatment. Medical management and acute post stroke care should follow the ASA guidelines.
- Any neurological determination should be evaluated by urgent CT scan and other evaluations as indicated according to investigator/hospital best practice.
- As in all surgical interventions, monitoring of intra-procedural blood loss is recommended so that appropriate management may be instituted.
- Limit the usage of the AXS Vecta Aspiration Catheter to arteries greater than the catheter's outer diameter.
- Excessive aspiration with the distal tip of the AXS Vecta Aspiration Catheter covered by the vessel wall may cause vessel injury. Carefully investigate location of the distal tip under fluoroscopy prior to aspiration.
- There is an inherent risk with the use of angiography and fluoroscopy.
- When transporting the VC-701 Clqi Pump, utilize the pump handle.



Stryker Neurovascular

47900 Bayside Parkway

Fremont, CA 94538

strykerneurovascular.com

Date of Release: MAY/2019

EX_EN_US

Ingest more.



Empowering first pass retrieval
with AXS Vecta 71 Aspiration
Catheter **now powered by** the
Dual Action Aspiration of Medela
Dominant Flex.

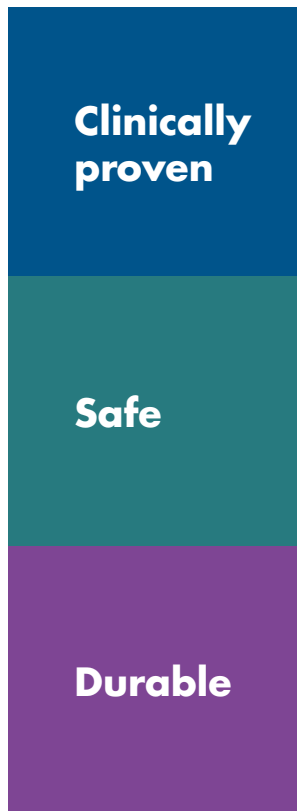
AXS Vecta™ 71 Aspiration Catheter

Testing completed by Stryker. Data on file at Stryker.

The AXS Vecta 71 Aspiration Catheter has a larger lumen compared to the AXS Catalyst 6 Distal Access Catheter, which is cleared for use with the Dominant Flex, sold as the AXS Universal Aspiration System. A larger lumen provides more aspiration power and more room for clot ingestion.

The results say it all

Now **PMA** approved



84.7%

Primary efficacy endpoint

4.4%

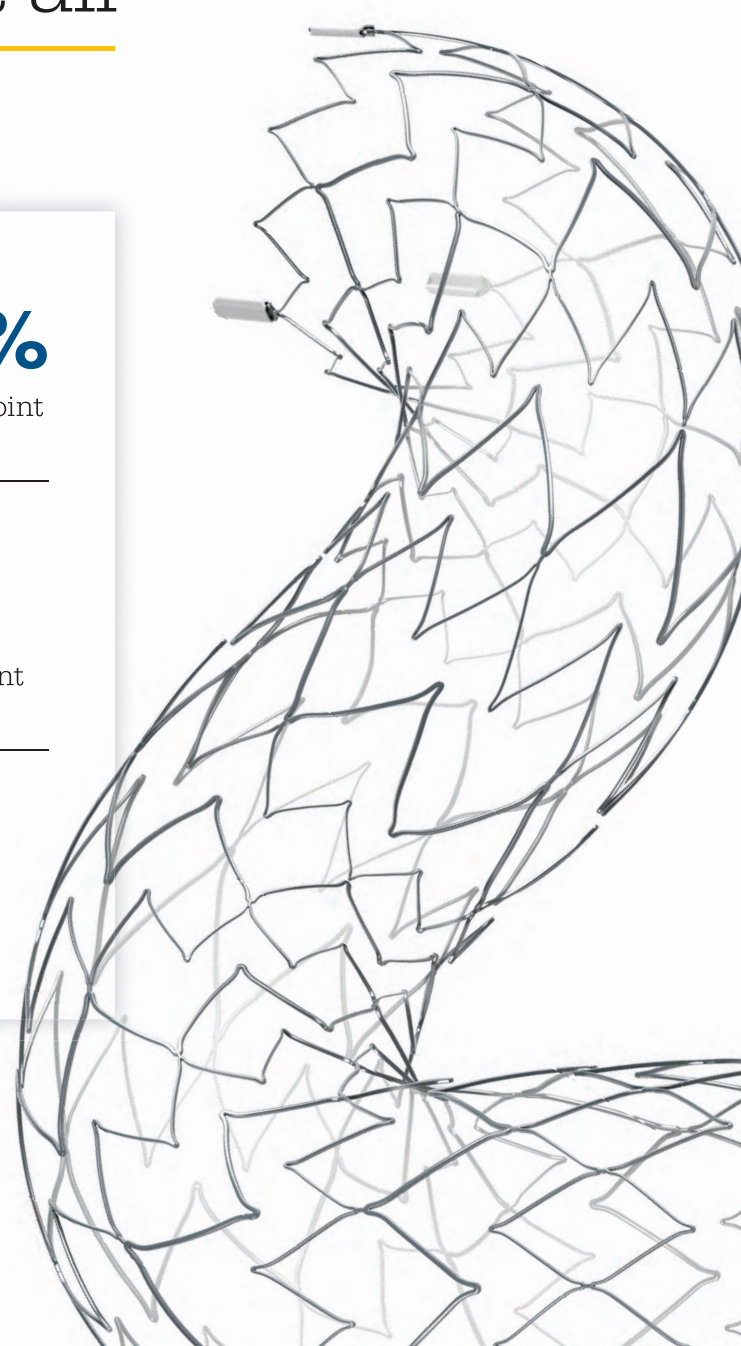
Primary safety endpoint

3.8%

Retreatment rate

The ATLAS IDE Study is the largest of its class with **182 patients treated.**

Neuroform Atlas[®]
Stent System



AJNR

AMERICAN JOURNAL OF NEURORADIOLOGY

JULY 2019
VOLUME 40
NUMBER 7
WWW.AJNR.ORG

Publication Preview at www.ajnr.org features articles released in advance of print. Visit www.ajnrblog.org to comment on AJNR content and chat with colleagues and AJNR's News Digest at <http://ajnrdigest.org> to read the stories behind the latest research in neuroimaging.

1083 **PERSPECTIVES** *E.C. Kavanagh*

REVIEW ARTICLE

 1084 **A Practical Review of Functional MRI Anatomy of the Language and Motor Systems** *V.B. Hill, et al.* **FUNCTIONAL**

PRACTICE PERSPECTIVES

1091 **Assessment of Explicitly Stated Interval Change on Noncontrast Head CT Radiology Reports** *M. Braileanu, et al.*

GENERAL CONTENTS

    1095 **3T MRI Whole-Brain Microscopy Discrimination of Subcortical Anatomy, Part 2: Basal Forebrain** *M.J. Hoch, et al.* **ADULT BRAIN**

1106 **Wall Contrast Enhancement of Thrombosed Intracranial Aneurysms at 7T MRI** *T. Sato, et al.* **ADULT BRAIN**

1112 **Gadolinium Enhancement of the Aneurysm Wall in Unruptured Intracranial Aneurysms Is Associated with an Increased Risk of Aneurysm Instability: A Follow-Up Study** *M.D.I. Vergouwen, et al.* **ADULT BRAIN**

   1117 **Assessing Postconcussive Reaction Time Using Transport-Based Morphometry of Diffusion Tensor Images** *S. Kundu, et al.* **ADULT BRAIN**
FUNCTIONAL

 1124 **Association of Fractional Flow on 3D-TOF-MRA with Cerebral Perfusion in Patients with MCA Stenosis** *X. Ge, et al.* **ADULT BRAIN**
FUNCTIONAL

 1132 **Quantitative Delta T1 (dT1) as a Replacement for Adjudicated Central Reader Analysis of Contrast-Enhancing Tumor Burden: A Subanalysis of the American College of Radiology Imaging Network 6677/Radiation Therapy Oncology Group 0625 Multicenter Brain Tumor Trial** *K.M. Schmainda, et al.* **ADULT BRAIN**

   1140 **Brain Tumor-Enhancement Visualization and Morphometric Assessment: A Comparison of MPRAGE, SPACE, and VIBE MRI Techniques** *L. Danieli, et al.* **ADULT BRAIN**

 1149 **Extent of Surgical Resection in Lower-Grade Gliomas: Differential Impact Based on Molecular Subtype** *S.H. Patel, et al.* **ADULT BRAIN**

  1156 **Normal-Appearing Cerebellar Damage in Neuromyelitis Optica Spectrum Disorder** *J. Sun, et al.* **ADULT BRAIN**

AJNR (Am J Neuroradiol ISSN 0195–6108) is a journal published monthly, owned and published by the American Society of Neuroradiology (ASNR), 800 Enterprise Drive, Suite 205, Oak Brook, IL 60523. Annual dues for the ASNR include \$170.00 for journal subscription. The journal is printed by Cadmus Journal Services, 5457 Twin Knolls Road, Suite 200, Columbia, MD 21045; Periodicals postage paid at Oak Brook, IL and additional mailing offices. Printed in the U.S.A. POSTMASTER: Please send address changes to American Journal of Neuroradiology, P.O. Box 3000, Denville, NJ 07834, U.S.A. Subscription rates: nonmember \$410 (\$480 foreign) print and online, \$320 online only; institutions \$470 (\$540 foreign) print and basic online, \$935 (\$1000 foreign) print and extended online, \$380 online only (basic), extended online \$825; single copies are \$35 each (\$40 foreign). Indexed by PubMed/Medline, BIOSIS Previews, Current Contents (Clinical Medicine and Life Sciences), EMBASE, Google Scholar, HighWire Press, Q-Sensei, RefSeek, Science Citation Index, SCI Expanded, Meta/CZI and ReadCube. Copyright © American Society of Neuroradiology.



1162 Comparison of Multiple Sclerosis Cortical Lesion Types Detected by Multicontrast 3T and 7T MRI *J. Maranzano, et al.*

ADULT BRAIN



1170 Improving Detection of Multiple Sclerosis Lesions in the Posterior Fossa Using an Optimized 3D-FLAIR Sequence at 3T *A. Lecler, et al.*

ADULT BRAIN

1177 Impact of Skull Defects on the Role of CTA for Brain Death Confirmation *D.M. Nunes, et al.*

ADULT BRAIN



1184 Diagnosis and Prediction of Relapses in Susac Syndrome: A New Use for MR Postcontrast FLAIR Leptomeningeal Enhancement *S. Coulette, et al.*

ADULT BRAIN



1191 Long-Term Results and Follow-Up Examinations after Endovascular Embolization for Unruptured Cerebral Aneurysms *T. Murakami, et al.*

INTERVENTIONAL



1197 Flow-Pattern Details in an Aneurysm Model Using High-Speed 1000-Frames-per-Second Angiography *J.M. Krebs, et al.*

INTERVENTIONAL



1201 Antiplatelet Therapy in Patients with Aneurysmal SAH: Impact on Delayed Cerebral Ischemia and Clinical Outcome. A Meta-Analysis *F. Cagnazzo, et al.*

INTERVENTIONAL

1207 Comparison of Carotid Endarterectomy and Stenting for Symptomatic Internal Carotid Artery Near-Occlusion *J. Kim, et al.*

EXTRACRANIAL VASCULAR INTERVENTIONAL



1213 Functional Connectivity Associated with Health-Related Quality of Life in Children with Focal Epilepsy *H. Nawani, et al.*

PEDIATRICS FUNCTIONAL

1221 Quantitative Analysis of Punctate White Matter Lesions in Neonates Using Quantitative Susceptibility Mapping and R2* Relaxation *Y. Zhang, et al.*

PEDIATRICS FUNCTIONAL



1227 Predictive Value of MRI in Diagnosing Brain AVM Recurrence after Angiographically Documented Exclusion in Children *A. Jhaveri, et al.*

PEDIATRICS

1236 Quantification of DTI in the Pediatric Spinal Cord: Application to Clinical Evaluation in a Healthy Patient Population *B.B. Reynolds, et al.*

SPINE PEDIATRICS

1242 Subject-Specific Studies of CSF Bulk Flow Patterns in the Spinal Canal: Implications for the Dispersion of Solute Particles in Intrathecal Drug Delivery *W. Coenen, et al.*

SPINE FUNCTIONAL

1250 35 YEARS AGO IN AJNR

ONLINE FEATURES

LETTERS

E34 Polymer Embolism from Bioactive and Hydrogel Coil Embolization Technology: Considerations for Product Development *A.M. Chopra, et al.*

E36 Optic Nerve Evaluation in Idiopathic Intracranial Hypertension *M. De Bernardo, et al.*

E37 Reply *T.A. Kennedy*

E38 Automated Segmentation of Hippocampal Volume: The Next Step in Neuroradiologic Diagnosis of Mesial Temporal Sclerosis *N. Damodaran, et al.*

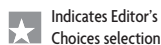
E39 ERRATUM

BOOK REVIEWS *R.M. Quencer, Section Editor*

Please visit www.ajnrblog.org to read and comment on Book Reviews.



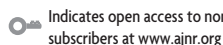
Difference among the MPRAGE (A), SPACE (B), and VIBE (C) conspicuities at the level of the faintly enhancing inferolateral border of the lesion (arrows), which is better represented on the SPACE and VIBE images, compared with MPRAGE. This component of the tumor is not included in the MPRAGE lesion segmentation (D); however, it is captured completely on SPACE (E) and partially on VIBE (F) images. The tractographic reconstruction of the optic radiation trajectory (G) demonstrates the close proximity of the tumor to this tract.



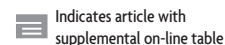
Indicates article with supplemental on-line photo



Indicates article with supplemental on-line video



Evidence-Based Medicine Level 1



Evidence-Based Medicine Level 2

Official Journal:

American Society of Neuroradiology
American Society of Functional Neuroradiology
American Society of Head and Neck Radiology
American Society of Pediatric Neuroradiology
American Society of Spine Radiology

EDITOR-IN-CHIEF

Jeffrey S. Ross, MD

Professor of Radiology, Department of Radiology,
Mayo Clinic College of Medicine, Phoenix, AZ

SENIOR EDITORS

Harry J. Cloft, MD, PhD

Professor of Radiology and Neurosurgery,
Department of Radiology, Mayo Clinic College of
Medicine, Rochester, MN

Thierry A.G.M. Huisman, MD

Radiologist-in-Chief, Texas Children's Hospital,
Houston, TX

Yvonne W. Lui, MD

Associate Professor of Radiology,
Chief of Neuroradiology,
New York University School of Medicine,
New York, NY

C.D. Phillips, MD, FACR

Professor of Radiology, Weill Cornell Medical
College, Director of Head and Neck Imaging,
New York-Presbyterian Hospital, New York, NY

Lubdhra M. Shah, MD

Associate Professor of Radiology and Director of
Spine Imaging, University of Utah Department of
Radiology and Imaging Sciences, Salt Lake City, UT

Charles M. Strother, MD

Professor of Radiology, Emeritus, University of
Wisconsin, Madison, WI

STATISTICAL SENIOR EDITOR

Bryan A. Comstock, MS

Senior Biostatistician,
Department of Biostatistics,
University of Washington, Seattle, WA

ARTIFICIAL INTELLIGENCE DEPUTY EDITOR

Christopher G. Filippi, MD

Professor and Vice Chair of Biomedical and
Translational Science,
Donald and Barbara Zucker School of Medicine at
Hofstra/Northwell,
Lenox Hill Hospital and Greenwich Village
Healthplex, New York, NY

EDITORIAL BOARD

Ashley H. Aiken, Atlanta, GA
Lea M. Alhilali, Phoenix, AZ
Kubilay Aydin, Istanbul, Turkey
John D. Barr, Dallas, TX
Ari Blitz, Baltimore, MD
Barton F. Branstetter IV, Pittsburgh, PA
Jonathan L. Brisman, Lake Success, NY
Keith Cauley, Danville, PA
James Y. Chen, San Diego, CA
Asim F. Choudhri, Memphis, TN
Daniel Chow, Irvine, CA
J. Matthew Debnam, Houston, TX
Seena Dehkharghani, New York, NY
Yonghong Ding, Rochester, MN
Clifford J. Eskey, Hanover, NH
Saeed Fakhran, Phoenix, AZ
Massimo Filippi, Milan, Italy
Reza Forghani, Montreal, Quebec, Canada
Nils D. Forkert, Calgary, Alberta, Canada
Wende N. Gibbs, Phoenix, AZ
Christine M. Glastonbury, San Francisco, CA
John L. Go, Los Angeles, CA
Philipp Göllitz, Erlangen, Germany
Allison Grayev, Madison, WI
Brent Griffith, Detroit, MI
Ajay Gupta, New York, NY
Rakesh Kumar Gupta, Haryana, India
Lotfi Hacein-Bey, Sacramento, CA
Christopher P. Hess, San Francisco, CA
Andrei Holodny, New York, NY
Benjamin Huang, Chapel Hill, NC
Mahesh V. Jayaraman, Providence, RI
Valerie Jewells, Chapel Hill, NC
Christof Karmonik, Houston, TX
Timothy J. Kaufmann, Rochester, MN
Hillary R. Kelly, Boston, MA
Toshibumi Kinoshita, Akita, Japan
Kenneth F. Layton, Dallas, TX
Alexander Lerner, Los Angeles, CA
Michael Lev, Boston, MA
Karl-Olof Lovblad, Geneva, Switzerland
Franklin A. Marden, Chicago, IL
Joseph C. McGowan, Merion Station, PA
Stephan Meckel, Freiburg, Germany
Christopher J. Moran, St. Louis, MO
Takahisa Mori, Kamakura City, Japan
Suresh Mukherji, Ann Arbor, MI
Alexander J. Nemeth, Chicago, IL
Renato Hoffmann Nunes, Sao Paulo, Brazil
Sasan Partovi, Cleveland, OH
Laurent Pierot, Reims, France
Jay J. Pillai, Baltimore, MD
Whitney B. Pope, Los Angeles, CA
Joana Ramalho, Lisbon, Portugal
Otto Rapalino, Boston, MA

Álex Rovira-Cañellas, Barcelona, Spain
Paul M. Ruggieri, Cleveland, OH
Amit M. Saindane, Atlanta, GA
Maksim Shapiro, New York, NY
Timothy Shepherd, New York, NY
Mark S. Shiroishi, Los Angeles, CA
Bruno P. Soares, Baltimore, MD
Maria Vittoria Spampinato, Charleston, SC
Khin Khin Tha, Sapporo, Hokkaido, Japan
Krishnamoorthy Thamburaj, Hershey, PA
Cheng Hong Toh, Taipei, Taiwan
Aquila S. Turk, Greenville, SC
Anja G. van der Kolk, Utrecht, the Netherlands
Willem Jan van Rooij, Tilburg, Netherlands
Arastoo Vossough, Philadelphia, PA
Elysa Widjaja, Toronto, Ontario, Canada
Max Wintermark, Stanford, CA
Ronald L. Wolf, Philadelphia, PA
Kei Yamada, Kyoto, Japan
Carlos Zamora, Chapel Hill, NC
Vahe M. Zohrabian, New Haven, CT

EDITORIAL FELLOW

Hediyeh Baradaran, Salt Lake City, UT

SPECIAL CONSULTANTS TO THE EDITOR

AJNR Blog Editor

Neil Lall, Denver, CO

Case of the Month Editor

Nicholas Stence, Aurora, CO

Case of the Week Editors

Juan Pablo Cruz, Santiago, Chile
Sapna Rawal, Toronto, Ontario, Canada

Classic Case Editor

Sandy Cheng-Yu Chen, Taipei, Taiwan

Health Care and Socioeconomics Editor

Pina C. Sanelli, New York, NY

Physics Editor

Greg Zaharchuk, Stanford, CA

Podcast Editor

Wende N. Gibbs, Phoenix, AZ

Twitter Editor

Jennifer McCarty, Houston, TX

Founding Editor
Juan M. Taveras

Editors Emeriti
Mauricio Castillo, Robert I. Grossman,
Michael S. Huckman, Robert M. Quencer

Managing Editor
Karen Halm

Assistant Managing Editor
Laura Wilhelm

Communications Coordinator
Rebecca Artz

Executive Director, ASNR
Mary Beth Hepp



Title: Pollen Explosion. This picture was taken while visiting Chamonix Mont-Blanc in May 2018. It shows a “pollen explosion,” a rare natural phenomenon but a nightmare for hay fever sufferers! The photo was taken on a Huawei P20 Smartphone.

Eoin C. Kavanagh, Clinical Professor, University College Dublin; Consultant Radiologist, Mater Misericordiae University Hospital, Cappagh National Orthopaedic Hospital, Dublin, Ireland

A Practical Review of Functional MRI Anatomy of the Language and Motor Systems

 V.B. Hill,  C.Z. Cankurtaran,  B.P. Liu,  T.A. Hijaz,  M. Naidich,  A.J. Nemeth,  J. Gastala,  C. Krumpelmann,  E.N. McComb, and  A.W. Korutz



ABSTRACT

SUMMARY: Functional MR imaging is being performed with increasing frequency in the typical neuroradiology practice; however, many readers of these studies have only a limited knowledge of the functional anatomy of the brain. This text will delineate the locations, anatomic boundaries, and functions of the cortical regions of the brain most commonly encountered in clinical practice—specifically, the regions involved in movement and language.

ABBREVIATIONS: FFA = fusiform face area; IPL = inferior parietal lobule; PPC = posterior parietal cortex; SMA = supplementary motor area; VOTC = ventral occipitotemporal cortex

This article serves as a review of the functional areas of the brain most commonly mapped during presurgical fMRI studies, specifically targeting movement and language. We have compiled what we hope is a useful, easily portable, and concise resource that can be accessible to radiologists everywhere. We begin with a review of the language-processing system. Then we describe the gross anatomic boundaries, organization, and function of each anatomic region.

Dorsal and Ventral Streams in Language and Visual Processing

Two anatomically and functionally differentiated parallel processing streams serve as a theoretic model for higher order cognitive processes: the ventral and dorsal streams. These concepts of ventral and dorsal streams as well as their functional and anatomic connectivity are introduced here and will be referenced later in this article. The dual-stream model was first conceptualized for vision by Ungerleider and Mishkin in their seminal work,¹ hypothesizing that dual and distinct computational streams for vision proceeded in parallel, with the dorsal stream

servicing to analyze spatial position and the ventral stream working to identify what an object is. Influenced by the dorsal and ventral stream model of vision, Hickok and Poeppel² hypothesized a similar framework for language. In this model, the ventral stream, or lexical-semantic system, is involved in sound-to-meaning mappings associated with language comprehension and semantic access. A prototype task of the ventral stream is listening to and deriving meaning from speech.³ The dorsal stream, or phonological system, is involved in sound-to-motor mappings associated with producing and articulating language.^{2,3} Hence, a prototype task of the dorsal stream is repeating speech.³

The dorsal stream of language originates in the peri-Sylvian region within the superior temporal gyrus and superior temporal sulcus and travels through the supramarginal gyrus to the frontal lobe, including the premotor cortex and inferior frontal gyrus. The major fiber tract of the dorsal stream is the superior longitudinal fasciculus/arcuate fasciculus, connecting the classic posterior temporal receptive language area (Wernicke area) with the frontal expressive language area (Broca area), as well as additional extensions to the inferior premotor cortex within the frontal lobe (Fig 1).⁴⁻⁶ The model of the Broca and Wernicke language areas devoted to the production and understanding of speech, respectively, has become richer across the years so that now receptive and expressive language understanding is more complex, with dependence of both on larger areas of the network and with substantial individual variation.⁷ Studies have suggested that the superior longitudinal fasciculus/arcuate fasciculus can be separated into 4 subcomponents (superior longitudinal fasciculus I–III) with the arcuate fasciculus composing the fourth subcomponent.^{8,9} Specifically, the superior longitudinal fasciculus III and arcuate fasciculus play a major role in the dorsal language stream.⁶

Received November 26, 2018; accepted after revision April 24, 2019.

From the Departments of Radiology (V.B.H., C.Z.C., B.P.L., T.A.H., M.N., A.J.N., J.G., C.K., E.N.M., A.W.K.), Neurology (A.J.N.), and Radiation Oncology (B.P.L.), Northwestern University Feinberg School of Medicine, Chicago, Illinois.

B.P.L. is supported by P50CA221747 SPORE for Translational Approaches to Brain Cancer. A.J.N. is supported by RO1HL092259, SP0039078: Cerebral Autoregulation Monitoring to Reduce Brain Injury from Cardiac Surgery.

Please address correspondence to Virginia B. Hill, MD, Neuroradiology, Northwestern University Feinberg School of Medicine, Suite 1400, 676 N. St. Clair St, Chicago, IL 60611; e-mail virginiahill2@mac.com or virginia.hill@nm.org; @virginiahill

 Indicates open access to non-subscribers at www.ajnr.org

<http://dx.doi.org/10.3174/ajnr.A6089>

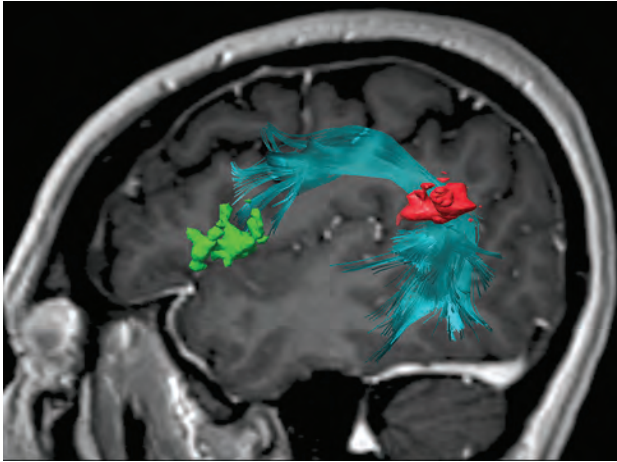


FIG 1. Sagittal 3D-FLAIR image with a superimposed diffusion tensor image of the arcuate fasciculus between the inferior parietal lobule (pars opercularis and pars triangularis) (green) and the angular gyrus (red). The frontotemporal segment of the arcuate fasciculus connects the Broca area at the inferior frontal gyrus with the Wernicke area more posteriorly, traditionally at the posterior superior temporal gyrus. However, this connection is variable, and in this case, it is at the angular gyrus/posterior superior temporal area.

The ventral stream of language involves the middle and inferior temporal gyri, anterior temporal lobe, and ventrolateral prefrontal cortex.¹⁰ The major tract of the ventral stream is the inferior occipitofrontal fasciculus, with additional contributions by the uncinate fasciculus, extreme capsule, middle longitudinal fasciculus, and inferior longitudinal fasciculus.^{5,6,10,11} While the dorsal stream is left-lateralized, the ventral stream is bilateral.^{3,12} Evidence suggests that while there are some tasks that segregate the ventral and dorsal streams, successful execution requires complex collaboration and seamless integration of processing between the 2 systems.¹³

Primary Motor and Primary Sensory Cortices

General Anatomic Borders. The primary motor and sensory cortices occupy the pre- and postcentral gyri, respectively (Fig 2A). The precentral gyrus, bounded anteriorly by the precentral sulcus and posteriorly by the central sulcus, extends inferiorly toward the lateral sulcus and becomes contiguous with the inferior aspect of the postcentral gyrus. The superior aspect of the gyrus extends onto the medial surface of the cerebral hemisphere and merges with the anterior paracentral lobule. The postcentral gyrus, bounded anteriorly by the central sulcus and posteriorly by the postcentral sulcus, extends inferiorly and joins the precentral gyrus just above the lateral sulcus. Superiorly, the gyrus passes over the midline of the hemisphere and terminates in the posterior paracentral lobule.¹⁴

Anatomic Organization. The primary motor cortex does not encompass the entire precentral gyrus but rather tapers inferiorly along the posterior margin of the gyrus. The nonmotor cortex occupies the remainder of the gyrus.¹⁵⁻¹⁷

The motor and sensory cortices have a well-defined somatotopic organization. In other words, each part of the body can be reliably and predictably mapped to a specific region of the contralateral cortex. Specifically, the cells of the motor and sensory

cortices responsible for the lips and face occupy the inferior segments, followed superiorly by the regions for the fingers and hands and a small region for the trunk. The final component, corresponding to the leg and foot, bridges the superior aspect of the gyrus and extends onto the medial surface of the hemisphere. The amount of cortex devoted to any anatomic region is proportional to the degree of precision or discrimination necessary for optimal function of that body part. The resultant distorted homunculus emphasizes the face and lips and the fingers and hands.^{18,19}

Function.

Primary Motor Cortex. The primary motor cortex initiates voluntary movement through the corticospinal tract (Fig 2B), which also receives contributions from the premotor cortex, supplementary cortex, and somatosensory cortex.¹⁷ A large percentage of the corticospinal tract fibers cross in the pyramidal decussation and connect to motor neurons in the contralateral spinal cord to trigger movement. The motor cortex also connects with the cerebellum and brain stem.¹⁹ Through this network, subcortical regions and other cortical areas influence the input and output of the primary motor cortex.²⁰

A lesion in the primary motor cortex, such as an acute infarct, classically results in motor weakness (Fig 3).

Primary Somatosensory Cortex. The primary somatosensory cortex processes tactile and proprioceptive information, receiving fine-touch and proprioception input from the dorsal column-medial lemniscus pathway and information regarding pain, temperature, and touch from the lateral and ventral spinothalamic tracts.^{17,19} Similar to its motor counterpart, the somatosensory cortex also receives input from other cortical regions, and subcortical areas modify the output from this region.²¹

Supplementary Motor Area

The supplementary motor area (SMA) and the pre-SMA are discussed separately in this article, with the acknowledgment that their functions are nuanced, their borders are indistinct and functionally variable, and the 2 likely represent a continuum rather than discrete anatomic areas.²²

General Anatomic Borders. The SMA occupies the dorsomedial aspect of the superior frontal gyrus, immediately anterior to the foot motor representation, and is bounded medially by the interhemispheric falx and laterally by the premotor cortex (Fig 2A).²³ The cingulate sulcus is inferior to the SMA. The anterior margin of the SMA is defined by a perpendicular line through the corpus callosum rostrum. The V line, a vertical line through the posterior aspect of the anterior commissure, differentiates the rostral from the caudal SMA.²⁴

Anatomic Organization. The SMA demonstrates somatotopic organization. From anterior to posterior, the SMA represents the head, trunk, upper extremity, and lower extremity, with some studies showing more detailed somatotopy of the face, neck, and proximal/distal upper and lower extremities.²³ While the SMA demonstrates greater activation with tasks performed using the contralateral side of the body, humans do have a dominant SMA that can show bilateral activation.²³ Word generation and working memory tasks activate the rostral SMA predominantly on the left side; complex motor and sensory tasks activate the contralateral caudal SMA.²⁴

Function. The SMA receives input from the motor, premotor, and sensory cortices and provides a wide array of outputs, including those to the primary motor cortex, basal ganglia, thalamus,

subthalamic nucleus, brain stem, contralateral SMA, and cervical motor neurons (primarily contralaterally).^{22,23} Projections from the SMA join those from the premotor cortex and compose approximately one-third of the corticospinal tract.²⁵ The SMA is involved in the planning, coordination, and initiation of movement, particularly complex hand motions and action sequences that involve both sides of the body.²²⁻²⁴ Learning new motion sequences activates the rostral SMA, but the performance of those sequences activates the caudal SMA. The SMA is also involved in posture, selection of the laterality of a movement, speech (such as word generation and comprehension of the spoken word), working memory, and pain sensation (Fig 4).^{23,24}

Lesions of the dominant SMA such as tumors or anterior cerebral artery infarctions result in abulia, gait apraxia, and transient weakness.²² Resection of the nondominant SMA also can inhibit speech (Fig 5). “SMA Syndrome” results from unilateral resection of the SMA and is characterized by contralateral akinesia and mutism, but preservation of extremity muscle strength.²⁶ Lesions can also result in “alien limb” syndrome in which spontaneous movements of the limb, such as grasping, are uncontrollable by the patient, often countering the patient’s attempted goal-directed motion.²² Left middle cerebral artery infarct causing aphasia can prompt compensation by and reorganization of speech function to the SMA.²⁴

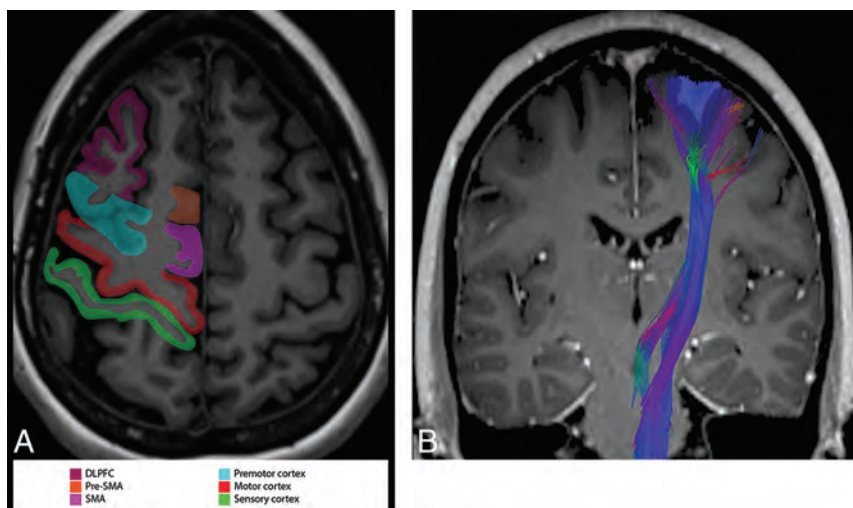


FIG 2. A, Axial MPRAGE image through the sensorimotor cortex with functional areas labeled in the right cerebral hemisphere. B, Coronal contrast-enhanced MPRAGE image with superimposed diffusion tensor imaging view of the corticospinal tract. DLPCF, dorsolateral prefrontal cortex; SMA, supplementary motor area.

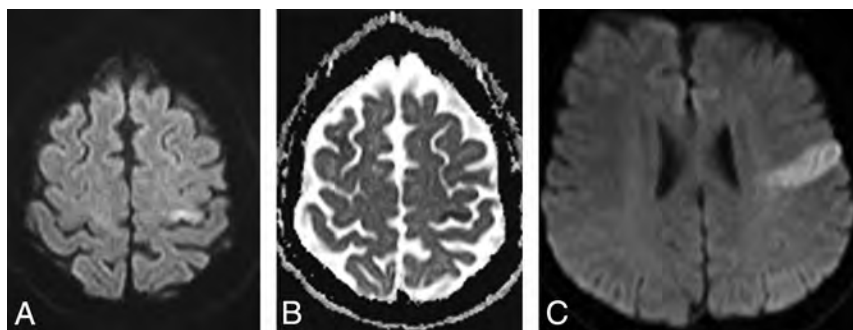


FIG 3. DWI (A) and ADC map (B) demonstrate a left hand/arm motor infarct in a patient with sudden onset of right-arm weakness. C, DWI demonstrates a left facial motor infarct in a patient with facial weakness.

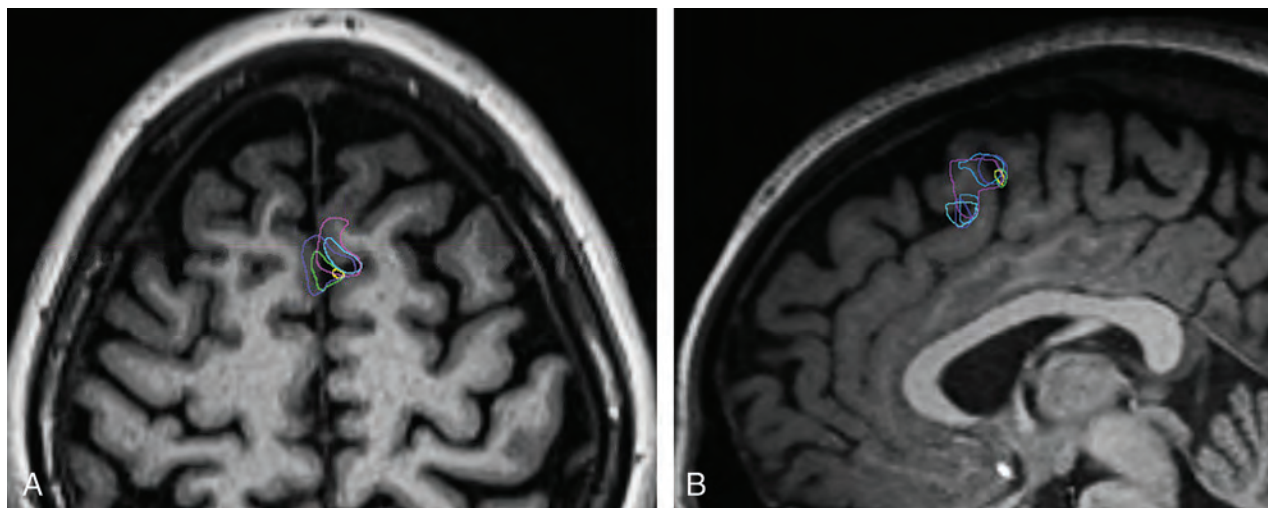


FIG 4. Functional MR imaging blood oxygen level–dependent activation of the SMA superimposed on axial (A) and sagittal (B) MPRAGE images. Dark blue designates activation during antonym generation; turquoise, during picture naming; purple, during rhyming; light blue, during silent word generation; yellow, during finger movement; and green, during lip movement.

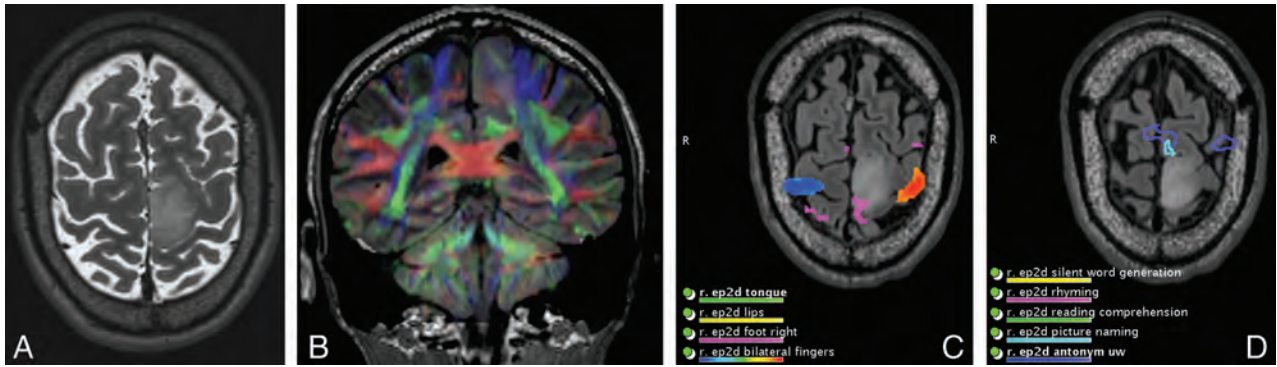


FIG 5. A patient with a left precentral gyrus/paracentral lobule and an SMA mass who initially presented with seizure. A, Axial T2-weighted MR imaging shows a left SMA mass. The patient underwent subtotal resection complicated by transient postoperative right hemiparesis (SMA syndrome). Pathology showed a diffuse infiltrating astrocytoma, *isocitrate dehydrogenase*-mutant, World Health Organization grade II. DTI superimposed on coronal FLAIR (B) and axial functional MR imaging show right foot (C) and language (D) SMA activation at the margins of the mass.

Presupplementary Motor Area

General Anatomic Borders. The pre-SMA is located anterior to the SMA within the dorsal aspect of the superior frontal gyrus (Fig 2A). Similar to the SMA, the pre-SMA is bounded medially by the interhemispheric falx and laterally by the premotor cortex. The ventral (inferior) boundary of the pre-SMA is the anterior cingulate motor area.^{23,24}

Anatomic Organization. Somatotopy of the pre-SMA is similar to that of the SMA, albeit cruder, with the head, upper extremity, and lower extremity represented from anterior to posterior.²³

Function. The pre-SMA is activated when learning new sequential movements²⁴ and when incorporating visual input into planning internally generated tasks.²³ In addition, the predominantly left-sided pre-SMA is activated when performing word-generation and working-memory tasks.²⁴

Premotor Region Proper

General Anatomic Borders. The premotor area comprises the dorsal superior frontal gyrus, dorsal middle frontal gyrus, and the anterior bank of the precentral gyrus, ventral to the primary motor area (Fig 2A).²³

Anatomic Organization. Somatotopic organization of the premotor area is similar to but cruder than that of the primary motor cortex, with medial-to-lateral representations for the leg, trunk, arm, face, and mouth.²⁵

Function. The premotor area integrates auditory, visual, and somatosensory stimuli in the selection of movement, initiation of movement, and performance of movement-related tasks. The premotor area attends to externally guided movement, in contradistinction to the SMA and pre-SMA, which are involved in self-initiated movements. Similar to the SMA, the premotor region also helps determine the laterality of motion.²³

The premotor cortex contains “mirror neurons,” as does the posterior parietal cortex (PPC). These neurons are active when a person performs or watches another perform a series of movements; this observation allows us to tap into our own advanced motor circuits to understand the actions of others.

Posterior Parietal Cortex

General Anatomic Borders. The PPC is caudal and posterior to the primary somatosensory cortex and postcentral sulcus. The PPC comprises the superior parietal lobule and the inferior parietal lobule (IPL), which are separated by the intraparietal sulcus. The medial portion of the superior parietal lobule is the precuneus, located on the medial surface of each cerebral hemisphere in front of the parietal-occipital sulcus and cranial and anterior to the cuneus. The marginal ramus of the cingulate sulcus separates the paracentral lobule from the precuneus, and the subparietal sulcus separates the precuneus from the posterior cingulate cortex. The subparietal sulcus forms the ventral margin of the superior parietal lobule on the medial surface.

The IPL is further divided into 2 gyri: Caudally, the angular gyrus caps the end of the superior temporal sulcus and is continuous with the middle temporal gyrus; rostrally, the supramarginal gyrus caps the end of the Sylvian fissure (Fig 6A). The supramarginal gyrus is continuous anteriorly with the postcentral gyrus and posteriorly with the superior temporal gyrus.²⁷⁻²⁹

Function. The PPC is known for neural processes underlying attention. The important role of the PPC to attention is perhaps best demonstrated by parietal insults or lesions that result in hemispatial or contralateral neglect. The most common lesion site in patients with hemispatial neglect is the right temporoparietal junction, a part of the ventral attention network, and the adjacent superior temporal gyrus. Damage to the nondominant PPC can result in left hemispatial neglect.^{27,28,30}

Left-hemispheric PPC lesions in humans result in apraxia and extinction, demonstrating the role of the PPC in high-order motor functions. Functional imaging studies demonstrate that rostral IPL areas activate during the planning of a motor response or movement execution. The IPL is also activated with grasping, viewing graspable objects, conceptualizing actions, evaluating the motor significance of sensory stimuli, basing decisions on perceptions, and judging and observing actions. The intraparietal sulcus and portions of the superior parietal lobule are involved in visuomotor integration. A major function of the PPC is the maintenance of a spatial reference for goal-directed movements.^{27,28,31,32}

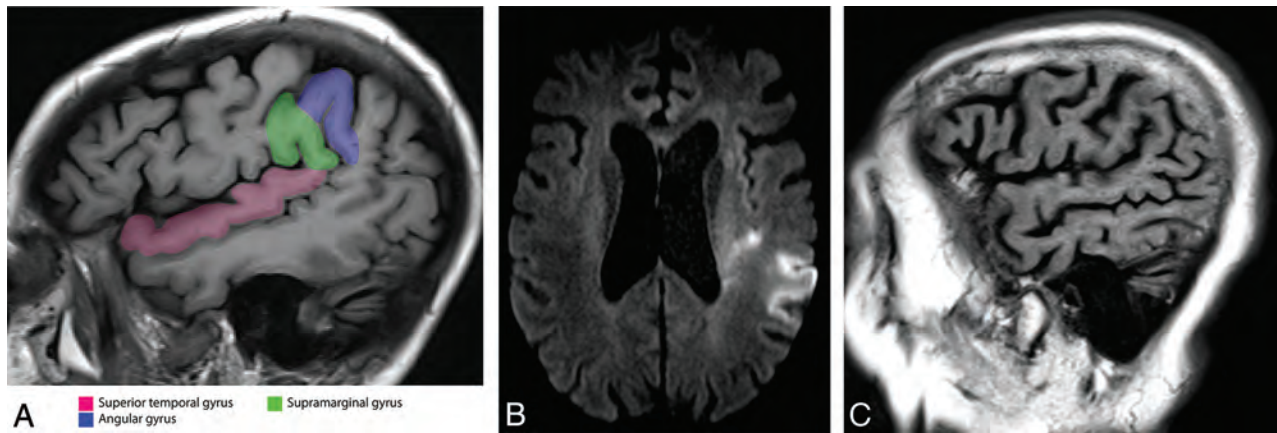


FIG 6. A, Sagittal MPRAGE image through the inferior parietal lobe demonstrates the supramarginal gyrus and angular gyrus. The superior temporal gyrus also is highlighted. Axial DWI (B) and sagittal T1-weighted (C) images of a left IPL infarct. The patient presented with the inability to understand and could not produce any comprehensible speech. The IPL is involved in semantic and phonologic processing. Patients with an infarct in this region have severe word- and sentence-comprehension deficits due to a transcortical sensory aphasia. Subdivisions of the arcuate fasciculus connect the IPL to the posterior temporal area as well as the IPL to the Broca area.

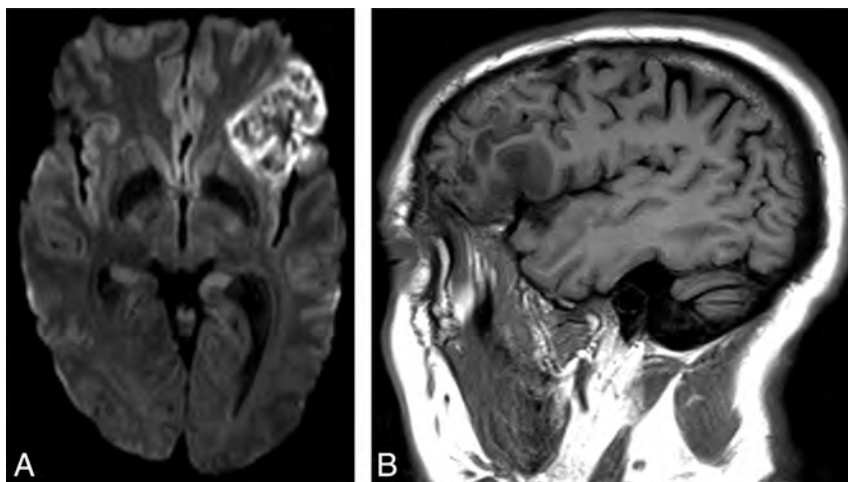


FIG 7. A left Broca infarct with classic expressive aphasia. A, Axial diffusion-weighted image demonstrates restricted diffusion at the classic Broca area. B, Sagittal T1-weighted image demonstrates hypointensity due to edema from the infarct.

A language-related area exists within the posterior IPL (Fig 6B, -C), mainly within the angular gyrus. The PPC, particularly the IPL, performs semantic and phonologic processing. The angular gyrus with the adjacent white matter is the most common parietal lesion site in patients with severe word and sentence comprehension deficits due to transcortical sensory aphasia. The PPC is also involved in verbal fluency tasks.^{27,28,33} Studies of white matter connectivity using diffusion-tensor imaging found that subdivisions of the arcuate fasciculus connect the Broca area to the rostral IPL or the IPL to posterior temporal areas; this feature may account for different manifestations of aphasia resulting from damage to different points along the arcuate fasciculus (Fig 1).^{34,35}

Arithmetic operations and the processing and understanding of numbers are also functions of the PPC. Injury to the PPC can result in dyscalculia, as is seen in Gerstmann syndrome. Gerstmann syndrome results from damage to the angular gyrus of the language-dominant hemisphere and is characterized by agnosia, agraphia or dysgraphia, dyslexia, right-left disorientation, as well as acalculia or dyscalculia. In some instances, Gerstmann syndrome is also associated with aphasia.²⁷

Posterior Superior Temporal Lobe

General Anatomic Borders. The posterior superior temporal lobe (Fig 6A) includes the posterior two-thirds of the superior temporal gyrus and the cortex extending medially into the posterosuperior aspect of the Sylvian fissure. The superior surface of the superior temporal gyrus, located within the Sylvian fissure, contains 3 distinct areas: the planum polare anteriorly, transverse temporal (Heschl) gyri medially, and the planum temporale posteriorly.

Function. Functional and anatomic studies localize the primary auditory cortex to the transverse temporal (Heschl) gyri and the secondary auditory cortex to the surrounding territory.^{36,37}

Damage to projections from the secondary auditory cortex into the posterior Sylvian fissure results in pure word deafness with preserved nonspeech hearing.^{38,39} In the language-dominant hemisphere, the area receiving these projections, area Spt, plays a role in sensorimotor integration as the beginning of the dorsal language stream. Area Spt is located in the Wernicke area (Fig 1); however, damage to area Spt usually results in conductive aphasia.⁴⁰ Recent research questions the exact location of the Wernicke area. Classic receptive aphasia is often associated with lesions outside the traditional boundaries of the Wernicke area.^{41,42}

Ventrolateral Prefrontal Cortex

General Anatomic Borders. The ventrolateral prefrontal cortex is located within the inferior frontal gyrus.

Function. The Broca area is part of a larger network dedicated to language processing and production, most commonly lateralizing to the left hemisphere. Traditionally, the Broca area represents where speech is articulated into meaningful sounds.²⁴ Lesion studies suggest a role in internal conflict resolution by selecting

among competing linguistic representations as part of the cognitive control domain of the lateral prefrontal cortex.⁴³ Lesions typically result in motor aphasia with maintained speech comprehension (Fig 7).

Cingulate Cortex

General Anatomic Borders. The cingulate gyrus, coursing parallel to the corpus callosum, derives its name from the Latin for “belt.” The superior frontal gyrus lies anterior and superior to it, and the precuneus abuts it posteriorly.

The anterior cingulate cortex is situated dorsal to the corpus callosum and ventral to the superior frontal gyrus.⁴⁴ The posterior cingulate cortex lies at the medial aspect of the inferior portion of the parietal lobe. Superiorly, it is defined by the marginal ramus of the cingulate sulcus and inferiorly by the corpus callosum. Anteriorly, the posterior cingulate cortex is defined by the midcingulate region and posteriorly by the parieto-occipital sulcus. Along with the precuneus and retrosplenial cortex, it constitutes the posteromedial cortex, and with the retrosplenial cortex, it forms the retrosplenial gyrus.⁴⁵

Function. The midcingulate region contains motor function with corticospinal tract projections.⁴⁵ An fMRI study suggested 3 somatotopically organized motor zones, distinct from SMA activation, in the cingulate/paracingulate region.⁴⁶

Ventral Occipitotemporal Cortex

General Anatomic Borders. The division between the temporal and occipital lobes is the lateral parietotemporal line, an imaginary boundary extending from the superolateral terminus of the parieto-occipital fissure inferiorly to the preoccipital notch. Several gyri and sulci are continuous between the temporal and occipital lobes across this line; those on the inferior (ventral) aspect of the brain, the lingual gyrus and fusiform gyrus, make up the ventral occipitotemporal cortex (VOTC).

Function. The VOTC forms the path of the ventral visual stream, which maps perceptions of the visual system to conceptual representations.⁴⁷ There is evidence for several areas of functional specialization within the extrastriate ventral stream, each responsible for identifying a particular type of stimulus. Primarily located within the right fusiform gyrus, the fusiform face area (FFA) is responsible for the identification of particular faces.⁴⁸⁻⁵⁰ Injury to the FFA can result in prosopagnosia, the inability to recognize familiar faces with the retained ability to identify that a visual stimulus is a face. The corresponding functional unit within the left fusiform gyrus is the visual word form area,⁵¹⁻⁵³ injury to which causes pure alexia where a patient cannot read but can speak and comprehend language normally.⁵⁴ Bilateral lesions involving the VOTC can result in agnosia of other types of visual objects, with the retained ability to identify the objects using other sensory inputs.⁵⁵ The lingual gyrus is continuous rostrally with the parahippocampal gyrus and caudally with the superior visual field region of the primary visual cortex. Injuries to the lingual gyri and portions of the fusiform gyri can result in the inability to appreciate color (achromatopsia) and the inability to name colors (color anomia).⁵⁵ The lingual gyrus also may significantly link the

visual system and the limbic system, mediating the formation of visual memories and the emotional attachments to images.^{55,56}

CONCLUSIONS

We hope this review of the anatomy and function of the major cortical regions of the brain will foster a better understanding of cortical organization and function.

Disclosures: Virginia B. Hill—UNRELATED: Consultancy: Google.

REFERENCES

1. Ungerleider LG, Mishkin M. **Two cortical visual systems.** In: Ingle D, Goodale MA, Mansfield RJ, eds. *Analysis of Visual Behavior.* Cambridge: MIT Press; 1982:549–86
2. Hickok G, Poeppel D. **Dorsal and ventral streams: a framework for understanding aspects of the functional anatomy of language.** *Cognition* 2004;92:67–99 CrossRef Medline
3. Hickok G, Poeppel D. **The cortical organization of speech processing.** *Nat Rev Neurosci* 2007;8:393–402 CrossRef Medline
4. Smits M, Jiskoot LC, Papma JM. **White matter tracts of speech and language.** *Semin Ultrasound CT MR* 2014;35:504–16 CrossRef Medline
5. Axer H, Klingner CM, Prescher A. **Fiber anatomy of dorsal and ventral language streams.** *Brain Lang* 2013;127:192–204 CrossRef Medline
6. Dick AS, Bernal B, Tremblay P. **The language connectome: new pathways, new concepts.** *Neuroscientist* 2014;20:453–67 CrossRef Medline
7. Binder JR. **fMRI is a valid noninvasive alternative to Wada testing.** *Epilepsy Behav* 2011;20:214–22 CrossRef Medline
8. Yeterian EH, Pandya DN, Tomaiuolo F, et al. **The cortical connectivity of the prefrontal cortex in the monkey brain.** *Cortex* 2012;48: 58–81 CrossRef Medline
9. Makris NK, Kennedy DN, McInerney S, et al. **Segmentation of subcomponents within the superior longitudinal fasciculus in humans: a quantitative, in vivo, DT-MRI study.** *Cereb Cortex* 2005; 15:854–69 CrossRef Medline
10. Saur D, Kreher BW, Schnell S, et al. **Ventral and dorsal pathways for language.** *Proc Natl Acad Sci U S A* 2008;105:18035–40 CrossRef Medline
11. Parker GJ, Luzzi S, Alexander DC, et al. **Lateralization of ventral and dorsal auditory-language pathways in the human brain.** *Neuroimage* 2005;24:656–66 CrossRef Medline
12. Fridriksson JY, Bonilha L, Basilakos A, et al. **Revealing the dual streams of speech processing.** *Proc Natl Acad Sci U S A* 2016;113: 15108–13 CrossRef Medline
13. Cloutman LL. **Interaction between dorsal and ventral processing streams: where, when and how?** *Brain Lang* 2013;127:251–63 CrossRef Medline
14. Tamraz JC, Comair YG. *Atlas of Regional Anatomy of the Brain Using MRI: With Functional Correlations.* Berlin: Springer; 2005
15. Binkofski F, Fink GR, Geyer S, et al. **Neural activity in human primary motor cortex areas 4a and 4p is modulated differentially by attention to action.** *J Neurophysiol* 2002;88:514–19 CrossRef Medline
16. Geyer S, Ledberg A, Schleicher A, et al. **Two different areas within the primary motor cortex of man.** *Nature* 1996;382:805–07 CrossRef Medline
17. Vanderah TW, Gould DJ, Nolte J. *Nolte's The Human Brain: An Introduction to its Functional Anatomy.* Philadelphia: Elsevier; 2016
18. Overduin SA, Servos P. **Distributed digit somatotopy in primary somatosensory cortex.** *Neuroimage* 2004;23:462–72 CrossRef Medline
19. Watson C, Kirkcaldie M, Paxinos G. *The Brain: An Introduction to Functional Neuroanatomy.* Amsterdam: Elsevier; 2010

20. Chouinard PA, Paus T. **The primary motor and premotor areas of the human cerebral cortex.** *Neuroscientist* 2006;12:143–52 CrossRef Medline
21. Geyer S, Schleicher A, Zilles K. **Areas 3a, 3b, and 1 of human primary somatosensory cortex.** *Neuroimage* 1999;10:63–83 CrossRef Medline
22. Nachev P, Kennard C, Husain M. **Functional role of the supplementary and pre-supplementary motor areas.** *Nat Rev Neurosci* 2008;9:856–69 CrossRef Medline
23. Naidich TPY, Yousry TA. **Functional neuroanatomy.** In: Stippich C, ed. *Clinical Functional MRI: Presurgical Functional Neuroimaging*. 2nd ed. Berlin: Springer; 2015:xvi
24. Chung GH, Han YM, Jeong SH, et al. **Functional heterogeneity of the supplementary motor area.** *AJNR Am J Neuroradiol* 2005;26:1819–23 Medline
25. Nolte J. **Overview of motor system.** In: Nolte J, Sundstein J. *The Human Brain: An Introduction to its Functional Anatomy*. 4th ed. St. Louis: Mosby; 1999:441–43
26. Potgieser AR, de Jong BM, Wagemakers M, et al. **Insights from the supplementary motor area syndrome in balancing movement initiation and inhibition.** *Front Hum Neurosci* 2014;8:960 CrossRef Medline
27. Zilles K, Amunts K. **Architecture of the cerebral cortex.** In: Mai K, Paxinos G, eds. *The Human Nervous System*. 3rd ed. Amsterdam: Elsevier Academic Press; 2012
28. Caspers S, Amunts K, Zilles K. **Posterior parietal cortex: multimodal association cortex.** In: Mai K, Paxinos G, eds. *The Human Nervous System*. 3rd ed. Amsterdam: Elsevier Academic Press; 2012
29. Cavanna AE, Trimble MR. **The precuneus: a review of its functional anatomy and behavioural correlates.** *Brain* 2006;129:564–83 CrossRef Medline
30. Shomstein S. **Cognitive functions of the posterior parietal cortex: top-down and bottom-up attentional control.** *Front Integr Neurosci* 2012;6:38 CrossRef Medline
31. Culham JC, Valyear KF. **Human parietal cortex in action.** *Curr Opin Neurobiol* 2006;16:205–12 CrossRef Medline
32. Vingerhoets G. **Contribution of the posterior parietal cortex in reaching, grasping, and using objects and tools.** *Front Psychol* 2014; 5:151 CrossRef Medline
33. Seghier ML. **The angular gyrus: multiple functions and multiple subdivisions.** *Neuroscientist* 2013;19:43–61 CrossRef Medline
34. Catani M, Jones DK, ffytche DH. **Perisylvian language networks of the human brain.** *Ann Neurol* 2005;57:8–16 CrossRef Medline
35. Kamali A, Sair HI, Radmanesh A, et al. **Decoding the superior parietal lobule connections of the superior longitudinal fasciculus/arculate fasciculus in the human brain.** *Neuroscience* 2014;277:577–83 CrossRef Medline
36. Da Costa S, van der Zwaag W, Marques JP, et al. **Human primary auditory cortex follows the shape of Heschl's gyrus.** *J Neurosci* 2011; 31:14067–75 CrossRef Medline
37. Hackett TA. **Anatomic organization of the auditory cortex.** *Handb Clin Neurol* 2015;129:27–53 CrossRef Medline
38. Poeppel D. **Pure word deafness and the bilateral processing of the speech code.** *Cognit Sci* 2001;25:679–93 CrossRef
39. Stefanatos GA, Gershkoff A, Madigan S. **On pure word deafness, temporal processing, and the left hemisphere.** *J Int Neuropsychol Soc* 2005;11:456–70; discussion 455 CrossRef Medline
40. Buchsbaum BR, Baldo J, Okada K, et al. **Conduction aphasia, sensory-motor integration, and phonological short-term memory: an aggregate analysis of lesion and fMRI data.** *Brain Lang* 2011;119:119–28 CrossRef Medline
41. Tremblay P, Dick AS. **Broca and Wernicke are dead, or moving past the classic model of language neurobiology.** *Brain Lang* 2016;162:60–71 CrossRef Medline
42. Mesulam MM, Thompson CK, Weintraub S, et al. **The Wernicke conundrum and the anatomy of language comprehension in primary progressive aphasia.** *Brain* 2015;138:2423–37 CrossRef Medline
43. Ongür D, Price JL. **The organization of networks within the orbital and medial prefrontal cortex of rats, monkeys and humans.** *Cereb Cortex* 2000;10:206–19 CrossRef Medline
44. Gasquoine PG. **Localization of function in anterior cingulate cortex: from psychosurgery to functional neuroimaging.** *Neurosci Biobehav Rev* 2013;37:340–48 CrossRef Medline
45. Leech R, Sharp DJ. **The role of the posterior cingulate cortex in cognition and disease.** *Brain* 2014;137:12–32 CrossRef Medline
46. Amiez C, Petrides M. **Neuroimaging evidence of the anatomo-functional organization of the human cingulate motor areas.** *Cereb Cortex* 2014;24:563–78 CrossRef Medline
47. Ungerleider LG, Haxby JV. **'What' and 'where' in the human brain.** *Curr Opin Neurobiol* 1994;4:157–65 Medline
48. Kanwisher N, Yovel G. **The fusiform face area: a cortical region specialized for the perception of faces.** *Philos Trans R Soc Lond B Biol Sci* 2006;361:2109–28 CrossRef Medline
49. Kanwisher N, McDermott J, Chun MM. **The fusiform face area: a module in human extrastriate cortex specialized for face perception.** *J Neurosci* 1997;17:4302–11 Medline
50. Rossion B, Jacques C, Jonas J. **Mapping face categorization in the human ventral occipitotemporal cortex with direct neural intracranial recordings.** *Ann N Y Acad Sci* 2018 CrossRef Medline
51. Cohen L, Dehaene S. **Specialization within the ventral stream: the case for the visual word form area.** *Neuroimage* 2004;22:466–76 CrossRef Medline
52. Seghier ML, Price CJ. **Explaining left lateralization for words in the ventral occipitotemporal cortex.** *J Neurosci* 2011;31:14745–53 CrossRef Medline
53. Glezer LS, Jiang X, Riesenhuber M. **Evidence for highly selective neuronal tuning to whole words in the "visual word form area".** *Neuron* 2009;62:199–204 CrossRef Medline
54. Leff AP, Spitsyna G, Plant GT, et al. **Structural anatomy of pure and hemianopic alexia.** *J Neurol Neurosurg Psychiatry* 2006;77:1004–07 CrossRef Medline
55. Mendoza JE, Foundas AL. **The cerebral cortex.** *Clinical neuroanatomy: a neurobehavioral approach*. New York: Springer; 2008:271–499
56. Bogousslavsky J, Miklossy J, Deruaz JP, et al. **Lingual and fusiform gyri in visual processing: a clinico-pathologic study of superior altitudinal hemianopia.** *J Neurol Neurosurg Psychiatry* 1987;50:607–14 CrossRef Medline

Assessment of Explicitly Stated Interval Change on Noncontrast Head CT Radiology Reports

 M. Braileanu,  K. Crawford,  S.R. Key, and  M.E. Mullins

ABSTRACT

BACKGROUND AND PURPOSE: Consistent and standardized reporting of interval change for certain diagnoses may improve the clinical utility of radiology reports. The purpose of this study was to assess explicitly stated interval change of various findings in noncontrast head CT reports.

MATERIALS AND METHODS: A retrospective review was performed on successive noncontrast head CT radiology reports from the first 2 weeks of January 2014. Reports with at least 1 prior comparison CT scan were included. Reports with normal examination findings and those that made comparison with only other types of examinations (eg, MR imaging) were excluded. Descriptive and subgroup statistical analyses were performed.

RESULTS: In total, 200 patients with 230 reports and 979 radiographic findings were identified. The average interval between reports was 344.9 ± 695.9 days (range, 0–3556 days). Interval change was mentioned 67.3% ($n = 659$) of the time for all findings ($n = 979$). Explicitly stated interval change was significantly associated with nonremote findings ($P < .001$) and generalized statements of interval change ($P < .001$). The proportion of interval change reported ranged from 95.3% of the time for hemorrhagic to 36.4% for soft-tissue/osseous categorizations.

CONCLUSIONS: Interval change reporting was variable, mentioned for 67.3% of noncontrast head CT report findings with a prior comparison CT scan. Structured radiology reports may improve the consistent and clear reporting of interval change for certain findings.

ABBREVIATION: IC = interval change

The radiology report is essential in helping clinicians assess patient care, especially during changing treatment plans or prolonged hospital stays.^{1,2} Given the large amount of data primary teams have to review, careful summarization of radiographic findings provides an efficient evaluation of diagnostic abnormalities.³ Assessment of interval change (IC) through comparison with prior radiology reports may improve communication with the primary team, provide excellent patient care, and have important medicolegal implications.^{4,5} However, there are limited published data in the scientific literature on this topic.³ The purpose of this study was to assess explicitly stated IC, specifically for different individual findings, in noncontrast head CT radiology reports.

MATERIALS AND METHODS

A retrospective review was performed on all noncontrast head CT radiology reports from the first 2 weeks of January 2014. Reports from this time period were requested through our institutional data-request system and then were successively analyzed. Studies could be from the emergency department, inpatient floors, or outpatient clinic. At our institution, many radiologists from the neuroradiology department, community radiology specialists, and emergency and trauma imaging radiology divisions interpret noncontrast head CTs. This study was institutional review board–approved.

Reports within that time period with at least 1 explicitly stated prior noncontrast head CT comparison were included. Interval change was defined as an explicit reference to the prior report and/or radiographic images. A full date (day, month, year) was required for inclusion; nonsensical dates were excluded. The accuracy of the prior dates was assumed, and we did not verify prior dates because it was outside the scope of the study. Normal examination findings, outside hospital comparisons/priors, and comparisons with other types of examinations (eg, MR imaging and/or CTA) were excluded. All reports within the 2-week period were reviewed, including repeat examinations of the same patient. If there were multiple noncontrast

Received February 27, 2019; accepted after revision April 24.

From the Department of Radiology and Imaging Sciences, Emory University School of Medicine, Atlanta, Georgia.

Paper previously presented at: Annual Meeting of the American Society of Neuroradiology, May 18–23, 2019; Boston, Massachusetts.

Please address correspondence to Maria Braileanu, MD, Department of Radiology and Imaging Sciences, Emory University School of Medicine, Emory University Hospital, Suite BG23, 1364 Clifton Rd NE, Atlanta, GA 30322; e-mail: mbraile@emory.edu; @maria_braileanu

<http://dx.doi.org/10.3174/ajnr.A6081>

Table 1: Categorization of radiology report findings

Finding	Elaboration
Hemorrhage	Intraparenchymal, intraventricular, subdural, subarachnoid, extra-axial hemorrhages/suspicious collections
Infarct/ischemia	Transcortical, ischemia, encephalomalacia
Intracranial mass	Known and unknown diagnosis; including intraparenchymal, sellar, pineal, and so forth
Mass effect	Herniation, midline shift, diffuse edema, sulcal effacement, ventricular effacement
Microvascular	Chronic ischemic microvascular white matter changes, lacunar infarctions
Pneumocephalus	Intraparenchymal, extra-axial, intraventricular
Postprocedural	Craniotomy, craniectomy, ventricular catheters/drains, drains, cataract surgery, lines
Sinus	Acute or chronic paranasal or mastoid disease
Soft-tissue/osseous	Any abnormalities pertaining to these structures Exception: postsurgical or related to the sinuses
Ventricular caliber	Hydrocephalus, ex vacuo dilation, ventriculomegaly, prominent Exception: effacement caused by mass effect
Volume loss	Cortical atrophy/volume loss, both diffuse and focal Exception: ventriculomegaly likely secondary to volume loss
Other	Malformations, abnormal calcification, dural thickening, artifacts, and so forth

head CT priors, the most recent date was used. Images were not reviewed; as highly important as they are in general, the diagnostic accuracy of the reports was considered irrelevant for this study. Reports were both structured and narrative.

All radiographic findings described in the reports were collected. “Finding” was defined as a radiographic diagnosis or abnormality; a formal diagnosis was not required. For example, an unknown calcification and a pathologically proved meningioma would both be included. When appropriate, findings were grouped together (ie, bilateral lacunar infarcts versus listing each lacunar infarction separately) unless the IC was described separately in the report (ie, bilateral lacunar infarction with 1 new lacunar infarction).

All abnormalities were categorized into the following: hemorrhage, infarct/ischemia, intracranial mass, mass effect, microvascular, pneumocephalus, postprocedural, sinus, soft-tissue/osseous, ventricular caliber, volume loss, and other (Table 1). In addition, whether the finding was remote or typically chronic in the given clinical setting was collected. For example, explicitly stated “old craniotomy” was included as remote. Typically, chronic abnormalities such as microvascular ischemic changes or vascular calcifications were also considered remote. If a finding appeared unchanged after at least 6 months, it was included in this category, such as ex vacuo ventriculomegaly.

Interval change could include improvement, worsening/new, or stability of a radiographic finding as long as it was explicitly stated, similar to a previous study by Hassanpour et al.³ Ambiguous terminology (eg, “evolving,” “persistent,” “re-demonstrated,” “again”) was included as an IC but marked separately. However, for statistical analysis, these terms were included under the stable/unchanged categorization. Chronologic terminology without a modifier was not deemed indicative of IC. For example, “old subdural hematoma” would indicate a chronic process but not necessarily an explicit IC. Similarly, “acute infarction” does not necessarily specify whether the prior examination had the finding.

Whether the IC was mentioned in the body or impression of the report was collected for all findings. Use of generalized statements was noted and assumed to apply to all diagnoses (eg, “Impression: No interval change” or “All other findings are unchanged”). However, if the statement was ambiguous or contradictory, it was not applied but collected separately. If both direct and ambiguous terminology were used in the body and impression, the most explicit IC was collected.

Descriptive and subgroup statistical analyses were performed using STATA Statistical Software: Release 14, 2015 (StataCorp, College Station, Texas). Subgroup analysis was assessed using the χ^2 likelihood ratio test. All *P* values were reported as 2-sided. A *P* value < .05 was statistically significant.

RESULTS

Of the 869 reports reviewed from January 1–13, 2014, two hundred thirty reports were included. In total, 200 patients with 979 radiographic findings were identified. There were 19 patients with 1–4 additional reports within that time period. The mean age ($n = 200$) was 68.9 ± 19.1 years (range, 19–101 years) with 56% ($n = 112$) women. The average interval between reports ($n = 230$) was 344.9 ± 695.9 days (range, 0–3556 days). The time interval between reports was <31 days for 57.5% ($n = 563$) of all findings ($n = 979$). In total, 42.0% ($n = 412$) of findings were typically remote/chronic. There were 40 reports of 230 (17.4%) with generalized statements of interval change, of which 3 were contradictory and not applied to individual findings.

Interval change was described in 67.3% ($n = 659$) of all findings ($n = 979$) (Table 2), with 58.3% ($n = 571$) in the body, 42.6% ($n = 417$) in the impression, and 34.2% ($n = 335$) in both. Explicit IC ($n = 659$) was categorized as “stable” in 40.2% ($n = 394$), “improved” in 9.8% ($n = 96$), “worsened/new” in 9.8% ($n = 96$), or “ambiguous” in 7.5% ($n = 73$) of findings.

Interval change for individual findings was significantly more likely to be explicitly stated with the time between reports being <31 days ($P < .001$), and with generalized statements of interval change in the report ($P < .001$); it was less likely with remote findings ($P < .001$) (Table 2).

In subgroup analysis (Table 3), IC was significantly less likely to be explicitly stated or placed in the impression with microvascular ($P < .001$, $P = .01$), sinus ($P < .001$, $P = .009$), soft-tissue/osseous ($P < .001$, $P < .001$), and volume loss ($P < .001$, $P < .001$) categorizations relative to all findings, respectively. Explicitly stated interval change was significantly more likely in hemorrhage ($P < .001$), intracranial mass ($P = .02$), and mass effect ($P = .001$) categorizations. Mention of IC in the impression was more likely for hemorrhage ($P < .001$) and mass effect ($P = .01$). All other categories were not significantly different from all findings.

DISCUSSION

The American College of Radiology Practice Parameters recommends that every report should include comparison with prior examinations when available and appropriate as part of the radiologic consultation.¹ In this study, we found variable IC reporting mentioned in 67.3% of noncontrast head CT report findings with a prior examination. Whether IC was explicitly stated depended on multiple factors, including categorization of findings, chronicity of findings, and time interval between studies.

Finding categorization revealed variable application of IC. Typically, “acute” categories such as hemorrhage (95.3%), infarct/ischemia (76.8%), and mass effect (82.1%) had significantly higher but not perfect IC reporting. Hemorrhage and mass effect were more likely to have explicit IC mentioned in the impression, an appropriate approach given the acute clinical significance of any change in these findings. Intracranial mass also had high IC reporting (92.9%), which may be important for tumor monitoring and treatment planning.⁶ Most interesting, IC for intracranial mass was less likely to be in the impression; on a noncontrast head CT with probable advance imaging follow-up, IC of a mass may be less important than having the mass. The rate of IC reporting of pneumocephalus was only 71.4% and not significantly different from the rate for all findings, a concerning result given that pneumocephalus can be a potentially serious finding.⁷ The rate of explicit IC of ischemia/infarction (76.8%) and postprocedural (69.7%) and ventricular caliber (72.8%) IC reporting for these categories was not significantly different from all findings, likely representing a combination of “important” (acute hydrocephalus) and “secondary” (ex vacuo dilation) findings as determined by the reading radiologist.⁸

Stereotypically chronic (microvascular, 50.9%; volume loss, 47.1%) or typically “secondary” (sinus, 43.7%; soft-tissue/osseous, 36.4%) categories were less likely to have an explicitly stated IC. Given the relative ambiguity of the American College of Radi-

ology recommendations, exclusion of these findings is likely appropriate.^{2,8} However, in certain clinical settings, these findings, even chronic white matter microvascular ischemic changes,^{9,10} may be relevant to patient care. Furthermore, the ordering provider may consider a certain diagnosis more important than a radiologist does. For example, prior studies have noted inconsistent reporting of the sinuses on CT with associated dissatisfaction among otolaryngologists.^{11,12} Although it is likely appropriate to not mention IC for these typically chronic and “secondary” findings, careful examination of the study indication and patient presentation should always be considered before excluding IC.⁸

The higher rate of explicitly stated IC was significantly associated with the time interval between reports being <31 days ($P < .001$). Mention of IC may be important even if the interval time is >1 month. For example, conservative management of intracranial vascular abnormalities or surveillance after treatment may require prolonged observation and interval follow-up.¹³⁻¹⁵ Similarly, chronic findings were less likely to have explicitly stated IC ($P < .001$). However, monitoring chronic findings for long periods may have clinical significance. For example, longitudinal volume loss is important in predicting risk and clinical outcomes in different types of dementia.¹⁶⁻¹⁸

Structured reporting with clear terminology may improve the reporting of IC as well as the clinical utility of radiology reports. When IC was stated in our study, it was in ambiguous terms 7.5% of the time. Clear and standardized radiographic terminology may decrease confusion and make comparison with prior examinations easier.^{6,19} For our retrospective review, both structured and narrative reports were reviewed with no standardization of IC. Currently, our institution uses structured reports nearly exclusively, though IC is not included. The use of a generalized statement increased the likelihood of IC reporting in our study ($P < .001$), and in certain respects, it may be considered a proxy for standardization. Structured radiology reports may result in improved understanding of radiographic findings and clinical utility compared with narrative reports.^{2,6,20-22} Furthermore, studies have shown that clinicians may prefer standardized reports to narrative find-

Table 2: Analysis of IC for all findings (n = 979)

	Total (%) (No.)	IC Stated (%) (No.)	χ^2 Likelihood Ratio	χ^2 Likelihood Ratio P Value
All findings	100% (979)	67.3% (659)		
Interval <31 days	57.5% (563)	74.1% (417)	27.3	<.001 ^a
Remote finding	42.1% (412)	52.2% (215)	73.9	<.001 ^a
Generalized statement	14.1% (138)	100% (138)	120.0	<.001 ^a

^aStatistically significant.

Table 3: Subgroup analysis of IC for finding categorization

Finding	Total (%) (No.)	Interval Change (%) (No.)	χ^2 Likelihood Ratio	χ^2 Likelihood Ratio P Value	IC in the Impression (%) (No.)	χ^2 Likelihood Ratio	χ^2 Likelihood Ratio P Value
Total	100% (979)	67.3% (659)			42.6% (417)		
Hemorrhage	13.0% (127)	95.3% (121)	67.5	<.001 ^a	67.7% (86)	37.5	<.001 ^a
Infarct/ischemia	7.0% (69)	76.8% (53)	3.2	.07	42.0% (29)	0.01	.9
Intracranial mass	1.4% (14)	92.9% (13)	5.4	.02 ^a	57.1% (8)	1.2	.3
Mass effect	9.7% (95)	82.1% (78)	11.5	.001 ^a	54.7% (52)	6.3	.01 ^a
Microvascular	16.6% (163)	50.9% (83)	22.8	<.001 ^a	33.7% (55)	6.4	.01 ^a
Pneumocephalus	2.9% (28)	71.4% (20)	0.2	.6	46.4% (13)	.2	.7
Postprocedural	14.8% (145)	69.7% (101)	0.4	.5	41.4% (60)	0.1	.7
Sinus	5.8% (57)	43.9% (25)	14.1	<.001 ^a	26.3% (15)	6.9	.009 ^a
Soft-tissue/osseous	4.5% (44)	36.4% (16)	18.5	<.001 ^a	11.4% (5)	21.5	<.001 ^a
Ventricular caliber	11.6% (114)	72.8% (83)	1.8	.2	50.9% (58)	3.6	.06
Volume loss	8.7% (85)	47.1% (40)	16.3	<.001 ^a	24.7% (21)	12.9	<.001 ^a
Other	3.9% (38)	68.4% (26)	0.02	.9	39.5% (15)	0.2	.7

^aStatistically significant.

ings.^{6,20,21,23} In addition, important features are less likely to be missed on structured reports.^{20,21}

Given our findings of overall poor reporting of IC, the higher percentage of reporting with generalized IC statements, and the literature regarding structured reporting, we propose including IC as a part of the standardized radiology report. An IC section should include options for overall no interval change, significant interval change as described in the report, or no comparable priors.

There are several limitations to this study. First, this was a retrospective study with reports being examined by multiple readers from different hospital settings; furthermore, retrospective categorization of patient location, given the dynamics of care transition at our institution, was impractical. However, all findings were statistically significant. Next, only noncontrast head CTs were included for simplification. It is assumed that similar patterns would be observed in different radiologic subspecialties and modalities. Similarly, comparisons with other modalities such as CTAs and MRIs were not included; however, this feature should not significantly bias the results because they were excluded. Next, the accuracy of every aspect of the reports was not verified. Although highly important, it was considered outside the scope of this study, which focused on how IC of individual findings is used in the report. In addition, we attempted to evaluate IC from both a radiologist's and referring clinician's perspectives. For practical purposes, basic accuracy was assumed. Finally, the definition of an explicitly stated IC in this study may be seen as overly exacting, though similar to definitions used in the literature.³ In addition, given the relative paucity of prior precedent in the scientific literature,³ our finding categorizations were arbitrary. Some of the findings we identified would not be anticipated to have changed in most settings. However, our definitions fulfilled our most important criterion: Would a clinician with no knowledge of the case be able to discern whether there was a prior study. Furthermore, the use of simple phrases like "unchanged" and "otherwise unchanged," we would argue, is straightforward for clinicians to understand and not overly demanding for radiologists to use.

CONCLUSIONS

We found variable explicit IC reporting that was mentioned for 67.3% of noncontrast head CT findings with a prior examination. The increased likelihood of IC being stated was significantly associated with the time between reports being <31 days ($P < .001$), non-remote findings ($P < .001$), and generalized statements of interval change ($P < .001$). Explicit IC reporting also varied on the basis of finding type, ranging from 95.3% of the time for hemorrhagic to 36.4% for soft-tissue/osseous categorizations. Consistent reporting of interval change for certain diagnoses may improve the clinical utility of radiology reports. This may be achieved through the use of standardized and structured radiographic reports and terminology to improve the clear reporting of IC.

REFERENCES

1. Cynthia JS, Marks A, Leonard B, et al. **ACR practice parameter for communication of diagnostic imaging findings.** https://www.acr.org/-/media/ACR/Files/Practice-Parameters/Communication_Diag.pdf. Accessed February 27, 2019
2. Ganeshan D, Duong PAT, Probyn L, et al. **Structured reporting in radiology.** *Acad Radiol* 2018;25:66–73 CrossRef Medline
3. Hassanpour S, Bay G, Langlotz CP. **Characterization of change and significance for clinical findings in radiology reports through natural language processing.** *J Digit Imaging* 2017;30:314–22 CrossRef Medline
4. Berlin L. **Comparing new radiographs with those obtained previously.** *Am J Roentgenol* 1999;172:3–6 CrossRef Medline
5. Wallis A, McCoubrie P. **The radiology report: are we getting the message across?** *Clin Radiol* 2011;66:1015–22 CrossRef Medline
6. Gore A, Hoch MJ, Shu HG, et al. **Institutional implementation of a structured reporting system: our experience with the brain tumor reporting and data system.** *Acad Radiol* 2019 Jan 17. [Epub ahead of print] CrossRef Medline
7. Cunqueiro A, Scheinfeld MH. **Causes of pneumocephalus and when to be concerned about it.** *Emerg Radiol* 2018;25:331–40 CrossRef Medline
8. Pandharipande PV, Herts BR, Gore RM, et al. **Rethinking normal: benefits and risks of not reporting harmless incidental findings.** *J Am Coll Radiol* 2016;13:764–67 CrossRef Medline
9. Geerlings MI, Appelman AP, Vincken KL, et al; SMART Study Group. **Association of white matter lesions and lacunar infarcts with executive functioning: the SMART-MR study.** *Am J Epidemiol* 2009;170:1147–55 CrossRef Medline
10. Xiong YY, Mok V. **Age-related white matter changes.** *J Aging Res* 2011;2011:617927 CrossRef Medline
11. Deutschmann MW, Yeung J, Bosch M, et al. **Radiologic reporting for paranasal sinus computed tomography: a multi-institutional review of content and consistency.** *Laryngoscope* 2013;123:1100–05 CrossRef Medline
12. Becker SS, O'Malley BB. **Evaluation of sinus computed tomography scans: a collaborative approach between radiology and otolaryngology.** *Curr Opin Otolaryngol Head Neck Surg* 2013;21:69–73 CrossRef Medline
13. Yang W, Wei Z, Wang JY, et al. **Long-term outcomes of patients with giant intracranial arteriovenous malformations.** *Neurosurgery* 2016;79:116–24 CrossRef Medline
14. Paul AR, Colby GP, Huang J, et al. **Selection of treatment modalities or observation of dural arteriovenous fistulas.** *Neurosurg Clin N Am* 2012;23:77–85 CrossRef Medline
15. Sorenson TJ, Brinjikji W, Bortolotti C, et al. **Recurrent brain arteriovenous malformations (AVMs): a systematic review.** *World Neurosurg* 2018;116:e856–66 CrossRef Medline
16. Reiter K, Nielson KA, Durgerian S, et al. **Five-year longitudinal brain volume change in healthy elders at genetic risk for Alzheimer's disease.** *J Alzheimers Dis* 2017;55:1363–77 CrossRef Medline
17. Okonkwo OC, Alosco ML, Jerskey BA, et al; Alzheimer's Disease Neuroimaging Initiative. **Cerebral atrophy, apolipoprotein E varepsilon4, and rate of decline in everyday function among patients with amnesic mild cognitive impairment.** *Alzheimers Dement* 2010;6:404–11 CrossRef Medline
18. Nedelska Z, Ferman TJ, Boeve BF, et al. **Pattern of brain atrophy rates in autopsy-confirmed dementia with Lewy bodies.** *Neurobiol Aging* 2015;36:452–61 CrossRef Medline
19. European Society of Radiology (ESR). **ESR paper on structured reporting in radiology.** *Insights Imaging* 2018;9:1–7 CrossRef Medline
20. Franconeri A, Fang J, Carney B, et al. **Structured vs narrative reporting of pelvic MRI for fibroids: clarity and impact on treatment planning.** *Eur Radiol* 2018;28:3009–17 CrossRef Medline
21. Tuncyurek O, Garces-Descovich A, Jaramillo-Cardoso A, et al. **Structured versus narrative reporting of pelvic MRI in perianal fistulizing disease: impact on clarity, completeness, and surgical planning.** *Abdom Radiol (NY)* 2019;44:811–20 CrossRef Medline
22. Bosmans JML, Weyler JJ, Parizel PM. **Structure and content of radiology reports, a quantitative and qualitative study in eight medical centers.** *Eur J Radiol* 2009;72:354–58 CrossRef Medline
23. Park SB, Kim MJ, Ko Y, et al. **Structured reporting versus free-text reporting for appendiceal computed tomography in adolescents and young adults: preference survey of 594 referring physicians, surgeons, and radiologists from 20 hospitals.** *Korean J Radiol* 2019;20:246–55 CrossRef Medline

3T MRI Whole-Brain Microscopy Discrimination of Subcortical Anatomy, Part 2: Basal Forebrain

M.J. Hoch, M.T. Bruno, A. Faustin, N. Cruz, A.Y. Mogilner, L. Crandall, T. Wisniewski, O. Devinsky, and T.M. Shepherd



ABSTRACT

BACKGROUND AND PURPOSE: The basal forebrain contains multiple structures of great interest to emerging functional neurosurgery applications, yet many neuroradiologists are unfamiliar with this neuroanatomy because it is not resolved with current clinical MR imaging.

MATERIALS AND METHODS: We applied an optimized TSE T2 sequence to washed whole postmortem brain samples ($n = 13$) to demonstrate and characterize the detailed anatomy of the basal forebrain using a clinical 3T MR imaging scanner. We measured the size of selected internal myelinated pathways and measured subthalamic nucleus size, oblique orientation, and position relative to the intercommissural point.

RESULTS: We identified most basal ganglia and diencephalon structures using serial axial, coronal, and sagittal planes relative to the intercommissural plane. Specific oblique image orientations demonstrated the positions and anatomic relationships for selected structures of interest to functional neurosurgery. We observed only 0.2- to 0.3-mm right-left differences in the anteroposterior and superoinferior length of the subthalamic nucleus ($P = .084$ and $.047$, respectively). Individual variability for the subthalamic nucleus was greatest for angulation within the sagittal plane (range, 15° – 37°), transverse dimension (range, 2–6.7 mm), and most inferior border (range, 4–7 mm below the intercommissural plane).

CONCLUSIONS: Direct identification of basal forebrain structures in multiple planes using the TSE T2 sequence makes this challenging neuroanatomy more accessible to practicing neuroradiologists. This protocol can be used to better define individual variations relevant to functional neurosurgical targeting and validate/complement advanced MR imaging methods being developed for direct visualization of these structures in living patients.

ABBREVIATIONS: DBS = deep brain stimulation; DRT = dentatorubrothalamic tract; PLIC = posterior limb of the internal capsule; STN = subthalamic nucleus; SUDC = sudden unexplained death of childhood; Vim = thalamic ventrointermedius nucleus; ZI = zona incerta

Deep to the cortical surface, the basal ganglia, thalamus, and subthalamus are vital basal forebrain structures involved in the regulation of autonomic, motor, sensory, limbic, and endocrine functions.^{1,2} The metabolic demand of the basal forebrain

exceeds the cerebral cortex in the resting state.³ Focal pathologic functional or structural changes can have serious clinical consequences due to the compact organization of the basal forebrain. The thalamus is a complex hub receiving subcortical sensory and motor input that projects to both the cortex and striatum.⁴ Thalamic infarction, demyelination, tumors, and other pathologies can cause chronic pain,⁵ sensory loss in multiple modalities, amnesia,⁶ dystonia,⁷ and other disorders.^{8,9} The subthalamus modulates basal ganglia output.¹⁰ Ischemic and hyperglycemic injuries of the subthalamic nucleus can result in hemiballism.^{11,12} The basal ganglia have complex connections to the cortical motor areas, including the precentral gyrus, supplementary motor area, and frontal eye fields.¹³ Basal ganglia pathologies cause

Received March 9, 2019; accepted after revision April 22.

From the Department of Radiology and Imaging Sciences, (M.J.H.), Emory University, Atlanta, Georgia; Departments of Radiology (M.T.B., N.C., T.M.S.), Pathology (A.F., T.W.), Neurosurgery (A.Y.M.), Neurology (L.C., T.W., O.D.), and Psychiatry (T.W.), New York University, New York, New York; SUDC Foundation (L.C., O.D.), New York, New York; and Center for Advanced Imaging Innovation and Research (T.M.S.), New York, New York.

This study was funded by the SUDC Foundation, the Taylor McKeen Shelton Foundation, and the Finding a Cure for Epilepsy and Seizures fund. T.M.S. received research support from the National Institute of Aging (grant AG048622). T.W. and A.F. received research support from the National Institute of Aging (grant AG008051). This work was supported, in part, by the Center for Advanced Imaging Innovation and Research, a National Institutes of Health–National Institute of Biomedical Imaging and Bioengineering Biomedical Technology Resource Center (Grant P41EB017183).

Please address correspondence to Timothy Shepherd, 660 First Ave, Room 226, New York, NY, 10016; e-mail: timothy.shepherd@nyumc.org

 Indicates open access to non-subscribers at www.ajnr.org

 article with supplemental on-line photos.

 Indicates article with supplemental on-line videos.

<http://dx.doi.org/10.3174/ajnr.A6088>

movement disorders (eg, Parkinson, Huntington, and Wilson diseases), developmental disorders (eg, autism), or neuropsychiatric disorders (eg, Tourette syndrome and obsessive-compulsive disorder).¹⁴⁻¹⁷

Functional neurosurgery is a rapidly evolving field with multiple basal forebrain targets to reversibly inhibit selected structures with deep brain stimulation (DBS) or ablate those structures using MR imaging–guided focused sonography. The subthalamic nucleus (STN), globus pallidus internus, and thalamic ventrointermedius nucleus (Vim) are common targets to treat medically refractory hypo- and hyperkinetic movement disorders.¹⁸ Exploratory targets include the habenulopeduncular pathway or nucleus accumbens for treating refractory depression and substance abuse.^{19,20} Chronic electrical stimulation of selected thalamic subnuclei can reduce seizures in patients with epilepsy.²¹ Despite therapeutic successes, the mechanisms of DBS remain incompletely explained, partially due to limited anatomic and functional understanding of key structures. For example, DBS of the STN is used to treat Parkinson disease, though some suggest zona incerta stimulation may also be clinically important.^{22,23}

Imaging tools to precisely define basal forebrain structures remain relatively unchanged despite rapid advances in therapeutics. To better understand the best anatomic targets and the actual mechanism for clinical improvement observed with functional neurosurgery, we need to directly visualize the relevant functional anatomy before and ideally after treatment. Conventional MR imaging has limited contrast resolution for basal forebrain anatomy; this is an active goal of MR imaging research. Susceptibility-weighted MR imaging,²⁴⁻²⁶ ultra-high-field in vivo MR imaging,²⁷⁻²⁹ and advanced diffusion techniques³⁰⁻³² can improve localization of key basal forebrain structures but are challenging to implement into routine clinical practice. Independent validation of diffusion methods has been limited.³³ We developed a rapid 3T postmortem anatomic MR imaging protocol³⁴ using an optimized 2D-TSE sequence with a clinical 3T MR imaging system and head coil available at most institutions. This protocol produces exquisite anatomic contrast for subcortical structures comparable to neuroanatomic atlases with histologic stains.^{2,35-37} Here, we demonstrate how this TSE sequence can precisely delineate basal forebrain anatomy across multiple samples. This can inform future translational research efforts to better identify these structures using in vivo MR imaging.

MATERIALS AND METHODS

Sample Procurement and Preparation

Whole-brain samples were obtained from an institutional review board–approved and Health Insurance Portability and Accountability Act–compliant multisite research study, the Sudden Unexplained Death of Childhood (SUDC) Registry and Research Collaborative,³⁸ which used ex vivo MR imaging screening before gross pathologic assessment, brain cutting, and histopathology for forensic investigation. For each subject, the postmortem brain was removed intact by the local medical examiner, then suspended in a 4% formaldehyde solution for at least 21 days to reach near-equilibrium from presumed fixative-induced nervous tissue T2 changes.³⁹ The brain was shipped to our institution, then washed continuously in water for 48 hours to eliminate MR im-

aging relaxation changes from the free aldehyde fixative solution.⁴⁰ Individual brains with MR imaging data included for the figures ($n = 13$) in this study met the following criteria: 1) minimal injury to cerebral hemispheres or callosum from procurement, 2) no MR imaging or pathologic abnormality (outside the hippocampus) identified by a board-certified neuroradiologist and neuropathologist, respectively, 3) no T1-hyperintense fixation bands in the basal forebrain structures due to variable fixation penetration,⁴¹ and 4) a prerefrigeration postmortem interval of <24 hours.⁴² One of 14 consecutive SUDC samples was rejected due to procurement-induced division of the midbrain. The mean postnatal age for included specimens was 47.3 ± 34.8 months with a range between 22 and 142 months (10/13 specimens were between 24 and 48 months of age); 6/13 specimens were from male subjects with SUDC. After imaging was completed, brains were returned to the SUDC research study for brain cutting within 7–10 days.

Whole-Brain MR Imaging Protocol

Each brain was immersed in water inside a custom 3D-printed container specifically designed to conform to a 64-channel head and neck coil on a 3T Prisma MR imaging scanner (Siemens, Erlangen, Germany). Sealed water-filled disposable powderless latex medical gloves were gently wedged between the container and brain to prevent motion. Scout sequences identified the brain position, and then 2D, high-resolution TSE MR imaging sequences of the whole brain were obtained in coronal, sagittal, and axial planes relative to the intercommissural plane. Optimization of sequence parameters for contrast resolution of small structures in the postmortem brain using TSE sequences with 3T MR imaging was reported separately.³⁴ T2-weighted TSE sequence parameters were the following: TR = 5380 ms, TE = 53 ms, echo-train length = 7, echo spacing = 10.8 ms, bandwidth = 415 Hz/pixel, slice thickness and number = 0.8 mm \times 116 (no interslice gap), in-plane resolution = 0.35 \times 0.35 mm, concatenations = 2, averages = 10, total time = 2 hours (full protocol available on request). The current scanner software limits the number of slices to 128, so whole-brain imaging with *isotropic* 350- μ m voxels was not possible. In selected cases, additional images were obtained empirically by stepwise angular rotations relative to the cardinal image planes to illustrate specific anatomic relationships within the basal forebrain.

MR Image Analysis

For each subject, we identified basal forebrain structures at 6 axial, sagittal, and coronal levels (Fig 1). The MR images were labeled with standard nomenclature.^{35,36,43,44} All figures used radiologic image orientation, and only structures identified in all samples by consensus between 2 board-certified neuroradiologists were reported. Terminology for the relative course and spatial positions of adjacent structures was limited to superior versus inferior, medial versus lateral, and anterior versus posterior to avoid confusion. Measurements of the right and left subthalamic nucleus and selected left hemisphere structures were obtained by a single board-certified neuroradiologist for 11 samples (2 samples did not have coregistered sagittal images). The anterior-posterior and left-right dimensions were measured in the axial plane for the left

mammillothalamic tract, column of the fornix, and postcommissural fornix (above and below the anterior commissure, respectively). The anteroposterior and superoinferior dimensions of the left ansa lenticularis were measured in the sagittal plane 5 mm off midline. For these measurements, the area of an ellipse was calculated. The largest in-plane dimension of the left and right subthalamic nuclei was measured in each cardinal plane using the image in which the subthalamic nucleus appeared largest. Similarly, the angle formed by the long axis of the subthalamic nucleus in each cardinal image plane relative to the orthogonal plane was measured; the structure was oriented inferomedial to superolateral in the coronal plane, anteromedial to posterolateral in the axial plane, and anterosuperior to posteroinferior in the sagittal plane.

The neuroradiologist determined the stereotactic coordinates relative to the intercommissural point for the most inferior, lateral, and posterior point of the subthalamic nucleus where it

forms a discrete border with the more hyperintense inferior zona incerta. Note that this fiducial will usually be inferior and lateral to the desired deep brain stimulator (DBS) electrode tip target but was chosen because it can be precisely measured to assess right-left and individual variability in the STN position. The within-sample differences between each of the above right and left measurements were compared using paired-sample Wilcoxon signed rank tests, with $P < .05$ considered significant. The mean difference detectable with 80% statistical power for $n = 11$ samples was estimated by multiplying the SD of the difference by 0.94. A global coefficient of variation was calculated (right- and left-sided data combined, $n = 22$) to estimate variability for each of these features. In addition, the neuroradiologist identified which segment of the subthalamic nucleus was targeted by using the a priori coordinates for DBS electrode tip placement in the medial-posterior-inferior subthalamus at our institution (11 mm lateral, 4 mm posterior, and 5 mm inferior to the intercommissural point); for this, the long axis of the subthalamic nucleus was divided into thirds, and the short axis was divided into quadrants defined as inferior-superior and medial-lateral (hence, 12 potential segments).

RESULTS

Diencephalic structures are shown in selected axial, coronal, and sagittal images (Fig 2 and On-line Figs 1 and 2). On-line videos also are provided for all 3 planes. On-line Fig 3 demonstrates the reproducibility of anatomic contrast for 4

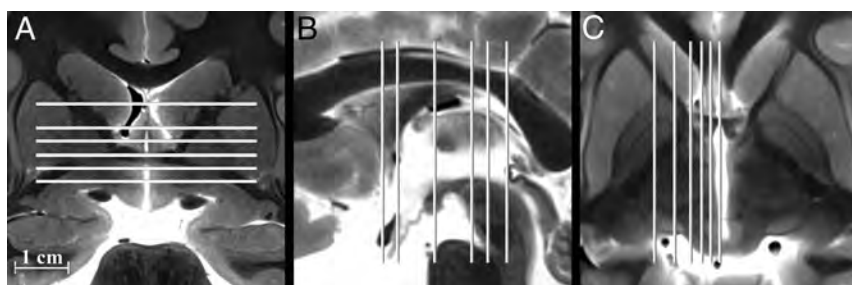


FIG 1. Selected coronal, sagittal, and axial images of the postmortem basal forebrain illustrating the serial imaging planes for Fig 2 and On-line Figs 1 and 2, respectively. Table 1 provides a complete list of labeled anatomy for all figures, indicated by the numbers in parentheses in the legends. The familiarity of T2 contrast and multiple imaging planes provided in this study should help facilitate learning the complex neuroanatomy of the basal forebrain.

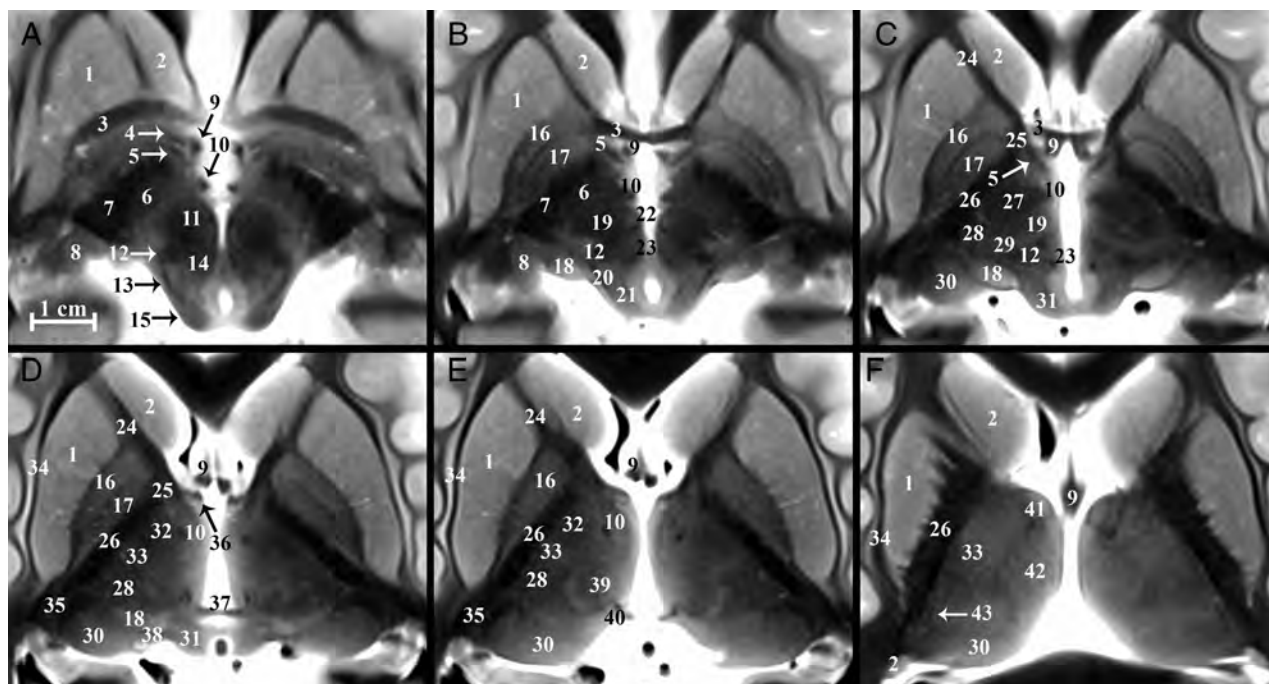


FIG 2. Serial inferior-to-superior axial images of the postmortem basal forebrain parallel to the commissural plane (A-F, -4, -2, 0, 2, 4, and 8 mm relative to the intercommissural plane, respectively). The globus pallidus internus (17) is a therapeutic DBS target for Parkinson disease and dystonia.¹⁸ The globus pallidus internus is separated from the externus (16) by a thin hypointense band, the internal medullary lamina (55 in On-line Fig 1). Note the 2 divisions of the globus pallidus internus (medial and lateral) separated by the accessory medullary lamina in B and C. Contrast is less conspicuous in the more superior thalamus.

Table 1: Basal forebrain structures

Labeling Key
1) Putamen
2) Caudate nucleus
3) Anterior commissure
4) Ansa peduncularis (inferior thalamic peduncle)
5) Ansa lenticularis
6) Subthalamic nucleus
7) Cerebral peduncle
8) Lateral geniculate nucleus
9) Fornix
10) Mammillothalamic tract
11) Red nucleus
12) Medial lemniscus
13) Spinothalamic tract
14) Central tegmental tract
15) Inferior colliculus
16) Globus pallidus externus
17) Globus pallidus internus
18) Medial geniculate nucleus
19) Dentatorubrothalamic tract
20) Brachium of the inferior colliculus
21) Mesencephalic trigeminal nucleus
22) Habenulopeduncular tract (fasciculus retroflexus)
23) Posterior commissure
24) Anterior limb of the internal capsule
25) Genu of the internal capsule
26) Posterior limb of the internal capsule
27) Thalamic fasciculus (H1)
28) Nucleus ventrocaudalis anterior
29) Nucleus ventrocaudalis posterior
30) Pulvinar
31) Superior colliculus
32) Nucleus lateropolaris
33) Nucleus ventrooralis
34) External capsule
35) Retrolenticular internal capsule
36) Direct hippocampal tract
37) Habenular commissure
38) Brachium of the superior colliculus
39) Nucleus centralis
40) Nucleus habenuaris
41) Anterior thalamic nuclear group
42) Nucleus medialis
43) External medullary lamina (thalamus)
44) Extreme capsule
45) Claustrum
46) Caudolenticular gray bridges (pontes grisei caudatolenticulares)
47) Olfactory tubercle
48) Accumbens area
49) Medial forebrain bundle
50) Optic tract
51) External medullary lamina (globus pallidus)
52) Diagonal band of Broca
53) Basal nucleus of Meynert
54) Hypothalamic nuclei
55) Internal medullary lamina (globus pallidus)
56) Mammillary body
57) Optic radiations
58) Lenticular fasciculus (H2)
59) Substantia nigra
60) Massa intermedia
61) Nucleus dorsalis superficialis
62) Nucleus dorsalis oralis
63) Internal medullary lamina (thalamus)
64) Auditory radiations

Table 1: Continued

Labeling Key
65) Periaqueductal gray matter
66) Supraoptic decussation
67) Optic chiasm
68) Superior cerebellar peduncle (crossed)
69) Decussation of the superior cerebellar peduncle
70) Medial longitudinal fasciculus
71) Splenium
72) Hypothalamic sulcus
73) Oculomotor nerve (cranial nerve III)
74) Stratum opticum
75) Nucleus ventrointermedius
76) Nucleus parafascicularis
77) Eninger comb system
78) Nucleus of field of Forel (H)
79) Internal capsule
80) Principal mammillary tract
81) Subthalamic fasciculus
*"Zona incerta"

specimens in selected axial and coronal planes. All labeled structures were identified for each subject by both board-certified neuroradiologists (Table 1), and the numbers in parentheses from this point on refer to Table 1. The TSE MR imaging contrast qualitatively correlated inversely with myelin staining for basal forebrain structures in histologic atlases.^{2,35,36,37} The darkest structures included the internal capsule (79), callosum (71), lenticular fasciculus (58), and postcommissural fornix (9). Intermediate hypointensity was observed in other myelinated structures, including the distal mammillothalamic tract (10), the thalamic internal medullary lamina (63), and the dentatorubrothalamic tract (19). The brightest structures included the posterior hypothalamus (54), geniculate nuclei (8 and 18), substantia nigra (59), and zona incerta (asterisk). We briefly describe and illustrate the complex anatomy of several basal forebrain structures of particular interest as current and emerging functional neurosurgery targets (all measurements are reported as mean \pm SD for $n = 11$ specimens).

Subthalamic Nucleus

The subthalamic nucleus (6) modulates basal ganglia output and is the most common target of DBS for Parkinson disease.¹⁰ The STN is a biconvex hypointense structure at the mesencephalic-diencephalic junction, oriented oblique to all 3 standard planes (Fig 3). The anterolateral STN border is the more hypointense internal capsule, whereas the zona incerta (asterisk) is a thin hyperintense structure abutting the posterior and medial borders of the STN. The substantia nigra (59) is the inferomedial margin of the STN. Together, the corticonigral, pallidonigral, and nigrostriatal fibers appear as a thin, dark bundle dividing the posterolateral third of the substantia nigra as they course inferior, posterior, and lateral from the posterior inferior tip of the STN (Fig 2A and On-line Fig 1E). The subthalamic fasciculus (81) arises from the inferolateral STN border with bidirectional fibers that cross the internal capsule, connecting the STN and globus pallidus (17) (Fig 4D). Table 2 reports measurements of the STN and its oblique orientation relative to imaging planes defined by the commissures, along with stereotactic coordinates for its easily defined lateral-posterior-inferior border. There appeared to be 0.2- to

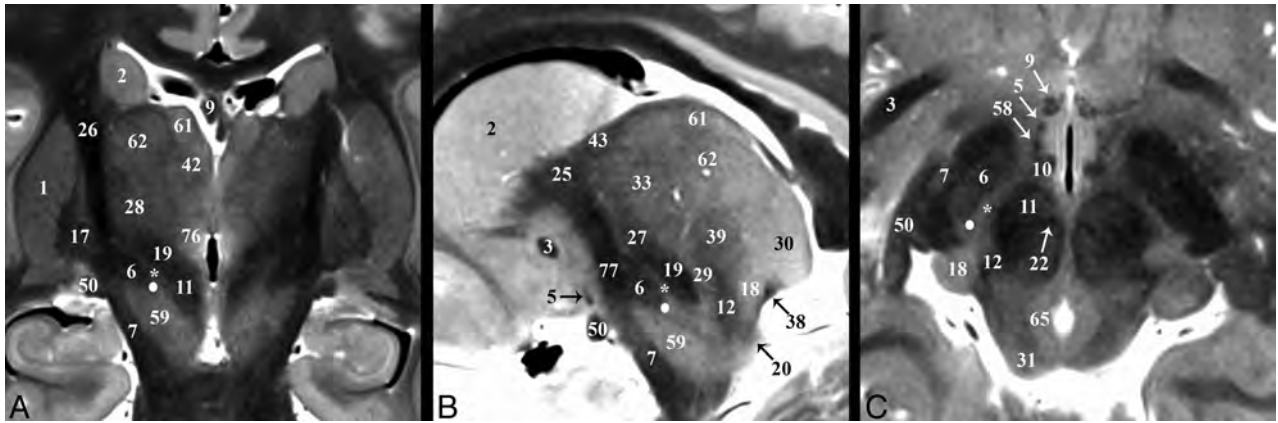


FIG 3. Selected images illustrating the subthalamic nucleus (6) in the basal forebrain. Coronal, sagittal, and axial images show the subthalamic nucleus as a biconvex hypointense structure nestled along the medial margin of the internal capsule (26). *B*, The darkest portion of the internal capsule just anterior to the subthalamic nucleus represents the Edinger comb system (77) containing the pallidosubthalamic, pallidonigral, and nigrostriatal tracts. The *small white circle* represents the potential DBS electrode tip placement site (Table 2) in the inferior portion of the zona incerta (*asterisk*), which corresponds with a better therapeutic profile according to Plaha et al.²²

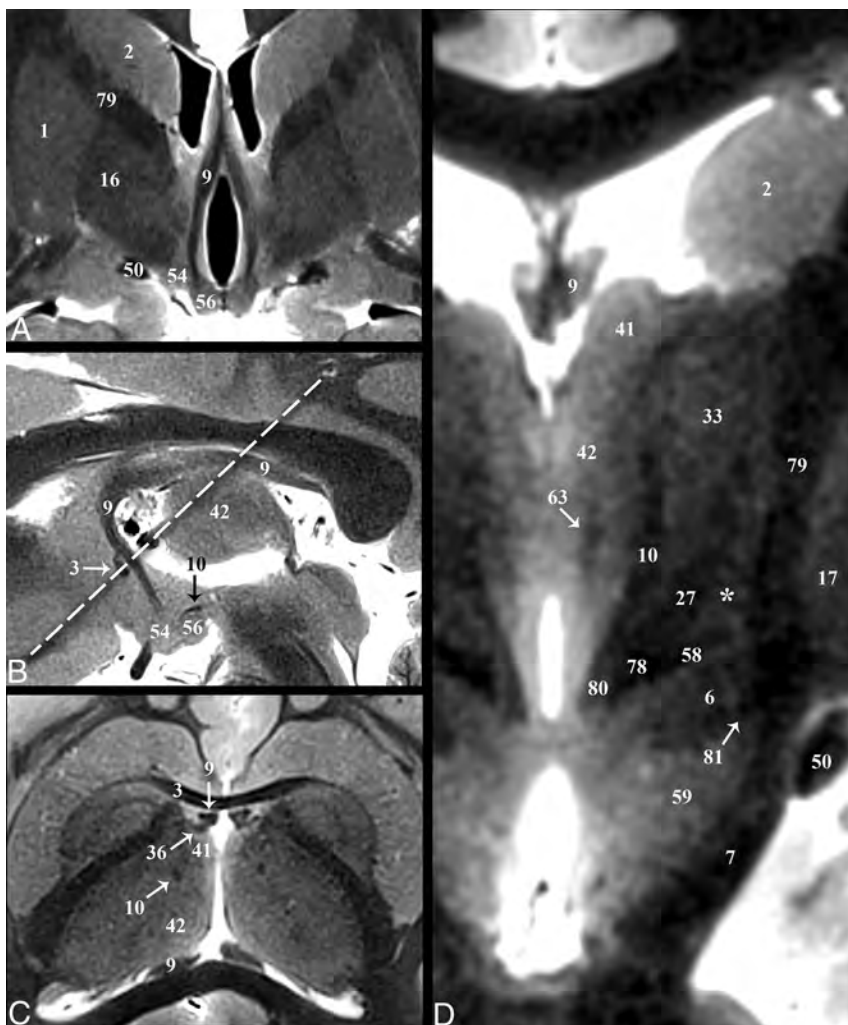


FIG 4. Selected images illustrating the hippocampal-thalamic pathways. Coronal, sagittal, oblique axial (the *dashed line* in *B* represents the oblique imaging plane for *C*), and magnified coronal images of the fornix (9) and mammillothalamic tract (10). *A* and *B*, The decreased size of the postcommissural fornix as it approaches the mammillary bodies (56) is likely due, in part, to the direct hippocampal pathway (36) in *C*, which bypasses the mammillary bodies to reach the anterior thalamic nuclei (41). *D*, Just medial to the Fields of Forel (78) and pallidofugal tracts, the principal mammillary tract (80) gives rise to the ascending mammillothalamic tract. Note the subthalamic fasciculus (81) and zona incerta (*asterisk*).

0.3-mm right-left differences in the anterior-posterior and superior-inferior lengths of the STN ($P = .084$ and $.047$, respectively); otherwise, no significant differences were observed. Individual variability for the subthalamic nucleus (ie, coefficient of variation) was greatest for long-axis angulation in the sagittal plane (range, 15° – 37°), largest transverse dimension (range, 2–6.7 mm), and most inferior border (range, 4–7 mm below the intercommissural plane). The a priori institutional coordinates for targeting the electrode tip into the subthalamic nucleus were centered in the inferior-posterior third for 21/22 subthalamic nuclei and the inferior-middle third in 1/22 (right and left data combined; no anterior third targeting was identified). Lateral-half targeting was present in 6/11 nuclei both for right and left subthalamic nuclei (or 55% of targets).

Zona Incerta

The functions of the zona incerta (ZI) are poorly understood, but it appears to involve sensory processing.⁴⁵ We have used an asterisk to denote the ZI to visually emphasize that this structure is better defined by bordering structures and changes in shape at different points along the neuroaxis. The superior portion of the ZI appears as a thin hyperintense band on the TSE sequence superomedial to the inferior portion of the genu of the internal capsule (79), superior to the lenticular fasciculus (58), inferior to the thalamic fasciculus (27) (Figs 3 and 5*B*), and anterolateral to

Table 2: Measurements of the subthalamic nucleus in SUDC brains using TSE MRI contrast (n = 11)^a

Measurement/ Dimension/Plane	Right	Left	Difference ^b	P Value ^c	COV ^d
Length ^e (mm)					
Anteroposterior	9.6 ± 0.9	9.9 ± 0.8	-0.3 ± 0.6	.084	8.8%
Mediolateral	4.2 ± 1.2	4.1 ± 1.0	0.0 ± 0.4	.910	26.0%
Superoinferior	6.0 ± 0.6	5.8 ± 0.7	0.2 ± 0.3	.047	10.8%
Angle ^f					
Coronal	58.7° ± 6.5°	58.0° ± 6.6°	0.7° ± 5.8°	.414	10.9%
Axial	135.5° ± 4.8°	131.6° ± 5.8°	3.8° ± 5.9°	.590	4.1%
Sagittal	26.5° ± 6.6°	28.5° ± 7.0°	-1.9° ± 5.4°	.188	24.3%
Stereotactic coordinates ^g (mm)					
Lateral	13.5 ± 1.0	13.5 ± 1.1	0.1 ± 0.5	1.000	7.8%
Posterior	4.8 ± 0.6	4.7 ± 0.5	0.1 ± 0.3	1.000	11.1%
Inferior	5.5 ± 0.9	5.4 ± 0.7	0.1 ± 0.5	1.000	14.7%

Note:—COV indicates coefficient of variation.

^a Data are means ± standard deviation unless otherwise indicated.

^b Right-sided measurement minus left-sided measurement.

^c Paired-sample Wilcoxon signed rank test.

^d Global COV for right and left data combined (n = 22).

^e Largest dimension in each plane.

^f The angle formed by the long axis of the subthalamic nucleus relative to the orthogonal imaging plane where angulation is inferomedial to superolateral in the coronal plane, anteromedial to posterolateral in the axial plane, and anterosuperior to posteroinferior in the sagittal plane.

^g Coordinates relative to the intercommissural point where the most inferior, lateral, and posterior point of the subthalamic nucleus forms a distinct border with the inferior portion of the zona incerta. This point will usually be inferior and lateral to the desired DBS electrode tip target but can be measured precisely to assess individual and right-left variation in the subthalamic nucleus position.

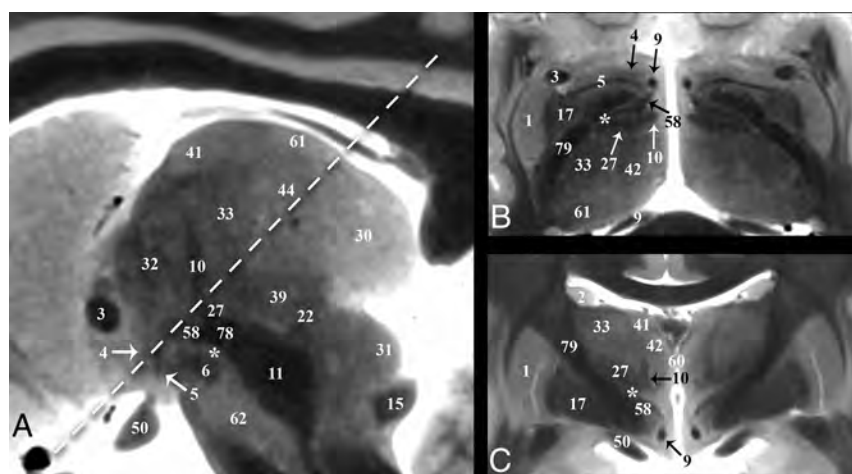


FIG 5. Selected images illustrating the pallidothalamic tracts. Sagittal, oblique axial (the *dashed line* in A represents the oblique imaging plane for B), and coronal images illustrating the complex 3D shapes and spatial relationships of the ansa lenticularis (5), lenticular fasciculus (58), and thalamic fasciculus (27). B, The ansa lenticularis originates from the inferomedial globus pallidus internus (17) and joins the lenticular fasciculus (H2 field of Forel) in the very hypointense prerubral H Fields of Forel (78). These pallidal efferents then ascend as the thalamic fasciculus (H1 Fields of Forel) to the ventral thalamus. The zona incerta (*asterisk*) is the bright signal intensity region in between lenticular and thalamic fasciculi in B and C. The subthalamic nucleus (6) can be seen in relationship to these structures in A. Note the dark structure just inferior to the 44 label and the *dashed line* is a thalamic perforating vessel.

the dentatorubrothalamic tract (19) (Fig 6A). DBS inhibition of the mid- and inferior portions of the ZI may represent therapeutic targets for Parkinson disease.^{22,46} The midportion of the ZI appears as a thin hyperintense band medial to the STN and lateral to the red nucleus (Fig 3C). The medial border of the ZI in this region cannot be distinguished from the prelemniscal radiation by TSE MR imaging; histology shows that the latter abuts the lateral margin of the red nucleus. The most inferior portion of the

ZI is a round hyperintense region in the axial plane (Fig 3C) that is posterior to the STN and medial to the posterior internal capsule.

Pallidothalamic Tracts

The pallidothalamic tracts carry efferents from the globus pallidus to the ventral thalamic nuclei (Fig 5).⁴⁷ The ansa lenticularis (5) consists of fibers from the inferior globus pallidus internus (17) passing immediately inferior to the internal capsule genu, (79), which turns from an anterolateral to posteromedial position (Fig 5B) and ascends slightly to meet the descending lenticular fasciculus (58) just anterolateral to the proximal ascending portion of the mammillothalamic tract (10). The ansa lenticularis measured 1.8 ± 0.3 by 0.8 ± 0.1 mm in the sagittal plane (or a 1.1 ± 0.3 mm² area). The lenticular fasciculus (field H2) represents confluent projections from the more central and superior portions of the internal globus pallidus that pass through the posterior limb of the internal capsule (PLIC) (this aspect is difficult to visualize because both structures are dark on TSE). These fibers become confluent along the medial border of the anterior third of the PLIC (Fig 3A, 4D, and 5B) and course inferomedially to meet the ansa lenticularis and form the thalamic fasciculus (27; field H1). Notably, this prerubral junction within the field of Forel (78; H) is one of the most hypointense structures visualized in the basal forebrain, suggesting dense myelination. The thalamic fasciculus fibers project posteriorly (lateral to the mammillothalamic tract) and then curve posterolaterally and superiorly to reach the lateropolaris (32) and ventrooralis (33) thalamic nuclei. The thalamic fasciculus is posterior and slightly superior to the lenticular fasciculus, but almost parallel, and the 2 structures are separated by the hyperintense superior portion of the ZI.

The ansa peduncularis (4) is a functionally unrelated but spatially proximate pathway to the pallidothalamic tracts that represents confluent projections from the amygdala, temporal, and olfactory cortex to the dorsomedial thalamic nucleus.^{48,49} This structure appears continuous with the anterior inferior thalamic peduncle, appearing as a sheet-like vertically oriented structure lateral to the postcommissural fornix, anterosuperior to the ansa lenticularis, posteroinferior to the anterior commissure, and su-

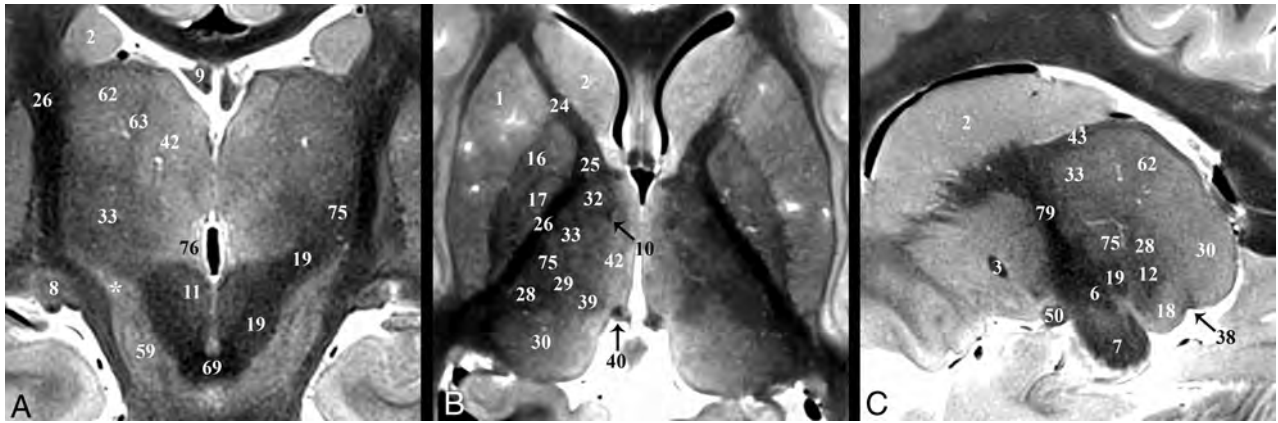


FIG 6. Coronal, axial, and sagittal images illustrating the superior ascent of the dentatorubrothalamic tract (19) to the Vim nucleus (75). A, Slight obliquity of the image allows depiction of the Vim and DRT on the left and the posterior aspect of the relatively more hyperintense nucleus ventrooralis (33) on the right (zona incerta labeled with asterisks). The relationship of the PLIC (26), nucleus ventrocaudalis anterior (28), and nucleus ventrocaudalis posterior (29) nuclei to the Vim is also illustrated. For completeness, the interested reader can find the proximal or prerubral component of the dentatorubrothalamic pathway also demonstrated in On-line Fig 3 of the previous report.⁵⁷

terior to the optic tract (Fig 2A, On-line Fig 2D, and Fig 5). It is less compact and hypointense compared with the ansa lenticularis.

Thalamus and Dentatorubrothalamic Tract

Major thalamic nuclei, especially inferior and lateral ones, can be identified with TSE contrast. The medial PLIC border (26) was easily discriminated from the adjacent lateral sensorimotor thalamic nuclei: from anterior to posterior: nucleus lateropolaris (32), nucleus ventrooralis (33), Vim (75), nucleus ventrocaudalis posterior (29), and nucleus ventrocaudalis anterior (28) (Fig 6B). Functional neurosurgeons traditionally use a nomenclature for the thalamic nuclei whereby the ventralis lateralis (VL) nucleus is subdivided into an anterior nucleus ventrooralis posterior (Vop) and posterior Vim nucleus. Extending from the contralateral brain stem via the decussation of the superior cerebellar peduncle (69) is the dentatorubrothalamic tract (19, DRT), which envelops the red nucleus (11) before terminating in the Vim (75) (Fig 6A). An additional cerebellar thalamic connection that bypasses the red nucleus can be seen in On-line Fig 2E, -F and Fig 3B between the cerebellothalamic tract (inseparable from the DRT [19] with TSE) and the thalamic fasciculus (27). The Vim is an intermediate-intensity nucleus located in the midportion of the inferolateral thalamus and serves as a common target for DBS treatment of essential tremor.¹⁸ It is posterior to the inferior half of the relatively more hyperintense nucleus ventrooralis (33) (Fig 6A, -B). The hyperintense nucleus dorsalis oralis (62) sits along the superior border of the Vim (Fig 6A, -C). The nucleus ventrocaudalis anterior and nucleus ventrocaudalis posterior make up the posterior and posteromedial borders of the Vim and are slightly more hypointense and hyperintense, respectively (On-line Fig 2E, -F and Fig 6B, -C).

The internal medullary lamina is visible as a thin dark sheet that envelops the centralis nucleus (39) (Fig 2E and On-line Fig 1F) and the anterior nucleus (41) anterosuperiorly (Fig 2F and On-line Fig 1E). The dark fibers of the medial lemniscus (12) define the inferior margins of the nucleus ventrocaudalis anterior and the anterior margin of the hyperintense medial geniculate nucleus (18) (On-line Fig 2F). The medial geniculate nucleus is

further bordered inferomedially and superolaterally by the brachium of the inferior colliculus (20) and superior colliculus, respectively (38) (Fig 2B, -C). The hyperintense lateral geniculate nucleus (8) is best identified in the coronal plane at the terminations of the hypointense optic tract (50) (On-line Fig 1D, -F).

Fornix and Mammillothalamic Tract

The fornix (9) is the major output pathway from the hippocampus to the medial diencephalon and serves episodic memory.^{50,51} The fornix originates from the fimbria of the hippocampus and then curves superiorly and then anteriorly (posterior and/or superior to the medial thalamus and third ventricle). Anteriorly, the compact hypointense fornix columns are superior to the anterior commissure (3), forming the anteromedial margins of the foramen of Monro (Fig 4). Projections of the precommissural fornix are not distinct from the septal and other nuclei. The diagonal band of Broca (52) appears as a faint dark band anterior to the commissure but does not appear continuous with the fornix columns (On-line Fig 1A). The fornix and postcommissural fornix immediately above and below the anterior commissure measured 3.5 ± 0.9 by 1.8 ± 0.4 mm and 2.4 ± 0.4 by 1.8 ± 0.2 mm, respectively, (anterior-posterior by left-right in the axial plane). Below the commissure was a 1.4-mm^2 or 39% decrease in cross-sectional area (*t* test, *P* = .001). Posterior and slightly superior to where this focal narrowing occurs (Fig 4A, -B) is a separate hypointense compact lateral projection (Fig 4C). This represents the less well-understood direct hippocampal-diencephalic pathway (36) that bypasses the mammillary bodies and may be important for recollective recognition memory.⁵⁰ The proximal aspect of this projection abuts the inferolateral margin of the stria medullaris. It then ascends superiorly and spreads/thins across the anterior surface of anterior thalamic nucleus (41). The postcommissural fornix descends and curves posteriorly to envelope the superolateral surface of the hyperintense mammillary bodies (56) (On-line Figs 1C and 2B and Fig 4A).

The mammillothalamic tract (10) is a separate hypointense white matter bundle originating from the anteromedial and superomedial surfaces of the mammillary bodies, which first courses posterolaterally for 8–10 mm (with a concave appearance

directed anterior and lateral) (On-line Fig 2B, -C). Medial to the thalamic fasciculus (27), the mammillothalamic tract turns sharply upward and ascends vertically to envelope the most inferior and inferolateral surfaces of the anterior nucleus of the thalamus (Fig 4D). The proximal vertical portion of the mammillothalamic tract measured 1.8 ± 0.4 by 1.4 ± 0.2 mm in the axial plane (or a 1.9 ± 0.5 mm² area) with the more distal portion becoming less compact and distinct.

DISCUSSION

We used a standard clinical 3T MR imaging system and 2D-TSE sequence to generate excellent contrast resolution of basal forebrain anatomy from multiple ex vivo whole-brain specimens. Previous postmortem MR imaging microscopy studies have benefited from ultra-high-field MR imaging (>3T)^{29,52,53} but required dissected samples, long acquisition times, special radiofrequency coils, and a dedicated research support staff, which limits widespread application. Excellent anatomic contrast was derived from the MR imaging sequence without time-consuming off-line mathematic analysis or model-based reconstructions for relaxation mapping^{54,55} or advanced analytical diffusion representations.^{30,56} Validation of tractography and other advanced diffusion contrasts remains limited,³³ whereas TSE contrast largely recapitulates contrast observed over the past 100+ years in histology atlases of the human brain. The current TSE protocol can be used to both validate and complement diffusion MR imaging and tractography for visualizing these structures (or other novel advanced MR imaging methods). Our protocol can be used by many readers using available clinical equipment with reasonable scan times. We are currently developing a similar 3D-TSE approach that overcomes coverage limitations of the 2D sequence, facilitates higher isotropic spatial resolutions, and can more efficiently generate multiplanar reformats from a single acquisition.

We sought to create an accessible introduction to the subcortical anatomy poorly visualized with current clinical MR imaging protocols. This TSE sequence was previously applied to brain stem anatomy.⁵⁷ Here, we focused on potential functional neurosurgery targets that are not well-understood by clinical neuroradiologists. Almost all clinical brain MR imaging protocols include T2-weighted contrast so that neuroanatomy using this TSE protocol may be easier to learn, retain, and mentally map onto clinical MR imaging scans obtained at lower spatial resolution. Compared with using postmortem brains for gross dissection for teaching neuroanatomy, MR microscopy quickly produces “digital specimens” that do not degrade with time or repeated use. The same specimen can be scanned orthogonally or in many different oblique planes and at different spatial resolutions without tissue destruction. Furthermore, these specimens can be reviewed using clinical PACS or other readily available software tools and can be easily shared across individual teaching sites. Finally, it is straightforward to apply this protocol to multiple whole-brain samples, increasing trainee exposure to normal individual anatomic variations (On-line Fig 3).

The direct or indirect imaging identification of target basal forebrain structures is a key requirement for modern functional neurosurgery. However, conventional MR imaging poorly displays internal anatomic boundaries of several clinically targeted

structures. Functional surgery therefore relies on indirect targeting using measurements of intercommissural distances, third ventricle widths, or other calculations from stereotactic atlases⁵⁸ originally derived from internal landmarks on pneumoencephalography.⁵⁹ A common concern is that indirect targeting methods are vulnerable to individual variability in subthalamic and thalamic nuclei positions, or even right-left asymmetries within the same individual.⁶⁰⁻⁶⁵ This vulnerability may result in a decreased therapeutic profile and increased risk for adverse effects such as motor contractions, perioral numbness, and imbalance when targeting the thalamic Vim in patients with essential tremor.⁶⁶

A previous study reported a large range of coronal angulations for the long axis of the subthalamic nucleus in the sagittal plane (range, 15°–57°) that resulted in the DBS electrode tip sometimes terminating in the zona incerta instead of the inferomedial subthalamus. This zona incerta stimulation was associated with potentially better therapeutic outcomes, but different adverse events.²² Hence, 1- to 2-mm targeting differences can be quite clinically important in the complex, compactly-organized basal forebrain. In 11 SUDC brains, we only observed small 0.2- to 0.3-mm right-left differences for superior-inferior and anterior-posterior lengths in the STN ($P = .047$ and $.084$, respectively) (Table 2). The results had an estimated 80% statistical power to detect a right-left difference of greater than 0.3- to 0.6-mm length, 5.1°–5.5° angulation, or 0.3–0.5 mm in stereotactic coordinates. Institutional coordinates resulted in similar target locations for right and left nuclei, but with equal placement of the electrode tip in either the medial or lateral segment of the posterior third of the STN. The medial-lateral dimensions of the subthalamic nuclei also showed the largest coefficient of variation (Table 2). This may be because of less contrast resolution between the STN and adjacent inferior internal capsule. The angulation in the sagittal plane and the most inferior stereotactic point for the subthalamic nucleus also showed larger individual variation as reflected by the coefficient of variation. Similarly, Morel⁶⁷ reported greater individual variation in lateral measurements for thalamic structures relative to the midsagittal plane and recorded a ~1.5-mm variation in microelectrode depth for entering the posterior subthalamus in 20 patients. Other measurements showed little individual variability, and we observed much less angular variation in the coronal plane (range, 48°–69°) compared with a previous report.²² These data illustrate that postmortem MR imaging with high-resolution TSE sequences facilitates performing these types of measurements in many brain samples, and further research using this paradigm may be used to better understand stereotactic targeting.

Size measurements for selected myelinated structures within the basal forebrain reflect dark structure to bright background contrast. These measurements may be affected by the degree of myelination and the number and diameter of axons. The post-commissural fornix was continuous with the column of the fornix, but 39% smaller just below the anterior commissure. This caliber change appears posterior to the commissure in Fig 4B. Despite axonal projections from the fornix to the anterior septal nuclei (eg, diagonal band of Broca),⁵⁰ we did not visualize a discrete projection from the fornix columns on TSE contrast, whereas a large portion of dark, presumably myelinated fibers

project from the fornix columns first lateral and then arching superiorly into the anterior nucleus of the thalamus just above the commissure (Figs 2D and 4C) (the “direct” pathway).⁵⁰ Because this projection has a similar MR imaging appearance to the column and postcommissural fornix, we suggest that this projection may be the dominant source of reduced caliber instead of projections to the precommissural fornix and thus a major efferent projection.

The ansa lenticularis, a key projection from the globus pallidus internus, is easily recognized on TSE MR imaging contrast (Figs 4B and 5E). In the axial plane the lateral two-thirds of this structure gently arcs with posterior concavity inferior to the globus pallidus, then near the midline the terminal aspects of the structure sharply and compactly curve posterior and superiorly to meet the lenticular fasciculus in a complex configuration that is challenging to appreciate with individual 2D images. The ansa lenticularis is relatively small with a cross-sectional area of $1.1 \pm 0.3 \text{ mm}^2$ when the lateral proximal portion is measured transverse to its long axis in the sagittal plane. If we calculate the ansa lenticularis volume as a cylinder, this implies that even if centered and linearly oriented within a 2-mm isotropic voxel, this structure would only occupy 28% of the volume. This small occupancy and its true looping course illustrate the difficulty of resolving internal medial forebrain pathways with lower SNR techniques such as diffusion MR imaging, for which acquiring isotropic voxels below 2 mm is challenging on current MR imaging systems. TSE or other non-diffusion-weighted sequences can be used to complement and validate future diffusion-based methods to resolve these functionally important structures with emerging clinical interest.

The external validity of the contrast and reported measurements may be affected by formaldehyde fixation,^{39–41} postmortem interval,⁴² agonal changes,⁶⁸ SUDC pathology,⁶⁹ pediatric brains,^{70,71} or distortion/relaxation of the brain by removal during postmortem examination. Preliminary experiments have not identified contrast differences between pediatric and elderly cadaver brains using the TSE sequence, though this requires future investigation. SUDC brain measurements may not reflect larger right-left asymmetries or individual variability that develop later in adulthood. However, the anterior-posterior commissure distance in 11 SUDC samples was $23.8 \pm 2.4 \text{ mm}$, similar to adult brains.^{67,72} Previous work in adult brains also demonstrated that this distance only differed by 2%–4% between premorbid in vivo MR imaging and postmortem measurement following formaldehyde fixation, sectioning, and histologic staining⁶⁷ (note, these latter 2 steps were not performed prior to imaging SUDC brains). Several of the potential confounding factors listed above may also affect histology data in stereotactic atlases currently used for functional neurosurgery planning in living patients.^{58,67} In previous atlases, anatomic assignments were determined on the basis of perceived semiquantitative changes to cell shape, size, volume fraction, staining affinity, and the density of myelin present.⁶⁴ The boundaries were often determined by a single experienced individual (eg, Dr Hassler).⁵⁸ The location and area/volume of anatomic assignments based on TSE appear largely concordant with histology atlases, but there may be differences between anatomic assignments using TSE MR imaging and existing atlases, particularly for regions with less contrast such as the internal thalamic

nuclei.^{37,64,73,74} A detailed correlation of postmortem TSE contrast and measurements to histology is planned. The inherent portability of MR imaging data, multiplanar capabilities, reproducibility across multiple samples, and a more quantifiable basis for image contrast suggest that TSE MR imaging data could be used to create a compelling complementary atlas of the basal forebrain.

CONCLUSIONS

A modified TSE T2-weighted sequence generated excellent contrast resolution of basal forebrain structures relevant to emerging functional neurosurgery applications using relatively short scan times and a widely available 3T MR imaging system. Multiplanar images provided excellent visualization of specific nuclei and small internal myelinated pathways not well-understood by clinical neuroradiologists.

ACKNOWLEDGMENTS

The authors thank the medical examiners, coroners, and the SUDC families for their support of this research. The senior author thanks Jim Babb, PhD, for assistance with the statistical analysis.

Disclosures: Laura Crandall—RELATED: Grant: SUDC Foundation and Finding a Cure for Epilepsy and Seizures*; Support for Travel to Meetings for the Study or Other Purposes: SUDC Foundation, Comments: travel reimbursement only for meetings attended on behalf of the Foundation; Other: Lange Shaw Donor-Advisor Fund, Comments: Funds support my effort in the study*; UNRELATED: Board Membership: SUDC Foundation, Comments: volunteer position; Travel/Accommodations/Meeting Expenses Unrelated to Activities Listed: SUDC Foundation, Comments: travel reimbursement only for meetings attended on behalf of the Foundation. Thomas Wisniewski—RELATED: Grant: National Institute on Aging, National Institutes of Health grant No. AG08051.* Orrin Devinsky—UNRELATED: Board Membership: SUDC Foundation, Comments: research grants to New York University Langone Health*; Other: National Institute of Neurological Disorders and Stroke, Comments: research support for Sudden unexpected death in epilepsy (SUDEP) research. Timothy M. Shepherd—RELATED: Grant: SUDC Foundation, Taylor McKeen Shelton Foundation, Finding a Cure for Epilepsy and Seizures fund, National Institutes of Health—National Institute on Aging AG048622.* Alon Y. Mogilner—UNRELATED: Consultancy: Medtronic, St. Jude, Brainlab, Boston Scientific, Alpha Omega, Comments: consulting for issues related to deep brain stimulation; Stock/Stock Options: ElectroCORE, Comments: Stock warrants were not exercised. *Money paid to institution.

REFERENCES

1. Carpenter MB, Strong OS, Truex RC. *Human Neuroanatomy: (Formerly Strong and Elwyn's Human Neuroanatomy)*. 7th ed. Baltimore: Lippincott Williams and Wilkins; 1976
2. Haines DE. *Neuroanatomy: An Atlas of Structures, Sections and Systems*. 6th ed. Philadelphia: Lippincott Williams and Wilkins; 2004
3. Kochunov P, Ramage AE, Lancaster JL, et al. **Loss of cerebral white matter structural integrity tracks the gray matter metabolic decline in normal aging.** *Neuroimage* 2009;45:17–28 CrossRef Medline
4. Nieuwenhuys R, Voogd J, van Huijzen C. *The Human Central Nervous System*. 4th ed. Berlin: Springer-Verlag; 2008
5. Gustin SM, Peck CC, Wilcox SL, et al. **Different pain, different brain: thalamic anatomy in neuropathic and non-neuropathic chronic pain syndromes.** *J Neurosci* 2011;31:5956–64 CrossRef Medline
6. Danet L, Barbeau EJ, Eustache P, et al. **Thalamic amnesia after infarct: the role of the mammillothalamic tract and mediodorsal nucleus.** *Neurology* 2015;85:2107–15 CrossRef Medline
7. Krystkowiak P, Martinat P, Defebvre L, et al. **Dystonia after striato-pallidal and thalamic stroke: clinicoradiological correlations and pathophysiological mechanisms.** *J Neurol Neurosurg Psychiatry* 1998;65:703–08 CrossRef Medline

8. Minagar A, Barnett MH, Benedict RH, et al. **The thalamus and multiple sclerosis: modern views on pathologic, imaging, and clinical aspects.** *Neurology* 2013;80:210–19 CrossRef Medline
9. Aggleton JP, Pralus A, Nelson AJ, et al. **Thalamic pathology and memory loss in early Alzheimer's disease: moving the focus from the medial temporal lobe to Papez circuit.** *Brain* 2016;139(Pt 7):1877–90 CrossRef Medline
10. Hamani C, Saint-Cyr JA, Fraser J, et al. **The subthalamic nucleus in the context of movement disorders.** *Brain* 2004;127:4–20 CrossRef Medline
11. Etemadifar M, Abtahi SH, Abtahi SM, et al. **Hemiballismus, hyperphagia, and behavioral changes following subthalamic infarct.** *Case Rep Med* 2012;2012:768580 CrossRef Medline
12. Kim HJ, Moon WJ, Oh J, et al. **Subthalamic lesion on MR imaging in a patient with nonketotic hyperglycemia-induced hemiballismus.** *AJNR Am J Neuroradiol* 2008;29:526–27 CrossRef Medline
13. Lanciego JL, Luquin N, Obeso JA. **Functional neuroanatomy of the basal ganglia.** *Cold Spring Harb Perspect Med* 2012;2:a009621 CrossRef Medline
14. Anderson JC, Costantino MM, Stratford T. **Basal ganglia: anatomy, pathology, and imaging characteristics.** *Curr Probl Diagn Radiol* 2004;33:28–41 CrossRef Medline
15. Maximo JO, Kana RK. **Aberrant “deep connectivity” in autism: a cortico-subcortical functional connectivity magnetic resonance imaging study.** *Autism Res* 2019;12:384–400 CrossRef Medline
16. Pagnozzi AM, Conti E, Calderoni S, et al. **A systematic review of structural MRI biomarkers in autism spectrum disorder: a machine learning perspective.** *Int J Dev Neurosci* 2018;71:68–82 CrossRef Medline
17. Walkup JT, Mink JW, Hollenbeck PJ, eds. *Advances in Neurology: Tourette Disorder.* Vol. 99. Philadelphia: Lippincott Williams and Wilkins; 2006
18. Miciocinovic S, Somayajula S, Chitnis S, et al. **History, applications, and mechanisms of deep brain stimulation.** *JAMA Neurol* 2013;70:163–71 CrossRef Medline
19. Benabid AL, Torres N. **New targets for DBS.** *Parkinsonism Rel Disord* 2012;18(Suppl 1):S21–23 CrossRef Medline
20. Peisker CB, Schüller T, Peters J, et al. **Nucleus accumbens deep brain stimulation in patients with substance use disorders and delay discounting.** *Brain Sci* 2018;8:21 CrossRef Medline
21. Fisher R, Salanova V, Witt T, et al; SANTE Study Group. **Electrical stimulation of the anterior nucleus of thalamus for treatment of refractory epilepsy.** *Epilepsia* 2010;51:899–908 CrossRef Medline
22. Plaha P, Ben-Shlomo Y, Patel NK, et al. **Stimulation of the caudal zona incerta is superior to stimulation of the subthalamic nucleus in improving contralateral parkinsonism.** *Brain* 2006;129:1732–47 CrossRef Medline
23. Blomstedt P, Fytagoridis A, Åström M, et al. **Unilateral caudal zona incerta deep brain stimulation for Parkinsonian tremor.** *Parkinsonism Rel Disord* 2012;18:1062–66 CrossRef
24. Manova ES, Habib CA, Boikov AS, et al. **Characterizing the mesencephalon using susceptibility-weighted imaging.** *AJNR Am J Neuroradiol* 2009;30:569–74 CrossRef Medline
25. Santin MD, Didier M, Valabrègue R, et al. **Reproducibility of R2* and quantitative susceptibility mapping (QSM) reconstruction methods in the basal ganglia of healthy subjects.** *NMR Biomed* 2017;30 CrossRef Medline
26. Doganay S, Gumus K, Koc G, et al. **Magnetic susceptibility changes in the basal ganglia and brain stem of patients with Wilson's disease: evaluation with quantitative susceptibility mapping.** *Magn Reson Med Sci* 2018;17:73–79 CrossRef Medline
27. Xiao Y, Zitella LM, Duchin Y, et al. **Multimodal 7T imaging of thalamic nuclei for preclinical deep brain stimulation applications.** *Front Neurosci* 2016;10:264. CrossRef Medline
28. Lenglet C, Abosch A, Yacoub E, et al. **Comprehensive in vivo mapping of the human basal ganglia and thalamic connectome in individuals using 7T MRI.** *PLoS One* 2012;7:e29153 CrossRef Medline
29. Massey LA, Miranda MA, Zrinzo L, et al. **High resolution MR anatomy of the subthalamic nucleus: imaging at 9.4 T with histological validation.** *Neuroimage* 2012;59:2035–44 CrossRef Medline
30. Calamante F, Oh SH, Tournier JD, et al. **Super-resolution track-density imaging of thalamic substructures: comparison with high-resolution anatomical magnetic resonance imaging at 7.0T.** *Hum Brain Mapp* 2013;34:2538–48 CrossRef Medline
31. Cho ZH, Law M, Chi JG, et al. **An anatomic review of thalamolimbic fiber tractography: ultra-high resolution direct visualization of thalamolimbic fibers anterior thalamic radiation, superolateral and inferomedial medial forebrain bundles, and newly identified septum pellucidum tract.** *World Neurosurg* 2015;83:54–61 CrossRef Medline
32. Rozanski VE, da Silva NM, Ahmadi SA, et al. **The role of the pallidothalamic fibre tracts in deep brain stimulation for dystonia: a diffusion MRI tractography study.** *Hum Brain Mapp* 2017;38:1224–32 CrossRef Medline
33. Maier-Hein KH, Neher PF, Houde J, et al. **The challenge of mapping the human connectome based on diffusion tractography.** *Nature Commun* 2017;8:1–13 CrossRef Medline
34. Miller S, Goldberg J, Bruno M, et al. **Intrinsic T2-weighted MRI contrast of the subcortical human brain.** In: *Proceedings of the Scientific Assembly and National Meeting of the Radiological Society of North America*, Chicago, Illinois. November 26 to December 1, 2017; Abstract ID: 27997
35. Warner JJ. *Atlas of Neuroanatomy: With Systems Organization and Case Correlations.* Boston: Butterworth-Heinemann; 2001
36. DeArmond SJ, Fusco MM, Dewey MM. *Structure of the Human Brain: A Photographic Atlas.* 3rd ed. New York: Oxford University Press; 1989
37. Olszewski J, Baxter D. *Cytoarchitecture of the Human Brain Stem.* 2nd ed. New York: Karger; 1982
38. Crandall L, Devinsky O. **Sudden unexplained death in children.** *Lancet Child Adolesc Health* 2017;1:8–9 CrossRef Medline
39. Dawe RJ, Bennett DA, Schneider JA, et al. **Postmortem MRI of human brain hemispheres: T2 relaxation times during formaldehyde fixation.** *Magn Reson Med* 2009;61:810–18 CrossRef Medline
40. Shepherd TM, Thelwall PE, Stanis GJ, et al. **Aldehyde fixative solutions alter the water relaxation and diffusion properties of nervous tissue.** *Magn Reson Med* 2009;62:26–34 CrossRef Medline
41. Yong-Hing CJ, Obenaus A, Stryker R, et al. **Magnetic resonance imaging and mathematical modeling of progressive formalin fixation of the human brain.** *Magn Reson Med* 2005;54:324–32 CrossRef Medline
42. Shepherd TM, Flint JJ, Thelwall PE, et al. **Postmortem interval alters the water relaxation and diffusion properties of rat nervous tissue: implications for MRI studies of human autopsy samples.** *Neuroimage* 2009;44:820–26 CrossRef Medline
43. Naidich TP, Duvernoy HM, Delman BN, et al. *Duvernoy's Atlas of the Human Brain Stem and Cerebellum.* New York: Springer-Verlag/Wien; 2009
44. Hassler R. **Anatomy of the thalamus.** In: Schaltenbrand G, Bailey P, eds. *Introduction to Stereotaxis with an Atlas of the Human Brain.* Stuttgart: Thieme; 1959:230–90
45. Mitrofanis J. **Some certainty for the “zone of uncertainty”? Exploring the function of the zona incerta.** *Neuroscience* 2005;130:1–15 CrossRef Medline
46. Nagaseki Y, Shibasaki T, Hirai T, et al. **Long-term follow-up results of selective VIM-thalamotomy.** *J Neurosurg* 1986;65:296–302 CrossRef Medline
47. Gallay MN, Jeanmonod D, Liu J, et al. **Human pallidothalamic and cerebellothalamic tracts: anatomical basis for functional stereotactic neurosurgery.** *Brain Struct Funct* 2008;212:443–63 CrossRef Medline
48. Pascalau R, Popa Stanila R, Sfrangeu S, et al. **Anatomy of the limbic white matter tracts as revealed by fiber dissection and tractography.** *World Neurosurg* 2018;113:e672–89 CrossRef Medline
49. Averbach P. **Lesions of the nucleus ansae peduncularis in neuropsychiatric disease.** *JAMA Neurol* 1981;38:230–35 Medline

50. Aggleton JP, O'Mara SM, Vann SD, et al. **Hippocampal-anterior thalamic pathways for memory: uncovering a network of direct and indirect actions.** *Eur J Neurosci* 2010;31:2292–307 CrossRef Medline
51. Bubb EJ, Kinnavane L, Aggleton JP. **Hippocampal - diencephalic - cingulate networks for memory and emotion: an anatomical guide.** *Brain Neurosci Adv* 2017;1 CrossRef Medline
52. Fatterpekar GM, Delman BN, Boonn WW, et al. **MR microscopy of normal human brain.** *Magn Reson Imaging Clin N Am* 2003;11:641–53 CrossRef Medline
53. Lemaire JJ, Sakka L, Ouchchane L, et al. **Anatomy of the human thalamus based on spontaneous contrast and microscopic voxels in high-field magnetic resonance imaging.** *Neurosurgery* 2010;66(3 Suppl Operative):161–72 CrossRef Medline
54. Deoni SC, Josseau MJ, Rutt BK, et al. **Visualization of thalamic nuclei on high resolution, multi-averaged T1 and T2 maps acquired at 1.5 T.** *Hum Brain Mapp* 2005;25:353–59 CrossRef Medline
55. Traynor CR, Barker GJ, Crum WR, et al. **Segmentation of the thalamus in MRI based on T1 and T2.** *Neuroimage* 2011;56:939–50 CrossRef Medline
56. Lambert C, Simon H, Colman J, et al. **Defining thalamic nuclei and topographic connectivity gradients in vivo.** *Neuroimage* 2017;158:466–79 CrossRef Medline
57. Hoch MJ, Bruno MT, Faustin A, et al. **3T MRI whole-brain microscopy discrimination of subcortical anatomy, part 1: brain stem.** *AJNR Am J Neuroradiol* 2019;40:401–07 CrossRef Medline
58. Schaltenbrand G, Wahren W. *Atlas of Stereotaxy of the Human Brain.* 2nd ed. Stuttgart: Thieme; 1977
59. Spiegel EA, Wycis HT, Marks M, et al. **Stereotaxic apparatus for operations on the human brain.** *Science* 1947;106:349–50 CrossRef Medline
60. Daniluk S, G Davies K, Ellias SA, et al. **Assessment of the variability in the anatomical position and size of the subthalamic nucleus among patients with advanced Parkinson's disease using magnetic resonance imaging.** *Acta Neurochir (Wien)* 2010;152:201–10; discussion 210 CrossRef Medline
61. Littlechild P, Varma TR, Eldridge PR, et al. **Variability in position of the subthalamic nucleus targeted by magnetic resonance imaging and microelectrode recordings as compared to atlas co-ordinates.** *Stereotact Funct Neurosurg* 2003;80:828–27 Medline
62. Brierley JB, Beck E. **The significance in human stereotactic brain surgery of individual variation in the diencephalon and globus pallidus.** *J Neurol Neurosurg Psychiatry* 1959;22:287–98 CrossRef Medline
63. Eidelberg D, Galaburda AM. **Symmetry and asymmetry in the human posterior thalamus, I: cytoarchitectonic analysis in normal persons.** *Arch Neurol* 1982;39:325–32 CrossRef Medline
64. Van Buren JM, Borke RC. *Variations and Connections of the Human Thalamus.* Berlin: Springer-Verlag; 1972
65. Vayssiere N, Hemm S, Cif L, et al. **Comparison of atlas- and magnetic resonance imaging-based stereotactic targeting of the globus pallidus internus in the performance of deep brain stimulation for treatment of dystonia.** *J Neurosurg* 2002;96:673–79 CrossRef Medline
66. Ohye C. **Selective thalamotomy and gamma thalamotomy for parkinson disease.** In: Lozano AM, Gildenberg PL, Tasker RR, eds. *Textbook of Stereotactic and Functional Neurosurgery.* 2nd ed. Berlin: Springer-Verlag; 2009
67. Morel A. *Stereotactic atlas of the human thalamus and basal ganglia.* New York: Informa Healthcare; 2007
68. dos Santos BL, Del-Bel EA, Pittella JE, et al. **Influence of external factors on the preservation of human nervous tissue for histological studies: review article.** *J Bras Patol Med Lab* 2014;50:438–44
69. Krous HF, Chadwick AE, Crandall LA, et al. **Sudden unexpected death in childhood: a report of 50 cases.** *Pediatr Dev Pathol* 2005;8:307–19 CrossRef Medline
70. Gay CT, Hardies LJ, Rauch RA, et al. **Magnetic resonance imaging demonstrates incomplete myelination in 18q- syndrome: evidence for myelin basic protein haploinsufficiency.** *Am J Med Genet* 1997;74:422–31 CrossRef Medline
71. Baierl P, Forster Ch, Fendel H, et al. **Magnetic resonance imaging of normal and pathological white matter maturation.** *Pediatr Radiol* 1988;18:183–89 CrossRef Medline
72. Choi CY, Han SR, Yee GT, et al. **Central core of the cerebrum.** *J Neurosurg* 2011;114:463–69 CrossRef Medline
73. Duvernoy H. *The Human Brain. Surface, Three-Dimensional Sectional Anatomy and MRI.* New York: Springer-Verlag; 1991
74. Morel A, Magnin M, Jeanmonod D. **Multiarchitectonic and stereotactic atlas of the human thalamus.** *J Comp Neurol* 1997;387:588–630 CrossRef Medline

Wall Contrast Enhancement of Thrombosed Intracranial Aneurysms at 7T MRI

¹T. Sato, ²T. Matsushige, ³B. Chen, ⁴O. Gembruch, ⁵P. Dammann, ⁶R. Jabbarli, ⁷M. Forsting, ⁸A. Junker, ⁹S. Maderwald, ¹⁰H.H. Quick, ¹¹M.E. Ladd, ¹²U. Sure, and ¹³K.H. Wrede

ABSTRACT

BACKGROUND AND PURPOSE: The pathophysiology of wall contrast enhancement in thrombosed intracranial aneurysms is incompletely understood. This in vivo study aimed to investigate wall microstructures with gadolinium-enhanced 7T MR imaging.

MATERIALS AND METHODS: Thirteen patients with 14 thrombosed intracranial aneurysms were evaluated using a 7T whole-body MR imaging system with nonenhanced and gadolinium-enhanced high-resolution MPRAGE. Tissue samples were available in 5 cases, and histopathologic findings were correlated with 7T MR imaging to identify the gadolinium-enhancing microstructures.

RESULTS: Partial or complete inner wall enhancement correlated with neovascularization of the inner wall layer and the adjacent thrombus. Additional partial or complete outer wall enhancement can be explained by formation of vasa vasorum in the outer aneurysm wall layer. The double-rim enhancement correlated with perifocal edema and wall histologic findings suggestive of instability.

CONCLUSIONS: Two distinct aneurysm wall microstructures responsible for gadolinium enhancement not depictable at lower spatial resolutions can be visualized in vivo using high-resolution gadolinium-enhanced 7T MR imaging.

Treatment of thrombosed intracranial aneurysms, most of which are large (12–24 mm) or giant (>25 mm), is complex and associated with a high risk of complications.^{1,2} Previous studies have suggested a different pathophysiology of thrombosed intracranial aneurysms compared with nonthrombosed aneurysms.^{3,4} The mechanisms on the cellular level remain unclear, but histopathologic studies have improved our understanding of the pathophysiology.⁵

Histopathologic studies regarding the thrombosed intracranial aneurysm wall showed neovascularization or vascular chan-

nel lining of the intima, as well as thrombus formation in the aneurysm dome far away from the parent artery. These findings seem to play an important role in aneurysm growth.^{4,6–8} In rare cases of giant fusiform thrombosed aneurysms, persistent growth was observed even after proximal occlusion and trapping.^{3,9}

Wall-enhancement patterns of thrombosed intracranial aneurysms on CT and MR imaging are recognized as one of the clinical-alert signs indicating their unstable behavior.^{3,9} However, in current imaging techniques, wall enhancement is visualized as a single rim due to insufficient spatial resolution, and the microstructures cannot be discriminated in vivo.

Recent research has shown that ultra-high spatial resolution 7T MR imaging is an excellent tool for in vivo visualization of aneurysm microstructures.¹⁰ This study therefore aimed to investigate the microstructure of thrombosed intracranial aneurysm wall-enhancement patterns using ultra-high-field 7T contrast-enhanced MR imaging with direct comparison with histopathologic findings.

MATERIALS AND METHODS

Study Design and Patient Cohort

The study was conducted according to the principles of the Declaration of Helsinki and was Health Insurance Portability and Accountability Act–compliant. The authorized ethics committee of the University Duisburg-Essen approved the study, and all patients provided written informed consent before the examination.

Received February 15, 2019; accepted after revision April 25.

From the Department of Neurosurgery (T.S., T.M., B.C., O.G., P.D., R.J., U.S., K.H.W.), University Hospital Essen, Department of Diagnostic and Interventional Radiology and Neuroradiology (M.F.), Institute of Neuropathology (A.J.), High Field and Hybrid MR Imaging (H.H.Q.), and Erwin L. Hahn Institute for Magnetic Resonance Imaging (T.S., T.M., B.C., O.G., P.D., S.M., H.H.Q., M.E.L., K.H.W.), University Duisburg-Essen, Essen, Germany; Department of Neurosurgery (T.S.), Fukushima Medical University, Fukushima, Japan; Department of Neurosurgery (T.M.), Graduate School of Biomedical and Health Sciences, Hiroshima University, Hiroshima, Japan; Department of Neurosurgery and Interventional Neuroradiology (T.M.), Hiroshima City Asa Citizens Hospital, Hiroshima, Japan; Medical Physics in Radiology (M.E.L.), German Cancer Research Center, Heidelberg, Germany; and Faculty of Physics and Astronomy and Faculty of Medicine (M.E.L.), University of Heidelberg, Heidelberg, Germany.

Karsten H. Wrede, Bixia Chen, and Oliver Gembruch were supported by the University Duisburg-Essen (Programm zur internen Forschungsförderung Essen).

Please address correspondence to Taku Sato, MD, PhD, University Hospital Essen, Department of Neurosurgery, Hufelandstr 55, 45147 Essen, Germany; e-mail: Taku.Sato@uk-essen.de

<http://dx.doi.org/10.3174/ajnr.A6084>

Patient demographics and anatomic characteristics

Aneurysm No.	Patient No.	Age (yr)	Sex	Location	Maximum Diameter		Wall		Perifocal Edema	Treatment	Pathology
					(mm)	Thrombosis	Contrast-Enhancement Pattern				
1 ^a	2	75	M	BA	27.2	Complete	Double (partial)	+	Observation	—	
2 ^a	3	80	M	MCA	29.0	Complete	Double (complete)	+	Observation	—	
3 ^a	4	61	F	MCA	26.0	Partial	Double (complete)	+	Clipping	+	
4	8	56	M	MCA	29.6	Partial	Double (Partial)	+	Clipping	+	
5	10	53	M	MCA	14.2	Partial	Double (Partial)	+	Clipping	+	
6	13	44	F	MCA	28.2	Partial	Double (Partial)	+	Clipping	+	
7	5	55	M	MCA	25.0	Partial	Double (complete)	+	Clipping	—	
8	5	55	M	dACA	11.0	Partial	Single	—	Clipping	—	
9 ^a	1	56	F	ICA	37.9	Partial	Single	—	Endovascular ^b	—	
10	6	52	F	ICA	23.2	Partial	Single	—	Endovascular	—	
11	7	63	F	ICA	21.4	Partial	Single	—	Endovascular	—	
12	9	70	F	MCA	15.6	Partial	Single	—	Clipping	—	
13	11	43	M	ICA	36.0	Partial	Single	—	Endovascular ^b	—	
14	12	50	F	MCA	21.6	Partial	Single	—	Clipping	+	

Note:—BA indicates basilar artery; dACA, distal anterior cerebral artery; +, Yes; —, No.

^a Aneurysms 1, 2, 3 and 9 have been reported in the context of giant intracranial aneurysms imaged at 7T MRI.¹⁰

^b Parent vessel occlusion.

Patients were prospectively included between January 2011 and November 2018. The study cohort comprised 6 men and 7 women with an average age of 58.3 years (range, 43–80 years). Inclusion criteria were the following: 1) patients with a thrombosed intracranial aneurysm diagnosed by digital subtraction angiography and conventional CT or 3T MR imaging, 2) 18 years of age or older, and 3) able to give informed consent. Exclusion criteria were the following: 1) presence of a cardiac pacemaker or any other electronic implant, 2) pregnancy or breastfeeding, 3) claustrophobia, or 4) patients needing permanent monitoring (eg, subarachnoid hemorrhage). Aneurysms 1, 2, 3, and 9 have previously been presented in a different context of giant intracranial aneurysm imaging.¹⁰

High-Resolution 7T MR Imaging

All subjects were evaluated with a 7T whole-body MR system (Magnetom 7T; Siemens, Erlangen, Germany) equipped with a 1/32-channel Tx/Rx head radiofrequency coil (Nova Medical, Wilmington, Massachusetts). The gradient system provides 40-mT/m maximum amplitude and a slew rate of 200 mT/m/ms. A modified MPRAGE sequence was obtained with the following parameters: FOV = 270 × 236 mm², matrix = 384 × 336, resolution = 0.7 × 0.7 mm², slice thickness = 0.7 mm, TR = 2500 ms, TE = 1.54 ms, flip angle = 7°, bandwidth = 570 Hz/pixel, acquisition time = 6 minutes 13 seconds.^{11,12} Gadolinium contrast-enhanced images were acquired 10 minutes after intravenous administration of a gadobutrol-based macrocyclic contrast agent (1 mmol/mL/10 kg of body weight). High-resolution T2-weighted images were acquired by a modified TSE sequence with the following parameters: FOV = 176 × 256 mm², matrix = 512 × 384, resolution = 0.45 × 0.5 mm², slice thickness = 2 mm, TR = 6000 ms, TE = 100 ms, flip angle = 180°, bandwidth = 264 Hz/pixel, acquisition time = 4 minutes 1 second.

Image Analysis

Two raters assessed the following characteristics in multiplanar image reconstruction using an open-source medical image viewer (Horos, Version 2.0.1; <http://www.horosproject.org/>) in consen-

sus reading: 1) aneurysm wall contrast patterns and 2) presence of perifocal edema.

Histopathologic Examination

Histopathologic samples of 5 thrombosed intracranial aneurysms (aneurysms 3, 4, 5, 6, and 14), harvested during microsurgical clipping of the aneurysm, were analyzed and compared with MR imaging findings. Histopathologic sections from areas corresponding to MR imaging ROIs were prepared with 5- μ m thickness and were stained with hematoxylin-eosin, Verhoeff-Van Gieson, Prussian blue, and CD68. The degree of macrophage infiltration was evaluated with the ImageJ software package (National Institutes of Health, Bethesda, Maryland).¹³ First, CD68 immunostainings were digitized using an Aperio AT2 slide scanner (Leica Microsystems, Wetzlar, Germany). From the scanned files, 4 images with an edge length of 300 μ m and the highest macrophage activity covering the complete thickness of the aneurysm wall were extracted for further analysis. The CD68-positive areas of all 4 ROIs were measured and calculated as a percentage using the ImageJ functions “color threshold” and “analyze particles.”

Statistical Analysis

Due to the limited number of cases, only small-sample tests could be applied. A χ^2 test was used to evaluate the perifocal edema and the contrast-enhancement pattern. Correlation between size and contrast-enhancement patterns was analyzed by a Mann-Whitney *U* test. Significance level α was defined as $P < .05$.

RESULTS

All patients were examined without any adverse events, and all MR imaging sequences were successfully acquired. Basic demographic data for all patients and major anatomic features of the aneurysms are summarized in the Table. Imaging studies revealed complete thrombosis of 2 aneurysms and partial thrombosis in 12 aneurysms. One patient (patient 5) had 2 aneurysms (both with partial thrombosis). The mean diameter of aneurysms was 24.7 mm (standard deviation, 7.4 mm; range, 11.0–37.9 mm). All aneurysms were partially or completely surrounded by brain parenchyma, with perifocal edema present in 7 aneurysms. All throm-

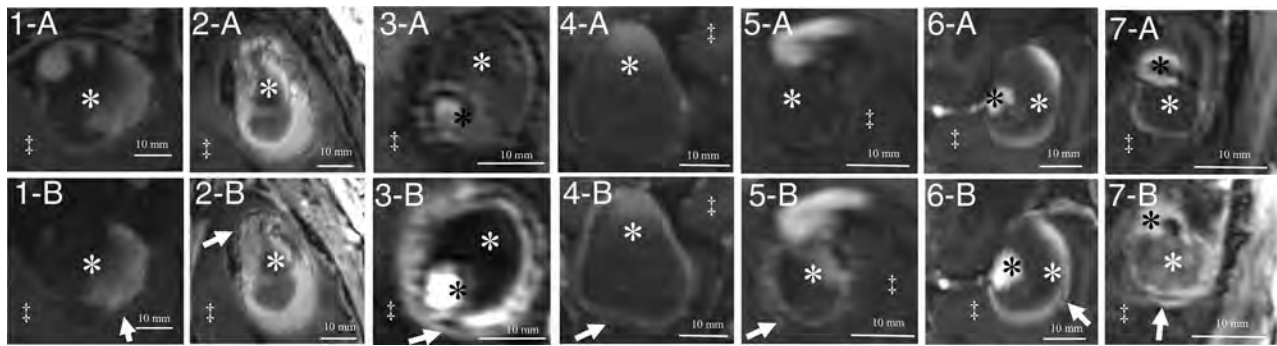


FIG 1. Delineation of thrombosed intracranial aneurysms (A, Nonenhanced MPRAGE; B, Gadolinium-enhanced MPRAGE) with double-rim (aneurysms 1–7) enhancement patterns. Identical structures are marked in all subfigures as follows: *White arrows* indicate a double-rim pattern of the aneurysm walls; *white asterisks*, intraluminal thrombus; *black asterisks*, aneurysm lumen; *double daggers*, brain parenchyma.

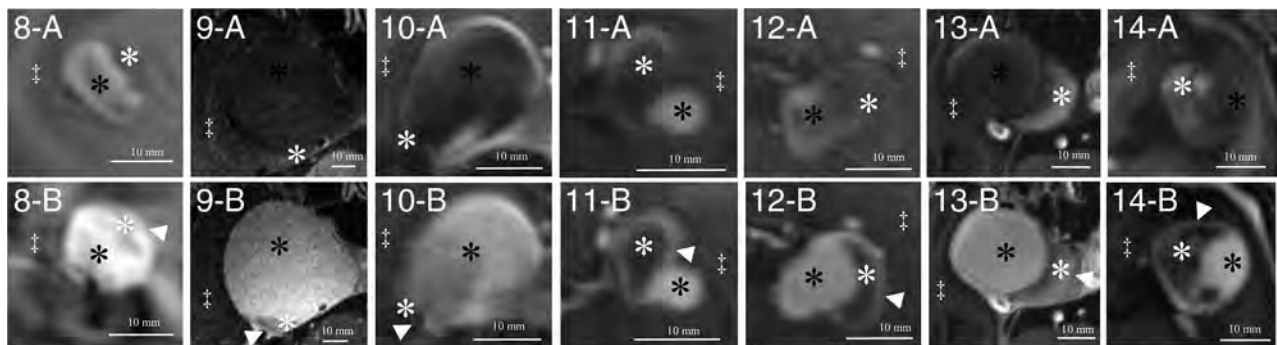


FIG 2. Delineation of thrombosed intracranial aneurysms (A, Nonenhanced MPRAGE; B, Gadolinium-enhanced MPRAGE) with single-rim (aneurysms 8–14) enhancement patterns. Identical structures are marked in all subfigures as follows: *White asterisks* indicate intraluminal thrombus; *black asterisks*, aneurysm lumen; *double daggers*, brain parenchyma; *white arrowheads*, single-rim pattern of the aneurysm walls.

bosed intracranial aneurysms showed partial or complete rim enhancement of the inner wall layer (Figs 1 and 2). Additionally, in 7 aneurysms, the outer aneurysm wall layer showed either partial or complete rim enhancement (Fig 1). All thrombosed intracranial aneurysms with double-rim enhancement presented with perifocal edema ($P < .01$). The maximum aneurysm diameter and presence of perifocal edema showed no correlation ($P = .456$).

In 5 aneurysms, partial resection of the aneurysm dome was required during the microsurgical procedure to expose the neck, and these specimens were suitable for histologic examination. Four of these aneurysms presented with perifocal edema and double-rim enhancement (Fig 3). The thick wall showed vascularization of the intima and the fresh thrombus adjacent to the inner aneurysm layer. The outer signal of the double-rim enhancement correlated with vasa vasorum developing in the outer aneurysm wall layer and macrophage invasion in the media and adventitia. The region with only single-rim enhancement showed an undeveloped vasa vasorum and fewer macrophages (Fig 4). The average CD68-positive areas in the 4 double-rim pattern aneurysm walls were large ($19.5\% \pm 6.4\%$) compared with the single-rim case with a CD68-positive area ($13.9\% \pm 7.5\%$).

DISCUSSION

The overall prevalence of thrombosed intracranial aneurysms is unknown, but postmortem series reported it to be 9% of all intracranial aneurysms.¹⁴ Nevertheless, large and giant aneurysms show partial thrombosis much more frequently (48%–76%), and

the frequency seems to correlate with aneurysm size.^{3,15} Furthermore, the presence of partial thrombosis has been identified as a clinical biomarker for aneurysm histologic findings suggestive of instability and risk of rupture. Both completely thrombosed aneurysms were treated conservatively, though aneurysm size, shape, and contrast-enhancement patterns indicated treatment. These patients (80 and 75 years of age) had severe comorbidities and therefore refused microsurgical treatment. Clinical impact of the presented findings remains unclear because the treatment indication was given in all presented cases due to large aneurysm sizes. Because the results cannot be generalized to smaller aneurysms, further studies in larger patient cohorts are needed.

Ollikainen et al¹⁶ have shown that aneurysm wall remodeling and histologic findings suggestive of instability are associated with chronic inflammation in histopathology. Lack of internal elastic lamina, erosion of the luminal endothelium, infiltration of inflammatory cells, apoptosis of smooth-muscle cells, and the presence of myointimal hyperplasia, fibrosis, and thrombus are characteristics of aneurysm wall remodeling. These processes are also associated with neovascularization of the intima and formation of vasa vasorum and finally wall degeneration. Neovascularization of the intima and within the thrombus as seen in the histopathology of thrombosed intracranial aneurysm walls farthest away from the parent artery has been reported previously and seems to play an important role in aneurysm growth, histologic findings suggestive of instability, and rupture.^{4,17}

Frösen et al⁶ have also proposed several explanations for iron

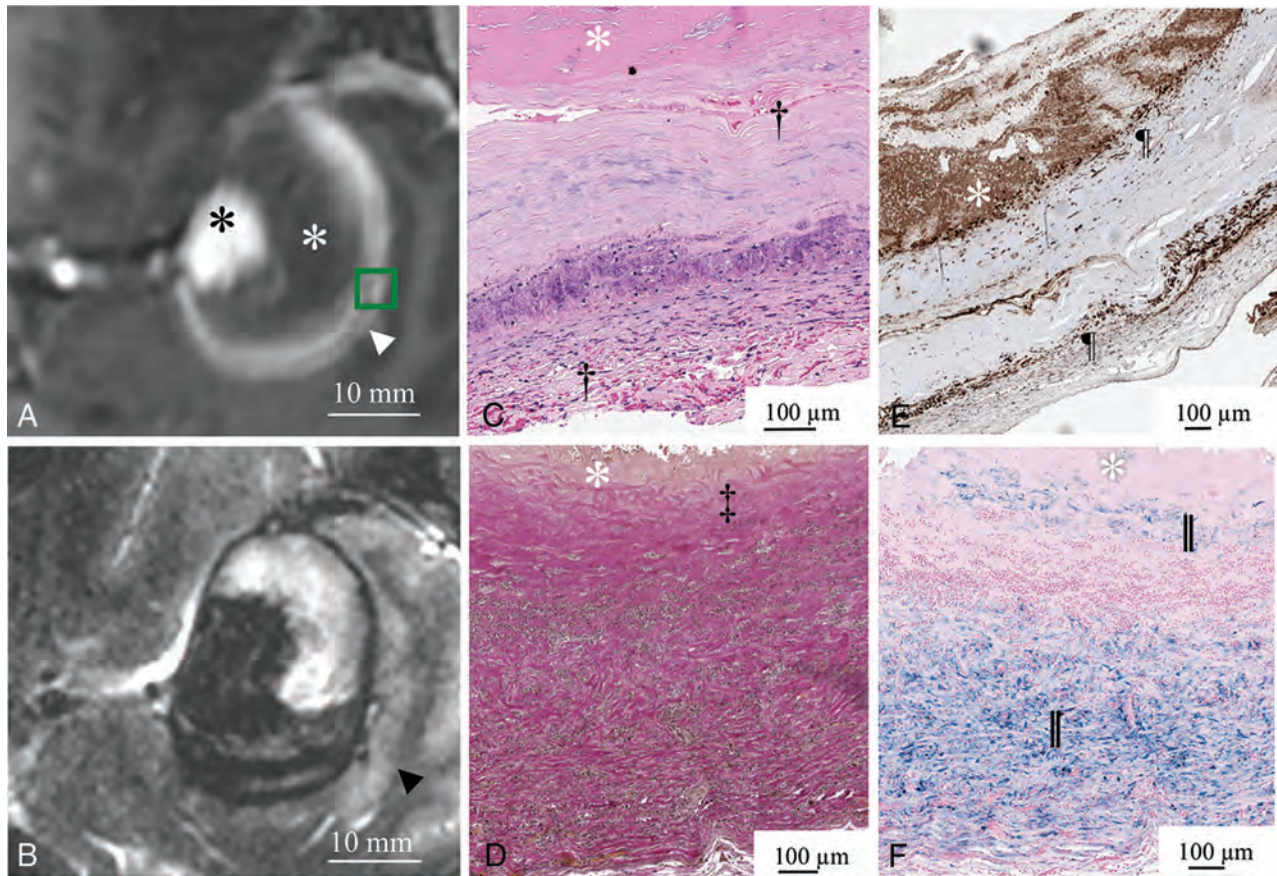


FIG 3. Gadolinium-enhanced MPRAGE shows a double-rim pattern of the aneurysm wall (*white arrowhead*) in aneurysm 6 (*white asterisk*, intraluminal thrombus; *black asterisk*, aneurysm lumen). The *green box* indicates the area of the histopathologic specimen (A). Perifocal edema (*black arrowhead*) adjacent to the double-rim enhancement delineated in T2-weighted MR imaging (B). The *white asterisk* indicates intraluminal thrombus (C–F). Good correspondence between the double-rim pattern of the aneurysm wall and neovascularization of the inner wall layer (*upper dagger*) and developed vasa vasorum (*lower dagger*) in hematoxylin-eosin staining (C). Loss of elastic fibers in the inner aneurysm wall layer in Van Gieson elastic staining (*double daggers*) (D). Abundant macrophages (*pilcrow sign*) in the inner and outer layers of the aneurysm wall visualized in CD68 immunostaining (E). Iron deposition (*double vertical lines*) in the inner and outer aneurysm wall layers stained with Prussian blue (F).

deposition and macrophage accumulation in unstable aneurysm walls. Interstitial iron results from erythrocytes seeping into the interstitial space from leaky vessels. This iron is then phagocytosed by macrophages migrating into the aneurysm wall. Prussian blue staining and immunostaining (eg, CD163) can reveal these processes in histologic specimens. On the other hand, macrophage infiltration was also present in most aneurysm walls without iron deposition, supporting the assumption that different inflammatory processes are involved in macrophage migration. The average CD68-positive areas in the 4 double-rim-pattern aneurysm walls were large ($19.5\% \pm 6.4\%$) compared with the single-rim case with a CD68-positive area ($13.9\% \pm 7.5\%$), but there were too few histopathologic samples to statistically evaluate the difference. Nevertheless, the macrophage infiltration seems to be one of the important pathophysiologic mechanisms involved in wall enhancement in thrombosed aneurysms. Even though part of thrombosed intracranial aneurysm pathophysiology has already been explained, several aspects still remain unclear, and in vivo evaluation is not feasible with current clinical imaging methods.^{3,9,15,18}

Vessel wall imaging with gadolinium-enhanced MR imaging has become more popular in the past years and might be a clinical

biomarker for histologic findings suggestive of aneurysm instability.^{19,20} Nevertheless, due to the variety of different vessel wall imaging techniques, generalizability of the published results remains limited. Restricted by spatial resolution, wall enhancement has been described as a partial or complete single rim using current clinical CT or MR imaging systems, and the actually enhancing wall microstructure could not be identified in vivo. MR imaging at 7T has demonstrated a great advantage in detecting aneurysm wall microstructures. The higher signal-to-noise ratio makes voxel sizes feasible for in vivo imaging that are significantly smaller than the wall thickness.^{10–12} The presented study reports distinct single- and double-rim enhancement patterns in thrombosed intracranial aneurysms using ultra-high-field 7T MR imaging for the first time. Quantifying a normalized degree of enhancement was not feasible, due to intersubject variance of pharmacokinetics and non-normalized MR imaging signal intensities. Quantitative T1 and T2 mapping sequences might make this possible in the future.

Our results suggest that 2 distinct aneurysm wall microstructures are responsible for gadolinium wall enhancement in thrombosed intracranial aneurysms that cannot be discriminated at a lower spatial resolution. The partial or complete inner wall en-

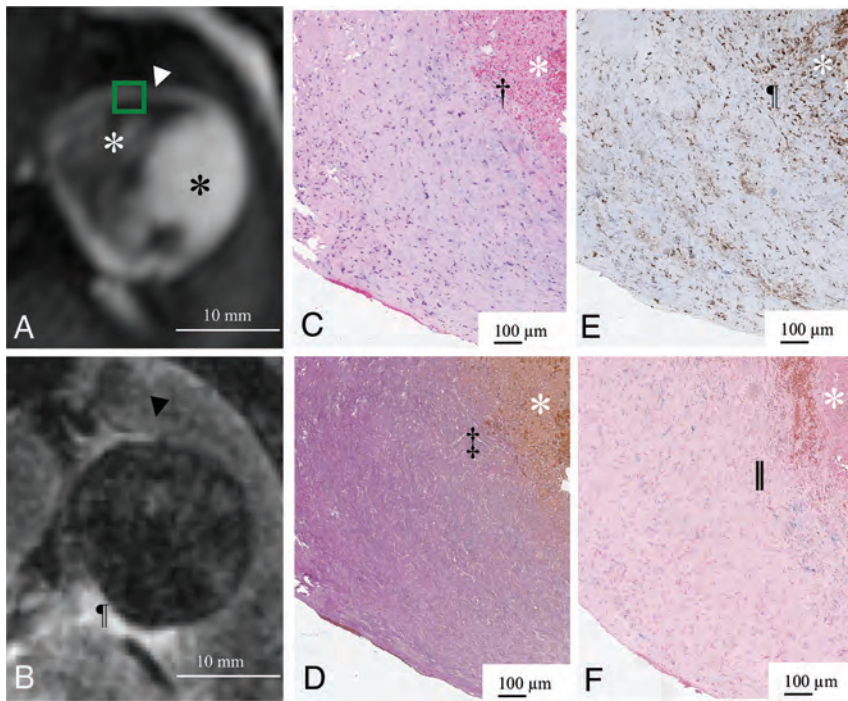


FIG 4. Gadolinium-enhanced MPRAGE shows a single-rim pattern (white arrowhead) in aneurysm 14 (white asterisk, intraluminal thrombus; black asterisk, aneurysm lumen). The green box indicates the area of the histopathologic specimen (A). No perifocal edema (black arrowhead) adjacent to the single-rim enhancement can be delineated in T2-weighted MR imaging. Cisternal CSF is delineated with hyperintense signal (pilcrow sign) (B). The white asterisk indicates intraluminal thrombus (C–F). Good correspondence between the single-rim pattern of the aneurysm wall and neovascularization of the inner wall layer (dagger) and missing vasa vasorum of the outer wall layer in hematoxylin-eosin staining (C). Loss of elastic fibers in the inner aneurysm wall layer in Van Gieson elastic staining (double daggers) (D). Abundant macrophages (pilcrow sign) in the inner layer and few in the outer layer of the aneurysm wall visualized in CD68 immunostaining (E). Iron deposition (double vertical lines) in the inner and less in the outer aneurysm wall layers stained with Prussian blue (F).

enhancement seen in all presented cases correlates with neovascularization of the inner wall layer and the adjacent thrombus. Furthermore, neovascularization of the inner wall layer has also been reported in histologic examinations of nonthrombosed aneurysms.⁸ The additional partial or complete outer wall enhancement seen in 7 of the presented patients (Table) can be explained by formation of vasa vasorum in the outer aneurysm wall layer. This double-rim pattern correlates with wall degeneration and histologic findings suggestive of instability. Furthermore, the vasa vasorum interface with pial vessels and therefore induce perifocal edema. These results are in line with previously proposed perifocal edema induction, not by mass effect but by direct interaction of the aneurysm wall with the pial surface.¹⁵ If direct correlation between perifocal edema adjacent to the aneurysm wall and the absence or presence of double-rim wall enhancement in 7T MR imaging can be shown in a larger patient cohort, these results would have an important clinical impact because perifocal edema can be easily visualized using lower magnetic-field-strength MR imaging. On the other hand, the pathophysiology of double-rim wall enhancement and perifocal edema is still not completely understood. Cavernous ICA aneurysms were not associated with perifocal edema, even though they exert mass effect on the brain, and their separation from the brain parenchyma by the dura mater may prevent the diffusion of edema-inducing factors despite

the presence of partial thrombosis. Dengler et al¹⁵ reported that direct contact between the partially thrombosed surface of an aneurysm and the brain parenchyma may be crucial for perifocal edema formation. However, histopathologic correlations were pending.

Limitations

There are some limitations to the current study. The study cohort comprised only 13 patients with 14 thrombosed intracranial aneurysms. This is mainly due to the low prevalence of thrombosed intracranial aneurysms and the even lower rate of unruptured thrombosed intracranial aneurysms. Histopathologic correlations were only possible in 5 aneurysms. Only 1 case with single-rim wall enhancement was available for histopathologic analysis, restricting the comparison of both enhancement patterns. Identical enhancement patterns could be shown in various locations, thus indicating that these patterns are a general feature of thrombosed intracranial aneurysms.

CONCLUSIONS

Two distinct aneurysm wall microstructures responsible for gadolinium enhancement not depictable at a lower spatial resolution can be visualized in vivo using high-resolution gadolinium-

enhanced 7T MR imaging. Partial or complete inner wall enhancement correlates with neovascularization of the inner wall layer as well as the adjacent thrombus. Additional partial or complete outer wall enhancement can be explained by formation of vasa vasorum in the outer aneurysm wall layer. The double-rim enhancement correlates with perifocal edema and wall histologic findings suggestive of instability.

Disclosures: Bixia Chen—RELATED: Grant: Programm zur internen Forschungsförderung Essen grant, Comments: scientific grant of the University of Duisburg-Essen.* Oliver Gembruch—RELATED: Grant: Interne Forschungsförderung Essen, Comments: The grant is a scientific grant given by the University Duisburg-Essen.* Harald H. Quick—RELATED: Other: Siemens Healthcare, Erlangen, Germany, Comments: The Erwin L. Hahn Institute for MR Imaging, University Duisburg-Essen, has an established research cooperation with Siemens Healthcare, Erlangen, Germany.* Karsten H. Wrede—RELATED: Grant: Programm zur internen Forschungsförderung Essen grant, Comments: grant for scientific work from the University Duisburg Essen.* *Money paid to the institution.

REFERENCES

1. Roccatagliata L, Guédin P, Condetto-Auliac S, et al. **Partially thrombosed intracranial aneurysms: symptoms, evolution, and therapeutic management.** *Acta Neurochir (Wien)* 2010;152: 2133–42 CrossRef Medline
2. Miyamoto S, Funaki T, Iihara K, et al. **Successful obliteration and shrinkage of giant partially thrombosed basilar artery aneurysms**

- through a tailored flow reduction strategy with bypass surgery. *J Neurosurg* 2011;114:1028–36 CrossRef Medline
3. Krings T, Alvarez H, Reinacher P, et al. **Growth and rupture mechanism of partially thrombosed aneurysms.** *Interv Neuroradiol* 2007;13:117–26 CrossRef Medline
 4. Nagahiro S, Takada A, Goto S, et al. **Thrombosed growing giant aneurysms of the vertebral artery: growth mechanism and management.** *J Neurosurg* 1995;82:796–801 CrossRef Medline
 5. Lehman VT, Brinjikji W, Mossa-Basha M, et al. **Conventional and high-resolution vessel wall MRI of intracranial aneurysms: current concepts and new horizons.** *J Neurosurg* 2018;128:969–81 CrossRef Medline
 6. Frösen J, Tulamo R, Paetau A, et al. **Saccular intracranial aneurysms: pathology and mechanisms.** *Acta Neuropathol* 2012;123:773–86 CrossRef Medline
 7. Cebal J, Ollikainen E, Chung BJ, et al. **Flow conditions in the intracranial aneurysm lumen are associated with inflammation and degenerative changes of the aneurysm wall.** *AJNR Am J Neuroradiol* 2017;38:119–26 CrossRef Medline
 8. Tulamo R, Frösen J, Hernesniemi J, et al. **Inflammatory changes in the aneurysm wall: a review.** *J Neurointerv Surg* 2010;2:120–30 CrossRef Medline
 9. Iihara K, Murao K, Yamada N, et al. **Growth potential and response to multimodality treatment of partially thrombosed large or giant aneurysms in the posterior circulation.** *Neurosurgery* 2008;63:832–42; discussion 842–43 CrossRef Medline
 10. Matsushige T, Chen B, Ringelstein A, et al. **Giant intracranial aneurysms at 7T MRI.** *AJNR Am J Neuroradiol* 2016;37:636–41 CrossRef Medline
 11. Umutlu L, Theysohn N, Maderwald S, et al. **7 Tesla MPRAGE imaging of the intracranial arterial vasculature: nonenhanced versus contrast-enhanced.** *Acad Radiol* 2013;20:628–34 CrossRef Medline
 12. Wrede KH, Johst S, Dammann P, et al. **Caudal image contrast inversion in MPRAGE at 7 Tesla: problem and solution.** *Acad Radiol* 2012;19:172–78 CrossRef Medline
 13. Schneider CA, Rasband WS, Eliceiri KW. **NIH image to ImageJ: 25 years of image analysis.** *Nat Methods* 2012;9:671–75 CrossRef Medline
 14. Housepian EM, Pool JL. **A systematic analysis of intracranial aneurysms from the autopsy file of the Presbyterian Hospital, 1914 to 1956.** *J Neuropathol Exp Neurol* 1958;17:409–23 CrossRef Medline
 15. Dengler J, Maldaner N, Bijlenga P, et al; Giant Intracranial Aneurysm Study Group. **Perianeurysmal edema in giant intracranial aneurysms in relation to aneurysm location, size, and partial thrombosis.** *J Neurosurg* 2015;123:446–52 CrossRef Medline
 16. Ollikainen E, Tulamo R, Frösen J, et al. **Mast cells, neovascularization, and microhemorrhages are associated with saccular intracranial artery aneurysm wall remodeling.** *J Neuropathol Exp Neurol* 2014;73:855–64 CrossRef Medline
 17. Nakatomi H, Segawa H, Kurata A, et al. **Clinicopathological study of intracranial fusiform and dolichoectatic aneurysms: insight on the mechanism of growth.** *Stroke* 2000;31:896–900 CrossRef Medline
 18. Schubiger O, Valavanis A, Wichmann W. **Growth-mechanism of giant intracranial aneurysms; demonstration by CT and MR imaging.** *Neuroradiology* 1987;29:266–71 CrossRef Medline
 19. Matouk CC, Mandell DM, Günel M, et al. **Vessel wall magnetic resonance imaging identifies the site of rupture in patients with multiple intracranial aneurysms: proof of principle.** *Neurosurgery* 2013;72:492–96; discussion 496 CrossRef Medline
 20. Shimonaga K, Matsushige T, Ishii D, et al. **Clinicopathological insights from vessel wall imaging of unruptured intracranial aneurysms.** *Stroke* 2018;49:2516–19 CrossRef Medline

Gadolinium Enhancement of the Aneurysm Wall in Unruptured Intracranial Aneurysms Is Associated with an Increased Risk of Aneurysm Instability: A Follow-Up Study

M.D.I. Vergouwen, D. Backes, I.C. van der Schaaf, J. Hendrikse, R. Kleinloog, A. Algra, and G.J.E. Rinkel

ABSTRACT

BACKGROUND AND PURPOSE: Previous studies have suggested that gadolinium enhancement of the wall of unruptured intracranial aneurysms on MR imaging may reflect aneurysm wall instability. However, all previous studies were cross-sectional. In this longitudinal study, we investigated whether aneurysm wall enhancement is associated with an increased risk of aneurysm instability.

MATERIALS AND METHODS: We included all patients 18 years of age or older with ≥ 1 unruptured aneurysm from the University Medical Center Utrecht, the Netherlands, who were included in 2 previous studies with either 3T or 7T aneurysm wall MR imaging and for whom it was decided not to treat the aneurysm but to monitor it with follow-up imaging. We investigated the risk of growth or rupture during follow-up of aneurysms with and without gadolinium enhancement of the aneurysm wall at baseline and calculated the risk difference between the 2 groups with corresponding 95% confidence intervals.

RESULTS: We included 57 patients with 65 unruptured intracranial aneurysms. After a median follow-up of 27 months (interquartile range, 20–31 months), growth ($n = 2$) or rupture ($n = 2$) was observed in 4 of 19 aneurysms (21%; 95% CI, 6%–54%) with wall enhancement and in zero of 46 aneurysms (0%; 95% CI, 0%–8%) without enhancement (risk difference, 21%; 95% CI, 3%–39%).

CONCLUSIONS: Gadolinium enhancement of the aneurysm wall on MR imaging is associated with an increased risk of aneurysm instability. The absence of wall enhancement makes it unlikely that the aneurysm will grow or rupture in the short term. Larger studies are needed to investigate whether aneurysm wall enhancement is an independent predictor of aneurysm instability.

ABBREVIATION: PHASES = Population, Hypertension, Age, Size of Aneurysm, Earlier Subarachnoid Hemorrhage from Another Aneurysm, and Site of Aneurysm

The prevalence of unruptured intracranial aneurysms is approximately 3% in adults.¹ Aneurysm rupture results in subarachnoid hemorrhage, a subtype of stroke with a poor prognosis.² In patients with an unruptured intracranial aneurysm, the only available treatment options to prevent SAH and improve life expectancy with good quality of life are surgical clipping and endovascular treatment. Because these treatment options have a risk of complications, the risk of aneurysm rupture needs to be weighed against the risk of treatment complications.³ If the predicted risk of aneurysm rupture is small, patients are usually fol-

lowed across time with repeat imaging to detect possible aneurysm growth, which is a marker of aneurysm instability and a predictor of rupture.

Current risk prediction of aneurysm growth and rupture is mainly based on aneurysm size, location, and demographics.^{4,5} Although small aneurysms have a low risk of rupture, most episodes of SAH come from small aneurysms because small aneurysms are much more prevalent.⁶ Currently, most small aneurysms remain untreated because the risk of rupture is smaller than the risk of treatment complications. The clinical challenge is to identify the subgroup of small aneurysms with a high risk of rupture.

Several studies have shown that the wall of an intracranial aneurysm can enhance after administration of gadolinium using MR imaging.^{7–14} Enhancement of the aneurysm wall may represent aneurysm instability and therefore may be a novel biomarker to identify unstable aneurysms. However, previous studies had a cross-sectional design. Here we present the results of the first longitudinal study investigating whether gadolinium enhancement of the aneurysm wall at baseline is associated with aneurysm growth or rupture during follow-up.

Received February 8, 2019; accepted after revision May 14.

From the Department of Neurology and Neurosurgery (M.D.I.V., D.B., A.A., G.J.E.R.), Brain Center Rudolf Magnus, Department of Radiology (I.C.v.d.S., J.H.), and Julius Center for Health Sciences and Primary Care, (G.J.E.R.), University Medical Center Utrecht, Utrecht University, Utrecht, the Netherlands; Department of General Practice (D.B.), Erasmus Medical Center, Rotterdam, the Netherlands; and Department of Neurology (R.K.), Academic Medical Center, Amsterdam, the Netherlands. Please address correspondence to Mervyn D.I. Vergouwen, MD, PhD, Department of Neurology and Neurosurgery, Room G3.228, Brain Center Rudolf Magnus, University Medical Center Utrecht, Utrecht University, PO Box 85 500, 3500 GA Utrecht, the Netherlands; e-mail: m.d.i.vergouwen@umcutrecht.nl

<http://dx.doi.org/10.3174/ajnr.A6105>

MATERIALS AND METHODS

This study was performed at the University Medical Center Utrecht, the Netherlands. Approval for this study was obtained from the local institutional review board. All patients provided written informed consent. We included all patients 18 years of age or older with ≥ 1 unruptured aneurysm who were included in 2 previous studies with either 3T or 7T aneurysm wall MR imaging, in whom it was decided not to treat the aneurysm but to monitor it with follow-up imaging.^{12,15} In our center, the decision as to whether an aneurysm should be treated is based on the following parameters: the Population, Hypertension, Age, Size of Aneurysm, Earlier Subarachnoid Hemorrhage from Another Aneurysm, and Site of Aneurysm (PHASES) score for estimating the 5-year risk of rupture, the assumed risk of complications from preventive endovascular or neurosurgical aneurysm treatment, life expectancy, and patient anxiety.⁴

At baseline, 3T or 7T aneurysm wall MR imaging was performed. Follow-up imaging was performed with MR angiography or CT angiography to determine potential aneurysm growth across time.

Baseline Imaging

Patients scanned on 3T MR imaging were included in the gadolinium-enhanced aneurysm wall Imaging of Non-ruptured intracranial Aneurysms (LUMINA) study.¹² In short, LUMINA was a cross-sectional study in which patients 18 years of age or older with ≥ 1 unruptured intracranial aneurysm were included if the treating physician decided on follow-up imaging instead of preventive aneurysm occlusion. Exclusion criteria were impaired renal function (glomerular filtration rate of < 30 mL/min/1.73 m), gadolinium contrast allergy, or pregnancy. In total, 79 patients with 89 aneurysms were recruited for the LUMINA study between October 2014 and October 2015.

Patients scanned on 7T MR imaging were recruited between February and May 2014 for a study focusing on aneurysm volume pulsation.¹⁵ In short, patients 18 years of age or older diagnosed with a saccular intradural unruptured intracranial aneurysm who were either scheduled for treatment of their aneurysm or were in follow-up to detect possible aneurysm growth were recruited through the outpatient clinic of the Department of Neurology and Neurosurgery. Exclusion criteria were the presence of contraindications for 7T MR imaging (eg, claustrophobia and metal objects such as dental implants or prostheses in or on the body), presence of an aneurysm associated with a vascular malformation other than an aneurysm (eg, an arteriovenous malformation), impaired renal function (glomerular filtration rate of < 30 mL/min/1.73 m), and gadolinium contrast allergy.

Imaging Protocol

A 3T whole body scanner (Philips Achieva, Philips Healthcare, Best, The Netherlands) and a 7T whole-body system (Philips Healthcare, Cleveland, OH) were used to acquire aneurysm wall imaging before and after administration of a single intravenous injection of a gadolinium-based contrast agent, gadobutrol (Gadovist, 0.1 mmol/kg body weight; Bayer Schering Pharma, Berlin, Germany). Imaging protocols for 3T and 7T aneurysm wall imaging were described previously.^{12,15,16}

Assessment of Baseline MR Imaging

Two neuroradiologists (J.H. or I.C.v.d.S.) reviewed the baseline MR images blinded to patient-specific characteristics and recorded aneurysm size (maximum diameter on a 0.1-mm scale), aneurysm location, aneurysm shape (regular or irregular shape defined as the presence of blebs, aneurysm wall protrusions, or multiple lobes), and the presence of gadolinium enhancement of the aneurysm wall (defined as present or absent).

Assessment of Outcome

The outcome measure was aneurysm instability, which was defined as aneurysm growth or rupture. The minimal follow-up time was 12 months. Aneurysm growth was defined as growth of ≥ 1 mm in at least 1 direction. We used radiology reports of follow-up MRA and CTA scans to determine whether aneurysm growth occurred. Radiologists who assessed the aneurysm size at follow-up imaging were blinded to the findings of aneurysm wall imaging at baseline. We checked the medical records of all patients who had aneurysm wall imaging for aneurysm rupture during follow-up. In case of death, the general practitioner was contacted to verify the cause of death.

Statistical Analysis

We investigated the risk of growth or rupture during follow-up of aneurysms with and without gadolinium enhancement of the aneurysm wall at baseline. In addition, we determined the risk difference between the 2 groups with an accompanying 95% confidence interval.

RESULTS

Follow-up imaging was available for 55 patients with 63 asymptomatic aneurysms who had aneurysm wall MR imaging at 3T and for 2 patients with 2 asymptomatic aneurysms who had aneurysm wall imaging at 7T. The last follow-up imaging was MRA for 56 aneurysms and CTA in 9 aneurysms. Reasons for not having follow-up imaging available were the following: 1) patient discharged from further follow-up because of advanced age ($n = 6$); 2) aneurysm treated after baseline MR imaging ($n = 2$); or 3) patient awaiting follow-up imaging because of a short follow-up time ($n = 13$), death from lung cancer ($n = 1$), SAH before scheduled follow-up imaging ($n = 1$), and the patient never wanting to be treated for unruptured intracranial aneurysm ($n = 1$). None of the patients were lost during follow-up. Reasons for aneurysm treatment after baseline imaging were aneurysm growth compared with earlier imaging and bilobar configuration of the aneurysm, which was not visible on the earlier scan of lower quality. In both patients, the aneurysm was not symptomatic.

Patient and aneurysm characteristics of the included patients are shown in the Table. At baseline, 19 aneurysms (29%; 95% CI, 18%–46%) had gadolinium enhancement of the wall. After a median follow-up of 27 months (interquartile range, 20–31 months), an outcome event occurred in 4 of 19 aneurysms (21%; 95% CI, 6%–54%) with enhancement and in zero of 46 aneurysms (0%; 95% CI, 0%–8%) without enhancement (risk difference, 21%; 95% CI, 3%–39%). Growth without rupture was observed in 2 aneurysms and was detected with CTA for 1 aneurysm and with MRA for 1 aneurysm (Fig 1). Aneurysm rupture occurred in 2 aneurysms (Fig 2).

DISCUSSION

Our follow-up study showed that gadolinium enhancement of the aneurysm wall is associated with an increased risk of aneurysm instability during follow-up. One of 5 aneurysms with wall enhancement had growth or rupture, while no

growth or rupture was observed in aneurysms without wall enhancement.

The current study differs from previous studies. This is the first longitudinal study to investigate whether gadolinium enhancement of the aneurysm wall is associated with aneurysm instability

during follow-up, while previous studies had a cross-sectional design.^{7-11,14} Those studies often compared the proportion of patients with gadolinium enhancement of the aneurysm wall in stable and unstable (mostly ruptured) intracranial aneurysms.^{7-11,14} In a small study of 5 patients with subarachnoid hemorrhage of whom 3 had multiple intracranial aneurysms, gadolinium enhancement of the aneurysm wall was present in all ruptured but not in the unruptured aneurysms.⁷ The second study found aneurysm wall enhancement in 29% of the 77 unruptured aneurysms, and in 87% of 31 unstable aneurysms, which were defined as a recently ruptured aneurysm, symptomatic aneurysm, or an aneurysm undergoing morphologic change.⁸ A third study found aneurysm wall enhancement in 18% of 83 unruptured intracranial aneurysms and in 98% of 61 ruptured intracranial aneurysms.⁹ A fourth study found aneurysm wall enhancement in 11% of the 18 unruptured, stable aneurysms and in all

Patient and aneurysm characteristics at baseline^a

	Wall Enhancement (n = 19)		No Wall Enhancement (n = 46)
	Unstable during FU (n = 4)	Stable during FU (n = 15)	
Median age (IQR) (yr)	50 (47–53)	60 (55–68)	55 (52–61)
Female sex	4 (100)	11 (73)	37 (80)
Hypertension	2 (50)	9 (60)	21 (46)
Smoking status			
Current smoker	2 (50)	3 (20)	14 (30)
Previous smoker	1 (25)	10 (67)	25 (54)
Never smoked	1 (25)	2 (13)	7 (15)
Previous SAH	–	3 (20)	11 (24)
Family history of intracranial aneurysms	1 (25)	–	10 (22)
Aneurysm location			
ICA (excluding PcomA)	–	1 (7)	16 (35)
PcomA	–	1 (7)	3 (7)
ACA/AcomA/pericallosal artery	–	1 (7)	9 (20)
MCA	4 (100)	11 (73)	12 (26)
Basilar artery	–	1 (7)	2 (4)
Other posterior circulation	–	–	4 (9)
Aneurysm size (mm)			
1.0–2.9	–	1 (7)	16 (35)
3.0–4.9	–	3 (20)	16 (35)
5.0–6.9	3 (75)	6 (40)	11 (24)
≥7.0	1 (25)	5 (33)	3 (7)
Irregular shape	–	6 (40)	9 (20)
Median follow-up duration (IQR) (mo)	15 (12–28)	27 (19–31)	27 (24–32)

Note:—PcomA indicates posterior communicating artery; AcomA, anterior communicating artery; ACA, anterior cerebral artery; FU, follow-up; IQR, interquartile range; MCA, middle cerebral artery; SAH, subarachnoid hemorrhage; –, no patients.

^aData are aneurysm-based instead of patient-based and are presented as number (%) unless stated otherwise.

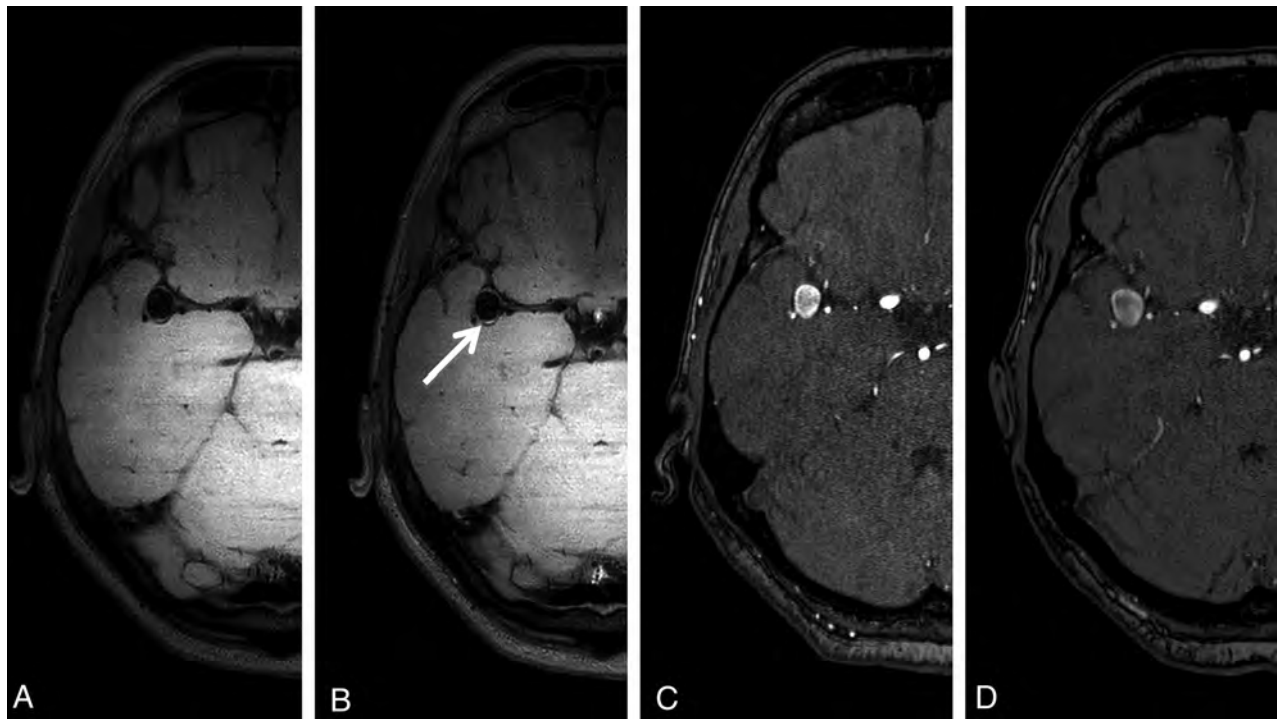


FIG 1. Aneurysm wall imaging of a patient with aneurysm growth at follow-up. A 63-year-old woman with a right middle cerebral artery aneurysm. A, Aneurysm wall imaging without gadolinium. B, Aneurysm wall imaging after administration of gadolinium shows focal posterior enhancement (arrow). C, TOF-MRA at baseline shows a 9-mm aneurysm. D, TOF-MRA after 12 months of follow-up shows a 12-mm aneurysm.

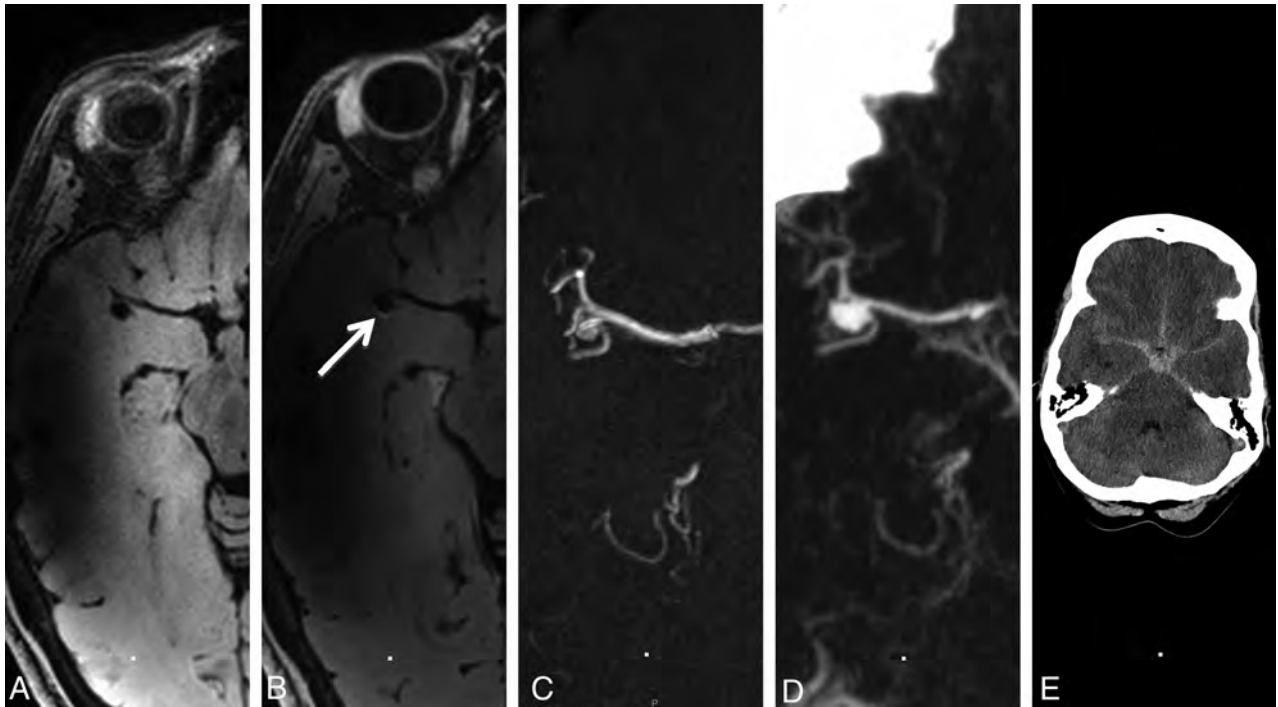


FIG 2. Aneurysm wall imaging of a patient with aneurysm rupture at follow-up. A 47-year-old woman with a right middle cerebral artery aneurysm. *A*, Aneurysm wall imaging without gadolinium. *B*, Aneurysm wall imaging after administration of gadolinium shows focal posterior enhancement (*arrow*). *C*, At baseline, the aneurysm is 4 mm. *D*, After 31 months, the aneurysm ruptured, with CTA showing aneurysm growth (7 mm). *E*, Head CT shows SAH.

12 unstable aneurysms, which were defined as a recently ruptured aneurysm, symptomatic aneurysm, or growing aneurysm.¹¹ A fifth study found aneurysm wall enhancement in 74% of unruptured intracranial aneurysms and in all 19 ruptured aneurysms.¹⁴ The LUMINA study did not include ruptured aneurysms and found wall enhancement in 29% of 89 small unruptured intracranial aneurysms.¹²

Current risk prediction for aneurysm growth and rupture is based on the earlier subarachnoid hemorrhage, location of the aneurysm, age >60 years, population, size of the aneurysm, and shape of the aneurysm (ELAPSS) and PHASES scores, which were designed on the basis of large cohorts of patients with unruptured intracranial aneurysms.^{4,5} In these scores, risk prediction is based on patient and aneurysm characteristics, with aneurysm size, aneurysm location, and demographics being the most important contributing variables. However, because most instances of SAH are caused by rupture of a small aneurysm, novel biomarkers are needed that predict aneurysm instability and will lead to a personalized approach to risk prediction. The results of our study suggest that aneurysm wall imaging with gadolinium administration is such a novel biomarker and therefore an ideal tool for accurately selecting patients who will have aneurysm instability in the short term.

A strength of our study is that it had a longitudinal instead of a cross-sectional design. In addition, all patients had aneurysm wall imaging before and after administration of gadolinium according to strict predefined protocols. We included patients in whom the treating physician had decided on follow-up imaging instead of preventive aneurysm occlusion. Specifically in this group of patients, novel biomarkers are

needed to better predict which aneurysms have an increased risk of instability during follow-up. Finally, because gadolinium contrast agents are safe and widely available, it is easy to implement MR imaging with gadolinium-enhanced aneurysm wall imaging in clinical care.

A limitation of our study is the single-center design, which limits generalization of our results to other populations. In addition, baseline imaging was either with 3T or 7T MR imaging. It remains unclear whether 7T is more sensitive to detect aneurysm wall enhancement than 3T MR imaging. Furthermore, follow-up imaging was performed with both CTA and MRA, instead of MRA only. Another limitation of our study is its relatively small sample size. Finally, because all aneurysms with instability during follow-up were >5 mm, it remains to be investigated whether aneurysm wall enhancement is a predictor of aneurysm instability independent of aneurysm size.

Our study has implications. The results of this study suggest that aneurysm wall MR imaging with gadolinium administration can be used to improve patient selection for preventive neurosurgical or endovascular aneurysm treatment in patients with small, unruptured intracranial aneurysms. However, because of the currently still imprecise results, larger studies are needed to confirm these findings and to investigate whether aneurysm wall enhancement has predictive information of future aneurysm instability in addition to the current predictors.

CONCLUSIONS

Gadolinium enhancement of the aneurysm wall on MR imaging is associated with an increased risk of aneurysm instability. The ab-

sence of wall enhancement makes it unlikely that the aneurysm will grow or rupture in the short term.

Disclosures: Mervyn Vergouwen—UNRELATED: Payment for Lectures Including Service on Speakers Bureaus: Cerenovus.* *Money paid to the institution.

REFERENCES

1. Vlak MH, Algra A, Brandenburg R, et al. **Prevalence of unruptured intracranial aneurysms, with emphasis on sex, age, comorbidity, country, and time period: a systematic review and meta-analysis.** *Lancet Neurol* 2011;10:626–36 CrossRef Medline
2. Vergouwen MD, Jong-Tjien-Fa AV, Algra A, et al. **Time trends in causes of death after aneurysmal subarachnoid hemorrhage: a hospital-based study.** *Neurology* 2016;86:59–63 CrossRef Medline
3. Algra AM, Lindgren A, Vergouwen MD, et al. **Procedural clinical complications, case-fatality risks, and risk factors in endovascular and neurosurgical treatment of unruptured intracranial aneurysms: a systematic review and meta-analysis.** *JAMA Neurol* 2018 Dec 28. [Epub ahead of print] CrossRef Medline
4. Greving JP, Wermer MJ, Brown RD Jr, et al. **Development of the PHASES score for prediction of risk of rupture of intracranial aneurysms: a pooled analysis of six prospective cohort studies.** *Lancet Neurol* 2014;13:59–66 CrossRef Medline
5. Backes D, Rinkel GJ, Greving JP, et al. **ELAPSS score for prediction of risk of growth of unruptured intracranial aneurysms.** *Neurology* 2017;88:1600–06 CrossRef Medline
6. Bender MT, Wendt H, Monarch T, et al. **Small aneurysms account for the majority and increasing percentage of aneurysmal subarachnoid hemorrhage: a 25-year, single institution study.** *Neurosurgery* 2018;83:692–99 CrossRef Medline
7. Matouk CC, Mandell DM, Günel M, et al. **Vessel wall magnetic resonance imaging identifies the site of rupture in patients with multiple intracranial aneurysms: proof of principle.** *Neurosurgery* 2013;72:492–96 CrossRef Medline
8. Edjlali M, Gentric JC, Régent-Rodriguez C, et al. **Does aneurysmal wall enhancement on vessel wall MRI help to distinguish stable from unstable intracranial aneurysms?** *Stroke* 2014;45:3704–06 CrossRef Medline
9. Nagahata S, Nagahata M, Obara M, et al. **Wall enhancement of the intracranial aneurysms revealed by magnetic resonance vessel wall imaging using three-dimensional turbo spin-echo sequence with motion-sensitized driven-equilibrium: a sign of ruptured aneurysm?** *Clin Neuroradiol* 2016;26:277–83 CrossRef Medline
10. Liu P, Qi H, Liu A, et al. **Relationship between aneurysm wall enhancement and conventional risk factors in patients with unruptured intracranial aneurysms: a black-blood MRI study.** *Interv Neuroradiol* 2016;22:501–05 CrossRef Medline
11. Hu P, Yang Q, Wang DD, et al. **Wall enhancement on high-resolution magnetic resonance imaging may predict an unsteady state of an intracranial saccular aneurysm.** *Neuroradiology* 2016;58:979–85 CrossRef Medline
12. Backes D, Hendrikse J, van der Schaaf I, et al. **Determinants of gadolinium-enhancement of the aneurysm wall in unruptured intracranial aneurysms.** *Neurosurgery* 2018;83:719–25 CrossRef Medline
13. Lv N, Tang H, Chen S, et al. **Morphological parameters related to aneurysmal wall enhancement in patients with multiple intracranial aneurysms.** *World Neurosurg* 2018;114:e338–43 CrossRef Medline
14. Wang GX, Wen L, Lei S, et al. **Wall enhancement ratio and partial wall enhancement on MRI associated with the rupture of intracranial aneurysms.** *J Neurointerv Surg* 2018;10:566–70 CrossRef Medline
15. Kleinloog R, Zwanenburg JJM, Schermers B, et al. **Quantification of intracranial aneurysm volume pulsation with 7T MRI.** *AJNR Am J Neuroradiol* 2018;39:713–19 CrossRef Medline
16. Kleinloog R, Korkmaz E, Zwanenburg JJ, et al. **Visualization of the aneurysm wall: a 7.0-Tesla magnetic resonance imaging study.** *Neurosurgery* 2014;75:614–22; discussion 622 CrossRef Medline

Assessing Postconcussive Reaction Time Using Transport-Based Morphometry of Diffusion Tensor Images

S. Kundu, A. Ghodadra, S. Fakhran, L.M. Alhilali, and G.K. Rohde



ABSTRACT

BACKGROUND AND PURPOSE: Cognitive deficits are among the most commonly reported post-concussive symptoms, yet the underlying microstructural injury is poorly understood. Our aim was to discover white matter injury underlying reaction time in mild traumatic brain injury DTI by applying transport-based morphometry.

MATERIALS AND METHODS: In this retrospective study, we performed DTI on 64 postconcussive patients (10–28 years of age; 69% male, 31% female) between January 2006 and March 2013. We measured the reaction time percentile by using Immediate Post-Concussion Assessment and Cognitive Testing. Using the 3D transport-based morphometry technique we developed, we mined fractional anisotropy maps to extract the common microstructural injury associated with reaction time percentile in an automated manner. Permutation testing established statistical significance of the extracted injuries. We visualized the physical substrate responsible for reaction time through inverse transport-based morphometry transformation.

RESULTS: The direction in the transport space most correlated with reaction time was significant after correcting for covariates of age, sex, and time from injury (Pearson $r = 0.44$, $P < .01$). Inverting the computed direction using transport-based morphometry illustrates physical shifts in fractional anisotropy in the corpus callosum (increase) and within the optic radiations, corticospinal tracts, and anterior thalamic radiations (decrease) with declining reaction time. The observed shifts are consistent with biologic pathways underlying the visual-spatial interpretation and response-selection aspects of reaction time.

CONCLUSIONS: Transport-based morphometry discovers complex white matter injury underlying postconcussive reaction time in an automated manner. The potential influences of edema and axonal loss are visualized in the visual-spatial interpretation and response-selection pathways. Transport-based morphometry can bridge the gap between brain microstructure and function in diseases in which the structural basis is unknown.

ABBREVIATIONS: FA = fractional anisotropy; ImPACT = Immediate Post-Concussion Assessment and Cognitive Testing; mTBI = mild traumatic brain injury; TBM = transport-based morphometry

Cognitive deficits are among the most commonly reported symptoms after mild traumatic brain injury (mTBI).^{1–6} Both transient and persistent deficits in processing speed, attention, and working memory are associated with mTBI.⁷ Furthermore, persistent cognitive deficits may accelerate aging-related cognitive decline.² Yet, despite its ubiquity, the microstructure under-

lying postconcussive cognitive deficit is difficult to assess. Routine CT and MR imaging findings are often negative. Although diffusion tensor imaging can capture diffuse white matter injury,⁸ mTBI is still diagnosed clinically because damage is subtle and spatially diffuse.^{7,9} The microstructural injury is challenging to

Received December 26, 2018; accepted after revision April 27, 2019.

From the Department of Biomedical Engineering, Electrical and Computer Engineering (G.K.R.), University of Virginia, Charlottesville, Virginia; Department of Biomedical Engineering at Carnegie Mellon University and Medical Scientist Training Program (S.K.), University of Pittsburgh Medical Center, Pittsburgh, Pennsylvania; Department of Radiology (A.G.), Banner Health and Hospital Systems, Mesa, Arizona; and Department of Neuroradiology (S.F.), Barrow Neurological Institute, Phoenix, Arizona. Dr Alhilali is currently at the Department of Internal Medicine, University of Pittsburgh Medical Center, Pittsburgh, Pennsylvania.

This work was supported, in part, by the National Science Foundation award CCF 1421502 and National Institutes of Health awards GM130825 and GM090033.

A subset of these results was presented at: Radiological Society of North America's Scientific Assembly and Annual Meeting: "Transport-Based Morphometry of Diffusion Tensor Images for Assessment of Postconcussive Reaction Time." November 27 to December 2, 2016; Chicago, Illinois.

Please address correspondence to Shinjini Kundu, MD, PhD, Medical Scientist Training Program, University of Pittsburgh/Carnegie-Mellon University, 526 Scaife Hall, 3550 Terrace St, Pittsburgh, PA 15261; e-mail: shk71@pitt.edu; @ShinjiniKundu

Indicates open access to non-subscribers at www.ajnr.org

Indicates article with supplemental on-line appendix.

Indicates article with supplemental on-line photos.

<http://dx.doi.org/10.3174/ajnr.A6087>

distinguish from a background of normal anatomic variability and accumulated insults with time.¹⁰

Given its complexity, traditional analysis has permitted only a limited view of the microstructural perturbations. Conventional methods have sought to index injuries to individual tracts (ie, ROI analysis; Tract-Based Spatial Statistics, TBSS; <http://fsl.fmrib.ox.ac.uk/fsl/fslwiki/TBSS>; and so forth) or individual voxels (ie, voxel-based analysis, potholes and molehills analysis, and so forth).^{7,10,11} However, techniques treating each voxel or ROI as an independent variable cannot provide adequate insight into the interconnectedness of injuries across multiple regions as a function of cognition.^{6,7} Furthermore, visual inspection is particularly insensitive to subtle- but-interconnected biophysical shifts in tissue architecture.¹²

In our prior work, we developed 3D transport-based morphometry (TBM) as a technique to assess complex physical changes in brain tissue that may be undetectable by visual inspection.¹³ By computing the effort needed to morph the brain tissue distribution in one image into another, TBM statistically mapped joint interaction across multiple brain regions.¹³ Unlike traditional approaches, TBM could explain the relevant microstructural shifts underlying the clinical assessment visually because it is a generative technique.¹³ Furthermore, TBM can discover the common substrate underlying reaction time in a fully automated manner.^{6,7}

This study investigated the brain microstructure associated with postconcussive reaction time, one of the most frequently reported cognitive deficits after mTBI.^{1,3,4,14,15} Given new interventions such as exercise rehabilitation,^{16,17} it is crucial to identify objective substrates underlying postconcussive cognition to assess progress in treatment and understand repair mechanisms. Particularly, studying the acute and postacute phases of recovery could reveal new targets for early treatment monitoring. TBM has never before been applied to investigate white matter injury associated with postconcussive cognition. Given the known limitations of traditional techniques, we hypothesize that if a common structural substrate underlying postconcussive reaction time exists, it can be uncovered using TBM.

MATERIALS AND METHODS

Subject Cohort

In this retrospective study, institutional review board approval was obtained, and informed consent was waived. The electronic medical record was searched for DTI studies performed for mTBI between January 1, 2006, and March 1, 2013, at the University of Pittsburgh Medical Center. Studies were identified using keywords “concussion,” “mild traumatic brain injury,” and “diffusion tensor imaging.” Inclusion criteria were the following: 10–50 years of age, witnessed closed head trauma, no focal neurologic deficit, loss of consciousness of <1 minute, posttraumatic amnesia of <30 minutes, English language proficiency, and available neurocognitive testing with Immediate Post-Concussion Assessment and Cognitive Testing (ImPACT; <https://scipol.duke.edu/track/immediate-post-concussion-assessment-and-cognitive-testing-impact>). Exclusion criteria were the following: prior neuropsychiatric illness (2 patients), abnormal CT or conventional brain MR imaging findings including large focal abnormalities such as encephalomalacia not attributable to current trauma (3 patients), history of substance abuse (3 patients), lack of DTI (4 patients), lack of neurocognitive assessment (6 patients), total symptom score of zero (3 patients), and

Table 1: Demographic information and causes of injury

Participant Characteristics	Number of Participants
Demographics	
Age, time of imaging (range) (mean) (yr)	10–28 (16.1 ± 2.9)
Male participants (%)	44 (68.8)
Time from injury to imaging (mean) (days)	55 ± 91
Causes of mTBI	
Sports injury (%)	42 (65.6%)
Motor vehicle collision (%)	6 (9.4%)
Bicycle accident (%)	2 (3.1%)
Fell down stairs (%)	2 (3.1%)
Fell off horse (%)	2 (3.1%)
Other ^a (%)	10 (15.6%)

^a Various civilian injuries.

inability to align fractional anisotropy (FA) images (2 patients). The cohort included patients in the immediate ($n = 13$), acute ($n = 30$), subacute ($n = 10$), and chronic ($n = 11$) phases of injury (acute, 1–6 weeks; subacute, 7–12 weeks; chronic, >12 weeks).¹⁸ The final cohort contained 64 subjects. A prior article¹¹ used this cohort to examine postconcussive headache. Demographic information and causes of injury are summarized in Table 1. Unlike voxel-based analysis or ROI techniques used in prior studies, we evaluated postconcussive reaction time using the TBM technique to enable both discovery and visualization of novel structural substrate.

A neuropsychological examination was performed by a single neuropsychologist with >15 years of experience in treating patients with mTBI. Reaction time was determined as part of the ImPACT.¹⁹ Although ImPACT included other cognitive measures, this study focused on reaction time, one of the most common postconcussive cognitive sequelae²⁰ and a sensitive marker of recovery following concussion.^{20,21} ImPACT reaction time for each subject is a percentile based on normative data from baseline testing of >17,000 athletes as part of presport participation. Percentile information accounts for both sex and age.

MR Imaging Acquisition and Preprocessing

All subjects underwent an identical imaging protocol on the same system during the imaging time period. DTI was performed with a 1.5T unit (Signa; GE Healthcare, Milwaukee, Wisconsin) and a standard head coil. A single-shot echo-planar sequence was used (TR = 4000 ms, TE = 80 ms, NEX = 2, section thickness = 5 mm, matrix = 128 × 128, FOV = 260 mm). Diffusion gradients were set in 25 noncollinear directions using 2 b-values ($b=0$ and 1000/mm²).

FA maps were generated to characterize white matter integrity using the Brain Diffusion Toolbox,^{22,23} which is part of the DTI pipeline of FSL.^{24,25} The FA maps included both gray and white matter and were registered to the Montreal Neurological Institute atlas by a 12-parameter affine transformation. A common reference image was computed through the Euclidean average of all images across the study population.

Analyzing FA Spatial Distribution Using Transport-Based Morphometry

The microstructure differentiating high and low reaction time was not perceptible visually as demonstrated in Fig 1, motivating the use of TBM^{13,26–28} to discover the complex pattern. Our 3D-TBM technique¹³ is an image-transformation framework that fa-

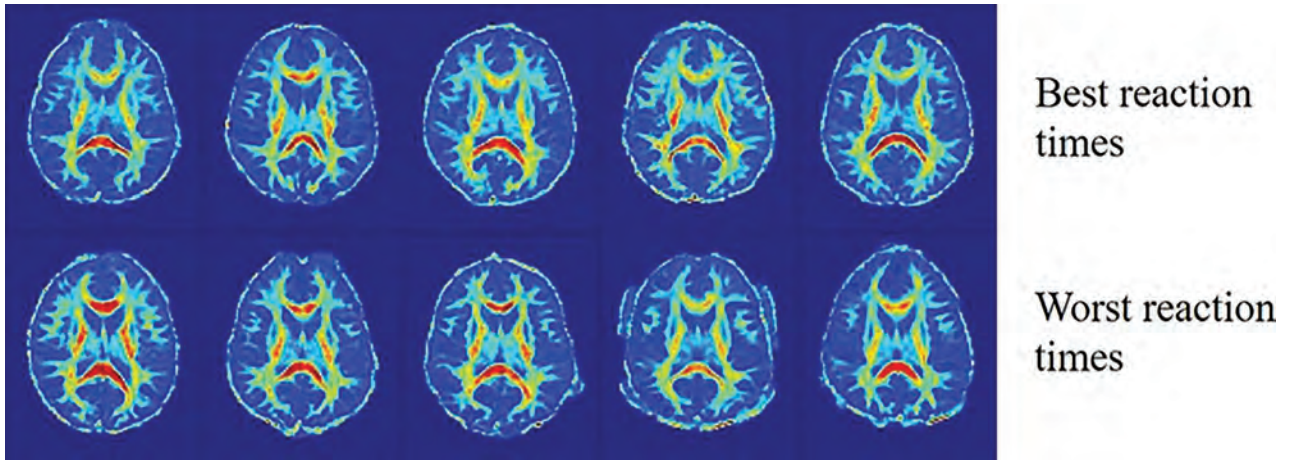


FIG 1. FA maps of 10 different postconcussive patients. The same axial slice is shown for patients with the best reaction time percentiles (*upper row*) and worst reaction time percentiles (*lower row*). These images illustrate the challenge that FA maps corresponding to the best and worst reaction times are not easily differentiated by visual inspection because the abnormal variations related to reaction time cannot be discerned from the other heterogeneous variations. Intelligent computer-aided techniques are needed to differentiate these images.

cilitates the discovery of this pattern through analysis in a transform domain.²⁶⁻²⁸ On-line Fig 1 illustrates the system diagram in the On-line Appendix. The interested reader is referred to Kundu et al¹³ for the mathematic derivation of 3D-TBM. We provide only a brief description here.

The similarity in the FA spatial distribution with respect to a reference is quantified in a transport map for each subject: a vector field morphing an individual FA image into the common reference. The optimal transport map minimizes FA transport to match the common reference. On-line Fig 2 shows FA maps and corresponding transport maps for 4 sample subjects.

The optimal transport map is unique for a pair of images,¹³ ensuring a bijective transformation. Equations A1 and A2 describe analysis and synthesis equations for forward and inverse transforms, respectively, in the On-line Appendix. Transformation is nonlinear; thus, complex patterns are more sparsely characterized in the transport domain and correspond to distances on the Riemannian manifold. Computing Riemannian distances with respect to a common template allows linearization of the optimal mass transport metric and reduces the number of operations from $N(N-1)/2$ to N . Prior work shows that pattern discrimination using the linear optimal transport distance is enabled when the template lies sufficiently close to the Riemannian manifold.^{27,28} Because the TBM transformation is bijective, we can generate de novo images along the regression direction in transport space through inverse transformation. The latter is enabled because TBM is generative. The ability to ultimately visualize the complex shift in microstructural profile initially imperceptible to visual inspection (Fig 1) is a unique contribution of TBM. We implemented all 3D-TBM codes in Matlab (MathWorks, Natick, Massachusetts) as described in Kundu et al.¹³

Assessing the Microstructural Relationship with Reaction Time

Statistical learning is performed in the transport domain to extract relevant image features. First, transport maps generated by the transformation are vectorized and concatenated into a standard data matrix. Then, the principal components analysis technique (Equation A3) is used to eliminate data dimensions con-

tributing little to the variance in the dataset. The data matrix is projected onto the topmost d eigenvectors associated with 90% of the variance in transport maps to create the reduced-dimension data matrix $X \in \mathbb{R}^d \times n$ ($d \ll n$). Let $v \in \mathbb{R}^n \times 1$ be the reaction time percentile mapped to squared values (to increase separation of lower from higher percentiles). The direction in transport space that results in the strongest linear correlation is computed with the reaction time percentile v (Equation 1)²⁶:

$$1) \quad w_{\text{corr}} = \arg \max_w \frac{w^T X v}{\sqrt{w^T w}} = \frac{X v}{\sqrt{v^T X^T X v}}$$

Here, w_{corr} is a vector field synthesized in the transport domain that quantifies the direction and amount of FA redistribution most correlated with the reaction time percentile. Covariates are removed according to Equation 2.

$$2) \quad v = y - Z(Z^T Z)^{-1} Z^T y.$$

Here, v describes the residual from the reaction time percentile ($y \in \mathbb{R}^n \times 1$) that is decorrelated and orthogonal to the c , confounding variables in $Z \in \mathbb{R}^n \times c$. This study corrects for age, sex, and time from injury as covariates. Statistical significance of the computed direction was assessed using permutation testing with $T = 1000$ tests. The reported P value is the fraction of times over T tests that the Pearson correlation coefficient was higher when labels v are randomly assigned to subject data than when computed based on the original assignment. We implemented all statistical analysis code in Matlab.

RESULTS

Assessing the Microstructural Relationship with Reaction Time

As illustrated in Fig 1, visual inspection does not elucidate the changes characteristic of poor postconcussive reaction time. The computed tissue distribution from the transport space was significantly associated with the reaction time percentile after correcting for covariates according to Equation 2 (Pearson $r = 0.44$, $P < .01$). The strength of the association is moderate. Furthermore, the pattern of injury identified by TBM is specific to cognitive

symptoms following mTBI because it is not significantly correlated with any other ImPACT measures except processing-speed percentile (Table 2).

On-line Fig 3 shows the scatterplot of subjects when their images are projected onto the most correlated direction computed in the transport space. The mean image $I_0(x)$ maps to a projection score of zero. Each point in the scatterplot represents a brain image in the dataset. According to the linear regression model constructed in the transport space, increasing reaction time percentile (faster reaction times) is associated with increasing projection scores, and decreasing reaction time percentile (slower reaction times) is associated with decreasing projection scores.

Understanding Complex Correlations Visually

In addition to confirming a correlation between the reaction time percentile and microstructure, projection scores can be interpreted clinically. Reverse TBM transformation can map any given projection score to visualize a computer-generated image. Figure 2 shows

Table 2: Correlation between TBM direction and other ImPACT measures

ImPACT Measure	Pearson Correlation	P
Anxiety	-0.06	.68
Cervicalgia	-0.06	.70
Headaches	-0.18	.91
Total ImPACT score	-0.29	.98
Processing speed percentile	0.31	<.01 ^a
Sleep-wake disturbance	-0.24	.97
Time to recovery	-0.05	.67
Tinnitus	-0.05	.61
Verbal memory	0.20	.06
Visual memory	0.20	.05

^a The discovered pattern of injury does not correlate with any other ImPACT measures except processing-speed percentile.

visualizations of dynamic brain morphology corresponding to varying projection scores. The images are synthesized on the basis of the study population. Note that simple linear regression in transport space can characterize the nonlinear, spatially diffuse, white matter injury pattern in the image domain.

The projection scores across the horizontal axis in Fig 2 correspond to those in the horizontal axis of On-line Fig 3. The images shown are computer-generated by TBM from points sampled along the line of best fit where the projection score spans -2 to $+2$ SDs from the mean. The FA maps are colored to aid in visualization. The values represent relative density, a measure of FA concentration. Two axial slices are shown that best summarize the morphologic differences from a low-reaction-time percentile to a high-reaction-time percentile. The population mean image $I_0(x)$ is indicated by the projection score zero in Fig 2. The images at the negative projection scores correlate most strongly with the low-reaction-time percentile, while the images at the positive projection scores correlate most strongly with high-reaction-time percentile (On-line Fig 3). Progressing from a low-to-high reaction time percentile, the statistical model illustrates that FA in the corpus callosum decreases while increasing in the optic radiations, corticospinal tract, and anterior thalamic tracts.

Individual Assessment of White Matter Injury Associated with Reaction Time

In addition to identifying common structural correlates of reaction time, TBM also identifies white matter injury in individual patients. The direction computed in transport space can clinically assess whether the patterns of white matter injury in Fig 2 are present in an individual patient. The transport map for an individual patient can be projected onto this direction to yield a projection score for the patient. The projection scores can be interpreted on the basis of the relationship with reaction time performance illustrated in On-line Fig 3 to evaluate whether cognitive deficits may be present. Figure 3

illustrates the FA map of a patient with a fast reaction time in the 94th percentile that maps to a high positive projection score and that of a patient with slow reaction time in the 21st percentile that maps to a low negative projection score, a potential metric by which to differentiate these patients. A key strength of TBM is its ability to assess spatially diffuse, complex white matter patterns that are not easily identified visually or by an ROI-based perspective.

Furthermore, Fig 3 shows that the transport map may reveal new numeric assessment tools. The determinant of the Jacobian computed from the transport maps measures the joint changes in FA concentration across multiple white matter tracts. An increase in FA concentration is indicated by a value of >1 , and decreases are indicated by a value of <1 . We see that the direction of FA change in multiple white matter tracts with respect

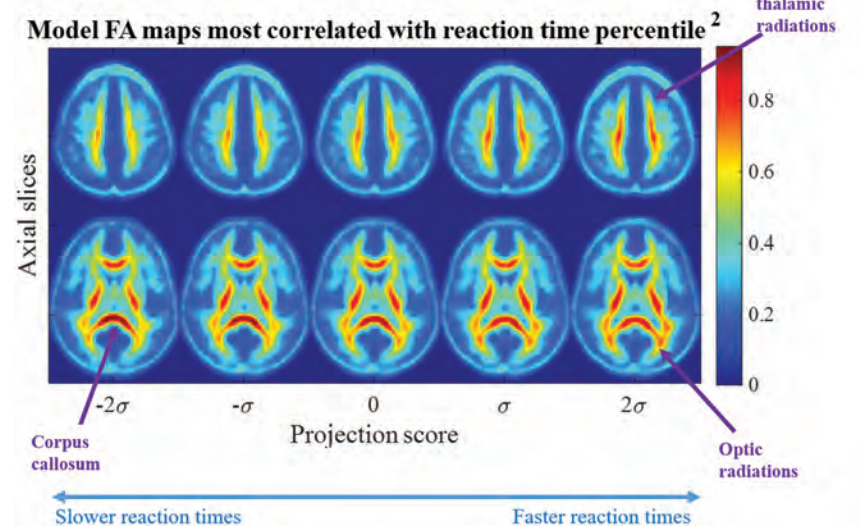


FIG 2. Most correlated direction. Images corresponding to the most correlated direction in transport space show decreasing FA in the corticospinal tracts, anterior thalamic radiations, and optic radiations with the low reaction time percentile corresponding to the scatterplot in On-line Fig 3. The FA in the corpus callosum increases as reaction time decreases.

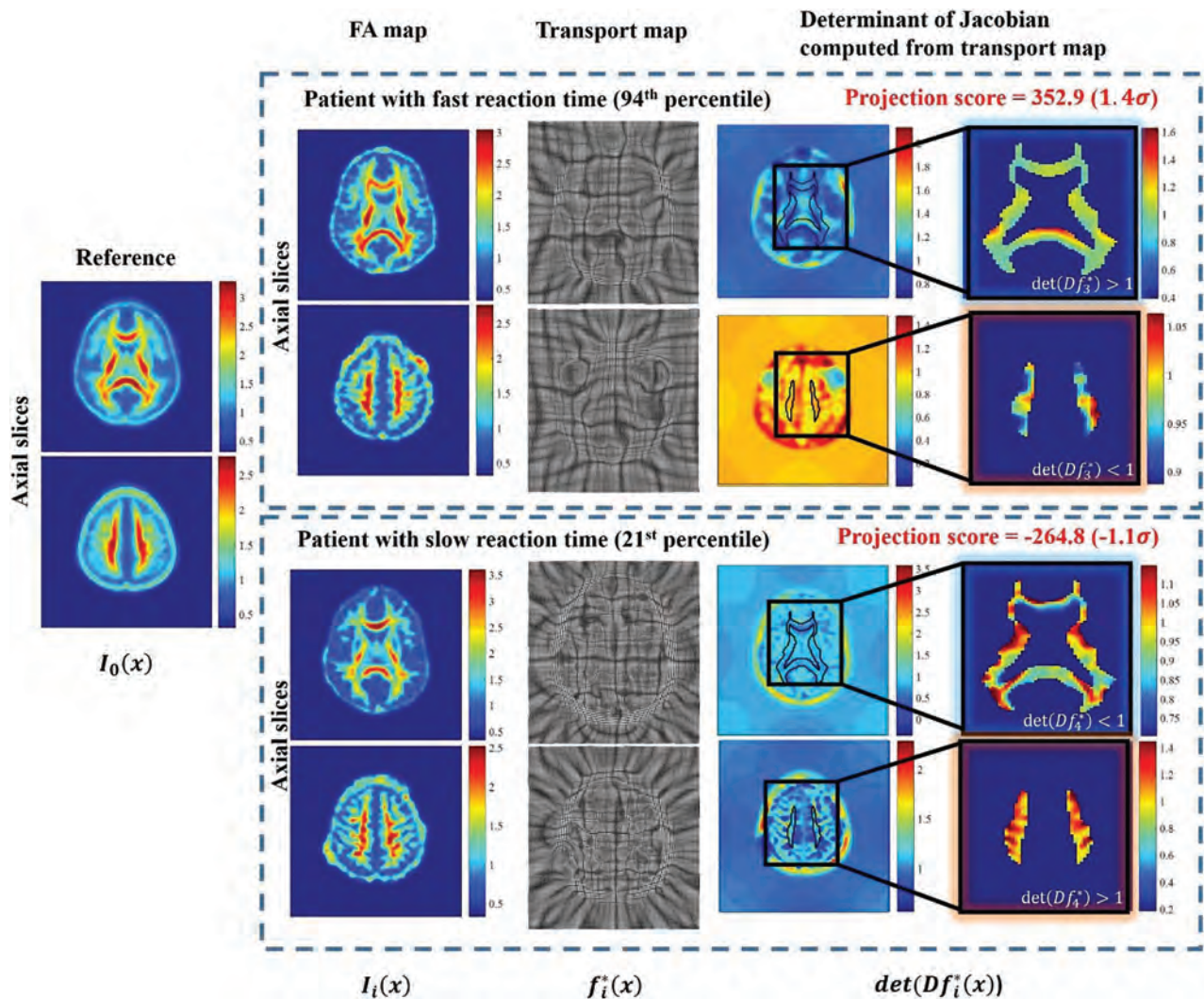


FIG 3. TBM can help assess cognitive deficits in individual patients using the computed direction to assess whether the complex and spatially distributed patterns of white matter injury identified by Fig 2 are present. When transport maps are projected onto this direction, a projection score is generated that can be used to differentiate patients according to the relationship in On-line Fig 3. The subjects shown correspond to $i = 3$ and 4 in Fig 1. The direction of FA change with respect to the reference in individual patients corroborates the patterns identified in Fig 2.

to the common reference corroborates those identified by Fig 2 for a patient with high and low reaction times.

DISCUSSION

This article investigates the microstructure underlying postconcussive reaction time. Our prior work developing 3D-TBM demonstrated its ability to uncover microstructural circuits not adequately assessed through visual inspection or conventional methods.¹³ This article builds on prior work to propose a new framework to bridge microstructure and postconcussive cognitive assessment. We discovered an FA spatial pattern that is significantly associated with reaction time and robust to covariates of age, sex, and time from injury. The discovered pattern is specific to cognitive symptoms and does not correlate with ImpACT measures outside of processing speed and reaction time. This article is the first to elucidate the influence of multiple regions jointly on postconcussive reaction time through visualizable FA images.

This work delves deeper in elucidating the link between postconcussive reaction time and brain microstructure than prior studies.²⁹⁻³² Previous studies investigated individual ROIs.

Womack et al²⁹ reported that the posterior corpus callosum is related to peripheral visual reaction time, and Arenth et al³⁰ reported that DTI parameters in the corpus callosum relate to impaired reaction time post-TBI. The prior findings, however, lack specificity to cognitive performance because the corpus callosum is commonly involved across mTBI populations.³¹ Our work uncovers microstructural circuitry that is specific to cognitive processing (ie, reaction time and processing speed). Other studies examining frontal ROIs^{12,32} found no consistent pattern between DTI variables on various ROIs and symptom scale scores. Most important, a prior study suggested that cognitive deficit is a diffuse process: the number of DTI lesions positively correlated with poorer cognitive measures.⁷ Our work offers a more complete map of the multiple microstructural lesions that jointly influence reaction time. This study uniquely visualizes the complex, dynamic microstructure opaque to visual interpretation and ROI-based approaches because TBM is generative.

Our work demonstrates a new approach for assessing latent microstructural patterns, especially those that are not discernible

visually. TBM addresses many shortcomings of traditional methods. Histogram analysis does not provide regionally specific answers,^{12,33} ROI-based techniques do not characterize spatially diffuse processes, and voxel-based analysis is sensitive to a priori structural/functional alignment,^{12,33,34} which produces false-positives in mTBI cohorts.¹⁰ Tractography visualizes *in vivo* pathways, but poorly understood interconnections are precisely the ones most difficult to characterize using tractography.³⁵ In contrast, TBM uncovers structure-function circuitry¹³ in an automated manner. Unlike traditional methods, TBM is generative and inverse transformation visualizes latent microstructure opaque to these methodologies. We see multiple white matter tracts dynamically interacting, providing novel insight into biophysical substrates. Our approach is widely applicable to future mTBI studies investigating the link between brain microstructure and clinical symptoms.

The microstructure we discovered is consistent with reaction time neurobiology. First, optic radiations interpret the initial stimulus and contribute to interindividual variability in reaction time.³⁶ Next, frontally mediated circuits help process the observed stimulus. In prior studies, damage to the anterior thalamic radiations led to impaired cognitive function³⁷ and was associated with reaction time deficits.³⁸ Following executive processing, interhemispheric transmission translates attention into a physical response. The corpus callosum mediates interhemispheric transmission and correlates with reaction time in both healthy and cognitively impaired individuals.^{33,39} Finally, the corticospinal tract generates a motor response.⁴⁰

In addition, this study illuminates interaction across multiple white matter tracts. The direction of FA varies among the corpus callosum and visual tracts, corticospinal tracts, and anterior thalamic radiations. Our corpus callosum findings are consistent with prior reports⁶ of increased FA with injury that suggest cytotoxic edema in the semiacute phase. However, other studies describe diffusely decreased FA with persistent cognitive symptoms, including in the corpus callosum.^{7,41} The acute/postacute imaging time period may be responsible for this finding. White matter injury in mTBI is dynamic, demonstrating increased FA early due to cytotoxic edema and decreased FA late, reflecting decreased white matter integrity and axonal loss.⁴² Our finding of mixed FA likely reflects a transitional time period. Some regions may have progressed to axonal loss, while others remain in earlier stages. This mixed response is seen during the semiacute interval.^{43,44} The corpus callosum is the largest fiber tract in the human brain⁴⁵; increased FA may represent residual edema from the immediate into the subacute phase of injury relative to smaller tracts.

There are several limitations of this study. We conducted a retrospective, single-center study. Future prospective, multi-center studies are needed to build on our results. Additionally, our patients ranged from pediatric to adult. White matter myelination may vary in the pediatric population. However, our model remained significant even after accounting for age covariation.⁴⁶ Furthermore, focusing on FA spatial distribution may be advantageous in mixed-age patient populations in which differences in head size may confound traditional voxel-based techniques. Our study included subjects imaged at heterogeneous intervals since traumatic injury, but the statistical model remained robust after

correcting for time from injury as a covariate. Furthermore, many patients with mTBI do not seek medical attention, and there is a possible selection bias toward more seriously injured or symptomatic patients. However, the bias may help direct toward patients who would benefit most from objective assessment. Finally, lack of universally accepted normative data limits quantitative use of DTI metrics in the clinical setting. Future studies will need to establish normative references for quantitative TBM in healthy patients and those with mTBI. This study motivates future investigation into causality between brain microstructure and mTBI symptoms.

CONCLUSIONS

In the future, 3D TBM may help provide prognostic markers to assess either recovery or progression to chronic stages in prospective longitudinal DTI studies.^{12,33} There is immense potential for 3D-TBM to be a novel diagnostic technology capable of investigating structure-function relationships in many diseases like mTBI that are still considered mysteries.

Disclosures: Gustavo K. Rohde—UNRELATED: Grants/Grants Pending: National Institutes of Health/National Science Foundation, Comments: I currently have 1 National Institutes of Health and National Science Foundation pending grant on developing the underlying technology that will support future studies using transport-based morphometry; Patents (Planned, Pending or Issued): United States Patent Office, Comments: I have 1 patent related to methods for measuring optimal transport between images.

REFERENCES

1. Vincent AS, Roebuck-Spencer TM, Cernich A, et al. **Cognitive changes and dementia risk after traumatic brain injury: implications for aging military personnel.** *Alzheimers Dement* 2014;10(3 Suppl):S174–87 CrossRef Medline
2. Himanen L, Portin R, Isoniemi H, et al. **Cognitive functions in relation to MRI findings 30 years after traumatic brain injury.** *Brain Inj* 2005;19:93–100 Medline
3. Grandhi R, Tavakoli S, Ortega C, et al. **A review of chronic pain and cognitive, mood, and motor dysfunction following mild traumatic brain injury: complex, comorbid, and/or overlapping conditions?** *Brain Sci* 2017;7 CrossRef Medline
4. Levin HS, Li X, McCauley SR, et al. **Neuropsychological outcome of mTBI: a principal component analysis approach.** *J Neurotrauma* 2013;30:625–32 CrossRef Medline
5. Hellowell DJ, Taylor RT, Pentland B. **Cognitive and psychosocial outcome following moderate or severe traumatic brain injury.** *Brain Inj* 1999;13:489–504 Medline
6. Wozniak JR, Krach L, Ward E, et al. **Neurocognitive and neuroimaging correlates of pediatric traumatic brain injury: a diffusion tensor imaging (DTI) study.** *Arch Clin Neuropsychol* 2007;22:555–68 Medline
7. Niogi SN, Mukherjee P, Ghajar J, et al. **Extent of microstructural white matter injury in postconcussive syndrome correlates with impaired cognitive reaction time: a 3T diffusion tensor imaging study of mild traumatic brain injury.** *AJNR Am J Neuroradiol* 2008;29:967–73 Medline
8. Mac Donald CL, Dikranian K, Bayly P, et al. **Diffusion tensor imaging reliably detects experimental traumatic axonal injury and indicates approximate time of injury.** *J Neurosci* 2007;27:11869–76 Medline
9. Davenport ND, Lim KO, Armstrong MT, et al. **Diffuse and spatially variable white matter disruptions are associated with blast-related mild traumatic brain injury.** *Neuroimage* 2012;59:2017–24 CrossRef Medline
10. Watts R, Thomas A, Filippi CG, et al. **Potholes and molehills: bias in**

- the diagnostic performance of diffusion-tensor imaging in concussion.** *Radiology* 2014;272:217–23 CrossRef Medline
11. Ghodadra A, Alhilali L, Fakhran S. **Principal component analysis of diffusion tensor images to determine white matter injury patterns underlying postconcussive headache.** *AJNR Am J Neuroradiol* 2016; 37:274–78 CrossRef Medline
 12. Niogi SN, Mukherjee P. **Diffusion tensor imaging of mild traumatic brain injury.** *J Head Trauma Rehabil* 2010;25:241–55 CrossRef Medline
 13. Kundu S, Kolouri S, Erickson KI, et al. **Discovery and visualization of structural biomarkers from MRI using transport-based morphometry.** *Neuroimage* 2018;167:256–75 CrossRef Medline
 14. Erlanger D, Saliba E, Barth J, et al. **Monitoring resolution of post-concussion symptoms in athletes: preliminary results of a web-based neuropsychological test protocol.** *J Athl Trai* 2001;36:280–87 Medline
 15. Collie A, Maruff P, Makdissi M, et al. **CogSport: reliability and correlation with conventional cognitive tests used in postconcussion medical evaluations.** *Clin J Sport Med* 2003;13:28–32 Medline
 16. Leddy JJ, Kozlowski K, Fung M, et al. **Regulatory and autoregulatory physiological dysfunction as a primary characteristic of post concussion syndrome: implications for treatment.** *NeuroRehabilitation* 2007;22:199–205 Medline
 17. Leddy JJ, Kozlowski K, Donnelly JP, et al. **A preliminary study of subsymptom threshold exercise training for refractory post-concussion syndrome.** *Clin J Sport Med* 2010;20:21–27 CrossRef Medline
 18. Department of Defense, Department of Veterans Affairs. VA/DoD Clinical Practice Guideline for Management of Concussion/Mild Traumatic Brain Injury. 2009. <https://www.rehab.research.va.gov/jour/09/46/6/pdf/cpg.pdf>. Accessed May 17, 2019
 19. Mayers LB, Redick TS. **Clinical utility of ImpACT assessment for postconcussion return-to-play counseling: psychometric issues.** *J Clin Exp Neuropsychol* 2012;34:235–42 CrossRef Medline
 20. Eckner JT, Kutcher JS, Richardson JK. **Effect of concussion on clinically measured reaction time in 9 NCAA division I collegiate athletes: a preliminary study.** *PMR* 2011;3:212–18 CrossRef Medline
 21. Lau B, Lovell MR, Collins MW, et al. **Neurocognitive and symptom predictors of recovery in high school athletes.** *Clin J Sport Med* 2009; 19:216–21 Medline
 22. Behrens TE, Woolrich MW, Jenkinson M, et al. **Characterization and propagation of uncertainty in diffusion-weighted MR imaging.** *Magn Reson Med* 2003;50:1077–88 Medline
 23. FDT. FMRIB's Diffusion Toolbox. <http://fsl.fmrib.ox.ac.uk/fsl/fsl-wiki/FDT>. Updated May 12, 2016. Accessed May 17, 2019
 24. Jenkinson M, Beckmann CF, Behrens TE, et al. **FSL.** *Neuroimage* 2012;62:782–90 CrossRef Medline
 25. FMRIB Software Library, Version 6.0. Analysis Group, FMRIB, Oxford, UK. <http://www.fmrib.ox.ac.uk/fsl>. Updated April 16, 2019. Accessed March 26, 2016
 26. Basu S, Kolouri S, Rohde GK. **Detecting and visualizing cell phenotype differences from microscopy images using transport-based morphometry.** *Proc Natl Acad Sci U S A* 2014;111:3448–53 CrossRef Medline
 27. Wang W, Slepčev D, Basu S, et al. **A linear optimal transportation framework for quantifying and visualizing variations in sets of images.** *Int J Comput Vis* 2013;101:254–69 CrossRef Medline
 28. Kolouri S, Tosun AB, Ozolek JA, et al. **A continuous linear optimal transport approach for pattern analysis in image datasets.** *Pattern Recognit* 2016;51:453–62 CrossRef Medline
 29. Womack KB, Paliotta C, Strain JF, et al. **Measurement of peripheral vision reaction time identifies white matter disruption in patients with mild traumatic brain injury.** *J Neurotrauma* 2017;34:1539–45 CrossRef Medline
 30. Arenth PM, Russell KC, Scanlon JM, et al. **Corpus callosum integrity and neuropsychological performance after traumatic brain injury: a diffusion tensor imaging study.** *J Head Trauma Rehabil* 2014;29: E1–10 CrossRef Medline
 31. Aoki Y, Inokuchi R, Gunshin M, et al. **Diffusion tensor imaging studies of mild traumatic brain injury: a meta-analysis.** *J Neurol Neurosurg Psychiatry* 2012;83:870–76
 32. Levin H, Wilde EA, Troyanskaya M, et al. **Diffusion tensor imaging of mild to moderate blast related TBI and its sequelae.** *J Neurotrauma* 2010;27:683–94 CrossRef Medline
 33. Grossman EJ, Inglese M, Bammer R. **Mild traumatic brain injury: is diffusion imaging ready for primetime in forensic medicine? Top Magn Reson Imaging 2010;21:379–86 CrossRef Medline**
 34. Bookstein FL. **“Voxel-based morphometry” should not be used with imperfectly registered images.** *Neuroimage* 2001;14:1454–62 Medline
 35. Jbabdi S, Johansen-Berg H. **Tractography: where do we go from here?** *Brain Connect* 2011;1:169–83 CrossRef Medline
 36. Tuch DS, Salat DH, Wisco JJ, et al. **Choice reaction time performance correlates with diffusion anisotropy in white matter pathways supporting visuospatial attention.** *Proc Natl Acad Sci U S A* 2005;102:12212–17 Medline
 37. Booth T, Bastin ME, Penke L, et al. **Brain white matter tract integrity and cognitive abilities in community-dwelling older people: the Lothian Birth Cohort, 1936.** *Neuropsychology* 2013;27:595–607 CrossRef Medline
 38. Righart RI, Duering M, Gonik M, et al. **Impact of regional cortical and subcortical changes on processing speed in cerebral small vessel disease.** *Neuroimage Clin* 2013;2:854–61 CrossRef Medline
 39. Anstey KJ, Mack HA, Christensen H, et al. **Corpus callosum size, reaction time speed and variability in mild cognitive disorders and in a normative sample.** *Neuropsychologia* 2007;45:1911–20 Medline
 40. Leocani L, Cohen LG, Wassermann EM, et al. **Human corticospinal excitability evaluated with transcranial magnetic stimulation during different reaction time paradigms.** *Brain* 2000;123(Pt 6): 1161–73 Medline
 41. Salmond CH, Menon DK, Chatfield DA, et al. **Diffusion tensor imaging in chronic head injury survivors: correlations with learning and memory indices.** *Neuroimage* 2006;29:117–24 Medline
 42. Eierud C, Craddock RC, Fletcher S, et al. **Neuroimaging after mild traumatic brain injury: review and meta-analysis.** *Neuroimage Clin* 2014;4:283–94 CrossRef Medline
 43. Mayer AR, Ling J, Mannel MV, et al. **A prospective diffusion tensor imaging study in mild traumatic brain injury.** *Neurology* 2010;74: 643–50 CrossRef Medline
 44. Bazarian JJ, Zhong J, Blyth B, et al. **Diffusion tensor imaging detects clinically important axonal damage after mild traumatic brain injury: a pilot study.** *J Neurotrauma* 2007;24:1447–59 Medline
 45. Aboitiz F. **Brain connections: interhemispheric fiber systems and anatomical brain asymmetries in humans.** *Biol Res* 1992;25:51–61 Medline
 46. Eckert MA, Keren NI, Roberts DR, et al. **Age-related changes in processing speed: unique contributions of cerebellar and prefrontal cortex.** *Front Hum Neurosci* 2010;4:10 CrossRef Medline

Association of Fractional Flow on 3D-TOF-MRA with Cerebral Perfusion in Patients with MCA Stenosis

X. Ge, H. Zhao, Z. Zhou, X. Li, B. Sun, H. Wu, J. Wan, J. Xu, J.P. Villablanca, and X. Liu



ABSTRACT

BACKGROUND AND PURPOSE: Fractional flow measured on 3D-TOF-MRA was proposed to quantify cerebral hemodynamic changes in patients with artery stenosis. We investigated the association between fractional flow and cerebral perfusion changes in patients with symptomatic MCA stenosis.

MATERIALS AND METHODS: This prospective study was approved by the institutional review board, and all participants provided written informed consent. From June 2015 to May 2018, four hundred twenty-nine patients with symptomatic intracranial arterial stenosis were consecutively recruited and underwent conventional brain MR imaging, 3D-TOF-MRA, and brain CTP. A total of 91 patients with unilateral M1 segment stenosis of the MCA and a stenosis degree of 50%~99% were included in the analysis. Fractional flow was measured by comparing distal and proximal signal intensity changes across the stenosis on 3D-TOF-MRA. The cutoff value for fractional flow for discriminating between normal perfusion and hypoperfusion was obtained from the receiver operating characteristic curve. Associations between fractional flow and hypoperfusion were assessed using univariate and multivariate analyses.

RESULTS: The receiver operating characteristic curve showed a significant fractional flow threshold value at 0.90 (sensitivity, 70.1%; 95% CI, 55.9%–81.2%; specificity, 69.6%; 95% CI, 47.6%–84.1%). Participants with a fractional flow of ≤ 0.90 were independently associated with cerebral hypoperfusion downstream from the stenosis site (adjusted OR, 3.68; 95% CI, 1.63–11.62; $P = .027$).

CONCLUSIONS: Fractional flow measured on 3D-TOF-MRA may serve as a noninvasive and practical tool for determining the cerebral hypoperfusion in patients with symptomatic MCA stenosis.

ABBREVIATIONS: FF = fractional flow; ICAS = intracranial arterial stenosis; rMTT = relative (affected side/contralateral side) MTT; rTTP = relative (affected side/contralateral side) TTP; SAG-C = stressed autoregulation compensated; SAG-D = stressed autoregulation decompensated; SI = signal intensity

Intracranial arterial stenosis (ICAS) is one of the main causes of ischemic stroke or TIA.¹ In addition to stenosis severity, several factors (such as plaque composition, collateral circulation status, and hemodynamic changes across the stenosis lesion) are closely associated with a risk of primary or recurrent stroke in patients with ICAS.^{2–4} Brain 3D-TOF-MRA has been widely used to diag-

nose ICAS in clinical practice. Recently, fractional flow (FF) measured on 3D-TOF-MRA, a new imaging parameter, was proposed to quantify cerebral hemodynamic changes in patients with ICAS.^{5–8}

Although FF predicted the risk of stroke in patients with ICAS in a secondary analysis of the Stroke Outcomes and Neuroimaging of Intracranial Atherosclerosis (SONIA) trial,⁷ the underlying mechanism has not been clarified. Cerebral hemodynamic changes caused by ICAS presumably reduce the perfusion pressure in the corresponding downstream region. Because CTP is a fast and reliable imaging option to visualize cerebral perfusion, Cianfoni et al⁹ and Siemund et al¹⁰ used CTP to characterize dynamic perfusion changes in response to a progressive decline in perfusion pressure: When perfusion pressure drops into an ischemic range, cerebral perfusion is maintained through autoregulatory vasodilation, which manifests with a normal or slightly increased CBF, elevated CBV, and a corresponding increase in MTT. As perfusion pressure continues to decline, cerebral arterioles are unable to dilate further, and CBF and CBV decrease as a consequence, as MTT is further prolonged. TTP,

Received December 11, 2018; accepted after revision May 3, 2019.

From the Departments of Radiology (X.G., H.Z., Z.Z., X. Li, B.S., J.X., X. Liu), Neurology (H.W.), and Neurosurgery (J.W.), Ren Ji Hospital, School of Medicine, Shanghai Jiao Tong University, Shanghai, P.R. China; and Department of Radiological Sciences and Neurosurgery (J.P.V.), David Geffen School of Medicine at University of California, Los Angeles, Los Angeles, California.

This research was supported by the National Natural Science Foundation of China (No. 81271575, 81401374, 81571630) and the Shanghai Jiao Tong University Medical-Engineering Cross-Cutting Research Project (No. YG2015M553, YG2015QN36).

Please address correspondence to Xiaosheng Liu, MD, PhD, Department of Radiology, Ren Ji Hospital, School of Medicine, Shanghai Jiao Tong University, 160 Pujian Rd, Shanghai 200127, China; e-mail: mi Xiaosheng@gmail.com

Indicates open access to non-subscribers at www.ajnr.org

<http://dx.doi.org/10.3174/ajnr.A6095>

an intuitive and straightforward parameter like MTT, is also extracted by some software packages.

Lan et al⁵ have explored the relationship between FF and cerebral perfusion in patients with ICAS and found that lower FF across the stenosis lesion could reflect delayed perfusion in the ipsilateral downstream region. However, their work was hindered by a long interval between MRA and CTP, a small sample size, and other potential confounders. In this study, we aimed to prospectively investigate the association between FF across the stenosis lesion and ipsilateral downstream perfusion on CTP in patients with symptomatic MCA stenosis and to assess the ability of the FF to discriminate cerebral hypoperfusion from normal perfusion in this clinical population.

MATERIALS AND METHODS

Participants

The study was approved by the Ethic Committee of Shanghai Renji Hospital, and all participants provided written informed consent. From September 2015 to May 2018, we consecutively recruited patients with ischemic stroke or TIA who were diagnosed by a physician from the department of neurology of our hospital. Ischemic stroke was defined as an episode of neurologic dysfunction persisting ≥ 24 hours or until death, caused by focal cerebral infarction on CT or MR imaging with other etiologies excluded.¹¹ TIA was defined as a transient episode of neurologic dysfunction lasting < 24 hours and caused by focal cerebral ischemia without a finding of acute infarction. The symptomatic MCA stenosis was defined as responsible for the neurologic dysfunction. All participants underwent conventional brain MR imaging, including 3D-TOF-MRA, and brain CTP within 1 day of enrollment. The location and degree of ICAS were evaluated on CTA from the arterial phases of CTP source data. Patients with unilateral MCA stenosis at the M1 segment and with a stenosis degree of 50%–90% were included for analysis. Exclusion criteria were as follows: 1) cardioembolic stroke, 2) coexistent extracranial arterial stenosis with the stenosis degree of $> 50\%$, 3) tandem stenosis at the MCA by CTA and MRA, 4) MR signal intensity (SI) and absent CTA density loss at the M1 segment of the MCA due to complete occlusion, and 5) contraindications to MR imaging or CTP (heart pacemaker, metallic implant, severe claustrophobia, pregnancy, allergy, or an estimated glomerular filtration rate of < 30 mL/min/1.73 m²). Demographic and clinical characteristics of enrolled subjects were recorded. Anatomically severe and moderate stenosis was determined to be 70%–99% and 50%–69% luminal stenosis measured on CTA, respectively.

Fractional Flow Measured on 3D-TOF-MRA

All participants underwent conventional brain MR imaging and 3D-TOF-MRA using a 3T whole-body MR imaging scanner (Achieva; Philips Healthcare, Best, the Netherlands) with the following sequences—1) axial T1WI: TR = 25 ms, TE = 2.3 ms; 2) axial T2WI: TR = 3000 ms, TE = 80 ms; 3) axial FLAIR: TR = 7000 ms, TE = 120 ms, TI = 2250 ms; and 4) axial DWI: TR = 2748 ms, TE = 97 ms, b-value = 1000. All axial MR images shared the following parameters: FOV = 230 × 230 mm, slice thickness = 5 mm, acquisition matrix = 230 × 230 (except DWI with the reconstructed matrix of 192 × 192). The parameters of

the 3D-TOF-MRA sequence were the following: slice thickness = 1.2 mm, TR = 23 ms, TE = 3.5 ms, flip angle = 18°, FOV = 199 × 199 mm, acquisition matrix = 500 × 332. Eighteen MIPs with 10° separation were constructed for anteroposterior and lateral views, respectively. The duration of MR imaging was 8 minutes 50 seconds.

FF was measured on an Extended MR Workspace 2.6.3.1 (Philips Healthcare) by 2 independent readers (X.G. and X. Liu with 3 and 15 years of experience in MR imaging interpretation, respectively), blinded to each other's readings and clinical data. According to the method proposed by Liebeskind et al,⁷ proximal and distal SIs across ICAS lesions were measured on the MIP image that showed the highest percentage of stenosis of the target lesion, using two 3-mm-length ROIs covering the entire vessel lumen (Fig 1). The boundary of the vessel edge was defined using a visual estimation of the full width at half maximum of the slice-sensitivity profile.¹² The background SI was estimated by the average SI in 2 circular ROIs (with an area of 15–20 mm²) placed symmetrically on both sides of the background on the same MIP image. The FF was calculated according to the following formula: $FF = (\text{Distal SI} - \text{Background SI}) / (\text{Proximal SI} - \text{Background SI})$. To avoid the possible impact of window width and level settings on the lesion appearance, we standardized viewing thresholds between the 2 readers. Each lesion was measured twice by each reader; then, the average of the 2 measures was the FF value of the lesion from this reader.

Acute cerebral infarctions were identified as hyperintense lesions on the DWI and hypointense lesions on apparent diffusion coefficient maps. The volumes of the acute cerebral infarctions involving the MCA regions were measured by an independent radiologist (J.X. with 20 years of experience in MR imaging interpretation) twice for each patient with acute ischemic stroke on the Extended MR workstation. The volumes of acute cerebral infarctions were determined using the image of the affected slices with hyperintense areas visible from the $b = 1000$ mm²/s² images. The sum of the volumes of the acute cerebral infarctions was recorded and averaged.

Brain CT Perfusion

All participants underwent cerebral CTP with a 64–detector row scanner (SOMATOM Sensation 64, Siemens, Forchheim, Germany). Scanning parameters of CTP were as follows: 100 kV, 150 mAs, 235 × 199 mm collimation, 11.4-cm scan volume in the z-axis, slice thickness = 5 mm using an adaptive spiral scanning technique (“shuttle mode”). Data were acquired at 40 time points separated by a repetition interval of 1.5 seconds. A total of 50 mL of nonionic iodinated contrast media, iohexol (Omnipaque 350; GE Healthcare, Piscataway, New Jersey), was injected at a rate of 5.0 mL/s, followed by a saline flush of 30 mL of sodium chloride at 5.0 mL/s and a start delay of 5 seconds. The total CT dose index volume was 198.25 mGy, and the total dose-length product was 2258 mGy × cm. The CTP processing analysis was performed on a multimodality workstation (Siemens syngo 2010B; Siemens) with the vendor-supplied Neuro-VPCT software based on the semiautomatic deconvolution algorithm “auto stroke.” Motion correction, bone segmentation, estimation of arterial input, and venous output function were performed automatically before

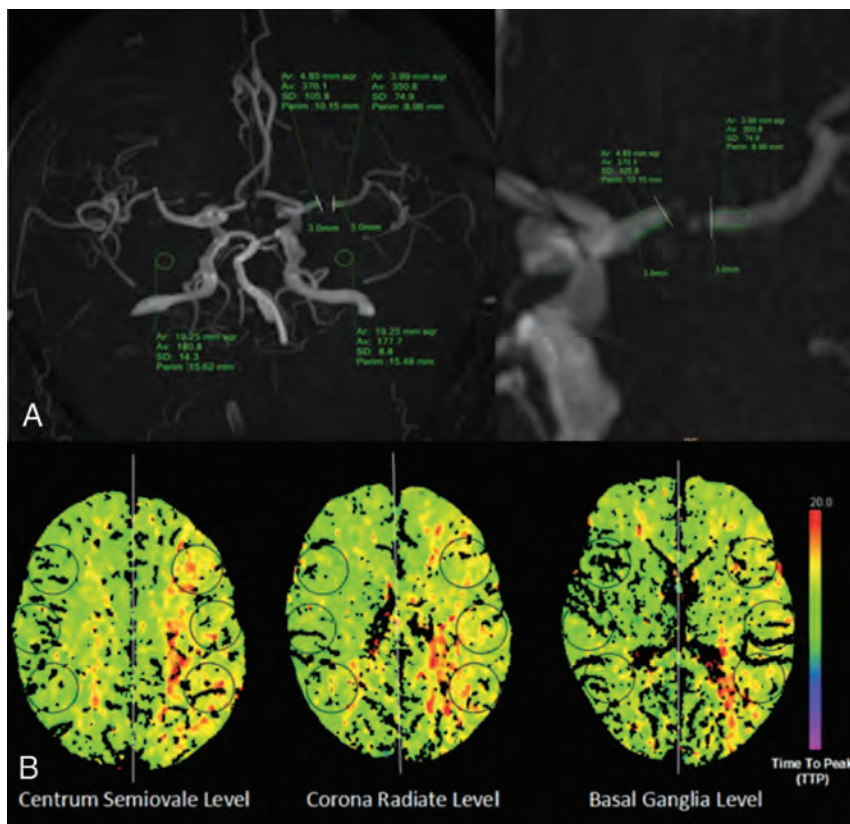


FIG 1. Illustration of fractional flow measurement and cerebral perfusion assessment. A, FF measurement: measurement of signal intensities proximal and distal to a stenosis located at the left MCA on a 3D-MIP image of TOF-MRA. B, Cerebral perfusion assessment: 6 circular ROIs were symmetrically drawn in the bilateral MCA territories at the centrum semiovale, corona radiata, and basal ganglia levels.

angiograms and color-coded perfusion parameter maps of MTT, TTP, CBF, and CBV were obtained.

The quantitative assessment of cerebral perfusion was performed by 2 independent radiologists (X. Li and Z.Z. with 4 and 10 years of experience in CTP interpretation, respectively) who were blinded to the FF outcome. Six circular ROIs (8–12 cm²) in either hemisphere were drawn manually and symmetrically in the bilateral MCA territories at 3 anatomic levels (the centrum semiovale, corona radiata, and basal ganglia levels) (Fig 1). The mean relative values of MTT (rMTT), TTP (rTTP), CBF, and CBV were calculated by the ratio of the mean value of the ROIs between the affected and contralateral sides. Ischemic penumbra was considered as a relative MTT increase of >145% with increased TTP, mildly decreased CBF, and normal or even increased CBV.¹³ Core infarction was an affected CBF reduction of >31% of the contralateral side, with increased MTT and TTP and decreased CBV.¹⁴ Radiologists needed to refer to the DWI to avoid missing small lacunar infarcts on color-coded perfusion parameter maps. Hypoperfusion was defined as ischemic penumbra and/or core infarction in the downstream region of the lesion and was graded as 1 of 2 stages: the stressed autoregulation compensated (SAG-C) stage (ischemic penumbra without core infarction) and the stressed autoregulation decompensated (SAG-D) stage (with core infarction) (Fig 2).

The degree of luminal stenosis and stenosis lengths were blindly measured twice by the same reader (B.S. with 5 years of experience in brain CT interpretation) for each patient, and the

values were averaged. The degree of stenosis on CTA was calculated by following equation: Percentage Stenosis = $[1 - (D_{\text{stenosis}} / D_{\text{normal}})] \times 100\%$. D_{stenosis} is the diameter of vessel at the side of stenosis. D_{normal} is the diameter of the vessel distal to the stenosis.¹⁵ Anatomically moderate and severe stenoses were determined as 50%–69% luminal stenosis and 70%–99% luminal stenosis, respectively.

Collateral circulation in MCA territories was assessed on the basis of a 6-point ordinal scale proposed by Menon et al.¹⁶ The 15th (the peak arterial phase), 20th, and 25th phases of the CTP original images were chosen to grade collateral scores. Two independent radiologists (H.Z. and B.S. with 10 and 5 years of experience in brain CT interpretation, respectively) who were blinded to the data of adjusted FF and CT perfusion compared the pial arterial filling between symptomatic and contralateral hemispheres in 3 CTP phases and then performed collateral scoring.

Statistical Analysis

Data were presented as mean \pm SD and median or count (percentage) as appropriate. The 1-way random intraclass correlation coefficient was performed to assess the interreader reproducibility of the FF. Mean FFs of 2 readers were compared using paired *t* tests. Interreader agreement on collateral scoring and hypoperfusion decision-making were assessed by the Cohen κ test. The κ value or intraclass correlation coefficient was interpreted as fair (0.20–0.40), moderate (0.41–0.60), good (0.61–0.80), or excellent (0.81–1.00) agreement. Receiver operating characteristic curves were used to calculate the sensitivity and specificity of the FF for distinguishing normal perfusion and hypoperfusion. The threshold was set according to the Youden index. The association between the FF and hypoperfusion was assessed using the logistic regression model. First, univariable association was determined, and a multivariable model was then used to adjust potential confounders with *P* values of < .05 in the univariable analysis. Correlations between FF and perfusion parameters, degree of luminal stenosis, stenosis lengths, the volumes of acute cerebral infarctions, and the degree of hypoperfusion were evaluated by either the Pearson or Spearman correlation coefficient. The 1-way ANOVA test followed by the least significant difference test was applied for multiple comparisons of FF among different degrees of cerebral hypoperfusion. Differences of FF between normal perfusion and hypoperfusion groups were analyzed by the independent-samples *t* test. SPSS software (Version 19.0; IBM, Armonk, New York) was used for statistical analysis. A *P* value < .05 was considered statistically significant.

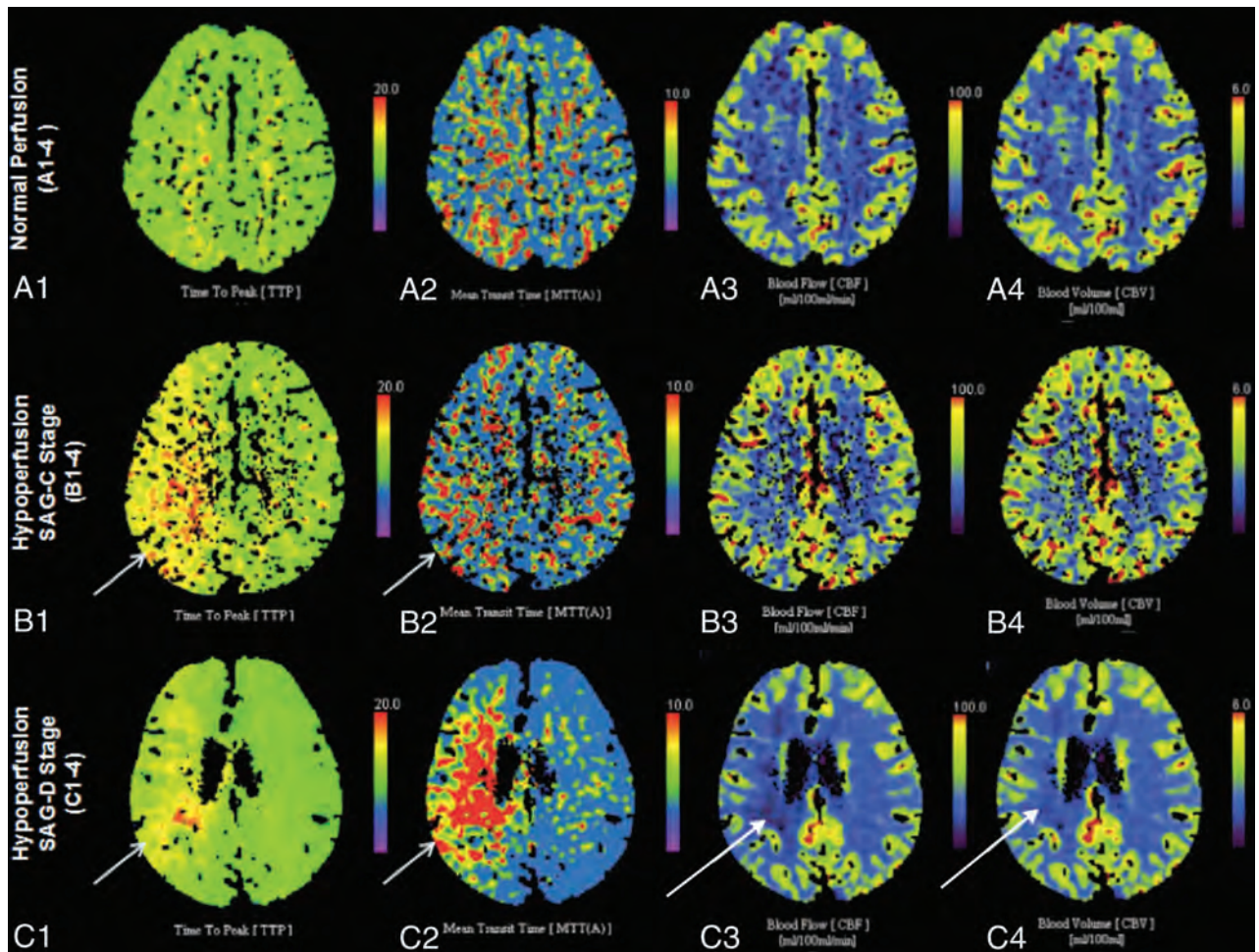


FIG 2. Color-coded perfusion parameter maps show the degree of cerebral hypoperfusion. A1–4, Normal perfusion. B1–4, Hypoperfusion on the stressed autoregulation compensated stage (ischemic penumbra without core infarction). C1–4, Hypoperfusion on the SAG-D stage (ischemic penumbra with core infarction). Short arrows show ischemic penumbra regions (increased TTP and MTT, normal CBF and CBV). The long arrows show core infarction regions (increased TTP and MTT, decreased CBF and CBV).

RESULTS

Characteristics of Participants

In total, 91 eligible participants (28 women and 63 men; mean age, 59.0 ± 9.6 years) were included in the analysis. Patients with stroke spanned the acute-to-chronic stage (median time since stroke, 22.7 days; interquartile range, 12.3–36.1 days). The percentage of patients with MCA stenosis was 89.0% ($n = 81$) on the symptomatic side and 11.0% ($n = 10$) on the asymptomatic side. A total of 338 participants were excluded due to cardioembolic stroke ($n = 21$), intracranial artery occlusion ($n = 68$), ICAS involving the posterior circulation or intracranial segment of the internal carotid artery ($n = 89$), multiple ICAS or extracranial arterial stenosis ($n = 118$), tandem stenosis at the MCA ($n = 37$), or poor image quality due to motion artifacts ($n = 5$). Participants with hypoperfusion were significantly different from those with normal perfusion in current smoking, anatomic severity of the lesion, collateral scoring, and FF ($P = .001$, $P = .004$, $P = .002$, and $P = .000$, respectively) (Table 1).

Mean FFs were not significantly different between 2 readers ($P = .309$, mean difference = $.008$). The interreader agreement was good for FF (intraclass correlation coefficient = 0.92), hypo-

perfusion assessment ($\kappa = 0.93$), and collateral circulation scoring ($\kappa = 0.90$).

FF Cutoff Value Determined from the Receiver Operating Characteristic Curve

Twenty-nine (31.9%) participants had normal perfusion, and 62 (68.1%) had hypoperfusion involving the ipsilateral MCA region. The mean FF value of the hypoperfusion group was significantly lower than that of normal-perfusion group (0.7 ± 0.2 versus 0.9 ± 0.2 ; $P = .000$). The receiver operating characteristic curve of FF to distinguish normal perfusion and hypoperfusion is shown in Fig 3. The area under the curve was 0.702. For the FF, the Youden index was greatest when a threshold value of 0.90 was applied (sensitivity, 70.1%; 95% CI, 55.9%–81.2%; specificity, 69.6%; 95% CI, 47.6%–84.1%).

Association between FF and Cerebral Perfusion

Table 2 shows the results of the logistic regression analyses of FF. In univariate analysis, there were significant differences between normal perfusion and hypoperfusion in the FF, collateral score, and current smoking ($P = .046$, $P = .049$, and $P = .043$, respec-

Table 1: Characteristics of patients and lesions

	With Normal Perfusion on Brain CTP (n = 29)	With Hypoperfusion on Brain CTP (n = 62)	P Value
Age (mean) (yr)	58.8 ± 9.2	61.5 ± 10.9	.237
Male sex (No.) (%)	16 (17.6%)	47 (51.6%)	.261
Current smoker (No.) (%)	4 (4.4%)	30 (33.0%)	.001
Hypertension history (No.) (%)	13 (14.3%)	38 (41.8%)	.073
Diabetes mellitus history (No.) (%)	5 (5.5%)	19 (20.9%)	.204
Blood pressure (mean) (mm Hg)			
SBP	139.6 ± 25.9	140.7 ± 24.1	.874
DBP	79.3 ± 14.3	83.1 ± 13.9	.283
Fasting blood glucose (mean) (mmol/L)	5.5 ± 1.1	6.4 ± 2.5	.069
Cholesterol (mean) (mmol/L)			
Total cholesterol	4.1 ± 0.8	4.0 ± 1.2	.814
HDL	1.1 ± 0.3	1.1 ± 0.4	.988
LDL	2.2 ± 0.7	2.2 ± 1.0	.954
Triglycerides	1.7 ± 0.9	1.5 ± 0.9	.494
Admitting diagnosis (No.) (%)			
Transient ischemic attack	10 (11.0%)	11 (12.1%)	.916
Acute ischemic stroke	8 (8.8%)	26 (28.6%)	.086
Chronic ischemic stroke	11 (12.1%)	25 (27.5%)	.541
Time from onset to CT/MRI (mean) (day)	29.1 ± 19.6	24.0 ± 18.9	.408
Median (interquartile range 25%–75%)	24 (15.5–46)	22 (11–30)	.536
Anatomic severity of lesion on CTA (No.) (%)			
Severe	10 (11.0%)	49 (53.8%)	.004
Moderate	19 (20.9%)	13 (14.3%)	.674
Stenosis length (mean) (mm)	4.7 ± 2.5	4.9 ± 2.7	.795
Collateral scoring on CTA	4.5 ± 0.4	3.7 ± 1.5	.002
Fractional flow on MRA	0.9 ± 0.2	0.7 ± 0.2	.000

Note:—HDL indicates high density lipoprotein; LDL, low density lipoprotein; SBP, systolic blood pressure; DBP, diastolic blood pressure.

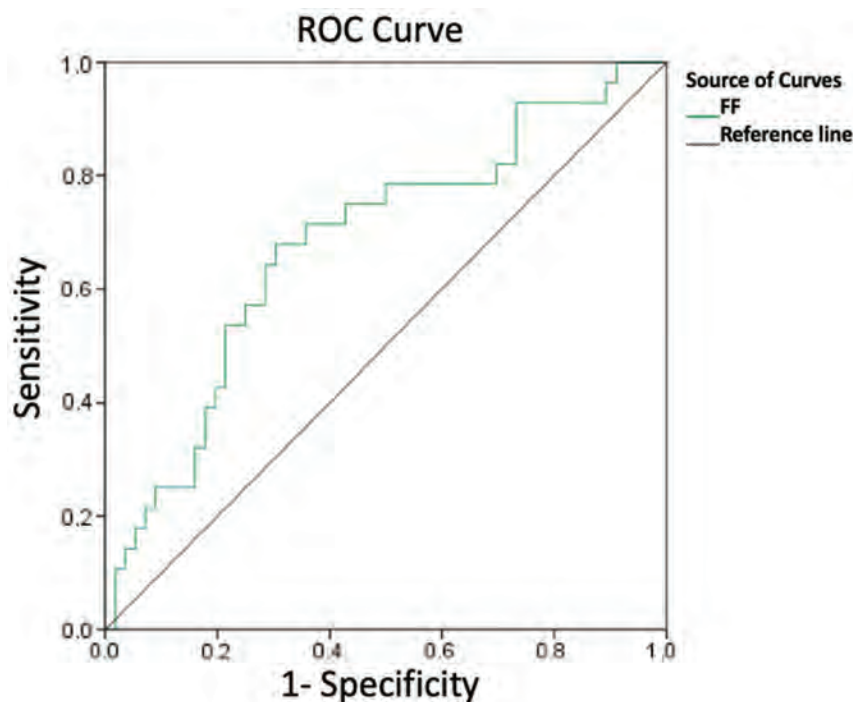


FIG 3. Receiver operating characteristic (ROC) curve of fractional flow to differentiate normal perfusion and hypoperfusion.

tively). In multivariate analysis, an FF of ≤ 0.90 was independently associated with cerebral hypoperfusion in the region downstream from a stenosis site (adjusted OR, 3.68; 95% CI, 1.63–11.62; $P = .027$) and after correcting for collateral score and current smoking

(OR, 0.26; 95% CI, 0.07–0.97; $P = .041$; OR, 7.20; 95% CI, 1.43–36.40; $P = .017$).

FF was different among normal (29, 31.9%), SAG-C (22, 24.2%), and SAG-D (40, 43.9%) perfusion stages ($P = .021$), and a negative correlation was found between FF and different cerebral perfusion stages ($\rho = -0.325$, $P = .010$). The mean FF at the normal stage (0.93 ± 0.15) was higher than that at SAG-C stage (0.86 ± 0.21 , $P = .024$) or at the SAG-D stage (0.72 ± 0.18 , $P = .011$). The mean FFs at SAG-C and SAG-D stages were not different ($P = .534$) (Fig 4). In terms of the perfusion parameters, the FF was correlated with rTTP ($r = -0.52$, $P < .001$), rMTT ($r = -0.57$, $P < .001$), and relative CBF ($r = 0.21$, $P = .043$), but not with relative CBV ($r = 0.16$, $P = .143$) in all eligible participants (Table 3). Stratification by the collateral score showed that the correlations between FF and rTTP and rMTT in poor collateral circulation (collateral score 0–3 group; $r = -0.485$, $P = .001$; $r = -0.414$, $P = .001$) were stronger than those in good collateral circulation (collateral score 4–5 group; $r = -0.250$, $P = .004$; $r = -0.361$, $P = .002$).

Neither the degree of luminal stenosis nor stenosis lengths were significantly correlated with FF ($r = -0.217$, $P = .089$; $r = -0.163$, $P = .315$). In patients with acute cerebral infarctions, there was no significant correlation between FF and the volume of acute cerebral infarctions ($r = -0.119$, $P = .076$).

DISCUSSION

In this study, there was an independent association between the FF across the stenosis site and cerebral hypoperfusion in the downstream region in participants with ICAS at the M1 segment of the MCA. FF could discriminate cerebral hypoperfusion from normal perfusion at a cutoff value of 0.90 with relatively high sensitivity and specificity. The interreader reproducibility of the FF measurement was good, a finding consistent with the results of a prior study.¹⁷ These findings suggest that FF measured on 3D-TOF-MRA could be adopted as a noninvasive and practical tool to determine the hemodynamic change in patients with ICAS.

Table 2: Association of participant characteristics with cerebral hypoperfusion in univariable and multivariable logistic regression models

	Univariable Model		Multivariable Model	
	P Value	OR (95% CI)	P Value	OR (95% CI)
Age (per 1-yr increase)	.542	0.98 (0.90–1.05)		
Male vs female	.254	0.38 (0.07–2.01)		
Current smoker (Y vs N)	.043	8.06 (1.06–60.71)	.017	7.20 (1.43–36.40)
Hypertension history (Y vs N)	.072	3.99 (0.89–18.06)		
Diabetes mellitus history (Y vs N)	.847	1.18 (0.21–6.51)		
SBP (per 1-mm Hg increase)	.141	0.96 (0.91–1.01)		
DBP (per 1-mm Hg increase)	.615	1.02 (0.94–1.16)		
Fasting blood glucose (per 1-mmol/L increase)	.081	1.75 (0.93–3.14)		
HDL (per 1-mmol/L increase)	.427	3.19 (0.14–75.54)		
LDL (per 1-mmol/L increase)	.299	3.37 (0.19–60.23)		
Triglycerides (per 1-mmol/L increase)	.180	0.53 (0.23–1.41)		
Total cholesterol (per 1-mmol/L increase)	.300	0.17 (0.07–4.72)		
Time from onset to CT/MRI (per 1-day lapse)	.451	0.98 (0.95–1.03)		
Anatomic severity of ICAS on CTA (severe vs moderate)	.274	0.59 (0.48–12.86)		
Stenosis length (per 1-mm increase)	.262	0.54 (0.45–13.06)		
Collateral score on CTA (per 1-score increase)	.049	0.28 (0.06–1.22)	.041	0.26 (0.07–0.97)
Fractional flow on MRA (≤ 0.90 vs > 0.90)	.046	7.28 (1.03–51.35)	.027	3.68 (1.63–11.62)

Note:—Y indicates yes; N, no; HDL, high density lipoprotein; LDL, low density lipoprotein; SBP, systolic blood pressure; DBP, diastolic blood pressure.

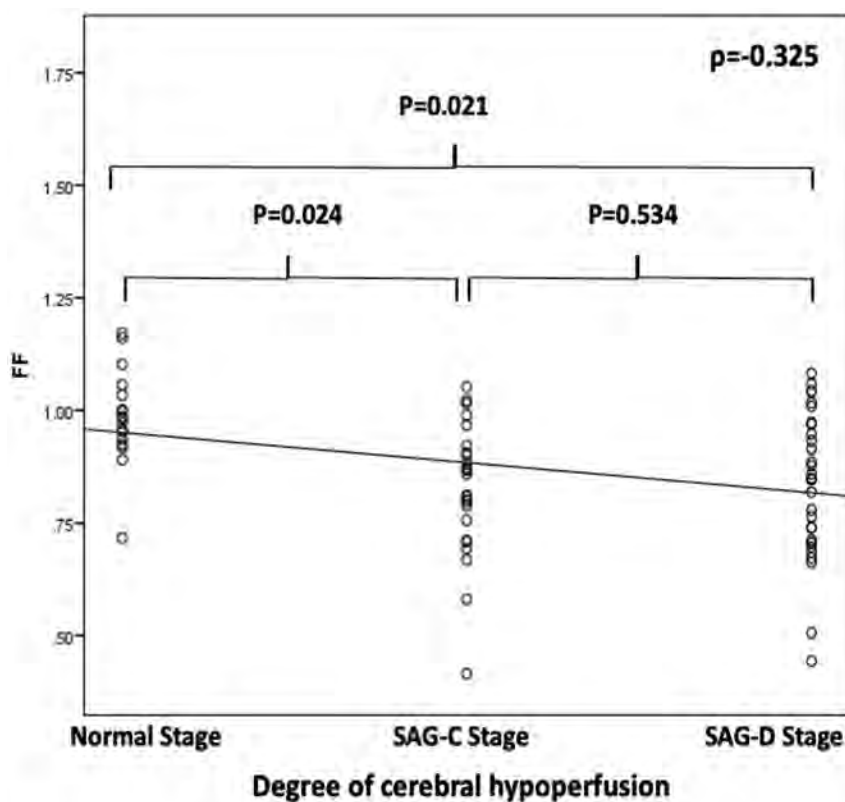


FIG 4. Correlations between fractional flow and the degree of cerebral hypoperfusion.

Previous studies have reported that 3D-TOF-MRA was not only able to diagnose ICAS but also provide information on hemodynamic changes due to stenotic lesions. Leng et al⁶ reported that SI changes across a stenosis on 3D-TOF-MRA were correlated with acute infarct volume on DWI. Lan et al⁵ found that reduced SI was associated with delayed ipsilateral cerebral perfusion. However, the threshold FF value for determining hemodynamically significant ICAS is still unknown. In this study, the dichotomous FF was used in the analysis of its association with cerebral perfusion. We found that FF could discriminate cerebral

hypoperfusion from normal perfusion at the cutoff value of 0.90. In addition, we used reasonable ROIs in the bilateral MCA territories on the CTP maps, examined a larger sample size, and took more confounders into consideration, including stenosis severity, collateral circulation scores, and the interval time between CT and MR imaging.

Liebeskind et al⁷ reported that FF could predict the risk of stroke in patients with ICAS. The underlying mechanism might be the mediation of cerebral perfusion impairment caused by a hemodynamic change.^{18,19} Most interesting, our FF cutoff value (0.90) in the discrimination of hypoperfusion from normal perfusion is almost the same as that (0.9) in the prediction of stroke risk in patients with MCA stenosis.⁷ A further prospective cohort study is needed to confirm the underlying mechanism by taking stroke events as the outcome and analyzing both FF and cerebral perfusion at baseline. According to the flow-related enhancement theory, an SI change of vessel lumen across the stenosis site on 3D-TOF-MRA is nonlinearly

correlated with the change of blood flow velocity caused by luminal stenosis.^{20–22} A nonlinear formula for FF calculation still awaits development.

We found that FF was significantly correlated with some of the perfusion parameters that are sensitive to perfusion pressure. Our results on the correlation between FF and rMTT were also confirmed in a prior study.⁵ The possible mechanisms may be that TTP and MTT were sensitive to perfusion pressure, and CBV and CBF were mainly influenced by the autoregulation mechanism and collateral circulation.⁹ In addition, the flow direction postste-

Table 3: Correlations between FF and perfusion parameters in different subgroups

Groups	Collateral Score				Current Smoking				All	
	0~3 (n = 26; 28.6%)		4~5 (n = 65; 71.4%)		Yes (n = 34; 37.4%)		No (n = 57; 62.6%)		(n = 91; 100%)	
	r	P	r	P	r	P	r	P	r	P
rTTP	-0.485	.001	-0.250	.004	-0.509	.018	-0.502	.017	-0.517	.000
rMTT	-0.414	.001	-0.361	.002	-0.454	.019	-0.507	.011	-0.569	.000
rCBF	-0.103	.739	0.079	.592	0.270	.046	0.203	.167	0.213	.043
rCBV	0.033	.914	0.004	.977	-0.172	.400	0.128	.384	0.155	.143

Note:—rCBV indicates relative CBV; rCBF, relative CBF.

nosis may be reversed and may create a low signal on 3D-TOF-MRA distal to the stenosis in case of good collateral flow, providing a false impression that the stenosis is hemodynamically relevant. The FF had a limited ability to detect the preservation or a slight decrease in relative CBF and relative CBV. Thus, there was no significant difference in FF between SAG-C and SAG-D stages in our study, SAG-C and SAG-D stages graded according to the decrease of CBF and CBV.

Collateral blood is one of the key factors in maintaining normal cerebral perfusion in ischemic regions when primary sources of flow have become compromised.²³ To reduce the effect of cerebral collateral circulation on the results, we chose the unilateral MCA stenosis at the M1 segment, which could avoid the compensation of communicating arteries of the circle of Willis. In addition, we also took the secondary collateral pathways into account, consisting of intracranial leptomeningeal anastomoses. Also, we found that correlations between FF and rTTP and rMTT in the collateral score 0–3 group were stronger than those in the collateral score 4–5 group. The reason may be that hemodynamic changes across the ICAS lesion may directly influence downstream perfusion when collateral blood is poor.

Strengths of this study included the prospective design, relatively large sample size, short interval between MR imaging and CT, and adjusting clinical or imaging confounders related to the cerebral perfusion. This study also had several limitations. First, we recruited only participants with ICAS at the unilateral M1 segments of the MCA. Therefore, generalization of the conclusions from the current study may be limited by the selection bias. The application of FF in patients with ICAS at multiple sites will be further explored in future studies. Second, our sample size was not large enough for subgroup analysis, so a prospective study with more participants is needed. Furthermore, several factors could affect the SI across the stenosis site on TOF-MR imaging, such as vessel orientation, vessel tortuosity, natural vessel-caliber change, and mineralized atherosclerotic plaques, which could induce potential bias. We did not evaluate the possible impact of variable imaging and postprocessing parameters, such as slice thickness, flip angle, and reconstruction interval on FF values, and we emphasize that the cutoff values we obtained may be specific to the imaging protocol used in this study. Finally, although CTP is a widely available technique in the clinical application, the accuracy of CTP results is challenging and is affected by multiple factors such as arterial input function selection, arterial curves, and less sensitivity for lacunar infarcts.

CONCLUSIONS

This study demonstrates that an FF of < 0.90 measured on 3D-TOF-MRA can independently predict the risk of cerebral hypo-

perfusion in the region downstream from the MCA stenosis. Its ability to discriminate between normal perfusion and hypoperfusion in patients with ischemic stroke or TIA suggests that it may serve as a simple tool for risk stratification in routine clinical practice.

Disclosures: Xiaoqian Ge—*RELATED: Grant:* National Natural Science Foundation of China (No. 81271575, 81401374, 81571630) and the SJTU Medical-Engineering Cross-Cutting Research Project (No. YG2015MS53, YG2015QN36).* Huijin Zhao—*RELATED: Grant:* National Natural Science Foundation of China (grants 81571630, 81401374), Shanghai Jiao Tong University (YG2016MS56), and Renji Hospital (RJZZ18–001).* Zien Zhou—*UNRELATED: Grants/Grants Pending:* University of New South Wales Sydney. *Comments:* Scientia PhD Scholarship (2018–2022). Xiao Li—*RELATED: Grant:* National Natural Science Foundation of China (No. 81271575, 81401374, 81571630) and the SJTU Medical-Engineering Cross-Cutting Research Project (No. YG2015MS53, YG2015QN36).* Beibei Sun—*RELATED: Grant:* This research was supported by the National Natural Science Foundation of China (No. 81271575, 81401374, 81571630) and the SJTU Medical-Engineering Cross-Cutting Research Project (No. YG2015MS53, YG2015QN36).* Hengqu Wu—*RELATED: Grant:* National Natural Science Foundation of China (No. 81271575, 81401374, 81571630) and the SJTU Medical-Engineering Cross-Cutting Research Project (No. YG2015MS53, YG2015QN36).* Xiaosheng Liu—*RELATED: Grant:* the National Natural Science Foundation of China (No. 81271575, 81401374, 81571630) and the SJTU Medical-Engineering Cross-Cutting Research Project (No. YG2015MS53, YG2015QN36).* *Money paid to the institution.

REFERENCES

- Holmstedt CA, Turan TN, Chimowitz MI. **Atherosclerotic intracranial arterial stenosis: risk factors, diagnosis, and treatment.** *Lancet Neurol* 2013;12:1106–14 [CrossRef Medline](#)
- Pu Y, Lan L, Leng X, et al. **Intracranial atherosclerosis: from anatomy to pathophysiology.** *Int J Stroke* 2017;12:236–45 [CrossRef Medline](#)
- Lan L, Leng X, Ip V, et al. **Prolonged perfusion predicts recurrent ischemic stroke but not transient ischemic attack in patients with symptomatic intracranial stenosis.** *Curr Neurovasc Res* 2017;14:149–57 [CrossRef Medline](#)
- Lu SS, Ge S, Su CQ, et al. **MRI of plaque characteristics and relationship with downstream perfusion and cerebral infarction in patients with symptomatic middle cerebral artery stenosis.** *J Magn Reson Imaging* 2018;48:66–73 [CrossRef Medline](#)
- Lan L, Leng X, Abrigo J, et al. **Diminished signal intensities distal to intracranial arterial stenosis on time-of-flight MR angiography might indicate delayed cerebral perfusion.** *Cerebrovasc Dis* 2016;42:232–39 [CrossRef Medline](#)
- Leng X, Wong KS, Soo Y, et al. **Magnetic resonance angiography signal intensity as a marker of hemodynamic impairment in intracranial arterial stenosis.** *PLoS One* 2013;8:e80124 [CrossRef Medline](#)
- Liebeskind DS, Kosinski AS, Lynn MJ, et al. **Noninvasive fractional flow on MRA predicts stroke risk of intracranial stenosis.** *J Neuroimaging* 2015;25:87–91 [CrossRef Medline](#)
- Liebeskind DS, Feldmann E. **Fractional flow in cerebrovascular disorders.** *Intervent Neurol* 2012;1:87–99 [CrossRef](#)
- Cianfoni A, Colosimo C, Basile M, et al. **Brain perfusion CT: principles, technique and clinical applications.** *Radiol Med* 2007;112:1225–43 [CrossRef Medline](#)

10. Siemund R, Cronqvist M, Andberg G, et al. **Cerebral perfusion imaging in hemodynamic stroke: be aware of the pattern.** *Interv Neuroradiol* 2009;15:385–94 CrossRef Medline
11. Sacco RL, Kasner SE, Broderick JP, et al; American Heart Association Stroke Council, Council on Cardiovascular Surgery and Anesthesia, Council on Cardiovascular Radiology and Intervention, Council on Cardiovascular and Stroke Nursing, Council on Epidemiology and Prevention, Council on Peripheral Vascular Disease, Council on Nutrition, Physical Activity and Metabolism. **An updated definition of stroke for the 21st century: a statement for healthcare professionals from the American Heart Association/American Stroke Association.** *Stroke* 2013;44:2064–89 CrossRef Medline
12. Greene TC, Rong XJ. **Evaluation of techniques for slice sensitivity profile measurement and analysis.** *J Appl Clin Med Phys* 2014;15:4042 CrossRef Medline
13. Wintermark M, Flanders AE, Velthuis B, et al. **Perfusion-CT assessment of infarct core and penumbra: receiver operating characteristic curve analysis in 130 patients suspected of acute hemispheric stroke.** *Stroke* 2006;37:979–85 CrossRef Medline
14. Campbell BC, Christensen S, Levi CR, et al. **Cerebral blood flow is the optimal CT perfusion parameter for assessing infarct core.** *Stroke* 2011;42:3435–40 CrossRef Medline
15. Samuels OB, Joseph GJ, Lynn MJ, et al. **A standardized method for measuring intracranial arterial stenosis.** *AJNR Am J Neuroradiol* 2000;21:643–46 Medline
16. Menon BK, D'Este CD, Qazi EM, et al. **Multiphase CT angiography: a new tool for the imaging triage of patients with acute ischemic stroke.** *Radiology* 2015;275:510–20 CrossRef Medline
17. Leng X, Ip HL, Soo Y, et al. **Interobserver reproducibility of signal intensity ratio on magnetic resonance angiography for hemodynamic impact of intracranial atherosclerosis.** *J Stroke Cerebrovasc Dis* 2013;22:e615–19 CrossRef Medline
18. Markus H, Cullinane M. **Severely impaired cerebrovascular reactivity predicts stroke and TIA risk in patients with carotid artery stenosis and occlusion.** *Brain* 2001;124:457–67 CrossRef Medline
19. Jongen LM, Hendrikse J, Moll FL, et al. **Cerebral perfusion affects the risk of ischemia during carotid artery stenting.** *Cerebrovasc Dis* 2010;29:538–45 CrossRef Medline
20. Kodama T, Watanabe K. **Influence of imaging parameters, flow velocity, and pulsatile flow on three-dimensional time-of-flight MR angiography: experimental studies.** *Eur J Radiol* 1997;26:83–91 CrossRef Medline
21. Wilcock DJ, Jaspan T, Worthington BS. **Problems and pitfalls of 3-D TOF magnetic resonance angiography of the intracranial circulation.** *Clin Radiol* 1995;50:526–32 CrossRef Medline
22. Mustert BR, Williams DM, Prince MR. **In vitro model of arterial stenosis: correlation of MR signal dephasing and trans-stenotic pressure gradients.** *Magn Reson Imaging* 1998;16:301–10 CrossRef Medline
23. Ginsberg MD. **The cerebral collateral circulation: Relevance to pathophysiology and treatment of stroke.** *Neuropharmacology* 2018;134:280–92 CrossRef Medline

Quantitative Delta T1 (dT1) as a Replacement for Adjudicated Central Reader Analysis of Contrast-Enhancing Tumor Burden: A Subanalysis of the American College of Radiology Imaging Network 6677/Radiation Therapy Oncology Group 0625 Multicenter Brain Tumor Trial

K.M. Schmainda, M.A. Prah, Z. Zhang, B.S. Snyder, S.D. Rand, T.R. Jensen, D.P. Barboriak, and J.L. Boxerman

ABSTRACT

BACKGROUND AND PURPOSE: Brain tumor clinical trials requiring solid tumor assessment typically rely on the 2D manual delineation of enhancing tumors by ≥ 2 expert readers, a time-consuming step with poor interreader agreement. As a solution, we developed quantitative dT1 maps for the delineation of enhancing lesions. This retrospective analysis compares dT1 with 2D manual delineation of enhancing tumors acquired at 2 time points during the post therapeutic surveillance period of the American College of Radiology Imaging Network 6677/Radiation Therapy Oncology Group 0625 (ACRIN 6677/RTOG 0625) clinical trial.

MATERIALS AND METHODS: Patients enrolled in ACRIN 6677/RTOG 0625, a multicenter, randomized Phase II trial of bevacizumab in recurrent glioblastoma, underwent standard MR imaging before and after treatment initiation. For 123 patients from 23 institutions, both 2D manual delineation of enhancing tumors and dT1 datasets were evaluable at weeks 8 ($n = 74$) and 16 ($n = 57$). Using dT1, we assessed the radiologic response and progression at each time point. Percentage agreement with adjudicated 2D manual delineation of enhancing tumor reads and association between progression status and overall survival were determined.

RESULTS: For identification of progression, dT1 and adjudicated 2D manual delineation of enhancing tumor reads were in perfect agreement at week 8, with 73.7% agreement at week 16. Both methods showed significant differences in overall survival at each time point. When nonprogressors were further divided into responders versus nonresponders/nonprogressors, the agreement decreased to 70.3% and 52.6%, yet dT1 showed a significant difference in overall survival at week 8 ($P = .01$), suggesting that dT1 may provide greater sensitivity for stratifying subpopulations.

CONCLUSIONS: This study shows that dT1 can predict early progression comparable with the standard method but offers the potential for substantial time and cost savings for clinical trials.

ABBREVIATIONS: 2D-T1 = 2D manual delineation of enhancing tumor; dT1 = delta T1; NR-NP = nonresponder/nonprogressor; OS = overall survival; R = response; RANO = Response Assessment in Neuro-Oncology; ACRIN = American College of Radiology Imaging Network; RTOG = Radiation Therapy Oncology Group

Objective, accurate, and reproducible methods to measure glioblastoma volume are important for clinicians to assess treatment response and guide appropriate therapy, both in daily practice and in clinical trials. Contrast-enhanced MR imaging is the most widely used approach and the focus of recent consensus brain tumor imaging protocol recommendations.¹ However, although contrast-enhanced MR imaging has excellent spatial res-

olution, even slight variations in image-acquisition parameters or vendor platforms can greatly impact image quality, lesion conspicuity, and measurement of tumor volume.² These problems are compounded by the fact that glioblastoma is histopathologically and radiographically heterogeneous in appearance, with geographically irregular margins, variable contrast enhancement, and regions of central necrosis or cystic changes.³ Furthermore, assessment of posttreatment tumor volume can be confounded by the presence of blood products that appear bright on post-contrast MR imaging and that mimic contrast-enhancing tumor,⁴ or in the context of therapies reducing blood-brain barrier permeability and contrast agent extravasation. For ex-

Received January 28, 2019; accepted after revision May 8.

From the Departments of Biophysics (K.M.S., M.A.P.) and Radiology (K.M.S., S.D.R.), Medical College of Wisconsin, Milwaukee, Wisconsin; Department of Biostatistics (Z.Z.) and Center for Statistical Sciences (Z.Z., B.S.S.), Brown University School of Public Health, Providence, Rhode Island; Jensen Informatics LLC (T.R.J.), Brookfield, Wisconsin; Department of Radiology (D.P.B.), Duke University Medical Center, Durham, North Carolina; Department of Diagnostic Imaging (D.P.B., J.L.B.), Rhode Island Hospital, Providence, Rhode Island; and Warren Alpert Medical School of Brown University (J.L.B.), Providence, Rhode Island.

Funding support was provided through the National Institutes of Health/National Cancer Institute grants R01 CA082500, R44 CA134031, R41 NS076149, U01-CA079778, U01-CA080098, and U01-CA176110 and the Robert C. Olson MD Endowment.

Please address correspondence to Kathleen M. Schmainda, PhD, Department of Biophysics, Medical College of Wisconsin, 8701 Watertown Plank Rd, Milwaukee, WI 53226; e-mail: kathleen@mcw.edu

Indicates open access to non-subscribers at www.ajnr.org

<http://dx.doi.org/10.3174/ajnr.A6110>

ample, bevacizumab,⁵ used to treat recurrent glioblastoma, can decrease contrast agent extravasation independent of its effect on tumor biology.^{3,6} These challenges contribute to large interobserver differences (up to 50%–60%) in assessing tumor burden and evaluating treatment responses that impact both daily practice and clinical trials.^{4,7}

As a solution, difference maps, created from the subtraction of precontrast from postcontrast images, have been used to highlight regions of contrast enhancement.⁸ However, unlike x-ray angiography or CT, pixel values in MR images can vary widely due to multiple factors, even for identical pulse sequences and tissue types; this variation can result in nonenhancing regions appearing in the subtraction image. In response, we developed quantitative dT1 images of contrast enhancement, which eliminate much of the normal variability in image contrast due to MR imaging system instabilities, field strength, slight differences in imaging parameters (TR, TE, and so forth), and sources of bright signal apparent on precontrast T1WI.^{9,10} Because dT1 images are quantitative, delineation of enhancing lesions can be automated by applying the same predetermined threshold across time points and patients.

Consequently, the dT1 tool has the potential to cause a paradigm shift in how brain tumor burden is assessed. This study compares the use of dT1 technology for semiautomatic lesion identification with the accepted standard that relies on expert readers to manually delineate enhancing lesions. The approach was to determine whether the semiautomatic determination of ROIs using dT1 images would compare with the adjudicated reads from the American College of Radiology Imaging Network 6677/Radiation Therapy Oncology Group 0625 central reader study (as reported in the primary article¹¹) with regard to association with patient outcome.

MATERIALS AND METHODS

The Radiation Therapy Oncology Group (RTOG, now NRG Oncology), in collaboration with the American College of Radiology Imaging Network (ACRIN, now Eastern Cooperative Oncology Group [ECOG]-ACRIN), both funded by the National Cancer Institute, conducted a prospective, randomized, Phase II multicenter trial (ACRIN 6677/RTOG 0625) of bevacizumab in recurrent glioblastoma multiforme. Each participating institution obtained institutional review board approval before subject accrual and conducted the trial in compliance with the Health Insurance Portability and Accountability Act. Informed consent was obtained for all subjects.

Patients

A total of 123 patients from 23 institutions with recurrent histologically proved glioblastoma or gliosarcoma were enrolled in the ACRIN 6677/RTOG 0625 trial. Detailed inclusion and exclusion criteria are available on the RTOG Web site (<https://www.rtog.org/ClinicalTrials/ProtocolTable/StudyDetails.aspx?study=0625>).

All patients were treated with bevacizumab (10 mg/kg IV on days 1 and 15 of a 28-day cycle) in combination with either temozolomide or irinotecan.¹¹

Of the 123 patients enrolled, 107 patients met the inclusion

criteria, defined as having imaging beyond baseline and progression data. Of these, 105 datasets could be analyzed by central reader analysis of 2D manual delineation of enhancing tumor (2D-T1), which required having an interpretable baseline image and at least 1 additional interpretable time point. Of the 105 datasets, matched pre- and postcontrast T1 images were available for 83 patients, enabling the creation of dT1 images. A matched dataset is defined as one for which the same imaging sequence and the same scanning options (eg, flow-compensation is either on or off for both) are used for both the pre- and postcontrast T1WI. Slight differences in TR and TE between the pre- and postcontrast images are acceptable. When we restricted attention to the weeks 8 and 16 time points, 74 patients were evaluable for comparison between the same 2D-T1 and dT1 image datasets at week 8 and 57 patients were evaluable for comparison at week 16.

Data-Acquisition Methods

MR imaging was performed at both 1.5T (Espree, Magnetom Avanto, Siemens, Erlangen, Germany; Signa Excite, Signa HDx, GE Healthcare, Milwaukee, Wisconsin) and 3T (Signa HDx, Signa Excite; GE Healthcare). Conventional MR imaging included precontrast T1WI, T2WI, FLAIR, and diffusion-weighted imaging.¹¹ For both pre- and postcontrast T1WI, all sites were required to collect the data using a spin-echo sequence with the following parameter ranges: TE/TR = minimum (<15 ms)/400–600 ms, FOV = 220–240 mm, phase FOV = 75%, slice thickness/gap = 5/1 mm, matrix = 256 × 256, NEX = 1. The imaging protocol remained fixed at each site and across all time points. Following IV injection of 0.1 mmol/kg of a standard gadolinium-based contrast agent (the brand used was dictated by the preference of each site), axial 2D spin-echo (2D-T1) and 3D volumetric T1WI postcontrast images were acquired. Patients participating in the optional advanced component of the trial had dynamic contrast-enhanced, dynamic susceptibility contrast, and/or spectroscopic MR imaging at baseline, week 2, and after every 2 cycles of treatment. Results from these advanced imaging cohorts were previously reported.^{12–14} A complete listing of all MR imaging parameters for this protocol can be found on the ACRIN Web site (<https://www.acrin.org/PROTOCOLSUMMARYTABLE/PROTOCOL6677/6677ImagingMaterials.aspx>).

Image Analysis

Central Reader Analysis. As previously described,¹¹ all local imaging was transmitted to ACRIN for central review by 2 primary readers and 1 adjudicator, each with neuroradiology Certificates of Added Qualification and 8, 6, and 3 years, respectively, of post-fellowship experience. For each distinct contrast-enhancing target lesion (≥ 1 -cm diameter, ≥ 1 cm from other enhancing lesions), the largest diameter of contrast enhancement and its maximum perpendicular diameter were measured. A 2D tumor area was computed by summing over all lesions the product of maximum perpendicular diameters. Pre- and postcontrast images were reviewed simultaneously to exclude blood products from 2D measurements.

For all evaluable patients, images at each available time point were presented in random order to both primary readers who

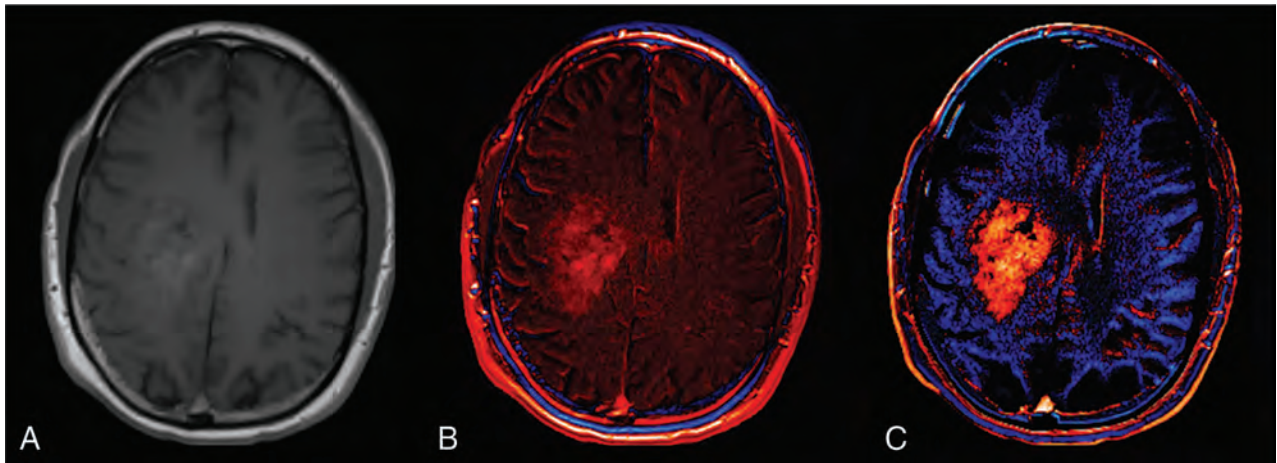


FIG 1. Standardization is required for the creation of robust dT1 maps. A, Postcontrast T1WI obtained in a patient with a glioblastoma. B, A difference map created without calibration. C, A dT1 map created from the difference between calibrated post- and precontrast T1WI.

then independently made 2D-T1 measurements. After completing measurements for all time points, the primary readers were unblinded to the order of examinations. Consistent with the Macdonald and Response Assessment in Neuro-Oncology (RANO) criteria, each reader determined the time of progression on 2D-T1 when there was a $>25\%$ increase with respect to the nadir in maximal cross-sectional enhancing areas or the appearance of any new measurable enhancing tumor. Radiologic response was defined as a $\geq 50\%$ decrease with respect to baseline, confirmed on the subsequent time point. Steroid dosage and clinical status were unavailable to the readers for this study. The adjudicator settled discordant times to progression between the readers by opining on the most correct times to progression. FLAIR images were not used to determine outcomes for either the 2D-T1 or dT1 analysis.

Creation of dT1 Maps

The dT1 method quantitatively compares calibrated pre-(T1) and postcontrast anatomic images, in which the calibration rule was machine-learned from input data of a given type (eg, T1WI spin-echo).^{9,10} Specifically, learning the calibration rule (historically referred to as the “standardization step”)^{15,16} requires the determination of mean intensity values at predefined landmarks, which correspond to percentiles in the distribution of pixel values, using a dataset of training images. This training step is performed only once. Next, each new input image of a given type is transformed to the standardized space (ie, calibrated) using a piecewise linear-intensity mapping function. The result is a constant dynamic range for the calibrated images so that for a given tissue type, it is possible to establish fixed gray-level windows without the need for a per-case window level adjustment.¹⁶

For routine analysis, 2D pre- and postcontrast 2D-T1 images were coregistered using a rigid mutual-information cost function, followed by application of the machine-learned calibration rule to each T1-weighted image. The calibrated-registered precontrast T1WI was subtracted from the calibrated-registered postcontrast T1WI, resulting in a dT1 image. Figure 1 illustrates the superior conspicuity of a glioblastoma with dT1 compared with a simple difference map constructed from noncalibrated images.

Because dT1 maps are quantitative, delineation of enhancing lesions can be semiautomated by choosing a fixed threshold and applying it consistently across time points and patients. The threshold of 3000 (calibrated units) was determined by an experienced (>20 years) neuroradiologist (S.D.R.), as previously described.¹⁰ Briefly, dT1 voxels were spatially correlated with raw dynamic susceptibility contrast MR imaging data. Voxels with no visually discernable dynamic susceptibility contrast MR imaging signal (ie, a lack of perfused tissue) were used to confirm a lack of contrast agent–perfused tissue and, thus, a lack of contrast agent enhancement. A threshold of 3000 was found to reliably make this distinction and is now routinely applied to dT1 images for the semiautomatic determination of contrast agent–enhancing ROIs. Note that the perfusion signal was used for the initial determination of a threshold. Its collection and use are not required for the routine use of dT1 maps. Generation of dT1 images was built into the IB Delta Suite software (Imaging Biometrics, Elm Grove, Wisconsin) used for this study.

A nonexpert reader (ie, an engineer with <4 years of MR imaging experience at the time of annotation) blinded to the central reader analyses coarsely defined the bounding region on each image slice using the dT1 maps. Care was taken to exclude the choroid plexus, vessels, and scalp. All pixels within the bounding region that were above 3000 were included as the final enhancing-tumor ROI. No manipulation of the tumor ROI was performed beyond identification of the initial bounding region. An experienced neuroradiologist (S.D.R.), blinded to the central reader results, reviewed and approved the final ROIs for any difficult cases. This approach mimics the current practice of having technologists preprocess data and radiologists perform a final review.

Statistical Analysis

2D-T1 results were reported previously.¹¹ Using dT1, for each post-baseline time point, we measured the dT1 volume against the nadir value, and progression and response (R) were determined as described above for the central reader analysis. If neither the progression nor R criteria were satisfied, the time point was

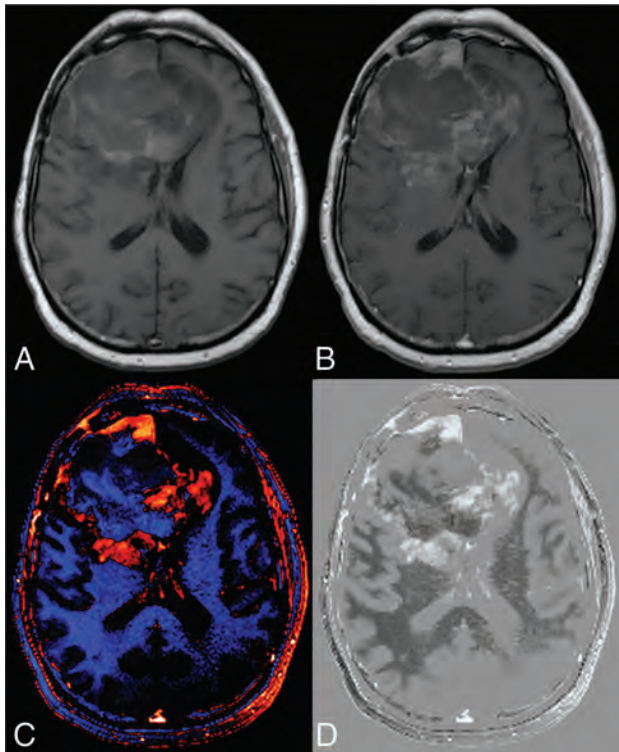


FIG 2. Benefit of creating a dT1 map. Shown are the pre- (A) and postcontrast (B) T1-weighted images from a patient with recurrent glioblastoma treated with bevacizumab and enrolled in the ACRIN 6677 trial. The bright signal on the precontrast image and the subtle enhancement on the postcontrast image make it difficult to determine the extent of enhancing tumor. Alternatively, the dT1 map created from the difference between calibrated pre- and calibrated postcontrast T1-weighted images clearly delineates enhancing tumor as displayed with either color (C) or in gray-scale (D).

labeled as nonresponder/nonprogressor (NR-NP). Uninterpretable time points were ignored.

Agreement between the adjudicated 2D-T1 assessments and the dT1 assessments at weeks 8 and 16 was determined using a simple percentage agreement, as well as the Krippendorff α statistic. The latter statistic corrects for chance agreement,¹⁷ when the methods agree perfectly, $\alpha = 1$, and when the methods agree as if chance had produced the results, $\alpha = 0$.

For both 2D-T1 and dT1, separate landmark analysis sets were created for progression by weeks 8 and 16, and association with overall survival (OS) was reported using Kaplan-Meier curves with the log-rank test.

Statistical computations were performed using SAS Version 9.4 software (SAS Institute, Cary, North Carolina) or R Version 3.4.4 software (R project; <http://www.r-project.org/>), with $P < .05$ considered statistically significant.

RESULTS

An example of a dT1 image created from a study patient is shown in Fig 2. The dT1 map, shown in color and gray-scale (Fig 2C, -D), clearly highlights the enhancing tumor without being confounded by the bright signal on precontrast T1WI (Fig 2A) or subtle enhancement on the postcontrast T1WI (Fig 2B).

By means of dT1, a total of 7/74 (9%) cases progressed by week 8, and 26/57 (46%) cases progressed by week 16. Of the cases that

did not progress by week eight, 28/67 (42%) were R and 39/67 (58%) were NR-NP; the counts at week 16 were 23/31 (74%) and 8/31 (26%), respectively.

Cross-tabulation of week 8 status revealed perfect agreement for progression between dT1 and the adjudicated 2D-T1 reads. When nonprogressors were further subdivided into R versus NR-NP, the percentage agreement was 70.3% (95% CI, 59.1%–79.5%) with a Krippendorff α of 0.52 (95% CI, 0.35–0.70). Agreement for progression by week 16 decreased, with a percentage agreement of 73.7% (95% CI, 61.0%–83.4%) and a Krippendorff α of 0.46 (95% CI, 0.21–0.68). The percentage agreement further decreased when nonprogressors were subdivided into R versus NR-NP (percentage agreement = 52.6%; 95% CI, 39.9%–65.0%; Krippendorff $\alpha = 0.45$; 95% CI, 0.22–0.65).

Given the perfect agreement for progression at week 8 between dT1 and the adjudicated 2D-T1 reads, the Kaplan-Meier curves for both methods were identical (Table 1 and Fig 3A), with a significant difference in OS ($P < .0001$). While 2D-T1 did not further distinguish between R and NR-NP ($P = .35$), there was a significant difference in OS between R and NR-NP for dT1 ($P = .01$; Table 1 and Fig 3B).

At week 16, a highly significant difference in OS was observed between progressors and nonprogressors for both T1 and dT1 ($P < .0001$, $P = .006$; Table 2 and Fig 3C). No difference in OS was observed between R and NR-NP for either method ($P = .73$ and $P = .61$; Table 2 and Fig 3D).

DISCUSSION

The results of this study support the integration of dT1 into central reader analysis for the delineation of contrast-enhancing brain tumor. The dT1 method was comparable with expert reads for determination of early tumor progression and proved superior for further distinguishing R versus NR-NP at the week 8 time point. While agreement between the methods decreased at week 16, both methods showed a significant difference in OS based on progression status.

The result that dT1 proved better for stratifying subpopulations may be explained in several possible ways: First, due to the process of standardization (calibration) followed by subtraction, dT1 provides a consistent and objective delineation of enhancing lesions. It is less confounded by both systematic differences (vendor platforms, slight variations in imaging settings) and the subjectivity (interreader differences) that influences current approaches. This feature, in turn, can result in an improved sensitivity to enhancing lesions, that may not be apparent on postcontrast images, as illustrated in Fig 4. In addition, the superiority of using dT1 may be explained by the demonstrated benefit of volumetric measurements over standard bidimensional approaches for measuring tumor size¹⁸ and the application of a fixed physiology-based threshold to dT1 images to determine enhancing tumor burden.

Before 2010, the MacDonald criteria were widely used to assess treatment response of high-grade gliomas¹⁹ and included the 2D measurement of enhancing tumor in conjunction with a clinical assessment and corticosteroid dose. Tumor progression on FLAIR and the recognition that contrast enhancement is nonspecific prompted the development of the updated RANO criteria,

Table 1: Overall survival stratified by progression status at week 8

Sequence	Progression by Week 8?		Progression by Week 8? (R vs NR-NP)		
	No	Yes	R	NR-NP	P
	N (%), Median OS (days) (95% CI)	N (%), Median OS (days) (95% CI)	N (%), Median OS (days) (95% CI)	N (%), Median OS (days) (95% CI)	N (%), Median OS (days) (95% CI)
2D	67 (91%) 303 (232–400)	7 (9%) 110 (74–192)	18 (24%) 364 (280–510)	49 (66%) 268 (217–378)	7 (9%) 110 (74–192)
	$P < .0001^a$ ($n = 74$)		$P = .35$: R vs NR-NP		
dT1	67 (91%) 303 (232–400)	7 (9%) 110 (74–192)	28 (38%) 425.5 (311–660)	39 (53%) 223 (180–276)	7 (9%) 110 (74–192)
	$P < .0001^a$ ($n = 74$)		$P = .01^a$: R vs NR-NP		

Note:—N indicates number of patients; R, responder; NR-NP, non-responder/non-progressor; P, progression.

^a Significant.

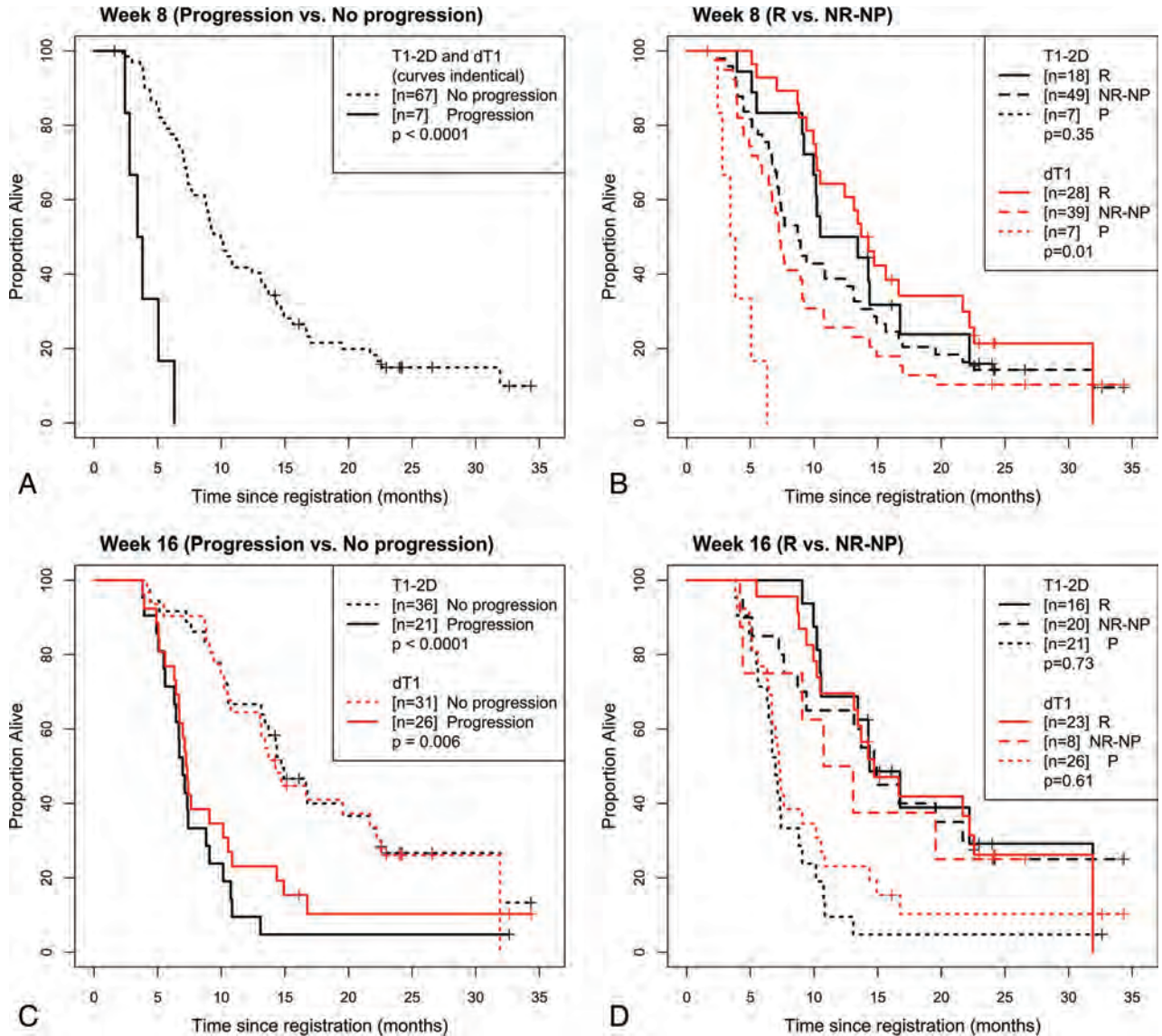


FIG 3. Kaplan-Meier curves for 2D-T1 and dT1-determined enhancing tumor. Shown are overall survival curves stratified by whether the participant progressed at or before week 8 (A), progressed at or before week 8, broken into progressing (P), responding, and nonresponding/nonprogressing (B), progressed at or before week 16 (C) and had progressed at or before week 16, broken into P, R, and NR-NP (D).

which added FLAIR to the MacDonald criteria.²⁰ However, FLAIR also have important limitations and remain controversial.²¹ In fact, the parent study did not find a statistically significant survival time reduction among the isolated FLAIR progressors compared with nonprogressors.¹¹ Even so, we are not

suggesting that dT1 replace RANO as the standard assessment criteria. Rather, the results of this study show that dT1 has the potential to replace the current approach for delineating enhancing-lesion volumes, which is one aspect of the RANO assessment.

Measurement of the contrast-enhancing lesion remains cen-

Table 2: Overall survival stratified by progression status at week 16

Sequence	Progression by Week 16?		Progression by Week 16? (R vs NR-NP)		
	No	Yes	R	NR-NP	P
	N (%), Median OS (days) (95% CI)	N (%), Median OS (days) (95% CI)	N (%), Median OS (days) (95% CI)	N (%), Median OS (days) (95% CI)	N (%), Median OS (days) (95% CI)
2D	36 (63%) 448 (321–660)	21 (37%) 212 (170–268)	16 (28%) 437 (319–971)	20 (35%) 451 (232–687)	21 (37%) 212 (170–268)
	$P < .0001^a$ ($n = 57$)		$P = .73$: R vs NR-NP		
dT1	31 (54%) 434 (319–676)	26 (46%) 221.5 (196–309)	23 (40%) 448 (319–687)	8 (14%) 362.5 (127, –)	26 (46%) 221.5 (196–309)
	$P = .006^a$ ($n = 57$)		$P = .61$: R vs NR-NP		

Note: — indicates those that were still alive at the end of study (i.e., no upper bound); N, number of patients; R, responder; NR-NP, non-responder/non-progressor; P, progressor.

^aSignificant.

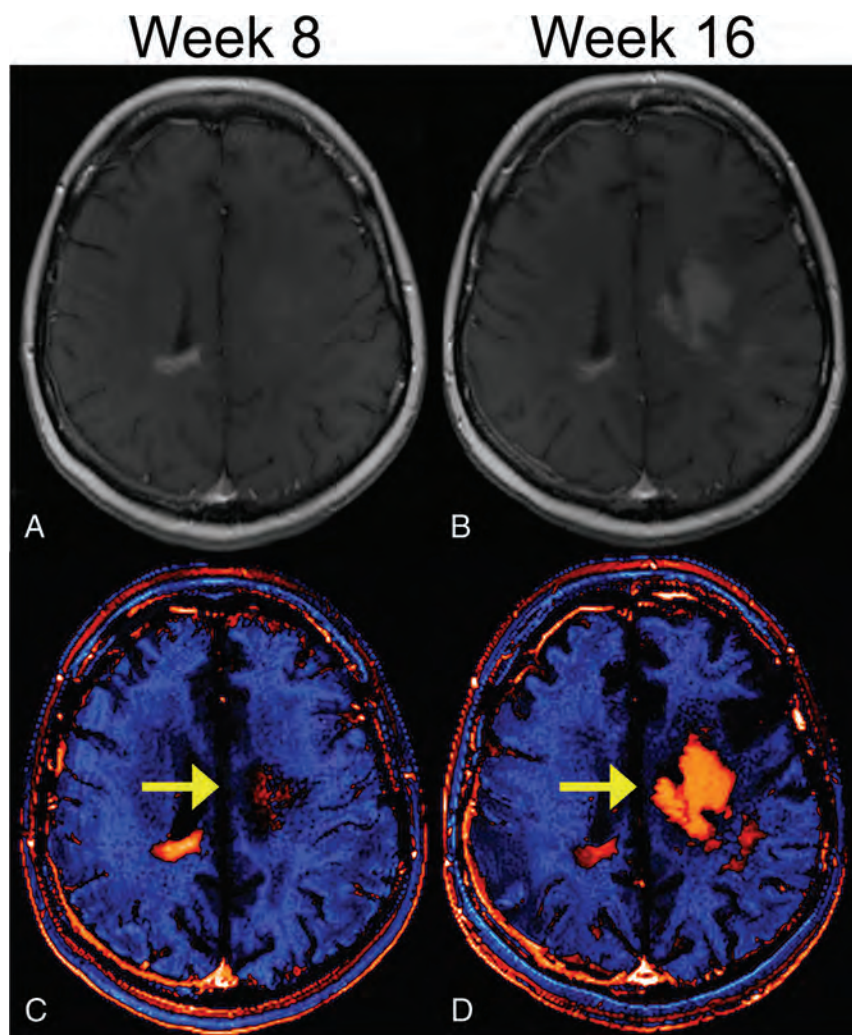


FIG 4. Potential of dT1 for improved sensitivity to the enhancing lesion. For postcontrast images (A and B), progression of the enhancing lesion, which is clearly visible at week 16 (B), was not discernable at week 8 (A). With dT1, the enhancing lesion visible earlier at week 8 (yellow arrow) (C) is becoming even more apparent at week 16 (D).

central to the assessment of treatment response and was the focus of a recent effort to standardize imaging protocols for tumor-volume assessment.¹ Even as new imaging biomarkers, such as those derived from perfusion- or diffusion-weighted MR imaging, are proving useful for the biologic assessment of tumor response, the analysis of such biomarkers depends on the accurate delineation of enhancing tumor. Therefore, it is necessary to be able to process

these pre- and postcontrast T1WI data in a robust manner for both routine care and clinical trials.

The standard approach for lesion segmentation is the labor-intensive and time-consuming manual delineation of contrast-enhancing lesions by expert readers. Due to the subjective nature of this approach, clinical trials rely on multiple expert readers and involve additional readers to adjudicate cases for which there is disagreement. In a study that enlisted 8 board-certified radiologists to measure high-grade tumor diameters, substantial interreader disagreement was demonstrated with a rate of consensus regarding tumor progression of only 45% and only moderate reproducibility.²² This lack of agreement necessitates frequent adjudication. The primary study, from which this secondary analysis obtained its data, reported a 43% adjudication rate when using 2D-T1 and 42% for 3D-T1.¹¹ Even more detrimental, the turnaround time for central analysis may preclude certain study designs that require assessment of progression within 48 hours, for example.

By comparison, the dT1 technology can be used by nonradiologists, as demonstrated in the present study, and requires only seconds to identify enhancing lesions. Because it is a semiautomated, dT1 overcomes the subjectivity that confounds current methods and, therefore, has the potential to provide greater consistency in lesion identifica-

tion across time points and patients. These capabilities derive from the unique standardization (calibration) algorithm incorporated into the process of creating dT1 maps.^{10,15,23} The standardization algorithm serves to diminish slight differences in TE and TR settings for a given sequence type¹⁶ and thus lessens the importance of such variations that can result in differences in lesion conspicuity. Finally, the standardization algorithm, which

has also been trained for use in the creation of relative CBV maps, resulted in substantial improvement in repeatability²⁴ as well as consistency across time.²³ Therefore, it is expected that dT1 should also result in greater repeatability; an hypothesis that should be tested in prospective studies.

The dT1 images are different from the subsequently developed, yet possibly better known, Gaussian-normalized difference maps.⁸ Gaussian-normalized maps require the determination of a new normalization for each patient and image, both pre- and postcontrast, which raises questions about consistency across time points and patients. dT1 uses the same calibration and threshold for each patient and image, enabling consistent quantification and automation across time points, patients, and sites.

Simple difference images, which eliminate some confounding bright signal on precontrast T1WI, are limited by variations in sequence parameter settings (eg, Fig 1). Furthermore, simple difference maps are not quantitative, thereby precluding the ability to automate lesion identification and resulting in little improvement over current methods. Consequently, the dT1 technology has the greatest likelihood of offering a substantial improvement over similar tools, with a greater potential for automation and clinical use.

Also of particular interest is that, in this study, only dT1 could predict differences in outcome for the NR-NP tumors at week 8. This greater sensitivity may result from more accurate and possibly more sensitive delineation of enhancing tumor (Fig 4) by dT1, free of precontrast bright signal, or it may be attributed to the physiologically motivated threshold used with dT1. Thus, a quantitative dT1-determined lesion may more accurately reflect active brain tumor. However, whether this same threshold should be used for other contrast-enhancing tumor types is unknown and will be the topic of future studies.

A limitation of this study is that only 1 nonradiologist determined the enhancing ROIs using dT1. A separate study characterizing the interreader agreement using the dT1 technology is warranted. Also, it is likely that all cases, particularly those with more complicated lesions, will still require expert review. Yet expert sign-offs are routine, and improving the initial step of tumor delineation with dT1 should result in improved time efficiencies to the radiologists' workflow.

Another perceived limitation is that fewer datasets could be analyzed with dT1 compared with 2D-T1. However, this limitation is not intrinsic to the dT1 method. Rather, it is because this is a retrospective analysis of data that were not collected for the purpose of creating dT1 images. Although dT1 is amenable to slight variations in parameter settings such as TE and TR and works well across vendor platforms and field strengths, it requires that the same sequence be used to collect both the pre- and post-contrast T1WI. Consequently, the issue of limited application is not of concern for prospective clinical trials.

A final limitation is that the response assessment using dT1 did not explicitly include the appearance of new lesions as an indicator of progression. However, for all cases included in this study, no new measurable lesions of >1 mL were present at the time of review. Thus, all statements of progression were made on the basis of the findings at the primary tumor site only. Future studies will explicitly include the presence of new lesions as an additional criterion to determine progression.

Overall, the potential impact of dT1 technology is far-reaching, given the approximately 117,000 new diagnoses of primary brain tumor per year,²⁵ the >300,000 patients living with brain tumors who undergo repeat imaging follow-ups as part of their standard of care, and the 475 active clinical studies for glioblastoma multiforme (<https://clinicaltrials.gov/>). Therefore, the potential impact of the dT1 technology for daily practice and clinical trials is immense.

CONCLUSIONS

This study shows that dT1 can predict early progression comparable with the standard method, may be superior for substratification, and offers the potential for substantial time and cost savings for clinical trials.

ACKNOWLEDGMENTS

We acknowledge Imaging Biometrics LLC (IQ-AI Ltd) for technical support, software development, and assistance with data analysis. No direct funding support was provided by Imaging Biometrics LLC for this study.

Disclosures: Kathleen M. Schmainda—*RELATED: Grant:* National Institutes of Health, *Comments:* The dT1 technology discussed was developed in the lab with National Institutes of Health funding (R01 CA082500 and U01CA176110)*; *UNRELATED: Stock/Stock Options:* Imaging Biometrics LLC/IQ-AI Ltd, *Comments:* ownership interest. Bradley S. Snyder—*RELATED: Grant:* ECOG-ACRIN, *Comments:* ACRIN 6677 was conducted under the auspices of ACRIN (now ECOG-ACRIN), a National Cancer Institute-funded cancer cooperative group. The Center for Statistical Sciences in the Brown University School of Public Health, where I am employed, is part of the Biostatistics Center of ECOG-ACRIN*. Todd R. Jensen—*UNRELATED: Consultancy:* Imaging Biometrics LLC, *Comments:* I am a software developer who helped carry out the dT1 method and implementation. I work as an independent medical imaging and informatics consultant, primarily doing software development. Other entities in this field that have retained my services in addition to Imaging Biometrics LLC include ADM Diagnostics Inc and Change Healthcare; *Patents (Planned, Pending or Issued):* Imaging Biometrics and Change Healthcare. Daniel P. Barboriak—*RELATED: Grant:* ECOG-ACRIN, *Comments:* The data used in this article came from a legacy ACRIN grant. My involvement in this project is part of my duties as imaging Co-Chair of the Brain Tumor Working Group at ECOG-ACRIN. My involvement is supported by the grant to ECOG-ACRIN from the National Cancer Institute*; *UNRELATED: Consultancy:* Blue Earth Diagnostics, *Comments:* I was compensated for participation in a medical advisory board meeting concerning the PET agent fluciclovine. This has minimal, if any, relevance to the submission; *Grants/Grants Pending:* National Institutes of Health, *Comments:* I have grants in the planning stages that concern segmentation for brain tumor images obtained in clinical trials*; *OTHER RELATIONSHIPS:* My lab has developed a method of performing difference imaging for measuring tumor enhancement that could be compared with this method at some point. *Money paid to the institution.

REFERENCES

1. Ellingson BM, Bendszus M, Boxerman J, et al; Jumpstarting Brain Tumor Drug Development Coalition Imaging Standardization Steering Committee. **Consensus recommendations for a standardized Brain Tumor Imaging Protocol in clinical trials.** *Neuro Oncol* 2015; 17:1188–98 CrossRef Medline
2. Eisenhauer EA, Therasse P, Bogaerts J, et al. **New response evaluation criteria in solid tumours: revised RECIST guideline (version 1.1).** *Eur J Cancer* 2009;45:228–47 CrossRef Medline
3. Henson JW, Ulmer S, Harris GJ. **Brain tumor imaging in clinical trials.** *AJNR Am J Neuroradiol* 2008;29:419–24 CrossRef Medline
4. Kubben PL, Postma AA, Kessels AG, et al. **Intraobserver and interobserver agreement in volumetric assessment of glioblastoma multiforme resection.** *Neurosurgery* 2010;67:1329–34 CrossRef Medline
5. Hurwitz H, Fehrenbacher L, Novotny W, et al. **Bevacizumab plus irinotecan, fluorouracil, and leucovorin for metastatic colorectal cancer.** *N Engl J Med* 2004;350:2335–42 CrossRef Medline

6. Norden AD, Young GS, Setayesh K, et al. **Bevacizumab for recurrent malignant gliomas: efficacy, toxicity, and patterns of recurrence.** *Neurology* 2008;70:779–87 CrossRef Medline
7. Provenzale JM, Ison C, Delong D. **Bidimensional measurements in brain tumors: assessment of interobserver variability.** *AJR Am J Roentgenol* 2009;193:W515–22 CrossRef Medline
8. Ellingson BM, Kim HJ, Woodworth DC, et al. **Recurrent glioblastoma treated with bevacizumab: contrast-enhanced T1-weighted subtraction maps improve tumor delineation and aid prediction of survival in a multicenter clinical trial.** *Radiology* 2014;271:200–10 CrossRef Medline
9. Jensen TR, Schmainda KM. **Computer-aided detection of brain tumor invasion using multiparametric MRI.** *J Magn Reson Imaging* 2009;30:481–89 CrossRef Medline
10. Bedekar D, Jensen T, Rand S, et al. **Delta T1 method: an automatic post-contrast ROI selection technique for brain tumors.** In: *Proceedings of the Annual Meeting of the International Society for Magnetic Resonance in Medicine*, Stockholm, Sweden. May 1–7, 2010
11. Boxerman JL, Zhang Z, Safriel Y, et al. **Early post-bevacizumab progression on contrast-enhanced MRI as a prognostic marker for overall survival in recurrent glioblastoma: results from the ACRIN 6677/RTOG 0625 Central Reader Study.** *Neuro Oncol* 2013;15:945–54 CrossRef Medline
12. Schmainda KM, Zhang Z, Prah M, et al. **Dynamic susceptibility contrast MRI measures of relative cerebral blood volume as a prognostic marker for overall survival in recurrent glioblastoma: results from the ACRIN 6677/RTOG 0625 multicenter trial.** *Neuro Oncol* 2015;17:1148–56 CrossRef Medline
13. Ellingson BM, Kim E, Woodworth DC, et al. **Diffusion MRI quality control and functional diffusion map results in ACRIN 6677/RTOG 0625: a multicenter, randomized, phase II trial of bevacizumab and chemotherapy in recurrent glioblastoma.** *Int J Oncol* 2015;46:1883–92 CrossRef Medline
14. Ratai EM, Zhang Z, Snyder BS, et al. **Magnetic resonance spectroscopy as an early indicator of response to anti-angiogenic therapy in patients with recurrent glioblastoma: RTOG 0625/ACRIN 6677.** *Neuro Oncol* 2013;15:936–44 CrossRef Medline
15. Nyúl LG, Udupa JK. **On standardizing the MR image intensity scale.** *Magn Reson Med* 1999;42:1072–81 CrossRef Medline
16. Nyúl LG, Udupa JK, Zhang X. **New variants of a method of MRI scale standardization.** *IEEE Trans Med Imaging* 2000;19:143–50 CrossRef Medline
17. Krippendorff K. **Agreement and information in the reliability of coding.** *Communication Methods and Measures* 2011;5:93–112 CrossRef
18. Dempsey MF, Condon BR, Hadley DM. **Measurement of tumor “size” in recurrent malignant glioma: 1D, 2D, or 3D?** *AJNR Am J Neuroradiol* 2005;26:770–76 Medline
19. MacDonald DR, Cascino TL, Schold SC Jr, et al. **Response criteria for phase II studies of malignant glioma.** *J Clin Oncol* 1990;8:1277–80 CrossRef Medline
20. Wen PY, Macdonald DR, Reardon DA, et al. **Updated response assessment criteria for high-grade gliomas: Response Assessment in Neuro-Oncology working group.** *J Clin Oncol* 2010;28:1963–72 CrossRef Medline
21. Wen PY, Norden AD, Drappatz J, et al. **Response assessment challenges in clinical trials of gliomas.** *Curr Oncol Rep* 2010;12:68–75 CrossRef Medline
22. Provenzale JM, Ison C, Delong D. **Bidimensional measurements in brain tumors: assessment of interobserver variability.** *AJR Am J Roentgenol* 2009;193:W515–22 CrossRef Medline
23. Bedekar D, Jensen TR, Schmainda KM. **Standardization of relative cerebral blood volume (rCBV) image maps for ease of both inter- and inpatient comparisons.** *Magn Reson Med* 2010;64:907–13 CrossRef Medline
24. Prah MA, Stufflebeam SM, Paulson ES, et al. **Repeatability of standardized and normalized relative CBV in patients with newly diagnosed glioblastoma.** *AJNR Am J Neuroradiol* 2015;36:1654–61 CrossRef Medline
25. Ostrom QT, Gittleman H, Fulop J, et al. **CBTRUS Statistical Report: Primary Brain and Central Nervous System Tumors Diagnosed in the United States in 2008–2012.** *Neuro Oncol* 2015;17(Suppl 4):iv1-iv62 CrossRef Medline

Brain Tumor-Enhancement Visualization and Morphometric Assessment: A Comparison of MPRAGE, SPACE, and VIBE MRI Techniques

L. Danieli, G.C. Riccitelli, D. Distefano, E. Prodi, E. Ventura, A. Cianfoni, A. Kaelin-Lang, M. Reinert, and E. Pravatà



ABSTRACT

BACKGROUND AND PURPOSE: Postgadolinium MR imaging is crucial for brain tumor diagnosis and morphometric assessment. We compared brain tumor enhancement visualization and the “target” object morphometry obtained with the most commonly used 3D MR imaging technique, MPRAGE, with 2 other routinely available techniques: sampling perfection with application-optimized contrasts by using different flip angle evolutions (SPACE) and volumetric interpolated brain examination (VIBE).

MATERIALS AND METHODS: Fifty-four contrast-enhancing tumors (38 gliomas and 16 metastases) were assessed using MPRAGE, VIBE, and SPACE techniques randomly acquired after gadolinium-based contrast agent administration on a 3T scanner. Enhancement conspicuity was assessed quantitatively by calculating the contrast rate and contrast-to-noise ratio, and qualitatively, by consensus visual comparative ratings. The total enhancing tumor volume and between-sequence discrepancy in the margin delineation were assessed on the corresponding 3D target objects contoured with a computer-assisted software for neuronavigation. The Wilcoxon signed rank and Pearson χ^2 nonparametric tests were used to investigate between-sequence discrepancies in the contrast rate, contrast-to-noise ratio, visual conspicuity ratings, tumor volume, and margin delineation estimates. Differences were also tested for 1D (Response Evaluation Criteria in Solid Tumors) and 2D (Response Assessment in Neuro-Oncology) measurements.

RESULTS: Compared with MPRAGE, both SPACE and VIBE obtained higher contrast rate, contrast-to-noise ratio, and visual conspicuity ratings in both gliomas and metastases (*P* range, <.001–.001). The between-sequence 3D target object margin discrepancy ranged between 3% and 19.9% of lesion tumor volume. Larger tumor volumes, 1D and 2D measurements were obtained with SPACE (*P* range, <.01–.007).

CONCLUSIONS: Superior conspicuity for brain tumor enhancement can be achieved using SPACE and VIBE techniques, compared with MPRAGE. Discrepancies were also detected when assessing target object size and morphology, with SPACE providing more accurate estimates.

ABBREVIATIONS: CEL = contrast-enhancing lesion; GBCA = gadolinium-based contrast agent; RANO = Response Assessment in Neuro-Oncology; RECIST = Response Evaluation Criteria in Solid Tumors; SPACE = sampling perfection with application-optimized contrasts using different flip angle evolution; TV = tumor volume; VIBE = volumetric interpolated brain examination

Postcontrast MR imaging plays a fundamental role in brain tumor diagnosis, anatomic delineation, and treatment re-

sponse. 3D sequences obtained after gadolinium-based contrast agent (GBCA) injection can illustrate BBB disruption in brain tumors.^{1–3} They can also provide 3D spatial representations of the enhancing part of the tumor for guiding treatment, biopsy planning, and/or allowing a precise dose delivery during stereotactic radiosurgery.^{4–7} However, various MR imaging techniques can be chosen, each with inherently different characteristics. The most used post-GBCA sequence is MPRAGE, an inversion recovery fast gradient recalled-echo sequence.^{8,9} This technique emphasizes the anatomic brain tissue contrast between gray and white matter

Received December 18, 2018; accepted after revision May 8, 2019.

From the Departments of Neuroradiology (L.D., D.D., E.P., E.V., A.C., E.P.), Neurology (G.C.R., A.K.-L.), and Neurosurgery (M.R.), Neurocenter of Southern Switzerland, Lugano, Switzerland; Neuroimaging Research Unit (G.C.R.), Institute of Experimental Neurology, Division of Neuroscience, San Raffaele Scientific Institute, Vita-Salute San Raffaele University, Milan, Italy; Departments of Neuroradiology (A.C.) and Neurology (A.K.-L.), Inselspital, Bern University Hospital, University of Bern, Bern, Switzerland; and Faculty of Biomedical Sciences (A.K.-L., M.R.), Università della Svizzera Italiana, Lugano, Switzerland.

Lucia Danieli received a grant from the Scientific Research Advisory Board of the Ente Ospedaliero Cantonale (grant number 107.99501) for conducting this study.

Paper previously presented as an oral communication at: European Congress of Radiology, February 28 to March 2, 2018, Vienna, Austria; and Annual Meeting of the American Society of Neuroradiology and the Foundation of the ASNR Symposium, Vancouver, British Columbia, Canada, June 2–7, 2018.

Please address correspondence to Emanuele Pravatà, MD, Via Tesserete 46, 6900, Lugano, Switzerland; e-mail: emanuele.pravata@eoc.ch

 Indicates article with supplemental on-line tables.

 Indicates article with supplemental on-line photos.

<http://dx.doi.org/10.3174/ajnr.A6096>

due to the inversion recovery preparation pulse. It was recommended for use in brain tumor clinical trials, in both the “Consensus Recommendations for a Standardized Brain Tumor Imaging Protocol in Clinical Trials”¹⁰ and in the modified Response Assessment in Neuro-Oncology (RANO) criteria.⁹ However, MPRAGE images exhibit suboptimal postgadolinium enhancement visualization, particularly in lesions with low gadolinium concentration.^{8,11,12} On the other hand, in previous investigations, 2 alternative techniques available for clinical use, the sampling perfection with application-optimized contrasts using different flip-angle evolution (SPACE sequence; Siemens, Erlangen, Germany) and the volumetric interpolated brain examination (VIBE) demonstrated a higher sensitivity to enhancing brain lesions.^{13–17} SPACE is a 3D-TSE technique¹⁸ that intrinsically provides higher sensitivity to low gadolinium concentrations and is more resilient to the effects of tumoral hemosiderin and/or calcium deposits, which may reduce enhancement visualization.^{5,13,18,19} VIBE is a fast gradient recalled-echo T1-weighted sequence without an inversion recovery preparation pulse, originally used in brain imaging for contrast-enhanced MR imaging venography studies, which use a partial *k*-space acquisition with a “centric-ordering” filling, to obtain both time-efficient and contrast-enhancement sensitive images.¹⁶

Awareness about MR imaging sequence–related differences in the sensitivity to GBCA enhancement may be particularly useful to decide the most appropriate sequence to use in cases in which a GBCA dose reduction is considered, such as in pregnant women and/or other vulnerable patient populations.^{20–24} In this study, we hypothesized the following: 1) Compared with MPRAGE, SPACE and VIBE may provide superior tumor-enhancement visualization, and 2) morphometric discrepancies may occur among these sequences when contouring the corresponding contrast-enhancing lesions (CELs). We evaluated 54 tumors, comprising both gliomas and metastases amenable to surgical interventions and/or stereotactic radiosurgery, comparing MPRAGE with SPACE and VIBE images with respect to the following: 1) tumor-enhancement contrast rate and contrast-to-noise ratio and visual conspicuity, and 2) tumor volume (TV) and margin delineation of the 3D “target” objects created for treatment planning. As an additional aim, we tested potential differences when using 1D (Response Evaluation Criteria in Solid Tumors [RECIST]²⁵) and 2D (RANO^{9,26}) standard measurements for treatment-response assessment. Finally, the number of metastases not visualized on MPRAGE images was recorded.

MATERIALS AND METHODS

This study was approved by the local ethics committee of Canton Ticino after obtaining written informed consent from all patients.

Between April 2015 and May 2017, one hundred ninety-six consecutive adult patients undergoing brain MR imaging for suspected or known tumor or tumor relapse following an operation were prospectively enrolled and examined on a 3T scanner (Magnetom Skyra; Siemens) with a 20-channel head coil. Inclusion criteria were the following: enhancing intra-axial tumors that were candidates for neuronavigation-assisted biopsy, surgical removal, and/or stereotactic radiosurgery treatment based on the literature recommendations^{27–29} and multidisciplinary tumor board consensus. Forty-one patients with intra-axial tumors were

reviewed; of these, 3 were excluded for movement artifacts, and 1 for incomplete protocol acquisition. In patients with multiple discrete foci of enhancement separated by nonenhancing parenchyma, these were considered individual lesions. Three additional metastases, which were not detected on MPRAGE (see also “Visual Conspicuity” below), were not included in the subsequent analyses. Fifty-four CELs (38 gliomas in 29 patients, and 16 metastases in 8 patients) were finally included. In 38/38 gliomas and 10/16 metastases, the final diagnosis was based on pathology. The diagnoses for the remaining lesions were based collectively on imaging characteristics, clinical history, evidence of remote (non-brain) malignancy, and MR imaging follow-up. In patients with tumor relapse (16 gliomas), differentiating tumor from treatment-related enhancement was based on perfusion and diffusion imaging, morphology (nodular/expansile versus linear/nonspecific), and sequential MR imaging follow-up.

MR Imaging Sequences

For MPRAGE and SPACE, we adapted the sequence default parameters recommended by the vendor, including a sagittally oriented slab with a symmetric *k*-space acquisition in all encoding directions, resulting in 1-mm³ isotropic voxels. For VIBE, which uses an asymmetric *k*-space acquisition,¹⁶ we obtained sagittally oriented slabs with a 1 × 1 × 1.27 mm actual voxel size, resulting into a 1-mm isotropic voxel after zero-filling interpolation. To minimize the potential bias related to the time gap between the first and last acquired images after injection, we reduced the scan duration using parallel imaging.³⁰ As previously proposed,^{17,31} a relatively higher acceleration factor was used for SPACE (×4), to account for the longer acquisition time. Finally, because patients had to be investigated for metastases potentially occurring in nonbrain tissues, fat suppression was also applied to improve contrast enhancement at this level. Scan durations were 1 minute 57 seconds for VIBE, 3 minutes 10 seconds for SPACE, and 3 minutes 46 seconds for MPRAGE. A summary of the main parameters of the sequences is reported in On-line Table 1.

All patients underwent our standard brain tumor MR imaging protocol, including FLAIR, DWI, T2*, T2 TSE, and PWI. For the precontrast T1-weighted images, 1 sequence was randomly chosen among MPRAGE, SPACE, and VIBE. A constant dose of 0.1 mL/Kg of gadobutrol, followed by a saline flush, was administered IV in all examinations. Finally, MPRAGE, SPACE, and VIBE sequences were consecutively performed in a randomized order, starting 5 minutes after contrast injection.

Image Analysis

Quantitative Conspicuity. Two measures, the contrast rate and contrast-to-noise ratio, were calculated with previously used formulas:

$$\text{Contrast Rate} = [(SI_{\text{lesion}} - SI_{\text{parenchyma}}) / SI_{\text{parenchyma}}] \times 100,^{13,32}$$

$$\text{Contrast-to-Noise Ratio} = (SI_{\text{lesion}} - SI_{\text{parenchyma}}) / SD_{\text{parenchyma}},^{17,31}$$

Where SI_{lesion} and $SI_{\text{parenchyma}}$, respectively, represent the CEL and the adjacent parenchyma average signal intensity, and $SD_{\text{parenchyma}}$ represents the standard deviation in $SI_{\text{parenchyma}}$. As

previously suggested,^{17,31} because parallel imaging was used, SI and SD for noise calculation were taken in the adjacent parenchyma, instead of background air. By means of iPlan, Version 3.0 (Brainlab, Munich, Germany), ROIs were drawn by an expert neuroradiologist (L.D., with 7 years of experience in neuroimaging). For SI_{lesion}, ROIs were drawn distant from lesion edges to avoid partial volume effects (average ROI size = 11.88 mm²). For SI_{parenchyma}, a relatively larger ROI (average size = 74.71 mm²) was placed in the adjacent parenchyma, including the gray and white matter to account for signal intensity differences among the tissues,¹³ and avoiding CSF and vessels.

Visual Conspicuity. As previously noted,^{13,17} it is not possible to perform a visual evaluation blinded to the sequence type because expert readers would easily recognize the distinguishing features of the various sequences. Here, 1 neuroradiologist (E.P.) and 1 neurosurgeon (M.R.) with 10 and 15 years of experience, respectively, unaware of the clinical data and quantitative results, assessed all 3 sequence types in each patient. The 3 sequences were presented sequentially for each patient, in a random order, using the Brainlab DICOM viewer. They provided a consensus visual score, aimed at comparing the quality of CEL conspicuity among sequences in a competitive manner and ranking (“best,” “intermediate,” and “worst”), taking into account the following: 1) enhancement conspicuity, 2) clarity of CEL separation from adjacent vessels, and 3) impact of artifacts from paramagnetic deposits from hemorrhage/calcifications. When the overall visual conspicuity of a given lesion was assessed as similar between 2 or among all 3 sequences, the same ranking was assigned to each. Finally, during a separate session, the number of small metastases visible on SPACE and/or VIBE, but not on MPRAGE images, was retrospectively recorded.

Volume and Margin Delineation. Analyses were performed using a semiautomated tool based on a region-growing algorithm (SmartBrush 2.5; Brainlab). This is previously validated software that demonstrated excellent reliability for brain tumor segmentation.^{33,34} All segmentations were performed by a single neuroradiologist (L.D.) to avoid interrater bias.³⁴ After image coregistration among all sequences, they were presented independently to the reader. Region-growing 2D segmentations of the CELs were drawn on perpendicular slices and automatically 3D-interpolated by the software. Then, margin refinements were manually performed with the help of the region-growing algorithm.³³

Within-sequence reproducibility was performed by repeating segmentations in a randomly chosen subset of 27 (50%) CELs during a subsequent separate session and by calculating the corresponding intraclass correlation coefficients with a 2-way mixed consistency, average-measured approach.^{33,35} Consistent with previous validation studies,³³ intraclass correlation coefficient values were excellent: 0.998 for MPRAGE, 95% CI, 0.995–0.999; 0.997 for VIBE, 95% CI, 0.993–0.999; and 0.999, 95% CI, 0.997–0.999 for SPACE.

The potential discrepancy occurring between the objects contoured using the different techniques was further assessed concerning lesion margin spatial mismatch. Using the Brainlab object manipulation tool, objects were reciprocally subtracted: 1)

$|CEL_{MPRAGE}| - |CEL_{SPACE}|$; 2) $|CEL_{SPACE}| - |CEL_{MPRAGE}|$; 3) $|CEL_{MPRAGE}| - |CEL_{VIBE}|$; and 4) $|CEL_{VIBE}| - |CEL_{MPRAGE}|$. We defined the resulting differences as margin extent discrepancy. This quantified the mismatch volume of the regions where a given sequence exceeded another and vice versa (see the explanatory diagram in Fig 1). The amount of mismatch with respect to the entire CEL was assessed by calculating the ratio (expressed in percentages) between the margin extent discrepancy and the median MPRAGE TV as a reference.

1D and 2D Measurements. In a subsequent session, 3 expert neuroradiologists (L.D., D.D., E.P.), with 7, 8, and 10 years of experience in brain tumor imaging, respectively, each independently measured the longest CEL diameter (1D RECIST²⁵) and the product of the 2 longest perpendicular diameters (2D RANO⁹), excluding cystic cavities and lesions with poorly defined margins. Only lesions of diameter ≥ 10 mm were considered measurable. Twenty-nine CELs (22 gliomas, 7 metastases) were evaluated and randomly presented to the readers, while varying sequences and patients. Finally, for each lesion, the 3 readers' measurements were averaged to perform sequence comparisons.

Statistical Analysis

All computations were performed using the SPSS software package, Version 22.0 (IBM, Armonk, New York). Normal distribution assumptions were checked by Kolmogorov-Smirnov and Shapiro-Wilk tests. Descriptive analyses for quantitative variables used median and interquartile range, while frequencies were used for the qualitative measures. In all CELs, as well as gliomas and metastases separately, differences between pairs of sequences in the contrast rate, contrast-to-noise ratio, and TV were investigated using the nonparametric Wilcoxon test. The visually estimated conspicuity ranking scores among sequences were compared using the χ^2 test. Bland-Altman diagrams were performed to represent the agreement of TV measures between sequences, and the corresponding repeatability coefficients were calculated.^{36,37} As for 1D and 2D measurements, given the limited sample size, analyses were performed in all CELs only. Interreader reproducibility of 1D and 2D measurements was estimated using the intraclass correlation coefficient.

The FSL General Linear Model (<http://fsl.fmrib.ox.ac.uk/fsl/fslwiki/GLM>) for repeated measures was used to adjust for the potential confound effect of the acquisition order between compared sequences, with respect to the contrast rate, contrast-to-noise ratio, TV, and 1D and 2D differences on Poisson distribution. The General Linear Model was also applied to test the potential confound of postsurgical and posttreatment tissue changes, which can influence the enhancement intensity at different CEL sites.³⁸ This potential confounding factor was addressed through testing the interaction effect of recurrence (as a binomial variable) on TV differences with the General Linear Model. The level of significance was set at $P < .05$.

RESULTS

Of 57 CELs detected by SPACE, 3 small (≤ 2 -mm diameter) metastases (5.3% of all lesions, 15.8% of all metastases) were missed

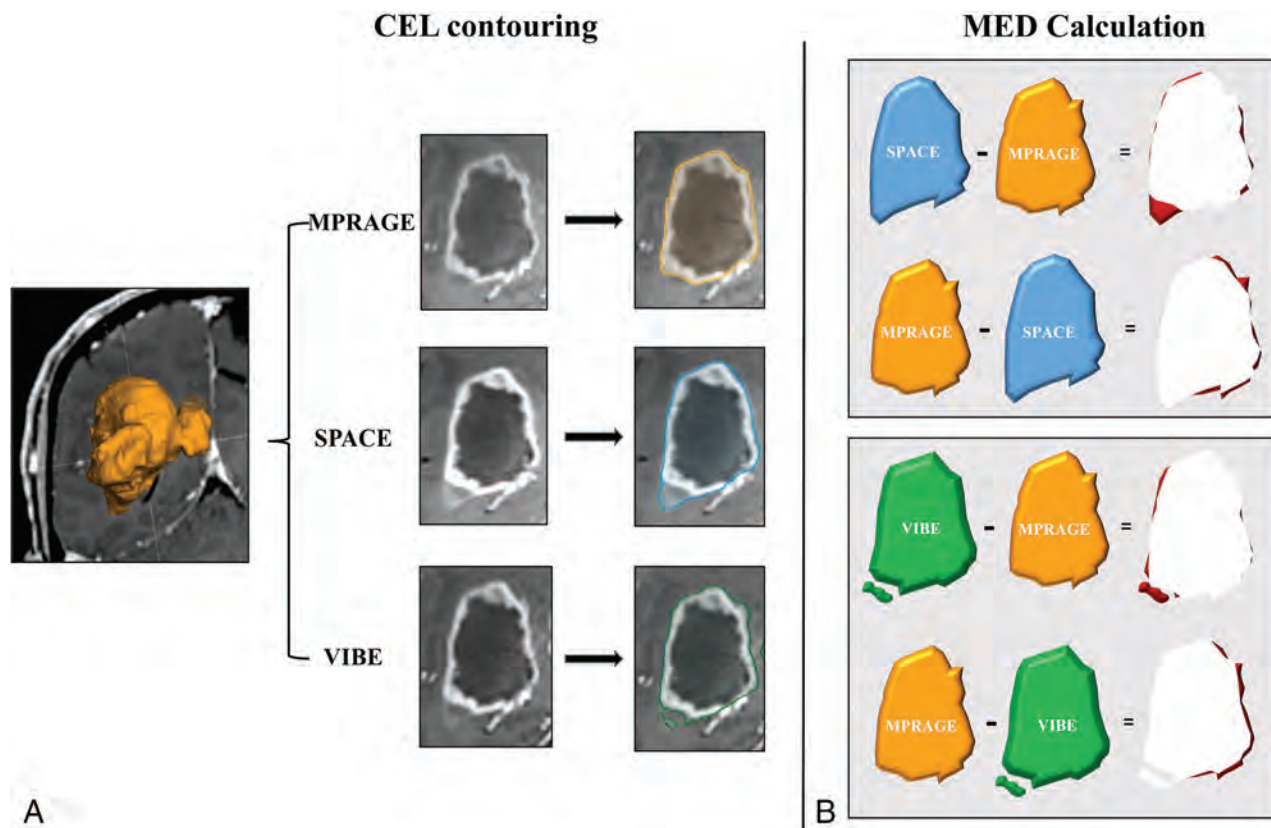


FIG 1. Diagram showing the contrast-enhancing lesion margin extent discrepancy (MED) estimation procedure. This approach is aimed at highlighting the spatial mismatch of the tumor border segmentation obtained from MPRAGE, with respect to SPACE and VIBE, and vice versa. *A*, First, for each CEL and sequence type, volume segmentation is performed using a validated computer-assisted tool dedicated to pretreatment planning and neuronavigation (SmartBrush 2.5; Brainlab). Segmentations obtained on MPRAGE, SPACE, and VIBE images are, respectively, represented in orange, blue, and green. *B*, The segmented volumes are reciprocally subtracted, generating maps of the areas where SPACE and VIBE volumes, respectively, exceed MPRAGE, and vice versa. Finally, the resulting MED areas are represented in red.

Table 1: Quantitative and qualitative conspicuity assessment

	CR Median (IQR)	CNR Median (IQR)	Visual Score		
			Best ^a	Intermediate	Worst
All CELs (<i>n</i> = 54)					
3D-IR GRE MPRAGE	80.88 (43.71–125.65)	10.02 (5.71–16.06)	15 (27.8%)	26 (48.1%)	13 (24.1%)
3D-TSE SPACE	100.92 ^{b,c} (73–191.59)	19.17 ^{b,c} (13.21–36.01)	54 (100%)	0	0
3D-GRE VIBE	85.86 ^{b,c} (43.71–135.22)	16.76 ^{b,c} (11–37.22)	24 (44.4%) ^b	25 (46.3%)	5 (9.3%) ^b
Gliomas (<i>n</i> = 38)					
3D-IR GRE MPRAGE	90.01 (48.29–125.21)	10.51 (5.68–17.33)	9 (23.7%)	19 (50%)	10 (26.3%)
3D-TSE SPACE	125.64 ^{b,c} (88.41–187.45)	24.46 ^{b,c} (12.55–41.23)	38 (100%)	0	0
3D-GRE VIBE	94.19 ^{b,c} (58.34–88.95)	16.22 ^{d,c} (9.89–27.25)	16 (42.1%) ^d	18 (47.4%)	4 (10.5%) ^d
Metastases (<i>n</i> = 16)					
3D-IR GRE MPRAGE	54.71 (35.24–130.01)	9.30 (6.77–12.29)	6 (37.5%)	7 (43.8%)	3 (18.8%)
3D-TSE SPACE	80.04 ^{b,c} (63.13–200)	17.15 ^{b,c} (13.63–21.26)	16 (100%)	0	0
3D-GRE VIBE	72.95 ^{b,c} (54.19–154.43)	17.26 ^{b,c} (12.14–31.18)	8 (50%)	7 (43.8%)	1 (6.3%)

Note:—IR indicates inversion recovery; GRE, gradient recalled-echo; CR, contrast rate; CNR, contrast-to-noise ratio; IQR, interquartile range.

^a Because SPACE in the visual assessment was constantly rated as best in all cases, no statistical comparison tests were performed in this analysis.

^b *P* < .001.

^c *P* ≤ .01 (adjusted for the order of sequence acquisition; FSL General Linear Model).

^d *P* = .001 (compared with MPRAGE, Wilcoxon test).

on MPRAGE. The remaining 54 CELs were included in the subsequent analyses. Patients' main demographics and CEL characteristics are presented on On-line Table 2.

Conspicuity Assessment

Both the contrast rate and contrast-to-noise ratio were significantly higher on either SPACE and VIBE images compared with MPRAGE, in all groups. Differences remained significant after

adjusting for the acquisition order of the compared sequences (Table 1). For visual assessment, in all CELs, MPRAGE obtained the best ranking in 15/54 (27.8%), intermediate in 26/54 (48.1%), and worst in 13/54 (24.1%). SPACE provided the best CEL visualization in all cases (54/54, 100%); therefore, no statistical comparison was performed with MPRAGE. VIBE obtained a higher frequency of best (24/54, 44.4%) and a lower frequency of worst

ratings (5/54, 9.3%) compared with MPRAGE ($P < .001$), whereas the frequency of intermediate ratings was not significantly different (25/54, 46.3%). Similar results were obtained by VIBE in the glioma subgroup ($P = .001$), while no significant differences were found in metastases subgroup. Two illustrative cases, with an example of a tiny metastasis not visible on MPRAGE images, are presented in Fig 2.

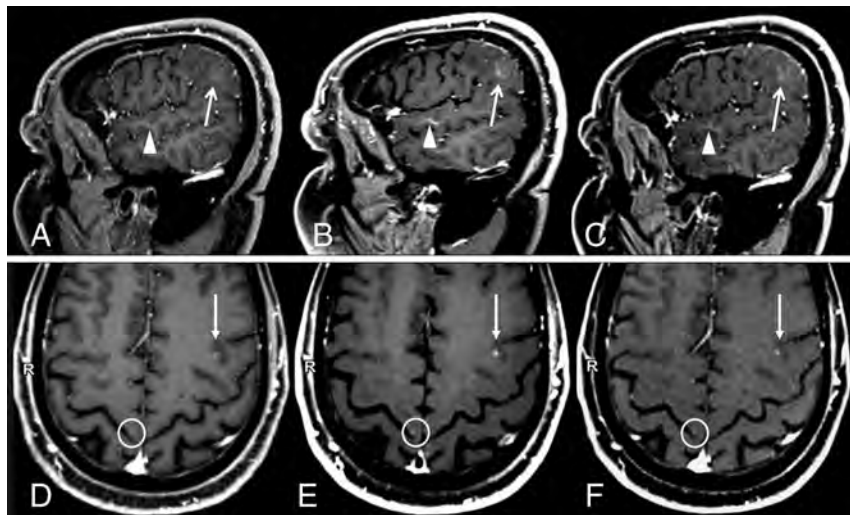


FIG 2. Two sample cases showing differences in contrast-enhancing lesion conspicuity between sequences. A and D, MPRAGE. B and E, SPACE. C and F, VIBE. A–C, Case 1: a patient with a faintly enhancing glioblastoma. Compared with MPRAGE (A), the lesion enhancement (arrows) and its boundary demarcations are much better appreciated on SPACE and VIBE images. The corresponding contrast rate/contrast-to-noise ratio values are 24.75/2.45, 51.32/8.96, and 41.23/6.25, and the rankings are worst, best, and intermediate, respectively, for MPRAGE, SPACE, and VIBE. Also incidentally noted is a developmental venous anomaly (arrowheads), which shows a strong contrast enhancement on black-blood SPACE images. This is probably related to the extremely slow flow seen in such small venous malformations. Images were acquired at 5 minutes after contrast injection in the following order: VIBE, SPACE, MPRAGE. D–F, Case 2: a patient with metastases from renal carcinoma (D, MPRAGE. E, SPACE. F, VIBE). A small CEL is seen in the left frontal lobe (arrows) whose conspicuity with respect to the background parenchyma was ranked worst on MPRAGE, intermediate on VIBE, and best on SPACE images. The corresponding contrast rate/contrast-to-noise ratio values are 8.85/3.08, 18.96/9.15, and 16.63/6.89, respectively. An example of a very tiny metastasis in the right precentral gyrus cortex, which was missed when inspecting MPRAGE images alone but was visible on SPACE and VIBE, is highlighted by circles. This lesion was not included in the analyses. Images were acquired after 5 minutes from contrast injection in the following order: SPACE, VIBE, and MPRAGE.

Volume and Margin Delineation Assessment

Between-sequence TV and margin extent discrepancy estimations are summarized in Table 2. As for the TV, significantly discrepant measurements were obtained between MPRAGE and SPACE in all groups (P range, .001–.007), with SPACE generating larger volumes. The corresponding measure agreement distribution is illustrated by the Bland-Altman plots in On-line Fig 1. The repeatability coefficient was 2.03 cm³. After adjusted for the compared sequence-acquisition order, differences remained significant in all CELs and gliomas and approached significance for metastases ($P = .075$) (Table 2). No significant interaction effect of recurrence (previously treated lesions) was detected ($F = 0.958$, $P = .332$). No discrepancy was found between MPRAGE and VIBE in all groups (P range, .201–.343).

The margin extent discrepancy analysis results are reported in Table 2. As for the $|\text{CEL}_{\text{MPRAGE}}| - |\text{CEL}_{\text{SPACE}}|$ comparison (quantifying the areas where MPRAGE exceeded SPACE margins), the margin extent discrepancy represented 7.4% (all lesions), 6% (gliomas), and 6.1% (metastases) of the TV, whereas for the reciprocal $|\text{CEL}_{\text{SPACE}}| - |\text{CEL}_{\text{MPRAGE}}|$ subtraction (quantifying the areas where SPACE exceeded MPRAGE margins), the margin extent discrepancy was 19.9% (all lesions), 14.2% (gliomas), and 15.2% (metastases). Regarding the $|\text{CEL}_{\text{MPRAGE}}| - |\text{CEL}_{\text{VIBE}}|$ mismatch, the margin extent discrepancy was 11% (all lesions), 7% (gliomas), and 3% (metastases) of the TV, whereas for the $|\text{CEL}_{\text{VIBE}}| - |\text{CEL}_{\text{MPRAGE}}|$ mismatch, it was 11% (all lesions), 7.6% (gliomas), and

Table 2: Morphometric assessment

	All CELs (n = 54)	Gliomas (n = 38)	Metastases (n = 16)
TV (median/IQR) (mL)			
MPRAGE	1.36/0.18–10.93	3.02/0.44–28.93	0.33/0.006–2.81
SPACE	1.78/0.20–11.00	3.5/0.49–29.73	0.39/0.006–3.2
VIBE	1.62/0.16–10.35	3.39/0.43–27.48	0.40/0.007–2.84
TV, SPACE vs MPRAGE			
p^a	.001 ^b	.007 ^b	.003 ^b
P (adjusted for sequence acquisition order) ^c	.034 ^b	.033 ^b	.075
TV, VIBE vs MPRAGE			
p^a	.259	.201	.343
P (adjusted for sequence acquisition order) ^c	.521	.538	.706
MED (median/% of TV)			
$ \text{CEL}_{\text{MPRAGE}} - \text{CEL}_{\text{SPACE}} $	0.10 mL/7.4%	0.18 mL/6%	0.02 mL/6.1%
$ \text{CEL}_{\text{SPACE}} - \text{CEL}_{\text{MPRAGE}} $	0.27 mL/19.9%	0.43 mL/14.2%	0.05 mL/15.2%
$ \text{CEL}_{\text{MPRAGE}} - \text{CEL}_{\text{VIBE}} $	0.15 mL/11%	0.21 mL/7%	0.01 mL/3%
$ \text{CEL}_{\text{VIBE}} - \text{CEL}_{\text{MPRAGE}} $	0.15 mL/11%	0.23 mL/7.6%	0.05 mL/15.2%

Note:—MED indicates margin extent discrepancy; IQR, interquartile range.

^a Wilcoxon signed rank test.

^b Statistically significant differences.

^c General Linear Model.

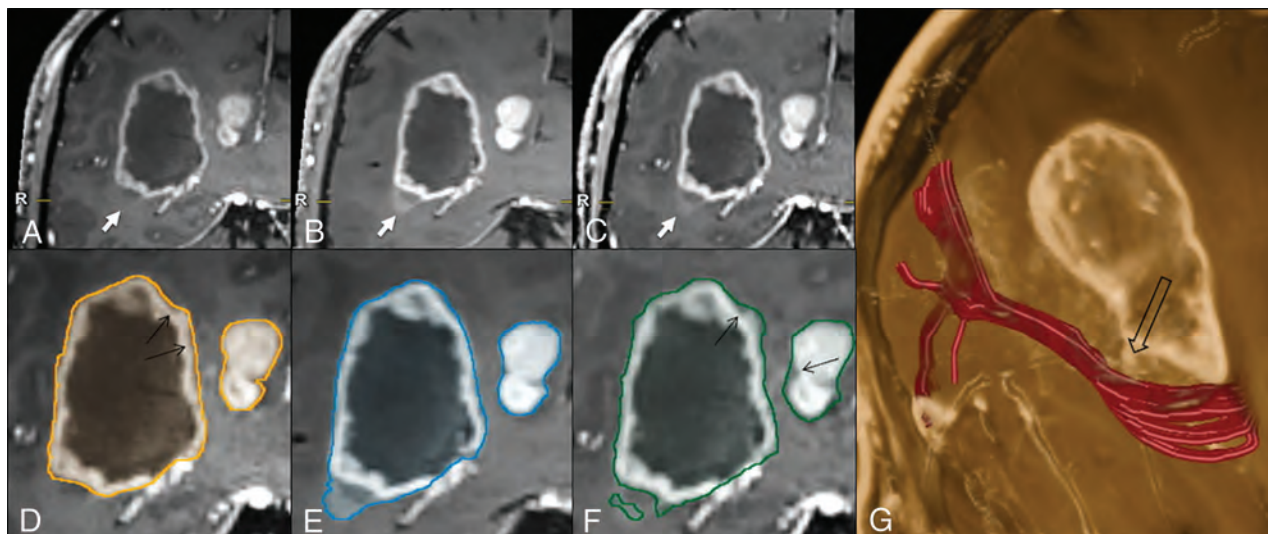


FIG 3. Illustrative case comparing the 3D target-object-creation results in a glioblastoma, obtained on MPRAGE, SPACE, or VIBE images (see the text and Fig 1 for method explanation). There is a clear difference among the MPRAGE (A), SPACE (B), and VIBE (C) conspicuities at the level of the faintly enhancing inferolateral border of the lesion (arrows), which is better represented on the SPACE and VIBE images, compared with MPRAGE. This part of the tumor is not included in the MPRAGE lesion segmentation (D); however, it is captured completely on SPACE (E) and partially on VIBE (F) images. The tractographic reconstruction of the optic radiation trajectory (G, in red) demonstrates the close proximity of the tumor to this tract (empty arrow). The black arrows in D and F indicate some thin areas of tumor margin overestimation on MPRAGE and VIBE, respectively, which are not seen on SPACE images. Images were acquired after 5 minutes from contrast injection in the following order: MPRAGE, VIBE, and SPACE.

15.2% (metastases). Segmentation examples are provided in Fig 3 and in On-line Fig 2, highlighting sources of mismatch related to differences in the enhancement sensitivity, erroneous margin estimation, and vessel segmentation, as well as susceptibility artifacts.

1D and 2D Assessment

The interobserver reproducibility, investigated with intraclass correlation coefficient single measurements, showed good agreement among the 3 readers for both 1D (MPRAGE: intraclass correlation coefficient = 0.69, 95% CI, 0.56–0.79; VIBE: intraclass correlation coefficient = 0.73, 95% CI, 0.61–0.82; and SPACE: intraclass correlation coefficient = 0.74, 95% CI, 0.63–0.83), and 2D (MPRAGE: intraclass correlation coefficient = 0.74, 95% CI, 0.63–0.83; VIBE: intraclass correlation coefficient = 0.81, 95% CI, 0.72–0.88; and SPACE: intraclass correlation coefficient = 0.81, 95% CI, 0.72–0.88). At the between-sequence comparison (On-line Table 3), both measurements were significantly discrepant between MPRAGE and SPACE ($P < .001$ and $.001$, respectively). Differences were also significant after adjusting for the acquisition order of compared sequences (On-line Table 3). No significant discrepancies with VIBE images were found.

DISCUSSION

Contrast enhancement refers to hyperintensity on T1-weighted images following GBCA administration, which is the result of extravasation of gadolinium-containing macromolecules through a leaky BBB. GBCA accumulates within tumor interstitium, resulting in longitudinal relaxation time shortening and consequent T1 signal hyperintensity.¹ Contrast enhancement helps CEL detection, characterization, and pretreatment anatomic assessment and represents a biomarker of potential high-grade tumor within malignant gliomas.^{2,3,6,39} A number of factors are known to in-

fluence the CEL conspicuity with respect to the background parenchyma: the BBB ultrastructural characteristics,⁴⁰ magnetic field strength,⁴¹ GBCA concentration, relaxivity properties, time from injection, and MR imaging technique. Here, we quantitatively and qualitatively show that tumor-enhancement visualization with SPACE and VIBE is superior to that in MPRAGE, the currently recommended standard technique for brain tumor clinical trials.^{9,10} In this study, SPACE and VIBE demonstrated significantly superior visual conspicuity ratings across all the CEL assessments, with SPACE having the best enhancement visualization in 100% of cases and VIBE in 44%, compared with 27.8% for MPRAGE. Conversely, MPRAGE received the worst ranking among sequences in 24.1% of all CELs, compared with only 9.3% for VIBE. On image inspection, we found that subtly enhancing parts of the tumors detected by SPACE and VIBE may be crucially missed by MPRAGE. Accordingly, 3 very small metastases could be detected only by SPACE. These results confirm and extend previous investigations conducted on metastatic lesions. Kato et al¹³ and Komada et al⁴² documented higher contrast rate and contrast-to-noise ratio estimated by SPACE. In addition, a retrospective study by Kammer et al¹⁷ showed that the use of SPACE allowed increased sensitivity and diagnostic confidence in the detection of small lesions. Previous information about VIBE performance was remarkably scarce: only 1 previous study conducted at 1.5T by Wetzel et al¹⁶ reported higher contrast-to-noise ratio values and visual conspicuity in a heterogeneous group of brain tumors, compared with MPRAGE.

To the best of our knowledge, this is the first study providing information about morphometric discrepancies occurring with brain tumor segmentation, related to sequence-enhancement conspicuity differences. First, we found that discrepant and significantly larger TV estimates were obtained using SPACE com-

pared with MPRAGE, both in all lesions and in gliomas and metastases considered separately. However, the use of VIBE images did not lead to significantly different TV estimates with respect to MPRAGE. Second, consistent with the larger TV estimates, SPACE contours exceeded those created with MPRAGE by 12.8% of the TV in all CELs. Most important, despite providing smaller TV estimates, MPRAGE margins exceeded SPACE margins by 6.2% of the TV, as well. Factors contributing to such a spatial delineation discrepancy included the different techniques sensitive to subtle enhancement, overestimation of tumor borders, erroneous vessel contouring, and/or interference from hemorrhagic/calcium deposit–related susceptibility artifacts (Fig 3 and Online Figs 2 and 3). Although an *in vivo* reference standard is not available to establish the CEL TV and morphology, the fact that SPACE images obtained higher contrast rate and contrast-to-noise ratio and visual conspicuity ratings from expert readers⁴³ reasonably supports the higher accuracy of this technique compared with MPRAGE for CEL boundary delineation. Furthermore, because high-flow intracranial arteries or venous sinuses appear dark on TSE images due to the flow void effect, they could be more accurately separated from the adjacent CEL than on fast gradient recalled-echo images, which conversely display enhancing vessels due to the flow-related enhancement effect.^{10,13,17}

Our findings have several practical implications. First, the use of SPACE and/or VIBE sequences may facilitate the identification of areas with relatively higher grade malignancy within gliomas. This is important for guiding accurate biopsy sampling and consequent correct histologic grading and treatment decision-making. Second, because achieving maximal tumor resection may lead to more favorable patient outcomes and the extent of resection may be increased with image-guided approaches,⁴⁴ optimizing target delineation accuracy facilitates precision surgery in individual patients. In the setting of stereotactic radiosurgery planning, using low-conspicuity images could also hinder target-volume margin delineation and result in suboptimal dose delivery to all CEL sites and/or in unnecessary dose delivery to surrounding eloquent brain structures.⁴⁻⁷ An exemplary case, demonstrating MPRAGE underestimation of tumor margins adjacent to the optic radiation, is presented in Fig 3.

Third, accurate count of brain metastases for radiosurgery planning is important to decide between stereotactic radiosurgery and whole-brain treatment approaches. This importance is underscored by a previous study⁴⁵ that emphasized the use of double-dose GBCA to improve MR imaging lesion-detection sensitivity for treatment planning. In contrast, maximizing image sensitivity to low-GBCA concentrations may play a crucial role whenever dose reduction is deemed appropriate to limit a patient's gadolinium tissue deposition.^{20-24,41} Fourth, the varied postcontrast conspicuity should be taken into account for follow-up examinations when different techniques are used, because this has the potential to confound treatment-response assessment, both in terms of enhancement degree and TV. Finally, our findings lend strength to designing data-acquisition strategies dedicated to MR imaging computer-assisted metastasis detection,⁴⁶ as well as multiparametric diagnostic and prognostic assessment of gliomas,⁴⁷⁻⁵⁰ which rely on highly accurate and standardized measures of tumor MR imaging features.

The RECIST²⁵ and RANO^{9,26} criteria, which represent standardized methodologies for the assessment of tumor response to treatment, respectively rely on 1D and 2D CEL measurements. In line with 3D-TV findings, both the 1D and 2D estimates performed in all measurable CELs were larger when using SPACE compared with MPRAGE. However, the limited number of measurable lesions available in this study did not allow a specific assessment of glioma and metastasis tumor types. Nevertheless, if confirmed in larger series, the present results might suggest the use of 3D-TSE techniques rather than MPRAGE to improve diagnostic accuracy in the design of clinical trials and in clinical practice.

Because the main goal of the present study was to test whether SPACE and/or VIBE may represent valid alternatives to MPRAGE, a direct comparison between SPACE and VIBE was not performed. However, we found that contrary to SPACE, VIBE did not lead to significant differences of morphometric assessment. We speculate that these differences are due to varied technique characteristics. For example, in SPACE sequences, the magnetization refocusing is obtained by radiofrequency pulses, which increase image resistance to magnetic field inhomogeneity.¹⁵ Another limitation with VIBE is the use of partial *k*-space acquisition to increase time efficiency¹⁶ so that the acquired voxel size is larger than the final interpolated size, thus potentially having a blurring effect. In addition, VIBE images show vessel enhancement, which may confound CEL boundary segmentation.

Limitations and Future Perspectives

While our sample size is relatively small, thorough selection was performed to represent cases potentially encountered in a routine neurosurgical and/or stereotactic radiosurgery treatment setting. The time gap between image acquisition and contrast agent injection represents a potential bias for the comparison of sequences acquired during the same examination because a larger GBCA amount may accumulate in the tumor within this time. However, obtaining data acquisition at exactly the same time for all test sequences would ideally require repeat contrast injections, resulting in an unnecessary dose increase to patients.^{20,21} We limited this bias by the following: 1) randomizing the sequence-acquisition order, 2) starting image acquisition 5 minutes after injection to allow a plateau phase, 3) reducing scan duration using parallel imaging, and 4) repeating quantitative analyses after adjusting for the acquisition order of compared sequences. Another potential confounding factor included different characteristics of GBCA uptake within posttreatment change.³⁸ In principle, this factor may bias morphometry assessment in previously treated (relapsing) gliomas. However, all these were carefully selected to differentiate tumor from posttreatment-related change, by using perfusion and diffusion imaging, morphology, and sequential MR imaging follow-up. In addition, we detected no significant effect on the between-sequence volume differences. The potential variability across different magnetic field intensities and vendors providing 3D-TSE T1 (eg, CUBE, GE Healthcare, Milwaukee, Wisconsin; VISTA, Philips Healthcare, Best, the Netherlands) and/or 3D-fast gradient recalled echo volume-interpolated T1 (LAVA; General Electric) techniques was not assessed in this study. Finally, we did not focus on reproducibility assessment across dif-

ferent software tools, or operators performing segmentations. Further investigations are warranted to extrapolate our results to additional treatment centers using different computer-assisted segmentation approaches and varied operator experience levels.

CONCLUSIONS

SPACE and VIBE postcontrast techniques may provide better visualization of brain tumor enhancement than MPRAGE. Morphometric discrepancies existed among sequences, with SPACE leading to potentially more accurate contouring estimates.

ACKNOWLEDGMENTS

We would like to thank Dr Rachel Delfanti for help in editing this article. This study received a grant from the Scientific Research Advisory Board of the Ente Ospedaliero Cantonale, Bellinzona, Ticino, Switzerland.

Disclosures: Lucia Danieli—*RELATED: Grant:* Advisory Board for Research of the Ente Ospedaliero Cantonale, *Comments:* I received a grant from the Advisory Board for Research of the Hospital Cooperation (Ente Ospedaliero Cantonale) (grant No. 107.99501) for conducting this study. Alain Kaelin-Lang—*UNRELATED: Consultancy:* Advisory Boards (Merz Pharma, Zambon)*; *Employment:* Medical and Scientific Director of the Neurocenter of Southern Switzerland; *Grants/Grants Pending:* Fondazione Svizzera per la Ricerca sulle Malattie Muscolari Switzerland, Swiss Parkinson Biotech; *Payment for Lectures including Service on Speakers Bureaus:* sponsored lectures (Merz Pharma)*. Michael Reinert—*UNRELATED: Grants/grants pending:* Lega Cancro Ticinese, Gabruelle Charitable Foundation, *Comments:* Neurooncology Research Group. *Money paid to the institution.

REFERENCES

- Gadian DG, Payne JA, Bryant DJ, et al. **Gadolinium-DTPA as a contrast agent in MR imaging—theoretical projections and practical observations.** *J Comput Assist Tomogr* 1985;9:242–51 CrossRef Medline
- Healy ME, Hesselink JR, Press GA, et al. **Increased detection of intracranial metastases with intravenous Gd-DTPA.** *Radiology* 1987; 165:619–24 CrossRef Medline
- Sze G, Milano E, Johnson C, et al. **Detection of brain metastases: comparison of contrast-enhanced MR with unenhanced MR and enhanced CT.** *AJNR Am J Neuroradiol* 1990;11:785–91 Medline
- Zhao F, Li M, Kong L, et al. **Delineation of radiation therapy target volumes for patients with postoperative glioblastoma: a review.** *Onco Targets Ther* 2016;9:3197–204 CrossRef Medline
- Cao Y, Tseng CL, Balter JM, et al. **MR-guided radiation therapy: transformative technology and its role in the central nervous system.** *Neuro Oncol* 2017;19:ii16–29 CrossRef Medline
- Wang LL, Leach JL, Breneman JC, et al. **Critical role of imaging in the neurosurgical and radiotherapeutic management of brain tumors.** *Radiographics* 2014;34:702–21 CrossRef Medline
- Farace P, Giri MG, Meliàdò G, et al. **Clinical target volume delineation in glioblastomas: pre-operative versus post-operative/pre-radiotherapy MRI.** *Br J Radiol* 2011;84:271–78 CrossRef Medline
- Mugler JP 3rd, Brookeman JR. **Theoretical analysis of gadopentetate dimeglumine enhancement in T1-weighted imaging of the brain: comparison of two-dimensional spin-echo and three-dimensional gradient-echo sequences.** *J Magn Reson Imaging* 1993;3:761–69 CrossRef Medline
- Ellingson BM, Wen PY, Cloughesy TF. **Modified criteria for radiographic response assessment in glioblastoma clinical trials.** *Neurotherapeutics* 2017;14:307–20 CrossRef Medline
- Ellingson BM, Bendszus M, Boxerman J, et al. **Jumpstarting Brain Tumor Drug Development Coalition Imaging Standardization Steering Committee. Consensus recommendations for a standardized brain tumor imaging protocol in clinical trials.** *Neuro Oncol* 2015; 17:1188–98 CrossRef Medline
- Schmilz BL, Aschoff AJ, Hoffmann MH, et al. **Advantages and pitfalls in 3T MR brain imaging: a pictorial review.** *AJNR Am J Neuroradiol* 2005;26:2229–37 Medline
- Blüml S, Schäd LR, Scharf J, et al. **A comparison of magnetization prepared 3D gradient-echo (MP-RAGE) sequences for imaging of intracranial lesions.** *Magn Reson Imaging* 1996;14:329–35 CrossRef Medline
- Kato Y, Higano S, Tamura H, et al. **Usefulness of contrast-enhanced T1-weighted sampling perfection with application-optimized contrasts by using different flip angle evolutions in detection of small brain metastasis at 3T MR imaging: comparison with magnetization-prepared rapid acquisition of gradient echo imaging..** *AJNR Am J Neuroradiol* 2009;30:923–29 CrossRef Medline
- Hodel J, Outteryck O, Ryo E, et al. **Accuracy of postcontrast 3D turbo spin-echo MR sequence for the detection of enhanced inflammatory lesions in patients with multiple sclerosis.** *AJNR Am J Neuroradiol* 2014;35:519–23 CrossRef Medline
- Reichert M, Morelli JN, Runge VM, et al. **Contrast-enhanced 3-dimensional SPACE versus MP-RAGE for the detection of brain metastases: considerations with a 32-channel head coil.** *Invest Radiol* 2013;48:55–60 CrossRef Medline
- Wetzel SG, Johnson G, Tan AGS, et al. **Three-dimensional, T1-weighted gradient-echo imaging of the brain with a volumetric interpolated examination.** *AJNR Am J Neuroradiol* 2002;23:995–1002 Medline
- Kammer NN, Copenrath E, Treitl KM, et al. **Comparison of contrast-enhanced modified T1-weighted 3D TSE black-blood and 3D MP-RAGE sequences for the detection of cerebral metastases and brain tumours.** *Eur Radiol* 2016;26:1818–25 CrossRef Medline
- Mugler JP 3rd, Bao S, Mulkern RV, et al. **Optimized single-slab three-dimensional spin-echo MR imaging of the brain.** *Radiology* 2000;216:891–99 CrossRef Medline
- Chappell PM, Pelc NJ, Foo TK, et al. **Comparison of lesion enhancement on spin-echo and gradient-echo images.** *AJNR Am J Neuroradiol* 1994;15:37–44 Medline
- Ramalho J, Semelka RC, Ramalho M, et al. **Gadolinium-based contrast agent accumulation and toxicity: an update.** *AJNR Am J Neuroradiol* 2016;37:1192–98 CrossRef Medline
- Thomsen HS, Morcos SK, Almen T, et al. **ESUR Contrast Medium Safety Committee. Nephrogenic systemic fibrosis and gadolinium-based contrast media: updated ESUR Contrast Medium Safety Committee guidelines.** *Eur Radiol* 2013;23:307–18 CrossRef Medline
- Gathings RM, Reddy R, Santa Cruz D, et al. **Gadolinium-associated plaques: a new, distinctive clinical entity.** *JAMA Dermatol* 2015;151: 316–19 CrossRef Medline
- Khawaja AZ, Cassidy DB, Al Shakarchi J, et al. **Revisiting the risks of MRI with gadolinium based contrast agents: review of literature and guidelines.** *Insights Imaging* 2015;6:553–58 CrossRef Medline
- Gong E, Pauly JM, Wintermark M, et al. **Deep learning enables reduced gadolinium dose for contrast-enhanced brain MRI.** *J Magn Reson Imaging* 2018;48:330–40 CrossRef Medline
- Therasse P, Arbuck SG, Eisenhauer EA, et al. **New guidelines to evaluate the response to treatment in solid tumors: European Organization for Research and Treatment of Cancer, National Cancer Institute of the United States, National Cancer Institute of Canada.** *J Natl Cancer Inst* 2000;92:205–16 CrossRef Medline
- Wen PY, Macdonald DR, Reardon DA, et al. **Updated response assessment criteria for high-grade gliomas: Response Assessment in Neuro-Oncology Working Group.** *J Clin Oncol* 2010;28:1963–72 CrossRef Medline
- Paek SH, Audu PB, Sperling MR, et al. **Reevaluation of surgery for the treatment of brain metastases: review of 208 patients with single or multiple brain metastases treated at one institution with modern neurosurgical techniques.** *Neurosurgery* 2005;56:1021–34; discussion 1021–34 Medline
- Sahgal A, Ruschin M, Ma L, et al. **Stereotactic radiosurgery alone for multiple brain metastases? A review of clinical and technical issues.** *Neuro Oncol* 2017;19:ii2–15 CrossRef Medline
- Kondziolka D, Kano H, Harrison GL, et al. **Stereotactic radiosurgery**

- as primary and salvage treatment for brain metastases from breast cancer: clinical article. *J Neurosurg* 2011;114:792–800 CrossRef Medline
30. Robson PM, Grant AK, Madhuranthakam AJ, et al. **Comprehensive quantification of signal-to-noise ratio and g-factor for image-based and k-space-based parallel imaging reconstructions.** *Magn Reson Med* 2008;60:895–907 CrossRef Medline
 31. Sommer NN, Saam T, Coppens E, et al. **Multiple sclerosis: improved detection of active cerebral lesions with 3-dimensional T1 black-blood magnetic resonance imaging compared with conventional 3-dimensional T1 GRE imaging.** *Invest Radiol* 2018;53:13–19 CrossRef Medline
 32. Rand S, Maravilla KR, Schmiedl U. **Lesion enhancement in radio-frequency spoiled gradient-echo imaging: theory, experimental evaluation, and clinical implications.** *AJNR Am J Neuroradiol* 1994;15:27–35 Medline
 33. Huber T, Alber G, Bette S, et al. **Reliability of semi-automated segmentations in glioblastoma.** *Clin Neuroradiol* 2017;27:153–61 CrossRef Medline
 34. Huber T, Alber G, Bette S, et al. **Progressive disease in glioblastoma: benefits and limitations of semi-automated volumetry.** *PLoS One* 2017;12:e0173112 CrossRef Medline
 35. McGraw KO, Wong SP. **Forming inferences about some intraclass correlation coefficients.** *Psychol Methods* 1996;1:30–46 CrossRef
 36. Bland JM, Altman DG. **Statistical methods for assessing agreement between two methods of clinical measurement.** *Lancet* 1986;1:307–10 Medline
 37. Peat J, Barton B. *Medical Statistics: A Guide to Data Analysis and Critical Appraisal.* Oxford: Blackwell Publishing; 2005
 38. Zach L, Guez D, Last D, et al. **Delayed contrast extravasation MRI for depicting tumor and non-tumoral tissues in primary and metastatic brain tumors.** *PLoS One* 2012;7:e52008 CrossRef Medline
 39. Balériaux D, Colosimo C, Rusalleda J, et al. **Magnetic resonance imaging of metastatic disease to the brain with gadobenate dimeglumine.** *Neuroradiology* 2002;44:191–203 CrossRef Medline
 40. Cha S, Lupo JM, Chen MH, et al. **Differentiation of glioblastoma multiforme and single brain metastasis by peak height and percentage of signal intensity recovery derived from dynamic susceptibility-weighted contrast-enhanced perfusion MR imaging.** *AJNR Am J Neuroradiol* 2007;28:1078–84 CrossRef Medline
 41. Krautmacher C, Willinek WA, Tschampa HJ, et al. **Brain tumors: full- and half-dose contrast-enhanced MR imaging at 3.0 T compared with 1.5 T—initial experience.** *Radiology* 2005;237:1014–19 CrossRef Medline
 42. Komada T, Naganawa S, Ogawa H, et al. **Contrast-enhanced MR imaging of metastatic brain tumor at 3 Tesla: utility of T(1)-weighted SPACE compared with 2D spin echo and 3D gradient echo sequence.** *Magn Reson Med Sci* 2008;7:13–21 CrossRef Medline
 43. Reitsma JB, Rutjes AW, Khan KS, et al. **A review of solutions for diagnostic accuracy studies with an imperfect or missing reference standard.** *J Clin Epidemiol* 2009;62:797–806 CrossRef Medline
 44. Sanai N, Berger MS. **Surgical oncology for gliomas: the state of the art.** *Nat Rev Clin Oncol* 2018;15:112–25 CrossRef Medline
 45. Garcia MA, Lazar A, Duriseti S, et al. **Discovery of additional brain metastases on the day of stereotactic radiosurgery: risk factors and outcomes.** *J Neurosurg* 2017;126:1756–63 CrossRef Medline
 46. Yang S, Nam Y, Kim MO, et al. **Computer-aided detection of metastatic brain tumors using magnetic resonance black-blood imaging.** *Invest Radiol* 2013;48:113–19 CrossRef Medline
 47. Cui Y, Tha KK, Terasaka S, et al. **Prognostic imaging biomarkers in glioblastoma: development and independent validation on the basis of multiregion and quantitative analysis of MR images.** *Radiology* 2016;278:546–53 CrossRef Medline
 48. Caulo M, Panara V, Tortora D, et al. **Data-driven grading of brain gliomas: a multiparametric MR imaging study.** *Radiology* 2014;272:494–503 CrossRef Medline
 49. Narang S, Lehrer M, Yang D, et al. **Radiomics in glioblastoma: current status, challenges and potential opportunities.** *Transl Cancer Res* 2016;5:383–97 CrossRef
 50. Gillies RJ, Kinahan PE, Hricak H. **Radiomics: images are more than pictures, they are data.** *Radiology* 2016;278:563–77 CrossRef Medline

Extent of Surgical Resection in Lower-Grade Gliomas: Differential Impact Based on Molecular Subtype

S.H. Patel, A.G. Bansal, E.B. Young, P.P. Batchala, J.T. Patrie, M.B. Lopes, R. Jain, C.E. Fadul, and D. Schiff



ABSTRACT

BACKGROUND AND PURPOSE: Diffuse lower-grade gliomas are classified into prognostically meaningful molecular subtypes. We aimed to determine the impact of surgical resection on overall survival in lower-grade glioma molecular subtypes.

MATERIALS AND METHODS: For 172 patients with lower-grade gliomas (World Health Organization grade II or III), pre- and postsurgical glioma volumes were determined using a semiautomated segmentation software based on FLAIR or T2-weighted MR imaging sequences. The association of pre- and postsurgical glioma volume and the percentage of glioma resection with overall survival was determined for the entire cohort and separately for lower-grade glioma molecular subtypes based on *isocitrate dehydrogenase (IDH)* and 1p/19q status, after adjustment for age, sex, World Health Organization grade, chemotherapy administration, and radiation therapy administration.

RESULTS: For the entire cohort, postsurgical glioma volume (hazard ratio, 1.80; 95% CI, 1.18–2.75; $P = .006$) and the percentage of resection (hazard ratio, 3.22; 95% CI, 1.79–5.82; $P < .001$) were associated with overall survival. For *IDH*-mutant 1p/19q-codeleted oligodendrogliomas, the percentage of resection (hazard ratio, 6.69; 95% CI, 1.57–28.46; $P = .01$) was associated with overall survival. For *IDH*-mutant 1p/19q-noncodeleted astrocytomas, presurgical glioma volume (hazard ratio, 3.20; 95% CI, 1.22–8.39; $P = .018$), postsurgical glioma volume (hazard ratio, 2.33; 95% CI, 1.32–4.12; $P = .004$), and percentage of resection (hazard ratio, 4.34; 95% CI, 1.74–10.81; $P = .002$) were associated with overall survival. For *IDH*-wild-type lower-grade gliomas, pre-/postsurgical glioma volume and percentage of resection were not associated with overall survival.

CONCLUSIONS: The extent of surgical resection has a differential survival impact in patients with lower-grade gliomas based on their molecular subtype. *IDH*-mutant lower-grade gliomas benefit from a greater extent of surgical resection, with the strongest impact observed for *IDH*-mutant 1p/19q-noncodeleted astrocytomas.

ABBREVIATIONS: LGG = lower-grade glioma; mut = mutation; WHO = World Health Organization; *IDHmut-Noncodeled* = LGGs with an *IDH* mutation but lacking 1p/19q codeletion; *IDHmut-Codel* = LGGs with an *IDH* mutation and codeletion of chromosome arms 1p and 19q; *IDHwt* = LGGs in *IDH*-wild-type subgroup

Diffuse lower-grade gliomas (LGGs) are World Health Organization (WHO) grade II and III infiltrative brain neoplasms. In 2016, the WHO updated the classification of diffuse LGGs by integrating molecular markers with histopathology.¹ Between 70% and 80% of LGGs are now known to have a prognostically favorable mutation in the *isocitrate dehydrogenase (IDH)* gene.^{2,3} Oligodendrogliomas (grade II) and anaplastic oligoden-

drogliomas (grade III) are defined by the presence of both an *IDH* mutation and codeletion of chromosome arms 1p and 19q (heretofore collectively referred to as *IDHmut-Codel*). LGGs with an *IDH* mutation but lacking 1p/19q codeletion include diffuse astrocytomas (grade II) and anaplastic astrocytomas (grade III) (heretofore collectively referred to as *IDHmut-Noncodeled*).^{1,3-5} These *IDH*-mutant LGG subgroups have distinct prognostic and therapeutic profiles.³⁻⁷ The *IDH*-wild-type subgroup of LGGs (heretofore collectively referred to as *IDHwt*) is associated with the most aggressive clinical behavior and worst outcome, similar to that of glioblastomas (WHO grade IV), though heterogeneity in the behavior and molecular features within this subgroup is being increasingly recognized.⁸⁻¹¹

Received March 27, 2019; accepted after revision May 12.

From the Departments of Radiology and Medical Imaging (S.H.P., A.G.B., E.B.Y., P.P.B.), Public Health Sciences (J.T.P.), and Pathology (M.B.L.), Divisions of Neuropathology and Molecular Diagnostics, and Division of Neuro-Oncology (C.E.F., D.S.), University of Virginia Health System, Charlottesville, Virginia; and Departments of Radiology (R.J.) and Neurosurgery (R.J.), New York University School of Medicine, New York, New York.

S.H. Patel received a Radiological Society of North America Research Scholar Grant (RSCH1819).

Paper previously presented at: American Society of Neuroradiology Annual Meeting and the Foundation of the ASNR Symposium, May 18–23, 2019; Boston, Massachusetts.

Please address correspondence to Sohil H. Patel, MD, Department of Radiology and Medical Imaging, University of Virginia Health System, PO Box 800170, Charlottesville, VA 22908; e-mail: shp4k@virginia.edu

Indicates article with supplemental on-line photo.

<http://dx.doi.org/10.3174/ajnr.A6102>

Multiple studies have provided evidence supporting the maximum safe surgical resection as the front-line treatment of diffuse LGGs.¹²⁻¹⁹ However, most studies were undertaken before the 2016 WHO update for the classification of diffuse LGGs, without accounting for defining molecular markers. It is unknown to what extent these earlier study results are confounded by the use of older nonmolecular classification schema. Only recently have volumetric MR imaging studies incorporated *IDH* and 1p/19q-codeletion status when assessing the impact of surgical resection on patient outcomes in LGGs.^{20,21}

The purpose of our study was to determine the effect of surgical resection extent on overall survival in a patient cohort with LGGs stratified by molecular subtype. Among the *IDH*-mutant LGGs, we hypothesized that the extent of surgery might have greater impact among *IDHmut-Noncodel* subtypes than the *IDHmut-Codel* subtypes, given the overall worse prognosis among the former subtype. We hypothesized that surgery would have prognostic impact among the *IDHwt* subtypes as well, though these results might be confounded by the molecular heterogeneity of this subtype.

MATERIALS AND METHODS

This retrospective study of patient data was Health Insurance Portability and Accountability Act-compliant and was approved by our institutional review board (University of Virginia Health System).

Patient Selection

The patients included in this study were selected from an institutional neuro-oncology/neuroradiology diffuse glioma data base maintained at our institution, containing a total of 429 diffuse glioma cases diagnosed between 2000 and 2018. All patients who are seen by Medical Neuro-Oncology at our institution are added to our data base. From this data base, patients were selected on the basis of the following inclusion criteria: 1) diagnosed with a diffuse LGG (WHO grades II and III), 2) a known molecular subtype based on *IDH* and 1p/19q-codeletion status, 3) available presurgical and postsurgical MR images, and 4) known chemotherapy and radiation therapy history at the last follow-up. After review of the electronic medical record and PACS, we excluded 176 cases with grade IV histology (ie, glioblastomas) and 49 LGGs with unknown molecular status. Of the remaining 204 cases, we excluded 20 cases for lack of pre- or postsurgical MR imaging and 12 cases for unknown chemotherapy or radiation therapy history at time of the last follow-up. A total of 172 patients met the criteria for study inclusion. The mean time interval between the presurgical MR imaging and the operation was 5.18 days, and the mean time interval between the postsurgical MR imaging and the operation was 79.3 days. As per the methodology of Wijnenga et al,²⁰ we preferentially avoided using the immediate postsurgical MR imaging scans for performing volume measurements to avoid including postsurgical edema or ischemia in our measurements.

Neuroimaging Analysis

Pre- and postsurgical MR images were analyzed by a board-certified neuroradiologist with a Certificate of Added Qualification in diagnostic neuroradiology and 6 years of experience. Measure-

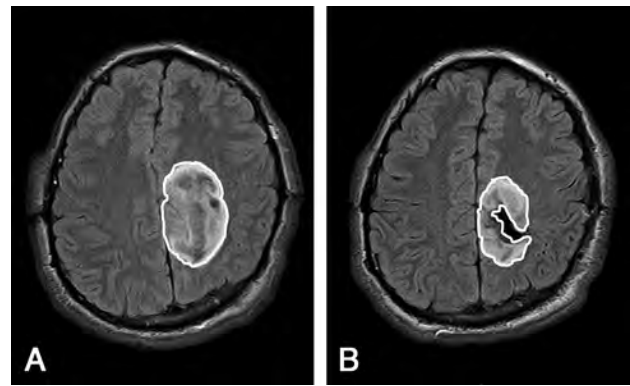


FIG 1. Glioma segmentation shown on axial FLAIR images of presurgical MR imaging (A) and postsurgical MR imaging (B) in a patient with a diffuse *IDH*-mutant astrocytoma who underwent subtotal resection.

ments of glioma volume on the presurgical and postsurgical MR imaging examinations were undertaken using the semiautomated lesion-management tool in the PACS using FLAIR or T2-weighted imaging (3D sequences were used when possible). MR imaging examinations analyzed in this study were performed on various 1.5T and 3T MR imaging scanners, and pulse sequences with variable parameters were used. On 3T MR imaging, the 3D-T2WI and FLAIR sequences used the following parameters—3D-T2WI: FOV = 256 mm, slice thickness = 1.0 mm, matrix = 256 × 256, TR = 3200 ms, TE = 413 ms, NEX = 1; 3D-FLAIR: FOV = 256 mm, slice thickness = 1.0 mm, matrix = 256 × 256, TR = 5000 ms, TI = 1800 ms, TE = 386 ms, NEX = 1. To create glioma volumes of interest, the neuroradiologist reader manually traced the contour of the glioma using axial images from the highest quality FLAIR or T2-weighted sequence on the presurgical and postsurgical MR images (Fig 1), and the software calculated a 3D volume based on the neuroradiologist's segmentation. For the presurgical volume measurements, in cases in which peritumoral edema could not be confidently distinguished from infiltrative glioma, the neuroradiologist reader erred on the side of including any high signal present on the T2/FLAIR sequences within the volume measurements. Based on presurgical and postsurgical glioma volumes, the percentage of glioma resection was calculated as $100\% \times (1 - [\text{Postsurgical Glioma Volume}] / [\text{Presurgical Glioma Volume}])$.

Neuropathology

Glioma histology and grade and *IDH* and 1p/19q statuses were retrieved from the electronic medical record. *IDH* and 1p/19q statuses were tested in the Clinical Laboratory Improvement Amendments-certified molecular pathology laboratory at our institution. *IDH*-mutation status was first tested by immunohistochemistry using an *IDH1* R132H-mutant-specific antibody. Immunohistochemistry was performed on 4- μ m-thick sections from formalin-fixed paraffin-embedded tissue following the manufacturer's recommended protocol (Bond-III; Leica Biosystem, Newcastle Upon Tyne, UK). Commercially purchased antibodies against *IDH1* (R132H) mutant protein (DIA-H09; Dianova, Hamburg, Germany) were used.^{22,23} In cases with negative findings on immunohistochemistry, *IDH1/2*

Table 1: Summary of patient characteristics^a

	<i>IDHmut-Codel</i> (n = 68)	<i>IDHmut-Noncodel</i> (n = 63)	<i>IDHwt</i> (n = 41)
Sex			
Female	37 (54.4%)	30 (47.6%)	18 (43.9%)
Male	31 (45.6%)	33 (52.4%)	23 (56.1%)
Age (yr) ^a	45.5 (35.5–53)	33 (27–42.8)	57.0 (49.5–63.3)
WHO grade			
II	50 (73.5%)	46 (73.0%)	25 (61.0%)
III	18 (26.5%)	17 (27.0%)	16 (39.0%)
Chemotherapy			
Yes	55 (80.9%)	53 (84.1%)	30 (73.2%)
No	13 (19.1%)	10 (15.9%)	11 (26.8%)
Radiation therapy			
Yes	45 (66.2%)	53 (84.1%)	31 (75.6%)
No	23 (33.8%)	10 (15.9%)	10 (24.4%)
Presurgical glioma volume (cm ³) ^a	56.4 (26.5–111.6)	55.0 (31.0–116.2)	47.7 (18.0–86.4)
Postsurgical glioma volume (cm ³) ^a	28.4 (13.2–59.1)	29.3 (1.2–65.6)	30.1 (8.4–64.4)
Mortality events	12 (17.6%)	14 (22.2%)	13 (31.7%)

^aData are listed as median and interquartile range. All other data are listed as absolute values and percentages.

mutation status was assessed by the clinically validated DNA pyrosequencing assay, using the PyroMark Q24 system, following the manufacturer's recommended protocol (QIAGEN; <https://www.qiagen.com/us/products/discovery-and-translational-research/pyrosequencing/instruments/pyromark-q24/#orderinginformation>).

We used the following primers—*IDH1* forward primer: 5'-Biot.-CATAATGTTGGCGTCAAATGTG-3'; *IDH1* reverse primer: 5'-ACATGCAAAATCACATTATTGCC-3'; *IDH1* sequencing primer: 5'-TGATCCCCATAAGCAT-3'; *IDH2* forward primer: 5'-GTTCAAGCTGAAGAAGATGTGG-3'; *IDH2* reverse primer: 5'-Biot.-GTGGCCTTGACTGCAGAG-3'; *IDH2* sequencing primer: and 5'-AGCCCATCACATTGG-3'. The pyrosequencing assay is designed to detect mutations within codon 132 of *IDH1* and codon 172 of *IDH2*, as described previously.²⁴ The 1p/19q-codeletion status was determined using dual-color fluorescence in situ hybridization on formalin-fixed paraffin-embedded tissue. Commercial human probes were applied to localize 1p36, 1q25, 19p13 (Vysis; Abbott Molecular, Abbott Park, Illinois), and DAPI (Insitus Biotechnologies, Albuquerque, New Mexico) was used as a nuclear counterstain.

Statistical Analysis

Categorical variables are summarized by frequencies and percentages, and molecular subtype comparisons of categorical variables were conducted using the Fisher exact test. Continuous scale variables are summarized by the median, interquartile range, and range of the distribution, and molecular subtype comparisons of continuous scale variables were performed using the Wilcoxon rank sum test. Multivariate Cox proportional hazards regression was used to examine whether presurgical glioma volume, postsurgical glioma volume, and the percentage of glioma resection are uniquely associated with overall survival time for all cases and for cases in the 3 molecular subtypes. In total, 12 multivariate Cox models were constructed, and each model was identically specified with the only between-model difference being the variable of interest (presurgical glioma volume, postsurgical volume, or percentage of glioma resection) and the molecular subtype

(*IDHmut-Codel*, *IDHmut-Noncodel*, *IDHwt*, or all molecular subtypes combined). Per variable of interest (eg, presurgical glioma volume) and per molecular subtype of patients (eg, the *IDHmut-Noncodel* molecular subtype), the regression model included not only the variable of interest (eg, presurgical glioma volume) but also patient age and sex, WHO grades II and III, chemotherapy administration status (yes, no), and radiation therapy administration status (yes, no) as concomitant variable predictors of survival time. For all 12 multivariate Cox models, the survival times of patients who were known to be alive at last follow-up were treated as right-censored observations. With regard to hypothesis testing, the type III version of

the Wald χ^2 statistic served as the pivotal quantity for testing the null hypothesis that there is no unique association between the variable of interest (eg, presurgical glioma volume) and survival time after accounting for patient age and sex, WHO grade, chemotherapy administration status, and radiation therapy administration status associations with survival time. A $P \leq .05$ decision rule was established a priori as the null hypothesis rejection rule for testing for predictor variable-versus-survival time unique association, and the strength of the predictor variable versus survival time unique association was quantified by the adjusted hazard ratio.

RESULTS

Among the 172 study patients, there were 85 females (49.4%) and 87 males (50.6%). The median age was 43 years (interquartile range, 31–54 years; range, 17–76 years). Patient characteristics per molecular subtype are shown in Table 1. There were significant differences in age in each of the 3 molecular subgroups ($P \leq .001$), with patients with *IDHwt* being the oldest and those with *IDHmut-Noncodel* being the youngest. There were a total of 39 deaths. Median overall survival time was 16.5 years among patients with *IDHmut-Codel*, 12.1 years among those with *IDHmut-Noncodel*, and 6.3 years among those with *IDHwt*. Overall survival curves for the LGG subtypes are shown in Fig 2. Overall survival curves differed between patients with *IDHmut-Codel* and *IDHwt* ($P < .001$) and between those with *IDHmut-Noncodel* and *IDHwt* ($P < .001$). Overall survival curves did not significantly differ between patients with *IDHmut-Codel* and *IDHmut-Noncodel* ($P = .125$).

Among all cases, the median presurgical glioma volume was 54.7 cm³ (interquartile range, 27.6–107.6 cm³; range, 1.1–340 cm³) and the median postsurgical glioma volume was 29.7 cm³ (interquartile range, 6.5–62.8 cm³; range, 0–339 cm³). There was no significant difference in presurgical glioma volume or postsurgical glioma volume among the 3 LGG molecular subtypes. Patients with *IDHwt* were associated with a smaller percentage of resection compared with those with *IDHmut-Noncodel* ($P = .01$).

Associations among presurgical glioma volume, postsurgical

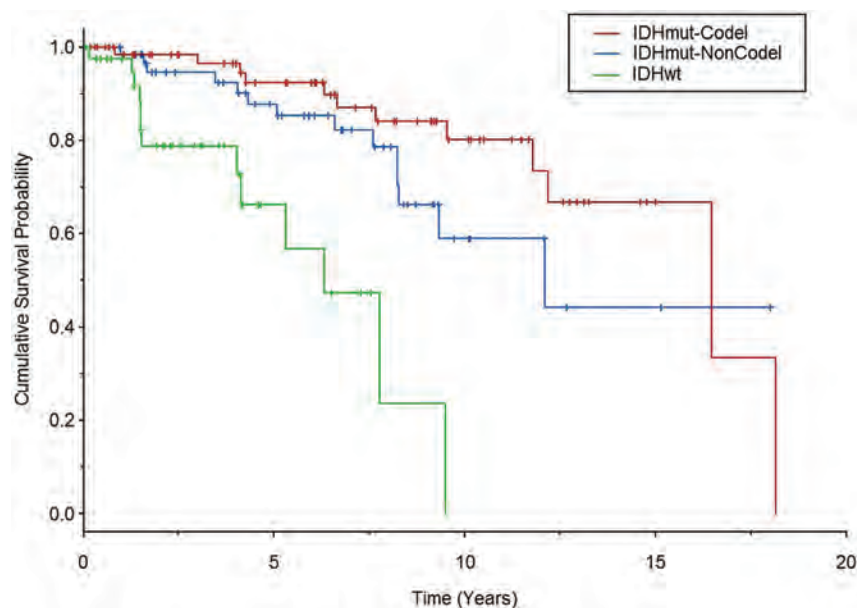


FIG 2. Kaplan-Meier curves for overall patient survival based on the LGG molecular subtype. Vertical line segments along the curve identify right-censored survival times. *IDHwt* LGGs were associated with significantly worse overall survival compared with both *IDH*-mutant subtypes.

Table 2: Survival analysis^a

Predictor	Ratio	Adjusted Hazard Ratio (95% CI)	P Value
All LGGs			
Presurgical glioma volume	3rd Q:1st Q	1.14 (0.79–1.64)	.479
Postsurgical glioma volume	3rd Q:1st Q	1.80 (1.18–2.75)	.006
Percentage glioma resection	25%:75%	3.22 (1.79–5.82)	<.001
<i>IDHmut-Codel</i>			
Presurgical glioma volume	3rd Q:1st Q	1.11 (0.53–2.33)	.781
Postsurgical glioma volume	3rd Q:1st Q	1.67 (0.82–3.48)	.170
Percentage glioma resection	25%:75%	6.69 (1.57–28.46)	.010
<i>IDHmut-Noncodel</i>			
Presurgical glioma volume	3rd Q:1st Q	3.20 (1.22–8.39)	.018
Postsurgical glioma volume	3rd Q:1st Q	2.33 (1.32–4.12)	.004
Percentage glioma resection	25%:75%	4.34 (1.74–10.81)	.002
<i>IDHwt</i>			
Presurgical glioma volume	3rd Q:1st Q	2.18 (0.47–10.15)	.319
Postsurgical glioma volume	3rd Q:1st Q	1.34 (0.28–4.76)	.653
Percentage glioma resection	25%:75%	0.91 (0.29–2.82)	.874

Note:—Q indicates quartile.

^a Predictor variables for overall survival are presurgical glioma volume, postsurgical glioma volume, and percentage glioma resection. Adjusted hazard ratios are listed for the entire cohort and for the 3 molecular subtypes, with age, sex, glioma grade, and chemotherapy and radiation therapy administration as the adjustment variables.

glioma volume, and the percentage of glioma resection and overall survival are shown in Table 2, after adjustment for patient age, sex, glioma grade, and chemo-radiation therapy administration. Among all LGGs in the cohort, postsurgical glioma volume ($P = .006$) and the percentage of glioma resection ($P < .001$) were associated with overall survival. However, associations varied among the 3 LGG molecular subtypes. For those with *IDHmut-Codel*, the percentage of resection was associated with overall survival ($P = .01$), but pre- or postsurgical glioma volumes were not. For those with *IDHmut-Noncodel*, presurgical glioma volume ($P = .018$), postsurgical glioma volume ($P = .004$), and the percentage of glioma resection ($P = .002$) were each associated with overall survival. For the *IDHwt* subtype, there was no association of presurgical glioma volume, postsurgical glioma volume, or

percentage of glioma resection with overall survival. Figure 3 shows overall survival curves according to the percentage of glioma resection for each of the molecular subtypes, and the On-line Figure shows overall survival curves according to postsurgical glioma volume strata. There were 13 patients with 0 mL of postsurgical residual glioma (*IDHmut-Codel*, $n = 1$; *IDHmut-Noncodel*, $n = 9$; *IDHwt*, $n = 3$), and all these patients were alive at the time of last follow-up.

DISCUSSION

Our study supports an association between a greater degree of surgical resection and overall survival in patients with *IDH*-mutant LGGs. We note an association between the extent of surgical resection and overall survival among both molecularly defined *IDH*-mutant astrocytomas and oligodendrogliomas; however, the impact of surgical resection extent on overall survival appears stronger for astrocytomas. The reason for the relatively stronger association with astrocytomas might relate to the relatively better responsiveness to nonsurgical therapies for oligodendrogliomas or oligodendrogliomas generally having longer survival times than astrocytomas, thus making it more difficult to demonstrate a survival benefit with an operation.^{3–7} We further note that the percentage of glioma resection was more strongly associated with overall survival than presurgical glioma volume or postsurgical glioma volume. Finally, we found no association between surgical resection and overall survival in *IDHwt* LGGs.

Prior studies have investigated the impact of surgical resection on the outcomes of patients with LGGs. Among the older studies, many used nonvolumetric approximations of residual glioma extent.^{15,25–27} Additionally, most prior studies were undertaken before the 2016 WHO update for CNS neoplasm classification and thus did not strictly classify their patient cohorts by *IDH* and 1p/19q-codeletion status.^{13,14,16} Only recently have studies provided evidence of the impact of surgical resection after stratification by defining molecular markers.^{20,21,28,29}

The most important of this recent literature is the work from Wijnenga et al, in 2018,²⁰ who evaluated the impact of surgery in a large cohort of molecularly defined grade II diffuse gliomas, determining that larger postoperative glioma volume was associated with worse overall survival (hazard ratio, 1.01 per 1 cm³ increase in residual glioma volume). They noted that the amount

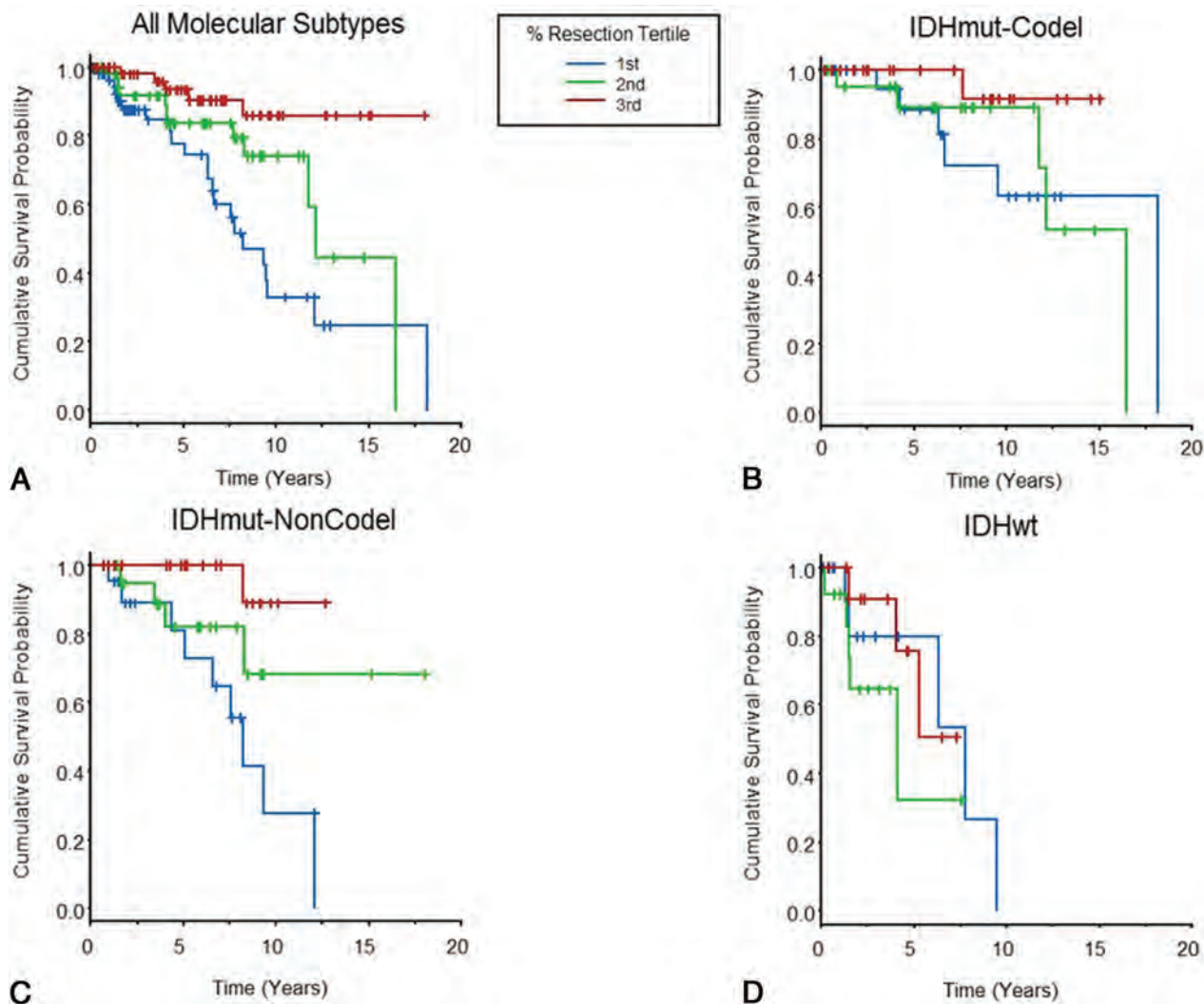


FIG 3. Kaplan-Meier curves in which overall patient survival is evaluated according to the percentage of glioma resection tertiles. Vertical line segments along the curve identify right-censored survival times. Data are shown for all patients with LGGs in the cohort (A) and separately for the 3 molecular subtypes (B–D).

of residual postsurgical glioma was more strongly associated with survival among *IDH*-mutant astrocytomas compared with oligodendrogliomas, similar to our results. Kawaguchi et al, in 2016,²⁸ evaluated a cohort of WHO grade III diffuse gliomas, undertaking an impressively comprehensive molecular analysis of their glioma specimens given the timing of their study. They found that gross total resection (as determined by postoperative MR imaging analysis) was significantly associated with improved overall survival among the *IDHmut-Noncodel* subgroup, but not for the *IDHmut-Codel* or the *IDHwt* subgroup. Study limitations included their binary stratification of surgical resection (yes/no gross total resection) and their choice of measuring residual glioma differently for enhancing and nonenhancing gliomas.

Eseonu et al, in 2017,²¹ evaluated a cohort of low-grade (presumably WHO grade II) diffuse gliomas. Molecular information was only available in a 51-patient subset of the patient cohort, among whom the extent of resection was associated with improved survival for the codeleted oligodendroglioma subgroup and *IDH*-wild-type subgroup (they did not have sufficient *IDH*-

mutant astrocytomas for analysis). Patel et al, in 2018,²⁹ evaluated a cohort of 74 patients with WHO grade II diffuse gliomas and, most interesting, found that the extent of glioma resection was associated with overall survival for the *IDH*-wild-type subgroup but not for the *IDH*-mutant subgroup, differing from our findings. Study limitations included lack of a description of *IDH*-mutation testing (with apparent lack of *IDH2*-mutation testing) and lack of stratification by 1p/19q-codeletion status.

The primary advantages of our study design include strict molecular classification of our patients with LGG, consistent with WHO guidelines, as well as volumetric measurement of pre- and postsurgical gliomas. Unlike most prior studies, we included both WHO grade II and III LGGs because WHO grade assignment among LGGs is subject to sampling bias and known to have significant interobserver variability.³⁰ Moreover, we ensured that our statistical analysis controlled for tumor grade. We also controlled for additional potentially confounding variables such as patient age, sex, and chemo-radiation therapy administration by the time of last follow-up. Our finding that the extent of surgical resection impacts overall survival in patients with *IDH*-mutant

LGGs, particularly in patients with *IDHmut-Noncodel* LGGs, supports most of the recent literature. Our finding that surgical resection does not impact survival in *IDHwt* LGGs is not broadly supported in the literature and requires further study. We speculate that disparate results regarding *IDHwt* LGGs may relate to the known clinical and molecular heterogeneity of this subgroup, especially among grade II *IDHwt* LGGs,^{8–10} and further stratification of this subgroup may be forthcoming in future WHO classification schemes.¹¹

Our study has limitations. Its retrospective design may have introduced unanticipated biases that affected the results. Our analysis might be limited by our cohort size and follow-up time, given the number of mortality events. For example, our relatively smaller cohort of *IDHwt* LGGs might have impacted our ability to discern survival benefits from surgical resection in this subgroup. Moreover, although we adhered to the latest WHO criteria, we did not include more detailed molecular testing of *IDHwt* LGGs (eg, *TERT* promoter mutation, chromosome 7/10 alterations, *EGFR* gene amplification) that might have allowed relevant substratification of this subgroup. Our volume measurements were performed using FLAIR and T2WI, and we recognize that edema and gliosis might have been inadvertently included within measurements due to their overlapping appearance with infiltrative gliomas on these imaging sequences. Finally, we measured tumor volumes using MR imaging scans acquired on various scanners with variable image quality; such variables might have affected the volume measurements.

CONCLUSIONS

The extent of surgical resection differentially impacts overall survival among patients with LGGs based on molecular subtypes as defined by the WHO. Increased extent of surgical resection significantly benefits patients with *IDH*-mutant LGGs, with the impact strongest for *IDHmut-Noncodel* astrocytomas. We found no survival benefit from greater surgical resection in *IDHwt* LGGs. Further study of the *IDHwt* subgroup, with larger cohort sizes and molecular substratification, is warranted.

Disclosures: Sohil H. Patel—RELATED: Grant: Radiological Society of North American Research Scholar Grant (RSCH1819)*; UNRELATED: Expert Testimony: LeClairRyan Law Firm.* M. Beatriz Lopes—UNRELATED: Royalties: Elsevier, Comments: book chapter royalties; Travel/Accommodations/Meeting Expenses Unrelated to Activities Listed: International Society of Neuropathology, Comments: travel expenses to attend the international meeting in Tokyo, Japan, October 2018. Camilo E. Fadul—UNRELATED: Grants/Grants Pending: Novartis, Comments: clinical trial for recurrent glioblastoma.* *Money paid to institution.

REFERENCES

- Louis DN, Perry A, Reifenberger G, et al. **The 2016 World Health Organization Classification of Tumors of the Central Nervous System: a summary.** *Acta Neuropathol* 2016;131:803–20 CrossRef Medline
- Yan H, Parsons DW, Jin G, et al. **IDH1 and IDH2 mutations in gliomas.** *N Engl J Med* 2009;360:765–73 CrossRef Medline
- Brat DJ, Verhaak RG, Aldape KD, et al; Cancer Genome Atlas Research Network. **Comprehensive, integrative genomic analysis of diffuse lower-grade gliomas.** *N Engl J Med* 2015;372:2481–98 CrossRef Medline
- Eckel-Passow JE, Lachance DH, Molinaro AM, et al. **Glioma groups based on 1p/19q, IDH, and TERT promoter mutations in tumors.** *N Engl J Med* 2015;372:2499–508 CrossRef Medline
- Ceccarelli M, Barthel FP, Malta TM, et al. **Molecular profiling reveals biologically discrete subsets and pathways of progression in diffuse glioma.** *Cell* 2016;164:550–63 CrossRef Medline
- Cairncross G, Wang M, Shaw E, et al. **Phase III trial of chemoradiotherapy for anaplastic oligodendroglioma: long-term results of RTOG 9402.** *J Clin Oncol* 2013;31:337–43 CrossRef Medline
- van den Bent MJ, Brandes AA, Taphoorn MJ, et al. **Adjuvant procarbazine, lomustine, and vincristine chemotherapy in newly diagnosed anaplastic oligodendroglioma: long-term follow-up of EORTC brain tumor group study 26951.** *J Clin Oncol* 2013;31:344–50 CrossRef Medline
- Di Carlo DT, Duffau H, Cagnazzo F, et al. **IDH wild-type WHO grade II diffuse low-grade gliomas: a heterogeneous family with different outcomes—systematic review and meta-analysis.** *Neurosurg Rev* 2018 Jun 26. [Epub ahead of print] CrossRef Medline
- Aibaidula A, Chan AK, Shi Z, et al. **Adult IDH wild-type lower-grade gliomas should be further stratified.** *Neuro Oncol* 2017;19:1327–37 CrossRef Medline
- Poulen G, Goze C, Rigau V, et al. **Huge heterogeneity in survival in a subset of adult patients with resected, wild-type isocitrate dehydrogenase status, WHO grade II astrocytomas.** *J Neurosurg* 2018 Apr 20:1–10. [Epub ahead of print] CrossRef Medline
- Brat DJ, Aldape K, Colman H, et al. **cIMPACT-NOW update 3: recommended diagnostic criteria for “diffuse astrocytic glioma, IDH-wildtype, with molecular features of glioblastoma, WHO grade IV.”** *Acta Neuropathol* 2018;136:805–10 CrossRef Medline
- Hervey-Jumper SL, Berger MS. **Evidence for improving outcome through extent of resection.** *Neurosurg Clin N Am* 2019;30:85–93 CrossRef Medline
- Smith JS, Chang EF, Lamborn KR, et al. **Role of extent of resection in the long-term outcome of low-grade hemispheric gliomas.** *J Clin Oncol* 2008;26:1338–45 CrossRef Medline
- Ius T, Isola M, Budai R, et al. **Low-grade glioma surgery in eloquent areas: volumetric analysis of extent of resection and its impact on overall survival—a single-institution experience in 190 patients: clinical article.** *J Neurosurg* 2012;117:1039–52 CrossRef Medline
- McGirt MJ, Chaichana KL, Attenello FJ, et al. **Extent of surgical resection is independently associated with survival in patients with hemispheric infiltrating low-grade gliomas.** *Neurosurgery* 2008;63:700–07; author reply 707–08 CrossRef Medline
- Roelz R, Strohmaier D, Jabbarli R, et al. **Residual tumor volume as best outcome predictor in low grade glioma: a nine-years near-randomized survey of surgery vs. biopsy.** *Sci Rep* 2016;6:32286 CrossRef Medline
- Thon N, Kreth FW, Tonn JC. **The role of surgery in grade II/III oligodendroglial tumors.** *CNS Oncol* 2015;4:317–23 CrossRef Medline
- Jakola AS, Myrmet KS, Kloster R, et al. **Comparison of a strategy favoring early surgical resection vs a strategy favoring watchful waiting in low-grade gliomas.** *JAMA* 2012;308:1881–88 CrossRef Medline
- Duffau H, Lopes M, Arthuis F, et al. **Contribution of intraoperative electrical stimulations in surgery of low grade gliomas: a comparative study between two series without (1985–96) and with (1996–2003) functional mapping in the same institution.** *J Neurol Neurosurg Psychiatry* 2005;76:845–51 CrossRef Medline
- Wijnenga MM, French PJ, Dubbink HJ, et al. **The impact of surgery in molecularly defined low-grade glioma: an integrated clinical, radiological, and molecular analysis.** *Neuro Oncol* 2018;20:103–12 CrossRef Medline
- Eseonu CI, Eguia F, ReFaey K, et al. **Comparative volumetric analysis of the extent of resection of molecularly and histologically distinct low grade gliomas and its role on survival.** *J Neurooncol* 2017;134:65–74 CrossRef Medline
- Capper D, Weissert S, Balss J, et al. **Characterization of R132H mutation-specific IDH1 antibody binding in brain tumors.** *Brain Pathol* 2010;20:245–54 CrossRef Medline
- Capper D, Zentgraf H, Balss J, et al. **Monoclonal antibody specific for IDH1 R132H mutation.** *Acta Neuropathol* 2009;118:599–601 CrossRef Medline
- Felsberg J, Wolter M, Seul H, et al. **Rapid and sensitive assessment of the IDH1 and IDH2 mutation status in cerebral gliomas based on DNA pyrosequencing.** *Acta Neuropathol* 2010;119:501–07 CrossRef Medline

25. Ahmadi R, Rezvan A, Dictus C, et al. **Long-term outcome and survival of surgically treated supratentorial low-grade glioma in adult patients.** *Acta Neurochir (Wien)* 2009;151:1359–65 CrossRef Medline
26. McGirt MJ, Chaichana KL, Gathinji M, et al. **Independent association of extent of resection with survival in patients with malignant brain astrocytoma.** *J Neurosurg* 2009;110:156–62 CrossRef Medline
27. Yeh SA, Ho JT, Lui CC, et al. **Treatment outcomes and prognostic factors in patients with supratentorial low-grade gliomas.** *Br J Radiol* 2005;78:230–35 CrossRef Medline
28. Kawaguchi T, Sonoda Y, Shibahara I, et al. **Impact of gross total resection in patients with WHO grade III glioma harboring the IDH 1/2 mutation without the 1p/19q co-deletion.** *J Neurooncol* 2016;129:505–14 CrossRef Medline
29. Patel T, Bander ED, Venn RA, et al. **The role of extent of resection in IDH1 wild-type or mutant low-grade gliomas.** *Neurosurgery* 2018; 82:808–14 CrossRef Medline
30. van den Bent MJ. **Interobserver variation of the histopathological diagnosis in clinical trials on glioma: a clinician's perspective.** *Acta Neuropathol* 2010;120:297–304 CrossRef Medline

Normal-Appearing Cerebellar Damage in Neuromyelitis Optica Spectrum Disorder

J. Sun, N. Zhang, Q. Wang, X. Zhang, W. Qin, L. Yang, F.-D. Shi, and C. Yu



ABSTRACT

BACKGROUND AND PURPOSE: The cerebellum plays an important role in motor and cognitive functions. However, whether and how the normal-appearing cerebellum is impaired in patients with neuromyelitis optica spectrum disorders remain unknown. We aimed to identify the occult structural damage of the cerebellum in neuromyelitis optica spectrum disorder and its possible causes at the level of substructures.

MATERIALS AND METHODS: Normal-appearing gray matter volume of the cerebellar lobules and nuclei and normal-appearing white matter volume of the cerebellar peduncles were compared between patients with neuromyelitis optica spectrum disorder and healthy controls.

RESULTS: The cerebellar damage of patients with neuromyelitis optica spectrum disorder in the hemispheric lobule VI, vermis lobule VI, and all cerebellar nuclei and peduncles was related only to spinal lesions; and cerebellar damage in the hemispheric lobules VIII and X was related only to the aquaporin-4 antibody. The mixed cerebellar damage in the hemispheric lobules V and IX and vermis lobule Crus I was related mainly to spinal lesions; and mixed cerebellar damage in the hemispheric lobule VIIb was related mainly to the aquaporin-4 antibody. Other cerebellar substructures showed no significant cerebellar damage.

CONCLUSIONS: We have shown that the damage in cerebellar normal-appearing white matter and normal-appearing gray matter is associated with aquaporin-4-mediated primary damage or axonal degeneration secondary to spinal lesions or both. The etiologic classifications of substructure-specific occult cerebellar damage may facilitate developing neuroimaging markers for assessing the severity and the results of therapy of neuromyelitis optica spectrum disorder occult cerebellar damage.

ABBREVIATIONS: AQP4-Ab = aquaporin-4 antibody; HC = healthy control; ICP = inferior cerebellar peduncle; LSCL = length of the spinal cord lesion; MCP = middle cerebellar peduncle; NAGM = normal-appearing gray matter; NAWM = normal-appearing white matter; NMOSD = neuromyelitis optica spectrum disorder; SCI = spinal cord injury; SCN = spinal cord normal; SCP = superior cerebellar peduncle; SUIT = Spatially Unbiased Atlas Template of the Cerebellum and Brainstem

Neuromyelitis optica is an inflammatory demyelinating disorder characterized by recurrent optic neuritis and longitudinally extensive spinal cord myelitis.¹ As an expansion of neuromyelitis optica, the diagnosis of neuromyelitis optica spectrum

disorder (NMOSD) also includes patients who share critical features (for example, the antibody against aquaporin-4 [AQP4-Ab]) but cannot be currently diagnosed as having neuromyelitis optica.² NMOSD clinical symptoms may arise from neural impairment resulting from both visible lesions and invisible pathologies on conventional MR imaging.³

Although many previous studies have reported structural damage in normal-appearing gray (NAGM) and white matter (NAWM) of the cerebrum in NMOSD,^{4,5} our knowledge regarding damage to the cerebellum is very limited. Identifying structural damage in the normal-appearing cerebellum may improve our understanding of cerebellum-related dysfunction in NMOSD, because the cerebellum plays an important role in motor and cognitive functions.⁶

The AQP4-Ab has been identified as a highly specific serum marker⁷ and plays a pathogenic role in NMOSD.⁸ The cerebellum shows the highest AQP4 expression throughout the brain; thus,

Received March 19, 2019; accepted after revision May 9.

From the Department of Radiology and Tianjin Key Laboratory of Functional Imaging (J.S., N.Z., Q.W., X.Z., W.Q., C.Y.), and Department of Neurology (L.Y., F.-D.S.), Tianjin Medical University General Hospital, Tianjin, China

This work was supported by the National Key Research and Development Program of China (2018YFC1314301), the Natural Science Foundation of China (81425013), the Tianjin Key Technology R&D Program (17ZXMFSY00090), and Natural Science Foundation of Tianjin City (18JCQNJC80200).

Please address correspondence to Chunshui Yu, MD, PhD, Radiological Department, Tianjin Medical University General Hospital, No. 154 Anshan Rd, Heping District, Tianjin 300052, China; e-mail: chunshuiyu@tjmu.edu.cn

Indicates open access to non-subscribers at www.ajnr.org

Indicates article with supplemental on-line appendix and tables.

<http://dx.doi.org/10.3174/ajnr.A6098>

the AQP4-related immune response may result in primary occult damage in the cerebellum in NMOSD. Because NMOSD-specific lesions assumed to be caused by the AQP4-related immune damage are not equally distributed in the brain, we speculated that cerebellar substructures may be unequally affected. Because there are dense connections between the spinal cord and cerebellum,⁹⁻¹¹ it is plausible to hypothesize that spinal lesions may result in secondary cerebellar damage via axonal degeneration in NMOSD. Considering that the connection densities between cerebellar substructures and the spinal cord are largely heterogeneous, we further hypothesized that cerebellar substructures are unequally affected. Most important, we hypothesized that we could differentiate the possible causes of the occult cerebellar damage on the basis of its association with spinal lesions and AQP4-Ab status.

In this study, we aimed not only to investigate the structural damage in NAGM and NAWM of the cerebellum in NMOSD but also to explore the possible types of normal-appearing cerebellar damage in different cerebellar substructures.

MATERIALS AND METHODS

Subjects

This study included 36 patients with NMOSD and 20 healthy controls (HCs). All subjects signed a written informed consent form that was approved by the Medical Research Ethics Committee of Tianjin Medical University. NMOSD was diagnosed according to the 2015 criteria.¹² Patients were excluded from the study if they met any of the following criteria: 1) beyond the range of 18–55 years of age to exclude developmental- and age-related structural changes, 2) complications from other autoimmune disorders, 3) a history of other neuropsychiatric diseases, 4) poor image quality, or 5) contraindications to MR imaging. We recorded the following information for each patient: AQP4-Ab status and brain and spinal cord MR imaging assessment. Two radiologists assessed the cerebellar lesions on brain axial T2-weighted images independently, referring to the T2-FLAIR images and excluding the subjects with visible cerebellar lesions on T2-weighted or T2-FLAIR images.¹²

AQP4 Antibody Testing

AQP4-Ab was tested using a cell-based array through quantitative flow cytometry. For each patient with NMOSD, a serum sample was isolated from whole blood and stored in a -80°C freezer. We fixed a sample of 293 human embryonic kidney cells expressing *AQP4-M23-EGFP*-fused genes. Then we used a fluorescence microscope to detect the binding of the sera to the cells after incubation with Alexa Fluor 568-conjugated anti-human immunoglobulin G.¹³

MR Imaging Data Acquisition

Conventional brain and spinal MRIs and brain structural imaging were acquired using a 3T MR imaging system (Discovery MR750; GE Healthcare, Milwaukee, Wisconsin). The specific imaging parameters are described in the On-line Appendix. All images were visually inspected to ensure that only images without visible artifacts were included in the subsequent analyses.

Assessment of Spinal Cord Lesions

The length of the spinal cord lesion (LSCL) was estimated on the basis of spinal sagittal T2-weighted images by 2 radiologists independently, referring to the axial images. Interobserver agreement was assessed on the basis of weighted κ values. The LSCL values from the 2 investigators were averaged to represent the value of each patient.

Definition of Cerebellar Regions

The cerebellar regions were defined by the Spatially Unbiased Atlas Template of the Cerebellum and Brainstem (SUIT) (<http://www.diedrichsenlab.org/imaging/suit.htm>) embedded in the Statistical Parametric Mapping program (SPM12; <http://www.fil.ion.ucl.ac.uk/spm>). SUIT provides a high-resolution template of the human cerebellum derived from 20 healthy young individuals,¹⁴ which preserves anatomic details of cerebellar regions using automated nonlinear normalization methods with a high accuracy in alignment among subjects.¹⁵ SUIT provides a probabilistic atlas of cerebellar lobules and nuclei.¹⁶ Each cerebellar hemisphere was divided into lobules I–IV, V, VI, Crus I, Crus II, VIIa, VIIb, VIIIa, VIIIb, IX, and X, and the vermis was divided into lobules VI, Crus I, Crus II, VIIa, VIIIa, VIIIb, IX, and X.⁶ The dentate, interposed nucleus (the combination of the globose and emboliform nuclei) and the fastigial nucleus were extracted as cerebellar nuclei. After reslicing the SUIT cerebellar template into the Montreal Neurological Institute space, we could extract cerebellar regions from the template. As the major cerebellar white matter fiber tracts connected to other parts of the CNS, the superior (SCP), middle (MCP), and inferior (ICP) cerebellar peduncles were defined by the Johns Hopkins University white-matter tractography atlas by averaging the results of deterministic tractography of 28 healthy subjects.¹⁷

Calculation of Volumes of Cerebellar Regions

With SPM8, the structural images were segmented into gray matter, white matter, and CSF by a standard unified segmentation model; then, the segmented images were normalized to the Montreal Neurological Institute template by affine and nonlinear registration.¹⁸ After inverse transformation, the transformation parameters from the Montreal Neurological Institute to native space were obtained and used to register the SUIT cerebellar subregions in Montreal Neurological Institute space to individual space. Then we could estimate the volume of each cerebellar region for each subject by counting the number of voxels in each region. To quantitatively compare NAGM volume reduction in the cerebellum, we calculated the ratio of volume reduction using the following equation: $\text{NAGM Volume Reduction Ratio} = (\text{Mean NAGM Volume of Controls} - \text{Mean NAGM Volume of NMOSD}) / \text{Mean NAGM Volume of Controls}$.

Types of Normal-Appearing Cerebellar Damage

To explore the association of spinal cord lesions with cerebellar impairment in NMOSD, we divided 36 patients with NMOSD into spinal cord injury (SCI) and spinal cord normal (SCN) groups based on the presence or absence of the spinal cord lesion. Similarly, patients with NMOSD were divided into seropositive and seronegative groups based on the state of AQP4-Ab.

Table 1: Five different types of normal-appearing cerebellar damage in NMOSD

Types of Occult Cerebellar Damage	SCI vs HC		AQP4-Ab (+) vs HC	
	Without Controlling for AQP4-Ab Status	Controlling for AQP4-Ab Status	Without Controlling for LSCL	Controlling for LSCL
Type 1: only related to spinal lesions	Significant or not	Significant	Nonsignificant	Nonsignificant
Type 2: only related to AQP4-Ab	Nonsignificant	Nonsignificant	Significant or not	Significant
Type 3: mainly related to spinal lesions	Significant	Nonsignificant	Nonsignificant	Nonsignificant
Type 4: mainly related to AQP4-Ab	Nonsignificant	Nonsignificant	Significant	Nonsignificant
Type 5: no cerebellar damage	Nonsignificant	Nonsignificant	Nonsignificant	Nonsignificant

Note:—+ indicates seropositive.

Table 2: Demographics and clinical features in subjects^a

	SCI	SCN	AQP4-Ab (+)	AQP4-Ab (-)	HC	P ₁	P ₂	P ₃	P ₄	P ₅	P ₆
No.	17	19	27	9	20	NA	NA	NA	NA	NA	NA
Age (yr)	41.0 (20.5)	41.0 (15.0)	41.0 (12.0)	41.0 (28.0)	42.5 (7.5)	.297 ^b	.428 ^b	.827 ^b	.336 ^b	.390 ^a	.565 ^b
Sex (M/F)	3:14	4:15	2:25	5:4	7:13	.383 ^c	.522 ^c	.797 ^c	.026 ^{c,d}	.422 ^c	.006 ^{c,d}
Education (yr)	9.0 (8.0)	12.0 (3.0)	12.0 (6.0)	12.0 (3.5)	9.0 (6.3)	.517 ^b	.095 ^b	.076 ^b	.570 ^b	.594 ^b	.667 ^b
LSCL (VS)	3.0 (5.0)	0.0 (0.0)	2.0 (5.0)	0.0 (2.5)	0.0 (0.0)	NA	NA	NA	NA	NA	.218 ^b
AQP4-Ab (+/-)	15/2	14/5	27/0	0/9	0/0	NA	NA	.271 ^c	NA	NA	NA

Note:—VS indicates vertebral segments; +, seropositive; -, seronegative; NA, not applicable.

^a P₁; comparison between the SCI and HC groups; P₂; comparison between the SCN and HC groups; P₃; comparison between the SCI and SCN groups; P₄; comparison between the AQP4-Ab-seropositive and HC groups; P₅; comparison between the AQP4-Ab-seronegative and HC groups; P₆; comparison between the AQP4-Ab-seropositive and -seronegative groups. Variables are presented as median (interquartile range).

^b The P value was obtained with the Mann-Whitney U test.

^c The P value was obtained with the χ^2 test.

^d Significant.

Normal-appearing cerebellar volumetric analysis was performed by the Statistical Package for the Social Sciences version 19.0 (SPSS, Chicago, IL) using General Linear Model. General Linear Model was used to compare volumetric differences in each cerebellar substructure between each pair of groups (SCI versus HC; SCN versus HC; SCI versus SCN; AQP4-Ab-seropositive versus HC; AQP4-Ab-seronegative versus HC; AQP4-Ab-seropositive versus AQP4-Ab-seronegative. All intergroup comparisons were controlled for the effects of age, sex, and educational years. The volumetric differences in cerebellar substructures between each pair of the SCI, SCN, and HC groups were also compared, further controlling for the status of AQP4-Ab. Similarly, the volumetric differences in cerebellar substructures between each pair of the AQP4-Ab seropositive, seronegative, and HC groups were also compared, further controlling for the LSCL. For exploratory analysis, an uncorrected threshold of $P < .05$ was considered significant.

According to these intergroup comparisons, the occult damage of cerebellar substructures could be categorized into 5 subtypes (Table 1)—type 1: cerebellar damage only related to spinal lesions when there was a significant difference between SCI and HC groups while controlling for the AQP4-Ab status; type 2: cerebellar damage related only to AQP4-Ab when a significant difference was found between only AQP4-seropositive and HC groups while controlling for the LSCL; type 3: mixed cerebellar damage related mainly to spinal lesions when there was a significant difference between only SCI and HC groups without controlling for the AQP4-Ab status; type 4: mixed cerebellar damage related mainly to AQP4-Ab when a significant difference was present between only AQP4-seropositive and HC groups without controlling for the LSCL; and type 5: no cerebellar damage when all comparisons were nonsignificant.

Statistical Analyses for Demographic Variables

Statistical analyses for demographic variables were performed using the Statistical Package for the Social Sciences, Version 19.0 (IBM, Armonk, New York). Variables are presented as median (interquartile range). The Mann-Whitney U test was used to detect differences in age and educational years between each pair of groups. The χ^2 test was used to detect the sex differences between each pair of groups. $P < .05$ was considered statistically significant.

RESULTS

Demographic and Clinical Features of the Subjects

The demographic and clinical features of the subjects are summarized in Table 2. The LSCL values showed high agreement ($\kappa = 0.99$) between the 2 radiologists. There were no significant differences in age, sex, and educational years between each pair of the HC ($n = 20$), SCI ($n = 17$), and SCN ($n = 19$) groups. Although there were no significant differences in age and educational years between each pair of the HC ($n = 20$), AQP4-Ab-seropositive ($n = 27$), and AQP4-Ab-seronegative ($n = 9$) groups, the AQP4-Ab-seropositive group showed more significant female preponderance than the other 2 groups. Moreover, there were no significant differences in the presence of AQP4-Ab between the SCI and SCN groups and in the LSCL between the AQP4-Ab-seropositive and -seronegative groups.

Group Differences in Normal-Appearing Cerebellar Volume

The NAGM and NAWM volumetric differences of cerebellar substructures between each pair of groups are shown in On-line Table 1. Volumes in normal-appearing cerebellar substructures in HC and NMOSD groups are shown in On-line Table 2. Only the SCI group showed significant cerebellar damage relative to the

HC group, without controlling for the AQP4-Ab status. Compared with the HC group, the SCI group showed a lower NAGM volume in the hemispheric lobules V (6.7% reduction, $P = .016$), VIIIa (9.5% reduction, $P = .036$), IX (16.7% reduction, $P = .036$), and X (12.8% reduction, $P = .036$); vermis lobules VI (7.6% reduction, $P = .028$) and Crus I (32.2% reduction, $P = .005$); the dentate nucleus (6.3% reduction, $P = .032$); the interposed nucleus (9.1% reduction, $P = .006$); and the fastigial nucleus (9.4% reduction, $P = .034$); and lower NAWM volume in the ICP (6.7% reduction, $P = .021$). When we further controlled for the AQP4-Ab status, compared with the HC group, the SCI group still showed lower NAGM volume in the dentate nucleus ($P = .025$), interposed nucleus ($P = .034$), and fastigial nucleus ($P = .001$) and lower NAWM volume in the ICP ($P = .026$). We additionally found a volumetric reduction in hemispheric lobule VI ($P = .048$), the SCP (8.0% reduction, $P = .034$), and MCP (3.9% reduction, $P = .040$) in the SCI group. None of the cerebellar substructures showed any significant volumetric differences between the SCN and HC groups.

The AQP4-Ab-seropositive group showed significant cerebellar impairment relative to the HC group without controlling for LSCL results. Compared with the HC group, the AQP4-Ab-seropositive group showed lower NAGM volume in hemispheric lobules VIIb (6.8% reduction, $P = .047$), VIIIa (7.4% reduction, $P = .023$), VIIIb (10.4% reduction, $P = .028$), and X (12.9% reduction, $P = .047$). When we further controlled for the LSCL, compared with the HC group, the AQP4-Ab-seropositive group still showed lower NAGM volume in the hemispheric lobules VIIIa ($P = .041$), and VIIIb ($P = .014$). We did not find volumetric reduction in the NAGM of any vermis and nuclei and in the NAWM of peduncles between the AQP4-Ab-seropositive and HC groups. None of the cerebellar substructures showed significant differences between the AQP4-Ab-seronegative and HC groups.

According to these comparisons, the occult damage of the cerebellar substructures could be categorized into 5 types—type 1: hemispheric lobule VI, vermis lobule VI, and all the cerebellar nuclei and peduncles; type 2: hemispheric lobules VIII and X; type 3: hemispheric lobules V and IX and vermis lobule Crus I; type 4: hemispheric lobule VIIb; and type 5: other cerebellar substructures. The distribution of each type of occult cerebellar cortical damage is shown in the Figure.

DISCUSSION

In this study, we provided evidence for the normal-appearing cerebellar damage in NMOSD and indications for the possible causes of the observed occult damage in cerebellar substructures. The occult cerebellar damage is associated with the presence of spinal lesions or AQP4-Ab or both. The substructure-specific occult cerebellar damage and its etiologic classifications may not only help in the explanation of cerebellar dysfunction in NMOSD but may also facilitate developing neuroimaging markers for assessing etiology-specific cerebellar damage.

The volumetric reductions in several cerebellar substructures were only to hemispheric lobule VI, vermis lobule VI, and the cerebellar nuclei and peduncles, or mainly hemispheric lobules V and IX and vermis lobule Crus I associated with spinal lesions, indicating that the occult damage in these cerebellar substructures

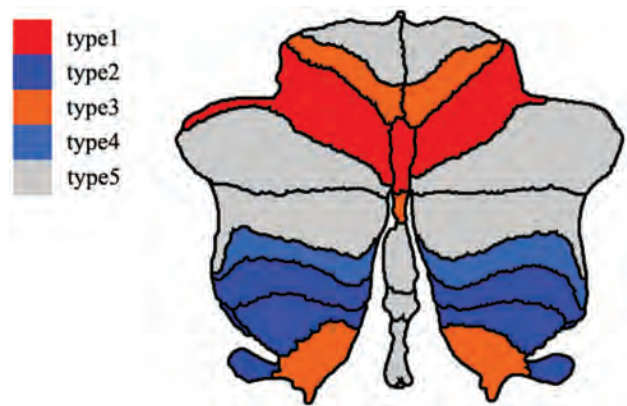


FIGURE. Spatial distribution of the occult cerebellar cortical damage in neuromyelitis optica spectrum disorder. Different colors represent the different types of normal-appearing cerebellar damage. Red denotes cerebellar subregions with occult damage related only to spinal lesions (type 1). Dark blue represents cerebellar subregions with occult damage related only to antibodies against aquaporin-4 antibody (type 2). Orange indicates cerebellar subregions with mixed occult damage mainly related to spinal lesions (type 3). Light blue suggests cerebellar subregions with mixed occult damage mainly related to the aquaporin-4 antibody (type 4). Gray denotes cerebellar subregions without occult damage (type 5).

is secondary to the spinal damage. There are many direct and indirect connections between spinal and cerebellar neurons. The spinocerebellar tract is the most important direct connection between spinal and cerebellar neurons and can be divided into the ventral, dorsal, and rostral spinocerebellar tracts.⁹⁻¹¹ These spinocerebellar tract fibers mainly project to cerebellar lobules I–V of the anterior lobe and lobules VI, VIII, and IX of the posterior lobe,^{19,20} especially the lobules I–V, which play an important role in motor control via various connections.⁶ Moreover, the cerebellar neurons indirectly connect with spinal neurons via a variety of nuclei in the brain stem, such as the cuneate, reticular, and inferior olivary nuclei, especially for lobules VI–VII.^{21,22}

In patients with NMOSD, the spinal lesions result in damage to spinal neurons that send afferent fibers to the cerebellum. These impaired spinal neurons may lead to structural damage in the corresponding cerebellar regions via a mechanism of Wallerian degeneration through spinal-cerebellar circuitry. The axonal degeneration may better account for the NAGM reduction in these cerebellar cortices in patients with NMOSD with spinal lesions. Spinal neurons can directly connect to cerebellar nuclei, especially the interposed nucleus, via the spinocerebellar tracts and spinoreticulocerebellar tracts.²³ Moreover, the cerebellar nuclei also indirectly connect with spinal neurons via the cerebellar cortices²⁴ and brain stem nuclei, such as the inferior olive,²⁵ lateral reticular nucleus,²⁶ red nucleus,²⁷ and vestibular nuclei.²⁸ Based on the direct and indirect connections between the cerebellar nuclei and spinal neurons, the axonal degeneration secondary to spinal cord damage may explain why the NAGM volume of the cerebellar nuclei is reduced in NMOSD. The spinocerebellar tract fibers enter into the cerebellum directly via the SCP and ICP. More than 80% of spinocerebellar tract fibers connect with the cerebellum via the ICP, and the other spinocerebellar tract fibers link to the cerebellum via the SCP.⁹⁻¹¹ Moreover, most of the MCP fibers are afferent fibers from the pontine nuclei indirectly

connecting with spinal and cerebral neurons.²⁹ Because they are important components of the spinocerebellar and cerebroprotine-cerebellar pathways, damage to the cerebellar peduncles can be explained by axonal degeneration secondary to the spinal and cerebral lesions.

The volumetric reductions in several cerebellar substructures were only to hemispheric lobules VIII and X, or mainly to hemispheric lobule VIIb, associated with the presence of AQP4-Ab, indicating that the occult damage in these cerebellar substructures is caused by AQP4-mediated immune damage. AQP4 is a transmembrane protein expressed on astrocytic end-feet surrounding blood vessels and regulates water movement among blood, brain, and CSF.³⁰ NMOSD is characterized by AQP4-mediated astrocyte damage,⁸ the binding of AQP4 antibody to AQP4 activates complement to form membrane attack complex that leads to astrocyte injury. The resulting astrocyte injury and inflammatory reaction may further result in damage to oligodendrocytes and neurons.³¹ The cerebellum has the highest AQP4 expression throughout the brain, and AQP4 is mainly rich in astrocyte cell membranes and their processes in both the granule cell and molecular layers of the cerebellum.^{32,33} Furthermore, AQP4 is highly expressed in cortices near the ventricular system.³⁴ The posterior cerebellar lobules are located proximal to the fourth ventricle and may show a high density of AQP4.³⁵ Thus the AQP4-mediated astrocyte damage can be another potential cause for the structural damage of the cerebellum in NMOSD.

Clinically, patients with NMOSD frequently have cerebellar symptoms such as ataxia, tremor, and cognitive deficits.⁶ Because some of these patients do not have visible cerebellar lesions on brain MR imaging, the occult damage may be the cause of these symptoms. The etiologic classifications of the occult damage in cerebellar substructures in NMOSD are clinically important. With this information, the volumes of cerebellar substructures with occult damage only or mainly caused by spinal lesions could be used to monitor the severity and the results of therapy of secondary cerebellar damage, and the volumes of cerebellar substructures with occult damage only or mainly caused by AQP4-mediated astrocyte damage could be used to monitor the severity and the results of therapy of the primary cerebellar damage in NMOSD.

Two limitations should be mentioned in this study. First, the cerebellar substructures were defined in standard space using different templates. The volumes of these substructures of each individual were calculated on the basis of the transformation parameters from the standard space to the individual space. Although advanced processing methods were used in this study, these methods may reduce interindividual volume variations. The loss of interindividual variations could influence correlation analyses between volumes of cerebellar substructures and other imaging or clinical measures. Second, our sample size was relatively small, and multiple comparisons were not corrected in this study. Thus, the results of this study should be validated in a larger sample with a more stringent statistical method.

CONCLUSIONS

By comparing structural imaging measures of the normal-appearing cerebellum between patients with NMOSD and healthy con-

trols, we found extensive cerebellar damage in patients with NMOSD. The occult cerebellar damage is related to either spinal lesions or AQP4-Ab or both with rather heterogeneous weights. The etiology-specific occult damage in cerebellar substructures may be used to assess the severity and the results of therapy of primary and secondary cerebellar damage in NMOSD.

ACKNOWLEDGMENTS

We thank Yujing Li, Ying Fu, and the neuroimmunology team at the General Hospital for patient recruitment and collection of clinical data.

REFERENCES

1. Wingerchuk DM, Lennon VA, Pittock SJ, et al. **Revised diagnostic criteria for neuromyelitis optica.** *Neurology* 2006;66:1485–89 CrossRef Medline
2. Wingerchuk DM, Lennon VA, Lucchinetti CF, et al. **The spectrum of neuromyelitis optica.** *Lancet Neurol* 2007;6:805–15 Medline
3. Wingerchuk DM, Hogancamp WF, O'Brien PC, et al. **The clinical course of neuromyelitis optica (Devic's syndrome).** *Neurology* 1999; 53:1107–14 CrossRef Medline
4. Yu C, Lin F, Li K, et al. **Pathogenesis of normal-appearing white matter damage in neuromyelitis optica: diffusion-tensor MR imaging.** *Radiology* 2008;246:222–28 CrossRef Medline
5. Rocca MA, Agosta F, Mezzapesa DM, et al. **A functional MRI study of movement-associated cortical changes in patients with Devic's neuromyelitis optica.** *Neuroimage* 2004;21:1061–68 CrossRef Medline
6. Manto M, Mariën P. **Schmahmann's syndrome: identification of the third cornerstone of clinical ataxiology.** *Cerebellum Ataxias* 2015;2:2 CrossRef Medline
7. Lennon VA, Wingerchuk DM, Kryzer TJ, et al. **A serum autoantibody marker of neuromyelitis optica: distinction from multiple sclerosis.** *Lancet* 2004;364:2106–12 CrossRef Medline
8. Matiello M, Schaefer-Klein J, Sun D, et al. **Aquaporin 4 expression and tissue susceptibility to neuromyelitis optica.** *JAMA Neurol* 2013;70:1118–25 CrossRef Medline
9. Geborek P, Bengtsson F, Jörntell H. **Properties of bilateral spinocerebellar activation of cerebellar cortical neurons.** *Front Neural Circuits* 2014;8:128 CrossRef Medline
10. Cohen O, Harel R, Aumann TD, et al. **Parallel processing of internal and external feedback in the spinocerebellar system of primates.** *J Neurophysiol* 2017;118:254–66 CrossRef Medline
11. Lan CT, Wen CY, Shieh JY. **Anatomical studies on the cuneocerebellar neurons in the gerbil by using HRP method.** *Ann Anat* 1994;176: 409–18 CrossRef Medline
12. Wingerchuk DM, Banwell B, Bennett JL, et al; International Panel for NMO Diagnosis. **International consensus diagnostic criteria for neuromyelitis optica spectrum disorders.** *Neurology* 2015;85:177–89 CrossRef Medline
13. Yang CS, Zhang DQ, Wang JH, et al. **Clinical features and sera anti-aquaporin 4 antibody positivity in patients with demyelinating disorders of the central nervous system from Tianjin, China.** *CNS Neurosci Ther* 2014;20:32–39 CrossRef Medline
14. Diedrichsen J. **A spatially unbiased atlas template of the human cerebellum.** *Neuroimage* 2006;33:127–38 CrossRef Medline
15. Diedrichsen J, Balsters JH, Flavell J, et al. **A probabilistic MR atlas of the human cerebellum.** *Neuroimage* 2009;46:39–46 CrossRef Medline
16. Schmahmann JD, Doyon J, McDonald D, et al. **Three-dimensional MRI atlas of the human cerebellum in proportional stereotaxic space.** *Neuroimage* 1999;10:233–60 CrossRef Medline
17. Hua K, Zhang J, Wakana S, et al. **Tract probability maps in stereotaxic spaces: analyses of white matter anatomy and tract-specific quantification.** *Neuroimage* 2008;39:336–47 CrossRef Medline
18. Ashburner J. **A fast diffeomorphic image registration algorithm.** *Neuroimage* 2007;38:95–113 CrossRef Medline
19. Sengul G, Fu Y, Yu Y, et al. **Spinal cord projections to the cerebellum**

- in the mouse. *Brain Struct Funct* 2015;220:2997–3009 CrossRef Medline
20. Necker R. Spinal neurons projecting to anterior or posterior cerebellum in the pigeon. *Anat Embryol (Berl)* 1992;185:325–34 Medline
 21. Serapide MF, Cicirata F, Sotelo C, et al. The pontocerebellar projection: longitudinal zonal distribution of fibers from discrete regions of the pontine nuclei to vermal and parafloccular cortices in the rat. *Brain Res* 1994;644:175–80 CrossRef Medline
 22. Glickstein M, Gerrits N, Kralj-Hans I, et al. Visual pontocerebellar projections in the macaque. *J Comp Neurol* 1994;349:51–72 CrossRef Medline
 23. Clendenin M, Ekerot CF, Oscarsson O, et al. Functional organization of two spinocerebellar paths relayed through the lateral reticular nucleus in the cat. *Brain Res* 1974;69:140–43 CrossRef Medline
 24. Ito M, Yoshida M. The origin of cerebral-induced inhibition of Deiters neurons, I: monosynaptic initiation of the inhibitory postsynaptic potentials. *Exp Brain Res* 1966;2:330–49 Medline
 25. Luque NR, Garrido JA, Carrillo RR, et al. Fast convergence of learning requires plasticity between inferior olive and deep cerebellar nuclei in a manipulation task: a closed-loop robotic simulation. *Front Comput Neurosci* 2014;8:97 CrossRef Medline
 26. Wu HS, Sugihara I, Shinoda Y. Projection patterns of single mossy fibers originating from the lateral reticular nucleus in the rat cerebellar cortex and nuclei. *J Comp Neurol* 1999;411:97–118 CrossRef Medline
 27. Hara S, Kaneyama T, Inamata Y, et al. Interstitial branch formation within the red nucleus by deep cerebellar nuclei-derived commissural axons during target recognition. *J Comp Neurol* 2016;524:999–1014 CrossRef Medline
 28. Witter L, De Zeeuw CI, Ruigrok TJ, et al. The cerebellar nuclei take center stage. *Cerebellum* 2011;10:633–36 CrossRef Medline
 29. Serapide MF, Zappalà A, Parenti R, et al. Laterality of the pontocerebellar projections in the rat. *Eur J Neurosci* 2002;15:1551–56 CrossRef Medline
 30. González C, González-Buitrago JM, Izquierdo G. Aquaporins, anti-aquaporin-4 autoantibodies and neuromyelitis optica. *Clin Chim Acta* 2013;415:350–60 CrossRef Medline
 31. Pereira WL, Reiche EM, Kallaur AP, et al. Epidemiological, clinical, and immunological characteristics of neuromyelitis optica: a review. *J Neurol Sci* 2015;355:7–17 CrossRef Medline
 32. Hubbard JA, Hsu MS, Seldin MM, et al. Expression of the astrocyte water channel aquaporin-4 in the mouse brain. *ASN Neuro* 2015;7 CrossRef Medline
 33. Neely JD, Amiry-Moghaddam M, Ottersen OP, et al. Syntrophin-dependent expression and localization of aquaporin-4 water channel protein. *Proc Natl Acad Sci U S A* 2001;98:14108–13 CrossRef Medline
 34. Bradl M, Misu T, Takahashi T, et al. Neuromyelitis optica: pathogenicity of patient immunoglobulin in vivo. *Ann Neurol* 2009;66:630–43 CrossRef Medline
 35. Amiry-Moghaddam M, Ottersen OP. The molecular basis of water transport in the brain. *Nat Rev Neurosci* 2003;4:991–1001 CrossRef Medline

Comparison of Multiple Sclerosis Cortical Lesion Types Detected by Multicontrast 3T and 7T MRI

J. Maranzano, M. Dadar, D.A. Rudko, D. De Nigris, C. Elliott, J.S. Gati, S.A. Morrow, R.S. Menon, D.L. Collins, D.L. Arnold, and S. Narayanan



ABSTRACT

BACKGROUND AND PURPOSE: Our aims were the following: 1) to compare multicontrast cortical lesion detection using 3T and 7T MR imaging, 2) to compare cortical lesion type frequency in relapsing-remitting and secondary-progressive MS, and 3) to assess whether detectability is related to the magnetization transfer ratio, an imaging marker sensitive to myelin content.

MATERIALS AND METHODS: Multicontrast 3T and 7T MR images from 10 participants with relapsing-remitting MS and 10 with secondary-progressive MS. We used the following 3T contrast sequences: 3D-T1-weighted, quantitative T1, FLAIR, magnetization-transfer, and 2D proton-density- and T2-weighted. We used the following 7T contrast sequences: 3D-T1-weighted, quantitative T1, and 2D-T2*-weighted.

RESULTS: Cortical lesion counts at 7T were the following: 720 total cortical lesions, 420 leukocortical lesions (58%), 27 intracortical lesions (4%), and 273 subpial lesions (38%). Cortical lesion counts at 3T were the following: 424 total cortical, 393 leukocortical (93%), zero intracortical, and 31 subpial (7%) lesions. Total, intracortical, and subpial 3T lesion counts were significantly lower than the 7T counts ($P < .002$). Leukocortical lesion counts were not significantly different between scanners. Total and leukocortical lesion counts were significantly higher in secondary-progressive MS, at 3T and 7T ($P \leq .02$). Subpial lesions were significantly higher in secondary-progressive MS at 7T ($P = .006$). The magnetization transfer ratio values of leukocortical lesions visible on both scanners were significantly lower than the magnetization transfer ratio values of leukocortical lesions visible only at 3T. No significant difference was found in magnetization transfer ratio values between subpial lesions visible only at 7T and subpial lesions visible on both 3T and 7T.

CONCLUSIONS: Detection of leukocortical lesions at 3T is comparable with that at 7T MR imaging. Imaging at 3T is less sensitive to intracortical and subpial lesions. Leukocortical lesions not visible on 7T T2*-weighted MRI may be associated with less demyelination than those that are visible. Detectability of subpial lesions does not appear to be related to the degree of demyelination.

ABBREVIATIONS: CL = cortical lesion; IC = intracortical; LC = leukocortical; MTR = magnetization transfer ratio; NAcGM = normal-appearing cortical GM; RRMS = relapsing-remitting MS; SP = subpial; SPMS = secondary-progressive MS

Multiple sclerosis is an inflammatory and neurodegenerative disease characterized by lesions that affect the white mat-

ter and gray matter of the central nervous system.¹ MR imaging of the brain is the criterion standard method to detect MS lesions in vivo,² allowing an accurate quantification of the WM component of MS. However, correlations between a patient's clinical status and WM lesion load remain modest^{3,4}, so it is

Received February 3, 2019; accepted after revision May 10.

From the Department of Anatomy (J.M.), University of Quebec in Trois-Rivieres, Trois-Rivieres, Quebec, Canada; McConnell Brain Imaging Centre (J.M., M.D., D.A.R., D.D.N., C.E., D.L.C., D.L.A., S.N.), Montreal Neurological Institute, McGill University, Montreal, Quebec, Canada; Department of Biomedical Engineering (M.D., D.A.R., D.L.C.), McGill University, Montreal, Quebec, Canada; Centre for Functional and Metabolic Mapping (J.S.G., R.S.M.), Robarts Research Institute, University of Western Ontario, London, Ontario, Canada; Department of Clinical Neurological Sciences (S.A.M.), London Health Sciences Centre, University of Western Ontario, London, Ontario, Canada; and Department of Medical Biophysics (R.S.M.), University of Western Ontario, London, Ontario, Canada

This study was supported by a Canadian Institutes of Health Research Grant (grant No. 201303MOP-302444- MPI-CFAA-23603).

This article is dedicated to the memory our dear friend and colleague, Dr Marcelo Kremenchtzky, Chair of Clinical MS Research at London Health Sciences Centre and a leading MS neurologist and clinician-scientist, who recently passed away. With regard to the current work, Dr Kremenchtzky made substantial contribu-

tions to the conception and design of this study and the acquisition and interpretation of data, and he critically revised the manuscript for intellectual content. May he rest in peace.

Please address correspondence to Josefina Maranzano, MD, PhD, University of Quebec in Trois-Rivieres, Department of Anatomy, Pavillon Leon-Provancher, Local 3501, 3351, Boulevard des Forges, Trois-Rivieres, QC, Canada, G8Z 4M3; McGill University, Department of Neurology and Neurosurgery, Montreal Neurological Institute, 3801 Rue University, Room WB327, Montreal, QC, Canada, H3A 2B4; e-mail: josefina.maranzano@uqtr.ca and josefina.maranzano@mail.mcgill.ca

Indicates open access to non-subscribers at www.ajnr.org

Indicates article with supplemental on-line tables.

Indicates article with supplemental on-line photo.

<http://dx.doi.org/10.3174/ajnr.A6099>

Table 1: Demographic and clinical characteristics of the participants

	Patients with RRMS	Patients with SPMS	Significant Differences (P Value)
Male/female	3:7	3:7	
EDSS score	Median, 1.5 Range, 1–3	Median, 4.5 Range, 3–6.5	.001 ^a
Age at Onset (yr)	Mean, 34 SD, 8.2	Mean, 30 SD, 6.5	.15 ^b
Disease duration (yr)	Mean, 12 SD, 7.8	Mean, 18 SD, 6.8	.04 ^b
White matter lesion volume (cm ³)	Median, 9.3 Range, 0.8–44.3	Median, 12.9 Range, 3.7–50.4	.18 ^a

Note:—EDSS indicates Expanded Disability Status Scale.

^a Mann-Whitney *U* test.

^b *T* test.

essential to accurately quantify GM lesions, especially in the cortex, which could increase clinical-imaging correlations.

MS cortical lesions (CLs) have been classified histopathologically into 4 types: type I leukocortical (LC), affecting the cortex and juxtacortical white WM; type II intracortical (IC), affecting only the cortex, without reaching the WM or subpial surfaces; type III subpial (SP), affecting the outer cortex along the SP boundary but not reaching the WM surface; and type IV, also SP but cortex-spanning, affecting all layers of the cortex.⁵ In many studies, types III and IV are grouped together as SP.

In vivo, CLs are detectable using MR imaging but are more difficult to visualize than WM lesions because of the lower myelin content in the cortex. Consequently, the change in myelin-related signal in CLs is smaller. CLs also generally exhibit less inflammation than WM lesions,⁶ leading to limited alteration of T1 and T2.^{4,7,8}

During the past 2 decades, there has been significant interest in improving MR imaging–based detection of CLs.^{8–12} At MR imaging field strengths of 1.5T and 3T, CLs are difficult to classify due to an insufficient signal-to-noise ratio (SNR), making the delineation of the boundaries between small CLs and surrounding normal tissue very challenging.¹⁰ At 7T, a classification of CLs that approximates that of histology is possible because of the increased SNR afforded by high-field MR imaging; hence, 7T MR imaging has emerged as the in vivo criterion standard for CL identification.^{8,13,14}

The reduced sensitivity of lower MR imaging field strengths for CL detection is reflected in postmortem studies. In particular, 1.5T and 3T MR imaging detect only a small fraction of the CLs, as low as 5%.¹⁵ MR imaging at 7T improves the detection rate¹⁶; however, a large number of CLs are still not captured. This is particularly true for type III lesions, for which 7%–32% detection sensitivities have been reported.¹⁴

The simultaneous use of multiple MR imaging contrasts improves CL detection over single-contrast reads at 3T, so multicontrast 3T MR imaging CL quantification may provide results closer to those from 7T.¹⁷

Our study presents the assessment of CL counts obtained with multicontrast reading protocols on both 3T¹⁷ and 7T MR images of the same MS cohort. Our goal was to establish which CL types were visible at 3T compared with 7T, using a multicontrast approach on coregistered images and to assess whether detectability was related to the degree of abnormality on

magnetization transfer imaging,^{18,19} as a measure of relative myelin content.

MATERIALS AND METHODS

Study Population

Twenty participants with MS (6 men, 14 women, between 38 and 56 years of age) followed at the London, Ontario MS clinic, were recruited as part of a larger prospective cohort study designed to assess CLs in MS. The first 10 participants with relapsing-remitting MS (RRMS) and the first 10 with secondary-progressive MS (SPMS) were included in the present cross-sectional analysis. The

median Expanded Disability Status Scale score was 3 (range, 1–6.5). The demographic details of the participants are presented in Table 1.

The study was approved by the institutional research ethics boards of the University of Western Ontario and McGill University. Each participant gave written informed consent.

MR Imaging Acquisition

All participants were imaged at the Centre for Functional and Metabolic Mapping at the Robarts Research Institute, University of Western Ontario. Subjects were imaged on a 3T Magnetom Prisma MR imaging scanner (Siemens, Erlangen, Germany). The same subjects were then scanned on a 7T Magnetom Step 2.3 (Siemens), using an 8-channel parallel-transmit configuration. Each participant was scanned at both 3T and 7T on the same day, except for 1 person whose scanning sessions were a week apart. None of the patients received treatment with corticosteroids during the month before the MR imaging.

The 3T MR imaging contrast sequences acquired were the following: 1) 3D-MP2RAGE sequence, yielding a 3D-T1-weighted image and a quantitative T1-map; 2) 3D-FLAIR; 3) 2D dual-echo, TSE, yielding proton-density-weighted and T2-weighted images; and 4) 3D-FLASH with and without a magnetization transfer pulse, to compute the magnetization transfer ratio (MTR) images.

On the 7T scanner, we obtained MP2RAGE and 2D-FLASH T2⁺-weighted image volumes. The detailed acquisition parameters are listed in Table 2.

MR Imaging Analysis

Image Processing. All 3T MR imaging contrast sequences were coregistered before CL segmentation, using the following image-processing pipeline: 1) brain mask extraction,²⁰ 2) bias field correction,^{21,22} 3) linear 9-parameter registration of the T1-weighted image to standard Montreal Neurological Institute stereotactic space²³ (transformations for registration were calculated using gradient orientations of minimal uncertainty),²⁴ 4) intermodality 6-parameter registration, and 5) resampling of all modalities to the T1-weighted image in Montreal Neurological Institute stereotactic space.²⁵

7T images were bias-field-corrected,²¹ and the MP2RAGE volumes (3D-T1WI and T1 map) were then linearly registered to the

Table 2: MRI acquisition parameters

	3T TIWI	3T PDw/ T2WI	3T FLAIR	3T MT On/Off	7T TIWI	7T T2*
Sequence	3D- MP2RAGE	2D-dual echo TSE	3D-TSE	3D-GRE	3D-MP2RAGE	2D-GRE
Orientation	Sagittal	Axial	Sagittal	Axial	Sagittal	Axial
TR (ms)	5000	2350	6000	36	6000	1000
TE (ms)	2.98	22 87	356	3.86	2.7	22
TI (ms)	700 2500	NA	2200	NA	800 2700	NA
Flip angle	4° 5°	120°	180°	10°	4° 5°	55°
Slices	176	120	176	192	224	60 (2 Stacks of 30)
Voxel size (mm)	1 × 1 × 1	1 × 1 × 1.5	1 × 1 × 1	1 × 1 × 1	0.7 × 0.7 × 0.7	0.3 × 0.3 × 1
Scan time (min:sec)	8:22	5:26	8:44	8:10	10:14	8:26 (per stack)

Note:—PDw indicates proton density-weighted; MT, magnetization transfer; GRE, gradient recalled-echo; NA, not applicable.

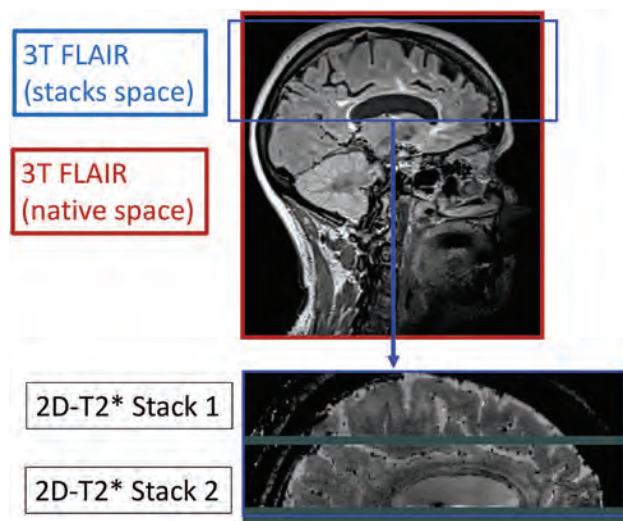


FIG 1. Multicontrast protocol volumetric area. Due to the sensitivity of 7T T2*-weighted acquisitions to magnetic susceptibility inhomogeneities present at the level of the posterior fossa and inferior temporal lobes, coverage of this interleaved, multislice acquisition is limited to the superior temporal lobes and above. Representation of the common volume of the brain is considered when comparing CL types detected on 3T and 7T.

T2*-weighted images, maintaining the high in-plane resolution of the T2*-weighted image that allows the classification of CL types.⁸

Once CL identification was performed (see the Cortical Lesion Quantification section below), we linearly registered all 3T MR imaging contrast sequences and their corresponding masks to 7T T2*WI space. This allowed accurate assessment of colocalization between CLs identified at 3T and 7T.

All comparisons between 3T and 7T scans were performed in the same volumetric area covered by the 7T T2*WI because this sequence does not include the inferior portion of the temporal lobes or the posterior fossa, while the 3T scans cover the whole brain (Fig 1).

Cortical Lesion Quantification. All MR images were segmented by an experienced rater (J.M. with >13 years of experience in lesion segmentation on MR imaging research scans of patients with MS), blinded to clinical status. Intra- and interrater reliability was assessed in 2 datasets (details presented in On-line Tables 1 and 2, respectively).

3T CL identification was performed in random order before 7T CL identification, with an interval of 3 months between reads.

CLs were manually segmented using the interactive software package “Display” (<https://github.com/BIC-MNI/Display>) developed at the McConnell Brain Imaging Center of the Montreal Neurological Institute. This program allows simultaneous viewing and lesion segmentation in the coronal, sagittal, and axial planes and cycling between multiple coregistered image contrasts. The program provides a “painting” tool for marking voxels with a given color (label number). These labels are saved in a separate label file that can be loaded for superimposition onto other brain images.²⁶

On 3T images, CLs were segmented and classified in a single group,¹⁷ providing a total CL count. This was done because the resolution at 3T does not allow a confident classification of CL types. Lesions had to be at least 3 voxels and have a high signal intensity on FLAIR and T2WI/proton-density weighted imaging and low signal intensity on T1WI in relation to the surrounding normal-appearing GM to be considered a 3T CL.

On 7T images, CLs were segmented as 3 different types (using 3 label numbers) following the classification by Bø et al (2003)^{5,27}: type I (LC), type II (IC), and types III/IV (SP). Figure 2 shows an example of these different types of lesions on our 7T T2*WI. All 7T contrasts were used to segment 7T CLs, which had to be at least 3 voxels and be hyperintense on T2*WI and the T1 map and hypointense on the 3D-T1WI contrast sequence in relation to the surrounding normal-appearing GM.

Once all scans were read, the 3T MR imaging contrast scans and CL masks of each patient were registered to the corresponding 7T T2*WI contrast. A side-by-side comparison of registered image slices allowed the categorization of CLs into those that had been identified on both 3T and 7T images (common lesions), CLs only identified at 3T (7T-negative lesions), and CLs only identified at 7T (3T-negative lesions). It also allowed us to determine the type of CL identified by 3T images: retrospective classification of 3T CL types.

White Matter Lesion Quantification. WM lesions were segmented using an automated Bayesian classifier followed by manual review and correction by an experienced rater (J.M.), as previously described.²⁸ The contrasts used for the classification and

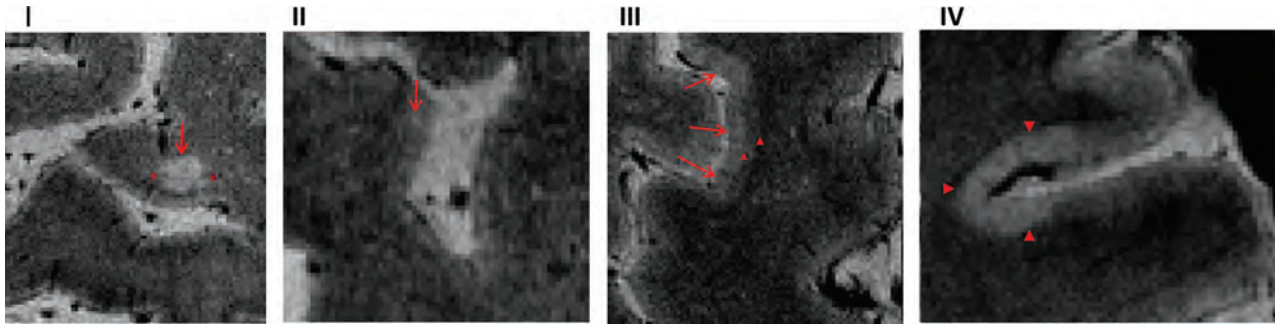


FIG 2. Cortical lesion classification. 7T T2* MR imaging cortical lesion classification (Bø et al 2003).⁵

manual correction of the WM lesions were 3T T1WI, FLAIR, and T2WI/proton-density-weighted.

Normal-Apparing Cortical Gray Matter Segmentation. Masks of normal-appearing cortical GM (NAcGM) adjacent to each CL were created by dilating the CL masks by 5 voxels in the 3 coordinate directions. A cortical GM tissue mask based on a multiatlas label fusion method²⁹ was used to avoid the inclusion of juxtacortical WM and CSF.

Statistical Analysis

Subject demographic data that were normally distributed were compared using a *t* test; otherwise, a Mann-Whitney *U* test was used. CL counts (3T versus 7T) were compared using a Wilcoxon signed rank test. The frequency of CL types in RRMS and SPMS was compared using a χ^2 test. The relationship between CL counts at 3T and 7T was evaluated with the Spearman correlation, and sensitivity [3T True-Positive/(3T True-Positive + 3T False-Negative) \times 100], specificity [3T True-Negative/(3T True-Negative + 3T False-Positive) \times 100], positive predictive value [3T True-Positive/(3T True-Positive + 3T False-Positive) \times 100], and negative predictive value [3T True-Negative/(3T True-Negative + 3T False-Negative) \times 100] of 3T counts with respect to 7T counts were calculated.

An Generalized Linear Model with a negative binomial distribution and a log-link function assessed the relationship of CL count as the outcome variable to the disease type (RRMS versus SPMS) as the predictor factor, adjusting for disease duration and age at symptom onset:

$$\text{CL Count} \sim (\text{Log-Link Function}) \text{ Disease Type} \\ + \text{Age at Symptom Onset} + \text{Disease Duration.}$$

The same type of GLM was used to determine the relationship between different CL types (LC and SP) and 4 predictor variables: 1) disease type, 2) age at symptom onset, 3) disease duration, and 4) WM lesion volume:

$$\text{LC/SP Lesion Count} \sim (\text{Log-Link Function}) \text{ Disease Type} \\ + \text{Age at Symptom Onset} + \text{Disease Duration} \\ + \text{WM Lesion Volume.}$$

We also assessed whether the number of SP lesions detected by 7T MR imaging was related to the total number of CLs detected by 3T MR imaging, using the same type of GLM:

$$7\text{T SP Lesion Count} \sim (\text{Log-Link Function}) 3\text{T Total CL count.}$$

A negative binomial regression model was chosen in all cases in which the CL count was the outcome variable, due to its overdispersion.³⁰

Finally, differences in MTR values across CL types were assessed and compared with the surrounding (NAcGM) using a mixed-effects model:

$$\text{Mean MTR} \sim 1 + \text{Lesion Type} + (1|\text{subject ID}).$$

All statistical analyses were performed using MATLAB R2018a and SPSS v.24.

RESULTS

Study Population Features

The male-female ratio was the same in the RRMS and SPMS groups: 3/7. The age at the onset of MS was not significantly different between RRMS and SPMS participants ($P = 0.15$). The disease duration was significantly longer for SPMS ($P = .04$). The Expanded Disability Status Scale scores were significantly higher in the SPMS group ($P = .001$) (Table 1).

The volume of WM lesions was not significantly different between RRMS and SPMS groups ($P = 0.18$).

Cortical Lesion Counts

Seven hundred twenty CLs were detected using the 7T multicontrast protocol. The median CL count was 24.5 per participant (range, 0–119). Of these, 420 (58%) were LC, 27 (4%) were IC, and 273 (38%) were SP.

Four hundred twenty-four CLs were detected using the 3T multicontrast protocol (count limited to the region covered by the 7T T2*WI scan). The median CL count was 13 per participant (range, 1–59). Of these, 393 (93%) were retrospectively determined to be LC, none were IC, and 31 (7%) were SP. The total 3T CL count, in the complete 3T volume, was 617, with a median count of 24.5 per participant (range, 1–85).

The 3T total CL, IC, and SP lesion counts were significantly lower than the respective 7T counts ($P = 0.39$). The LC lesion count was not significantly different between 3T and 7T.

One hundred twenty-six (30%) LC lesions were detected only on 3T MR imaging and were missed on 7T. On retrospective review, these LC lesions were visible at 7T on the MP2RAGE sequence but were not labeled as lesions due to the low signal on T2*WI. These 126 LC lesions did not show a preferential location

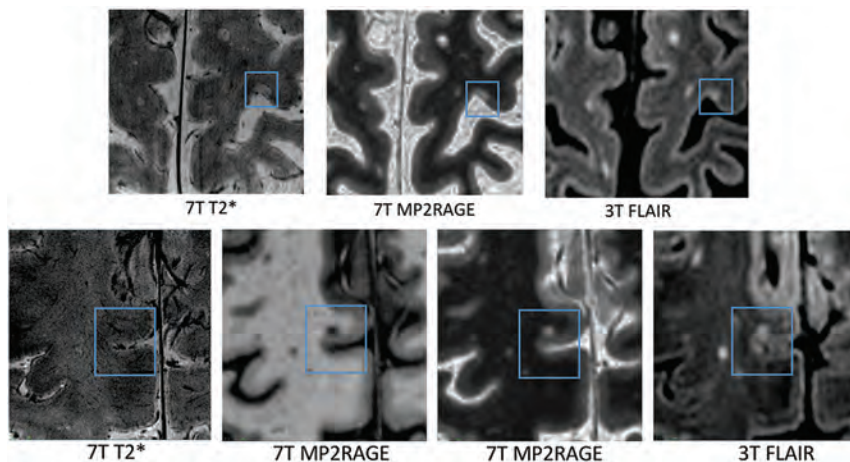


FIG 3. Example of CL lesions detected by 3T and 7T protocols. Example of 3T–7T common SP lesions (upper row) and 7T-negative LC lesions (lower row).

in the gyri; 43.6% affected the crown of the gyri, and 56.4% were located along the sulci. Finally, 50% of these LC lesions were located in the frontal lobes (see detailed localization and lobe distribution in On-line Tables 3 and 4).

Thirty-one (11%) SP lesions were detected on both 3T and 7T MR imaging (Fig 3).

At 7T total CL, LC, and SP lesion counts were significantly higher in SPMS participants after adjusting for disease duration and age at disease onset ($P = 0.01$, $P = 0.008$, and $P = 0.03$, respectively). The IC lesion counts were not significantly different across MS types ($P = 0.23$), likely due to their small numbers (9 in RRMS, 18 in SPMS).

At 3T, the proportions of LC and SP lesions of the total CL count were not significantly different between RRMS and SPMS ($P = 0.06$ and $P = 0.49$, respectively) (IC lesions were not detected at 3T). The proportions of CL types obtained on 7T MR imaging were significantly different between RRMS and SPMS when considering all 3 CL types ($P = .02$). However, when assessing differences between MS types in pairs of CL types, there were no significant differences in the proportions of LC and IC or IC and SP lesions. This finding is likely due to the small number of IC lesions that were identified. Conversely, the proportion of LC and SP lesions was significantly different between phenotypes ($P = 0.007$), with a higher proportion of LC lesions in SPMS. Details of the CL proportion by phenotype and tables used to calculate χ^2 are presented in On-line Tables 5–9.

The correlation between CL counts obtained at 3T and 7T, determined using a nonparametric test (Spearman ρ), was 0.96 for LC lesions ($P < 0.001$) and 0.78 for SP lesions ($P < 0.001$) (Fig 4).

The sensitivity of 3T counts with respect to 7T counts was 67.2% for LC lesions and 11.3% for SP lesions. The specificity of 3T counts, as well as the negative predictive values, could not be determined due to the inability to count true-negatives (cortex that appeared normal at both 3T and 7T). The positive predictive values for the 3T LC lesion count were 93.4% and 100% for SP lesions. However, these positive predictive values are relatively uninformative because the classification of CL 3T scans was only performed in a retrospective fashion.

Cortical Lesion Magnetization Transfer Characteristics

Mean MTR values of LC lesions visible on both scanners (3T–7T, common LC lesions) were significantly lower (mean MTR = 37.1 ± 3.0) ($P < 0.001$) than mean MTR values of LC lesions visible only on 3T (7T-negative LC lesions) (mean MTR = 38.3 ± 2.6).

The MTR of SP lesions visible on both 3T and 7T (common SP lesion) did not differ significantly from the MTR of SP lesions visible only on 7T (3T-negative SP lesion) ($P = .5$).

The mean MTR values in the GM voxels of each lesion type were also compared with surrounding NAcGM MTR values. LC lesions only visible on 3T scans or on both 3T and 7T scans showed significantly lower MTR values than the surrounding NAcGM ($P = .03$ and $.002$, respectively). In LC lesions visible only on 7T scans, the MTR difference compared with the surrounding cortex did not reach statistical significance (37.6 ± 2.1 versus 38.0 ± 1.6 , $P = .06$). IC lesions, only visible on 7T scans, did not show lower MTR values than the surrounding NAcGM. Finally, SP lesions detected on either 7T or both 3T and 7T showed significantly lower MTR values compared with the surrounding NAcGM ($P < 0.001$ and $.01$, respectively). Detailed MTR data are presented in On-line Table 10 and the On-line Figure.

Association of Cortical Lesion Counts with Clinical and MR Imaging Measures

We assessed the association between the 7T LC lesion count as the outcome variable and 4 predictors: MS type, disease duration, age at onset, and WM lesion volume. We found a significant association with SPMS ($P = .006$), a significant negative association with age at onset ($P = .05$), and a significant positive association with WM lesion volume ($P = .03$). When the same associations were evaluated for SP lesion as the outcome variable, only SPMS was found to have a significant association ($P = .03$).

Finally, we used a GLM to assess whether the total number of 3T CLs detected in the whole-brain volume could predict the number of SP lesions (3T total CL count = predictor; 7T SP lesion count = outcome variable), and we found a significant positive association ($P = .03$).

DISCUSSION

Comparison of our 2 multicontrast MR imaging reading protocols, using coregistered images derived from 3T and 7T scans, showed that LC lesions are detected with a comparable degree of accuracy and acceptable sensitivity on 3T scans: 3T LC sensitivity = 67.2% and 3T LC positive predictive value = 93.4%. Furthermore, we found that the correlation between LC lesion counts on 3T and 7T was very high: $r = 0.96$, $P < 0.001$. Thus, a 3T multicontrast detection of LC lesions could be considered equivalent to a 7T multicontrast assessment of LC lesions using T2* and MP2RAGE.

Our study also reproduces previous findings regarding the su-

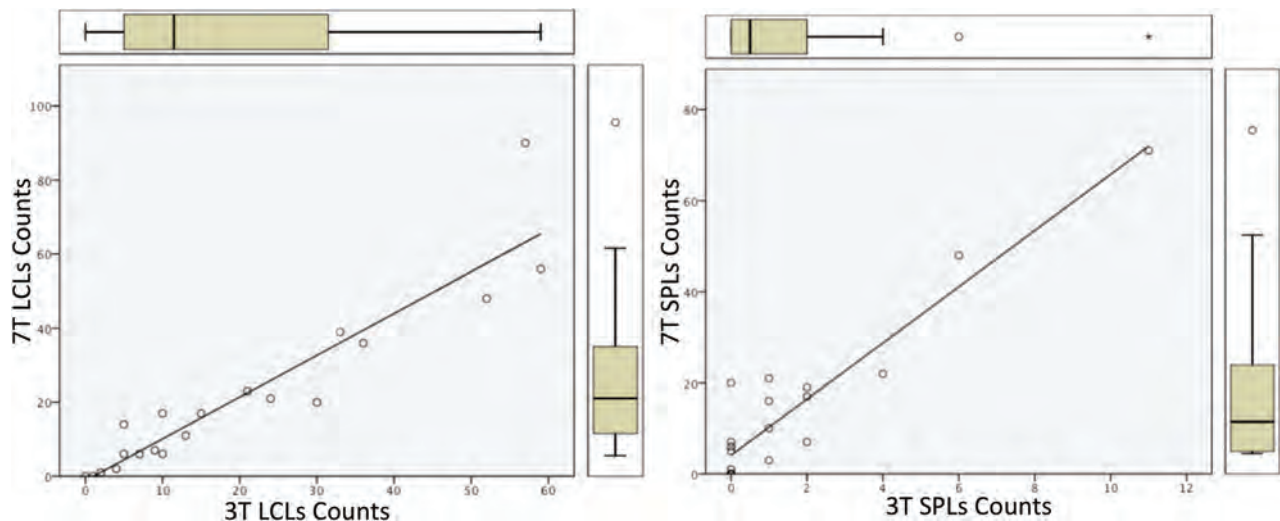


FIG 4. CL count correlations. Leukocortical and subpial lesion count correlations across scanners: 3T LC lesion counts and 7T LC lesion counts; 3T SP lesion counts and 7T SP lesion counts.

prior sensitivity of 7T MR imaging in the detection of SP and IC lesions, with a 3T sensitivity for SP lesions of only 11.3%.¹⁴ A slice-by-slice comparison of 3T images coregistered with 7T images revealed that 11% of SP lesions detected on 3T MR imaging could not be prospectively differentiated from LC lesions due to the lower resolution of the 3T scans. However, the number of 3T-positive SP lesions showed a high positive predictive value (100%) and a high correlation with the total SP lesion count at 7T ($r = 0.78$, $P < 0.001$), suggesting that the few SP lesions detected on 3T scans are all true-positives and that their distribution across participants would be representative of the distribution of SP lesions at 7T, albeit with a much lower sensitivity.

We also performed a slice-by-slice comparison of coregistered 3T and 7T images to assess CLs that were identified exclusively on 3T or 7T images. We found that 30% of LC lesions were not identified at 7T due to the absence of increased signal on the 7T T2*WI contrast, though they exhibited clear hypointensity on 3D-T1WI at 7T and elevated signal on the T1 map.¹⁴ Conversely, these negative-7T LC lesions were visible on 3T FLAIR,¹³ where they exhibited the classic hyperintensity of MS lesions. The finding of LC lesions negative on 7T T2*WI is in line with previous studies that reported a lower sensitivity of 7T T2*WI compared with 7T T2WI in the detection of LC lesions.^{14,31,32} Specifically, Kilsdonk et al, in 2016,¹⁴ performed an ex vivo comparison between 7T MR imaging CL detection by lesion type on various MR imaging contrast sequences versus histopathology, reporting that 7T T2*WI was able to detect only 50% of all LC lesions versus a detection of 100% using 7T T2WI. Due to both time constraints and inherent challenges related to whole-head B₁ shimming for T2WI acquisitions at 7T, it is not always possible to acquire both T2*WI and T2WI data in a single scan session. Consequently, researchers may favor 7T T2*WI, given its more sensitive performance in the assessment of SP lesions, which is the most difficult CL type to detect. However, if an MP2RAGE sequence is used at 7T, the sensitivity for LC lesions might be improved by increasing the weight of joint positivity on 3D-T1WI and the T1 map and relaxing the requirement for hyperintensity on T2*WI. Alternatively, the inclusion of a FLAIR contrast in the acquisition proto-

col of 7T scans may increase the LC lesion detection rate when combined with the MP2RAGE sequence.

Our finding that 7T-negative LC lesion had significantly higher MTR values than those found in 3T–7T common LC lesion suggests that negative LC lesion on 7T might be related to lower levels of demyelination.¹⁹ Additionally when comparing MTR values of LC lesions with the values of the surrounding NAcGM, 3T-negative LC lesions showed lower MTR values but did not reach statistical significance ($P = .06$). Conversely, common LC lesions and 7T negative did show significantly lower MTR values than the surrounding NAcGM ($P = 0.002$ and $P = 0.03$, respectively).

MTR was also used to characterize SP lesions visible on both 3T and 7T (common SP lesions) versus SP lesions only visible on 7T (3T-negative SP lesions). We did not find significant differences in MTR values, suggesting that the visibility of SP lesions on 3T images is not related to their degree of myelination/demyelination,¹⁹ but possibly to MR imaging resolution and T2 contrast characteristics of the lesions. We speculate that the inherently lower myelin content in cortical GM, particularly in the superficial layers,³³ may also, in part, be responsible for the lack of MTR differences between common SP lesions and 3T-negative SP lesions. However, when we performed the comparison of MTR values of these lesions with the surrounding NAcGM, both common SP lesions and 3T-negative SP lesions showed significantly lower values ($P = 0.01$ and $P < 0.001$, respectively).

Our study also assessed differences in CL types in the RRMS and SPMS groups. We did not find a higher proportion of SP lesions in SPMS, as suggested by ex vivo studies.^{34,35} This discrepancy could be related to the use of end-stage SPMS tissue samples in previous ex vivo studies. The participants with SPMS in our study had moderate disability and were of similar age to the those with RRMS. Another possible explanation could be related to pathologists typically only considering regions of complete demyelination as true lesions.³⁵ This type of definition is operationally impossible on MR imaging in vivo. When one applies MR imaging for in vivo identification of CLs, some LC lesions could represent areas of partial demyelination.³² This would increase the

MR imaging–based LC count in relation to a corresponding count using histology. In addition, on MR imaging, we were able to assess lesion counts over a larger volumetric area of the brain, as opposed to single slices evaluated in ex vivo studies.

Regarding the associations of CL counts and clinical and MR imaging measurements as predictors, we observed a significant association with MS type of both LC and SP lesions, with significantly higher counts in SPMS. However, while LC lesion counts also showed a significant positive association with WM lesion volumes and a significant negative association with age at disease onset, SP lesions did not. These differences could be related to variations in the dynamic aspects of the pathophysiologic evolution in the 2 lesion types. However, given the lower sensitivity of MR imaging to SP lesions, our sample size may be too small to observe significant associations with other predictors.¹⁴

Finally, the positive relationship of 3T total CL count to the 7T SP count, along with the strong relationship between LC lesion count at 3T and 7T, suggests that the overall CL identification performed on 3T is informative regarding the overall CL burden. The use of multicontrast acquisitions and reading protocol would allow many more centers without access to 7T scanning to assess CL pathology in MS.

Limitations

The absence of a histopathologic assessment is an obvious limitation of this study. As a consequence, we have characterized lesions as 3T positive/negative and 7T positive/negative because previous work using ex vivo MR imaging has shown that 7T still has sensitivity limitations in the detection of the different CL types.¹⁴ Nevertheless, we performed an analysis of sensitivity and calculated predictive values of 3T counts in relation to 7T counts, given the generally higher performance of 7T imaging. An ex vivo study has shown that partial demyelination in CLs is detectable on MR imaging³²; however, most ex vivo studies do not consider partially demyelinated lesions in their quantifications. We believe that this is a limiting factor in the interpretation of count data in comparing MR imaging and histology results.

CONCLUSIONS

3T multicontrast MR imaging is an adequate method to detect the number of LC lesions. 7T MR imaging is necessary for quantifying SP lesions and IC lesions in vivo. However, CLs detected at 3T include a fraction of SP pathology with a high predictive value that significantly correlates with SP lesions seen on 7T. This outcome suggests that a standardized, multicontrast 3T MR imaging reading protocol on coregistered images can be a valuable method to assess overall CL burden in vivo. We found that LC and SP lesions were higher in participants with SPMS, highlighting their association with progression in MS. Longitudinal studies are needed to assess the rate of accumulation of CLs and their association with change in clinical variables.

ACKNOWLEDGMENTS

We thank Dr Erin Beck, Clinical Fellow at the Translational Neuroradiology Section, Division of Neuroimmunology and Neurovirology, National Institute of Neurological Disorders and Stroke, National Institutes of Health, who performed 7T cortical lesion

segmentations in the dataset used to calculate the interrater reliability results.

Disclosures: Josefina Maranzano—RELATED: Grant: Canadian Institutes of Health Research*; UNRELATED: Grants/Grants Pending: Multiple Sclerosis Society of Canada, Comments: doctoral award from July 1, 2018, up to November 2018 (I completed my PhD in November, so the award was closed).* Colm Elliott—UNRELATED: Consultancy: F. Hoffmann-La Roche Ltd, Comments: Participated on an advisory board as a representative of NeuroRx Research*; Employment: NeuroRx Research. Sarah A. Morrow—RELATED: Grant: Canadian Institutes of Health Research.* Ravi S. Menon—RELATED: Grant: Canadian Institutes for Health Research.* D. Louis Collins—UNRELATED: Consultancy: NeuroRx Research, Comments: consultancy and training on image-processing procedures; Employment: McGill University, Comments: I am a professor at McGill University. Douglas L. Arnold—RELATED: Grant: Canadian Institutes of Health Research*; UNRELATED: Consultancy: Acorda Therapeutics, Biogen, Celgene, GeNeuro, Genentech, Hoffmann-La Roche, Merck, Novartis, Roche, Sanofi, Teva Pharmaceutical Industries, and Wave Life Sciences; Employment: NeuroRx Research; Grants/Grants Pending: Canadian Institutes of Health Research, Multiple Sclerosis Society of Canada, Biogen, Novartis, Immunotec; Stock/Stock Options: NeuroRx Research. Sridar Narayanan—UNRELATED: Employment: NeuroRx Research, Comments: Part-time; Grant: Immunotec. *Money paid to the Institution.

REFERENCES

1. Compston A, Coles A. **Multiple sclerosis.** *Lancet* 2008;372:1502–17 CrossRef Medline
2. Reich DS, Lucchinetti CF, Calabresi PA. **Multiple sclerosis.** *N Engl J Med* 2018;378:169–80 CrossRef Medline
3. Rocca MA, Messina R, Filippi M. **Multiple sclerosis imaging: recent advances.** *J Neurol* 2013;260:929–35 CrossRef Medline
4. Calabrese M, Filippi M, Gallo P. **Cortical lesions in multiple sclerosis.** *Nat Rev Neurol* 2010;6:438–44 CrossRef Medline
5. Bø L, Vedeler CA, Nyland HI, et al. **Subpial demyelination in the cerebral cortex of multiple sclerosis patients.** *J Neuropathol Exp Neurol* 2003;62:723–32 CrossRef Medline
6. Peterson JW, Bø L, Mörk S, et al. **Transected neurites, apoptotic neurons, and reduced inflammation in cortical multiple sclerosis lesions.** *Ann Neurol* 2001;50:389–400 CrossRef Medline
7. Absinta M, Sati P, Reich DS. **Advanced MRI and staging of multiple sclerosis lesions.** *Nat Rev Neurol* 2016;12:358–68 CrossRef Medline
8. Mainiero C, Benner T, Radding A, et al. **In vivo imaging of cortical pathology in multiple sclerosis using ultra-high field MRI.** *Neurology* 2009;73:941–48 CrossRef Medline
9. Seewann A, Kooi EJ, Roosendaal SD, et al. **Postmortem verification of MS cortical lesion detection with 3D DIR.** *Neurology* 2012;78:302–08 CrossRef Medline
10. Geurts JJ, Roosendaal SD, Calabrese M, et al; MAGNIMS Study Group. **Consensus recommendations for MS cortical lesion scoring using double inversion recovery MRI.** *Neurology* 2011;76:418–24 CrossRef Medline
11. Sethi V, Yousry TA, Muhlert N, et al. **Improved detection of cortical MS lesions with phase-sensitive inversion recovery MRI.** *J Neurol Neurosurg Psychiatry* 2012;83:877–82 CrossRef Medline
12. Nelson F, Poonawalla A, Hou P, et al. **3D MPRAGE improves classification of cortical lesions in multiple sclerosis.** *Mult Scler* 2008;14:1214–19 CrossRef Medline
13. Kilsdonk ID, de Graaf WL, Soriano AL, et al. **Multicontrast MR imaging at 7T in multiple sclerosis: highest lesion detection in cortical grey matter with 3D-FLAIR.** *AJNR Am J Neuroradiol* 2013;34:791–96 CrossRef Medline
14. Kilsdonk ID, Jonkman LE, Klaver R, et al. **Increased cortical grey matter lesion detection in multiple sclerosis with 7 T MRI: a post-mortem verification study.** *Brain* 2016;139:1472–81 CrossRef Medline
15. Geurts JJ, Bø L, Pouwels PJ, et al. **Cortical lesions in multiple sclerosis: combined postmortem MR imaging and histopathology.** *AJNR Am J Neuroradiol* 2005;26:572–77 Medline
16. Nielsen AS, Kinkel RP, Tinelli E, et al. **Focal cortical lesion detection**

- in multiple sclerosis: 3 Tesla DIR versus 7 Tesla FLASH-T2. *J Magn Reson Imaging* 2012;35:537–42 CrossRef Medline
17. Maranzano J, Rudko DA, Arnold DL, et al. **Manual segmentation of MS cortical lesions using MRI: a comparison of 3 MRI reading protocols.** *AJNR Am J Neuroradiol* 2016;37:1623–28 CrossRef Medline
 18. Brown RA, Narayanan S, Arnold DL. **Segmentation of magnetization transfer ratio lesions for longitudinal analysis of demyelination and remyelination in multiple sclerosis.** *Neuroimage* 2013;66:103–09 CrossRef Medline
 19. Chen JT, Easley K, Schneider C, et al. **Clinically feasible MTR is sensitive to cortical demyelination in MS.** *Neurology* 2013;80:246–52 CrossRef Medline
 20. Eskildsen SF, Coupé P, Fonov V, et al; Alzheimer's Disease Neuroimaging Initiative. **BEAST: brain extraction based on nonlocal segmentation technique.** *Neuroimage* 2012;59:2362–73 CrossRef Medline
 21. Sled JG, Zijdenbos AP, Evans AC. **A nonparametric method for automatic correction of intensity nonuniformity in MRI data.** *IEEE Trans Med Imaging* 1998;17:87–97 CrossRef Medline
 22. Tustison NJ, Avants BB, Cook PA, et al. **N4ITK: improved N3 bias correction.** *IEEE Trans Med Imaging* 2010;29:1310–20 CrossRef Medline
 23. Dadar M, Fonov VS, Collins DL. **A comparison of publicly available linear MRI stereotaxic registration techniques.** *Neuroimage* 2018;174:191–200 CrossRef Medline
 24. De Nigris D, Collins DL, Arbel T. **Multi-modal image registration based on gradient orientations of minimal uncertainty.** *IEEE Trans Med Imaging* 2012;31:2343–54 CrossRef Medline
 25. Maranzano J, Till C, Assemlal HE, et al; Canadian Pediatric Demyelinating Disease Network. **Detection and clinical correlation of leukocortical lesions in pediatric-onset multiple sclerosis on multi-contrast MRI.** *Mult Scler* 2018 May 1. [Epub ahead of print] CrossRef Medline
 26. Maranzano J, Rudko DA, Nakamura K, et al. **MRI evidence of acute inflammation in leukocortical lesions of patients with early multiple sclerosis.** *Neurology* 2017;89:714–21 CrossRef Medline
 27. Bø L, Vedeler CA, Nyland H, et al. **Intracortical multiple sclerosis lesions are not associated with increased lymphocyte infiltration.** *Mult Scler* 2003;9:323–31 CrossRef Medline
 28. Elliott C. *A Bayesian Framework for 4-D Segmentation of Multiple Sclerosis Lesions in Serial MRI in the Brain.* Doctoral thesis. Montreal: McGill University; 2016
 29. Sabuncu MR, Yeo BT, Van Leemput K, et al. **A generative model for image segmentation based on label fusion.** *IEEE Trans Med Imaging* 2010;29:1714–29 CrossRef Medline
 30. Sormani M, Stromillo ML, Battaglini M, et al. **Modelling the distribution of cortical lesions in multiple sclerosis.** *Mult Scler* 2012;18:229–31 CrossRef Medline
 31. Jonkman LE, Klaver R, Fleysher L, et al. **Ultra-high-field MRI visualization of cortical multiple sclerosis lesions with T2 and T2*: a postmortem MRI and histopathology study.** *AJNR Am J Neuroradiol* 2015;36:2062–67 CrossRef Medline
 32. Yao B, Hametner S, van Gelderen P, et al. **7 Tesla magnetic resonance imaging to detect cortical pathology in multiple sclerosis.** *PLoS One* 2014;9:e108863 CrossRef Medline
 33. Palomero-Gallagher N, Zilles K. **Cortical layers: cyto-, myelo-, receptor- and synaptic architecture in human cortical areas.** *Neuroimage* 2017 Aug 12. [Epub ahead of print] CrossRef Medline
 34. Kutzelnigg A, Lucchinetti CF, Stadelmann C, et al. **Cortical demyelination and diffuse white matter injury in multiple sclerosis.** *Brain* 2005;128:2705–12 CrossRef Medline
 35. Kutzelnigg A, Lassmann H. **Pathology of multiple sclerosis and related inflammatory demyelinating diseases.** *Handb Clin Neurol* 2014;122:15–58 CrossRef Medline

Improving Detection of Multiple Sclerosis Lesions in the Posterior Fossa Using an Optimized 3D-FLAIR Sequence at 3T

 A. Lecler,  I. El Sanharawi,  J. El Methni,  O. Gout,  P. Koskas, and  J. Savatovsky



ABSTRACT

BACKGROUND AND PURPOSE: There is no consensus regarding the best MR imaging sequence for detecting MS lesions. The aim of our study was to assess the diagnostic value of optimized 3D-FLAIR in the detection of infratentorial MS lesions compared with an axial T2-weighted imaging, a 3D-FLAIR with factory settings, and a 3D double inversion recovery sequence.

MATERIALS AND METHODS: In this prospective study, 27 patients with confirmed MS were included. Two radiologists blinded to clinical data independently read the following sequences: axial T2WI, 3D double inversion recovery, standard 3D-FLAIR with factory settings, and optimized 3D-FLAIR. The main judgment criterion was the overall number of high-signal-intensity lesions in the posterior fossa; secondary objectives were the assessment of the reading confidence and the measurement of the contrast. A nonparametric Wilcoxon test was used to compare the MR images.

RESULTS: Twenty-two patients had at least 1 lesion in the posterior fossa. The optimized FLAIR sequence detected significantly more posterior fossa lesions than any other sequence: 7.5 versus 5.8, 4.8, and 4.1 (*P* values of .04, .03, and .03) with the T2WI, the double inversion recovery, and the standard FLAIR, respectively. The reading confidence index was significantly higher with the optimized FLAIR, and the contrast was significantly higher with the optimized FLAIR than with the standard FLAIR and the double inversion recovery.

CONCLUSIONS: An optimized 3D-FLAIR sequence improved posterior fossa lesion detection in patients with MS.

ABBREVIATIONS: CNR = contrast-to-noise ratio; DIR = double inversion recovery; FLAIREd = FLAIR-enhanced detection; PSIR = phase-sensitive inversion recovery; SI = signal intensity

Multiple sclerosis is the most frequent chronic inflammatory disease of the central nervous system.¹⁻⁴ MR imaging has been shown to be the most efficient technique to image MS⁵ and has been included in the diagnostic work-up of the disease since 2001.^{6,7} The diagnosis of MS relies on proof of disease dissemination in space and time and exclusion of other disorders that can mimic MS. MR imaging is also the technique of choice in disease monitoring; in patients with clinically isolated syndromes sugges-

tive of MS, it has substantial prognostic value in the prediction of the conversion to definite MS.^{8,9}

MR imaging is performed in suspected or confirmed MS as a multisequence protocol, including minimally T2-weighted imaging and FLAIR sequences.¹⁰⁻¹⁴ The key sequence to detect brain demyelinating lesions is the 3D-FLAIR sequence, which offers better sensitivity than the 2D-FLAIR sequence and T2WI.^{15,16} 3D-FLAIR can achieve homogeneous CSF suppression, is minimally affected by artifacts,^{15,17,18} and provides a better resolution due to smaller slice thickness.¹⁹ It provides a higher contrast-to-noise ratio and allows multiplanar reconstructions. Its use is supported by international guidelines.^{10,12} However, FLAIR sequences were historically reported to be less sensitive than T2WI in the posterior fossa,²⁰ and conflicting results have been reported in the literature so far.^{15,18,19,21,22}

Many sequences have been tested to improve the detection of demyelinating encephalic lesions in patients with MS, such as magnetization transfer,²³ MPRAGE,²⁴ double inversion recovery (DIR),^{19,25-27} the phase-sensitive inversion recovery (PSIR) sequence,^{28,29} or 3D FLAIR-enhanced detection

Received April 8, 2019; accepted after revision May 14.

From the Departments of Neuroradiology (A.L., I.E.S., P.K., J.S.) and Neurology (O.G.), Fondation Ophtalmologique Adolphe de Rothschild, Paris, France; and Department of Biostatistics (J.E.M.), MAP5 Laboratory, Unité Mixte de Recherche Centre National de la Recherche Scientifique 8145, Paris Descartes University, Sorbonne Paris Cité, Paris, France.

Augustin Lecler and Imane El Sanharawi contributed equally to the work and are co-first authors.

Please address correspondence to Augustin Lecler, MD, PhD, Department of Neuroradiology, Fondation Ophtalmologique Adolphe de Rothschild, 25 rue Manin, 75019 Paris, France; e-mail: alecler@for.paris; @RothNeuroRad

 Indicates article with supplemental on-line photo.

<http://dx.doi.org/10.3174/ajnr.A6107>

Table 1: MRI sequence parameters

	TSE T2WI	DIR	FLAIR 4800	FLAIR 8000
TR (ms)	4545	5500	4800	8000
TE (ms)	80	277	245	328
TI (ms)	NA	2550	1650	2400
FOV (mm)	230 × 230	250 × 250	240 × 240	240 × 240
Acquisition matrix (mm)	384 × 299	200 × 200	240 × 243	240 × 243
Reconstruction matrix (mm)	512 × 512	256 × 256	256 × 256	256 × 256
Acquisition plane	Axial	Sagittal	Sagittal	Sagittal
Slice thickness (mm)	3	1.4	1	1
Gap (mm)	0	0	0	0
No. of slices	47	277	365	365
Flip angle	90°	90°	90°	90°
Echo-train	15	175	130	180
NEX	1	1	1	1
Fat-suppression	None	SPIR	SPIR	SPIR
Bandwidth/pixel (Hz)	202	1179	938	938
Scan time duration	2 min 34 sec	3 min 51 sec	3 min 41 sec	4 min 24 sec
Mode	2D	3D	3D	3D

Note:—SPIR indicates spectral presaturation with inversion recovery; NA, not applicable; TSE, turbo spin echo.

(FLAIRE).¹⁸ However, the posterior fossa remains a challenging area for MR imaging, and the quality of images and the sharpness of lesion visualization are not always optimal.²⁰ Yet, detecting posterior fossa lesions is essential for a diagnosis of MS and is 1 of the 4 areas of the CNS that must be explored according to the McDonald criteria.⁷ Lesion burden was reported to be highly correlated with long-term disability and lower sensory Functional System Scores.^{30,31}

The aim of our study was to evaluate the diagnostic value of an optimized 3D-FLAIR sequence at 3T to detect infratentorial MS lesions.

MATERIALS AND METHODS

Study Design

We conducted a prospective study (NCT 03108573) in a tertiary referral center (Fondation Ophtalmologique Adolphe de Rothschild, Paris, France) specializing in neurologic diseases. This study was approved by a national independent research ethics board and adhered to the tenets of the Declaration of Helsinki (institutional review board 2012-A00993–40). Signed informed consent was obtained from all subjects. This study follows the Standards for Reporting Diagnostic Accuracy Studies guidelines.³²

Twenty-seven patients were included. Inclusion criteria were older than 18 years of age with a confirmed diagnosis of MS as defined by the 2017 McDonald criteria.⁷ Patients with any MR imaging contraindication were not included. Exclusion criteria were insufficient quality for interpretation of any of the evaluated sequences and absence of our optimized 3D-FLAIR sequence with a TR of 8000 ms. Selection of patients is shown in the On-line Figure.

MR Imaging Protocol

All MRIs were performed on the same 3T Ingenia device (Philips Healthcare, Best, the Netherlands) with a 16-channel neurovascular coil. Each patient underwent the following standard MS protocol: axial turbo spin echo (TSE) T2WI and a standard 3D-FLAIR with factory settings as provided by the vendor. This protocol was completed by 2 supplementary sequences: a 3D-DIR

and an optimized 3D-FLAIR, which provided the best subjective contrast on a preliminary testing on 3 patients with MS not included in our study, as planned in the study design. We optimized this 3D-FLAIR by lengthening its TR to 8000 ms, modifying its TI value to allow satisfactory fluid suppression, increasing its turbo factor to partially compensate for the increased acquisition time induced by the higher TR, and, to maintain clinically acceptable examination duration, also setting its effective TE to be as short as possible.

The order of the sequences was randomized between participants to overcome a possible effect of contrast agent administration on lesion detection. An intravenous contrast injection of a single

dose of gadobutrol (Gadovist; Bayer Schering Pharma, Berlin, Germany) was performed for all patients at least 5 minutes before the MR imaging acquisition, as recommended by international guidelines.¹² Technical specifications are described in Table 1.

Image and Data Analysis

Two radiologists, blinded to patient identification, medical history, and lab results, independently read, in random order, the MR images. The first one was a senior neuroradiologist with 20 years of experience (P.K.), and the second was a junior radiologist with no experience in neurologic imaging (I.E.S.). Each of the 4 sequences from 1 patient was read separately and independently from the other sequences. Readers were not allowed to read >1 sequence of the same patient during the same reading session. A second reading was performed 3 weeks later. Discrepancies were resolved by a third radiologist specialized in neuroradiology with 7 years of experience (A.L.). All data were read on a dedicated workstation with the OsiriX imaging software (<http://www.osirix-viewer.com>).

The primary judgment criterion was the overall number of high-signal lesions detected in the posterior fossa. We also assessed the following MR imaging characteristics: the location of the lesions (either in the cerebellum or the brain stem); the length of the largest lesion in each location; and the confidence in the detection of the lesions, estimated as follows: 1 corresponding to a low confidence; 2, to a moderate-to-high confidence; and 3, to a very high confidence.

Signal and Contrast Properties

We measured the SNR using the National Electrical Manufacturers Association method,³³ which needed 2 images acquired within 5 minutes of each other with the exact same imaging parameters. Those 2 images were then subtracted to produce a third one. On each subtracted sequence for each patient, we placed 2 ROIs in the white matter of the right and left cerebellar hemispheres to measure their signal intensity (SI) and obtain the mean white matter SI (SI_{WM}). We took the SD of the value of the ROIs and extracted the average SD of the noise. For the contrast-to-noise ratio (CNR) of the lesions, we manually placed an ROI in each sequence for

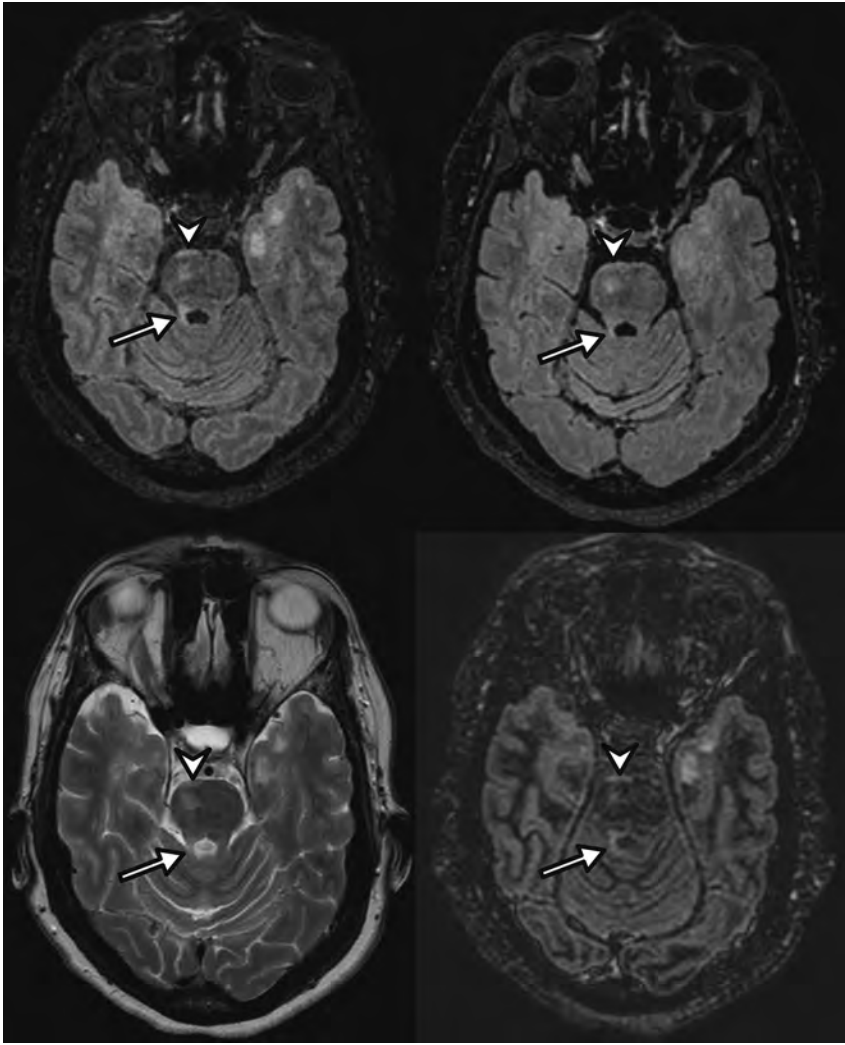


FIG 1. A 35-year-old woman with relapsing-remitting multiple sclerosis. 3D-optimized FLAIR (upper left), 3D standard FLAIR (upper right), axial T2WI (lower left), and 3D-DIR (lower right) MR imaging show a round lesion of the pons well-visualized on all sequences (arrowhead) and a lesion of the right superior cerebellar peduncle (arrow) more conspicuous on the optimized FLAIR sequence.

each patient in 2 nonenhancing lesions of significant size to measure their SI and obtain the mean lesion SI (SI_{lesion}). Those lesions had to be visible on all sequences and were the same on each sequence. Then, we calculated the SNR using the formula $SNR = \frac{SI_{WM} \times \sqrt{2}}{SD}$ and the CNR as follows: $CNR = \frac{SI_{\text{lesion}} - SI_{WM}}{SD}$.

Statistical Analysis

Analyses were conducted by a statistical analyst (J.E.M.) with 10 years of experience using R software, Version 3.3.2.³⁴ Categorical data were reported as number (percentage) as appropriate. Continuous data were reported as median with interquartile ranges or means \pm SD as appropriate. The nonparametric Wilcoxon test was used to compare the different MR images, using the Streitberg-Röhm algorithm in case of a tie. Because multiple tests were performed, the Bonferroni adjustment was used with an α level adjusted to a significance level of .005. *P* values $<$.05 were considered significant. The Cohen κ statistic

was used to assess inter- and intraobserver agreement for the MR imaging reading and was interpreted as follows: 0–0.20, poor agreement; 0.21–0.40, fair agreement; 0.41–0.60, moderate agreement; 0.61–0.80, good agreement; 0.81–1, almost perfect agreement.³⁵ The sample size was calculated on the basis of a minimum expected mean difference of 10% in detecting MS lesions between the optimized FLAIR and the T2WI and a common SD of 0.15. The statistical power was set at 0.9, and the significance criterion was set to .05, with a 2-tailed analysis.³⁶ Twenty-one patients would have been necessary for this statistical analysis. A final objective of 27 patients was set to anticipate secondary exclusions and unusable data.

RESULTS

Patient Characteristics

Twenty-seven patients with a confirmed diagnosis of MS (14 men and 13 women; mean age, 37 ± 10.7 years) were included. The mean Expanded Disability Status score was 3.2 ± 2.1 . The mean disease duration was 13.6 ± 9.2 years. The MS phenotype composition was as follows: 21 (78%) relapsing-remitting; 4 (15%) secondary-progressive; and 2 (7%) primitive-progressive.

Infratentorial Lesions

Of all 27 patients, 22 had at least 1 lesion in the posterior fossa detected with 1 of the 4 sequences, with a mean number of 5.6 ± 7.5 lesions per patient. There were 55, 57, 49, and 85 lesions in the cerebellum detected on T2WI, DIR, standard FLAIR, and optimized FLAIR, respectively. There were 102, 69, 63, and 108 lesions in the brain stem detected on T2WI, DIR, standard FLAIR, and optimized FLAIR, respectively. The largest lesion had a median length of 7.7 mm (interquartile range, 4.8–11.9 mm) and 9.2 mm (interquartile range, 5.9–12.0 mm) in the cerebellum and the brain stem, respectively.

Optimized FLAIR detected significantly more posterior fossa lesions than with T2WI, DIR, or standard FLAIR: 7.5 ± 9 versus 5.8 ± 8.6 ($P = .04$), 4.8 ± 7 ($P = .03$), and 4.1 ± 4.6 ($P = .03$), respectively, as shown on Figs 1 and 2. Subgroup comparisons are detailed in Table 2. Eight, 9, and 3 patients had no posterior fossa lesion detected with T2WI, DIR, and standard FLAIR, respectively, whereas they had at least 1 lesion detected with optimized FLAIR. Detailed intersequence comparisons are shown in Table 3.

The median values of the SNR and CNR were significantly higher with T2WI. The optimized FLAIR showed a higher CNR than DIR and standard FLAIR (Table 2).

The mean reading confidence index was significantly higher with

the optimized FLAIR sequence than with any other sequences: 2.8 versus 1.9 ($P = 5.10^{-6}$), 2.3 ($P = 5.10^{-3}$), and 2.0 ($P = 3.10^{-6}$) for T2WI, DIR, and the standard FLAIR sequences, respectively.

Inter- and Intraobserver Reproducibility

Interreader agreement was moderate for the overall number of lesions and for the cerebellum location and good for the brain stem location (κ values = 0.58, 0.49, and 0.67, respectively). Intraobserver agreement between the 2 readings was excellent for

the first reader and fair for the second reader (κ values = 0.90 and 0.33, respectively).

DISCUSSION

Our study showed that an optimized 3D-FLAIR sequence significantly improved the overall posterior fossa lesion detection in patients with MS, with a significantly higher reader-reported confidence, supporting a significantly higher number of detected lesions than would have normally been found with a T2WI, standard 3D-FLAIR with factory settings, or DIR sequence.

Many studies have tried to find the best MR image to accurately detect demyelinating encephalic lesions in patients with MS, such as T2WI,⁵ proton-density-weighted,¹⁵ 2D-FLAIR,^{19,37,38} magnetization transfer,²³ MPRAGE,²⁴ 3D-FLAIR,^{15,16,18,19,22} DIR,^{19,25-27} or PSIR.^{28,29} There have also been studies trying to improve the detection rate by combining sequences, such as the PT2³⁹ or FLAIR,⁴⁰ or by subtraction.¹⁹ However, we found only 1 study that specifically dealt with 3T 3D-FLAIR sequence optimization for identifying MS lesions by modifying the TE. In this study, the authors developed a 3D-FLAIREd with an iterative approach based on theoretic considerations. They obtained and analyzed a 3D spin-echo FLAIR with a longer contrast-equivalent TE than the effective TE of a 3D-FLAIR (600 versus 450 ms) without modifying the TR values held constant at 7000 ms. They showed that lesion recognition was improved in both supratentorial and infratentorial regions and that detection of cortical lesions increased with the 3D-FLAIREd.¹⁸ Our study is the first to evaluate the value of a FLAIR sequence with a long TR versus conventional 3D-FLAIR, axial T2WI, and DIR in the detection rate of infratentorial MS lesions specifically.

Our results are in agreement with those obtained by previously published studies, in which the FLAIR sequence

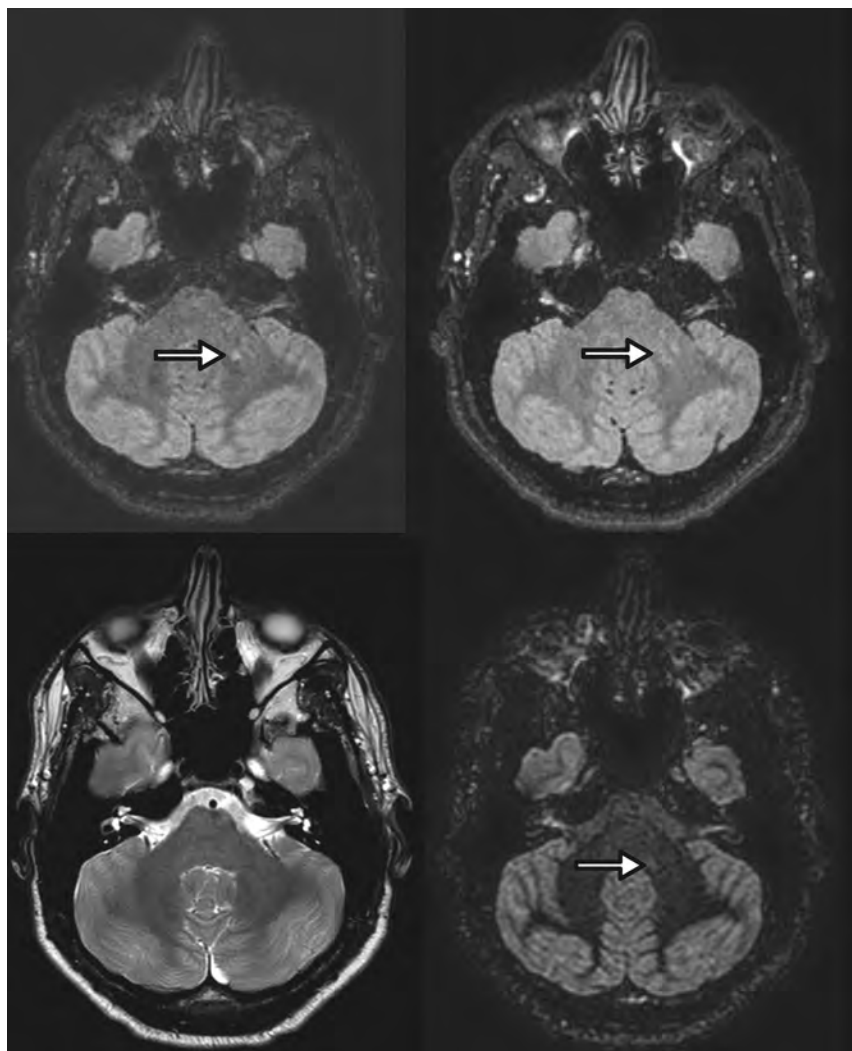


FIG 2. A 29-year-old woman with relapsing-remitting multiple sclerosis. 3D-optimized FLAIR (upper left), standard 3D-FLAIR (upper right), and 3D-DIR (lower right) MR imaging show a left middle cerebellar peduncle lesion not visible on the axial T2WI sequence (lower left). Note that the lesion is more conspicuous on the optimized FLAIR sequence.

Table 2: Description of the posterior fossa lesions and comparison of mean values of SNR and CNR

	T2	DIR	Standard FLAIR	Optimized FLAIR	T2/DIR ^a	T2/Standard FLAIR ^a	T2/Optimized FLAIR ^a	Standard FLAIR/DIR ^a	Optimized FLAIR/DIR ^a	Optimized FLAIR/Standard FLAIR ^a
Mean (SD) No. of lesions										
All locations	5.8 (8.6)	4.8 (7.0)	4.1 (4.6)	7.5 (9.0)	.6	.4	.04 ^b	.3	.03 ^b	.03 ^b
Cerebellum	2.0 (4.5)	2.2 (3.6)	1.8 (2.1)	3.5 (4.8)	.1	.05 ^b	7.10 ^{-4b}	.4	.01 ^b	.02 ^b
Brain stem	3.8 (4.8)	2.7 (3.9)	2.3 (2.8)	4.0 (4.9)	.2	.3	.3	.4	.2	.1
Mean SNR (SD)	112 (17.1)	16 (2.3)	34 (4.4)	29 (4.2)	5.10 ^{-5b}	8.10 ^{-5b}	7.10 ^{-5b}	2.10 ^{-3b}	3.10 ^{-3b}	.1
Mean CNR (SD)	45 (7.9)	9 (1.7)	11 (1.9)	14 (2.2)	4.10 ^{-4b}	4.10 ^{-4b}	6.10 ^{-4b}	.1	.01 ^b	.03 ^b

^a P value after comparison of the 2 groups with the nonparametric Wilcoxon test.

^b Significant differences after appropriate statistical correction.

Table 3: Number of patients with at least 1 lesion detected by 1 sequence only

	Patients with at Least 1 Lesion Detected			
	T2WI	DIR	Standard FLAIR	Optimized FLAIR
Patients with no lesion detected				
T2WI		1	5	8
DIR	2		6	9
Standard FLAIR	1	1		3
Optimized FLAIR	0	0	0	

was reported to depict more lesions than a conventional T2WI sequence.^{15,16,18,19,22,25,26,37} We did not find significant differences in the detection rate of infratentorial MS lesions among DIR, axial T2WI, and standard FLAIR, a finding concordant with the literature.^{19,25} However, we observed a significantly higher detection rate of MS lesions with the optimized FLAIR sequence than with the DIR sequence, as opposed to Wattjes et al,²⁶ who compared a DIR sequence with a FLAIR_{12,000} sequence. Moreover, optimized FLAIR detected at least 1 posterior fossa lesion in 8, 9, and 3 patients with no lesions detected on T2WI, DIR, and standard FLAIR, respectively, which is clinically very important because the posterior fossa is 1 of the 4 main locations taken into account for diagnosing MS.⁷ This might support earlier diagnosis and improve management of patients with MS. It might also be relevant for follow-up to avoid misclassifying patients as having no evidence of disease activity, which is increasingly considered the treatment goal.⁴¹

The posterior fossa is a challenging area for MR imaging. Image quality and sharpness of lesions are not always optimal, and the 2D-FLAIR sequence was historically reported as less sensitive than T2WI in this location,²⁰ mostly because of artifacts due to CSF and blood inflow or insufficient T2WI.³⁷ The use of 3D-FLAIR sequences overcomes these issues because they can achieve homogeneous CSF suppression, are minimally affected by artifacts,^{15,17,18} and provide a better resolution due to smaller slice thickness.¹⁹ The better performance of the optimized FLAIR sequence over the standard FLAIR may be explained by the intrinsic characteristics of the FLAIR sequence. The main parameters affecting the contrast of the FLAIR sequence are the TR, TE, TI, and flip angles. The TR seems to be the most relevant parameter to study because it is the main determinant of the intensity of the T2 signal. It is related to the T2 effect, and the augmentation of the effective TR attenuates the normal white matter signal, making lesions more easily depictable.^{18,42} We subjectively chose a TR of 8000 ms for our optimized 3D-FLAIR sequence because it provided the best subjective contrast on preliminary testing in our center. Most interesting, this value is very close to the TR of 7000 ms of the optimized FLAIRE sequence, which was considered as the most sensitive in the detection of MS lesions in both supra- and infratentorial regions¹⁸ and is close to the TR values of 8000–10,000 ms proposed to reach near-optimum contrast and high multisection efficiency as in a previous 2D-FLAIR optimization study at 1.5T.⁴²

A longer TR significantly increased the CNR in our series, allowing higher confidence in discriminating demyelinating lesions from normal-appearing white matter. We compared the

optimized FLAIR with the standard 3D-FLAIR with factory settings provided by most of the vendors at the time, with a TR of 4800 ms. This standard 3D-FLAIR is tested and normed on healthy volunteers and is not optimized to depict pathologic abnormalities of signal, even though it offers a good CSF suppression.

The DIR sequence, after attenuating the signal of both the white matter and the CSF,⁴³ was reported to allow a better delineation between white and gray matter and seems to be a sequence of choice for the detection of supratentorial lesions,^{19,25} especially the cortical ones. However, we did not note its superior detection in our study, probably due to increased noise at the CSF interfaces.

The most recent guidelines of the Consortium of Multiple Sclerosis Centers group¹² include a whole-brain 3D-T2-FLAIR and a 3D-T2WI, and the Magnetic Resonance Imaging in MS group¹⁰ recommended a standardized protocol, including axial T2WI and proton-density or T2-FLAIR sequences, and sagittal 2D or isotropic 3D-T2-FLAIR sequences. Our results suggest that the need for performing both a 3D-FLAIR sequence and a T2WI sequence for imaging of the posterior fossa in patients with MS might be questioned because no lesion seen on T2WI was missed on the optimized 3D-FLAIR either in our study or in the literature.¹⁵ We might advantageously reduce the MR imaging examination time by removing the T2WI sequence from our protocols.

Both the Consortium of Multiple Sclerosis Centers and the Magnetic Resonance Imaging in MS groups also recommend minimal technical specifications such as the maximum slice thickness, spatial resolution, voxel size, and duration time of the protocol. We believe that guidelines should also include recommendations on key parameters such as the TR. A TR of 8000 ms seems to be a good compromise for the FLAIR sequence, with reasonable acquisition time, good SNR and CNR, and a high confidence index, meaning an easier and more comfortable reading. The FLAIR sequence is widely available in all centers, and the modification of its parameters might be easily feasible on most clinical scanners. No extra time or specific software is needed for postprocessing, compared with other performant-sensitive sequences.^{39,40} It is simple and fits the clinical setting, and it may facilitate standardization of protocols among different centers worldwide.

An increase in the detection of posterior fossa lesions presents 2 major direct advantages for the patient: an earlier diagnosis and prognosis classification (especially for clinically or radiologically isolated syndromes)^{44,45} and a better follow-up due to an earlier diagnosis of new lesions. Those 2 elements have a deep impact on both the therapeutic decision-making and the patient's treatment.^{46,47} The presence of posterior fossa lesions is related to more substantial disability because the cerebellum and the brain stem serve critical functions and are often clinically eloquent locations.^{30,48,49} In our institution, we now routinely perform the optimized FLAIR sequence for suspected MS and MS follow-up.

Our study has some limitations: First, the results of the study are somewhat limited by the relatively small number of patients, and the results may be unique to the scanner and coil hardware used because no other systems were tested. Multicenter studies, including larger sample sizes, are necessary to confirm the results

and to also validate them for other MR imaging manufacturers. Second, we did not include other very effective sequences in depicting MS lesions, such as PSIR or other advanced techniques such as PT2, FLAIRE, or FLAIR.² Our study was not designed for this because its aim was to compare an optimized 3D-FLAIR with the most commonly used sequences used in clinical practice—that is, T2WI, standard 3D-FLAIR, and 3D-DIR.

Third, we compared 3D-FLAIR and DIR sequences with a 2D-T2WI and not a 3D-T2WI, which might have increased the detection rate of the T2WI. However, the specifications of the 2D-T2WI we used are compliant with international guidelines, and 2D-T2WI remains widely used to detect posterior fossa lesions worldwide.

Fourth, even though the examinations were anonymized and read in a random order and independently, the sequences tested had characteristics that could make them recognizable to readers, which could have led to a recognition bias.

Finally, we did not correlate results to pathology specimens and therefore cannot be sure that all lesions detected were, in fact, MS lesions. This correlation would have implied postmortem histologic examinations, which were not available.

CONCLUSIONS

Our study showed that an optimized 3D-FLAIR sequence significantly improved the overall posterior fossa lesion detection in patients with MS, with a significantly higher reader-reported confidence, supporting a significantly higher number of detected lesions than would have normally been found with a T2WI, standard 3D-FLAIR with factory settings, or DIR sequence.

ACKNOWLEDGMENTS

Laura McMaster provided professional English language medical editing of this article.

Disclosures: Jonathan El Methni—UNRELATED: Employment: Université Paris Descartes. Julien Savatovsky—UNRELATED: Payment for Lectures Including Service on Speakers Bureaus: Medtronic, Philips Healthcare, Sanofi, Biogen. Comments: Lecture fees were less than €1000; Travel/Accommodations/Meeting Expenses Unrelated to Activities Listed: Bayer Healthcare.

REFERENCES

1. Geurts JGG, Calabrese M, Fisher E, et al. **Measurement and clinical effect of grey matter pathology in multiple sclerosis.** *Lancet Neurol* 2012;11:1082–92 CrossRef Medline
2. Klaver R, De Vries HE, Schenk GJ, et al. **Grey matter damage in multiple sclerosis: a pathology perspective.** *Prion* 2013;7:66–75 CrossRef Medline
3. Messina S, Patti F. **Gray matters in multiple sclerosis: cognitive impairment and structural MRI.** *Mult Scler Int* 2014;2014:609694 CrossRef Medline
4. Pirko I, Lucchinetti CF, Sriram S, et al. **Gray matter involvement in multiple sclerosis.** *Neurology* 2007;68:634–42 CrossRef Medline
5. Runge VM, Price AC, Kirshner HS, et al. **Magnetic resonance imaging of multiple sclerosis: a study of pulse-technique efficacy.** *AJR Am J Roentgenol* 1984;143:1015–26 CrossRef Medline
6. McDonald WI, Compston A, Edan G, et al. **Recommended diagnostic criteria for multiple sclerosis: guidelines from the International Panel on the Diagnosis of Multiple Sclerosis.** *Ann Neurol* 2001;50:121–27 CrossRef Medline
7. Thompson AJ, Banwell BL, Barkhof F, et al. **Diagnosis of multiple sclerosis: 2017 revisions of the McDonald criteria.** *Lancet Neurol* 2018;17:162–73 CrossRef Medline
8. Barkhof F, Filippi M, Miller DH, et al. **Comparison of MRI criteria at first presentation to predict conversion to clinically definite multiple sclerosis.** *Brain J Neurol* 1997;120(Pt 11):2059–69 CrossRef Medline
9. Tintoré M, Rovira A, Martínez MJ, et al. **Isolated demyelinating syndromes: comparison of different MR imaging criteria to predict conversion to clinically definite multiple sclerosis.** *AJNR Am J Neuroradiol* 2000;21:702–06 Medline
10. Rovira A, Wattjes MP, Tintoré M, et al; MAGNIMS study group. **Evidence-based guidelines: MAGNIMS consensus guidelines on the use of MRI in multiple sclerosis-clinical implementation in the diagnostic process.** *Nat Rev Neurol* 2015;11:471–82 CrossRef Medline
11. Cotton F, Kremer S, Hannoun S, et al; Imaging Working Group of the Observatoire Français de la Sclérose en Plaques. **OFSEP, a nationwide cohort of people with multiple sclerosis: consensus minimal MRI protocol.** *J Neuroradiol* 2015;42:133–40 CrossRef Medline
12. Traboulsee A, Simon JH, Stone L, et al. **Revised Recommendations of the Consortium of MS Centers Task Force for a Standardized MRI Protocol and Clinical Guidelines for the Diagnosis and Follow-Up of Multiple Sclerosis.** *AJNR Am J Neuroradiol* 2016;37:394–401 CrossRef Medline
13. Simon JH, Li D, Traboulsee A, et al. **Standardized MR imaging protocol for multiple sclerosis: Consortium of MS Centers consensus guidelines.** *AJNR Am J Neuroradiol* 2006;27:455–61 Medline
14. Filippi M, Falini A, Arnold DL, et al; White Matter Study Group. **Magnetic resonance techniques for the in vivo assessment of multiple sclerosis pathology: consensus report of the white matter study group.** *J Magn Reson Imaging* 2005;21:669–75 CrossRef Medline
15. Gramsch C, Nensa F, Kastrup O, et al. **Diagnostic value of 3D fluid attenuated inversion recovery sequence in multiple sclerosis.** *Acta Radiol* 1987 2015;56:622–27 Medline
16. Tan IL, van Schijndel RA, Pouwels PJW, et al. **Serial isotropic three-dimensional fast FLAIR imaging: using image registration and subtraction to reveal active multiple sclerosis lesions.** *AJR Am J Roentgenol* 2002;179:777–82 CrossRef Medline
17. Barkhof F, Pouwels PJ, Wattjes MP. **The Holy Grail in diagnostic neuroradiology: 3T or 3D?** *Eur Radiol* 2011;21:449–56 CrossRef Medline
18. Polak P, Magnano C, Zivadinov R, et al. **3D FLAIRE: 3D fluid attenuated inversion recovery for enhanced detection of lesions in multiple sclerosis.** *Magn Reson Med* 2012;68:874–81 CrossRef Medline
19. Moraal B, Roosendaal SD, Pouwels PJW, et al. **Multi-contrast, isotropic, single-slab 3D MR imaging in multiple sclerosis.** *Eur Radiol* 2008;18:2311–20 CrossRef Medline
20. Gawne-Cain ML, O’Riordan JI, Thompson AJ, et al. **Multiple sclerosis lesion detection in the brain: a comparison of fast fluid-attenuated inversion recovery and conventional T2-weighted dual spin echo.** *Neurology* 1997;49:364–70 CrossRef Medline
21. Tan IL, Pouwels PJW, van Schijndel RA, et al. **Isotropic 3D fast FLAIR imaging of the brain in multiple sclerosis patients: initial experience.** *Eur Radiol* 2002;12:559–67 CrossRef Medline
22. Bink A, Schmitt M, Gaa J, et al. **Detection of lesions in multiple sclerosis by 2D FLAIR and single-slab 3D FLAIR sequences at 3.0 T: initial results.** *Eur Radiol* 2006;16:1104–10 CrossRef Medline
23. Iannucci G, Rovaris M, Giacomotti L, et al. **Correlation of multiple sclerosis measures derived from T2-weighted, T1-weighted, magnetization transfer, and diffusion tensor MR imaging.** *AJNR Am J Neuroradiol* 2001;22:1462–67 Medline
24. Nelson F, Poonawalla A, Hou P, et al. **3D MPRAGE improves classification of cortical lesions in multiple sclerosis.** *Mult Scler* 2008;14:1214–19 CrossRef Medline
25. Vural G, Keklikoglu HD, Temel S, et al. **Comparison of double inversion recovery and conventional magnetic resonance brain imaging in patients with multiple sclerosis and relations with disease disability.** *Neuroradiol J* 2013;26:133–42 CrossRef Medline

26. Wattjes MP, Lutterbey GG, Gieseke J, et al. **Double inversion recovery brain imaging at 3T: diagnostic value in the detection of multiple sclerosis lesions.** *AJNR Am J Neuroradiol* 2007;28:54–59 Medline
27. Geurts JJ, Pouwels PJ, Uitdehaag BM, et al. **Intracortical lesions in multiple sclerosis: improved detection with 3D double inversion-recovery MR imaging.** *Radiology* 2005;236:254–60 CrossRef Medline
28. Nelson F, Poonawalla AH, Hou P, et al. **Improved identification of intracortical lesions in multiple sclerosis with phase-sensitive inversion recovery in combination with fast double inversion recovery MR imaging.** *AJNR Am J Neuroradiol* 2007;28:1645–49 CrossRef Medline
29. Favaretto A, Poggiali D, Lazzarotto A, et al. **The parallel analysis of phase sensitive inversion recovery (PSIR) and double inversion recovery (DIR) images significantly improves the detection of cortical lesions in multiple sclerosis (MS) since clinical onset.** *PLoS One* 2015;10:e0127805 CrossRef Medline
30. Minneboo A, Barkhof F, Polman CH, et al. **Infratentorial lesions predict long-term disability in patients with initial findings suggestive of multiple sclerosis.** *Arch Neurol* 2004;61:217–21 CrossRef Medline
31. Quattrocchi CC, Cherubini A, Luccichenti G, et al. **Infratentorial lesion volume correlates with sensory functional system in multiple sclerosis patients: a 3.0-Tesla MRI study.** *Radiol Med* 2010;115:115–24 CrossRef Medline
32. Bossuyt PM, Reitsma JB, Bruns DE, et al; STARD Group. **STARD 2015: an updated list of essential items for reporting diagnostic accuracy studies.** *Radiology* 2015;277:826–32 CrossRef Medline
33. Goerner FL, Clarke GD. **Measuring signal-to-noise ratio in partially parallel imaging MRI.** *Med Phys* 2011;38:5049–57 CrossRef Medline
34. The R Foundation. **The R Project for Statistical Computing.** <https://www.R-project.org>. Accessed April 23, 2017
35. Landis JR, Koch GG. **An application of hierarchical kappa-type statistics in the assessment of majority agreement among multiple observers.** *Biometrics* 1977;33:363–74 CrossRef Medline
36. Eng J. **Sample size estimation: how many individuals should be studied?** *Radiology* 2003;227:309–13 CrossRef Medline
37. Okuda T, Korogi Y, Shigematsu Y, et al. **Brain lesions: when should fluid-attenuated inversion-recovery sequences be used in MR evaluation?** *Radiology* 1999;212:793–98 CrossRef Medline
38. Hashemi RH, Bradley WG Jr, Chen DY, et al. **Suspected multiple sclerosis: MR imaging with a thin-section fast FLAIR pulse sequence.** *Radiology* 1995;196:505–10 CrossRef Medline
39. Gaitán MI, Yañes P, Sati P, et al. **Optimal detection of infratentorial lesions with a combined dual-echo MRI sequence: “PT2.”** *Mult Scler* 2016;22:1367–70 CrossRef Medline
40. Wiggermann V, Hernández-Torres E, Traboulsee A, et al. **FLAIR2: a combination of FLAIR and T2 for improved MS lesion detection.** *AJNR Am J Neuroradiol* 2016;37:259–65 CrossRef Medline
41. Bevan CJ, Cree BA. **Disease activity free status: a new end point for a new era in multiple sclerosis clinical research?** *JAMA Neurol* 2014;71:269–70 CrossRef Medline
42. Rydberg JN, Riederer SJ, Rydberg CH, et al. **Contrast optimization of fluid-attenuated inversion recovery (FLAIR) imaging.** *Magn Reson Med* 1995;34:868–77 CrossRef Medline
43. Redpath TW, Smith FW. **Technical note: use of a double inversion recovery pulse sequence to image selectively grey or white brain matter.** *Br J Radiol* 1994;67:1258–63 CrossRef Medline
44. Wattjes MP, Harzheim M, Kuhl CK, et al. **Does high-field MR imaging have an influence on the classification of patients with clinically isolated syndromes according to current diagnostic MR imaging criteria for multiple sclerosis?** *AJNR Am J Neuroradiol* 2006;27:1794–98 Medline
45. Filippi M, Rocca MA, Ciccarelli O, et al; MAGNIMS Study Group. **MRI criteria for the diagnosis of multiple sclerosis: MAGNIMS consensus guidelines.** *Lancet Neurol* 2016;15:292–303 CrossRef Medline
46. Noyes K, Weinstock-Guttman B. **Impact of diagnosis and early treatment on the course of multiple sclerosis.** *Am J Manag Care* 2013;19(17 Suppl):s321–31 Medline
47. Tur C, Thompson AJ. **Early accurate diagnosis crucial in multiple sclerosis.** *Practitioner* 2015;259:21–7, 2–3 Medline
48. Tintore M, Rovira A, Arrambide G, et al. **Brainstem lesions in clinically isolated syndromes.** *Neurology* 2010;75:1933–38 CrossRef Medline
49. Preziosa P, Rocca MA, Mesaros S, et al. **Relationship between damage to the cerebellar peduncles and clinical disability in multiple sclerosis.** *Radiology* 2014;271:822–30 CrossRef Medline

Impact of Skull Defects on the Role of CTA for Brain Death Confirmation

 D.M. Nunes,  A.C.M. Maia Jr,  R.C. Boni, and  A.J. da Rocha

ABSTRACT

BACKGROUND AND PURPOSE: Intracranial pressure modifications caused by a skull defect, such as craniectomy or craniotomy, may change the hemodynamics and decrease the accuracy of CTA to confirm brain death. This study aimed to evaluate the impact of a skull defect and the interpretation criteria of images on this diagnostic test.

MATERIALS AND METHODS: A series of consecutive patients with a clinical diagnosis of brain death underwent CTA (case group), while the control group comprised patients with acute ischemic stroke in the same period. CTA criteria adopted to confirm brain death were the absence of opacification of the M4 branches and internal cerebral veins. The evaluation also included the presence of “stasis filling.” Cases were stratified as intact skull, craniotomy, and craniectomy. Three neuroradiologists evaluated all examinations independently.

RESULTS: In the case group, according to the Frampas criteria, the sensitivity of CTA to confirm brain death was 95.5% in patients with intact skull, 87.5% with craniotomy, and 60% with craniectomy. False-negative diagnoses of brain death were 15.6%, related to stasis filling in 71.4% ($P < .001$). However, according to the “modified Frampas criteria,” the sensitivity of CTA to confirm brain death was 100% in patients with intact skull, 93.8% with craniotomy, and 80% with craniectomy. False-negative diagnoses of brain death were found in 6.2% of patients, and there was no stasis filling. CTA showed 100% specificity in the control group. There were no disagreements among observers.

CONCLUSIONS: CTA had a high diagnostic accuracy and reproducibility to confirm brain death in patients with an intact skull. The modified Frampas criteria increased the sensitivity of CTA, particularly in patients with a skull defect. A concurrent skull defect, especially craniectomy, can decrease the sensitivity of CTA to confirm brain death.

ABBREVIATIONS: BD = brain death; ICM = iodinated contrast medium; ICV = internal cerebral vein; SD = skull defect; SF = stasis filling

Brain death (BD) is the result of diffuse, progressive, and irreversible brain damage clinically characterized by a deep unresponsive coma and the absence of spontaneous ventilation and brain stem reflexes.¹⁻³ Although the clinical criteria for the diagnosis of brain death assess the absence of brain stem functions, some countries have used the concept of global brain death, adding ancillary tests to show the absence of brain circulation or absence of electric activity or absence of metabolic activity, including the cerebral hemispheres.⁴⁻⁶ Circulatory evaluation is commonly used because it is subject to less pharmacologic inter-

ference (eg, the use of sedatives and occurrence of severe electrolyte and metabolic disorders).^{7,8}

Conventional angiography is the criterion standard to evaluate the circulatory system.⁹⁻¹¹ However, because this method is invasive, is not widely available, and requires specialized neuro-radiologic expertise to perform and interpret the results, other alternatives have been investigated, including CTA. The accuracy of CTA for a BD diagnosis was validated by Frampas et al¹² through the absence of intracranial arterial opacification of the distal branches (M4) and internal cerebral vein (ICV), both evaluated in the venous series of CTA, showing moderate sensitivity (85.7%) and high specificity (100%). Other studies have confirmed similar accuracies.¹³⁻¹⁸ Nevertheless, the interpretation criteria of the images used by Frampas et al¹² limited the applicability of CTA to confirm BD due to patients with false-negative findings (14.3%).

According to the Monro-Kellie doctrine, intracranial pressure is the result of the balance among the CSF, blood, and brain parenchyma inside the skull, a rigid compartment. Increased intra-

Received March 2, 2019; accepted after revision May 13.

From the Section of Neuroradiology (D.M.N., A.C.M.M.Jr., A.J.d.R.) and Section of Organ Procurement Organization (R.C.B.), Santa Casa de Misericórdia de São Paulo, São Paulo, SP, Brazil.

Please address correspondence to Douglas Mendes Nunes, MD, Santa Casa de Misericórdia de São Paulo, Serviço de Diagnóstico por Imagem, Rua Dr. Cesário Motta Junior 112, Vila Buarque, São Paulo, SP, Brazil, 01221-020; e-mail: douglasmendesnunes@gmail.com

<http://dx.doi.org/10.3174/ajnr.A6100>

cranial pressure results in pressure compensation through the displacement of the CSF to the spinal subarachnoid space, followed by intracranial vascular collapse. This collapse occurs initially in the venous compartment because of the increased compliance and lower intraluminal pressure and then in the arterial compartment, with consequent brain damage.¹⁹⁻²¹

Therefore, a skull defect (SD) in patients with suspected BD, such as extensive fracture or operation (craniectomy or craniotomy), may decrease the intracranial pressure, changing the intracranial hemodynamics and decreasing the diagnostic accuracy of ancillary tests that evaluate brain circulation.^{10,22,23} However, there are no specific studies evaluating the accuracy of CTA for BD confirmation in patients with SD, to our knowledge.

Our aim was to evaluate the impact of SDs and the interpretation criteria of imaging on the accuracy of CTA for BD confirmation.

MATERIALS AND METHODS

Study Design

This cross-sectional and observational study was conducted at a single hospital center (Santa Casa de Misericórdia de São Paulo) between June 2012 and July 2014. A case series of consecutive patients with a clinical diagnosis of BD (reference standard determination of BD) was evaluated according to the legal requirement,²⁴ the Brazilian BD protocol, which consists of 2 clinical examinations and some confirmatory ancillary tests, namely, transcranial Doppler (47 patients), conventional angiography (2 patients), and nuclear medicine (1 patient). In addition to the Brazilian BD protocol, these patients underwent CTA, the results of which did not interfere with the final diagnosis regarding BD. Due to the similarity between the stroke and BD protocols, the control group consisted of 22 patients with ischemic stroke who were candidates for thrombolysis and underwent CTA before any therapeutic proposal, in the same period. The institutional review board approved this study.

All patients older than 2 years of age with a BD clinical diagnosis, evaluated according to the legal requirements²⁴ of the Brazilian BD protocol, were enrolled after their legal guardian and 2 witnesses agreed to participate in the study by signing the free and informed consent form. Patients were excluded when they had a mean arterial pressure lower than 80 mm Hg, if the guardians did not authorize study enrollment, if contraindications or the inability to receive intravenous iodinated contrast medium (ICM) was present, or if the technical quality of the images was deemed inadequate. Demographic and clinical data, including age, sex, cause of BD, and the time interval between the BD diagnosis and CTA, were collected in a data base.

Technical Data

All examinations were acquired in a 64–detector row CT scanner (Version v2.6.2.22004; Brilliance™ CT 64-channel scanner; Philips Healthcare, Best, the Netherlands) with a minimum dose of ionizing radiation²⁵ following the CTA protocol proposed by Frampas et al.¹²

After lateral topography, 3 similar acquisitions were planned

starting at the C1–C2 level to the cranial vertex. The first acquisition was an NCCT scan (120 kV; 350 mA). Iso-osmolar, nonionic intravenous ICM (iopromide, Ultravist 300; Bayer HealthCare, Berlin, Germany) was injected through the right antecubital vein at a rate of 4–6 mL/s using a dual-head power injector (Medrad Stellant® D, Bayer HealthCare, Indianola, Pennsylvania) and a 16- to 22-ga catheter, with a pressure limit of 325 psi, depending on the age range. The total volume administered throughout the protocol was calculated on the basis of the estimated weight of the patient (2.0 mL/kg, reaching a maximum of 50 mL). The second (arterial) and third (venous) acquisitions (120 kV, 185 mAs, 0.67-cm thickness, 0.33-cm increments, FOV of 450 mm, and automatic settings for pitch and release) were performed, starting 20 and 60 seconds after the ICM injection commenced.

Image Analysis

To evaluate hemodynamic repercussions resulting from the SD, we divided the patients into 2 different groups: the intact skull and SD groups. The patients with SDs were divided into 2 subgroups, those with craniotomy and craniectomy.

The NCCT series confirmed the adequate passage of intravascular ICM in all patients by identifying opacification of the superficial temporal arteries and upper orbital veins during the examination as well as differentiating between spontaneously hyperattenuating vascular content and delayed, weak, persistent, and progressive vascular opacification (pseudo-subarachnoid hemorrhage versus true vascular opacification).

The arterial and venous series enabled the assessment of vessel opacification in the intracranial arterial and venous compartments via CTA based on MIP postprocessing algorithms (thickness: 10 mm) in workstation (Extended Brilliance™ Workspace, Version 3.5.0.2250; Philips Healthcare).

The progressive opacification of the intracranial arterial compartment between early (arterial) and delayed (venous) acquisitions of CTA was analyzed. The delayed, weak, persistent, and progressive opacification of the intracranial arterial compartment found between early (arterial) and delayed (venous) acquisitions of CTA is known as “stasis filling” (SF). This phenomenon is commonly observed in angiographic studies.^{10,26,27}

Three neuroradiologists with experience in the interpretation of CTA studies (9, 22, and 23 years, respectively) evaluated all the examinations independently using simultaneous viewing of images of the NCCT, arterial (early), and venous (delayed) CTA series. These findings were assessed to generate a single consensus report, which was compared with the BD clinical diagnosis (reference standard determination of BD).

Two sets of criteria were used to confirm BD by CTA. The original criteria proposed by Frampas et al,¹² which consist of the absence of opacification of the M4 branches and ICV, both evaluated in the venous series of the CTA; and another set, called in this study the “modified Frampas criteria,” consisting of the absence of opacification of the M4 branches in the arterial phase and ICV in the venous phase of the CTA. The rationale for using these modified criteria is to avoid false-negative findings due to SF because opacification of the intracranial arterial compartment was evaluated in the arterial phase of CTA.

Characterization of the groups according to the presence and type of skull defect^a

Variable	Controls, ISk (n = 22)	Patients with BD			P Value
		ISk (n = 22)	Craniotomy (n = 16)	Craniectomy (n = 10)	
Age (yr)	57.6 ± 16.4	42.8 ± 21.9	43.7 ± 18.8	47.4 ± 9.2	.811
Male sex	12 (54.5)	13 (59.1)	8 (50.0)	7 (70.0)	.600
Etiology					.287
SAH	0 (0.0)	6 (27.3)	8 (50.0)	3 (30.0)	
TBI	0 (0.0)	4 (18.2)	4 (25.0)	5 (50.0)	
HS	0 (0.0)	4 (18.2)	1 (6.3)	0 (0.0)	
IS	22 (100)	4 (18.2)	0 (0.0)	0 (0.0)	
Tumor	0 (0.0)	1 (4.5)	2 (12.5)	1 (10.0)	
GW	0 (0.0)	1 (4.5)	1 (6.3)	0 (0.0)	
Other	0 (0.0)	2 (9.1)	0 (0.0)	1 (10.0)	
Time interval from BD to CTA (min)	—	659 (274–964)	670 (269–1013)	483 (236–713)	.618

Note:—SAH indicates subarachnoid hemorrhage; TBI, traumatic brain injury; HS, hemorrhagic stroke; IS, ischemic stroke; GW, gunshot wound; ISk, intact skull; BD, brain death; —, no data.
^aData are presented as No. (%), except for age (mean ± SD) and time (median and quartile). P values are for comparison of the subgroups (ISk, craniotomy, and craniectomy).

Statistical Analysis

Categorical variables were described by the absolute and relative frequencies and were compared using the χ^2 test. The age and time interval between the clinical diagnosis of BD and CTA were assessed for normality using graphic methods and skewness and kurtosis values. Age was described using means and standard deviations and was compared using the Student *t* test for independent samples. The time interval was described using medians and quartiles and was compared using the Mann-Whitney test.

The accuracy of CTA in each group according to the presence and type of SD was determined using contingency tables and by calculating the sensitivity, specificity, and positive and negative predictive values. Interobserver agreement was evaluated using the Cohen κ , with the following interpretation: <0, no agreement; 0–0.19, very poor agreement; 0.20–0.39, poor; 0.40–0.59, moderate; 0.60–0.79, high; and 0.80–1.00, very high agreement.

All tests were 2-tailed, and *P* values < .05 were considered significant. Statistical analysis was performed using R statistical and computing software (<http://www.r-project.org>), SPSS (Version 24.0; IBM, Armonk, New York), and MedCalc for Windows (Version 15.2.0.0; MedCalc Software, Mariakerke, Belgium).

RESULTS

Seventy-two patients were evaluated, with 2 patients in the case group excluded because of poor image quality (poor contrast). Thus, 70 patients were included in the final analysis. The mean age of the sample was 48.3 ± 18.9 years (range, 2–84 years), and 57.1% were men. Forty-eight patients in the case group were diagnosed with BD. By contrast, 22 patients in the control group were candidates for thrombolysis to treat ischemic stroke. The patients in the case group were comparatively younger (44.0 ± 18.6 versus 57.6 ± 16.4 years; *P* = .005), but no significant differences were found in sex between the groups (58.3% versus 54.5%; *P* = .766).

The initial causes of coma were aneurysmal subarachnoid hemorrhage (*n* = 17, 35.4%), head trauma (*n* = 13, 27.1%), cerebral hemorrhage (*n* = 5, 10.4%), brain tumor (*n* = 4, 8.3%), ischemic stroke (*n* = 4, 8.3%), and gunshot wound (*n* = 2, 4.2%). Three other cases (6.3%) involved hydrocephalus due to ventriculoperitoneal shunt malfunction, hypoxic-ischemic encephalopathy after cardiorespiratory arrest due to respiratory causes, and a postoperative complication of Chiari malformation type I.

Twenty-six patients presented with SDs (16 craniotomies and 10 craniectomies). The median time interval between the final declaration of BD and CTA was 641 minutes (interquartile range, 269–883 minutes). Stratified analysis according to the presence and type of SD indicated no significant differences in age, sex, BD etiology, or the time interval between the declaration of BD and CTA. None of the patients in the control group had an SD (Table).

The 48 included patients in the case group were stratified according to the presence and type of SD. CTA demonstrated brain circulation arrest, defined according to the criteria of Frampas et al,¹² in 41 patients (41/48; sensitivity: 85.4% [95% CI, 72.2–93.9]). Among those with an intact skull, CTA was consistent with BD in 21 patients (21/22; sensitivity: 95.5% [95% CI, 77.2–99.9]). For those with an SD, CTA was consistent with BD in 20 patients (20/26; sensitivity: 76.9% [95% CI, 56.4–91.0]). The patients with an SD were subdivided into the craniotomy and craniectomy groups. CTA was consistent with BD in 14 patients with craniotomy (14/16; sensitivity: 87.5% [95% CI, 61.7–98.5]) and 6 patients with craniectomy (6/10; sensitivity: 60.0% [95% CI, 26.2–87.8]). The categorization of patients with BD according to the criteria of Frampas et al,¹² is summarized in Fig 1.

SF was diagnosed in 28 patients (28/45, 62.2%). Among these, 11 patients (11/20, 55.0%) had an intact skull, 10 patients (10/15, 66.7%) had undergone craniotomy, and 7 patients (7/10, 70.0%) had undergone craniectomy (*P* = .390).

Seven patients (7/48 = 14.6%) did not have a BD diagnosis from CTA using the criteria proposed by Frampas et al.¹² Among these, 5 patients (5/7, 71.4%) presented with SF (*P* < .001) and 2 patients (2/7, 28.6%) with craniectomy presented with arterial opacification of the distal branches (M4) in the arterial (early) acquisition of CTA. The false-negative CTA results were due to the SF phenomenon in 1 patient (1/20, 5.0%) with an intact skull, 2 patients (2/15, 13.3%) with craniotomy, and 2 patients (2/10, 20.0%) with craniectomy (*P* = .208) (Fig 2).

However, when the so-called modified Frampas criteria were applied, CTA demonstrated brain circulatory arrest in 45 patients (45/48; sensitivity: 93.8% [95% CI, 82.8–98.7]). Among those with an intact skull, CTA was consistent with BD in 22 patients (22/22; sensitivity: 100.0% [95% CI, 84.6–100.0]). For those with an SD, CTA was consistent with BD in 23 patients (23/26; sensi-

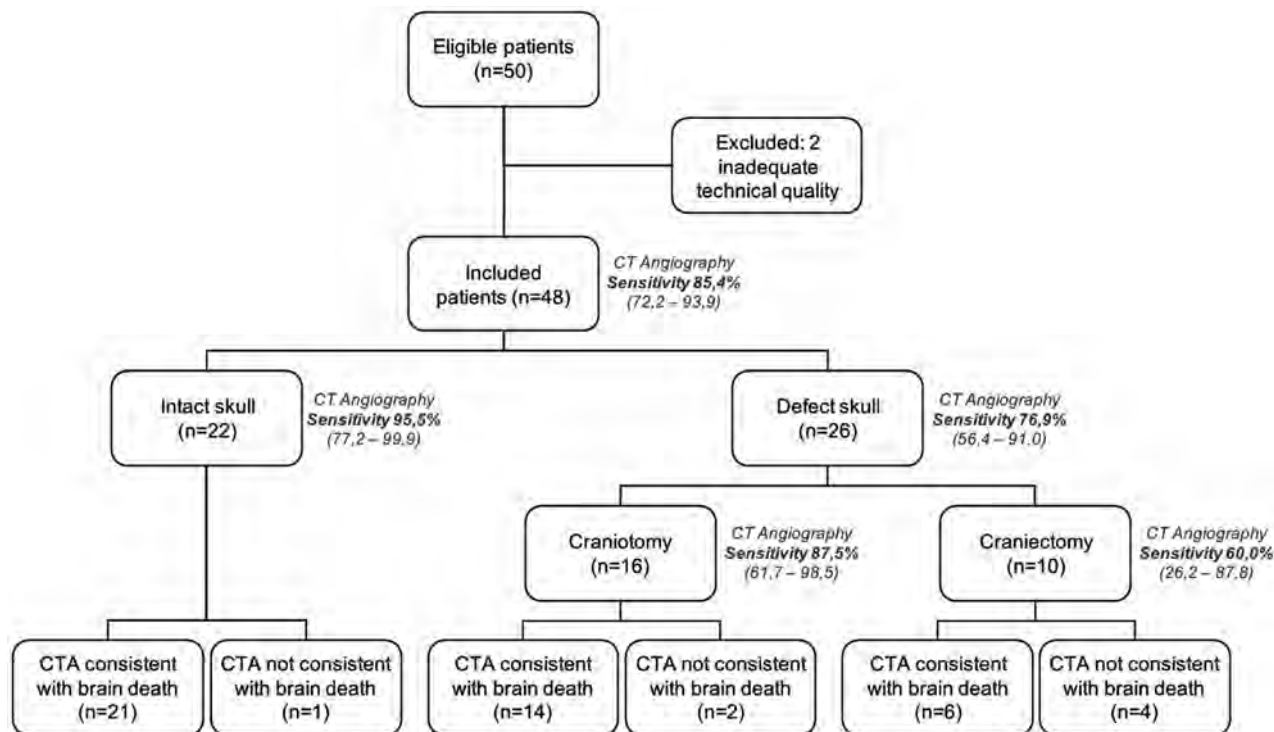


FIG 1. Flow chart of patients with a clinical diagnosis of brain death who underwent a CTA protocol proposed by Frampas et al,¹² according to the presence and type of skull defect. Application of the interpretation criteria of the images proposed by Frampas et al.

tivity: 88.5% [95% CI, 69.8–97.6]). The patients with an SD were subdivided into the craniotomy and craniectomy groups. CTA was consistent with BD in 15 patients with craniotomy (15/16; sensitivity: 93.8% [95% CI, 69.8–99.8]) and 8 with craniectomy (8/10; sensitivity: 80.0% [95% CI, 44.4–97.5]). The categorization of patients with BD according to the modified Frampas criteria is summarized in Fig 3.

Even with these modified criteria, 3 patients (3/48, 6.2%) did not have a BD diagnosis using CTA. These patients with false-negative findings of BD presented with arterial opacification of the distal branches (M4) in the arterial (early) acquisition of CTA: 1 patient (1/3, 33.3%) with craniotomy and 2 patients (2/3, 66.6%) with craniectomy.

There was a significant trend ($P = .037$) toward higher false-negative rates with more extensive SDs. Only 1 patient with craniectomy (1/45, 2.2%) showed opacification of the M4 branches and ICV in the arterial and venous series, respectively; in both, CTA criteria for BD were analyzed.

No association was found between the false-negative results and time interval between the diagnosis of BD and performance of CTA. The median time was 704 minutes (interquartile range 247–1157 minutes) among the cases with an incorrect diagnosis by CTA and 641 minutes (interquartile range 270–857 minutes) among the cases with a correct diagnosis ($P = .405$). Moreover, the percentage of incorrect diagnoses by CTA did not differ significantly among the time quartiles: first quartile, 93–270 minutes (2/12, 16.7%); second quartile, 270–641 minutes (1/13, 7.7%); third quartile, 641–857 minutes (1/11, 9.1%); fourth quartile, 857–1577 minutes (3/12, 25.0%) ($P = .551$). These results indicated that the accuracy of CTA is not affected by the time between the diagnosis of BD and the performance of CTA.

The specificity of CTA to confirm BD was 100% in patients with an intact skull—that is, no false-positive cases were found. The specificity in patients with SDs could not be estimated because the control group included no patient with an SD. There were no disagreements in the CTA analysis among the evaluators, resulting in a perfect Cohen κ of 1.0.

DISCUSSION

Despite the heterogeneity of protocols from CTA to confirm BD, the scientific literature has confirmed that CTA is a reliable, safe, fast, accessible, less invasive, reproducible, and auditable alternative ancillary confirmatory test in patients with the clinical criteria of BD.^{12-17,27-33} CTA has become increasingly common in the diagnosis of cerebral circulatory arrest and has already been licensed for use in many countries, such as Canada, Austria, Switzerland, France, the Netherlands, and Croatia.³⁴

Frampas et al¹² demonstrated the occurrence of cerebral circulatory arrest using CTA with moderate sensitivity (85.7%) and high specificity (100%), both by the absence of M4 branch and ICV opacification. Our study confirmed the reproducibility and diagnostic accuracy of CTA using the same criteria of 4 points proposed by Frampas et al,¹² with a similar sensitivity (85.4%), positive predictive value of 100%, and absence of disagreement in the CTA analysis among the evaluators.

As Leclerc et al³⁰ described and later studies have confirmed,^{13,31} the absence of ICV opacification constitutes the earliest and most sensitive (98.1%) finding to confirm the diagnosis of BD with CTA.¹² Our study also corroborated the high sensitivity (97.98%) of the absence of ICV opacification. However, the exclusive evaluation of the intracranial venous compartment for the diagnostic documentation of BD with CTA should be made

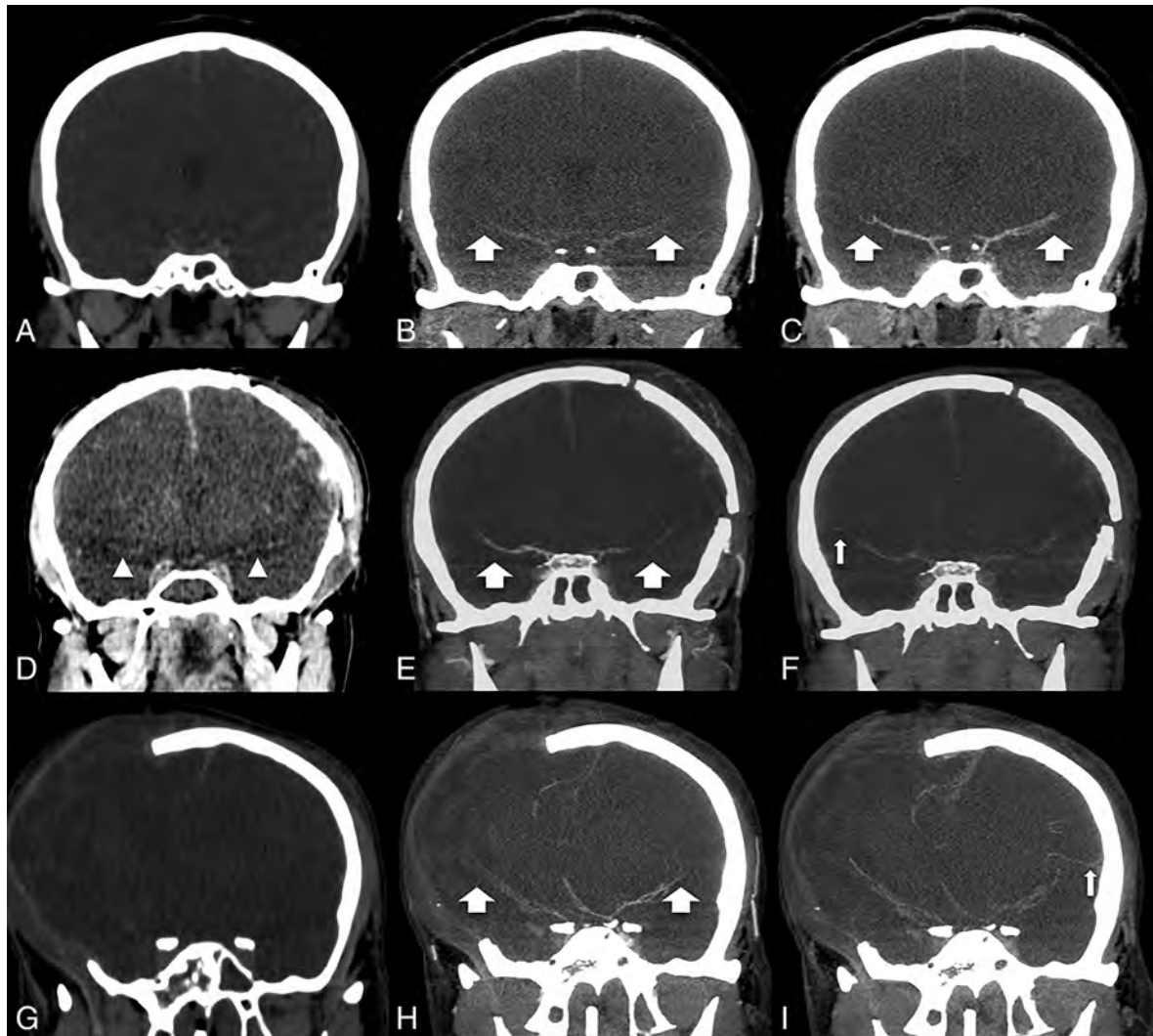


FIG 2. Comparison of CT images without contrast medium (A, D, and G) in the arterial (B, E, and H) and venous (C, F, and I) phases of CTA (MIP reformations in coronal plane) from 3 distinct patients with a brain death clinical diagnosis. In a patient with an intact skull (*upper row, A–C*), opacification was observed in the M1–M2 branches (*broad arrows*) in the arterial (B) and venous (C) phases and was more intense in the late phase. In a patient with craniotomy (*middle row, D–F*), one can appreciate the relative hyperattenuation of both M1 branches mimicking vascular opacification in noncontrast CT (*arrowheads* in D). Opacification was observed in both M2 branches (*broad arrows* in the arterial phase, E) and the right M3 branch in the venous phase (*thin arrow* in F), a phenomenon known as stasis filling. In a patient presenting with craniectomy (*lower row, G–I*), opacification was observed in both M2 branches (*broad arrows* in the arterial phase, H), the right M3 branch, and the left M4 branch in the venous phase (*thin arrow* in I) due stasis filling, a false-negative case of BD.

with caution, particularly among patients with intracranial hypertension, possibly reducing the specificity of the method. Moreover, the occurrence of deep cerebral venous thrombosis should always be considered to avoid possible false-positive results.

The protocol for BD diagnosis advocated by Frampas et al¹² includes image acquisitions of NCCT and biphasic CTA. Alternatively, Sawicki et al¹⁸ proposed optimizing the CTA technique by performing a single series with an acquisition delay of 40 seconds after the initiation of intravenous ICM infusion. Our study indicated that the maximum progression of the ICM in the intracranial vascular bed occurs during the late acquisition of CTA (venous phase), particularly among patients with concurrent SDs. However, the isolated evaluation of the late phase of CTA potentially limits the differentiation of spontaneously hyperattenuating vascular content, which was often found in our patients with extensive intra- and extracranial edema (pseudo-subarachnoid

hemorrhage versus true vascular opacification) because of the SF. This study reinforces the importance of the protocol proposed by Frampas et al¹² to avoid mistakes in diagnostic interpretation, thereby enabling comparisons between early and late acquisitions and providing reliable information for the correct evaluation of vascular opacification. The optimization of the interpretation criteria of the images proposed by Frampas et al¹² called the modified Frampas criteria, which consist of the absence of opacification of the M4 branches in the arterial phase and ICV in the venous series of the CTA, decreased the number of patients with false-negative findings due to a reduced influence of SF (which is usually present in the arteries during the venous phase), particularly with an SD.

Hemodynamic changes resulting from an SD might represent a confounding factor in the context of BD,^{10,22} thereby necessitating detailed studies to define the limits of the inter-

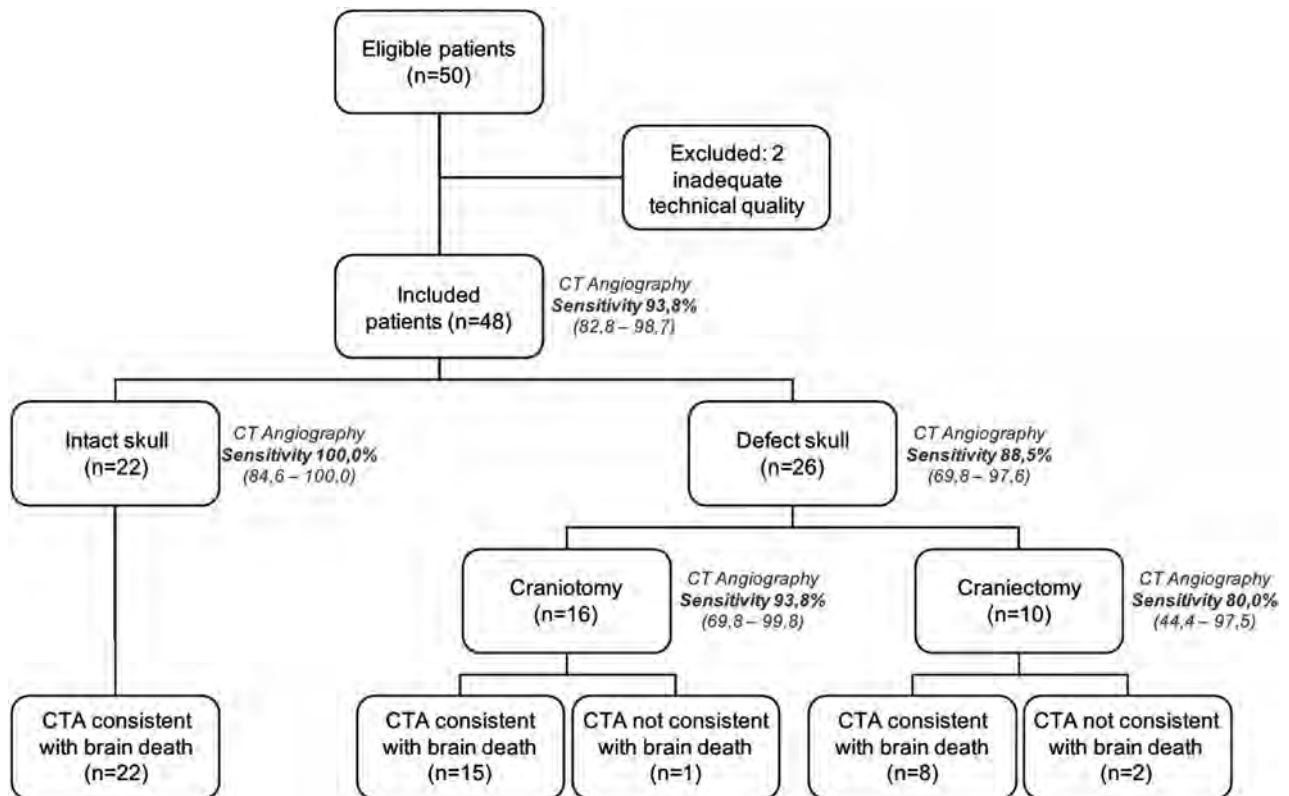


FIG 3. Flow chart of patients with a clinical diagnosis of brain death who underwent the CT angiography protocol proposed by Frampas et al, according to the presence and type of skull defect. Application of the interpretation criteria of the images of the modified Frampas criteria.

pretation for clinical purposes. Two distinct scenarios have been associated with the occurrence of false-negative results during the confirmation of BD in CTA studies: concomitant SD and acute hypoxic-ischemic encephalopathy after cardiorespiratory arrest.^{12,13,18,22,23,34} Our study confirmed that patients with an intact skull had high sensitivity and specificity for confirming BD by CTA, especially when the modified Frampas criteria were used for interpretation of the images, with results similar to those of conventional angiography (the criterion standard). There is a tendency for diagnostic errors to confirm BD by CTA (false-negative results) in patients with DS, particularly craniectomy, when the interpretation criteria of the images of Frampas et al¹² were used, probably because of lower intracranial pressure.³⁵⁻³⁷

First described in studies involving conventional angiography,^{10,26} the weak, slow, persistent, and progressive opacification of the intracranial arterial branches by ICM is known as SF.²⁶ This finding stems from the progression of intravascular ICM in a high-resistance distal vascular bed without the ability to perfuse the brain parenchyma.^{13,15,38} Recent studies using CTA have indicated a high prevalence of this finding, varying between 45% and 59% of all patients with confirmed BD.^{17,29,38} The present results indicated an intermediate rate (62.2%) of SF in the total sample when the criteria of Frampas et al¹² were used for interpretation of the images. The incorrect diagnosis of BD by CTA was meaningfully more common in patients with SF. Despite the small number of cases, this problem tends to occur more frequently in patients with SDs, especially those who have undergone craniectomy, with or without opacification of the venous compartment including the ICM. The interpretation of the images

according to modified Frampas criteria decreased the false-negative results and diagnostic mistakes.

Limitations of the present study include intracranial pressure not being measured; thus, establishing quantitative correlations with imaging findings was prevented. CTA to confirm BD also presented some drawbacks, such as the transportation of patients with hemodynamic instability and the difficulty of peripheral venous access in patients with edema.

Strategies to increase the accuracy of CT as a whole in the diagnosis of BD, which might be the object of future studies, include the use of CTP in addition to the standard protocol. CTP is a promising evidentiary method, given the increasing technologic development, the availability of equipment with higher temporal and spatial resolution, and reduced intravenous ICM use. However, some variations in the use of this technique demand the establishment and validation of new standard CTP protocols.

CONCLUSIONS

This study showed that the CTA protocol proposed by Frampas et al¹² has high sensitivity and reproducibility, as well as perfect specificity and interobserver agreement, for BD confirmation in patients with an intact skull. The optimization of the interpretation of the images according to the modified Frampas criteria increased the sensitivity of the CTA, particularly in patients with SDs. No control case was wrongly diagnosed as BD. These data add to the growing medical literature supporting the use of CTA as a reliable ancillary BD test. A concurrent SD, particularly craniectomy, can decrease the sensitivity of CTA for BD confirmation, mainly due to the SF phenomenon. The evaluation of CTA images

according to the modified Frampas criteria reduced false-negative findings, especially with craniectomy. Negative results may arise in this clinical scenario, requiring the consideration of other corroborating tests to confirm BD in patients with SD.

ACKNOWLEDGMENTS

We extend our appreciation to the Organ Procurement Organization, Santa Casa de Misericórdia de São Paulo Hospital, São Paulo, Brazil. The authors thank the institutional publishing support center (Núcleo de Apoio a Publicação) for technical assistance in publication.

REFERENCES

1. A definition of irreversible coma: report of the Ad Hoc Committee of the Harvard Medical School to examine the definition of brain death. *JAMA* 1968;205:337–40 CrossRef Medline
2. Wijdicks EF, Varelas PN, Gronseth GS, et al. Evidence-based guideline update: determining brain death in adults—report of the quality standards Subcommittee of the American Academy of Neurology. *Neurology* 2010;74:1911–18 CrossRef Medline
3. Nakagawa TA, Ashwal S, Mathur M, et al; Society of Critical Care Medicine, Section on Critical Care and Section on Neurology of American Academy of Pediatrics, Child Neurology Society. Clinical report: guidelines for the determination of brain death in infants and children—an update of the 1987 task force recommendations. *Pediatrics* 2011;128:e720–40 CrossRef Medline
4. Haupt WF, Rudolf J. European brain death codes: a comparison of national guidelines. *J Neurol* 1999;246:432–37 CrossRef Medline
5. Wijdicks EF. The diagnosis of brain death. *N Engl J Med* 2001;344:1215–21 CrossRef Medline
6. Kramer AH. Ancillary testing in brain death. *Semin Neurol* 2015;35:125–38 CrossRef Medline
7. Russo H, Bressolle F. Pharmacodynamics and pharmacokinetics of thiopental. *Clin Pharmacokinet* 1998;35:95–134 CrossRef Medline
8. Marrache F, Megarbane B, Pirnay S, et al. Difficulties in assessing brain death in a case of benzodiazepine poisoning with persistent cerebral blood flow. *Hum Exp Toxicol* 2004;23:503–05 CrossRef Medline
9. Bradac GB, Simon RS. Angiography in brain death. *Neuroradiology* 1974;7:25–28 CrossRef Medline
10. Braum M, Ducrocq X, Huot JC, et al. Intravenous angiography in brain death: report of 140 patients. *Neuroradiology* 1997;39:400–05 CrossRef Medline
11. Heran MK, Heran NS, Shemie SD. A review of ancillary tests in evaluating brain death. *Can J Neurol Sci* 2008;35:409–19 CrossRef Medline
12. Frampas E, Videcoq M, de Kerviler E, et al. CT angiography for brain death diagnosis. *AJNR Am J Neuroradiol* 2009;30:1566–70 CrossRef Medline
13. Escudero D, Otero J, Marqués L, et al. Diagnosing brain death by CT perfusion and multislice CT angiography. *Neurocrit Care* 2009;11:261–71 CrossRef Medline
14. Berenguer CM, Davis FE, Howington JU. Brain death confirmation: comparison of computed tomographic angiography with nuclear medicine perfusion scan. *J Trauma* 2010;68:553–59 CrossRef Medline
15. Bohatyrewicz R, Sawicki M, Walecka A, et al. Computed tomographic angiography and perfusion in the diagnosis of brain death. *Transplant Proc* 2010;42:3941–46 CrossRef Medline
16. Rieke A, Regli B, Mattle HP, et al. Computed tomography angiography (CTA) to prove circulatory arrest for the diagnosis of brain death in the context of organ transplantation. *Swiss Med Wkly* 2011;141:w13261 CrossRef Medline
17. Welschehold S, Kerz T, Boor S, et al. Detection of intracranial circulatory arrest in brain death using cranial CT-angiography. *Eur J Neurol* 2013;20:173–79 CrossRef Medline
18. Sawicki M, Bohatyrewicz R, Safranow K, et al. Computed tomographic angiography criteria in the diagnosis of brain death-comparison of sensitivity and interobserver reliability of different evaluation scales. *Neuroradiology* 2014;56:609–20 CrossRef Medline
19. Monro A. *Observations on Structure and Functions of the Nervous System*. London: Creech and Johnson; 1783
20. Kellie G. Appearance observed in the dissection of two individuals; death from cold and congestion of the brain. *Trans Med Chir Soc Edinb* 1824;1:84. <https://archive.org/details/b22384315>. Accessed December 20, 2018
21. Marshall SA, Kalanuria A, Markandaya M, et al. Management of intracerebral pressure in the neurosciences critical care unit. *Neurosurg Clin N Am* 2013;24:361–73 CrossRef Medline
22. Alvarez LA, Lipton RB, Hirschfeld A, et al. Brain death determination by angiography in the setting of a skull defect. *Arch Neurol* 1988;45:225–27 CrossRef Medline
23. Frisardi F, Stefanini M, Natoli S, et al. Decompressive craniectomy may cause diagnostic challenges to assess brain death by computed tomography angiography. *Minerva Anestesiol* 2014;80:113–18 Medline
24. Brasil. Conselho Federal de Medicina. Resolução No. 2.173, de 23 de Novembro de 2017. Define os critérios do diagnóstico de morte encefálica. Brasília (DF): CFM; 2017. Disponível em: <https://sistemas.cfm.org.br/normas/visualizar/resolucoes/BR/2017/2173>. Accessed December 20, 2018
25. American Association of Physicists in Medicine. The measurement, reporting and management of radiation dose in CT. Report of AAPM task group 23. AAPM report no. 96. https://www.aapm.org/pubs/reports/RPT_96.pdf. Accessed December 20, 2018
26. Kricheff II, Pinto RS, George AE, et al. Angiographic findings in brain death. *Ann N Y Acad Sci* 1978;315:168–83 CrossRef Medline
27. Savard M, Turgeon AF, Gariépy JL, et al. Selective 4 vessels angiography in brain death: a retrospective study. *Can J Neurol Sci* 2010;37:492–97 CrossRef Medline
28. Taylor T, Dineen RA, Gardiner DC, et al. Computed tomography (CT) angiography for confirmation of the clinical diagnosis of brain death. *Cochrane Database Syst Rev* 2014;CD009694 CrossRef Medline
29. Dupas B, Gayet-Delacroix M, Villers D, et al. Diagnosis of brain death using two-phase spiral CT. *AJNR Am J Neuroradiol* 1998;19:641–47 Medline
30. Leclerc X, Taschner CA, Vidal A, et al. The role of spiral CT for the assessment of the intracranial circulation in suspected brain-death. *J Neuroradiol* 2006;33:90–95 CrossRef Medline
31. Combes JC, Chomel A, Ricolfi F, et al. Reliability of computed tomographic angiography in the diagnosis of brain death. *Transplant Proc* 2007;39:16–20 CrossRef Medline
32. Brasil S, Bor-Seng-Shu E, de-Lima-Oliveira M, et al. Role of computed tomography angiography and perfusion tomography in diagnosing brain death: a systematic review. *J Neuroradiol* 2016;43:133–40 CrossRef Medline
33. Garrett MP, Williamson RW, Bohl MA, et al. Computed tomography angiography as a confirmatory test for the diagnosis of brain death. *J Neurosurg* 2018;128:639–44 CrossRef Medline
34. Welschehold S, Boor S, Reuland K, et al. Technical aids in the diagnosis of brain death: a comparison of SEP, AEP, EEG, TCD and CT angiography. *Dtsch Arztebl Int* 2012;109:624–30 CrossRef Medline
35. Miller K, Eljamel S. Does size and site matter in therapeutic decompressive craniectomy? A laboratory-based experimental study. *World Neurosurg* 2016;95:441–46 CrossRef Medline
36. Wang YS, Wang Y, Shi XW, et al. Size of bone flap and bone window area may impact the outcome of decompressive craniectomy using standard bone flap. *Eur Rev Med Pharmacol Sci* 2016;20:3679–82 Medline
37. Bor-seng-shu E, Figueiredo EG, Amorim RL, et al. Decompressive craniectomy: a meta-analysis of influences on intracranial pressure and cerebral perfusion pressure in the treatment of traumatic brain injury. *J Neurosurg* 2012;117:589–96 CrossRef Medline
38. Sawicki M, Bohatyrewicz R, Safranow K, et al. Dynamic evaluation of stasis filling phenomenon with computed tomography in diagnosis of brain death. *Neuroradiology* 2013;55:1061–69 CrossRef Medline

Diagnosis and Prediction of Relapses in Susac Syndrome: A New Use for MR Postcontrast FLAIR Leptomeningeal Enhancement

S. Coulette, A. Lecler, E. Saragoussi, K. Zuber, J. Savatovsky, R. Deschamps, O. Gout, C. Sabben, J. Aboab, A. Affortit, F. Charbonneau, and M. Obadia



ABSTRACT

BACKGROUND AND PURPOSE: Leptomeningeal enhancement can be found in a variety of neurologic diseases such as Susac Syndrome. Our aim was to assess its prevalence and significance of leptomeningeal enhancement in Susac syndrome using 3T postcontrast fluid-attenuated inversion recovery MR imaging.

MATERIALS AND METHODS: From January 2011 to December 2017, nine consecutive patients with Susac syndrome and a control group of 73 patients with multiple sclerosis or clinically isolated syndrome were included. Two neuroradiologists blinded to the clinical and ophthalmologic data independently reviewed MRIs and assessed leptomeningeal enhancement and parenchymal abnormalities. Follow-up MRIs (5.9 MRIs is the mean number per patient over a median period of 46 months) of patients with Susac syndrome were reviewed and compared with clinical and retinal fluorescein angiographic data evaluated by an independent ophthalmologist. Fisher tests were used to compare the 2 groups, and mixed-effects logistic models were used for analysis of clinical and imaging follow-up of patients with Susac syndrome.

RESULTS: Patients with Susac syndrome were significantly more likely to present with leptomeningeal enhancement: 5/9 (56%) versus 6/73 (8%) in the control group ($P = .002$). They had a significantly higher leptomeningeal enhancement burden with ≥ 3 lesions in 5/9 patients versus 0/73 ($P < .001$). Regions of leptomeningeal enhancement were significantly more likely to be located in the posterior fossa: 5/9 versus 0/73 ($P < .001$). Interobserver agreement for leptomeningeal enhancement was good ($\kappa = 0.79$). There was a significant association between clinical relapses and increase of both leptomeningeal enhancement and parenchymal lesion load: OR = 6.15 ($P = .01$) and OR = 5 ($P = .02$), respectively.

CONCLUSIONS: Leptomeningeal enhancement occurs frequently in Susac syndrome and could be helpful for diagnosis and in predicting clinical relapse.

ABBREVIATIONS: CIS = clinically isolated syndrome; CC = corpus callosum; FA = fluorescein angiography; LME = leptomeningeal enhancement; pcFLAIR = postcontrast FLAIR; SuS = Susac syndrome

Susac Syndrome (SuS) is a vasculopathy characterized by a triad of neurologic, hearing, and ophthalmologic disorders.¹⁻³ Fluorescein angiography (FA) typically shows branch retinal ar-

tery occlusions, and brain MR imaging shows FLAIR hyperintensities involving the corpus callosum (CC). Criteria were recently proposed for definite, probable, and possible SuS to guide diagnosis.⁴

The complete triad is present in only 13% of patients at disease onset.⁵ Peripherally located branch retinal artery occlusion may not result in visual symptoms, and its recognition requires review by experienced ophthalmologists. Therefore, MR imaging is often necessary to establish the diagnosis, but the primary radiologic misdiagnosis is multiple sclerosis, and immune treatment for MS may lead to exacerbation in patients with SuS.⁶⁻⁸

Several recent publications have investigated the presence of postcontrast FLAIR (pcFLAIR) leptomeningeal enhancement (LME) in a variety of neurologic diseases, particularly MS.⁹ Despite LME already being part of the diagnostic criteria proposed by Kleffner et al,⁴ there is scant literature devoted specifically to LME in SuS.¹⁰⁻¹²

Received November 4, 2018; accepted after revision May 13, 2019.

From the Neurology Department (S.C., R.D., O.G., C.S., J.A., M.O.), Neuroradiology Department (A.L., E.S., J.S., F.C.), Clinical Research Unit (K.Z.), and Ophthalmology Department (A.A.), Fondation Ophthalmologique Adolphe de Rothschild, Paris, France.

Sarah Coulette and Augustin Lecler contributed equally to the work

Kevin Zuber, MSc, Biostatistician, Clinical Research Unit, Fondation Ophthalmologique Adolphe de Rothschild conducted the statistical analysis.

Please address correspondence to Michael Obadia, MD, Department of Neurology, Fondation Ophthalmologique Adolphe de Rothschild, 29 rue Manin, 75019 Paris, France; e-mail: mobadia@for.paris; @RothNeuroRad; @FondARothschild



Indicates article with supplemental on-line photo.



Indicates article with supplemental on-line table.

<http://dx.doi.org/10.3174/ajnr.A6103>

The aim of our study was to evaluate the prevalence and significance of pcFLAIR LME at 3T in patients with SuS at onset and during follow-up.

MATERIALS AND METHODS

Study Design and Setting

We conducted a retrospective systematic chart review in a tertiary referral center specializing in ophthalmology and neurology interventions.

Ethics Approval, Patient Information, and Consent

This study was prospectively approved by our institutional research ethics board and adhered to the tenets of the Declaration of Helsinki. Informed consent was waived.

Patients

Susac Syndrome Group. We reviewed the medical charts of adult patients with SuS treated in our center from January 2011 to December 2017. All patients except one had a definite clinical diagnosis of SuS according to the 2016 criteria without relying on or including the presence of LME. The patient with a probable diagnosis of SuS had retinal and vestibular cochlear involvement without neurologic symptoms. All patients had branch retinal artery occlusion on FA. Brain MR imaging, FA, tonal audiometry, a complete serologic battery, and lumbar puncture were performed in all patients.

Treating neurologists determined the evaluation frequency and appropriate management with a systematic neurologic examination, completed by additional ear, nose, and throat and ophthalmologic examinations depending on symptoms. There are no standard algorithms for the use of steroids, antithrombotic therapy, or immunoglobulin intravenous or immunosuppressive therapy for SuS at our institution.

Follow-up included neurologic, ophthalmologic, and audiologic evaluations and FA and MR imaging. The MRIs and FAs were always performed within the same month as the clinical evaluations. A relapse was defined by the following: new neurologic symptoms, recent hearing loss and tinnitus or peripheral vertigo (peripheral vertigo should be supported by caloric testing of the vestibular organ, nystagmography, and/or vestibular evoked myogenic potentials), and/or a new vascular occlusion on FA. An ophthalmologist specialized in SuS with 10 years of experience (A.A.), blinded to clinical and radiologic data, independently reviewed all ophthalmologic data including FA for each eye. During follow-up, the severity of FA lesions was classified as unchanged, decreased, increased, or dissociated (defined as an increase in some lesions and decrease in others); in the case of dissociated evolution, the overall severity of the lesion was specified as unchanged, decreased, or increased.

Control Group. The control group included all consecutive patients who presented with acute optic neuritis with a definite diagnosis of MS or clinically isolated syndrome (CIS) during the same period. We chose this control group for 2 reasons: first, because of our recruitment as a tertiary referral center where many patients present with optic neuritis, either isolated or related to MS; second, because we perform the same imaging pro-

tol for all patients presenting with vision loss, thus allowing an accurate comparability regarding imaging technique and sequences between patients with SuS and the control group. From January 2011 to December 2017, seventy-three patients were included in the control group (56 patients with definite MS and 17 patients with CIS). A flowchart illustrating the selection of patients is shown in the On-line Figure.

MR Imaging Acquisition

All MR imaging examinations were performed with a 3T Ingenia device (Philips Healthcare, Best, the Netherlands) with a 32-channel head coil. Patients with SuS and those in the control group had the same protocol. An intravenous contrast injection of a single dose (0.1 mmol/kg) of gadolinium was administered 5 minutes before the first MR imaging acquisition. The common MR imaging protocol included postcontrast coronal T2 (TR/TE = 3000/75 ms, FOV = 150 × 150 mm, total acquisition time = 4 minutes 5 seconds), T1-weighted imaging (TR/TE = 497/7 ms, FOV = 150 × 150 mm, total acquisition time = 2 minutes 51 seconds), 3D pcFLAIR (TR/TE = 8000/388 ms, TI = 2400 ms, voxel size = 0.9 × 0.9 × 1 mm³, FOV = 240 × 240 × 175 mm³, total acquisition time = 4 minutes 24 seconds), and 3D postcontrast spin-echo T1-weighted imaging (TR/TE = 500/27 ms, voxel size = 1 × 1 × 1 mm³, FOV = 252 × 252 × 200 mm³, total acquisition time = 3 minutes 37 seconds).

MR Imaging Analysis

Two neuroradiologists (F.C. and E.S. with 12 and 7 years of experience, respectively), blinded to clinical, biologic, and FA data, independently analyzed the datasets in random order.

The readers assessed the following characteristics of patients' MR imaging at baseline and during follow-up: The primary judgment criterion was the presence of LME, defined as a pcFLAIR hyperintensity within the subarachnoid space substantially greater than that of the brain parenchyma (Fig 1). Secondary judgment criteria for LME were the number of regions of LME classified as few (<3) or multiple (≥3); their shape classified as punctate, linear, or mixed; their location classified as posterior fossa or supratentorial; an associated enhancement on postcontrast T1-weighted images; and their number classified as some or all regions of LME. Other secondary judgment criteria were the following: the presence of intraparenchymal focal pcFLAIR hyperintensities, their pattern defined as nonspecific, probably related to a small-vessel disease, or probably related to an inflammatory disease, according to international standards¹³⁻¹⁵; their location classified as posterior fossa, CC, or supratentorial; the precise location and shape of the CC lesions, classified as located in the central portion or the callosal-septal surface as "snowball," "icicle," or "spoke," respectively^{6,16}; and an associated enhancement on postcontrast T1-weighted images and the number classified as some or all intraparenchymal lesions.

During follow-up, LME and other encephalic lesion loads were classified as unchanged, decreased, increased, or dissociated (defined as an increase in some lesions and decrease in others); in case of dissociated evolution, the overall lesion load was specified as unchanged, decreased, or increased. Both readers were instructed to focus on and report LME as well as its characteristics

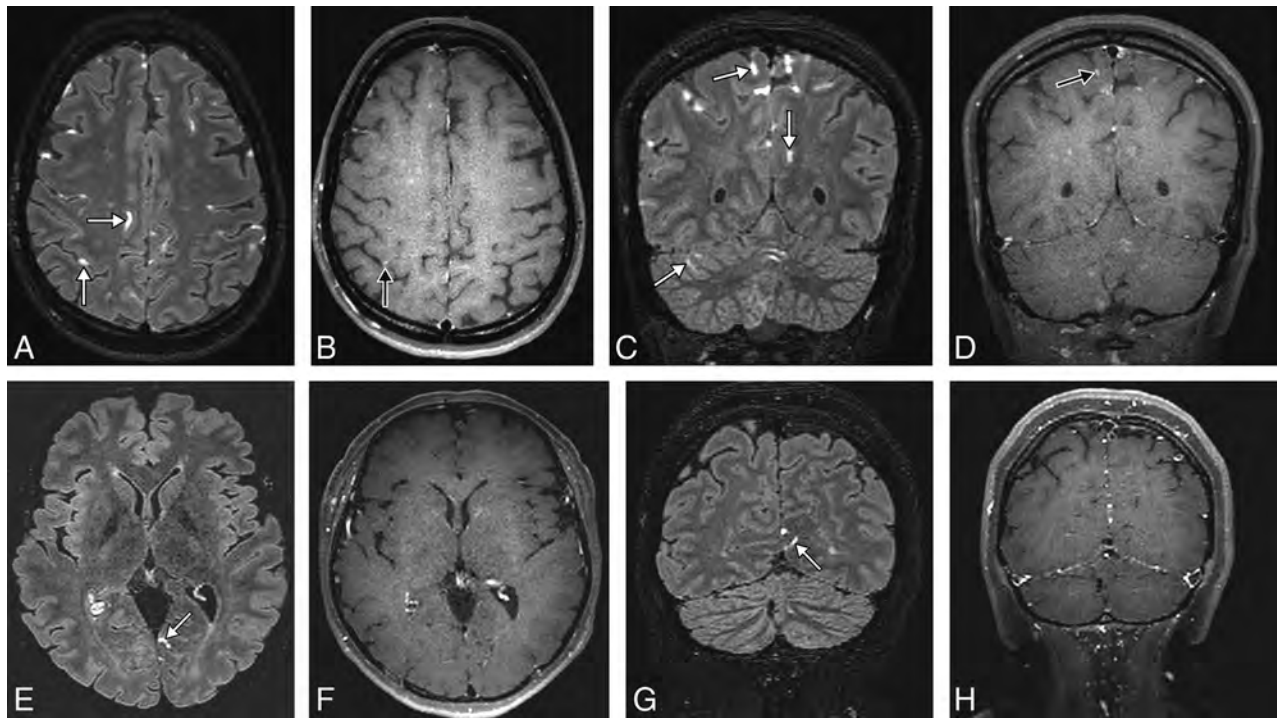


FIG 1. 3D postcontrast FLAIR and postcontrast T1-weighted MR images in the axial and coronal planes showing leptomeningeal enhancement (white arrows) in a patient with Susac syndrome (A–D) and one with multiple sclerosis (E–H). Note the multiple regions of leptomeningeal enhancement in the patient with Susac syndrome compared with the patient with MS. Only the MR imaging of the patient with Susac syndrome shows posterior fossa leptomeningeal enhancement. Some of the regions of leptomeningeal enhancement have an associated enhancement on postcontrast T1-weighted imaging (black arrows).

before looking at the intraparenchymal lesions to avoid any recognition bias.

Statistics

Quantitative variables are presented as mean (SD), median (interquartile range); and categoric variables, as percentages. Agreement between readers was assessed using the Cohen κ . Fisher tests were used to compare the SuS and control groups. Because multiple tests were performed, Bonferroni adjustment was used with an α level adjusted to a significance level of .005. Mixed-effects logistic models were used to assess the relationship between LME or parenchymal lesion load and relapse. Bias-corrected bootstrap 95% confidence intervals were obtained using 1000 bootstrap replicates. Post hoc power analyses were performed. All statistical analyses were performed by Kevin Zuber, MSc, Biostatistician, Clinical Research Unit, Fondation Ophthalmologique Adolphe de Rothschild, using R Statistical Software.¹⁷

RESULTS

Baseline

Demographic and Clinical Characteristics. Among the 9 patients included in the SuS group, 8 had definite SuS and 1 had a probable diagnosis (8 women and 1 man; mean age, 37.7 ± 11 years SD). At the first manifestation of the disease, 8 patients (89%) had a branch retinal artery occlusion on FA, 8 (89%) had neurologic symptoms (headache, $n = 6$; focal neurologic deficit, $n = 5$; or encephalopathy, $n = 4$), and 6 (67%) had auditory symptoms (hearing loss, $n = 5$; tinnitus, $n = 3$; or peripheral vertigo, $n = 1$). Only 5 patients (56%) fulfilled the SuS triad at the onset of the

disease. The mean time before diagnosis was 5 months (median, 0.4 months). The lumbar puncture findings were normal (<5 cells and 28–52 mg/dL of protein) in 2 patients and revealed a slight pleocytosis (mean, 12.3 cells/mm³; range, 0–67 cells/mm³) and an elevation of CSF protein (mean, 90 mg/dL; range, 31–274 mg/dL) in all others. Detailed clinical characteristics of the 73 patients are described in Table 1. Detailed characteristics of the 73 patients included in the control group are provided in Table 2.

MR Imaging Findings

LME. Patients with SuS were significantly more likely to present with LME: 5/9 (56%) versus 6/73 (8%) in the control group ($P = .002$). They had a significantly higher LME burden with ≥ 3 lesions in 5/9 patients versus 0/73 ($P < .001$). Regions of LME were significantly more likely to be located in the posterior fossa: 5/9 versus 0/73 ($P < .001$) (Fig 1).

There was significantly more associated postcontrast T1-weighted imaging enhancement in the SuS group than in the control group: 4/9 (44%) versus 4/73 (5%) ($P = .004$). Detailed MR imaging findings are presented in the On-line Table.

Intraparenchymal Focal pcFLAIR Hyperintensities. There was no significant difference between the 2 groups in the presence of intraparenchymal focal pcFLAIR hyperintensities: 9/9 (100%) versus 70/73 (96%). However, they were significantly more often described as inflammatory in the control group: 2/9 (22%) versus 62/73 (85%) ($P < .001$).

There was no significant difference between the 2 groups in the presence of CC focal pcFLAIR hyperintensities: 9/9 (100%) versus

Table 1: Clinical characteristics of patients with Susac syndrome at baseline and during follow-up

Patient	Sex	Age (yr)	Clinical Symptoms at Onset of the Disease			No. of Relapses	Susac Criteria	Treatments during Follow-Up	Follow-Up Duration (mo)
			Neurologic	Auditory	BRAO				
1	F	19	Y	Y	Y	0	Definite	P, AVK, ASA, IVIG	28
2	F	44	Y	Y	N	0	Definite	ASA, IVIG	53
3	F	43	Y	N	Y	7	Definite	P, ASA, IVIG, CP	46
4	F	32	Y	N	Y	1	Definite	P, AVK, ASA, IVIG, CP, MM	72
5	F	65	Y	Y	Y	2	Definite	P, ASA, IVIG, CP	37
6	F	29	Y	Y	Y	3	Definite	P, ASA, IVIG, CP	31
7	F	37	Y	Y	Y	0	Definite	P, ASA, IVIG	67
8	M	32	N	N	Y	1	Probable	ASA, MM	56
9	F	37	Y	Y	Y	3	Definite	P, ASA, IVIG, CP, RTX	1

Note:—Y indicates yes; N, no; BRAO, branch retinal artery occlusion; ASA, acetylsalicylic acid; AVK, anti-vitamin K; CP, cyclophosphamide; IVIG, intravenous immune globulin; MM, mycophenolate mofetil; P, prednisone; RTX, rituximab.

Table 2: Clinical characteristics of the control group at baseline

Characteristics	Number	Percentages
Sex		
Female	50	68
Male	23	32
Age at diagnosis		
Mean (IQR)	37.7	11
Medical history		
Multiple sclerosis	16	22
Inaugural optic neuritis	53	73
Recurrent optic neuritis	4	5
Expanded Disability Status Scale score		
Mean (range)	2.15 (1–5)	
Treatment		
No	68	93
Glatiramer acetate	2	3
Interferon	2	3
Mitoxantrone	1	1
MS course duration (yr)		
Mean (range)	6.1 (0–24)	
Final diagnosis after MRI		
Multiple sclerosis	56	77
Clinically isolated syndrome	17	23

Note:—IQR indicates interquartile range.

51/73 (70%). However, they were significantly more often described as located in the central portion of the CC in the SuS group: 7/9 (78%) versus 3/51 (6%) ($P < .001$). There was no statistically significant difference between the 2 groups for associated enhancement on postcontrast T1-weighted images.

Interobserver Agreement

Interobserver agreement was good for detecting LME and intraparenchymal lesions: $\kappa = 0.79$; 95% CI, 0.31–1 and $\kappa = 0.77$; 95% CI, 0.57–0.90, respectively.

Follow-up

Clinical Characteristics. The median follow-up time for the patients with SuS was 46 months (interquartile range, 25) with a total of 53 clinical evaluations. Seventeen relapses occurred during follow-up in 6 (67%) patients (median number, 1.5; interquartile range, 1.75 per patient). Throughout the course of the disease, all patients were treated with acetylsalicylic acid; 80%, with prednisone and intravenous immune globulin; and 70%, with immunosuppressive drugs. Five patients started immunosuppressive therapy after diagnosis, and 2, after a relapse. Detailed clinical follow-up characteristics are shown in Tables 1 and 3.

Thirty-six FAs were performed during the follow up, showing small, focal, and occlusive lesions of retinal arterioles in the retinal periphery in 6/9 (67%) patients. Of 72 eyes evaluated, worsening of the lesion severity was found for 14; stability, for 34; improvement, for 13; and dissociation, for 11.

MR Imaging Findings

Fifty-three MRIs were reviewed (mean number, 5.9 per patient). LME was seen in 7 of 9 (78%) patients on 40 (75%) follow-up MRIs. LME load remained unchanged in 23%, was decreased in 39%, and was increased in 39% of cases. It was dissociated in 50% of cases. (Fig 2). Intraparenchymal focal pcFLAIR hyperintensity lesion load remained unchanged in 36%, was decreased in 23%, and was increased in 41% of MRIs. It was dissociated in 18% of cases. Detailed MR imaging findings are shown in Table 3.

Association between MR Imaging Findings and Disease Course

There was a strong relationship between the occurrence of a clinical relapse and the increase of LME or intraparenchymal focal pcFLAIR hyperintensities: OR = 6.2; 95% CI, 1.6–59.7 and OR = 5; 95% CI, 1.3–37.7, respectively. There was a nonsignificant association between a worsening of the lesion severity on FA and an increase of LME or intraparenchymal focal pcFLAIR hyperintensities: OR = 2.8; 95% CI, 0.430 and OR = 3.6; 95% CI, 0.6–30, respectively.

Post Hoc Power Analyses

Post hoc power analyses performed on both groups for the appearance of leptomeningeal abnormalities showed a very high power of 90%. For the subgroup of patients with Susac, post hoc power analysis showed a power of 72%.

DISCUSSION

Our study showed that LME occurred frequently in SuS and may be helpful for diagnosis and in predicting clinical relapse. It is the first study to investigate the prevalence of LME on pcFLAIR at 3T MR imaging in SuS alongside the main differential diagnoses of MS or CIS. It is also the largest follow-up study of patients with SuS with MR imaging, to our knowledge. These results add to the body of knowledge regarding MR imaging findings in SuS as well as suggesting possible pathophysiologic mechanisms.

LME was more frequent in our study than in a previous

report using postcontrast T1-weighted imaging (56% versus 33%),¹⁰ but the pcFLAIR technique has shown greater ability to detect LME and is considered the reference technique to assess its presence.^{9,18-20}

LME is not specific to SuS and has been observed in various pathologies associated with blood-meningeal barrier dysfunction, such as after stroke,²¹ posterior reversible encephalopathy syndrome,²² brain tumors,²³ vasculitis,²⁴ neurosarcoidosis,²⁵ CNS infections, MS,^{20,26} HIV, or human T-cell lymphotropic virus type 1-associated myelopathy, but also in healthy volunteers.²⁶ However, LME is more frequent, and its pattern is unique in patients with SuS, which is highly relevant in clinical practice because it could be useful for differentiating SuS from its main dif-

ferential diagnoses such as MS or CIS. Posterior fossa lesions and a high lesion burden (≥ 3) were found in more than half of our patients but in none of the control group, which is in accordance with MS studies showing mostly supratentorial and uni- or bifocal lesions.^{27,28}

LME could also be useful for discriminating patients with SuS from those with neuromyelitis optica because the latter are much less likely to present with LME at onset or during follow-up.²⁹ The frequent involvement of the posterior fossa in SuS (cerebellum, middle cerebellar peduncles, and brain stem) has been reported previously, but only for white matter lesions.^{10,30} Moreover, during follow-up, our study showed that LME load was evolving with time with an increase of 39% and a decrease of 39% shown on follow-up MRIs. This finding was not reported in MS and could also be used to discriminate those with SuS from patients with MS or CIS. Therefore, LME might considerably strengthen the radiologic diagnostic criteria for SuS⁴ and should be included in further recommendations and guidelines. The overall number of regions of LME as well as their shape and location are the most important findings and should be reported to help radiologists and clinicians when diagnosing SuS.

Our findings might provide details concerning the possible pathophysiologic mechanisms of SuS. Pathophysiologically, CSF-restricted enhancement on pcFLAIR images is supposed to be an expression of a breakdown of the blood-meningeal barrier, directly related to ongoing inflammation and an immune-mediated neurologic condition in individuals infected with neurotropic viruses.²⁶ Therefore, the different patterns between the SuS and control groups could be explained by different blood-meningeal barrier dysfunctions: a specific focal reaction to the site of inflammation in MS and generalized angiopathy in SuS. Involvement of multiple foci in SuS likely represents contained areas of vascular leakage secondary to endotheliopathy. Likewise, histopathologic findings in SuS cases showed T-cell inflammation involving small-to-medium-sized leptomeningeal vessels.³¹ Other retinal histopathologic³² findings demonstrated vascular occlusion of retinal blood vessels without thrombosis and serous-filled spaces between the retinal blood vessels and the internal limiting membrane, resulting from the breakdown of the blood-retinal barrier. Decreased Adenosine diphosphatase (ADPase) activity in some

Table 3: Follow-up clinicoradiologic data of patients with Susac syndrome

Clinical Findings	No.	%
Relapse		
Yes	17	32
No	36	68
Neurologic symptoms	5	56
Auditory symptoms	8	89
FA abnormalities		
Occlusion	6	67
Vasculitis	6	67
Presence of LME		
Yes	40	75
No	13	25
No. of regions of LME		
<3	3	6
≥ 3	37	70
Location of regions of LME		
Supratentorial	20	38
Posterior fossa	33	62
Associated enhancement on postcontrast T1WI		
Yes	30	57
No	23	43
Evolution of the LME burden		
Decreased	17	39
Unchanged	10	23
Increased	17	39
Evolution of the intrafocal pcFLAIR hyperintensities		
Decreased	10	23
Unchanged	16	36
Increased	18	41

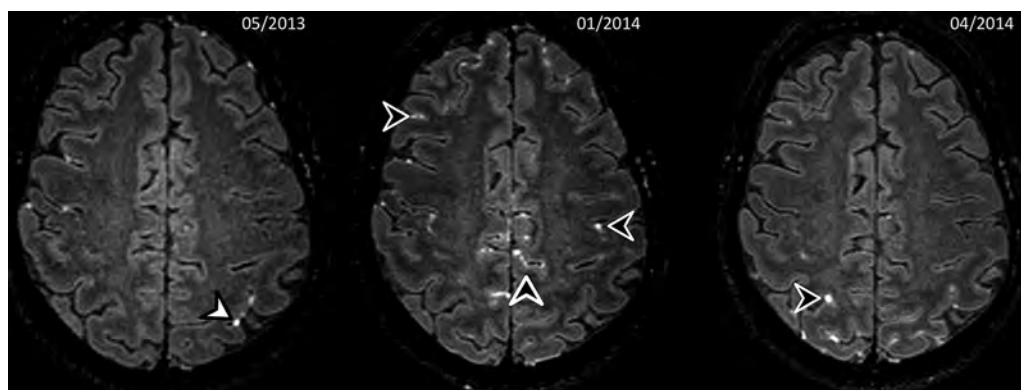


FIG 2. One-year follow-up 3D postcontrast FLAIR MR images in an axial plane showing a dissociated evolution of the regions of leptomeningeal contrast-enhancement in a patient with a Susac syndrome. Sequential MRIs show disappearance of the left parietal regions of leptomeningeal contrast enhancements (*white arrowhead*) and onset of multiple new regions of leptomeningeal contrast enhancement (*black arrowheads*), some of which disappeared during follow-up.

peripheral blood vessels also suggested endothelial cell dysfunction. The association of SuS with anti-endothelial cell antibodies further supports the role of endothelial pathology.³³ Vascular leakage could also be indicated by arteriolar wall hyperfluorescence observed on FA, known to be highly suggestive of SuS.³⁴

The other primary radiologic findings are in line with previous reports. We reported intraparenchymal focal pcFLAIR hyperintensities and CC involvement in all our patients with SuS, which is in accordance with the literature.^{5,10} The specificity of white matter lesions for diagnosis remains low. Lesions of the central portion of CC were significantly more frequent in patients with SuS in our study, as reported previously.^{6,10,16} This particular pattern is due to microinfarctions involving the microvascular blood supply of the CC.³⁵ Absinta et al^{26,27} showed that LME was dissociated from the formation of new white matter lesions in MS and suggested that LME might localize inflammation-related focal disruption of the blood-meningeal barrier and associated scarring. We believe that the pathophysiology is the same in patients with Susac syndrome, with LME reflecting a blood-meningeal barrier disruption, whereas intraparenchymal hyperintensities are due to microinfarctions.

During follow-up, there was a significant association between an increase in the number of regions of LME and clinical relapses in patients with SuS, with an OR of 6.2, confirming an observation on 2 patients in the literature.³⁰ LME could therefore become an interesting biomarker to monitor disease activity, predict clinical relapses, and plan the therapeutic approach, similar to the T2 lesion load in CIS³⁶ or MS.³⁷

This study has some limitations. First, the clinical retrospective design may have led to loss of clinical data capture, though regular and frequent follow-up at our institution with systematic neurologic examinations and hearing and visual evaluations with repeat FA may have limited such bias. Second, the sample was small due to the single-center study design and the rarity of the disease. Third, our control group consisted of patients with optic neuritis associated with MS or CIS, possibly lowering the probability of LME. Notably, LME was reported to be rare in relapsing-remitting MS and in CIS³⁸ and most common in patients with progressive forms of MS, half of whom showed pcFLAIR with a diagnosis of secondary-progressive MS.²⁸ Fourth, although radiologists were blinded to clinical data, SuS and MS/CIS have different morphologies, which might have led to a recognition bias. To minimize this effect, a double reading was performed independently by 2 trained and experienced neuroradiologists with instructions to focus and report LME before intraparenchymal lesions. Fifth, we compared patients with SuS with those with MS/CIS only, though it would have been interesting to compare them with patients with other autoimmune, inflammatory, or possibly infectious etiologies with LME. Sixth, we performed only postcontrast FLAIR and T1WI, thus preventing us from drawing conclusions about the underlying pathophysiological processes. Further studies including pre- and postcontrast imaging would allow us to determine whether LME is due to a leak of the contrast or is only from a T2 lesion with a leak of gadolinium due to an inflammatory process, with potential concerns regarding gadolinium accumulation.

CONCLUSIONS

Our study showed that LME occurred frequently in SuS and may be helpful for diagnosis and in predicting clinical relapse. Large multicenter studies are needed to confirm our findings and establish LME as a useful biomarker in SuS.

ACKNOWLEDGMENTS

Paul Kretchmer and Laura McMaster provided professional English language medical editing of this article.

Disclosures: Julien Savatovsky—UNRELATED: Payment for Lectures Including Service on Speakers Bureaus: Medtronic, Biogen, Sanofi; Travel/Accommodations/Meeting Expenses Unrelated to Activities Listed: Bayer Healthcare.

REFERENCES

1. Susac JO, Hardman JM, Selhorst JB. **Microangiopathy of the brain and retina.** *Neurology* 1979;29:313–16 CrossRef Medline
2. Susac JO. **Susac's syndrome: the triad of microangiopathy of the brain and retina with hearing loss in young women.** *Neurology* 1994;44:591–93 CrossRef Medline
3. Papo T, Biousse V, Lehoang P, et al. **Susac syndrome.** *Medicine (Baltimore)* 1998;77:3–11 CrossRef Medline
4. Kleffner I, Dörr J, Ringelstein M, et al; European Susac Consortium (EuSaC). **Diagnostic criteria for Susac syndrome.** *J Neurol Neurosurg Psychiatry* 2016;87:1287–95 CrossRef Medline
5. Dörr J, Krautwald S, Wildemann B, et al. **Characteristics of Susac syndrome: a review of all reported cases.** *Nat Rev Neurol* 2013;9:307–16 CrossRef Medline
6. Buzzard KA, Reddel SW, Yiannikas C, et al. **Distinguishing Susac's syndrome from multiple sclerosis.** *J Neurol* 2015;262:1613–21 CrossRef Medline
7. Sarbu N, Shih RY, Jones RV, et al. **White matter diseases with radiologic-pathologic correlation.** *Radiographics* 2016;36:1426–47 CrossRef Medline
8. Seifert-Held T, Langner-Wegscheider BJ, Komposch M, et al. **Susac's syndrome: clinical course and epidemiology in a Central European population.** *Int J Neurosci* 2017;127:776–780 CrossRef Medline
9. Zurawski J, Lassmann H, Bakshi R. **Use of magnetic resonance imaging to visualize leptomeningeal inflammation in patients with multiple sclerosis: a review.** *JAMA Neurol* 2017;74:100–09 CrossRef Medline
10. Susac JO, Murtagh FR, Egan RA, et al. **MRI findings in Susac's syndrome.** *Neurology* 2003;61:1783–87 CrossRef Medline
11. Sastre-Garriga J. **Leptomeningeal enhancement in Susac's syndrome and multiple sclerosis: time to expect the unexpected?** *Mult Scler* 2016;22:975–76 CrossRef Medline
12. Engisch R, Titelbaum DS, Chilver-Stainer L, et al. **Susac's syndrome: leptomeningeal enhancement on 3D FLAIR MRI.** *Mult Scler* 2016;22:972–74 CrossRef Medline
13. Fazekas F, Chawluk JB, Alavi A, et al. **MR signal abnormalities at 1.5 T in Alzheimer's dementia and normal aging.** *AJR Am J Roentgenol* 1987;149:351–56 CrossRef Medline
14. Filippi M, Rocca MA, Ciccarelli O, et al; MAGNIMS Study Group. **MRI criteria for the diagnosis of multiple sclerosis: MAGNIMS consensus guidelines.** *Lancet Neurol* 2016;15:292–303 CrossRef Medline
15. Wardlaw JM, Smith EE, Biessels GJ, et al; Standards for Reporting Vascular changes on nEuroimaging (STRIVE v1). **Neuroimaging standards for research into small vessel disease and its contribution to ageing and neurodegeneration.** *Lancet Neurol* 2013;12:822–38 CrossRef Medline
16. Rennebohm R, Susac JO, Egan RA, et al. **Susac's syndrome: update.** *J Neurol Sci* 2010;299:86–91 CrossRef Medline
17. R Core Team (2017). **R: A language and environment for statistical computing.** *R Foundation for Statistical Computing*, Vienna, Austria. <https://www.R-project.org/>. Accessed December 18, 2018
18. Mamourian AC, Hoopes PJ, Lewis LD. **Visualization of intrave-**

- nously administered contrast material in the CSF on fluid-attenuated inversion-recovery MR images: an in vitro and animal-model investigation. *AJNR Am J Neuroradiol* 2000;21:105–11 Medline
19. Mathews VP, Caldemeyer KS, Lowe MJ, et al. **Brain: gadolinium-enhanced fast fluid-attenuated inversion-recovery MR imaging.** *Radiology* 1999;211:257–63 CrossRef Medline
 20. Zivadinov R, Ramasamy DP, Hagemeyer J, et al. **Evaluation of leptomeningeal contrast enhancement using pre-and postcontrast subtraction 3D-FLAIR imaging in multiple sclerosis.** *AJNR Am J Neuroradiol* 2018;39:642–47 CrossRef Medline
 21. Latour LL, Kang DW, Ezzeddine MA, et al. **Early blood-brain barrier disruption in human focal brain ischemia.** *Ann Neurol* 2004;56:468–77 CrossRef Medline
 22. Hamilton BE, Nesbit GM. **Delayed CSF enhancement in posterior reversible encephalopathy syndrome.** *AJNR Am J Neuroradiol* 2008;29:456–57 CrossRef Medline
 23. Naul LG, Finkenstaedt M. **Extensive cerebrospinal fluid enhancement with gadopentetate dimeglumine in a primitive neuroectodermal tumor.** *AJNR Am J Neuroradiol* 1997;18:1709–11 Medline
 24. Salvarani C, Brown RD Jr, Calamia KT, et al. **Primary central nervous system vasculitis with prominent leptomeningeal enhancement: a subset with a benign outcome.** *Arthritis Rheum* 2008;58:595–603 CrossRef Medline
 25. Wengert O, Rothenfusser-Korber E, Vollrath B, et al. **Neurosarcoidosis: correlation of cerebrospinal fluid findings with diffuse leptomeningeal gadolinium enhancement on MRI and clinical disease activity.** *J Neurol Sci* 2013;335:124–30 CrossRef Medline
 26. Absinta M, Cortese ICM, Vuolo L, et al. **Leptomeningeal gadolinium enhancement across the spectrum of chronic neuroinflammatory diseases.** *Neurology* 2017;88:1439–44 CrossRef Medline
 27. Absinta M, Vuolo L, Rao A, et al. **Gadolinium-based MRI characterization of leptomeningeal inflammation in multiple sclerosis.** *Neurology* 2015;85:18–28 CrossRef Medline
 28. Zivadinov R, Uher T, Hagemeyer J, et al. **A serial 10-year follow-up study of brain atrophy and disability progression in RRMS patients.** *Mult Scler* 2016;22:1709–18 CrossRef Medline
 29. Kim W, Lee JE, Kim SH, et al. **Cerebral cortex involvement in neuromyelitis optica spectrum disorder.** *J Clin Neurol* 2016;12:188–93 CrossRef Medline
 30. White ML, Zhang Y, Smoker WRK. **Evolution of lesions in Susac syndrome at serial MR imaging with diffusion-weighted imaging and apparent diffusion coefficient values.** *AJNR Am J Neuroradiol* 2004;25:706–13 Medline
 31. Hardy TA, O'Brien B, Gerbis N, et al. **Brain histopathology in three cases of Susac's syndrome: implications for lesion pathogenesis and treatment.** *J Neurol Neurosurg Psychiatry* 2015;86:582–84 CrossRef Medline
 32. McLeod DS, Ying HS, McLeod CA, et al. **Retinal and optic nerve head pathology in Susac's syndrome.** *Ophthalmology* 2011;118:548–52 CrossRef Medline
 33. Magro CM, Poe JC, Lubow M, et al. **Susac syndrome: an organ-specific autoimmune endotheliopathy syndrome associated with anti-endothelial cell antibodies.** *Am J Clin Pathol* 2011;136:903–12 CrossRef Medline
 34. Egan RA, Hills WL, Susac JO. **Gass plaques and fluorescein leakage in Susac syndrome.** *J Neurol Sci* 2010;299:97–100 CrossRef Medline
 35. Garg N, Reddel SW, Miller DH, et al. **The corpus callosum in the diagnosis of multiple sclerosis and other CNS demyelinating and inflammatory diseases.** *J Neurol Neurosurg Psychiatry* 2015;86:1374–82 CrossRef Medline
 36. Barkhof F, Filippi M, Miller DH, et al. **Comparison of MRI criteria at first presentation to predict conversion to clinically definite multiple sclerosis.** *Brain J Neurol* 1997;120(Pt 11):2059–69 CrossRef Medline
 37. Paty DW, Li DK. **Interferon beta-1b is effective in relapsing-remitting multiple sclerosis, II. MRI analysis results of a multicenter, randomized, double-blind, placebo-controlled trial—UBC MS/MRI Study Group and the IFNB Multiple Sclerosis Study Group.** *Neurology* 1993;43:662–67 CrossRef Medline
 38. Eisele P, Griebel M, Szabo K, et al. **Investigation of leptomeningeal enhancement in MS: a postcontrast FLAIR MRI study.** *Neurology* 2015;84:770–75 CrossRef Medline

Long-Term Results and Follow-Up Examinations after Endovascular Embolization for Unruptured Cerebral Aneurysms

T. Murakami, T. Nishida, K. Asai, Y. Kadono, H. Nakamura, T. Fujinaka, and H. Kishima



ABSTRACT

BACKGROUND AND PURPOSE: The appropriate period of follow-up examinations after endovascular embolization for cerebral aneurysms using time-of-flight MR angiography is not well-known. We retrospectively investigated long-term results after endovascular embolization for unruptured cerebral aneurysms and evaluated the periods from embolization to recanalization and retreatment.

MATERIALS AND METHODS: Between April 2006 and March 2011, one hundred forty-eight unruptured aneurysms were treated with endovascular coil embolization. Among them, we investigated 116 unruptured aneurysms, which were followed up for >5 years. Time-of-flight MR angiography was performed at 1 day, 3–6 months, 1 year after the procedure, and every year thereafter.

RESULTS: The mean follow-up period was 7.0 ± 1.4 years. Recanalization was observed in 19 (16.3%) aneurysms within 2 years. Among them, retreatment for recanalization was performed in 8 (6.8%) aneurysms. No recanalization was detected in any aneurysms that had been stable in the first 2 years after embolization. A larger maximum aneurysm size was significantly correlated with recanalization ($P = .019$).

CONCLUSIONS: Aneurysms in which recanalization was not observed within 2 years after endovascular coil embolization were stable during a mean follow-up of 7 years. This result may be helpful in considering the appropriate span or frequency of follow-up imaging for embolized cerebral aneurysms.

ABBREVIATIONS: BA = basilar artery; CO = complete obliteration; RA = residual aneurysm; RN = residual neck

Endovascular coil embolization is one of the standard treatments for unruptured cerebral aneurysms.¹ A follow-up imaging study after embolization is crucial because the recanalization rate is 4.7%–33.6% and the retreatment rate is 4.7%–17.4%.^{2–10} Although DSA is the criterion standard for follow-up imaging studies, TOF-MRA is also an accurate method for detecting recanalization in cerebral aneurysms treated with coil embolization.¹¹ However, the appropriate span or frequency of follow-up imaging for embolized cerebral aneurysms using TOF-MRA is not well-known. Therefore, we retrospectively investigated long-term results after embolization for unruptured cerebral aneurysms and evaluated the periods from embolization to recanalization and retreatment to optimize follow-up examinations.

MATERIALS AND METHODS

Ethics

Ethics approval for the study was obtained from the Osaka University Hospital institutional review board (approval No. 16490).

Patient Population and Follow-Up Periods

In our institution, the treatment indication for unruptured cerebral aneurysms was decided according to the Japanese Guidelines for the Management of Stroke.¹² Endovascular coil embolization or surgical neck clipping was performed with the patient's informed consent. Endovascular coil embolization was selected in any aneurysm, except in those in which embolization was not applicable. In case of multiple aneurysms, coil embolization was also performed for any aneurysm, even if it was small, when it was technically possible. Between April 2006 and March 2011, one hundred forty-eight unruptured aneurysms in 126 patients were treated with endovascular coil embolization at Osaka University Hospital. Among the 148 unruptured aneurysms, 30 unruptured aneurysms in 27 patients could not be followed up for >5 years because patients had stopped coming to the hospital (non-follow-up group). There were also 3 cases of cerebral dissecting aneurysms. Among them, 2 cases were excluded because parent artery occlusion had been performed. Therefore, we assessed 116

Received March 19, 2019; accepted after revision May 13.

From the Department of Neurosurgery (T.M., T.N., K.A., Y.K., H.N., H.K.), Osaka University Graduate School of Medicine, Osaka, Japan; Department of Neurosurgery (T.F.), Osaka National Hospital, Osaka, Japan; and Department of Neurosurgery (T.M.), Osaka Neurological Institute, Osaka, Japan.

Please address correspondence to Hajime Nakamura, Department of Neurosurgery, Osaka University Graduate School of Medicine, 2-2 Yamadaoka, Suita, Osaka 565-0871, Japan; e-mail: hajime@nsurg.med.osaka-u.ac.jp

<http://dx.doi.org/10.3174/ajnr.A6101>

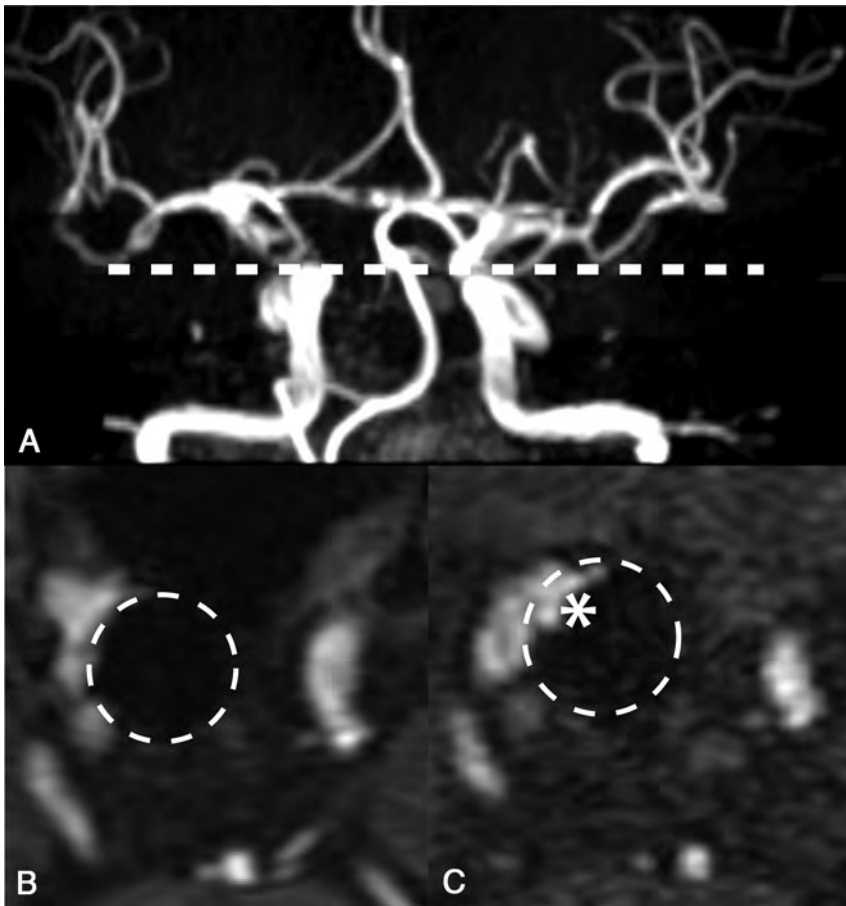


FIG 1. Evaluation of recanalization with MRA and TOF-MRA. *A*, At postprocedural day 1, we routinely evaluate the status of occlusion using MR angiography. The *dotted line* shows a cross-section of *B* and *C*. *B*, A residual neck is observed in the right internal carotid artery aneurysm after coil embolization at postprocedural day 1. *Dotted circles* show a coil mass. *C*, Blood flow signal of the residual neck has increased (*asterisk*) at 1 year after endovascular embolization compared with postprocedural day 1. This increased blood flow signal is regarded as recanalization.

unruptured aneurysms in 97 patients who were followed up for >5 years (follow-up group). The last follow-up data were collected in January 2017.

Aneurysm Measurement and Location

We measured the maximum size of aneurysms with 3D rotational angiography before treatment. We defined the bifurcation or nonbifurcation type of aneurysm as follows: The bifurcation type included all aneurysms that were located at an arterial bifurcation, such as the middle cerebral artery, anterior communicating artery, distal anterior cerebral artery, posterior communicating artery, ophthalmic artery, anterior choroidal artery, posterior inferior cerebellar artery, anterior inferior cerebellar artery and superior cerebellar artery, the top of the internal carotid artery, and the top of the basilar artery (BA). The nonbifurcation type of aneurysm was located at the arterial trunk, such as aneurysms at the dorsal wall of the internal carotid artery and BA trunk.

Endovascular Coil Embolization Procedure

Each endovascular embolization for an unruptured aneurysm was performed between April 2006 and March 2011 by a neurosurgeon who specialized in neurointervention (T.F.) To

avoid ischemic complications, we administered double antiplatelet drugs (aspirin, 100 mg, + clopidogrel, 75 mg, or aspirin, 100 mg, + cilostazol, 200 mg) 1 week before endovascular coil embolization. Double antiplatelet drugs were continued for 1–6 months after the procedure. A single antiplatelet drug was then continued for 6 months in patients without an assisting or for life in patients with a stent. An intravenous bolus injection of heparin was provided after arterial sheath insertion to maintain the activated clotting time at 250–300 seconds. Assisting devices, including balloons and stents, were selected according to the morphology and size of the neck and dome of the aneurysm. After a microcatheter was navigated into the aneurysm, platinum coils were placed in the aneurysm as long as the microcatheter was not pushed out of the aneurysm.

Angiographic Results and Follow-Up Evaluation

The immediate postprocedural angiographic results were classified using the Raymond-Roy occlusion classification¹³ by a neurosurgeon (T.F.) as follows: complete obliteration (CO), residual neck (RN), and residual aneurysm (RA). TOF-MRA was performed at 1 day, 3–6 months, 1 year after treatment, and every year thereafter. DSA at 1 year was

also routinely performed for monitoring embolized aneurysms. “Recanalization” was defined as an increasing blood flow signal in the aneurysm using TOF-MRA compared with a previous image (Fig 1). MR imaging was performed using either a 1.5T system (Ingenia; Philips Healthcare, Best, the Netherlands), or a 3T system (Discovery MR750 and MR750w; GE Healthcare, Milwaukee, Wisconsin, or Achieva; Philips Healthcare). Recanalization was judged by other neurosurgeons (H.N., T.N., and T.M.). These evaluations were performed independently and blindly. When there was a discrepancy, a decision was made by discussion with different neurosurgeons (K.A. and Y.K.). All neurosurgeons were board-certified as recorded by the Japan Neurosurgical Society. Therefore, they were well-informed regarding TOF-MRA technique properties, skills, artifacts, and limitations. These neurosurgeons were also experts in evaluating recanalization because they specialized in neurointervention. Furthermore, all neurosurgeons who evaluated recanalization were not involved in treating the cases of endovascular coil embolization. Retreatment was performed if the recanalization space was large enough for retreatment or it became larger or neurologic symptoms appeared.

Table 1: Analysis of recanalization after endovascular embolization of unruptured aneurysms

Parameters	Recanalization (n = 19)	Nonrecanalization (n = 97)	Total or Mean Value	P Value
Age (mean) (yr)	57.9 ± 12.1	59.6 ± 11.4	59.8 ± 11.3	.55 ^a
Sex (male/female)	3:16	31:66	34:82	.18 ^b
Location of the aneurysm (No.)				.72 ^b
MCA	1	10	11	
PcomA	1	7	8	
ICA	12	50	62	
BA tip	3	6	9	
Others	2	24	26	
Size of the aneurysm (No.) (mm)	9	6.8	7.1	.019 ^a
Balloon-assisted (No.)	17	69	86	.15 ^b
Stent-assisted (No.)	0	8	8	.34 ^b
CO/RN/RA (No.)	9/7/3	53/38/6	62/45/9 (53%/38%/7.7%)	.34 ^b

Note:—PcomA indicates posterior communicating artery.

^a *T* test.

^b Fisher exact test.

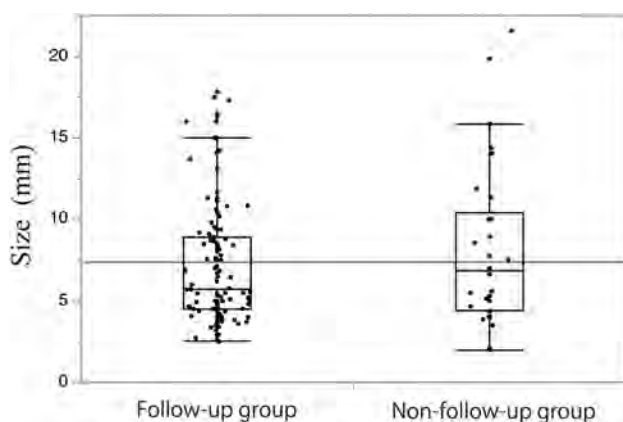


FIG 2. Comparison of the maximum size of aneurysms between the follow-up and non-follow-up groups. A total of 116 unruptured aneurysms were followed up for >5 years. These aneurysms were categorized as the follow-up-group. Thirty unruptured aneurysms could not be followed up for >5 years. These aneurysms were categorized as the non-follow-up group. The distribution of the maximum size of aneurysms between the follow-up and non-follow-up groups was not significantly different ($P = .24$, Student *t* test).

Statistical Analysis

Statistical analysis was performed with statistical software (JMP Pro 14.0.0; SAS Institute, Cary, North Carolina). Mean and frequency comparisons were analyzed simply. The nonrecanalized rate of embolized aneurysms was analyzed using the Kaplan-Meier method. The Bonferroni method was used for multiple comparisons. The relationships between recanalization and age, sex, initial angiographic results, aneurysm size, aneurysm site, and adjunctive technique (using balloon devices and stents) were also analyzed with the Student *t* test and Fisher exact test. Multivariable logistic regression was used for multivariate analysis. Differences were considered significant at $P < .05$.

RESULTS

Patients' Background and Details of Aneurysms

We investigated 116 unruptured aneurysms in 97 patients who were followed up for >5 years. The mean age of the patients was 59.8 ± 11.3 years, and 82 (70.6%) were women. Among the 116 aneurysms, 94 (81.0%) were located in the anterior circulation

and 22 (19.0%) were in the posterior circulation. Common aneurysmal locations are shown in Table 1. Fifty-eight (50.0%) aneurysms were the bifurcation type, and 58 (50.0%) were the nonbifurcation type. There was 1 case of a dissecting ICA aneurysm, which was categorized as a nonbifurcation-type aneurysm. The maximum diameter of aneurysms was measured on an angiogram, and the mean maximum size of aneurysms was 7.1 ± 3.7 mm. The distribution of the maximum size of each aneurysm was not significantly different between the follow-up and non-follow-up groups ($P = .24$, Fig 2). Furthermore, among the 97 patients, 33 (34.0%) patients had multiple aneurysms including untreated ones because of the small size. The mean number of aneurysms, including untreated aneurysms, was 1.4 ± 0.8 (range, 1–6).

Initial Angiographic Results and Recanalization

Endovascular procedures were performed with the patient under local anesthesia in 114 (98.2%) cases and under general anesthesia in 2 (1.8%) cases. In an immediate postprocedural angiogram, CO, an RN, and an RA were observed in 62 (53.4%), 45 (38.7%), and 9 (7.7%) aneurysms, respectively.

In our study, the mean follow-up period was 7.0 ± 1.4 years. In 116 unruptured aneurysms, recanalization was observed in 19 (16.3%). Three expert neurosurgeons (H.N., T.N., and T.M.) were in agreement regarding these results. There was 1 case of symptomatic recurrence (1/19, 5%), which was a visual disorder. Retreatment for recanalization was performed in 8 (6.8%) aneurysms. Among them, 3 (2.5%) aneurysms were retreated after >5 years from initial embolization. For all the retreated aneurysms, the 3 expert neurosurgeons were in agreement regarding the evaluation of the appearance of aneurysms on subsequent DSA. Figure 3 shows the Kaplan-Meier method for the nonrecanalization rate of the treated aneurysms with time. Aneurysms in which recanalization was not observed within 2 years after the procedure were not recanalized after this time.

Factors Associated with Recanalization

In univariate analysis, the maximum size of the aneurysm was significantly correlated with the recanalization rate ($P = .019$, Fig 4). Age ($P = .55$), sex ($P = .18$), and the location of the aneurysm ($P = .72$) were not significantly correlated with recanalization (Table 1). The immediate postprocedural angiographic results were not significantly related to recanalization ($P = .34$). Multivariable logistic regression also showed that only the maximum size of the aneurysm was significantly correlated with the recanalization rate (odds ratio = 1.24; 95% confidence interval, 1.05–1.43; $P = .006$; Table 2). There was no aneurysmal rupture in the follow-up period.

Relationship between the Size of the Aneurysm and the Nonrecanalization Rate

We stratified aneurysms into 3 groups (<5 mm, 5–10 mm, >10 mm) according to their dome size. The number of aneurysms

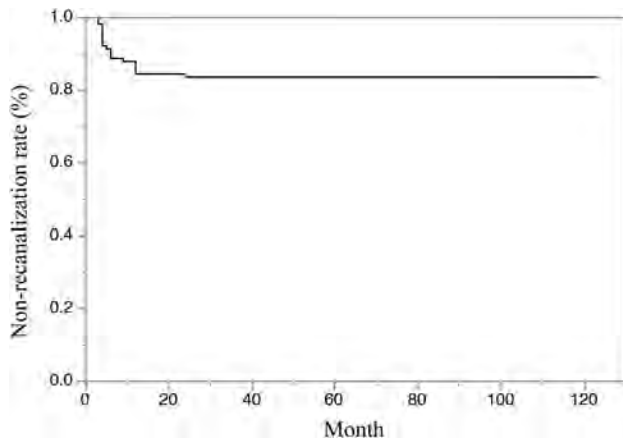


FIG 3. Kaplan-Meier analysis of the nonrecanalization rate. The non-recanalization rate of embolized aneurysms was decreased by 2 years, and there was no recanalization after this time.

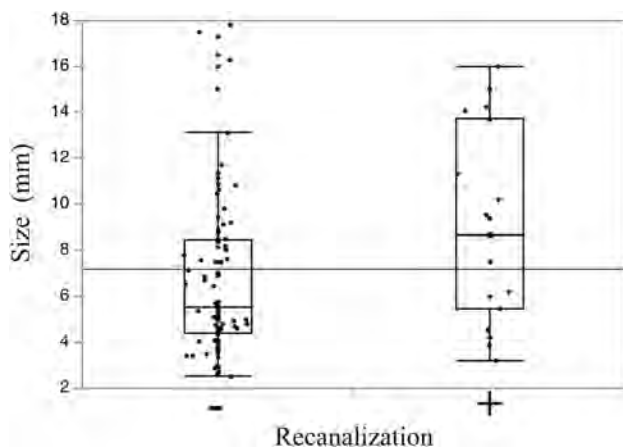


FIG 4. Correlation between recanalization and the size of aneurysms. The maximum size of aneurysms was significantly correlated with the recanalization rate ($P = .019$, Student t test).

Table 2: Multivariable logistic regression for recanalization

Variable	OR	95% CI	P Value
Age	0.99	0.95–1.04	.97
Sex	1.35	0.29–6.12	.69
Anterior/posterior	3.19	0.46–22.23	.22
Bifurcation type/nonbifurcation type	1.08	0.25–4.56	.91
Aneurysm location (ICA)	1.94	0.24–15.42	.52
Size (mm)	1.24	1.05–1.43	.006
No. of aneurysms	1.33	0.80–2.21	.27
Balloon-assisted	4.04	0.71–22.97	.084
Stent-assisted	0	0	.07
CO/RN/RA	1.05	0.38–2.86	.91
Follow-up period	1	0.99–1.00	.34

in these 3 groups was 44, 50, and 22, respectively. The nonrecanalization rate of embolized aneurysms in these 3 groups using the Kaplan-Meier method is shown in Fig 5. The group of aneurysms of >10 mm showed a significantly higher recanalization rate within 2 years compared with <5 mm ($P = .021$, Bonferroni method). Despite the size of the aneurysms, those in which recanalization was not observed within 2 years after the procedure were not recanalized during the follow-up period (Fig 5).

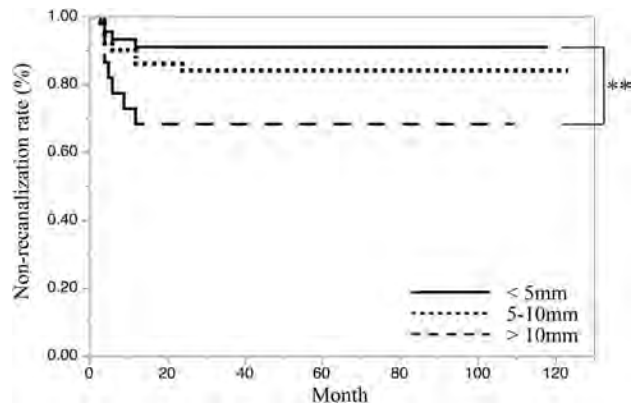


FIG 5. The relationship between the size of aneurysms and the nonrecanalization rate using the Kaplan-Meier method. Aneurysms were divided into <5 -mm, 5- to 10-mm, and >10 -mm groups. Using the Kaplan-Meier method, we analyzed the relationship between time (months) and the nonrecanalization rate of treated aneurysms in each group. The *thick line* indicates the nonrecanalization rate of the <5 -mm group. The *dotted line* indicates the 5- to 10-mm group. The *dashed line* indicates the >10 -mm group. The Bonferroni method showed that the >10 -mm group had a significantly higher recanalization rate within 2 years compared with the <5 -mm group. Despite the size of the aneurysms, aneurysms in which recanalization was not observed within 2 years after the procedure were not recanalized after this time. *Double asterisks* indicate $P = .021$.

DISCUSSION

Our study showed that the maximum size of aneurysms was significantly correlated with the recanalization rate. However, despite aneurysmal size, aneurysms in which recanalization was not observed within 2 years after endovascular coil embolization were stable during the follow-up period.

Endovascular coil embolization is accepted as a standard therapy for cerebral aneurysms worldwide.¹ Recanalization is one of the major concerns of endovascular coil embolization for cerebral aneurysms. Our study showed that recanalization and retreatment rates of embolized aneurysms were 16.3% and 6.8%, respectively, which are consistent with previous reports (recanalization rate: 4.7%–33.6%; retreatment rate: 4.7%–17.4%).^{2–10} A previous study reported that risk factors for recanalization were a ruptured aneurysm,⁴ a wide neck,³ a larger size,^{3,9,14–16} incomplete occlusion,^{9,17} a low-volume embolization rate,^{15,18,19} and a posterior circulation aneurysm.²⁰ In our study, a larger maximum size of the aneurysm was also significantly correlated with recanalization in univariate and multivariate analyses.

Incomplete occlusion, such as an RN and RA at the initial procedure, was not associated with recanalization in the present study. A previous report showed that coils in the acute phase facilitated coil-thrombus formation in the aneurysm, and this prevented inflow of blood.²¹ A coil-thrombus complex might have resulted in an increase in the volume-packing ratio and cases of CO, though tiny spaces between coils may actually exist. Therefore, the Raymond-Roy occlusion classification in the acute phase might have been inaccurate.

The recanalization rates of posterior circulation aneurysms and BA aneurysms are higher than those of aneurysms in other locations.²⁰ Although the recanalization rate of BA aneurysms was high (3/9, 30%) in our series, there was no significant difference in the recanalization rate between the posterior and

the anterior circulations. The reason might be because the proportion of BA aneurysms in the posterior circulation was smaller (9/24, 37.5%) in our series compared with that in the report of Nguyen et al,²⁰ though they did not show the specific number of aneurysms.

Three of 19 recanalized aneurysms were retreated >5 years after the initial treatment. These 3 aneurysms slightly recanalized within 2 years, were stable for the next 3 years, and then recanalized deeper >5 years after the first treatment. Therefore, if recanalization is detected within 2 years, we should continue imaging follow-up for >5 years. Significant risk factors for late deterioration are uncertain, but 2 of these 3 aneurysms were large (>14 mm). We suggest that early recanalized aneurysms should be followed up for >5 years, despite the extent of recanalization, especially in large aneurysms.

In our study, aneurysms stable for 2 years after the procedure were not recanalized. Raymond et al⁴ previously suggested that all patients should be followed up with noninvasive imaging studies for at least 3 years because 96.9% of all recanalizations were diagnosed by 3 years in their study. Furthermore, Holmin et al²² showed that stable angiographic findings during a 1-year interval predicted a low risk of recanalization. These reports are compatible with our results. If no recanalization is observed within 2 years after initial endovascular embolization for an unruptured aneurysm, further annual follow-up imaging studies in relation to treated aneurysms might be excessive. However, in the present study, development of new (de novo) aneurysms or enlargement of tiny or nontreated aneurysms coexisting with treated aneurysms was not evaluated. In managing patients with unruptured aneurysms, risk factors of growth and rupture need to be addressed. Awareness of a previous history of subarachnoid hemorrhage and risk factors, such as smoking, hypertension, and a family history, is considered important for preventing aneurysmal rupture and growth.²³ Therefore, a follow-up examination after coil embolization should be performed individually while considering de novo and nontreated aneurysms.

In the present study, relatively old imaging equipment was used. Newer instruments and technology in MRA for reducing artifacts and improving accuracy may be better for determining recanalization. However, because 3 expert neurosurgeons were in agreement about the results, our method of imaging was appropriate for evaluating recanalization of aneurysms. Additionally, in our institution, noncontrast TOF-MRA is routinely used to evaluate recanalization of aneurysms. Gadolinium-based enhanced MRA might be more accurate than TOF-MRA.^{24,25} van Amerongen et al¹¹ reported that the specificity of TOF-MRA was 84% with a sensitivity of 86% for discovery of aneurysm recanalization. For contrast-enhanced MRA, the specificity and sensitivity were 89% and 86%, respectively. However, we do not routinely select this method at our institution because contrast-enhanced MRA is more invasive and time-consuming than noncontrast MRA. However, contrast-enhanced MRA shows a higher quality view of stented parent arteries and fewer artifacts compared with TOF.^{24,26}

Our study has some limitations. First, although a wide neck and the volume embolization rate are correlated with recanalization,^{3,15,18,19} we were not able to evaluate these factors. We could

not collect sufficient data on the size of the neck or the volume embolization rate for further analysis because of the retrospective design of this study. However, our result about risk factors of recanalization could be acceptable because our other results are consistent with previous reports (eg, recanalization was correlated with a larger aneurysm size in the present study).^{3,9,14,15} Second, the mean observational span was 7 years. Earlier follow-up cases tended to be excluded because those patients had stopped coming to the hospital. Therefore, the mean follow-up period was 7.0 ± 1.4 years. Furthermore, whether a nonrecanalized aneurysm within 2 years after embolization will be secure for decades or a lifetime is unclear because late recanalization will probably occur in the future. Further studies on this issue for a longer period might be required. Third, this study had a retrospective design that was based on the clinical practice data. In the present study, a relatively large number of aneurysms ($n = 30$, non-follow-up group) could not be followed up. Considering the relatively small sample size in this study, loss in a non-follow-up group might have affected the significance of the results. However, the distribution of the maximum size of aneurysms between the follow-up and non-follow-up groups was not significantly different (Fig 2). Therefore, we consider that our results are acceptable, even though a relatively large number of aneurysms could not be followed up. Future studies on this issue are required in prospective and large cohorts.

CONCLUSIONS

Our study shows that aneurysms in which recanalization is not observed within 2 years after endovascular coil embolization are stable during a mean follow-up of 7 years. This result may be helpful in considering the appropriate span or frequency of follow-up imaging for embolized cerebral aneurysms.

ACKNOWLEDGMENTS

We thank Ellen Knapp, PhD, from the Edanz Group (www.edanzediting.com/ac) for editing a draft of the manuscript.

Disclosures: The authors declare that there is no conflict of interest.

REFERENCES

1. Molyneux AJ, Birks J, Clarke A, et al. **The durability of endovascular coiling versus neurosurgical clipping of ruptured cerebral aneurysms: 18-year follow-up of the UK cohort of the International Subarachnoid Aneurysm Trial (ISAT).** *Lancet* 2015;385:691–97 CrossRef Medline
2. Oishi H, Yamamoto M, Shimizu T, et al. **Endovascular therapy of 500 small asymptomatic unruptured intracranial aneurysms.** *AJNR Am J Neuroradiol* 2012;33:958–64 CrossRef Medline
3. Murayama Y, Nien YL, Duckwiler G, et al. **Guglielmi detachable coil embolization of cerebral aneurysms: 11 years' experience.** *J Neurosurg* 2003;98:959–66 CrossRef Medline
4. Raymond J, Guilbert F, Weill A, et al. **Long-term angiographic recurrences after selective endovascular treatment of aneurysms with detachable coils.** *Stroke* 2003;34:1398–403 CrossRef Medline
5. Gallas S, Pasco A, Cottier JP, et al. **A multicenter study of 705 ruptured intracranial aneurysms treated with Guglielmi detachable coils.** *AJNR Am J Neuroradiol* 2005;26:1723–31 Medline
6. Geyik S, Yavuz K, Ergun O, et al. **Endovascular treatment of intracranial aneurysms with bioactive Cerecye coils: effects on treatment stability.** *Neuroradiology* 2008;50:787–93 CrossRef Medline
7. Ries T, Siemonsen S, Thomalla G, et al. **Long-term follow-up of cerebral aneurysms after endovascular therapy prediction and**

- outcome of retreatment.** *AJNR Am J Neuroradiol* 2007;28:1755–61 CrossRef Medline
8. Renowden SA, Koumellis P, Benes V, et al. **Retreatment of previously embolized cerebral aneurysms: the risk of further coil embolization does not negate the advantage of the initial embolization.** *AJNR Am J Neuroradiol* 2008;29:1401–04 CrossRef Medline
 9. Campi A, Ramzi N, Molyneux AJ, et al. **Retreatment of ruptured cerebral aneurysms in patients randomized by coiling or clipping in the International Subarachnoid Aneurysm Trial (ISAT).** *Stroke* 2007;38:1538–44 CrossRef Medline
 10. Gallas S, Januel AC, Pasco A, et al. **Long-term follow-up of 1036 cerebral aneurysms treated by bare coils: a multicentric cohort treated between 1998 and 2003.** *AJNR Am J Neuroradiol* 2009;30:1986–92 CrossRef Medline
 11. van Amerongen MJ, Boogaarts HD, de Vries J, et al. **MRA versus DSA for follow-up of coiled intracranial aneurysms: a meta-analysis.** *AJNR Am J Neuroradiol* 2014;35:1655–61 CrossRef Medline
 12. Nihon-nousotyyuu-gakkai. **Nousotyyuu-guidline-iinkai.** *Nousotyyuu-tiryuu-guidline* (in Japanese). 2015. Kyowakikaku, Tokyo; 2015;230–35
 13. Roy D, Milot G, Raymond J. **Endovascular treatment of unruptured aneurysms.** *Stroke* 2001;32:1998–2004 CrossRef Medline
 14. Piotin M, Spelle L, Mounayer C, et al. **Intracranial aneurysms: treatment with bare platinum coils—aneurysm packing, complex coils, and angiographic recurrence.** *Radiology* 2007;243:500–08 CrossRef Medline
 15. Sluzewski M, Menovsky T, van Rooij WJ, et al. **Coiling of very large or giant cerebral aneurysms: long-term clinical and serial angiographic results.** *AJNR Am J Neuroradiol* 2003;24:257–62 Medline
 16. Koyanagi M, Ishii A, Imamura H. **Long-term outcomes of coil embolization of unruptured intracranial aneurysms.** *J Neurosurg* 2018;129:1492–98 CrossRef Medline
 17. Li MH, Gao BL, Fang C, et al. **Angiographic follow-up of cerebral aneurysms treated with Guglielmi detachable coils: an analysis of 162 cases with 173 aneurysms.** *AJNR Am J Neuroradiol* 2006;27:1107–12 Medline
 18. Tamatani S, Ito Y, Abe H, et al. **Evaluation of the stability of aneurysms after embolization using detachable coils: correlation between stability of aneurysms and embolized volume of aneurysms.** *AJNR Am J Neuroradiol* 2002;23:762–67 Medline
 19. Sugiyama S, Niizuma K, Sato K, et al. **Blood flow into basilar tip aneurysms: a predictor for recanalization after coil embolization.** *Stroke* 2016;47:2541–47 CrossRef Medline
 20. Nguyen TN, Hoh BL, Amin-Hanjani S, et al. **Comparison of ruptured vs unruptured aneurysms in recanalization after coil embolization.** *Surg Neurol* 2007;68:19–23 CrossRef Medline
 21. Bavinzski G, Talazoglu V, Killer M, et al. **Gross and microscopic histopathological findings in aneurysms of the human brain treated with Guglielmi detachable coils.** *J Neurosurg* 1999;91:284–93 CrossRef Medline
 22. Holmin S, Krings T, Ozanne A, et al. **Intradural saccular aneurysms treated by Guglielmi detachable bare coils at a single institution between 1993 and 2005: clinical long-term follow-up for a total of 1810 patient-years in relation to morphological treatment results.** *Stroke* 2008;39:2288–97 CrossRef Medline
 23. Sonobe M, Yamazaki T, Yonekura M, et al. **Small unruptured intracranial aneurysm verification study: SUAVE study, Japan.** *Stroke* 2010;41:1969–77 CrossRef Medline
 24. Anzalone N, Scomazzoni F, Cirillo M, et al. **Follow-up of coiled cerebral aneurysms at 3T: comparison of 3D time-of-flight MR angiography and contrast-enhanced MR angiography.** *AJNR Am J Neuroradiol* 2008;29:1530–36 CrossRef Medline
 25. Kaufmann TJ, Huston J 3rd, Cloft HJ, et al. **A prospective trial of 3T and 1.5T time-of-flight and contrast-enhanced MR angiography in the follow-up of coiled intracranial aneurysms.** *AJNR Am J Neuroradiol* 2010;31:912–18 CrossRef Medline
 26. Choi JW, Roh HG, Moon WJ, et al. **Time-resolved 3D contrast-enhanced MRA on 3.0T: a non-invasive follow-up technique after stent-assisted coil embolization of the intracranial aneurysm.** *Korean J Radiol* 2011;12:662–70 CrossRef Medline

Flow-Pattern Details in an Aneurysm Model Using High-Speed 1000-Frames-per-Second Angiography

J.M. Krebs, A. Shankar, S.V. Setlur Nagesh, J.M. Davies, K.V. Snyder, E.I. Levy, L.N. Hopkins, M. Mokin, D.R. Bednarek, A.H. Siddiqui, and S. Rudin



ABSTRACT

SUMMARY: Traditional digital subtraction angiography provides rather limited evaluation of contrast flow dynamics when studying and treating intracranial brain aneurysms. A 1000-frames-per-second photon-counting x-ray detector was used to image detailed iodine-contrast flow patterns in an internal carotid artery aneurysm of a 3D-printed vascular phantom. High-speed imaging revealed differences in vortex and inflow patterns with and without a Pipeline Embolization Device flow diverter in more detail and clarity than could be seen in standard pulsed angiography. Improved temporal imaging has the potential to impact the outcomes of endovascular interventions by allowing clinicians to better understand and act on flow dynamics in real-time.

ABBREVIATION: fps = frames per second

Hemodynamics are important in determining intervention outcomes. Conventional flat panel x-ray detectors operating at 30–60 frames per second (fps) offer limited visualization of aneurysmal flow patterns due to insufficient temporal resolution. Instead, studies seeking to understand the hemodynamics of intracranial arteries currently use computational fluid dynamics,¹ with complex algorithms to recreate flow patterns as opposed to directly measuring them. Although computational fluid dynamics is excellent for the display of detail in hemodynamics, it is an approximation of flow conditions and requires a long computational time to run the simulations, which significantly limits real-time applicability. We herein present a new method of using a new high-speed x-ray detector to visu-

alize the details of arterial hemodynamics during an interventional procedure.

Aneurysms are abnormal outpouchings on arteries, and 1 treatment option involves the use of flow-diverting stents, such as the Pipeline Embolization Device (PED; Covidien, Irvine, California). Flow diverters induce a modification of blood flow within and around the inflow zone of an aneurysm that leads to gradual intra-aneurysmal thrombosis and healing. During the intervention, clinicians must make critical judgements regarding placement, repositioning, and stacking of flow diverters that will ultimately impact treatment efficacy 6 months to a year later; thus, a detailed understanding of how flow is altered could critically impact treatment. In this work, we present the use of a 1000-fps single-photon-counting x-ray detector to visualize changes in detailed flow patterns in and around a 3D-printed flow-diverter-treated internal carotid artery aneurysm model in high spatial and temporal resolution.

MATERIALS AND METHODS

Detector Description

The Actaeon detector (XCounter, Danderyd, Sweden) is a single-photon-counting direct cadmium telluride detector with a 100- μm pixel pitch and a 256×256 matrix size, capable of acquisition speeds up to 1000 fps.²

Aneurysm Model Description

The process for fabricating 3D-printed models has been previously described.³ The model, simulating an internal carotid artery aneurysm, was connected to a pulsatile flow loop with water used

Received January 24, 2019; accepted after revision April 25.

From the Canon (formerly Toshiba) Stroke and Vascular Research Center (J.M.K., A.K., S.V.S.N., K.V.S., E.I.L., L.N.H., D.R.B., A.H.S., S.R.) and Departments of Biomedical Engineering (S.R.), Mechanical and Aerospace Engineering (S.R.), and Electrical Engineering (S.R.), University at Buffalo, State University of New York, Buffalo, New York; Department of Neurosurgery (J.M.D., K.V.S., E.I.L., L.N.H., A.H.S., S.R.), Gates Vascular Institute at Kaleida Health, Buffalo, New York; Departments of Neurosurgery (S.V.S.N., J.M.D., K.V.S., E.I.L., L.N.H., D.R.B., A.H.S., S.R.), Bioinformatics (J.M.D.), Radiology (E.I.L., L.N.H., D.R.B., A.H.S., S.R.), and Neurology (K.V.S.), Jacobs School of Medicine and Biomedical Sciences, University at Buffalo, State University of New York, Buffalo, New York; Jacobs Institute (J.M.D., K.V.S., E.I.L., L.N.H., A.H.S.), Buffalo, New York; and Department of Neurosurgery and Brain Repair (M.M.), University of South Florida, Tampa, Florida.

This work was partially supported by a research grant from Canon Medical Systems Corporation.

Please address correspondence to Stephen Rudin, PhD, Canon (formerly Toshiba) Stroke and Vascular Research Center, University at Buffalo, 875 Ellicott St, Buffalo, NY 14203; e-mail: srudin@buffalo.edu



Indicates article with supplemental on-line videos.

<http://dx.doi.org/10.3174/ajnr.A6090>

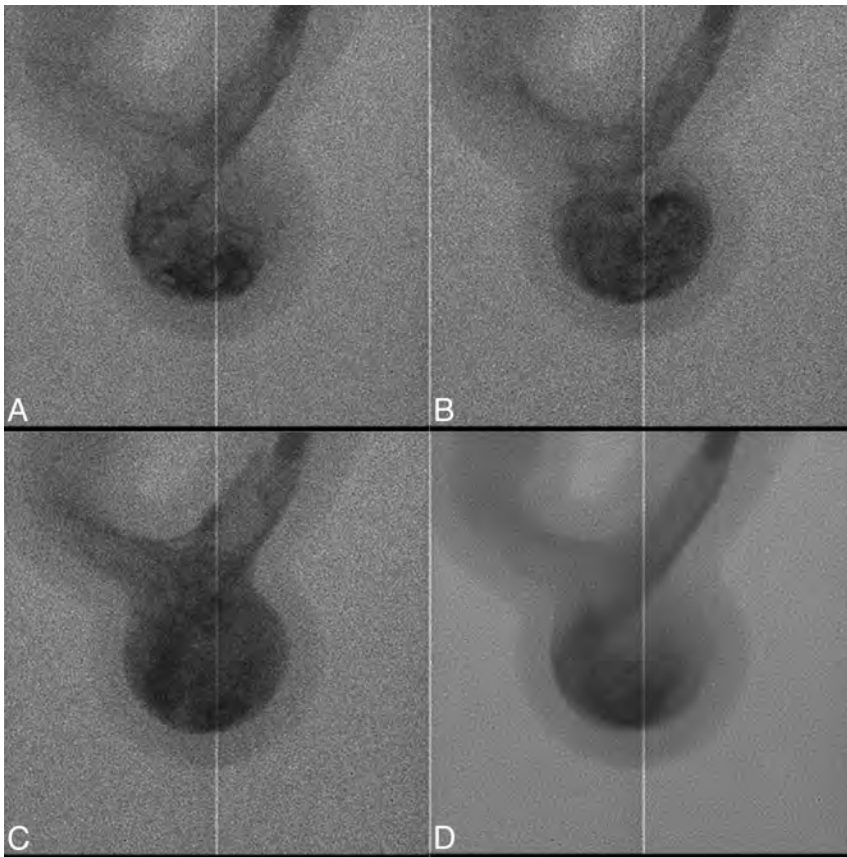


FIG 1. DSA images show flow detail in an internal carotid artery aneurysm model when no PED flow diverter is deployed, acquired at 1000 fps and separated by 25 frames each (A–C), and a single averaged image for one 40-ms x-ray pulse (D). The vertical line shows the 1-pixel boundary between detector modules. For the full sequence, see On-line Video 1.

as the circulating fluid. A 21-mm aluminum block was added underneath the model to approximate the x-ray attenuation of a human head (RQA5 attenuator, IEC 61267-1, 62220-1).

Image Acquisition

The detector was mounted on a Unistrut platform (Unistrut, Harvey, Illinois) and positioned 6 cm above the phantom, resulting in a magnification factor of 1.08, and was set to acquire continuously at 1000 fps. An Infinix biplane C-arm system (Model INFX-8000V; Canon, Otawara, Japan) was used as the x-ray source. Peak tube voltage was set to 92 kV, the tube current was set to 160 mA, and the exposure pulse width was set to 100 ms with a medium focal spot. A 6F catheter (Model 7512–23; Merit Medical, South Jordan, Utah) was placed proximal to the aneurysm region. With the catheter in place, an AutoSyringe (Model PPD11060507; Medrad, Warrendale, Pennsylvania) was used to inject a 10-mL burst of 350 mg of undiluted iodine per milliliter of contrast agent into the 3D printed vessel at 10 mL/s. The delay between the injection and the x-ray trigger was varied to observe contrast flow variation at different time intervals postinjection.

We acquired images of contrast flow before and after PED deployment. The PED was partially deployed, resulting in complete coverage of the aneurysmal ostia to accommodate multiple experiments. Images were acquired at 1000 fps, yielding 100 images for every 100-ms x-ray exposure period. For

comparison with standard angiography, we averaged 40 of these frames to simulate 1 image acquired with an exposure pulse width of 40 ms.

Exposure

The air kerma at the phantom entrance surface was measured using a 6-mL PTW ionization chamber and electrometer (Model T10023 Unidos; PTW, Freiburg, Germany).

RESULTS AND DISCUSSION

The air kerma per frame was $12.3 \mu\text{Gy}$ at the phantom entrance surface for each of the 1-ms images acquired at 1000 fps. The air kerma for frames integrated over a sequence of 100 ms was 1.23 mGy at the entrance surface. This is approximately the dose expected from a DSA run containing 20 frames.

Figure 1 (A–C) shows 3 images with no PED from a 100-image sequence acquired at 1000 fps. Figure 1D shows an image averaged over 40 frames from the same sequence with reduced noise and increased motion blurring. The blur for an actual DSA frame will depend on the pulse width used and the velocity of the blood flow. Noise reduction and blurring over a few tens of a millisecond

pulse width would correspond to those of a standard angiography frame. Future studies will be needed to better evaluate any potential effect of noise and noise variation across a nonhomogeneous phantom. Figure 2 shows the corresponding image datasets with a PED partially deployed.

Compared with standard angiographic images, Figs 1A–C and 2A–C demonstrate that additional information, such as detailed flow patterns in the aneurysm region, is visualized in images acquired at 1000 fps due to higher temporal resolution. When no PED flow diverter was deployed, images acquired at 1000 fps (Fig 1A–C and On-line Video 1) clearly show flow into the aneurysm with the development of vortices of contrast in the aneurysmal sac. Images acquired with a PED flow diverter in place (Fig 2A–C and On-line Video 2) show more diffuse flow of contrast into the aneurysm with lower apparent flow velocities and delayed development of vortices in the aneurysm sac. While with the flow phantom reported on here, changes in contrast media streamlines and blob shapes could easily be seen with 1-ms frame intervals, lower imaging speeds might be sufficient under certain circumstances. This will require further study.

For this demonstration, the synchronization between the high-speed detector and the x-ray source was done manually. The 100-ms exposure time used in this study is a limitation of the x-ray source.

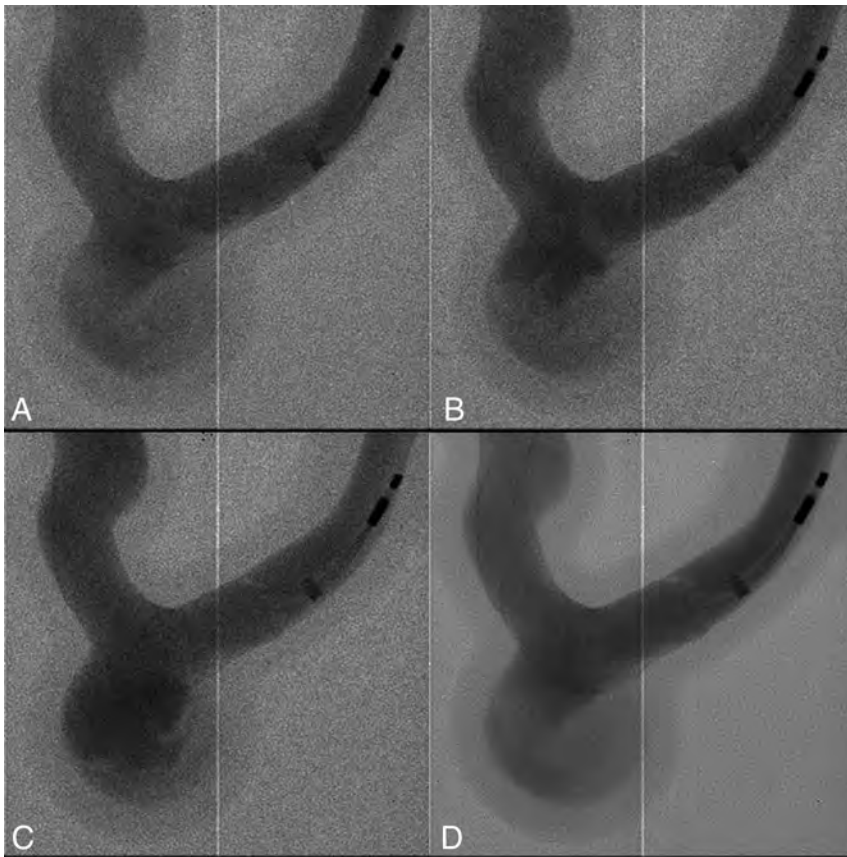


FIG 2. DSA images show flow detail in an internal carotid artery aneurysm model when a PED flow diverter is deployed, acquired at 1000 fps and separated by 25 frames each (A–C), and a single averaged image for one 40-ms x-ray pulse (D). For the full sequence, see On-line Video 2.

High-speed imaging, enabled by this new detector, allows clinicians to observe detailed flow patterns in the 3D-printed phantom, including differentiation of flow patterns into the target aneurysm versus the parent vessel. These gains in temporal information could potentially impact treatment decisions by allowing clinicians to assess flow patterns in real-time during a procedure. During treatment, clinicians assess the adequacy of stent placement by looking for indirect signs of flow diversion, such as evaluating wall apposition and looking for contrast stasis within the aneurysm sac. Detailed visualization of changes in flow dynamics could allow clinicians to directly assess factors that have been shown to improve the efficacy of flow diverters, such as decreases in flow vortices.⁴ Other potential clinical uses include the detection of endoleaks near an aneurysm, identification of residual flow that could cause an aneurysm to regrow, blood impingement pattern that could lead to coil compaction, and diversion of jets into an aneurysm at locations where flow may be less intuitive (such as at a bifurcation).

The imager described here is a small-FOV, ROI detector. It is contemplated that within a system that also provides a conventional full FOV capability, a high-speed unit somewhat larger than that shown here could be deployed during an interventional procedure in a manner similar to that of the Micro-Angiographic Fluoroscope (Canon Stroke and Vascular Research Center, University at Buffalo, Buffalo, New York), which has been previously

described⁵ and has evolved into the current Hi-Def Detector System (Canon Medical, Tustin, California).

CONCLUSIONS

Improvements in spatial and temporal resolution of angiography have the potential to significantly improve outcomes by giving clinicians additional real-time insights into the details of flow dynamics, which allow intraprocedural modifications to improve procedural safety and long-term efficacy.

Disclosures: Jordan M. Krebs—*RELATED: Grant:* Canon Medical Systems Corporation, *Comments:* research grant for Canon Stroke and Vascular Research Center, where the work took place*; *Grants/Grants Pending:* Canon Medical Systems Corporation, *Comments:* research grant for Canon Stroke and Vascular Research Center, where the work took place.* Alok Shankar—*RELATED: Grant:* Canon Medical Systems Corporation, Tokyo, Japan, *Comments:* research grant. Jason Davies—*UNRELATED: Employment:* Mr; *Grants/grants pending:* CTSR KL2.* Elad I. Levy—*UNRELATED: Board Membership:* Stryker, NeXtGen Biologics, MEDX, Cognition Medical, Endostream Medical, *Comments:* advisory board; *Consultancy:* Claret Medical, Gerson Lehrman Group Consulting, Guidepoint Global Consulting, Imperative Care, Medtronic, Rebound Therapeutics, StimMed; *Stock/Stock Options:* NeXtGen Biologics, Rapid Medical, Claret Medical, Cognition Medical, Imperative Care, Rebound Therapeutics, StimMed, Three Rivers Medical. Leo Nelson Hopkins—*UNRELATED: Board Membership:* Claret Medical; *Consultancy:* Boston Scientific, Abbott, Cordis, Medtronic; *Employment:*

University at Buffalo Neurosurgery, Jacobs Institute, Ka-leida Health; *Payment for Lectures Including Service on Speakers Bureaus:* Memorial Healthcare System, Complete Conference Management; *Stock/Stock Options:* Boston Scientific, Claret Medical, Augmenix, Endomation, Silk Road Medical, Ostial, Apama Medical, StimSox, Photolitec, ValenTx, Axtria, Ocular Therapeutix, The Stroke Project, *Comments:* financial interests, no money received. Maxim Mokin—*UNRELATED: Consultancy:* Cerebrotech Medical Systems, Canon Medical Systems Corporation, Imperative Care; *Royalties:* Oxford University Press. Daniel R. Bednarek—*RELATED: Grant:* Canon Medical Systems Corporation*; *UNRELATED: Grants/Grants Pending:* Canon Medical Systems Corporation*; *Royalties:* Canon Medical Systems Corporation, *Comments:* Dose Tracking System (DTS) licensing agreement.* Adnan H. Siddiqui—*UNRELATED: Consultancy:* Amnis Therapeutics, Boston Scientific, Canon Medical Systems USA, Cerebrotech Medical Systems, Cerenovus, Corindus Vascular Robotics, Endostream Medical, Guidepoint Global Consulting, Imperative Care, Integra, Medtronic, MicroVention, Northwest University; *Data and Safety Monitoring Board Chair for the HEAT Trial,* Penumbra, Q'Apel Medical, Rapid Medical, Rebound Therapeutics, Serenity Medical, Silk Road Medical, StimMed, Stryker, Three Rivers Medical, Vassol, W.L. Gore & Associates; *Stock/Stock Options:* Amis Therapeutics, BlinkTBI, Buffalo Technology Partners, Cardinal Consulting, Cerebrotech Medical Systems, Cognition Medical, Endostream Medical, Imperative Care, International Medical Distribution Partners, Neurovascular Diagnostics, Q'Apel Medical, Rebound Therapeutics, Rist Neurovascular, Serenity Medical, Silk Road Medical, StimMed, Synchron, Three Rivers Medical, Viseon Spine. Stephen Rudin—*RELATED: Grant:* Canon Medical Systems Corporation, *Comments:* An equipment grant from Canon is provided as well as partial research support*; *Provision of Writing Assistance, Medicines, Equipment, or Administrative Support:* Canon Medical Systems Corporation, *Comments:* Some x-ray equipment has been provided*; *Other:* National Institute of Biomedical Imaging and Bioengineering, National Institutes of Health, *Comments:* Partial support was provided in the past*; *UNRELATED: Patents (Planned, Pending or Issued):* Canon Medical Systems Corporation, *Comments:* There is an unrelated patent application pending*; *Royalties:* Canon Medical Systems Corporation, *Comments:* totally different project involving dose-tracking system software for clinical angiography equipment. *Money paid to the institution.

REFERENCES

1. Jiang J, Strother C. **Computational fluid dynamics simulations of intracranial aneurysms at varying heart rates: a “patient-specific” study.** *J Biomech Eng* 2009;131:091001 CrossRef Medline
2. Shankar A, Krebs J, Bednarek DR, et al. **Evaluation of a new photon-counting imaging detector (PCD) with various acquisition modes.** *Proc SPIE Int Soc Opt Eng* 2018;10573 CrossRef Medline
3. Russ M, O’Hara R, Setlur Nagesh SV, et al. **Treatment planning for image-guided neuro-vascular interventions using patient-specific 3D printed phantoms.** *Proc SPIE Int Soc Opt Eng* 2015;9417 CrossRef Medline
4. Dholakia R, Sadasivan C, Fiorella DJ, et al. **Hemodynamics of flow diverters.** *J Biomech Eng* 2017;139 CrossRef Medline
5. Binning MJ, Orion D, Yashar P, et al. **Use of the microangiographic fluoroscope for coiling of intracranial aneurysms.** *Neurosurgery* 2011;69:1131–38 CrossRef Medline

Antiplatelet Therapy in Patients with Aneurysmal SAH: Impact on Delayed Cerebral Ischemia and Clinical Outcome. A Meta-Analysis

F. Cagnazzo, I. Derraz, P.-H. Lefevre, G. Gascou, C. Dargazanli, C. Riquelme, P. Perrini, D. di Carlo, A. Bonafe, and V. Costalat



ABSTRACT

BACKGROUND AND PURPOSE: Delayed cerebral ischemia strongly impacts clinical outcome after aneurysmal SAH. The effect of antiplatelet therapy on delayed cerebral ischemia has been described with heterogeneous results. Our aim was to analyze the efficacy of antiplatelet therapy on delayed cerebral ischemia and clinical outcome in patients with SAH.

DATA SOURCES: A systematic search of 3 databases was performed for studies published from 1990 to 2019.

STUDY SELECTION: According to the Preferred Reporting Items for Systematic Reviews and Meta-Analyses guidelines, we included studies comparing the rates of delayed cerebral ischemia and clinical outcomes among patients with SAH with and without antiplatelet therapy.

DATA ANALYSIS: Random-effects meta-analysis was used to pool the following: delayed cerebral ischemia, mortality, and good outcome rates.

DATA SYNTHESIS: Including 7 studies, 1060 and 1762 patients with SAH were endovascularly or surgically treated with (cases) and without (controls) antiplatelet therapy, respectively. Overall, antiplatelet therapy did not significantly decrease delayed cerebral ischemia rates compared with the control group (219/1060 versus 485/1762, OR = 0.781; 95% CI, 0.46–1.31; $P = .33$). Among patients treated endovascularly, there was a trend toward lower delayed cerebral ischemia rates after antiplatelet therapy (157/778 versus 413/1410, OR = 0.552; 95% CI, 0.273–1.115; $P = .06$). Long-term (>2 weeks) antiplatelet therapy tended to be associated with a lower incidence of delayed cerebral ischemia (63/438 versus 96/353, OR = 0.379; 95% CI, 0.12–1.2; $P = .06$). The good-outcome rate was significantly higher (803/1144 versus 1175/1775, OR = 1.368; 95% CI, 1.117–1.676; $P = .002$) and the mortality rate was significantly lower (79/672 versus 97/571, OR = 0.656; 95% CI, 0.47–0.91; $P = .01$) among the antiplatelet therapy group.

LIMITATIONS: Heterogeneity was high for most outcomes.

CONCLUSIONS: Overall, the incidence of delayed cerebral ischemia seems not to be significantly reduced among the antiplatelet therapy group. However, delayed cerebral ischemia tended to be lower among subjects with both long-term antiplatelet therapy and endovascular treatment and antiplatelet administration. Poor outcome and mortality rates were significantly reduced among the antiplatelet therapy group.

ABBREVIATIONS: ASA = acetylsalicylic acid; AT = antiplatelet therapy; CV = cerebral vasospasm; DCI = delayed cerebral ischemia

Among patients with aneurysmal subarachnoid hemorrhage, delayed cerebral ischemia (DCI) represents a devastating complication that occurs in approximately 30% of subjects who survive the initial bleeding.¹ In general, DCI is defined as the development of new neurologic deficits, occurring most often

between 4 and 10 days after SAH, confirmed by new cerebral hypodense lesions on CT with no evidence of hydrocephalus or rebleed.^{2–5} The pathogenesis of DCI is still not completely clarified, and several mechanisms have been proposed, such as inflammatory activation, vasospasm, cortical spreading depolarization, and microthrombosis.¹ Along with the above-mentioned mechanisms, an increased platelet activity after SAH might also be involved in the development of DCI.^{6,7} Platelet aggregability and

Received March 3, 2019; accepted after revision April 25.

From the Neuroradiology Department (F.C., I.D., P.-H.L., G.G., C.D., C.R., A.B., V.C.), University Hospital Gui-de-Chauliac, Centre Hospitalier Universitaire de Montpellier, Montpellier, France; and Department of Neurosurgery (P.P., D.d.C.), University of Pisa, Pisa, Italy.

Please address correspondence to Federico Cagnazzo, MD, Neuroradiology Department, CHU Gui De Chauliac, 80 Ave Augustin Fliche, 34000 Montpellier, France; e-mail: f.cagnazzo86@gmail.com

Indicates article with supplemental on-line tables.

Indicates article with supplemental on-line photos.

<http://dx.doi.org/10.3174/ajnr.A6086>

the associated release of thromboxane B2 are increased in patients with SAH, especially in subjects with DCI.³ Accordingly, several studies indicated a possible preventive effect of antiplatelet therapy (AT), especially with aspirin, on the development of DCI in patients with SAH. However, the results are quite heterogeneous, and the efficacy of the platelet inhibitors for the prevention of DCI is still debated. Recently, 2 series of ruptured intracranial aneurysms treated by endovascular means showed that antiplatelet agents effectively reduced the risk of vasospasm and DCI.^{2,8} Our meta-analysis aimed to investigate the effect of antiplatelet drug administration on the prevention of DCI among patients with aneurysmal SAH. In addition, including recent series of endovascular treatments, we explored the effect of antiplatelet inhibitors in relation to the type of treatment.

MATERIALS AND METHODS

Literature Search

A comprehensive literature search of PubMed, Ovid EMBASE, and Scopus was conducted for studies published from January 1990 to January 2019. The Preferred Reporting Items for Systematic Reviews and Meta-Analyses (PRISMA) guidelines⁹ were followed. The key words and the detailed search strategy are reported in On-line Table 1, and the studies included in our review are reported in On-line Table 2. The main inclusion criteria were the following: 1) studies reporting patients with aneurysmal SAH who were treated with (cases) and without (controls) AT during the acute phase, 2) studies reporting clinical outcomes (incidence of DCI, cerebral vasospasm [CV], and neurologic outcome) of patients with aneurysmal SAH undergoing treatment with AT. In addition, the selection was restricted to studies reporting treatment with acetylsalicylic acid (ASA) (or ASA plus clopidogrel) given during the acute phase of SAH for the period of risk for CV and DCI (AT was continued for at least 2–3 weeks after SAH). Exclusion criteria were the following: 1) case reports, 2) review articles, 3) studies published in languages other than English, 4) in vitro/animal studies, and 5) studies reporting patients treated with other antiplatelet drugs different from ASA or clopidogrel, and 6) studies reporting patients for whom the AT was not continued during the period of risk for DCI and CV. In cases of overlapping patient populations, only the series with the largest number of patients or the most detailed data was included. Two independent readers screened articles in their entirety to determine eligibility for inclusion. A third author solved discrepancies.

Data Collection

We extracted the following: 1) incidence of DCI, 2) incidence of CV, 3) treatment-related complications, and 4) clinical outcome. The reported results were compared between patients treated (cases) and not treated (controls) with AT.

DCI was defined as the occurrence of new clinical features suggestive of DCI (gradually developed focal deficits, a decreased level of consciousness, or both) confirmed by new cerebral hypodense lesions on CT with no evidence of hydrocephalus or re-bleed.^{2–5} Good outcome was defined as a modified Rankin Scale score of 0–2 or a Glasgow Outcome Score of 4–5.

Outcomes

The primary objective of this study was to compare the incidence of DCI and good neurologic outcome between the AT and the control groups. The secondary objectives were to define the following: 1) the incidence of CV among the AT and the control groups, 2) the influence of AT on the occurrence of DCI based on the type of aneurysm treatment (endovascular versus surgical), and 3) the influence of the duration (short-term, <2 weeks versus long-term, >2 weeks) of the AT on the DCI rate.

Quality Scoring

The Newcastle-Ottawa Scale¹⁰ was used for the quality assessment of the included studies (details in On-line Table 3). The quality assessment was performed by 2 authors independently, and a third author solved discrepancies.

Statistical Analysis

We estimated, from each cohort, the cumulative prevalence (percentage) and 95% confidence interval for each outcome. Heterogeneity of the data was assessed I^2 , and subsequently, the DerSimonian and Laird random-effects model was applied. The graphic representation was performed by a forest plot. To evaluate the heterogeneity and bias, we analyzed the meta-regression and funnel plot followed by the Egger linear regression test, respectively. To verify the consistency of outcome meta-analysis results, the influence of each individual study on the summary effect estimate was assessed by the sensitivity analysis (“leave-one-out” approach) and the subgroups analysis. Differences were considered significant at $P < .05$. Meta-analysis was performed with ProMeta-2 (Internovi, Cesena, Italy) and OpenMeta[Analyst] (<http://www.cebm.brown.edu/openmeta/>).

RESULTS

Literature Review

Studies included in our meta-analysis are summarized in On-line Table 2. The search flow diagram is shown in On-line Fig 1.

A total of 7 studies and 2822 patients with aneurysmal SAH were included in our review. Overall, 1060 patients were treated with AT (cases), whereas 1762 patients did not receive antiplatelet agents (controls). All the included studies compared patients with SAH with and without AT during the acute phase.

Quality of Studies

Five studies presented a prospective design^{3–5,11,12}: Two studies were randomized controlled trials,^{3,5} 1 study was prospective,⁴ and 2 series were post hoc analyses from prospective randomized trials.^{11,12} Two studies had a retrospective design.^{2,8} Overall, all the reported articles were rated as “high-quality” studies based on the Newcastle-Ottawa Scale criteria.

Patient Population Characteristics

Detailed characteristics of the patient population are reported in On-line Tables 2 and 4. The mean age of patients was comparable between the 2 groups. The proportion of male patients was higher among the control group (49.9%; 95% CI, 47%–51% versus 43.7%; 95% CI, 41%–47%; $P = .006$). The proportion of high-grade SAH (Fisher 3–5) was slightly higher among the control

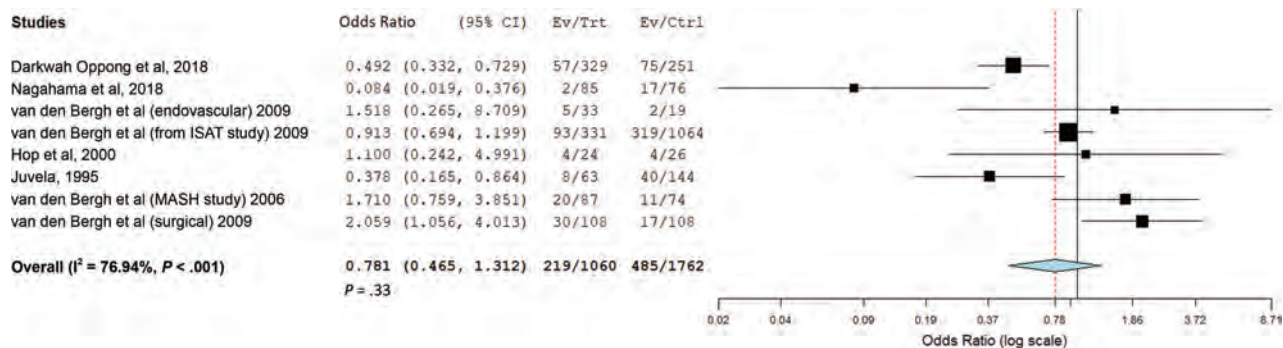


FIG 1. Forest plot with a random-effects model demonstrating the overall incidence (odds ratio meta-analysis) of DCI in the AT group compared with the control group. Ev indicates Events; Trt, Treated patients; Ctrl, Control.

Clinical outcomes after subarachnoid hemorrhage: comparison between the antiplatelet and the control groups

Outcomes	Antiplatelet Group vs Control Group (95% CI) (I^2)	No. of Articles	P Value
Overall rate of delayed cerebral ischemia	219/1060 vs 485/1762, OR = 0.781 (95% CI, 0.46–1.31) ($I^2 = 76.9\%$)	7	.33
Delayed cerebral ischemia endovascular group	157/778 vs 413/1410, OR = 0.552 (95% CI, 0.273–1.115) ($I^2 = 80.1\%$)	4	.06 ^a
Delayed cerebral ischemia surgical group	42/195 vs 61/278, OR = 0.952 (95% CI, 0.288–3.147) ($I^2 = 79.5\%$)	3	.5
Delayed cerebral ischemia long-term AT ^b	63/438 vs 96/353, OR = 0.379 (95% CI, 0.12–1.2) ($I^2 = 68\%$)	3	.06 ^a
Delayed cerebral ischemia short-term AT ^c	148/559 vs 349/1265, OR = 1.35 (95% CI, 0.81–2.23) ($I^2 = 80.1\%$)	4	.5
Cerebral vasospasm	79/414 vs 84/327, OR = 0.52 (95% CI, 0.2–1.5) ($I^2 = 83\%$)	2	.2
Good outcome	803/1144 vs 1175/1775, OR = 1.368 (95% CI, 1.117–1.676) ($I^2 = 9.3\%$)	8	.002 ^a
Mortality	79/672 vs 97/571, OR = 0.656 (95% CI, 0.47–0.91) ($I^2 = 0\%$)	5	.01 ^a
Overall rate of complications	40/438 vs 28/353, OR = 1.01 (95% CI, 0.34–3.01) ($I^2 = 42\%$)	3	.9
Overall rate of hemorrhagic complications	32/438 vs 15/353, OR = 1.7 (95% CI, 0.89–3.38) ($I^2 = 1\%$)	3	.1
Overall rate of major hemorrhagic events	8/438 vs 8/353, OR = 0.857 (95% CI, 0.32–2.28) ($I^2 = 10\%$)	3	.7

^a Significant.

^b Long-term AT = AT for 3 or 4 weeks.

^c Short-term AT = AT for <2 weeks.

group (67.7%; 95% CI, 65.6%–70% versus 60.6%; 95% CI, 57%–63.5%; $P = .001$). There were no aneurysms treated with stent-assisted coiling or flow diversion among the control group, whereas patients treated with coiling were slightly lower in the AT group (63.3%; 95% CI, 60%–66%) compared with controls (74%; 95% CI, 72%–76%; $P = .001$).

In all except 1 study, the AT consisted of ASA, 100 mg/day, started after the aneurysm occlusion (On-line Table 2). Dual AT was used in the series of Nagahama et al⁸ (clopidogrel, 600 mg, + ASA, 325/day, after aneurysm embolization). In 1 study,¹¹ the dose of ASA ranged between 75 mg and 325 mg/day.

The mean clinical follow-up was 5 months (median, 3.5 months; interquartile range, 2–6 months).

Treatment-Related Outcomes among the AT and Control Groups

Treatment-related outcomes were analyzed with the random-effects model because this model incorporates heterogeneity among studies. Overall, there was not a statistically significant reduction of the rate of DCI among the AT group compared with the control group (219/1060 versus 485/1762, OR = 0.781; 95% CI, 0.46–1.31; $P = .33$) (Fig 1 and Table). The funnel-plot, followed by the Egger linear regression test, excluded publication bias ($P = .8$). Meta-regression showed an insignificant variation of the effect size ($P = .5$) during the investigated period (On-line Fig 2).

The incidence of CV was not significantly reduced among the AT-versus-control groups (79/414 versus 84/327, OR = 0.52; 95% CI, 0.2–1.5; $P = .2$). On the other hand, the rate of good

outcome during follow-up was significantly higher among the AT group compared with the control group (803/1144 versus 1175/1775, OR = 1.368; 95% CI, 1.117–1.676; $P = .002$). The mortality rate during follow-up was significantly reduced among the AT group (79/672 versus 97/571, OR = 0.656; 95% CI, 0.47–0.91; $P = .01$).

Treatment-related complications were comparable among the 2 groups (40/438 versus 28/353, OR = 1.01; 95% CI, 0.34–3.01; $P = .9$), as well as the incidence of hemorrhagic events (32/438 versus 15/353, OR = 1.7; 95% CI, 0.89–3.38, 0.1).

Subgroup Analysis

Among the subgroup of patients treated endovascularly, there was a trend toward a lower rate of DCI after AT administration (157/778 versus 413/1410, OR = 0.552; 95% CI, 0.273–1.115; $P = .06$), whereas no difference was found between patients with and without AT among the surgical group (42/195 versus 61/278, OR = 0.952; 95% CI, 0.288–3.147; $P = .5$) (Table). There was a trend toward a lower incidence of DCI after long-term (> 2 weeks) AT (63/438 versus 96/353, OR = 0.379; 95% CI, 0.12–1.2; $P = .06$), whereas short-term antiplatelet administration (<2 weeks) was not associated with a significant reduction of the DCI rate (148/559 versus 349/1265, OR = 1.35; 95% CI, 0.81–2.23; $P = .5$).

Meta-regression demonstrated an association between the reduction of the rate of DCI after AT administration and the SAH grade: The higher the proportion of patients with low-grade SAH, the lower was the incidence of DCI after AT ($P = .06$) (Fig 2).

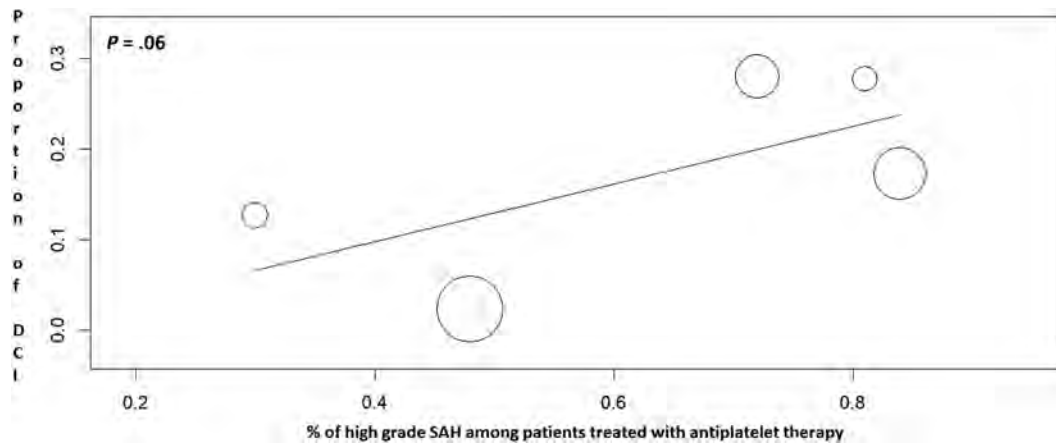


FIG 2. Meta-regression showing a trend toward a significant variation of the DCI rate after antiplatelet administration in relation to the proportion of patients with SAH with high-grade (Fisher 3–5) scores.

Sensitivity Analysis

Sensitivity analysis was performed with both the leave-one-out method and subgroup analysis. The leave-one-out meta-analysis showed that no individual study significantly influenced the investigated outcome (On-line Fig 3).

In addition, we divided the included studies as follows: retrospective, prospective, randomized controlled trials, and post hoc analysis from randomized controlled trials. Accordingly, we investigated the rate of DCI by performing a subgroup analysis based on the type of study (On-line Fig 4). The subgroup of retrospective studies was associated with a trend toward a lower rate of DCI among the AT group ($P = .06$), whereas the effect of the AT was not significant among the other subgroups. The subgroup of retrospective studies included the most recent series investigating AT among the endovascularly treated patients.

Study Heterogeneity

Substantial heterogeneity (>50%) was noted for most of the reported outcomes (rate of DCI, rate of DCI among the endovascular and surgical groups, rate of DCI after long- and short-term AT, and incidence of CV). Low heterogeneity was noted for the rates of good outcome, mortality, and complications.

DISCUSSION

Our meta-analysis of approximately 2800 patients with aneurysmal SAH highlighted several important findings about the impact of the AT on the rate of DCI and clinical outcome. Overall, this study did not show a significant beneficial effect of antiplatelet drugs on the occurrence of DCI. However, antiplatelet administration in the subgroup of patients with endovascular treatment and in the subgroup of long-term AT tended to be associated with a reduction of DCI. Despite the overall reduction of DCI not reaching a statistical significance, neurologic functional outcome in patients who received platelet inhibitors was significantly better, and mortality was significantly lower.

When we investigated the literature, data about the influence of AT on the occurrence of DCI after SAH are contradictory and quite heterogeneous. An older systematic review (2003) of clinical trials with 699 patients concluded that antiplatelet inhibitors reduced the risk of DCI, increasing the rate of good outcome in

patients with SAH.¹³ Similarly, a more recent Cochrane review (2007)¹⁴ indicated a trend toward better outcome and a lower incidence of DCI among patients treated with antiplatelet agents after SAH. However, the results were not statistically significant, and no definite conclusions were reached.

Studies included in these reviews had the following characteristics: 1) All series reported surgically treated patients, with only 1 study reporting both endovascular and surgical treatments; 2) different types of antiplatelet agents were administered (ASA, OKY, dipyridamole, ticlopidine); 3) some older series (before 1990) did not specifically investigate the incidence of DCI, reporting a general rate of neurologic deficit after treatment; and 4) other drugs, such as tranexamic acid, were used in some series in combination with ASA. Our study, the largest to date, presents more specific selection criteria: 1) Ninety-five percent of patients were treated with ASA, with only 1 very recent study reporting treatment with ASA + clopidogrel⁸; 2) DCI was the primary investigated outcome with a clear radiologic and clinical definition; and 3) 75% of patients were treated endovascularly, while 25% underwent surgical clipping (this is a more representative proportion of the modern treatment management of ruptured intracranial aneurysms); and finally 4) the effect of the AT was investigated in the endovascular and surgical groups, as well as in relation to the duration of the AT.

We found that the reduction of DCI ($OR = 0.78$, $P = .33$) and vasospasm ($OR = 0.52$, $P = .2$) after antiplatelet administration was not statistically significant. However, patients receiving antiplatelet agents had a better clinical outcome ($OR = 1.36$, $P = .002$) and lower mortality rate ($OR = 0.65$, $P = .01$). Reasons behind this benefit are difficult to explain,⁵ but antiplatelet drugs can be associated with a decreased occurrence of microemboli. Microemboli have been detected in both clinical series⁶ and autoptic studies of patients with SAH,⁷ representing a parallel pathogenic mechanism impacting the cerebral microcirculation and the neurologic outcome.^{5,7}

Similarly, in the Magnesium and Acetylsalicylic acid in Subarachnoid Hemorrhage (MASH) trial,⁵ there was not a significant beneficial effect of ASA on the incidence of DCI, despite ASA treatment resulting in a better functional outcome at follow-up.

The authors mentioned different factors that are likely associated with the lack of effect of ASA: 1) ASA alone, and the dose of aspirin (100 mg), might not be enough; 2) nearly 70% of patients were assigned to surgery, and it has been demonstrated that clipping might increase the risk of DCI compared with coiling¹⁵; and 3) ASA might not be the right antiplatelet drug. Dorhout Mees et al,¹³ in a meta-analysis of randomized trials, found a beneficial effect of AT mainly based on trials with antiplatelet agents different from aspirin. In addition, in the MASH trial, aspirin was given for 2 weeks after SAH. Our study found a trend toward lower DCI (OR = 0.37, $P = .06$) among patients treated with AT for longer than 2 weeks compared with those receiving antiplatelet drugs for a shorter period (≤ 2 weeks). In general, arterial narrowing starts 3–5 days after SAH, with the highest incidence of DCI and vasospasm between days 5 and 14 and gradually resolving between 2 and 4 weeks.^{16,17} Accordingly, it is likely that 2 weeks of AT might not give protection for the overall period of risk for CV and DCI (after 14 days).

Endovascular-versus-Surgical Groups

In a post hoc analysis of the MASH trial, van den Bergh et al¹¹ investigated the influence of aspirin on the subgroup of patients with SAH treated with coiling. The analysis found a relative risk of 1.3 (DCI clip/DCI coil ratio) in favor of endovascular treatment: The result implies that patients with endovascular coiling had a higher reduction of DCI after aspirin, compared with patients with neurosurgical clipping. Similarly, a recent series of patients treated endovascularly reported a significant positive impact of antiplatelet administration on the DCI risk. Darkwah Oppong et al² reported a series of 329 patients with ruptured aneurysms treated with endovascular techniques and receiving antiplatelet medication: ASA was independently associated with a reduced DCI risk (adjusted OR = 0.41, $P < .001$). In a very recent series of 161 patients with aneurysmal SAH treated by endovascular means, 85 received dual-antiplatelet therapy (ASA + clopidogrel) because of the use of additional stents, whereas 76 were allocated to the control group. The risk of clinical vasospasm (OR = 0.2, $P = .003$) and DCI (OR = 0.056, $P = .001$) was significantly lower in patients receiving dual-antiplatelet therapy.⁸ Accordingly, our meta-analysis found a trend toward a reduced incidence of DCI after antiplatelet treatment among the endovascular group (OR = 0.55, $P = .06$), but the reduction was not significant among the surgical group (OR = 0.95, $P = .5$). A large Cochrane meta-analysis¹⁸ comparing endovascular-versus-surgical treatment reported that DCI after SAH was observed in 292/1225 (24%) participants allocated to the endovascular group and in 349/1225 (28%) participants allocated to the surgical treatment group, with a relative and absolute risk reduction of coiling versus clipping of 16% (risk reduction, 0.84) and 4%, respectively. In the International Subarachnoid Aneurysm Trial (ISAT),¹⁵ clipping increased the risk of DCI compared with coiling in the 2143 patients (OR = 1.124). Expert opinions reported that manipulation of the brain and vessel wall during the operation increases the risk of vasospasm and DCI, though there is no reliable evidence supporting this theory.¹⁹ In conclusion, part of the reduction of DCI might be explained by a combination of the treatment (endovascular) and the use of antiplatelet drugs.

Relationship between the Grade of SAH and DCI Reduction after AT

The overall reduction of DCI after antiplatelet administration tended ($P = .06$) to be directly related to the proportion of patients with SAH with a low-grade (Fisher 1–2) score: In other words, the higher the SAH grade, the lower was the effect of antiplatelet agents on the DCI reduction (Fig 2). In general, the SAH grade is an independent risk factor for vasospasm and DCI,²⁰ and it is likely that AT had a lower effect among patients with larger amounts of cisternal blood. Finally, AT during endovascular treatment of acutely ruptured intracranial aneurysms might increase the risk of ventriculostomy-related hemorrhages. A recent meta-analysis²¹ reported that ventriculostomy-related hemorrhage rates were 20% and 9% among patients with SAH treated with and without AT, respectively, though major hemorrhages were low in both groups (4.4% and 1%, respectively).

Strength and Limitations

Our study has limitations. First, the heterogeneity among studies was high for most of the reported outcomes; this is likely related to the different treatment techniques and different doses of aspirin. Accordingly, our results should be interpreted with caution. The influence of the dose of AT was not investigated because the available data did not allow performing subgroup analysis. The P values of the subgroup analysis (endovascular-versus-surgical groups, long-term-versus-short-term AT) were around .05. Consequently, the results presented a certain degree of evidence,²² but they did not reach statistical significance. However, publication bias was reasonably excluded, and our study is the largest to date analyzing the use of antiplatelet drugs among patients with SAH.

CONCLUSIONS

In our study, the overall incidence of DCI among patients with SAH seems not to be significantly reduced after antiplatelet drug administration. However, DCI tended to be lower, both among subjects with long-term (> 2 weeks) AT and patients with endovascular treatment and antiplatelet administration. In addition, patients with AT and lower amounts of cisternal blood tend to have a lower incidence of DCI. Finally, poor outcome and mortality rates were significantly reduced among the AT group. Future randomized trials are needed to assess the benefits of AT among individuals with SAH allocated to the endovascular treatment.

Disclosures: Paolo Perrini—UNRELATED: Employment: University of Pisa, Comments: consultant neurosurgeon at University of Pisa. Vincent Costalat—UNRELATED: Consultancy: Balt, MicroVention, Medtronic; Grants/Grants Pending: Medtronic, Stryker*; Payment for Development of Educational Presentations: Balt, Medtronic, Stryker, MicroVention. Pierre-Henri Lefevre—UNRELATED: Payment for Development of Educational Presentations: Medtronic. Alain Bonafe—UNRELATED: Consultancy: Medtronic, Stryker, MicroVention.* *Money paid to the institution.

REFERENCES

1. Budohoski KP, Guilfoyle M, Helmy A, et al. **The pathophysiology and treatment of delayed cerebral ischaemia following subarachnoid haemorrhage.** *J Neurol Neurosurg Psychiatry* 2014;85:1343–53 CrossRef Medline
2. Darkwah Oppong M, Gembruch O, Pierscianek D, et al. **Post-treatment antiplatelet therapy reduces risk for delayed cerebral isch-**

- emia due to aneurysmal subarachnoid hemorrhage. *Neurosurgery* 2018 Dec 13. [Epub ahead of print] CrossRef Medline
3. Hop JW, Rinkel GJ, Algra A, et al. **Randomized pilot trial of postoperative aspirin in subarachnoid hemorrhage.** *Neurology* 2000;54: 872–78 CrossRef Medline
 4. Juvela S. **Aspirin and delayed cerebral ischemia after aneurysmal subarachnoid hemorrhage.** *J Neurosurg* 1995;82:945–52 CrossRef Medline
 5. van den Bergh WM, Algra A, Dorhout Mees SM, et al; MASH Study Group. **Randomized controlled trial of acetylsalicylic acid in aneurysmal subarachnoid hemorrhage: the MASH study.** *Stroke* 2006;37: 2326–30 CrossRef Medline
 6. Romano JG, Forteza AM, Concha M, et al. **Detection of microemboli by transcranial Doppler ultrasonography in aneurysmal subarachnoid hemorrhage.** *Neurosurgery* 2002;50:1026–30; discussion 1030–31 Medline
 7. Stein SC, Browne KD, Chen XH, et al. **Thromboembolism and delayed cerebral ischemia after subarachnoid hemorrhage: an autopsy study.** *Neurosurgery* 2006;59:781–87; discussion 787–88 CrossRef Medline
 8. Nagahama Y, Allan L, Nakagawa D, et al. **Dual antiplatelet therapy in aneurysmal subarachnoid hemorrhage: association with reduced risk of clinical vasospasm and delayed cerebral ischemia.** *J Neurosurg* 2018;129:702–10 CrossRef Medline
 9. Moher D, Liberati A, Tetzlaff J, et al. **Preferred reporting items for systematic reviews and meta-analyses: the PRISMA statement.** *Int J Surg* 2010;8:336–41 CrossRef Medline
 10. Wells G, Shea B, O'Connell D, et al. **The Newcastle-Ottawa Scale (NOS) for assessing the quality of nonrandomized studies in meta-analyses.** Ottawa: Ottawa Hospital Research Institute, 2011. http://www.ohri.ca/programs/clinical_epidemiology/oxford.asp. Accessed February 22, 2019
 11. van den Bergh WM, Algra A, Rinkel GJ, et al; MASH Study Group. **Magnesium and aspirin treatment in patients with subarachnoid haemorrhage: comparison of effects after endovascular and neurosurgical aneurysm occlusion.** *J Neurol* 2009;256:213–16 CrossRef Medline
 12. van den Bergh WM, Kerr RS, Algra A, et al; International Subarachnoid Aneurysm Trial (ISAT) Collaborative Group. **Effect of antiplatelet therapy for endovascular coiling in aneurysmal subarachnoid hemorrhage.** *Stroke* 2009;40:1969–72 CrossRef Medline
 13. Dorhout Mees SM, Rinkel GJ, Hop JW, et al. **Antiplatelet therapy in aneurysmal subarachnoid hemorrhage: a systematic review.** *Stroke* 2003;34:2285–89 CrossRef Medline
 14. Dorhout Mees SM, van den Bergh WM, Algra A, et al. **Antiplatelet therapy for aneurysmal subarachnoid haemorrhage.** *Cochrane Database Syst Rev* 2007;CD006184 Medline
 15. Dorhout Mees SM, Kerr RS, Rinkel GJ, et al. **Occurrence and impact of delayed cerebral ischemia after coiling and after clipping in the International Subarachnoid Aneurysm Trial (ISAT).** *J Neurol* 2012; 259:679–83 CrossRef Medline
 16. Vergouwen MD, Vermeulen M, van Gijn J, et al. **Definition of delayed cerebral ischemia after aneurysmal subarachnoid hemorrhage as an outcome event in clinical trials and observational studies: proposal of a multidisciplinary research group.** *Stroke* 2010; 41:2391–95 CrossRef Medline
 17. Weir B, Grace M, Hansen J, et al. **Time course of vasospasm in man.** *J Neurosurg* 1978;48:173–78 CrossRef Medline
 18. Lindgren A, Vergouwen MD, van der Schaaf I, et al. **Endovascular coiling versus neurosurgical clipping for people with aneurysmal subarachnoid haemorrhage.** *Cochrane Database Syst Rev* 2018;8: CD003085 CrossRef Medline
 19. Brilstra EH, Rinkel GJ, Algra A, et al. **Rebleeding, secondary ischemia, and timing of operation in patients with subarachnoid hemorrhage.** *Neurology* 2000;55:1656–60 CrossRef Medline
 20. Lee H, Perry JJ, English SW, et al. **Clinical prediction of delayed cerebral ischemia in aneurysmal subarachnoid hemorrhage.** *J Neurosurg* 2018 Jun 1:1–8. [Epub ahead of print] CrossRef Medline
 21. Cagnazzo F, Di Carlo DT, Petrella G, et al. **Ventriculostomy-related hemorrhage in patients on antiplatelet therapy for endovascular treatment of acutely ruptured intracranial aneurysms: a meta-analysis.** *Neurosurg Rev* 2018 Jul 2. [Epub ahead of print] CrossRef Medline
 22. Wood J, Freemantle N, King M, et al. **Trap of trends to statistical significance: likelihood of near significant P value becoming more significant with extra data.** *BMJ* 2014;348:g2215 CrossRef Medline

Comparison of Carotid Endarterectomy and Stenting for Symptomatic Internal Carotid Artery Near-Occlusion

J. Kim, S. Male, D. Damania, B.S. Jahromi, and R.P. Tummala

ABSTRACT

BACKGROUND AND PURPOSE: Carotid near-occlusion is defined as severe stenosis of the internal carotid artery with partial or full collapse of the distal vessel wall. The major studies evaluating carotid revascularization excluded patients with carotid near-occlusion. Given the paucity of data in the literature, we attempted to evaluate the safety of carotid endarterectomy and carotid artery stenting in carotid near-occlusion.

MATERIALS AND METHODS: A retrospective data base review was performed from January 2010 to December 2018 to identify patients who underwent carotid endarterectomy or carotid artery stenting for symptomatic ICA near-occlusion and had 1-month clinical and imaging follow-up with carotid sonography. The medical records and imaging studies of patients with ICA near-occlusion were selected for analysis.

RESULTS: Forty-five patients met the criteria for ICA near-occlusion, of whom 39 were included in the study, given insufficient 1-month follow-up on 6 patients. Of the 39 patients, 25 underwent carotid endarterectomy and 14 underwent carotid artery stenting. All patients had technically successful immediate revascularization of the ICA. Most (33 of 39) had 1-year follow-up postoperatively. Patients with carotid artery stenting had 20% restenosis and 79% vessel maturation rates, while patients with carotid endarterectomy had 17.4% restenosis and 84% vessel maturation. There was no significant difference in periprocedural complication rates between the 2 procedures.

CONCLUSIONS: Carotid artery stenting shows similar outcomes in restenosis and vessel maturation rates compared with carotid endarterectomy for ICA near-occlusion. There were no major differences between the 2 treatments in clinical outcomes or periprocedural complications. Carotid artery stenting is a revascularization option for carotid near-occlusion if the patient is considered at high risk for carotid endarterectomy.

ABBREVIATIONS: CAS = carotid artery stenting; CCA = common carotid artery; CEA = carotid endarterectomy; ECST = European carotid surgery trial; PSV = peak systolic velocity

Revascularization of symptomatic near-occlusion (also termed “pseudocclusion”) of the extracranial internal carotid artery is a controversial subject, partly due to an unclear natural history of the condition. Carotid artery near-occlusion was first described in 1970 as severe narrowing of the ICA with distal arterial narrowing secondary to hypoperfusion.¹ The NASCET² and the European Carotid Surgery Trial (ECST)³ collaborators defined near-occlusion as the presence of at least 2 of following 4 criteria: 1)

delayed contrast filling of the ipsilateral ICA compared with the external carotid artery, 2) evidence of collateral supply to the ipsilateral intracranial vessels, 3) reduction in the ipsilateral distal cervical ICA diameter compared with the contralateral ICA, and 4) reduction in the ipsilateral distal ICA diameter compared with the external carotid artery diameter beyond the facial and occipital artery origin.⁴ Originally, near-occlusion was defined in association with full collapse of the distal ICA, otherwise known as a “string sign,” but it was recently redefined, recognizing that near-occlusion without full collapse can progress eventually to full collapse with increasing risk of ipsilateral ischemic stroke.⁵ In this context, “collapse” refers to reduction of the vessel caliber secondary to poor filling. Currently, near-occlusion of the ICA is recognized as a spectrum of severe atherosclerotic stenosis with or without full collapse of the distal vessel: Full collapse of the ICA distal to the stenosis is threadlike, while partial collapse refers to a smaller caliber of the vessel than the original size but without the threadlike appearance.⁶ Due to concern for perioclusive embo-

Received February 24, 2019; accepted after revision April 22.

From the Departments of Neurology, Neurosurgery, and Radiology (J.K., S.M., R.P.T.), University of Minnesota, Minneapolis, Minnesota; Department of Medicine (D.D.), State University of New York, Downstate Medical Center, Brooklyn, New York; and Department of Neurological Surgery (B.S.J.), Northwestern University, Chicago, Illinois.

Please address correspondence to Jae Kim, MD, Department of Neurology, University of Minnesota, 420 Delaware St SE, Minneapolis, MN 55455; e-mail: kimx3990@umn.edu

<http://dx.doi.org/10.3174/ajnr.A6085>

lism, near-occlusions were revascularized historically with emergency carotid endarterectomy (CEA). Currently, emergency revascularization of near-occlusion is not routinely performed; moreover, the utility of treating these lesions at all with revascularization rather than medical therapy is questionable.

The risk of ipsilateral stroke increases with the degree of carotid stenosis, but paradoxically, the risk of stroke with near-occlusion is lower than that of severe (defined as 70%–99%) carotid stenosis. Analysis from a NASCET substudy reported a modest benefit with CEA, while the ECST reported no statistically significant benefit of surgical treatment of near-occlusion. Patient-level pooled analysis of NASCET and ECST found only a minor benefit of CEA in symptomatic carotid near-occlusion.⁴

Historically, revascularization of near-occlusion was thought to carry a high risk, but NASCET and ECST found no increased treatment risk in these patient subgroups compared with the severe-stenosis subgroups.⁷ Similar findings with endovascular treatment have also been described.^{8,9} Despite the reports of revascularization in carotid near-occlusion with CEA and carotid artery stenting (CAS), there are limited data available on the comparison of surgical treatment with endovascular treatment.¹⁰ In NASCET and ECST, a large number of patients met the criteria for near-occlusion on post hoc analysis. In these trials, 137 of 662 (21%) and 125 of 554 (23%), respectively, met the criteria for near-occlusion.¹¹ This finding meant that at least 1 in 5 patients with $\geq 70\%$ symptomatic carotid stenosis actually had near-occlusion on further analysis. More recent trials of CEA versus CAS for symptomatic stenosis have excluded this subgroup.^{12,13} Therefore, it is important to identify the merits and disadvantages of CAS versus CEA for revascularization of carotid near-occlusion. In this study, we report our experience of both of these revascularization strategies for symptomatic carotid near-occlusion.

MATERIALS AND METHODS

Patient Selection

From January 2010 to December 2018, we reviewed all patients who underwent CEA and CAS for symptomatic carotid stenosis and had 1-month clinical and sonography follow-up at 2 tertiary care centers. The diagnosis of near-occlusion, which met the criteria established previously, was made by reviewing catheter angiography imaging.⁴ The patients underwent CEA or CAS per risk stratification based on medical comorbidities and imaging findings. Patients underwent CAS only when they had high risk factors for CEA. The electronic medical record was reviewed to obtain demographic information as well as clinical follow-up, imaging studies, and operative notes.

Ethics

The institutional review boards of each institution approved the study procedures. Both institutional review boards (University of Minnesota, Minneapolis, Minnesota, and University of Rochester, Rochester, New York) approved a waiver of informed consent.

Technique for CEA

All patients received preoperative aspirin and/or clopidogrel and underwent surgery under general anesthesia with neurophysio-

logic monitoring, including somatosensory-evoked potentials and electroencephalography. Patients were anticoagulated with intravenous heparin before cross-clamping. After cross-clamping of the common carotid artery (CCA) and external and internal carotid arteries, an arteriotomy was performed to expose the plaque. The plaque was dissected off the intima until a smooth taper was achieved in the internal carotid artery. Back-bleeding from the internal carotid artery was confirmed in all patients before closure of the arteriotomy. Patch angioplasty was performed at the discretion of the surgeon on the basis of the caliber of the distal hypoplastic internal carotid artery.

Technique for CAS

All patients received daily aspirin and clopidogrel at least 5 days before the procedure, which was performed with the patient under conscious sedation and local anesthesia. A modified Seldinger technique was used for the transfemoral arterial access. All patients were loaded with 70–100 U per kilogram of body weight of intravenous heparin to maintain an activated clotting time between 250 and 350 seconds following placement of a 6F vascular-access sheath in the distal CCA. In most cases, a distal embolic protection device could not be advanced across the near-occlusion without predilation. A submaximal pre-stent angioplasty was performed using a Maverick balloon dilation catheter (Boston Scientific, Natick, Massachusetts) or a Gateway (Stryker, Kalamazoo, Michigan) noncompliant balloon over a 0.014-inch microwire. Next, a distal embolic protection system (Spider FX, Covidien, Plymouth, Minnesota; or FilterWire EZ, Boston Scientific) was navigated and deployed in the distal cervical ICA. A Precise self-expanding stent (Cordis, Fremont, California) was positioned over the stenotic segment, and the size of the stent was based on the distal CCA diameter. A poststent balloon angioplasty was performed if there was persistent stenosis of $>50\%$ following stent placement. Control cerebral angiography was performed after retrieval of the distal embolic filter.

Follow-Up and Assessment

A full neurologic examination was performed at the end of each procedure. Patients were observed for 24 hours with hourly neurologic examinations along with continuous cardiac monitoring. Patients were typically discharged on postoperative day 1 or 2. Patients having undergone CAS remained on aspirin and clopidogrel for at least 1 month and then aspirin thereafter. Patients having undergone CEA were continued on aspirin and/or clopidogrel. All patients had 1-month clinical and carotid sonography follow-up, while most patients (33/39) had 1-year clinical and imaging follow-up. Stroke was defined by any acute focal neurologic change as determined by a neurologist or neurosurgeon during the follow-up period. Carotid restenosis was defined as sonographic findings of an ICA peak systolic velocity (PSV) of ≥ 300 cm/s or an ICA/CCA PSV ratio of ≥ 3.8 , corresponding to $\geq 70\%$, and vessel maturation was defined as 1-year carotid sonography follow-up with a PSV of <200 and an ICA/CCA PSV ratio of <2 .¹⁴ Myocardial infarction was defined as an elevation of cardiac enzymes or electrocardiographic changes along with demonstration of abnormalities of cardiac wall motion.

Table 1: Demographics, vascular risk factors, and clinical/imaging findings

	CAS (n = 14)	CEA (n = 25)	P Value
Mean Age (y)	66.2	65.4	.80
Sex (%)			.16
Male	7 (50%)	19 (76%)	
Female	7 (50%)	6 (24%)	
Comorbidities (%)			
Hypertension	11 (79%)	19 (76%)	1.00
Smoking	6 (43%)	14 (56%)	.51
Hyperlipidemia	5 (36%)	11 (44%)	.74
Diabetes mellitus	2 (14%)	7 (28%)	.44
Coronary artery disease	2 (14%)	8 (32%)	.28
Clinical presentation (%)			.03
TIA	8 (57%)	5 (20%)	
Ischemic stroke	6 (43%)	20 (80%)	
Imaging finding (%)			
Full collapse	6 (43%)	14 (56%)	.51

Statistical Analysis

Comparisons between the 2 groups were performed with descriptive statistics and univariate comparison tests. For categorical variables, the Fisher exact test was used. For continuous variables, a 2-tailed Student *t* test was used. A *P* value < .05 was the threshold of statistical significance. All statistical analyses were performed with SPSS 24 (IBM, Armonk, New York).

RESULTS

From January 2010 through December 2018, a total of 45 patients who underwent either CEA or CAS for symptomatic near-occlusion were identified. Of these, only 39 patients who had 1-month clinical and sonographic follow-up were included in the study analysis. The distribution of baseline patient characteristics, comorbidities, and interventions is shown for the CEA and CAS groups in Table 1. The mean ages in the CEA and CAS groups were 65.4 (10) years and 66.2 (9) years, respectively. Seventy-six percent of patients in the CEA group were men compared with 50% in the CAS group. All patients had symptomatic ICA near-occlusion that was treated successfully with either CEA or CAS. Fourteen (56%) patients in the CEA group had full collapse, while 6 (43%) patients in the CAS group had full collapse. A significantly higher number of patients presented with ischemic stroke over TIA in the CEA group (80%) compared with the CAS group (43%). There were no significant differences between the 2 groups in demographics, comorbidities, and baseline imaging.

There was 1 periprocedural complication in the CEA group, which was due to reperfusion injury with resulting subarachnoid hemorrhage without neurologic consequences. There was 1 death in the CAS group due to acute heart failure 14 months after stent placement. One-year imaging data were available in 33 of 39 patients. At 1 year, restenosis of $\geq 70\%$ was identified in 4 of 23 (17.4%) patients in the CEA group and 2 of 10 (20%) patients in the CAS group using sonographic criteria. All patients who developed restenosis were asymptomatic. Vessel maturation with improvement in the distal vessel caliber occurred in most of the revascularized patients in the CEA and CAS groups, 84% and 79%, respectively (Table 2). There were no significant differences in clinical or imaging outcomes between the 2 groups.

Six patients (3 with CEA, 3 with CAS) were treated for symptomatic near-occlusion but were excluded from this study due to insufficient clinical and imaging follow-up. Of these 6 patients, no

Table 2: Outcomes for CEA and CAS groups

Outcome (%)	CAS (n = 14)	CEA (n = 25)	P Value
Restenosis	2/10 (20%)	4/23 (17.4%)	1.0
Follow-up intervention	1 (7%)	3 (12%)	1.0
Vessel maturation	11 (79%)	21 (84%)	0.7
Perioperative complication	0 (0%) ^a ; 1/17 (5.9%)	1 (4%) ^a ; 1/28 (3.6%)	1.0 ^a ; 1.0
Stroke/MI/death at 1 yr	1 (7%)	0 (0%)	.36

Note:—MI indicates myocardial infarction.

^a Perioperative complication rates after including an additional 6 patients (CAS = 3, CEA = 3) who were otherwise excluded from analyses due to insufficient follow-up.

patients in the CEA group developed complications, while 1 patient in the CAS group experienced a postoperative femoral pseudoaneurysm as well as reperfusion intracerebral hemorrhage. The perioperative complication rate between CEA and CAS groups, excluding these 6 patients, was 1/25 (4%) versus 0/14 (0%) (*p* = 1.0) compared with 1/28 (3.6%) versus 1/17 (5.9%) (*p* = 1.0) upon including these patients (Table 2). The patient who had complications was noted to have a femoral pseudoaneurysm at the end of angiography, and it was obliterated with sonography-guided manual compression. Within an hour after the procedure, the same patient developed hemiparesis and aphasia with an NIHSS score of 6 secondary to reperfusion intracerebral hemorrhage in the basal ganglia and subinsular region measuring 44 mL. The patient's examination findings remained stable, and the patient was discharged to an acute rehabilitation center on postoperative day 7. Subsequent follow-up data were insufficient.

Illustrative Cases

Patients with CEA. A 78-year-old man with coronary artery disease and hyperlipidemia was admitted with sudden onset of transient slurred speech and left facial droop. Initial MR angiography of the neck revealed an occluded right ICA, but subsequent conventional carotid angiography showed a right ICA near-occlusion with full collapse (Fig 1). On day 2 of the admission, the patient was brought to the operating room for CEA. Due to the very small caliber of the ICA, patch angioplasty was performed. The patient was extubated immediately after the procedure, and no neurologic changes were documented. He was discharged 3 days after the operation. On 1-month and 1-year follow-up, he was neurologically at baseline without deficit, with 1-year follow-up carotid sonography showing a right ICA PSV of 108 cm/s and a right ICA/CCA PSV ratio of 1.62.

Another patient, a 62-year-old woman with coronary artery disease, hypertension, diabetes mellitus, and hyperlipidemia, was admitted with intermittent left-arm numbness and weakness for 2 months. MR imaging revealed a subacute right parietal lobe infarct, and an initial MR angiogram of the neck revealed an occluded right ICA. Subsequent CT angiography of the neck and conventional carotid angiography showed a right ICA near-occlusion with full collapse. The patient underwent CEA with patch angioplasty and had no neurologic changes postoperatively. On 1- and 6-month follow-up, she was neurologically at baseline without deficit. At 6 months, she underwent a neck CTA that revealed no residual stenosis and complete resolution of vessel collapse compared with the baseline CTA (Fig 2).



FIG 1. A, Early arterial phase shows severe ICA stenosis (black arrows) with a larger caliber external carotid artery (white arrow). B, Later arterial phase shows delayed filling of distal ICA (black arrow). C, Collateral filling of the distal ICA by the ophthalmic artery (black arrow) from the internal maxillary artery branch (white arrows).

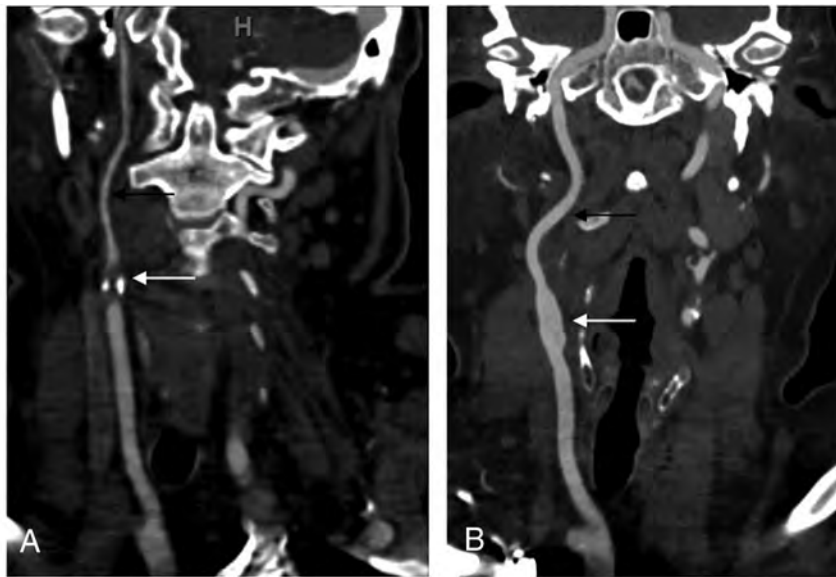


FIG 2. A, Baseline CTA of the neck revealing severe stenosis of the right ICA at the origin (white arrow) with collapse of the distal wall (black arrow). B, Follow-up CTA of the neck after treatment with CEA. There is no evidence of residual stenosis (white arrow) with maturation or regaining of the caliber of the distal ICA (black arrow).

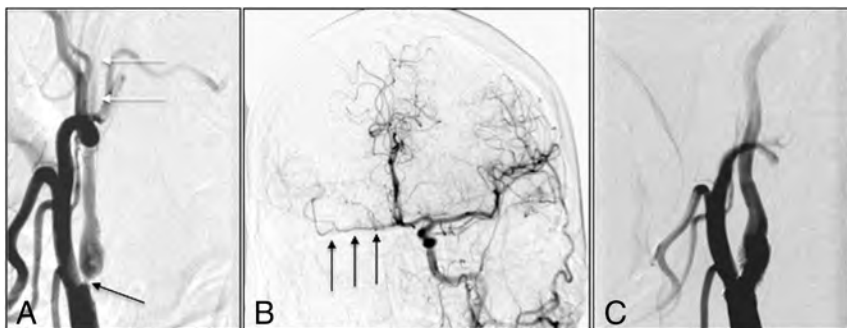


FIG 3. A, Early arterial phase shows severe right ICA stenosis (black arrow) with delayed distal ICA filling (white arrows). B, Cross-filling of the right middle cerebral artery (black arrows) after left carotid injection. C, Poststent right carotid injection shows brisk filling of distal ICA.

Patient with CAS. A 66-year-old man was admitted with left-arm and leg weakness for 2 weeks, with noncontrast CT of the head revealing a subacute right-frontal ischemic stroke. CT angiography showed severe stenosis of the right ICA, and the patient

underwent conventional angiography, which revealed near-occlusion of the right ICA without full collapse and delayed filling distally (Fig 3A). Left carotid injection showed cross-filling of the right middle cerebral artery (Fig 3B). Because of the patient's immobile neck, we decided to pursue stent revascularization. After positioning of the guide sheath in the distal CCA, predilation balloon angioplasty was performed under distal embolic protection followed by stent placement across the stenosis. Poststent right carotid injection showed increased perfusion of the distal right ICA (Fig 3C). There was no neurologic decline postprocedurally. The patient was discharged home on day 3 with a baseline neurologic examination. At 1-month and 1-year follow-up, there were no neurologic changes, and 1-year sonography revealed a left ICA PSV of 78 cm/s and a left ICA/CCA PSV ratio of 0.80.

DISCUSSION

Before the NASCET and ECST subgroup studies, carotid near-occlusion was thought to carry a high short-term stroke risk that required emergent revascularization.¹⁵ Re-analysis of the data showed that the risk is lower than originally thought. In pooled data for patients with near-occlusion from NASCET and ECST, the 3-year intention-to-treat risk of ipsilateral stroke was 15.1% for medically treated and 10.9% for surgically treated patients. In contrast, the pooled data for severe stenosis (70%–99%) without near-occlusion from NASCET and ECST described a 3-year intention-to-treat risk of ipsilateral stroke of 26.0% for medically treated and 8.2% for surgically treated patients.⁴ Although the benefit of CEA in near-occlusion did not reach statistical significance, there was a trend toward benefit with CEA compared with medical management. The risk of revascularization in near-occlusion was also thought initially to be high, but NASCET and ECST showed complication rates lower than in the severe stenosis (70%–99%) group. Our study also showed similar findings of relatively low periprocedural complications with either CEA or CAS. In our series, there was 1 complication periprocedurally in the CEA group due to reperfusion injury, resulting in subarach-

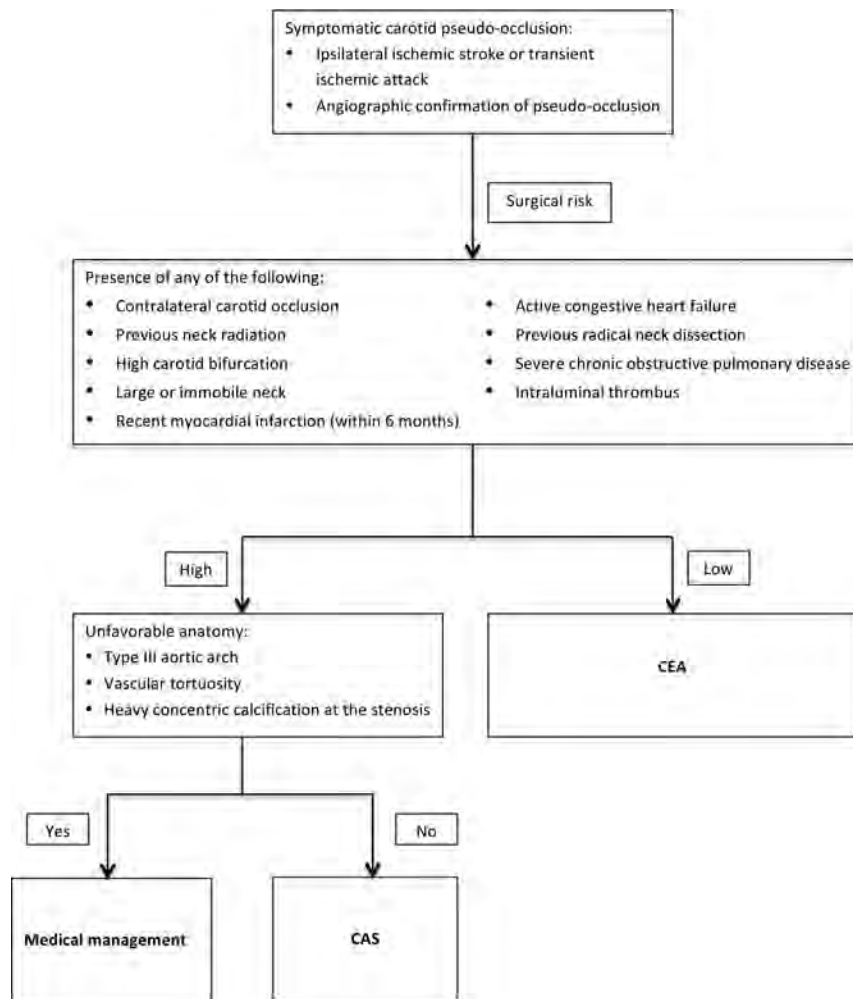


FIG 4. Algorithm for the management of symptomatic near-occlusion of the internal carotid artery.

noid hemorrhage with no neurologic deficit or any sequelae. At 1-year follow-up, no patients in either group experienced any strokes or myocardial infarctions. One patient in the CAS group died shortly after 1-year follow-up of a non-neurologic cause from acute heart failure. One patient who was not included in study analysis due to inadequate follow-up had femoral artery pseudoaneurysm and symptomatic reperfusion intracerebral hemorrhage.

The use of carotid stent placement has been accepted as an alternative option to CEA after approval by the Food and Drug Administration of CAS based on the Stenting and Angioplasty with Protection in Patients at High Risk for Endarterectomy (SAPPHIRE) trial.¹⁶ The Carotid Revascularization Endarterectomy versus Stenting Trial (CREST) also demonstrated no difference in composite outcomes (stroke, myocardial infarction, or death) between CEA and CAS.¹³ However, these studies did not include patients with near-occlusion. Near-occlusion would appear to be technically prohibitive of endovascular treatment, but in our series, only 1 patient selected for CAS had crossover to the CEA group. Due to tortuosity of the aortic arch as well as the degree of stenosis, the microwire and the microcatheter could not be crossed through the stenosis safely. The patient subsequently underwent technically successful CEA with patch angioplasty.

Until now, there has been scarce data on comparison between CEA and CAS in the literature for treatment of near-occlusion, and choosing 1 method for revascularization can be difficult. Our study shows similar outcomes and success rate as well as imaging outcomes in 1-year follow-up. As with any carotid revascularization, medical comorbidities and anatomic risk factors must be considered when choosing between CAS or CEA. We performed CAS on patients whom we determined had high risk factors for CEA. We determined that certain anatomic features of near-occlusion, including heavy concentric calcification (≥ 3 mm in width by at least 2 orthogonal views) or vascular tortuosity (≥ 2 bend point that exceeded 90° within 5 cm of the lesion), prohibited safe CAS placement.¹⁷ In these patients, we opted for CEA. High-risk anatomic factors for CEA include a high carotid bifurcation, intraluminal thrombus,¹⁸ a large or immobile neck, previous neck irradiation, prior neck operation, and contralateral carotid occlusion.

We used our algorithm (Fig 4) for selection of patients to CEA, CAS, or medical management. This algorithm does not depart greatly from our typical management of symptomatic carotid stenosis. The main difference in our management of near-occlusion is a higher threshold to perform stent placement.

A full collapse of the ICA distal to the near-occlusion will not allow a stent to expand fully, and this has deterred but not prohibited us from performing this procedure more frequently in this setting. While concentric calcification is an accepted contraindication to carotid stent placement, we have also been averse to placing carotid stents in near-occlusions with severe eccentric calcification. We have been concerned that the stent may not expand adequately against heavy calcification in an already constrained vessel.

Our clinical practice is to follow up all patients with carotid sonography at 1 month and 1 year. Near-occlusion typically results in decreased flow distal to the stenosis, resulting in a hypoplastic vessel. Vessel maturation was assessed at either 1-month or 1-year imaging in all patients. In our study, vessel maturation was noted in 21 (84%) patients in the CEA group and 11 (79%) patients in CAS group. However, our overall restenosis rate at 1 year ($\sim 20\%$) appears notably higher than that seen following revascularization of carotid stenosis without near-occlusion (4%–5%) at 1 year in CREST.¹⁹ Patients who had restenosis or occlusion did not have any recurrence of neurologic deficits; 4 of 6 patients were able to undergo additional angioplasty without complications. However, 2 patients did not undergo angioplasty

because they presented with delayed occlusion of the carotid artery after CEA with patch angioplasty, which is a higher rate of occlusion than that seen in CEA for severe stenosis without near-occlusion. Neither patient was symptomatic, and the acuity of the occlusion could not be assessed accurately due to occlusion being discovered during normal follow-up periods. While this outcome is consistent with assertions from NASCET authors⁴ that the stroke risk from near-occlusion is not a flow-related phenomenon but mostly an embolic phenomenon, it also suggests that revascularization after near-occlusion may have a higher risk of restenosis and/or occlusion, which has not been previously described.

Our data have several limitations, including the nonrandomized, retrospective nature of patient selection and follow-up. Patients were not randomly assigned to CEA versus CAS; CEA was the preferred option unless high-risk features favored CAS. We studied only patients with near-occlusion who underwent revascularization, and we did not include patients who underwent medical treatment alone. In patients at high risk of either CEA or CAS based on anatomic factors or comorbidities (eg, active congestive heart failure and concentrically calcified carotid near-occlusion), medical treatment may be the most reasonable option because the benefit of revascularization appears to be modest. Current medical management options have advanced since NASCET and ECST; this change may further improve outcomes of medically treated patients with near-occlusion. In addition, the sample size of our study is small, and to detect a difference between these 2 groups for periprocedural stroke rates for the treatment of symptomatic near-occlusion, we would need a sample size of 11,972.^{9,11}

CONCLUSIONS

Both CEA and CAS seem to be safe and effective treatments for patients with symptomatic carotid near-occlusion with low complication rates periprocedurally and at 1 year. CAS is a good alternative if the patient has a high risk for CEA.

Disclosures: Ramachandra P. Tummala—UNRELATED: Grants/Grants Pending: MicroVention, Comments: unrestricted fellowship education grant, not used for the submitted work.* *Money paid to the institution.

REFERENCES

- Lippman HH, Sundt TM Jr, Holman CB. **The poststenotic carotid slim sign: spurious internal carotid hypoplasia.** *Mayo Clin Proc* 1970; 45:762–67 Medline
- Ferguson GG, Eliasziw M, Barr HW, et al. **The North American Symptomatic Carotid Endarterectomy Trial: surgical results in 1415 patients.** *Stroke* 1999;30:1751–58 CrossRef Medline
- Randomised trial of endarterectomy for recently symptomatic carotid stenosis: final results of the MRC European Carotid Surgery Trial (ECST).** *Lancet* 1998;351:1379–87 CrossRef Medline
- Fox AJ, Eliasziw M, Rothwell PM, et al. **Identification, prognosis, and management of patients with carotid artery near occlusion.** *AJNR Am J Neuroradiol* 2005;26:2086–94 Medline
- Johansson E, Öhman K, Wester P. **Symptomatic carotid near-occlusion with full collapse might cause a very high risk of stroke.** *J Intern Med* 2015;277:615–23 CrossRef Medline
- Johansson E, Fox AJ. **Carotid near-occlusion: a comprehensive review, Part 1: definition, terminology, and diagnosis.** *AJNR Am J Neuroradiol* 2016;37:2–10 CrossRef Medline
- Morgenstern LB, Fox AJ, Sharpe BL, et al. **The risks and benefits of carotid endarterectomy in patients with near occlusion of the carotid artery. North American Symptomatic Carotid Endarterectomy Trial (NASCET) Group.** *Neurology* 1997;48:911–15 CrossRef Medline
- Terada T, Tsuura M, Matsumoto H, et al. **Endovascular treatment for pseudo-occlusion of the internal carotid artery.** *Neurosurgery* 2006;59:301–09; discussion 301–09 CrossRef Medline
- González A, Gil-Peralta A, Mayol A, et al. **Internal carotid artery stenting in patients with near occlusion: 30-day and long-term outcome.** *AJNR Am J Neuroradiol* 2011;32:252–58 CrossRef Medline
- Koutsoumpelis A, Kouvelos G, Peroulis M, et al. **Surgical and endovascular intervention on internal carotid artery near occlusion.** *Int Angiol* 2015;34:172–81 Medline
- Rothwell PM, Eliasziw M, Gutnikov SA, et al; Carotid Endarterectomy Trialists' Collaboration. **Analysis of pooled data from the randomised controlled trials of endarterectomy for symptomatic carotid stenosis.** *Lancet* 2003;361:107–16 CrossRef Medline
- Bonati LH, Dobson J, Featherstone RL, et al; International Carotid Stenting Study Investigators. **Long-term outcomes after stenting versus endarterectomy for treatment of symptomatic carotid stenosis: the International Carotid Stenting Study (ICSS) randomised trial.** *Lancet* 2015;385:529–38 CrossRef Medline
- Brott TG, Hobson RW 2nd, Howard G, et al; CREST Investigators. **Stenting versus endarterectomy for treatment of carotid-artery stenosis.** *N Engl J Med* 2010;363:11–23 CrossRef Medline
- Setacci C, Chisci E, Setacci F, et al. **Grading carotid intrastent restenosis: a 6-year follow-up study.** *Stroke* 2008;39:1189–96 CrossRef Medline
- Ringelstein EB, Berg-Dammer E, Zeumer H. **The so-called atheromatous pseudocclusion of the internal carotid artery: a diagnostic and therapeutical challenge.** *Neuroradiology* 1983;25:147–55 CrossRef Medline
- Yadav JS, Wholey MH, Kuntz RE, et al; Stenting and Angioplasty with Protection in Patients at High Risk for Endarterectomy Investigators. **Protected carotid-artery stenting versus endarterectomy in high-risk patients.** *N Engl J Med* 2004;351:1493–501 CrossRef Medline
- Roubin GS, Iyer S, Halkin A, et al. **Realizing the potential of carotid artery stenting: proposed paradigms for patient selection and procedural technique.** *Circulation* 2006;113:2021–30 CrossRef Medline
- Jahromi BS, Tummala RP, Yamamoto J, et al. **Early carotid stenting for symptomatic stenosis and intraluminal thrombus presenting with stroke.** *Neurology* 2008;71:1831–13 CrossRef Medline
- Brott TG, Howard G, Roubin GS, et al; CREST Investigators. **Long-term results of stenting versus endarterectomy for carotid-artery stenosis.** *N Engl J Med* 2016;374:1021–31 CrossRef Medline

Functional Connectivity Associated with Health-Related Quality of Life in Children with Focal Epilepsy

H. Nawani, M.L. Smith, A.L. Wheeler, and E. Widjaja



ABSTRACT

BACKGROUND AND PURPOSE: Although functional connectivity has been linked to cognitive function in epilepsy, its relationship with physical, psychological, or social dysfunction is unknown. This study aimed to assess the relationship between network architecture from resting-state fMRI and health-related quality of life in children with medically intractable focal epilepsy.

MATERIALS AND METHODS: Forty-seven children with nonlesional focal epilepsy were included; 22 had frontal lobe epilepsy and 15 had temporal lobe epilepsy. We computed graph metrics of functional connectivity, including network segregation (clustering coefficient and modularity) and integration (characteristic path length and participation coefficient). Health-related quality of life was measured using the Quality of Life in Childhood Epilepsy questionnaire. We examined the associations between graph metrics and the Quality of Life in Childhood Epilepsy total and domains scores, with age, sex, age at seizure onset, fMRI motion, and network density as covariates.

RESULTS: There was a negative relationship between the clustering coefficient and total Quality of Life in Childhood Epilepsy score [$t_{(40)} = -2.0$; $P = .04$] and social function [$t_{(40)} = -2.9$; $P = .005$]. There was a positive association between the mean participation coefficient and total Quality of Life in Childhood Epilepsy score [$t_{(40)} = 2.2$; $P = .03$] and cognition [$t_{(40)} = 3.8$; $P = .0004$]. In temporal lobe epilepsy, there was a negative relationship between the clustering coefficient and total Quality of Life in Childhood Epilepsy score [$t_{(8)} = -2.8$; $P = .02$] and social function [$t_{(8)} = -3.6$; $P = .0075$] and between modularity and total Quality of Life in Childhood Epilepsy score [$t_{(8)} = -2.5$; $P = .04$] and social function [$t_{(8)} = -4.4$; $P = .0021$]. In frontal lobe epilepsy, there was no association between network segregation and integration and Quality of Life in Childhood Epilepsy total or domain scores.

CONCLUSIONS: Our findings indicate that there are other higher order brain functions beyond cognition, which may be linked with functional connectivity of the brain.

ABBREVIATIONS: FLE = frontal lobe epilepsy; rsfMRI = resting-state fMRI; QOLCE = Quality of Life in Childhood Epilepsy; TLE = temporal lobe epilepsy

Resting-state functional MR imaging (rsfMRI) can measure spontaneous neural activity in the human brain noninvasively¹ and can be used to assess the interregional connectivity of

the brain. There are several approaches to assessing functional connectivity in the brain, including multivariate decompositions of fMRI data into intrinsic connectivity networks, specified connectivity between different brain units using a seed region, and graph theory–based approaches.² The graph theory–based approach models the brain as a complex network represented graphically by a collection of nodes and edges. The graph-based network approach has the advantage of characterizing unbiased patterns of whole-brain architecture. Globally, brain networks are optimized by achieving a balance between segregation of local specialized processing and integration of diverse modules across the brain.³

Epilepsy is considered a disorder of large neural networks.⁴ There is more heterogeneity with respect to etiology and location of epileptogenic zone in children with medically intractable epilepsy relative to adults,⁵ which may contribute to variability in the regions or networks that are disrupted. Global graph theoretic

Received February 26, 2019; accepted after revision May 16.

From Neurosciences and Mental Health (H.N., M.L.S., A.L.W., E.W.), Diagnostic Imaging (E.W.), and Division of Neurology (E.W.), Hospital for Sick Children, Toronto, Ontario, Canada; and Departments of Psychology (M.L.S.) and Physiology (A.L.W.), University of Toronto, Toronto, Ontario, Canada.

This work was supported by EpLink–The Epilepsy Research Program of the Ontario Brain Institute. The Ontario Brain Institute is an independent nonprofit corporation, funded partially by the Ontario government. Funding for data analysis was provided by the SickKids Foundation (A.L.W.).

The opinions, results, and conclusions are those of the authors and no endorsement by the Ontario Brain Institute is intended or should be inferred.

Please address correspondence to Anne Wheeler, MD, Hospital for Sick Children, 555 University Ave, Toronto, Ontario M5G 1X8, Canada; e-mail: anne.wheeler@sickkids.ca



Indicates article with supplemental on-line photos.

<http://dx.doi.org/10.3174/ajnr.A6106>

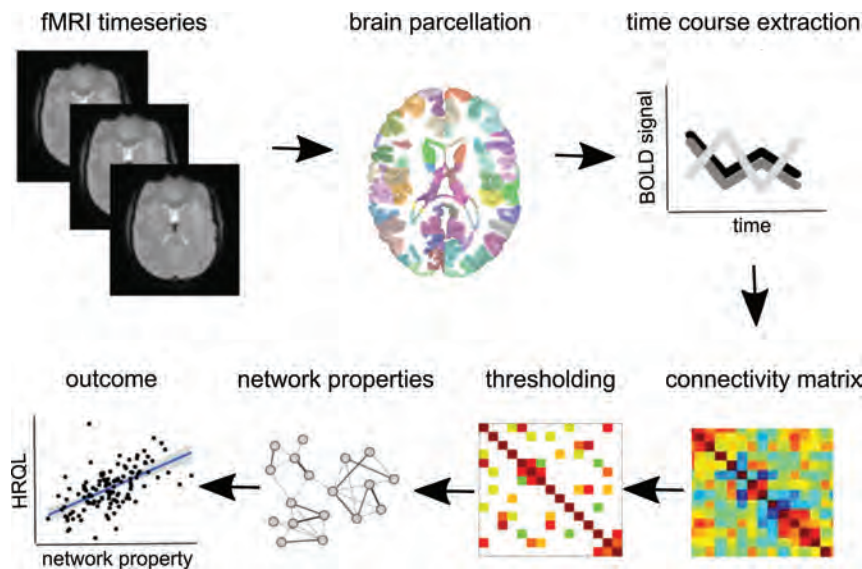


FIG 1. Summary of the analytic approach. For each participant, fMRI time-series were preprocessed, registered to their T1 anatomic scans, and parcellated into 268 regions. The mean blood oxygen level–dependent (BOLD) time course was extracted from each brain region, and correlations between regions were represented as a functional connectivity matrix. Each connectivity matrix was thresholded to create a weighted functional connectivity network. Network properties were computed, and their associations with health-related quality of life were assessed with linear models.

measures offer a robust means of capturing diverse sources and regions of brain dysfunction in children with medically intractable epilepsy. Abnormal functional connectivity has been linked to cognitive impairment in children with epilepsy. Higher modularity, implying that subnetworks were less interconnected, has been linked with impaired cognition, as measured by a computerized visual searching task, in children with frontal lobe epilepsy.⁶ Reduced centrality of the left inferior parietal lobule and segregated processing within the default mode network were associated with more favorable cognitive development in children with Rolandic epilepsy.⁷ Furthermore, clustering coefficient and path length have been shown to be associated with the full-scale intelligence quotient in children with focal epilepsy.⁸

Health-related quality of life (HRQL) is defined by the World Health Organization as a broad, multidimensional construct, including not only the disease state but also the person’s physical, psychological, and social well-being. This term refers to the impact, both subjective and objective, of dysfunction associated with illness or injury and treatment.⁹ Children with epilepsy frequently have impairment in multiple domains of HRQL and have higher rates of behavioral, cognitive, emotional, social, and academic problems compared with healthy children or children with other chronic health conditions.^{10–12} Clinical factors, including the duration of epilepsy, seizure type, frequency and severity, number and adverse effects of antiseizure medications, comorbidity, parental anxiety and depression, family socioeconomic status, and family function, have been shown to predict HRQL.^{13,14} Cognitive difficulties have also been shown to correlate with children’s HRQL.^{14,15} However, it is unclear whether there is a neural basis for impaired HRQL in children with epilepsy. Although functional connectivity has been linked to cognitive function in children with epilepsy, its relationship with broader dysfunctions

such as a person’s physical, psychological, and social well-being has not been explored in this population. The aim of the present study was to assess the relationship between graph theory metrics derived from rsfMRI and HRQL in children with focal epilepsy.

MATERIALS AND METHODS

Study Population

Children with medically intractable focal epilepsy who were evaluated for epilepsy surgery were recruited to the study ($n = 47$). Inclusion criteria were children 4–18 years of age with nonlesional epilepsy—that is, those with normal findings on 3T MR imaging acquired with the epilepsy protocol. The MRIs were reviewed by a pediatric neuroradiologist (E.W.) with expertise in epilepsy imaging to verify that there was no lesion seen on MR imaging. Exclusion criteria included prior resective or nonresective epilepsy surgery (eg, corpus callosotomy) and children/families who were unable to complete the HRQL

questionnaires. Demographics and clinical data, including the age, sex, age at seizure onset, duration of epilepsy, and number of antiepileptic drugs, were collected. The analytic approach is summarized in Fig 1. The study had the approval of the research ethics board of the Hospital for Sick Children.

Health-Related Quality of Life

Patient HRQL was measured using the Quality of Life in Childhood Epilepsy (QOLCE) questionnaire.¹⁶ The QOLCE is a 76-item parent-rated instrument covering 5 domains (physical activity, cognition, well-being, social activity, and behavior) and 16 subscales. Domain scores are derived from the unweighted average of the relevant items.¹⁶ The total QOLCE score is the unweighted average of 16 subscales, and higher scores indicate better HRQL. This instrument has been reported to have good validity and reliability.^{16,17}

MR Imaging and Resting-State fMRI

MR imaging was performed on a 3T scanner (Philips Achieva, Philips Healthcare, Best, the Netherlands) using an 8-channel phased array head coil in all patients. Patients were imaged using the epilepsy protocol, which included axial and coronal FLAIR (TR/TE = 10,000/140 ms, slice thickness = 3 mm, FOV = 22 cm, matrix = 316 × 290), axial and coronal T2 and proton-density (TR/TE = 4200/80/40 ms, slice thickness = 3 mm, FOV = 22 cm, matrix = 400 × 272), volumetric 3D-T1 (TR/TE = 4.9/2.3 ms, slice thickness = 1 mm, FOV = 22 cm, matrix = 220 × 220), and rsfMRI (TR = 2000 ms, TE = 30 ms, flip angle = 90°, FOV = 220 mm, matrix = 88 × 86 mm, slice thickness = 3.5 mm, 180 volumes acquired and aligned to the anterior/posterior commissure line, scan time = 6 minutes 8 seconds). rsfMRI was acquired with the patient’s eyes closed.

Characteristics of the whole sample and frontal and temporal lobe epilepsy subsamples

	Whole Sample (n = 47)	FLE (n = 22)	TLE (n = 15)
Age (yr)	13 (3)	13 (4)	13 (2)
Sex	23 F, 24 M	11 F, 11 M	6 F, 9 M
Type	22 Frontal 15 Temporal 8 Parietal or occipital 2 Multilobar	15 Left frontal 7 Right frontal	9 Left temporal 6 Right temporal
Mean age at seizure onset (SD), (yr)	8 (4)	8 (4)	10 (3)
Mean duration of epilepsy (SD), (yr)	5 (4)	5 (4)	4 (3)
No. of anti-epileptic drugs (range)	2 (0–4)	2 (1–4)	2 (0–3)
Frequency	15 Daily 20 Weekly 12 Monthly or less frequently	7 Daily 9 Weekly 6 Monthly or less frequently	4 Daily 9 Weekly 2 Monthly or less frequently
QOLCE (mean) (SD)			
Overall	63 (17)	62 (21)	67 (15)
Social function	66 (27)	64 (28)	67 (29)
Physical function	52 (18)	49 (22)	59 (13)
Emotional well-being	67 (17)	66 (19)	68 (16)
Cognition	67 (23)	66 (26)	77 (17)
Behavior	67 (15)	66 (15)	68 (18)

Note:—SD indicates standard deviation.

Image Processing and Analysis

Image Preprocessing. Preprocessing was performed using FSL, Version 5.0.9 (www.fmrib.ox.ac.uk/fsl). The first 4 scans were discarded, resulting in 176 blood oxygen level–dependent time-series at each voxel per acquisition. Brain extraction was performed using the FSL Brain Extraction Tool (<http://fsl.fmrib.ox.ac.uk/fsl/fslwiki/BET>)¹⁸; and motion correction, with MCFLIRT (<https://fsl.fmrib.ox.ac.uk/fsl/fslwiki/MCFLIRT>).¹⁹ Slice-timing correction was performed in ascending order, and spatial smoothing was performed using a Gaussian kernel of 5-mm full width at half maximum and high-pass temporal filtering at 100 seconds. Volumes from each fMRI acquisition were registered to each individual's high-resolution anatomic volume using linear registration. The images were then registered to the 2-mm³ stereotactic template of Montreal Neurological Institute 152 using nonlinear spatial normalization.²⁰ The coregistered T1 images were segmented into gray matter, white matter, and CSF using FSL FAST (<https://fsl.fmrib.ox.ac.uk/fsl/fslwiki/FAST>).²¹ Nuisance covariates, including CSF signal, white matter signal, and 6 rigid-body motion parameters, were regressed out of the data. The residual time courses were band-pass-filtered at 0.01–0.1 Hz.

Graph Theory Analysis. Mean time-series were extracted from 268 brain regions using an atlas-based parcellation of Shen et al.²² Pearson correlation coefficients were calculated for each pair of regions, from which a 268 × 268 correlation matrix representing interregional functional connectivity was produced for each participant. Connectivity matrices were thresholded at a maximum correlation value at which the network remained as 1 fully connected component in each participant (absolute *r* threshold = 0.34), and networks produced by a range of thresholds below this correlation value were also assessed to ensure that results were not dependent on threshold selection (*r* = 0.1: *r* = 0.34, in increments of 0.02). Edge weights were determined by normalizing correlation values. Topologic characteristics of weighted brain networks were

calculated using the Brain Connectivity Toolbox (www.brain-connectivity-toolbox.net).³ For each participant network, the mean clustering coefficient and modularity were computed as measures of network segregation, and characteristic path length and participation coefficient were computed as metrics of network integration. The clustering coefficient measures the magnitude of local interconnectivity of a network; specifically, it is the fraction of neighbors of nodes that are neighbors of each other. Modularity quantifies the degree to which the network may be subdivided into clearly delineated groups that maximize the number of within-group edges and minimize the number of between-group edges. Characteristic path length is a measure of network-wide integration and is defined as the average shortest path length in the network. The participation coefficient captures the diversity of intermodular connections of individual nodes.

Statistical Analysis

Linear models were used to examine associations between graph metrics and QOLCE scores. Age, sex, age at seizure onset, and fMRI motion (mean displacement values between 1 image and the next image in the series) were included in the model as covariates, along with network density as recommended by van den Heuvel et al.²³ The first level of analysis examined the relationships between the total QOLCE score (or overall HRQL) and the 4 metrics of network segregation and integration: 1) mean clustering coefficient, 2) characteristic path length, 3) modularity, and 4) mean participation coefficient. Network metrics that were associated with the total QOLCE score detected at an uncorrected *P* < .05 were then examined in relation to QOLCE domain scores using equivalent models. The significance of the relationships described in the second-level analysis of domain-specific scores was assessed with a *P* < .05, corrected for the 5 domains using a Bonferroni correction (ie, *P* < .01 considered significant). These analyses were repeated in separate subsamples of children with frontal lobe epilepsy (FLE) and temporal lobe epilepsy (TLE). Characteristics and QOLCE scores of the FLE and TLE subsamples were compared with *t* tests for continuous variables and χ^2 tests for categorical variables.

RESULTS

Forty-seven children with nonlesional focal epilepsy were included in this study. Twenty-two of these children had FLE, and 15 had TLE. Characteristics of the whole sample and FLE and TLE subsamples are summarized in the Table. Children with FLE were taking more antiepileptic drugs than those with TLE [$t_{(35)} = 2.0$; *P* = .05]. The FLE and TLE groups did not differ by any other characteristics (all, *P* > .05).

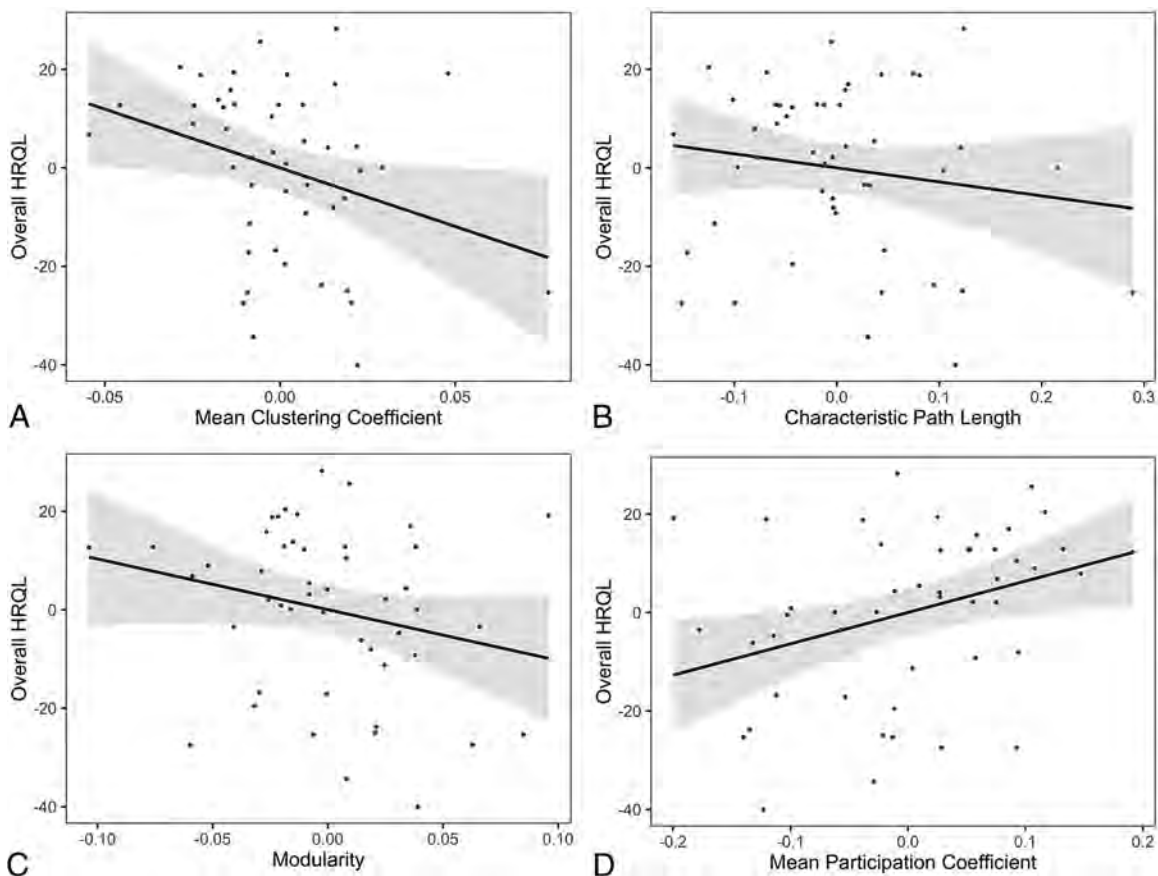


FIG 2. Associations between graph theory metrics and overall health-related quality of life (or total Quality of Life in Childhood Epilepsy score). The mean clustering coefficient shows a negative relationship with overall HRQL (A). Characteristic path length (B) and modularity (C) are not significantly associated with overall HRQL. The mean participation coefficient is positively associated with overall HRQL (D). Networks were thresholded at an absolute Pearson correlation coefficient of $r = 0.34$. Residuals after accounting for model covariates are plotted as relative measures along with regression lines with 95% confidence intervals.

HRQL

The mean total QOLCE scores as well as scores in each of the 5 domains are summarized for the whole sample and FLE and TLE subsamples in the Table. The samples of children with FLE and TLE did not differ in total score [$t_{(35)} = -0.93$; $P = .36$] or the 5 domain scores: social function [$t_{(35)} = -0.28$; $P = .78$], physical function [$t_{(35)} = -1.6$; $P = .13$], emotional well-being [$t_{(35)} = -0.35$; $P = .73$], cognition [$t_{(35)} = -1.4$; $P = .18$], and behavior [$t_{(35)} = -0.51$; $P = .61$].

Associations between Global Graph Theory Metrics and HRQL in the Whole Sample

A negative relationship between the total QOLCE score and the mean clustering coefficient [$t_{(40)} = -2.1$; $P = .04$] was detected, whereas the association between total QOLCE score and modularity did not reach our threshold for significance [$t_{(40)} = -1.7$; $P = .09$]. Overall, the total QOLCE score was positively associated with the mean participation coefficient [$t_{(40)} = 2.2$; $P = .04$], but there was no relationship between total QOLCE score and characteristic path length [$t_{(40)} = -0.92$; $P = .37$] (Fig 2).

Assessment of QOLCE domain scores revealed that there was a significant negative association between the mean clustering coefficient and the social function domain [$t_{(40)} = -2.9$; $P = .006$]

and a significant positive association between the participation coefficient and cognition [$t_{(40)} = 3.8$; $P = .0004$] (Fig 3). There were no significant relationships between the mean clustering coefficient and cognition [$t_{(40)} = -1.0$; $P = .30$], physical activity [$t_{(40)} = -0.49$; $P = .63$], emotional well-being [$t_{(40)} = -1.5$; $P = .14$], and behavior [$t_{(40)} = -1.7$; $P = .10$]. There were also no significant relationships between the participation coefficient and social function [$t_{(40)} = 0.39$; $P = .70$], physical activity [$t_{(40)} = 1.5$; $P = .15$], emotional well-being [$t_{(40)} = 1.5$; $P = .14$], and behavior [$t_{(40)} = 1.9$; $P = .07$]. Results for the total QOLCE and QOLCE domain scores were similar across network-generation thresholds (On-line Figs 1 and 2).

Associations between Global Graph Theory Metrics and HRQL in FLE and TLE Subsamples

In children with FLE, there were no significant relationships between the total QOLCE score and the clustering coefficient [$t_{(15)} = -1.3$; $P = .23$], characteristic path length [$t_{(15)} = -0.17$; $P = .86$], modularity [$t_{(15)} = -0.87$; $P = .40$], or participation coefficient [$t_{(15)} = 1.1$; $P = .27$] (On-line Fig 3), which were consistent across network-generation thresholds (On-line Fig 4).

In children with TLE, a negative relationship between the total QOLCE score, mean clustering coefficient [$t_{(8)} = -2.8$; $P = .02$],

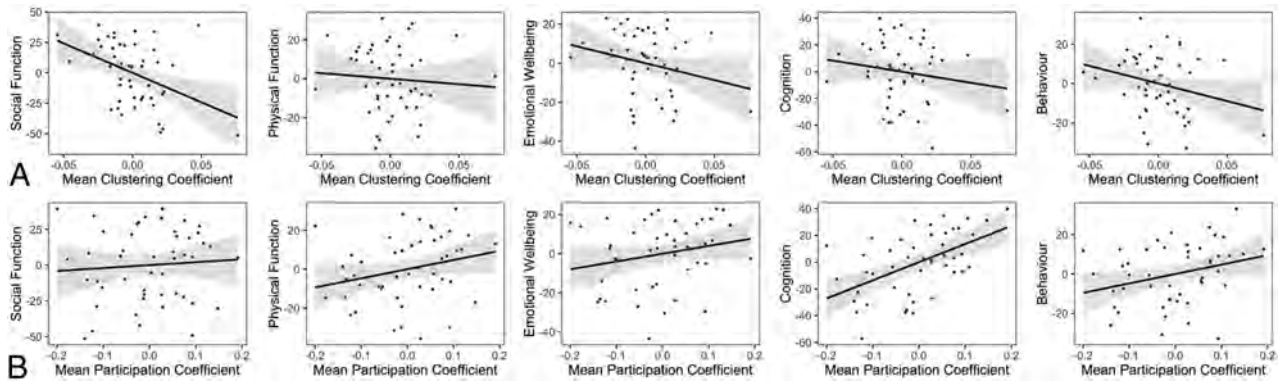


FIG 3. Associations between graph theory metrics and the domain-specific Quality of Life in Childhood Epilepsy score. The mean clustering coefficient shows a negative relationship with the social function domain of the QOLCE score only (A). The mean participation coefficient is positively associated with the cognition domain of the QOLCE score only (B). Networks were thresholded at an absolute Pearson correlation coefficient of $r = 0.34$. Residuals after accounting for model covariates are plotted as relative measures along with regression lines with 95% confidence intervals.

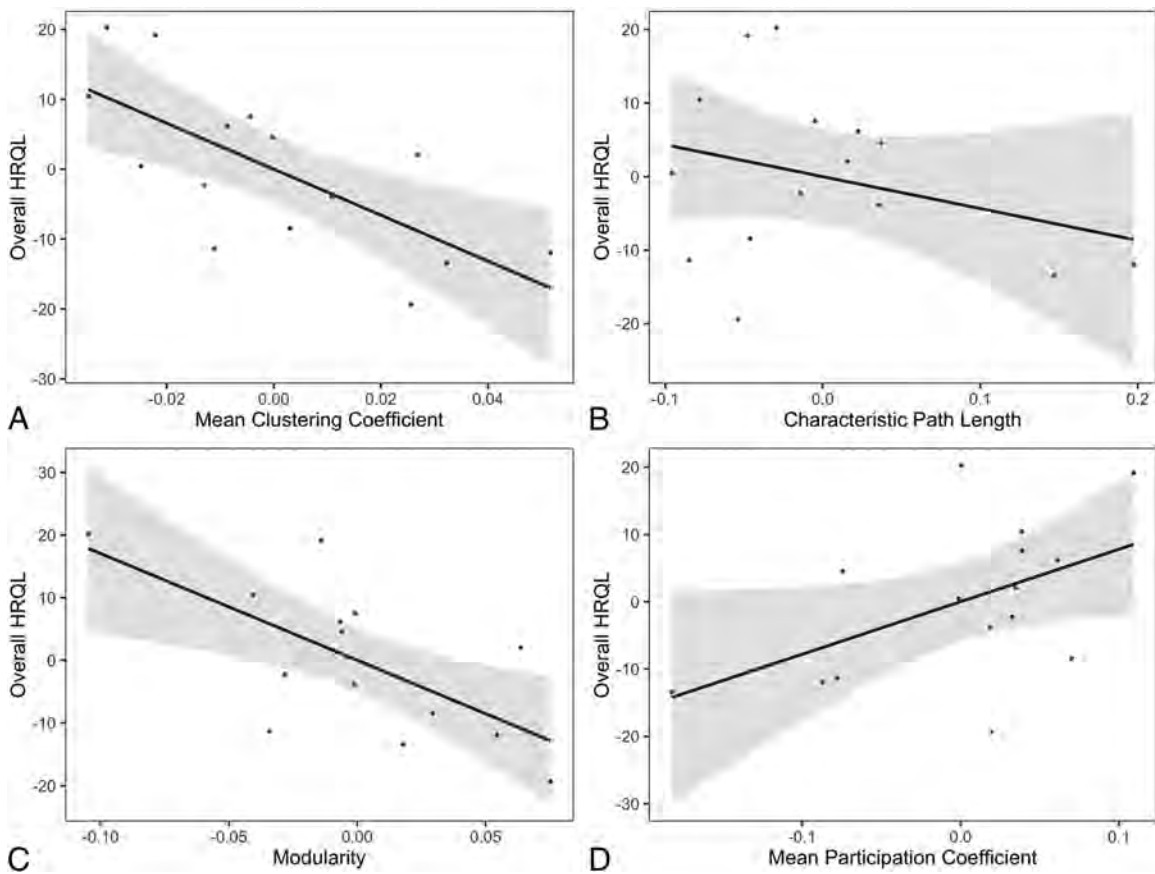


FIG 4. Associations between graph theory metrics and overall HRQL (or total Quality of Life in Childhood Epilepsy score) in patients with temporal lobe epilepsy. The mean clustering coefficient (A) and modularity (C) are negatively associated with overall HRQL. Characteristic path length (B) and the mean participation coefficient (D) are not significantly associated with overall HRQL. Networks were thresholded at an absolute Pearson correlation coefficient of $r = 0.34$. Residuals after accounting for model covariates are plotted as relative measures along with regression lines with 95% confidence intervals.

and modularity [$t_{(8)} = -2.5$; $P = .04$] was detected (Fig 4). Relationships were not significant among the total QOLCE score, characteristic path length [$t_{(8)} = -0.90$; $P = .39$], and the mean participation coefficient [$t_{(8)} = 1.6$; $P = .14$]. Assessment of HRQL domain scores revealed that there was a significant negative association between the mean clustering coefficient [$t_{(8)} = -3.6$; $P = .0075$] and modularity [$t_{(8)} = -4.4$; $P = .0021$] with

the social function domain (Fig 5). There were no significant associations between the clustering coefficient and physical function [$t_{(8)} = -2.4$; $P = .045$], emotional well-being [$t_{(8)} = -1.6$; $P = .16$], cognition [$t_{(8)} = -0.7$; $P = .48$], or behavior [$t_{(8)} = -1.5$; $P = .17$]. There was also no significant association between modularity and physical function [$t_{(8)} = -2.3$; $P = .054$], emotional well-being [$t_{(8)} = -1.7$; $P = .14$], cognition [$t_{(8)} = 0.11$;

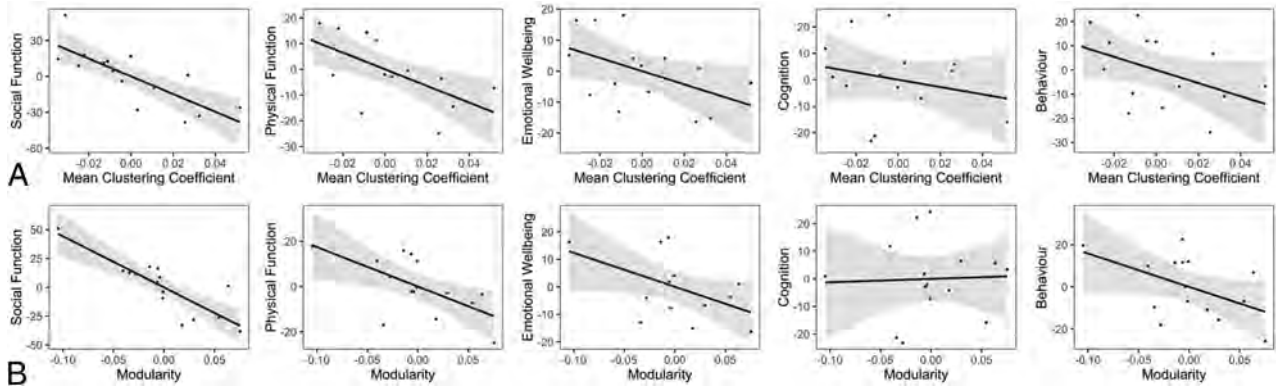


FIG 5. Associations between graph theory metrics and domain-specific Quality of Life in Childhood Epilepsy scores in patients with temporal lobe epilepsy. The mean clustering coefficient (A) and modularity (B) are negatively associated with the social function domain of the QOLCE score. Networks were thresholded at an absolute Pearson correlation coefficient of $r = 0.34$. Residuals after accounting for model covariates are plotted as relative measures along with regression lines with 95% confidence intervals.

$P = .91$], or behavior [$t_{(8)} = -1.6$; $P = .15$]. In the TLE subsample, results for total QOLCE and domain scores were similar across network-generation thresholds (On-line Figs 5 and 6).

DISCUSSION

A few studies have demonstrated the association between functional connectivity and HRQL in adults. Ren et al²⁴ have shown that a greater increase in the amplitude of low-frequency fluctuations of rsfMRI signal in the medial prefrontal cortex and superior frontal gyrus were significantly associated with HRQL in older adults with mild cognitive impairment. Greenberg et al²⁵ found an association between neural activity in the amygdala and the ventral prefrontal cortex during emotion processing as evaluated using fMRI and poor HRQL in young adults, and they found that state and trait anxiety mediated this relationship. This is the first study that has evaluated the link between global measures of functional connectivity and HRQL in children with focal epilepsy.

By computing graph-based measurements from rsfMRI, our study investigated the association between functional segregation and integration and overall HRQL. Clustering coefficient is a measure of the propensity of the brain to execute specialized processes within interconnected groups of brain regions or clusters and reflects functional segregation of brain networks.³ A high clustering coefficient indicates that the neighbors of a node are directly connected to each other.²⁶ An increased clustering coefficient has been reported in the bilateral cingulate, right perisylvian, and medial frontal lobes in children with focal epilepsy relative to controls,²⁷ in the polymicrogyria cortex relative to the normal cortex,²⁸ and in the affected hippocampus and anterior thalamus in patients with hippocampal sclerosis.²⁹ Participation coefficient measures the connectedness of a within-module node to a diverse set of segregated modules and hence the diversity of intermodular connections, which reflects network integration. A high overall participation coefficient of nodes in a network infers an increase in connector hubs, which are important for facilitating global intermodular integration.³ Lower levels of local information processing (that is, a lower mean clustering coefficient) and increased diversity of connections across modules (that is, a higher mean participation coefficient) contributed to higher levels of overall HRQL for children with focal epilepsy in this study.

Although the underlying mechanisms are not clear, these variations in network characteristics are likely influenced by seizures, antiseizure medication, or a combination of both.

During childhood and early adolescence, functional brain activity becomes more integrated,³⁰ and dynamic maturation of network modules in youth may be a critical driver for the development of cognition.³¹ In children with epilepsy, the ability to develop or maintain these network properties may be critical for the emergence and maintenance of cognitive abilities. We found a positive relationship between the participation coefficient, a measure of network integration, and cognitive domain scores. Paldino et al⁸ also showed an association between network integration, as measured by path length, and the intelligence quotient in children with epilepsy. Although our study and the study by Paldino et al showed similar findings of an association between network integration and cognition, details on the graph index measure that was associated with cognition differ in that we did not identify an association between path length and cognitive domain scores. These differences could be related to differences in study populations and/or analytic methods. We have included children with medically intractable epilepsy who have nonlesional epilepsy, while most of the children included in the study by Paldino et al had structural abnormalities. As with most graph theory analyses, there are many decision points in the analysis involving data preprocessing and graph construction that may influence the results. In this study, we constructed weighted networks and included network density as a covariate in the analyses, as recommended in recent publications.^{23,32} However, weighted networks and network density were not included in the analysis by Paldino et al.

We found an association between functional segregation, as measured by the clustering coefficient, and social function in children with focal epilepsy. Social functioning incorporates social interaction, which requires multiple higher order functions of the brain. Less is known about functional connectivity of the brain and higher order functions beyond cognitive function. There are some studies linking functional connectivity with emotion, one of the higher order functions. Emotion, such as depression, has been associated with a hyperactive default mode network.³³ Furthermore, default mode network activity of individuals with depres-

sion has been shown to be abnormally linked to other brain regions outside the default mode network.³⁴ We have not shown an association between global measures of graph indices and well-being, which incorporates measures from a variety of emotions. It is possible that the domain of well-being as measured by the QOLCE lacks specificity, and more specific measures of emotions may be linked to functional connectivity of specific regions or networks.

In the subsample with TLE, we also found a negative relationship between functional segregation and HRQL. However, there was no association between functional segregation and integration with HRQL in the subsample with FLE. The 2 subsamples demonstrated similarities in HRQL despite differences in the relationships between the functional connectivity and HRQL. A prior study has assessed structural connectivity in children with FLE and TLE and showed that the FLE subsample demonstrated more areas of reduced nodal efficiency and more impaired subnetworks than the TLE subsample.³⁵ The results of this study suggest that the architecture of brain-wide network connectivity is particularly relevant for higher order brain function when brain disruption originates in the temporal lobe. Further research is needed to distinguish differences in functional networks between TLE and FLE and their association with higher order brain function.

A limitation of this study is that we have not included a control group for comparison because the QOLCE is an epilepsy-specific HRQL instrument. A generic HRQL instrument would be required to compare the HRQL in children with epilepsy relative to controls and would permit correlation of graph-based measures of functional connectivity with generic HRQL within each of these groups. However, generic HRQL instruments may be less sensitive for assessing HRQL relative to disease-specific HRQL instruments. Future research could compare HRQL (as measured by a generic HRQL instrument) and functional connectivity among children with epilepsy versus controls and determine whether the correlations between HRQL and functional connectivity differ between children with focal epilepsy and controls.

CONCLUSIONS

This study showed a significant association between global measures of functional connectivity, including functional segregation and integration, with overall HRQL in children with medically intractable focal epilepsy. The negative association between the clustering coefficient, a measure of functional segregation, and HRQL was driven by social function. The positive association between the participation coefficient, a measure of functional integration, and HRQL, was driven by cognitive function. The findings indicate that there are other higher order brain functions beyond cognition, such as social function, which could be linked with functional connectivity of the brain. HRQL encompasses several different higher order functions such as cognition, emotion, social function, and behavior. Further studies are warranted to determine whether there are differences in brain networks among children with epilepsy with and without impairment in each of these higher order functions compared with healthy controls and whether the extent of alterations in brain networks correlates with the severity of higher order dysfunction.

Disclosures: Anne L. Wheeler—UNRELATED: Employment: Hospital for Sick Children; Grants/Grants Pending: I hold a Discovery Grant from the Natural Sciences and Engineering Research Council for unrelated research. I have a project grant under review at the Canadian Institutes for Health Research for unrelated research. Elysa Widjaja—RELATED: Grant: Ontario Brain Institute*; UNRELATED: Grants/Grants Pending: Canadian Institutes for Health Research.* *Money paid to institution.

REFERENCES

1. Biswal BB, Van Kylen J, Hyde JS. **Simultaneous assessment of flow and BOLD signals in resting-state functional connectivity maps.** *NMR Biomed* 1997;10:165–70 Medline
2. Wang J, Zuo X, He Y. **Graph-based network analysis of resting-state functional MRI.** *Front Syst Neurosci* 2010;4:16 CrossRef Medline
3. Rubinov M, Sporns O. **Complex network measures of brain connectivity: uses and interpretations.** *Neuroimage* 2010;52:1059–69 CrossRef Medline
4. Spencer SS. **Neural networks in human epilepsy: evidence of and implications for treatment.** *Epilepsia* 2002;43:219–27 CrossRef Medline
5. Rubinger L, Chan C, D'Arco F, et al. **Change in presurgical diagnostic imaging evaluation affects subsequent pediatric epilepsy surgery outcome.** *Epilepsia* 2016;57:32–40 CrossRef Medline
6. Vaessen MJ, Braakman HM, Heerink JS, et al. **Abnormal modular organization of functional networks in cognitively impaired children with frontal lobe epilepsy.** *Cereb Cortex* 2013;23:1997–2006 CrossRef Medline
7. Ofer I, Jacobs J, Jaiser N, et al. **Cognitive and behavioral comorbidities in Rolandic epilepsy and their relation with default mode network's functional connectivity and organization.** *Epilepsy Behav* 2018;78:179–86 CrossRef Medline
8. Paldino MJ, Golriz F, Chapieski ML, et al. **Brain network architecture and global intelligence in children with focal epilepsy.** *AJNR Am J Neuroradiol* 2017;38:349–56 CrossRef Medline
9. Spieth LE, Harris CV. **Assessment of health-related quality of life in children and adolescents: an integrative review.** *J Pediatr Psychol* 1996;21:175–93 CrossRef Medline
10. Austin JK, Risinger MW, Beckett LA. **Correlates of behavior problems in children with epilepsy.** *Epilepsia* 1992;33:1115–22 CrossRef Medline
11. Williams J, Steel C, Sharp GB, et al. **Anxiety in children with epilepsy.** *Epilepsy Behav* 2003;4:729–32 CrossRef Medline
12. Rodenburg R, Stams GJ, Meijer AM, et al. **Psychopathology in children with epilepsy: a meta-analysis.** *J Pediatr Psychol* 2005;30:453–68 CrossRef Medline
13. Ferro MA. **Risk factors for health-related quality of life in children with epilepsy: a meta-analysis.** *Epilepsia* 2014;55:1722–31 CrossRef Medline
14. Conway L, Smith ML, Ferro MA, et al. **Predictors of health-related quality of life in children with intractable epilepsy.** *Epilepsia* 2016;57:1256–64 CrossRef Medline
15. Sabaz M, Cairns DR, Lawson JA, et al. **The health-related quality of life of children with refractory epilepsy: a comparison of those with and without intellectual disability.** *Epilepsia* 2001;42:621–28 CrossRef Medline
16. Sabaz M, Cairns DR, Lawson JA, et al. **Validation of a new quality of life measure for children with epilepsy.** *Epilepsia* 2000;41:765–74 CrossRef Medline
17. Sabaz M, Lawson JA, Cairns DR, et al. **Validation of the quality of life in childhood epilepsy questionnaire in American epilepsy patients.** *Epilepsy Behav* 2003;4:680–91 CrossRef Medline
18. Smith SM. **Fast robust automated brain extraction.** *Hum Brain Mapp* 2002;17:143–55 CrossRef Medline
19. Jenkinson M, Bannister P, Brady M, et al. **Improved optimization for the robust and accurate linear registration and motion correction of brain images.** *Neuroimage* 2002;17:825–41 CrossRef Medline
20. Fonov V, Evans AC, Botteron K, et al; Brain Development Cooperative Group. **Unbiased average age-appropriate atlases for pediatric studies.** *Neuroimage* 2011;54:313–27 CrossRef Medline

21. Zhang Y, Brady M, Smith S. **Segmentation of brain MR images through a hidden Markov random field model and the expectation-maximization algorithm.** *IEEE Trans Med Imaging* 2001;20:45–57 CrossRef Medline
22. Shen X, Tokoglu F, Papademetris X, et al. **Groupwise whole-brain parcellation from resting-state fMRI data for network node identification.** *Neuroimage* 2013;82:403–15 CrossRef Medline
23. van den Heuvel MP, de Lange SC, Zalesky A, et al. **Proportional thresholding in resting-state fMRI functional connectivity networks and consequences for patient-control connectome studies: issues and recommendations.** *Neuroimage* 2017;152:437–49 CrossRef Medline
24. Ren P, Heffner KL, Jacobs A, et al. **Acute affective reactivity and quality of life in older adults with amnesic mild cognitive impairment: a functional MRI study.** *Am J Geriatr Psychiatry* 2017;25:1225–33 CrossRef Medline
25. Greenberg T, Bertocci MA, Chase HW, et al. **Mediation by anxiety of the relationship between amygdala activity during emotion processing and poor quality of life in young adults.** *Transl Psychiatry* 2017;7:e1178 CrossRef Medline
26. Watts DJ, Strogatz SH. **Collective dynamics of ‘small-world’ networks.** *Nature* 1998;393:440–42 CrossRef Medline
27. Takeda K, Matsuda H, Miyamoto Y, et al. **Structural brain network analysis of children with localization-related epilepsy.** *Brain Dev* 2017;39:678–86 CrossRef Medline
28. Sethi M, Pedersen M, Jackson GD. **Polymicrogyric cortex may predispose to seizures via abnormal network topology: an fMRI connectomics study.** *Epilepsia* 2016;57:e64–68 CrossRef Medline
29. Vaughan DN, Rayner G, Tailby C, et al. **MRI-negative temporal lobe epilepsy: a network disorder of neocortical connectivity.** *Neurology* 2016;87:1934–42 CrossRef Medline
30. Kundu P, Benson BE, Rosen D, et al. **The integration of functional brain activity from adolescence to adulthood.** *J Neurosci* 2018;38:3559–70 CrossRef Medline
31. Gu S, Satterthwaite TD, Medaglia JD, et al. **Emergence of system roles in normative neurodevelopment.** *Proc Natl Acad Sci U S A* 2015;112:13681–86 CrossRef Medline
32. Hallquist MN, Hillary FG. **Graph theory approaches to functional network organization in brain disorders: a new critique for a brave new small-world.** *Netw Neurosci* 2019;3:1–26 CrossRef Medline
33. Buckner RL, Andrews-Hanna JR, Schacter DL. **The brain’s default network: anatomy, function, and relevance to disease.** *Ann NY Acad Sci* 2008;1124:1–38 CrossRef Medline
34. Hwang JW, Xin SC, Ou YM, et al. **Enhanced default mode network connectivity with ventral striatum in subthreshold depression individuals.** *J Psychiatr Res* 2016;76:111–20 CrossRef Medline
35. Widjaja E, Zamyadi M, Raybaud C, et al. **Disrupted global and regional structural networks and subnetworks in children with localization-related epilepsy.** *AJNR Am J Neuroradiol* 2015;36:1362–68 CrossRef Medline

Quantitative Analysis of Punctate White Matter Lesions in Neonates Using Quantitative Susceptibility Mapping and R2* Relaxation

Y. Zhang, A. Rauscher, C. Kames, and A.M. Weber

ABSTRACT

BACKGROUND AND PURPOSE: It is difficult to distinguish punctate white matter lesions from focal hemorrhagic lesions in neonates on conventional MR imaging because both kinds of lesions show increased signal intensity on T1-weighted images and, frequently, decreased signal intensity on T2-weighted images. Our aim was to distinguish punctate white matter lesions and focal hemorrhagic lesions using quantitative measures.

MATERIALS AND METHODS: In the current study, we acquired multiecho gradient recalled-echo MR imaging data from 24 neonates with hypoxic-ischemic encephalopathy and postprocessed them as R2* relaxation maps and quantitative susceptibility maps. Seven subjects who were found to have multifocal punctate white matter lesions and/or focal hemorrhagic lesions on R2* maps were included (mean gestational age at birth, 33 ± 4.28 weeks; mean gestational age at scanning, 38 ± 2 weeks). Manually drawing ROIs on R2* maps, we measured R2* and magnetic susceptibility values of the lesions, along with white matter regions within the corpus callosum as healthy comparison tissue.

RESULTS: R2* and magnetic susceptibility values were both found to easily distinguish punctate white matter lesions, focal hemorrhagic lesions, and healthy white matter tissue from each other ($P < .05$), with a large Hedge g . R2* and magnetic susceptibility values were significantly increased in focal hemorrhagic lesions compared with punctate white matter lesions and healthy white matter tissue. Punctate white matter lesions were also found to have significantly increased values over healthy white matter tissue.

CONCLUSIONS: R2* and quantitative susceptibility maps can be used to help clinicians distinguish and measure focal hemorrhages, punctate white matter lesions, and healthy white matter tissue.

ABBREVIATIONS: GRE = gradient recalled-echo; PWML = punctate white matter lesion; QSM = quantitative susceptibility mapping

With benefits that come with improved neonatal intensive care, an increasing number of preterm neonates are surviving with reduced cystic periventricular leukomalacia and periventricular hemorrhagic infarction, which can be diagnosed by sonography.^{1,2} However, developmental outcomes following preterm birth remain poor, with 5%–10% having major motor def-

icits and more than half developing cognitive, behavioral, and social difficulties later in life.^{3,4}

Noncystic punctate white matter lesions (PWMLs) are detected by MR imaging in one-third of preterm neonates and are not accurately detected by sonography.^{5–9} Histologic and MR imaging studies suggest that PWMLs have intense macrophage and microglial infiltration and reduced astroglia, which coincide with microscopic necrosis and early gliosis.^{10,11} Whether these multifocal PWMLs in neonatal brain injuries are associated with neurodevelopmental outcomes is still a matter of debate.^{12–15}

The etiology of PWMLs remains unclear. Only sporadic reports exist of neonates presenting with perinatal asphyxia^{16–18} or convulsions¹⁹ accompanied by similar white matter lesions. Cornette et al¹⁵ reported the MR imaging characteristics and neurodevelopmental outcomes of PWMLs in a large cohort of preterm and term neonates and found that these lesions were pre-

Received December 14, 2018; accepted after revision April 29, 2019.

From the Department of Radiology (Y.Z.) and Ministry of Education Key Laboratory of Child Development and Disorders (Y.Z.), Children's Hospital of Chongqing Medical University, Chongqing, P.R. China; Key Laboratory of Pediatrics in Chongqing (Y.Z.), Chongqing, P.R. China; Chongqing International Science and Technology Cooperation Center for Child Development and Disorders (Y.Z.), Chongqing, P.R. China; and Division of Neurology (A.R., A.M.W.), Department of Pediatrics, University of British Columbia MRI Research Centre (A.R., A.M.W., C.K.), and Departments of Radiology, (A.R.) and Physics and Astronomy (C.K.), University of British Columbia, Vancouver, British Columbia, Canada.

Please address correspondence to Alexander Mark Weber, PhD, MSc, UBC MRI Research Centre, University of British Columbia, M10-Purdy Pavilion, 2221 Westbrook Mall, Vancouver, BC V6T 2B5; e-mail: alex.weber@ubc.ca; @rauscherMRI

<http://dx.doi.org/10.3174/ajnr.A6114>

dominantly associated with preterm birth but could also be seen in term infants.

PWMLs were defined as foci of T1- and T2-weighted hypointensity with no evidence of cystic degeneration.^{8,20} Previous MR imaging studies investigating PWMLs have been based on T1-weighted images, which have primarily evaluated the lesions by their number, diameter, and location.^{13,20,21} A grading system on MR imaging was developed to classify white matter abnormalities as normal (no periventricular white matter lesions), minimal (≤ 3 areas of T1-weighted signal abnormalities measuring < 2 mm), moderate (> 3 areas of T1-weighted signal abnormalities or areas measuring < 2 mm but $< 5\%$ of the hemisphere involved), and severe (T1-weighted signal abnormalities involving $> 5\%$ of the hemisphere).^{8,13} The degree of signal intensity of these lesions, however, is underestimated, which, in turn, is likely to result in a misdiagnosis of the degree of injury. On the other hand, it is difficult to distinguish PWMLs from focal hemorrhage on conventional MR imaging because both kinds of lesions show increased signal intensity on T1-weighted images and frequently decreased signal on T2-weighted images.^{22,23} Accurate predictive tools are essential for clinicians to identify and quantify brain injury and provide early interventions to improve clinical outcomes of these neonates.²¹

R2* mapping is a semiquantitative technique derived from multiecho gradient recalled-echo (GRE) MR imaging scans. R2* values are influenced by iron and myelin content and are relatively easy to calculate.²⁴ Quantitative susceptibility mapping (QSM), on the other hand, is a newer technique and can be derived from the same scan as R2* (or from a more common single-echo GRE scan) but which fully quantifies magnetic susceptibility using the phase data of the scan.²⁵ QSM has, until recently, been difficult to calculate, due to the ill-posed inverse field-to-susceptibility problem. In the current study, we acquired multiecho GRE scans in both preterm and term neonates to investigate PWML injuries with R2* and QSM maps. We hypothesized that these GRE-based MR imaging maps would allow us to distinguish PWMLs from hemorrhagic lesions with higher precision than conventional MR imaging scans.

MATERIALS AND METHODS

Patients

Between January 2017 and January 2018, preterm and term neonates with a clinical history of perinatal asphyxia and hypoxic-ischemic encephalopathy who transferred to the Children's Hospital of Chongqing Medical University intensive care nursery were approached for enrollment in a study evaluating the detection of brain injury by MR imaging. The institutional review board of Children's Hospital of Chongqing Medical University approved the study protocol, and informed consent was obtained from the parents. In total, 24 neonates were initially examined. The diagnostic criteria for PWMLs was foci of T1- and T2-weighted hypointensity with no evidence of cystic degeneration.^{8,20} Patients with T1 and T2 abnormalities were identified by 2 pediatric radiologists as part of the routine radiologic assessment, and any discrepancies were resolved through consensus. Eight neonates were found to

have multifocal PWMLs and/or focal hemorrhagic lesions and were included for further study.

MR Imaging Acquisition

Brain MR images were obtained on a 3T system (Achieva; Philips Healthcare, Best, the Netherlands) using an 8-channel sensitivity encoding head coil. Data for R2* mapping and QSM were collected using a 3D GRE sequence with 5 echoes (TR = 30 ms, TE₁ = 4.5 ms, echo spacing = 5.5 ms, $\alpha = 17^\circ$, FOV = $196 \times 154 \times 103$ mm³, acquired voxel size = $0.50 \times 0.75 \times 1.0$ mm³, reconstructed voxel size = $0.5 \times 0.5 \times 0.5$ mm³).²⁶ Other scans included the following: inversion recovery turbo spin-echo T1-weighting (TR/TI = 7000/600 ms, TE = 15 ms, slice thickness = 5 mm, FOV = $160 \times 151 \times 98$ mm³, acquisition matrix = 220×163); and turbo spin-echo T2-weighting (TR = 5000 ms, TE = 100 ms, slice thickness = 5 mm, FOV = $160 \times 149 \times 98$ mm³, acquisition matrix = 332×205). Total acquisition time was 9 minutes 39 seconds.

MR Image Analysis

R2* maps were calculated from the multi-GRE scans by fitting a monoexponential function to the magnitude signal decay in each voxel. QSM images of all 5 echoes were postprocessed from the phase data. Phase unwrapping was achieved using a 3D Laplacian algorithm,²⁷ while the background field was removed using the variable-kernel sophisticated harmonic artifact reduction for phase method.²⁸ Last, a Gaussian filter ($\sigma = 0.5$) was applied to the normalized field maps to smooth out high-frequency errors originating from the reconstruction steps before the inversion. A 2-step dipole inversion algorithm²⁹ was used to solve the dipole inversion problem. Finally, QSM images were then averaged across the third, fourth, and fifth echoes.

Authors Y.Z. and A.R. drew the ROIs independently. Neonates with scans with high motion or image artifacts were excluded. 3D ROIs encompassing PWMLs and focal hemorrhagic lesions were defined manually on consecutive slices of the R2* maps. Three ROIs of each subject were defined within the corpus callosum as normal white matter. For each ROI, the R2* and magnetic susceptibility values were measured.

Statistical Analysis

Statistical analysis was performed using R statistical and computing software (<http://www.r-project.org>). To assess interrater reliability, we calculated a 1-way intraclass correlation coefficient from the full set of R2* and QSM values obtained from the 2 different observers' ROIs. Due to the small sample size, a non-parametric Kruskal-Wallis rank sum test was used to test differences of R2* and magnetic susceptibility values among the different tissue types. Post hoc Dunn tests were performed with Holm-Bonferroni correction for multiple comparisons to test differences among the different tissue types (Tables 1 and 2). The Hedge g was used to estimate effect size.

RESULTS

In total, 8 subjects were found to have multifocal PWMLs and/or focal hemorrhagic lesions on R2* maps, with 1 patient with large

MR imaging artifacts being excluded. This resulted in 7 subjects being used (mean gestational age at birth, 33 ± 4.28 weeks; mean gestational age at scanning, 38 ± 2 weeks). Of these 7 subjects, 5 were preterm (Table 3).

In all, 18 PWMLs, 9 focal hemorrhagic lesions, and 21 normal white matter ROIs (3 ROIs within the corpus callosum of each subject) were identified in the 7 subjects we examined (Table 3 and Fig 1). PWMLs in preterm infants are usually linearly organized along the periventricular white matter. The PWMLs in term infants and focal hemorrhagic lesions are relatively isolated in the white matter.

The interclass correlation coefficient for the values obtained from the 2 observers' ROIs was calculated to be 0.98, which is defined as excellent by Koo and Li.³⁰

The $R2^*$ and magnetic susceptibility values for the 3 tissue types for each subject are shown in Fig 2. $R2^*$ and magnetic susceptibility boxplots are shown in Fig 3. The means and SDs of $R2^*$ and magnetic susceptibility values of the ROIs within the corpus callosum, PWMLs, and focal hemorrhagic lesions are listed in Table 4. The $R2^*$ and magnetic susceptibility values were found to be significantly different ($P < .05$), with a large Hedge g , among all 3 regions.

DISCUSSION

Paramagnetic hemorrhagic products substantially increase $R2^*$ relaxation rates and magnetic susceptibility.^{31,32} In our study, we have shown that $R2^*$ and magnetic susceptibility values of focal hemorrhagic lesions were significantly increased compared with PWMLs. Due to the magnetic susceptibility effect, signal increases indicating hemorrhage on $R2^*$

maps appear to be larger compared with the actual hyperintense signal area on T1-weighted images. In follow-up studies, hemorrhagic lesions can be absorbed and no longer seen on conventional scans, whereas PWMLs, which may represent early gliosis and evolve into early glial scars, can still be present.²² In a previous study, some PWMLs on T1-weighted scans of preterm neonates were absent or decreased near term-equivalent age, whereas others were worse on follow-up scans.²³ Thus, changes in $R2^*$ and magnetic susceptibility may provide a biomarker of PWML progression.

Previous MR imaging studies have been based on T1-weighted images evaluating PWMLs by features such as the number, diameter, and location of lesions.^{13,20,21} The signal intensity of these lesions, however, is likely underestimated¹³⁻¹⁵; this underestimation may result in a misdiagnosis of injury. For example, while Jeon et al¹² found that punctate lesions were significant predictors of cerebral palsy and Miller et al¹³ found that punctate lesions predicted a higher risk of neurodevelopmental disabilities, Dyet et al¹⁴ found that there were no significant differences in developmental outcomes between infants with and without PWMLs. Furthermore, Cornette et al¹⁵ found that isolated punctate lesions might imply a good prognosis because most subjects had a normal neurodevelopmental outcome at 29.5 months of age. It is difficult to distinguish PWMLs from focal hemorrhagic lesions on conventional MR imaging because both kinds of lesions show increased signal intensity on T1-weighted images and frequently decreased signal on T2-weighted images.^{22,23}

From the results we obtained, $R2^*$ and magnetic susceptibility values were able to easily distinguish healthy WM, PWMLs, and focal hemorrhagic lesions from each other. The $R2^*$ and magnetic susceptibility values of the PWMLs ranged from 9.76 to 17.06 Hz and from 0.002 to 0.035 ppm, respectively, which may be caused by the different disease stage and injury degree. The $R2^*$ and susceptibility values of the focal hemorrhagic lesions showed an even greater range, from 30.42 to 65.94 Hz and from 0.085 to 0.209 ppm, respectively. A large sample size and follow-up of the neonates is in progress, and it will be of interest to see whether there is a difference in outcome in those neonates with different $R2^*$ and magnetic susceptibility values of PWMLs.

While both $R2^*$ and QSM show great promise in measuring and differentiating PWMLs and focal hemorrhagic lesions, methodologic pros and cons should be weighed and discussed. $R2^*$ has historically been easier to postprocess because it requires simpler and fewer steps than QSM. Recently, however, QSM is becoming more mainstream, with wide dissemination possibly becoming feasible in the very near future.³³ $R2^*$, unlike QSM, may have

confounding factors such as fat, fibrosis, and edema³³ and saturation and blooming artifacts. For instance, QSM, compared with $R2^*$, has been shown to be more sensitive in identifying increased nigral iron in patients with Parkinson disease compared with healthy controls,³⁴ to have a superior contrast-to-noise ratio in locating and identifying the subthalamic nuclei,³⁵ and to be better at determining iron concentration of

Table 1: $R2^*$ —Dunn Kruskal-Wallis multiple comparisons^a

Comparison	Z	P.unadj	P.adj
CC FH	-5.88	4.05e-09	1.21e-08
CC PWML	-4.24	2.19e-05	4.38e-05
FH PWML	2.40	1.64e-02	1.64e-02

Note:—P.unadj indicates unadjusted P values; P.adj, adjusted P values; CC, corpus callosum; FH, focal hemorrhagic lesion.

^aP values were adjusted using the Bonferroni-Holm correction for multiple comparisons.

Table 2: QSM—Dunn Kruskal-Wallis multiple comparisons^a

Comparison	Z	P.unadj	P.adj
CC FH	-5.70	1.19e-08	3.58e-08
CC PWML	-3.75	1.75e-04	3.50e-04
FH PWML	2.61	9.04e-03	9.04e-03

Note:—P.unadj indicates unadjusted P values; P.adj, adjusted P values; CC, corpus callosum; FH, focal hemorrhagic lesion.

^aP values were adjusted using the Bonferroni-Holm correction for multiple comparisons.

Table 3: Clinical data and MR imaging findings in the study population

No.	GA (Birth) (wk)	BW (g)	Apgar	Sex	Scan Age (wk)	PWML	FH	IVH
1	39	3750	7	Male	41	2	2	Yes
2	38	3645	7	Male	40	4	2	Yes
3	31	1508	4	Female	37	8	0	No
4	28	1210	6	Female	37	2	1	Yes
5	29	1100	8	Female	35	2	0	No
6	35	2770	9	Male	38	0	2	No
7	34	1425	7	Female	38	0	2	No

Note:—GA indicates gestational age; BW, birth weight; Apgar, Apgar score (5 minutes); IVH, presence of intraventricular hemorrhage; FH, focal hemorrhagic lesion.

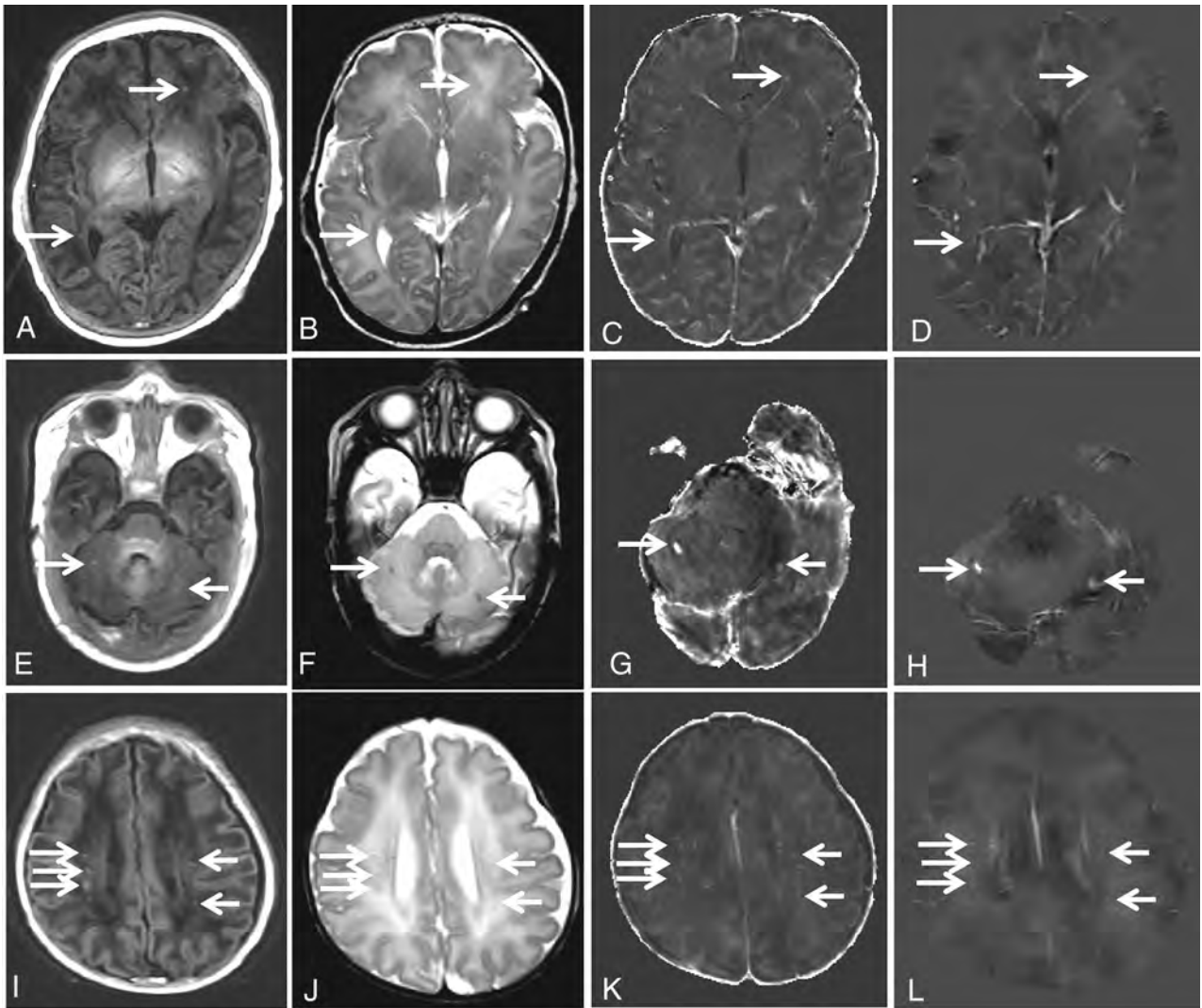


FIG 1. A–D, Punctate white matter lesions in a term neonate born at 38 weeks' gestational age, scanned at 40 weeks' gestational age (corresponding to case 2 in Table 3). A, T1-weighted axial image shows isolated high-intensity spots (*arrows*) corresponding to punctate white matter lesions in the white matter of the left frontal lobe and right posterior periventricular white matter. B, Corresponding T2-weighted axial image. Low-intensity spots (*arrows*) correspond to punctate lesions. C, R2* shows high signal in the punctate white matter lesions (*arrows*). D, QSM shows high signal at the punctate white matter lesions (*arrows*). E–H, Focal hemorrhagic lesions in a preterm neonate born at 35 weeks' gestational age, scanned at 38 weeks' gestational age (corresponding to case 6 in Table 3). E, T1-weighted axial image shows isolated high-intensity spots (*arrows*) corresponding to focal hemorrhagic lesions in the bilateral cerebellar hemispheres. F, Corresponding T2-weighted axial image. Low-intensity spots (*arrows*) correspond to focal hemorrhagic lesions. G and H, R2* and QSM, respectively, show very high signal at the focal hemorrhagic lesions (*arrows*), indicative of paramagnetic hemorrhagic products. I–L, Punctate white matter lesions in a preterm neonate born at 31 weeks' gestational age, scanned at 37 weeks' gestational age (corresponding to case 3 in Table 3). T1-weighted axial image (I), T2-weighted axial image (J), R2* (K), and QSM (L) through the body of the lateral ventricles show more punctate white matter lesions than the above term neonates in the 2 hemispheres (*arrows*). Lesions are linearly organized in the periventricular white matter.

various tissues, such as the liver, heart, and brain.^{33,36} On the other hand, our data suggest that R2* best distinguishes healthy white matter and PWMLs (see subject 7 in Fig 2 and the boxplots in Fig 3).

While QSM studies have often used well-characterized tissue as a reference to scale susceptibility values, such as CSF in the ventricles, recent studies have reported insignificant differences between raw and reference-normalized QSM.³⁷ To avoid making basic assumptions inherent in normalization, we decided to report raw values here.

Histologic and MR imaging studies suggest that PWMLs result in intense macrophage and microglial infiltration and reduced astroglia, which coincide with microscopic necrosis and early gliosis.^{10,11}

What components in these lesions lead to faster T2* signal decay and increased magnetic susceptibility? Is there an increase in iron content within PWMLs?³⁸ More histopathologic studies would be welcome. While iron can also be expected to be present in macrophages as hemosiderin deposits in the PWMLs, the lesions classified as focal hemorrhage might, as well, arise from a PWML, which has been hemorrhagically transformed. Of course, many focal hemorrhagic lesions are expected to be excluded from being falsely identified as PWMLs, but there might be an unknown proportion of actual PWMLs that have transformed hemorrhagically and are excluded from being further analyzed as PWMLs though they might be relevant according to disease outcome.

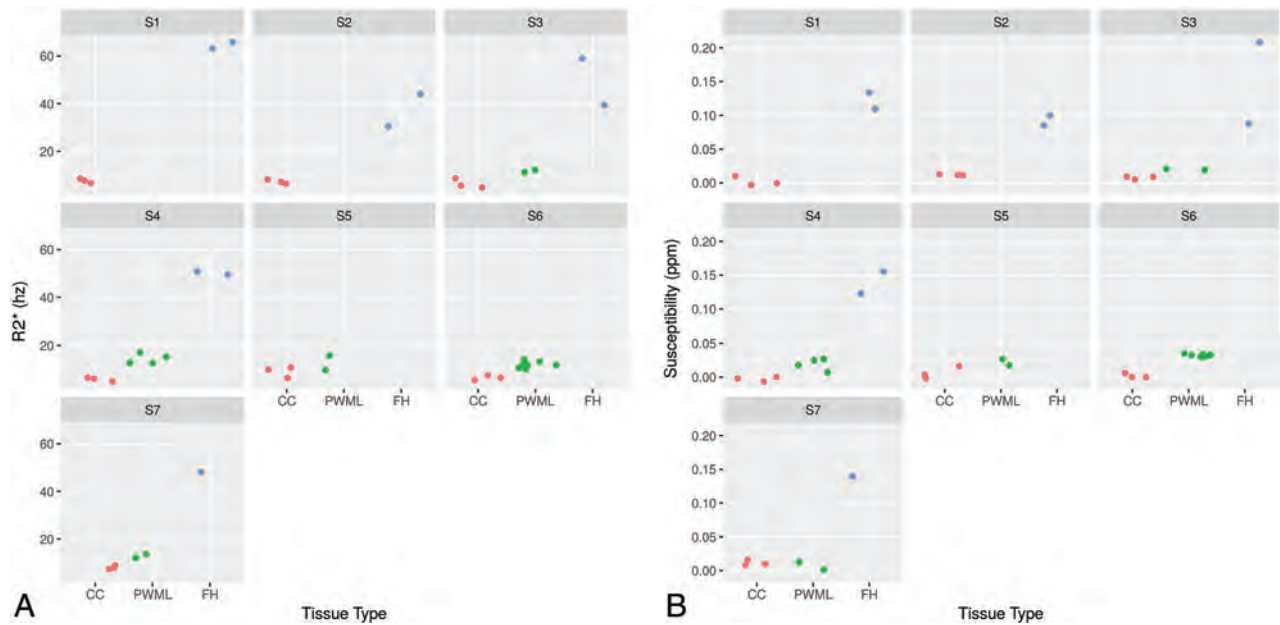


FIG 2. The R2* (A) and susceptibility (B) values for the 3 tissue/lesion types for each subject (S1–S7).

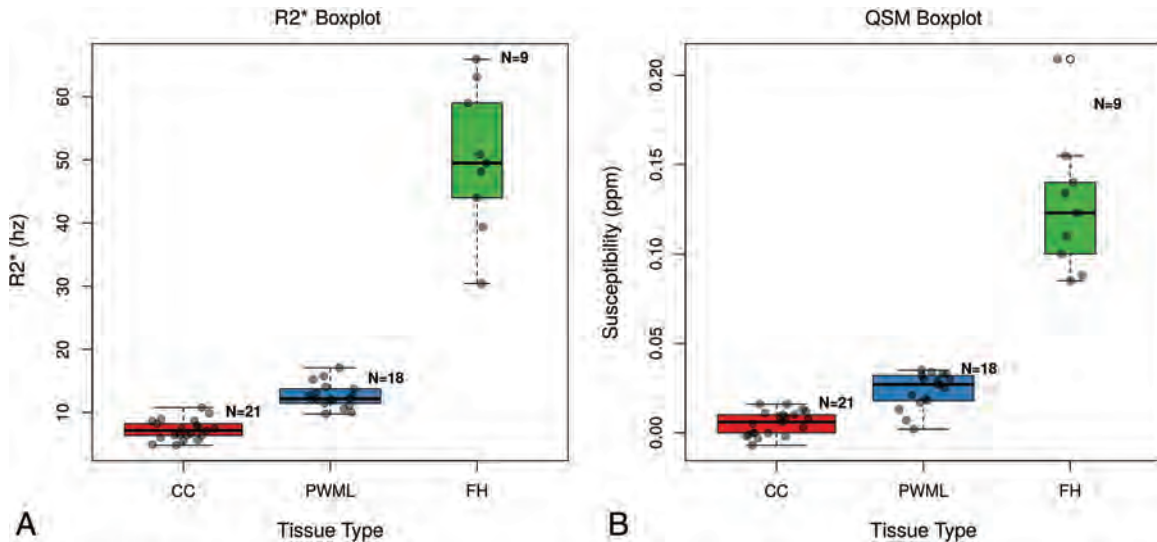


FIG 3. Boxplots of R2* (A) and susceptibility (B) values for the 3 tissue/lesion types.

Table 4: The mean and SD of R2* and susceptibility in 3 groups

ROIs	CC	PWMLs	FH
R2* (Hz)	7.23 ± 1.57	12.65 ± 1.94	50.04 ± 11.42
Susceptibility (ppm)	0.0054 ± 0.0067	0.024 ± 0.010	0.127 ± 0.039

Note:—CC indicates corpus callosum; FH, focal hemorrhagic lesion.

CONCLUSIONS

R2* relaxation and QSM can be used to distinguish PWMLs from focal hemorrhagic lesions and may be used as quantitative predictive tools to evaluate the correlation between PWMLs and neurodevelopmental outcomes in future studies.

REFERENCES

- Horbar JD, Badger GJ, Carpenter JH, et al; Members of the Vermont Oxford Network. **Trends in mortality and morbidity for very low birth weight infants, 1991–1999.** *Pediatrics* 2002;110(1 Pt 1):143–51 CrossRef Medline
- van den Hout BM, de Vries LS, Meiners LC, et al. **Visual perceptual impairment in children at 5 years of age with perinatal haemorrhagic or ischaemic brain damage in relation to cerebral magnetic resonance imaging.** *Brain Dev* 2004;26:251–61 CrossRef Medline
- Grunau RE, Whitfield MF, Davis C. **Pattern of learning disabilities in children with extremely low birth weight and broadly average intelligence.** *Arch Pediatr Adolesc Med* 2002;156:615–20 CrossRef Medline
- Hamrick SE, Miller SP, Leonard C, et al. **Trends in severe brain injury and neurodevelopmental outcome in premature newborn infants: the role of cystic periventricular leukomalacia.** *J Pediatr* 2004;145:593–99 CrossRef Medline
- Maalouf EF, Duggan PJ, Counsell SJ, et al. **Comparison of findings on cranial ultrasound and magnetic resonance imaging in preterm infants.** *Pediatrics* 2001;107:719–27 CrossRef Medline
- Inder TE, Anderson NJ, Spencer C, et al. **White matter injury in the premature infant: a comparison between serial cranial sonographic and MR findings at term.** *AJNR Am J Neuroradiol* 2003;24:805–09 Medline

7. Inder TE, Wells SJ, Mogridge NB, et al. **Defining the nature of the cerebral abnormalities in the premature infant: a qualitative magnetic resonance imaging study.** *J Pediatr* 2003;143:171–79 CrossRef Medline
8. Miller SP, Cozzio CC, Goldstein RB, et al. **Comparing the diagnosis of white matter injury in premature newborns with serial MR imaging and transfontanel ultrasonography findings.** *AJNR Am J Neuroradiol* 2003;24:1661–69 Medline
9. Debillon T, N'Guyen S, Muet A, et al. **Limitations of ultrasonography for diagnosing white matter damage in preterm infants.** *Arch Dis Child Fetal Neonatal Ed* 2003;88:F275–79 CrossRef Medline
10. Schouman-Claeys E, Henry-Feugas MC, Roset F, et al. **Periventricular leukomalacia: correlation between MR imaging and autopsy findings during the first 2 months of life.** *Radiology* 1993;189:59–64 CrossRef Medline
11. Riddle A, Dean J, Buser JR, et al. **Histopathological correlates of magnetic resonance imaging-defined chronic perinatal white matter injury.** *Ann Neurol* 2011;70:493–507 CrossRef Medline
12. Jeon TY, Kim JH, Yoo SY, et al. **Neurodevelopmental outcomes in preterm infants: comparison of infants with and without diffuse excessive high signal intensity on MR images at near-term-equivalent age.** *Radiology* 2012;263:518–26 CrossRef Medline
13. Miller SP, Ferriero DM, Leonard C, et al. **Early brain injury in premature newborns detected with magnetic resonance imaging is associated with adverse early neurodevelopmental outcome.** *J Pediatr* 2005;147:609–16 CrossRef Medline
14. Dyet LE, Kennea N, Counsell SJ, et al. **Natural history of brain lesions in extremely preterm infants studied with serial magnetic resonance imaging from birth and neurodevelopmental assessment.** *Pediatrics* 2006;118:536–48 CrossRef Medline
15. Cornette LG, Tanner SF, Ramenghi LA, et al. **Magnetic resonance imaging of the infant brain: anatomical characteristics and clinical significance of punctate lesions.** *Arch Dis Child Fetal Neonatal Ed* 2002;86:F171–77 CrossRef Medline
16. Keeney SE, Adcock EW, McArdle CB. **Prospective observations of 100 high-risk neonates by high-field (1.5 Tesla) magnetic resonance imaging of the central nervous system, II: lesions associated with hypoxic-ischemic encephalopathy.** *Pediatrics* 1991;87:431–38 Medline
17. Baenziger O, Martin E, Steinlin M, et al. **Early pattern recognition in severe perinatal asphyxia: a prospective MRI study.** *Neuroradiology* 1993;35:437–42 CrossRef Medline
18. Battin MR, Maalouf EF, Counsell SJ, et al. **Magnetic resonance imaging of the brain in very preterm infants: visualization of the germinal matrix, early myelination, and cortical folding.** *Pediatrics* 1998;101:957–62 CrossRef Medline
19. Mercuri E, Rutherford M, Cowan F, et al. **Early prognostic indicators of outcome in infants with neonatal cerebral infarction: a clinical, electroencephalogram, and magnetic resonance imaging study.** *Pediatrics* 1999;103:39–46 CrossRef Medline
20. Ramenghi LA, Fumagalli M, Righini A, et al. **Magnetic resonance imaging assessment of brain maturation in preterm neonates with punctate white matter lesions.** *Neuroradiology* 2007;49:161–67 CrossRef Medline
21. Cheng I, Miller SP, Duerden EG, et al. **Stochastic process for white matter injury detection in preterm neonates.** *Neuroimage Clin* 2015;7:622–30 CrossRef Medline
22. Niwa T, de Vries LS, Benders MJ, et al. **Punctate white matter lesions in infants: new insights using susceptibility-weighted imaging.** *Neuroradiology* 2011;53:669–79 CrossRef Medline
23. Gano D, Andersen SK, Partridge JC, et al. **Diminished white matter injury over time in a cohort of premature newborns.** *J Pediatr* 2015;166:39–43 CrossRef Medline
24. Yablonskiy DA, Haacke EM. **Theory of NMR signal behavior in magnetically inhomogeneous tissues: the static dephasing regime.** *Magn Reson Med* 1994;32:749–63 CrossRef Medline
25. Deistung A, Schweser F, Reichenbach JR. **Overview of quantitative susceptibility mapping.** *NMR Biomed* 2017;30 CrossRef Medline
26. Denk C, Rauscher A. **Susceptibility weighted imaging with multiple echoes.** *J Magn Reson Imaging* 2010;31:185–91 CrossRef Medline
27. Schofield MA, Zhu Y. **Fast phase unwrapping algorithm for interferometric applications.** *Opt Lett* 2003;28:1194–96 CrossRef Medline
28. Li W, Wu B, Liu C. **Quantitative susceptibility mapping of human brain reflects spatial variation in tissue composition.** *Neuroimage* 2011;55:1645–56 CrossRef Medline
29. Kames C, Wiggermann V, Rauscher A. **Rapid two-step dipole inversion for susceptibility mapping with sparsity priors.** *Neuroimage* 2018;167:276–83 CrossRef Medline
30. Koo TK, Li MY. **A guideline of selecting and reporting intraclass correlation coefficients for reliability research.** *J Chiropr Med* 2016;15:155–63 CrossRef Medline
31. Mori N, Miki Y, Kikuta K, et al. **Microbleeds in moyamoya disease: susceptibility-weighted imaging versus T2*-weighted imaging at 3 Tesla.** *Invest Radiol* 2008;43:574–79 CrossRef Medline
32. Nandigam RN, Viswanathan A, Delgado P, et al. **MR imaging detection of cerebral microbleeds: effect of susceptibility-weighted imaging, section thickness, and field strength.** *AJNR Am J Neuroradiol* 2009;30:338–43 CrossRef Medline
33. Wang Y, Spincemaille P, Liu Z, et al. **Clinical quantitative susceptibility mapping (QSM): biometal imaging and its emerging roles in patient care.** *J Magn Reson Imaging* 2017;46:951–71 CrossRef Medline
34. Barbosa JH, Santos AC, Tumas V, et al. **Quantifying brain iron deposition in patients with Parkinson's disease using quantitative susceptibility mapping, R2 and R2*.** *Magn Reson Imaging* 2015;33:559–65 CrossRef Medline
35. Liu T, Eskreis-Winkler S, Schweitzer AD, et al. **Improved subthalamic nucleus depiction with quantitative susceptibility mapping.** *Radiology* 2013;269:216–23 CrossRef Medline
36. Sharma SD, Fischer R, Schoennagel BP, et al. **MRI-based quantitative susceptibility mapping (QSM) and R2* mapping of liver iron overload: comparison with SQUID-based biomagnetic liver susceptometry.** *Magn Reson Med* 2017;78:264–70 CrossRef Medline
37. Acosta-Cabronero J, Betts MJ, Cardenas-Blanco A, et al. **In vivo MRI mapping of brain iron deposition across the adult lifespan.** *J Neurosci* 2016;36:364–74 CrossRef Medline
38. Meguro R, Asano Y, Odagiri S, et al. **Cellular and subcellular localizations of nonheme ferric and ferrous iron in the rat brain: a light and electron microscopic study by the perfusion-Perls and -Turnbull methods.** *Arch Histol Cytol* 2008;71:205–22 CrossRef Medline

Predictive Value of MRI in Diagnosing Brain AVM Recurrence after Angiographically Documented Exclusion in Children

 A. Jhaveri,  A. Amirabadi,  P. Dirks,  A.V. Kulkarni,  M.M. Shroff,  N. Shkumat,  T. Krings,  V.M. Pereira,  V. Rea, and  P. Muthusami



ABSTRACT

BACKGROUND AND PURPOSE: MRI is routinely performed following brain AVM after treatment in children. Our aim was to determine the predictive values of contrast-enhanced MR imaging and TOF-MRA for brain AVM recurrence in children, compared with conventional angiography and the role of 3D rotational angiography–MR imaging fusion in these cases.

MATERIALS AND METHODS: We included all pediatric patients with brain AVMs during an 18-year period with angiographically documented obliteration after treatment. Patients underwent 3T MR imaging, including contrast-enhanced MR imaging, TOF-MRA, and conventional angiography, with a subset undergoing 3D rotational angiography. The predictive values of contrast-enhanced MR imaging and TOF-MRA for brain AVM recurrence were determined. CTA sections reconstructed from 3D rotational angiography were coregistered with and fused to 3D-T1WI for analysis.

RESULTS: Thirty-nine children (10.8 ± 3.9 years of age; range, 2–17 years; male/female ratio, 19:20; mean Spetzler-Martin grade, 1.9 ± 0.6) met the inclusion criteria. Of these, 13 had angiographically confirmed brain AVM recurrence, 8 following surgery and 5 following embolization. Sensitivity, specificity, and positive and negative predictive values for recurrence were the following: contrast-enhanced MR imaging: 84.6%, 38.5%, 40.7%, 81.8%; TOF-MRA: 50.0%, 96.1%, 85.7%, 79.3%; both: 75.0%, 90.9%, 85.7%, 83.3%. 3D rotational angiography–MR imaging fused images confirmed or excluded recurrence in all available cases (13/13). Embolization-only treatment was a significant predictor of recurrence (OR = 32.4, $P = .006$). MR imaging features predictive of recurrence included a tuft of vessels on TOF-MRA and nodular juxtamural/linear enhancement with a draining vein on contrast-enhanced MR imaging.

CONCLUSIONS: MR imaging is useful for surveillance after brain AVM treatment in children, but conventional angiography is required for definitive diagnosis of recurrence. TOF-MRA and contrast-enhanced MR imaging provide complementary information for determining brain AVM recurrence and should be interpreted in conjunction. 3D rotational angiography–MR imaging fusion increases the diagnostic confidence regarding brain AVM recurrence and is therefore suited for intraoperative neuronavigation.

ABBREVIATIONS: bAVM = brain AVM; CA = conventional angiography; CEMRI = contrast-enhanced MR imaging; 3DRA = 3D rotational angiography; NPV = negative predictive value; PPV = positive predictive value; SM = Spetzler-Martin

The annual risk of brain arteriovenous malformation (bAVM) rupture is estimated at 2%–4%, with a 25% mortality rate per event.^{1–3} In children, bAVMs could remain undetected but usually present with rupture, accounting for most childhood intra-

cranial hemorrhages.^{4,5} Presentation with hemorrhage is a well-known risk factor for future bleeding from a bAVM.^{1,6,7} Modern treatment of bAVM comprises multimodality interventions alone or in combination: operation, stereotactic radiosurgery, and embolization. The results of A Randomized Trial of Unruptured Brain AVMs (ARUBA),⁸ which favored conservative management over active intervention for unruptured brain AVMs in adult patients, have been the subject of much debate.^{9–13} However, for ruptured bAVMs, complete angiographic obliteration is the accepted standard of care, due to a known increased risk of a second hemorrhage.

Recurrence after treatment of bAVMs in children is reported in 5%–15% of cases, which is higher than in adult patients.^{4,14} This necessitates angiographic documentation of complete obliteration, as well as close follow-up. There is no consensus regard-

Received April 2, 2019; accepted April 18.

From Pediatric Neuroradiology and Image Guided Therapy (A.J., A.A., M.M.S., N.S., V.R., P.M.), Diagnostic Imaging, and Division of Neurosurgery (P.D., A.V.K.), Department of Surgery, The Hospital for Sick Children, University of Toronto, Toronto, Ontario, Canada; and Divisions of Neuroradiology and Neurosurgery (T.K., V.M.P.), Departments of Medical Imaging and Surgery, University of Toronto, and Toronto Western Hospital, University Health Network, Toronto, Ontario, Canada.

Please address correspondence to Prakash Muthusami, MD, Diagnostic Imaging, IGT, The Hospital for Sick Children, 555 University Ave, Toronto, ON - M5G 1X8, Canada; e-mail: Prakash.muthusami@sickkids.ca; @PMuthusami

 Indicates article with supplemental on-line table.

<http://dx.doi.org/10.3174/ajnr.A6093>

ing the optimal timing and imaging technique for surveillance, with MR imaging, CTA, and conventional angiography (CA) playing an important role in the literature.^{5,15,16} CA is the criterion standard to document shunt obliteration, visualize recurrence, and tailor appropriate treatment in bAVMs. However, given its invasive nature, the potential risk of complications, need for general anesthesia in children, and exposure to ionizing radiation, there is interest in developing noninvasive methods that can yield similar results. Pediatric patients at our institution are followed up with MR imaging, with CA performed in case of abnormal MR imaging findings, and at 1 year in case of normal MR imaging findings. In cases with small recurrences or slow shunting, 3D rotational angiography is performed at the discretion of the interventional neuroradiologist, with subsequent fusion to 3D MR imaging (3DRA-MRI).

With the sensitivity of MRA being low for small recurrences,¹⁷⁻²⁰ contrast-enhanced MR imaging (CEMRI) is also performed as part of routine follow-up. However, CEMRI performed postsurgically is subject to false-positive enhancement related to reactive postoperative tissue along surgical margins or enhancement of dural folds within a hemorrhagic cavity or surgical bed.^{21,22} Additionally, there is emerging evidence in recent years of gadolinium deposition,^{23,24} with a concern for brain toxicity with repeat administrations.²⁵ It is therefore imperative that gadolinium be administered only when there is definite benefit,²⁶ especially for diseases like bAVM that require long-term follow-up. The adequacy of MR imaging for predicting recurrence of completely treated brain AVMs in children has not been studied, to the best of our knowledge. The additional benefit of performing CEMRI has also not been evaluated.

The primary objective of this study was to determine the predictive value of MR imaging as a surveillance tool for bAVM recurrence after angiographically documented obliteration in children. Secondary objectives were to assess whether CEMRI provided additional information not obtained from noncontrast MRA in this population and to assess whether 3D rotational angiography with MR imaging fusion increased diagnostic confidence for bAVM recurrence in children.

MATERIALS AND METHODS

Study Design

An institutional review board–approved retrospective study was undertaken in 236 consecutive patients with bAVMs, 18 years of age and younger, managed at the Hospital for Sick Children, Toronto, from January 2000 to February 2018. Currently, we follow a protocol of performing MR imaging with TOF-MRA and CEMRI at 3 months, 6 months, and 1 year following angiographically documented cure, with a conventional angiography performed at approximately 1 year or at any subsequent time point when there is suspicion of recurrence on surveillance MR imaging. Following a posttreatment 1-year CA with negative findings, children are followed up at our institution with MR imaging at increasing intervals until 18 years of age, after which time they are transitioned to an adult neurovascular service for continued follow-up. For this study, patients with reported complete cure following any therapeutic method including embolization, surgical excision, radiosurgery, or multimodal therapy were included,

with the first negative posttreatment angiography findings as a baseline. In addition, for historical cases treated before our current protocol, to be included in the study, patients had to have a posttreatment follow-up 3T MR imaging examination, which included a TOF-MRA and/or CEMRI, as well as a final CA examination at approximately 1 year following treatment, with these 2 examinations being no more than 6 months apart. Patients were excluded if they were managed conservatively ($n = 34$), had no intraoperative/posttreatment angiography ($n = 18$), no posttreatment follow-up 3T MR imaging available ($n = 101$), no documented cure after gamma knife treatment ($n = 26$) or follow-up CA was performed >6 months after follow-up MR imaging ($n = 18$).

For included cases ($n = 39$), data were collected on the following parameters: clinical details (patient sex and age, primary presentation), bAVM features (location, feeding arteries, and type: terminal or en passant or both; venous drainage: superficial or deep or both; presence of intranidal or postnidal aneurysms; presence of venous stenosis, Spetzler-Martin grade, and a compact/diffuse nidus), treatment details (treatment type: operation, endovascular, gamma knife, or combinations of these) and date, interval between treatment and first follow-up MR imaging, recurrence on TOF-MRA and CEMRI, and finally, the post-MR imaging CA interval and the presence of recurrence on CA and on 3DRA-MR imaging if performed. The presence of bAVM recurrence on CEMRI, TOF-MRA, and 3DRA-MR images, as well as descriptors for recurrence, were determined by the study neuroradiologist (P.M.), with analysis of PACS reports by another investigator (A.J.), blinded to each other's findings. Cases with discrepant findings were re-evaluated by another neuroradiologist (M.M.S.) to reach a consensus.

Imaging

MR imaging was performed on a 3T magnet (Magnetom Skyra, Siemens, Erlangen, Germany; or Achieva, Philips Healthcare, Best, the Netherlands) with a 32-channel transmit-receive head coil. The examination included standard T1-, T2-, and FLAIR-weighted sequences, followed by TOF-MRA with the following parameters: TR = 25 ms, TE = 3.81 ms, flip angle = 18°, bandwidth = 186 Hz, matrix size = 384 × 274, FOV = 180 × 180 mm², resulting in an in-plane spatial resolution of 0.2 × 0.2 mm² with 0.5-mm slice thickness. 3D-T1-turbo field echo images were acquired before and after the administration of 0.1 mmol/kg of gadolinium-based contrast agent (gadobutrol, Gadovist; Bayer Schering Pharma, Berlin, Germany) with the following parameters: TR = 2200 ms, TE = 3 ms, TI = 900 ms, flip angle = 9°, bandwidth = 240 Hz, matrix size = 224 × 224, FOV = 220 × 220 mm², resulting in an in-plane spatial resolution of 1.0 × 1.0 mm² with a 0.98-mm slice thickness. Conventional angiography was performed by 1 of 2 interventional neuroradiologists (P.M. or M.M.S.), either in a biplane neuroangiography suite (Artis Q BA Twin; Siemens) or intraoperatively in a hybrid suite (Artis Zeego; Siemens).

All procedures were performed with the patient under general anesthesia through femoral artery access. Angiography was performed using a 4F diagnostic catheter with standard projections, followed by rotational angiography being performed in the arte-

rial distribution of interest at the discretion of the operator, using the following parameters: 5-second rotational acquisition generating 133–248 projections for a total coverage of 200°, with a detector dose/frame of 100–360 μGy , reconstructions with a 512-matrix algorithm (0.20-mm³ voxel size), iodinated contrast agent (iohexol, Omnipaque 300 mg I/mL; GE Healthcare, Piscataway, New Jersey) injected through a power injector at 3–5 mL/s depending on the age and arterial size, 1- to 2-second x-ray acquisition delay after the start of contrast injection. For subtracted 3DRA, full-strength contrast was injected, whereas for unsubtracted 3DRA, contrast was diluted to 20% to reduce the total contrast volume and streak artifacts. Multiplanar and volume-rendered reformats were performed on a dedicated workstation (syngo MultiModality Workplace; Siemens) by a dedicated technologist (V.R.), supervised by the operating neuroradiologist. A 3D set of CT angiographic images was reconstructed from these images, which were subsequently fused to the patient's pregadolinium 3D T1 MR image set, yielding 3DRA-MR images.

Statistical Analysis

Statistical analysis was performed using the SPSS statistical software, Version 24 (IBM, Armonk, New York). Categorical variables were expressed as numbers and percentages. Continuous variables were described using median and interquartile range or mean and SD as appropriate. The χ^2 or Fisher exact test was used for evaluation of the association between the categorical variables, as appropriate. The sensitivity, specificity, and positive and negative predictive values of TOF-MRA and CEMRI were calculated using conventional angiography as the criterion standard. The diagnostic confidence scores for recurrence on MR imaging with 3DRA-MR imaging were compared using the Wilcoxon signed-rank test. The generalized score statistic test, based on generalized estimation equations, was used to compare the predictive values of MR imaging and DSA. Univariate and multiple logistic regression analyses were performed to evaluate the AVM risk factors. A 2-tailed $P < .05$ was considered statistically significant.

RESULTS

Patient Characteristics and Presentation

Thirty-nine children with bAVMs fulfilled the inclusion criteria for the study. The mean age of our patient cohort was 10.8 ± 3.9 years (range, 2–17 years). Of these, 20 (51.3%) were female, and 3 (7.7%) had a diagnosis of hereditary hemorrhagic telangiectasia. Hemorrhagic presentation was seen in 28/39 (71.2%) patients. Most (24/39, 61.5%) bAVMs in our patient cohort were Spetzler-Martin (SM) grade II (mean SM grade = 1.9 ± 0.6 ; range, I–IV). Terminal and en passant feeders were seen with similar frequency. Most bAVMs (31/39, 79.5%) had superficial venous drainage only, with venous stenosis seen in a minority (3/39, 7.7%). Clinical details and bAVM characteristics are summarized in Table 1.

Treatment

Treatment modalities received are shown in Table 1. All patients with bAVMs at our institution are discussed following initial diagnostic conventional angiography for management at a combined neurovascular conference with vascular neurosurgeons and

Table 1: Patient demographics in our cohort of pediatric bAVMs (N = 39)^a

Demographics	
Age (mean) (range) (yr)	10.8 \pm 3.9, 2–17
Male/female ratio	19/20
Presentation	
Hemorrhage	28 (71.2)
Seizures	5 (12.8)
HHT screening	3 (7.7)
Incidental (screening for headache)	2 (5.1)
Partially treated at outside institution	1 (2.6)
SM grade	
I	10 (26)
II	24 (61.5)
III	4 (10.3)
IV	1 (2.6)
Location	
Frontal	5 (12.8)
Parietal	9 (23.1)
Temporal	11 (28.2)
Occipital	9 (23.1)
Brain stem	1 (2.6)
Cerebellar	3 (7.7)
Choroidal	1 (2.6)
Arterial feeder type	
Terminal	19 (48.7)
En passant	20 (51.3)
Venous drainage	
Superficial only	31 (79.5)
Deep (\pm superficial drainage)	8 (20.5)
Venous stenosis	
Present	3 (7.7)
Absent	36 (92.3)
Compactness	
Compact	30 (76.9)
Diffuse	9 (23.1)
Treatment	
Surgery	20 (51.3)
Embolization	11 (28.2)
Radiosurgery	3 (7.7)
Multimodality	5 (12.8)

Note:—HHT indicates hereditary hemorrhagic telangiectasia.

^aData are numbers (%) unless otherwise indicated.

interventional neuroradiologists, and subsequently with the family. Most (20/39, 51.3%) bAVMs in our cohort, being small and compact, were amenable to surgical resection. Endovascular treatment was performed in the following manner: 1) as stand-alone treatment in 11/39 (28.2%), when associated with a terminal feeder; 2) presurgically in 2/39 (5.1%) to exclude a nonresectable nidus; 3) presurgically in 2/39 (5.1%) to target the rupture point in acute hemorrhage; or 4) to reduce nidal volume before radiosurgery in 1/39 (2.6%). Liquid embolics were used for all endovascular treatments, *n*-BCA (Histoacryl; Braun, Melsungen, Germany) with Lipiodol (Guerbet, Roissy, France) in 8/11 (72.7%); and Onyx (Covidien, Irvine, California) in 3/11 (27.3%). One patient received additional coil occlusion of a fistulous feeder. Only 3 patients with completed radiosurgical treatment met the inclusion criteria for this study.

Recurrent bAVM, Retreatment, and Recurrent Hemorrhage

Recurrence was confirmed by CA in 13 patients, following treatment with embolization in 8 patients, and by surgical ex-

cision in 5. No significant difference was noted between this group and those without recurrence with respect to age (10.4 ± 3.4 versus 11.0 ± 4.2 years, $P = .67$) or SM grade (1.7 ± 0.6 versus 2.0 ± 0.6 , $P = .20$). The mean interval between treatment and confirmation of recurrence was 43.8 ± 41.1 months (range, 9.1–156.9 months), with a trend toward longer recurrence-free intervals after surgical-versus-endovascular treatment (69.7 ± 60.5 versus 27.6 ± 16.8 months, $P = .08$). Four of these recurrences were diagnosed by MR imaging within 6 months of treatment, 2 of which were true-positives on con-

ventional angiography and underwent subsequent complete surgical resection. There were no rebleeds in our cohort. Multivariable analysis (Table 2) for predictors of bAVM recurrence showed no significant association with age, sex, SM grade, compactness of the nidus, type of feeder (terminal/en passant), presence of deep venous drainage, or presence of venous stenosis. However, we found a significant association of recurrence with embolization-only treatment (OR = 32.4; 95% CI, 2.7–386.3; $P = .006$), which was in line with the results of univariate analysis (OR = 12.27; 95% CI, 2.4–63.4; $P = .003$). This was independent of the type of embolic agent used. The multivariable model explained 47.0% (Nagelkerke R^2) of the variance in outcome and correctly classified 79.5% of cases. Because the type of feeder (terminal versus en passant) was significantly associated with the SM grade (Fisher Exact test, $P = .006$) and with the type of nidus (compact versus diffuse) (Fisher Exact test, $P = .02$), it was eliminated from our regression model.

Recurrence was diagnosed by CEMRI as enhancement with a sensitivity of 11/13 (84.6%) and specificity of 10/26 (38.5%), and

Table 2: Results of multivariable logistic regression model to predict bAVM recurrence

	Odds Ratio (95% CI)	P Value
Age at diagnosis (yr)	0.9 (0.7–1.3)	.914
Sex (M)	3.3 (0.4–28.7)	.287
SM grade	0.2 (0.0–1.2)	.079
Diffuse nidus (compact vs diffuse)	0.2 (0.0–2.8)	.256
Draining vein stenosis (yes vs no)	1.6 (0.0–130.3)	.831
Embolization only treatment (yes vs no)	32.4 (2.7–386.3)	.006

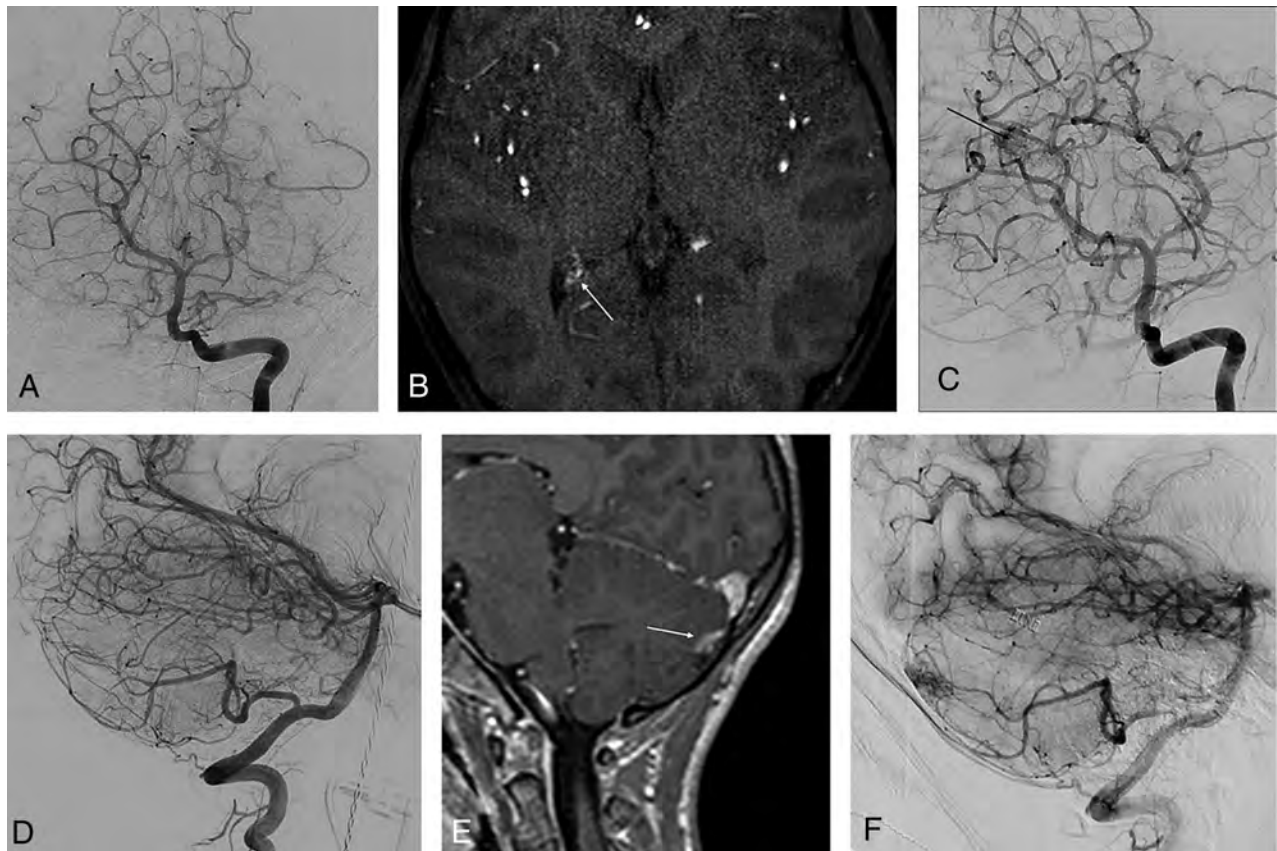


FIG 1. MR imaging appearances of true-positive AVM recurrence. *A*, Recurrent nidus in a 7-year-old girl with a right choroidal AVM that was embolized with *n*-BCA through a posterolateral choroidal feeder, with postembolization digital subtraction angiography confirming exclusion. *B*, Axial section from TOF-MRA performed 6 months posttreatment showing a tuft of vessels (*arrow*) posterior to the right lateral ventricular choroid plexus. This was also seen on contrast-enhanced MR imaging (not shown here) as exuberant and asymmetric choroid enhancement. *C*, Conventional angiogram, obtained 3 weeks after MR imaging, confirms an AVM nidus. Left vertebral artery injection confirms a right choroidal nidus (*arrow*) with deep venous drainage. The patient subsequently underwent radiosurgery. *D*, Recurrent cerebellar AVM in a 11-year-old girl with hereditary hemorrhagic telangiectasia lateral angiogram with negative findings immediately following endovascular embolization through a cerebellar branch of the right posterior inferior cerebellar artery. *E*, Sagittal section from postgadolinium MR imaging 3 months after treatment shows a nodular juxtamural focus of enhancement (*arrow*), with a vein traceable to the torcular. *F*, Conventional angiogram performed 1 month after MR imaging confirms this to be a recurrent nidus with early venous drainage. The recurrent AVM was surgically removed.

on TOF-MRA, as abnormal vessels with a sensitivity of 6/12 (50%, performed after contrast in 1 case) and specificity of 25/26 (96.1%). Positive and negative predictive values (PPV, NPV) for bAVM recurrence were CEMRI, 40.7% and 81.8%, and TOF-MRA, 85.7% and 79.3%. Looking specifically at the 13 recurrences (On-line Table), we found that MR imaging features predictive of recurrence included a tuft of vessels on TOF-MRA (Fig 1A–C), nodular juxtamural enhancement, or linear enhancement associated with a traceable draining vein on CEMRI (Fig 1D–F). When concordance of CEMRI and TOF-MRA findings was considered to make or exclude a recurrence, we found a sensitivity of 75%, specificity of 90.9%, PPV of 85.7%, and NPV of 83.3%

Table 3: Sensitivity, specificity, PPV, and NPV for CEMRI, TOF-MRA, and a combination of both to diagnose recurrent brain AVM after treatment in children

	CEMRI	TOF-MRA	CEMRI + TOF-MRA
Sensitivity	84.6%	50.0%	75.0%
Specificity	38.5%	96.1%	90.9%
PPV	40.7%	85.7%	85.7%
NPV	81.8%	79.3%	83.3%

(Table 3). Of the 13 recurrences, 8 underwent subsequent surgical resection; 4 were referred for radiosurgery; and 1, for endovascular embolization.

3DRA-MR Imaging Fusion for Confirmation of bAVM Recurrence

3DRA was performed in 14/39 (35.9%) patients, being technically adequate in 13/14 (92.9%) patients (suboptimal bolus timing in 1 patient). This yielded 13 patients for fusion with nongadolinium 3D T1 MR images. Although there were no additional findings or missed diagnoses on 2D-DSA, 3DRA-MR imaging information showed conclusively the presence of a nidus and abnormal/dysplastic vessels with contrast in a draining vein in 4 cases, of which 2 had been false-negative for recurrence on prior MR imaging (Fig 2), and conclusively excluded the presence of abnormal vascularity in an encephalomalacic cavity in 10 cases, of which 9 had shown false-positive enhancement on prior MR imaging (Fig 3). These “fused” 3D images, clearly defining the location and margins of the recurrent nidus, feeders, and draining veins, were used

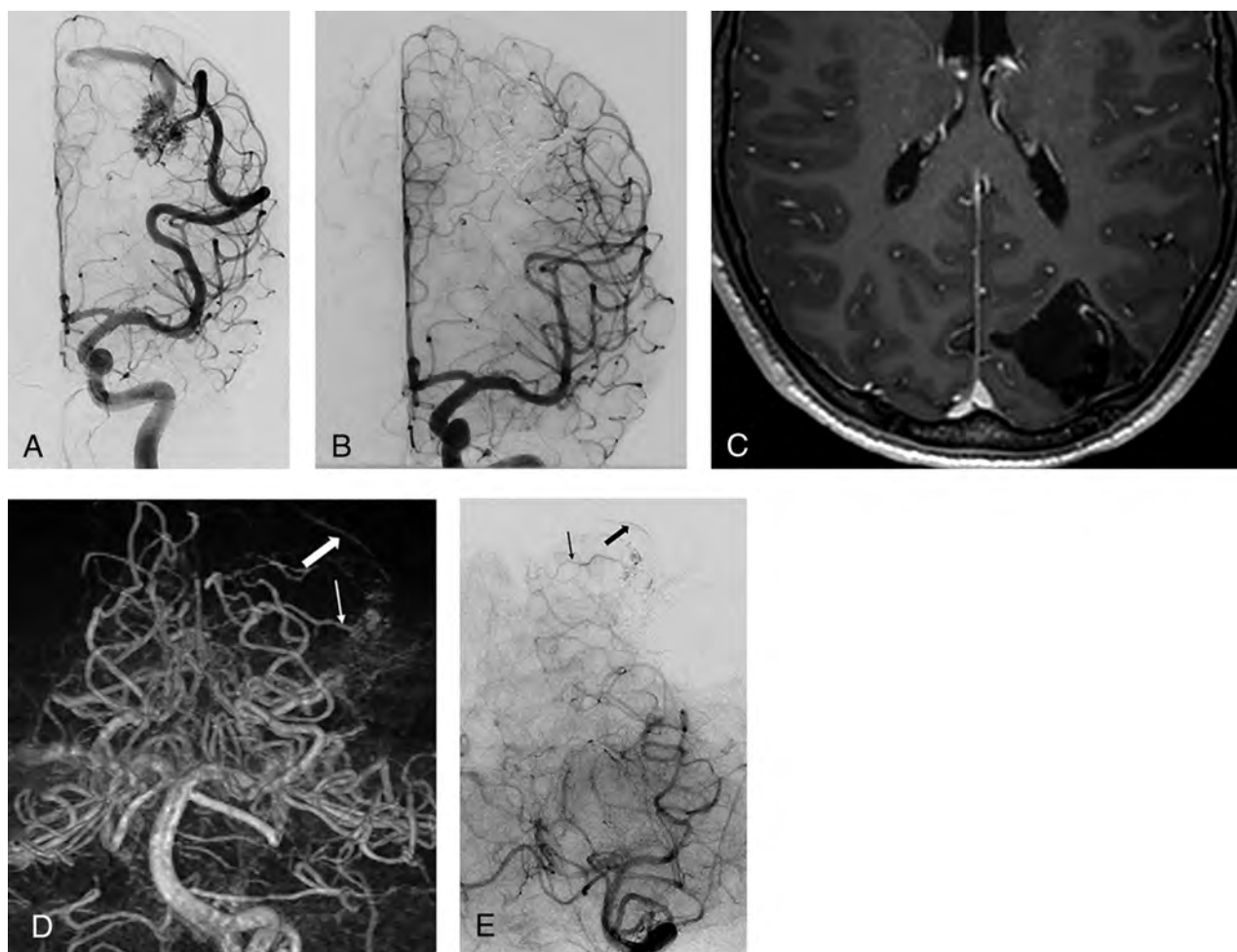


FIG 2. False-negative MR imaging findings for brain AVM recurrence, confirmed by digital subtraction and 3D rotational angiography. A 16-year-old boy with a left occipital AVM treated by embolization with Onyx. A, Frontal projection, left internal carotid angiography, shows a hypertrophied temporo-occipital middle cerebral artery branch supplying a compact nidus, with superficial venous drainage. B, Postembolization frontal angiogram shows complete exclusion of the shunt. C, Axial postgadolinium MR imaging section obtained 1 year after angiographically documented cure shows the hematoma cavity with artifacts from the Onyx cast within, but no suggestion of recurrence. D, Volume-rendered reformat obtained from 3D rotational angiography in the left vertebral artery shows a nidus behind the Onyx cast, with a prominent feeder (*thin arrow*) and early draining vein (*thick arrow*), which was also confirmed on digital subtraction angiography (E).

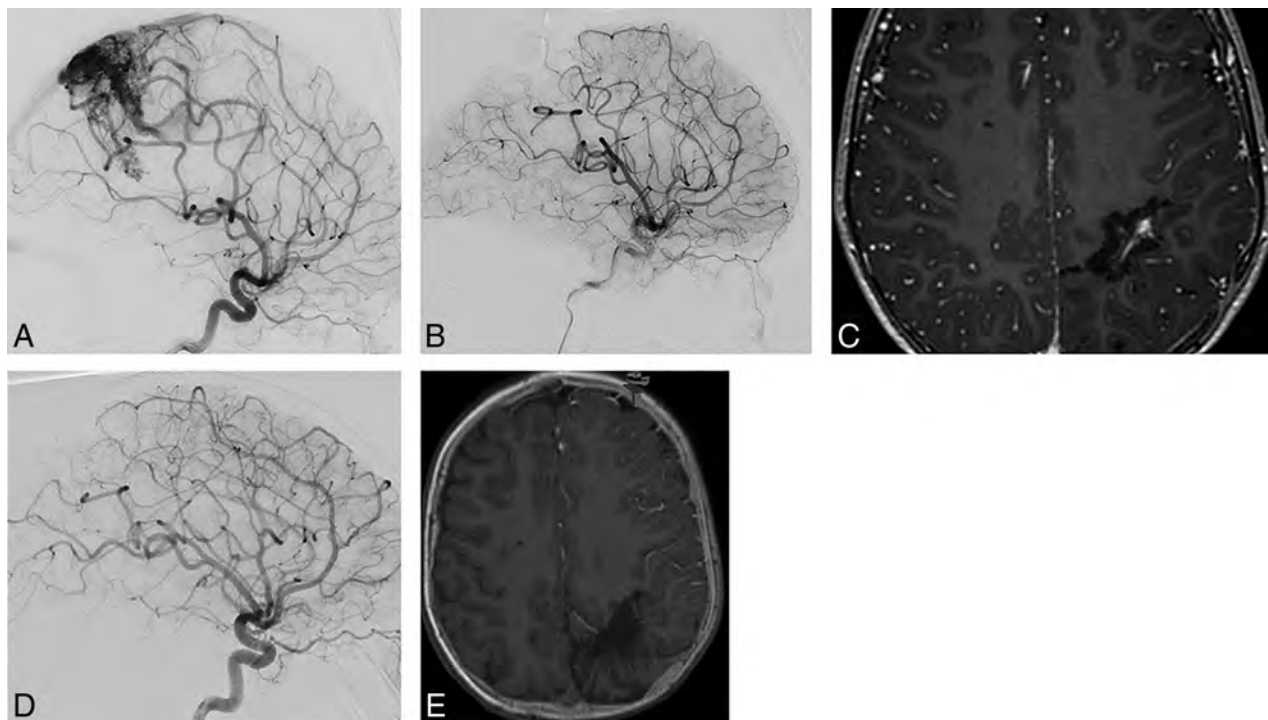


FIG 3. False-positive MR imaging for brain AVM recurrence, confirmed by conventional angiography and 3DRA-MR imaging fusion. A 5-year-old boy with a left parietal AVM. *A*, Left internal carotid injection in the lateral projection during conventional angiography shows a postcentral diffuse AVM nidus with a deep white matter component, hypertrophied anterior and middle cerebral arterial feeders, and venous drainage into the superior sagittal sinus. *B*, Complete surgical resection was performed after partial embolization, with cure confirmed with postresection angiography. *C*, Axial postgadolinium section from MR imaging performed 1 year after cure shows central linear and nodular enhancement suspicious for recurrence. *D*, Digital subtraction angiographic image, left internal carotid injection, shows no AVM recurrence. This was also confirmed from injections into the posterior circulation. *E*, 3DRA-MR imaging fusion shows no vascularity within the encephalomalacic cavity, excluding recurrence. MR imaging enhancement is believed to be related to scar tissue or dural folds.

for neuronavigation in 2 of these 4 recurrent cases that subsequently were resected (Fig 4).

DISCUSSION

Complete excision of the bAVM nidus with obliteration of arteriovenous shunting is required to eliminate the risk of hemorrhage. Although there is little in the neurosurgical literature about recurrent bAVMs, with sporadic case reports and series describing bAVM recurrence after angiographic confirmation of obliteration,²⁷⁻²⁹ they are likely more common than previously thought. A recent meta-analysis of this literature showed that bAVM recurrence occurred in 2.7% of reported adult series and in nearly 10%–15% of children.³⁰ There are several hypotheses about the pathophysiology of bAVM recurrence, as well as putative mechanisms to explain a higher incidence in children. Some authors have postulated a “reserve” nidus, which presumably finds expression after the primary nidus has been extirpated.⁷ Others have described, perhaps related, potentially unrecognized compartments at the time of treatment.⁸ Of course, neither of these would explain the increased rate of bAVM recurrence in children. Dysregulation of angiogenesis by vascular endothelial growth factor has been suggested as a possible cause, leading to endothelial cell activation and immature vessels sprouting from nearby normal arteries.⁹ Children, having higher vascular endothelial growth factor levels, stronger vascular endothelial growth factor receptor expression, and faster endothelial cell turnover, are be-

lieved to be at a higher risk of this angiodysgenesis.¹⁰ Finally, the veracity of a negative findings on immediate posttreatment angiography has been questioned: Acute changes in hemodynamics, along with edema and vasospasm, could theoretically mask a residual nidus that would later be deemed recurrent.¹¹

A recent systematic review in pediatric bAVMs showed that recurrence was detected significantly earlier in patients who underwent follow-up imaging than in those without it (3.56 ± 3.67 years versus 8.86 ± 5.61 years; $P = .017$).¹² More important, there was a significant difference in the rate of presentation with rupture with follow-up versus without it (13.3% versus 57.1%, $P = .04$). Not surprisingly, the acceptance of MR imaging for surveillance following bAVM treatment has been widespread.¹⁵ However, there are no data in the literature regarding the predictive value of positive or negative study findings. Our results showed that while the appearance of abnormal vessels on TOF-MRA had a high specificity (96%) and PPV (86%), it had a low sensitivity (50%). On the other hand, the presence of abnormal enhancement on CEMRI was a poor predictor (specificity and PPV approximately 40%) for recurrence, though the sensitivity was higher (85%). The combined sensitivity (75%), specificity (91%), and PPV (86%) values for both sequences taken together, along with noninvasiveness and absence of ionizing radiation, provide the rationale for use of MR imaging for surveillance in children after bAVM treatment and also show the complementary role of interpreting TOF-MRA and

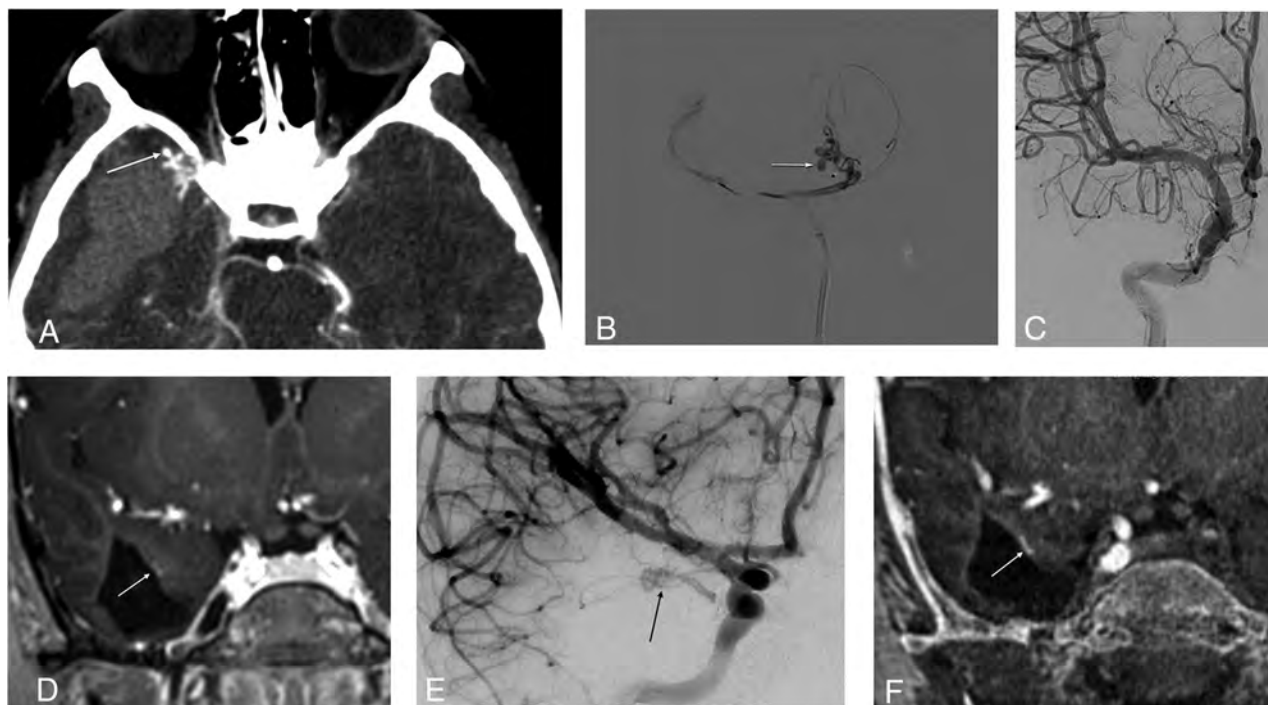


FIG 4. 3DRA-MR imaging fusion for accurate depiction of a small AVM recurrence. *A*, Axial CTA section in an 8-year-old child who presented with sudden reduced level of consciousness, showing a right temporal hematoma and an anterior temporal AVM with an anterolaterally directed pseudoaneurysm (*arrow*). *B*, Microcatheter injection into the temporopolar branch of the right middle cerebral artery shows the AVM and rupture point (*arrow*). *C*, This was embolized with *n*-BCA in Lipiodol, achieving a complete angiographic cure. *D*, MR imaging performed 1 year after treatment shows a small juxtamural nodular enhancement (*arrow*) on this postgadolinium coronal section. *E*, Basal view from a right internal carotid injection on subsequent conventional angiography confirms recurrent arteriovenous shunting (*arrow*). *F*, 3DR-MR imaging coronal fused image confirms CEMRI findings, as well as providing exquisite delineation of feeding arteries and draining vein (not shown here). This sequence, providing all requisite information for surgical resection, was used for intraoperative neuronavigation.

CEMRI findings together for these patients. However, the ability to exclude a recurrence was approximately 80% (NPV) for TOF-MRA and CEMRI, either independently or when combined.

To be useful as a screening tool for bAVM recurrence, a high NPV is critical to minimize the chance of missing patients who could have a recurrence. With 20% of recurrences not being detected on both sequences, a negative posttreatment MR imaging finding cannot completely exclude the need to perform conventional angiography. A recent study on 28 surgically resected pediatric bAVMs followed with conventional angiography showed that even an early (3- or 6-month) posttreatment conventional angiogram with negative findings could not exclude recurrence at 1 year.¹⁸ In that study, patients did not routinely undergo MR imaging surveillance, which could therefore not be compared against conventional angiography, and the authors highlighted the need for such data. Therefore, we maintain that a 1-year follow-up angiogram is imperative even in the presence of normal MR imaging examination findings, given the clinical consequences of recurrence. Although none of the recurrences in our cohort presented with hemorrhage, this outcome is likely testament to close surveillance and retreatment.

The low PPV of finding enhancement on MR imaging after bAVM treatment is not unexpected. Postsurgical nonvascular enhancement is reported after intracranial operations^{22,23} and is likely from reactive tissue or dural folds. We found that whereas a

vascular “tuft” on TOF-MRA within the cavity was a strong indicator of a recurrent nidus, patchy or nodular enhancement on CEMRI was not, unless located along a resection margin away from the dural surface. Linear vascular structures on TOF-MRA coursing into the cavity were more likely to reflect recurrence, whereas linear enhancement was not a good indicator of recurrence, either within the cavity or along its margins, unless traceable into a draining vein.

MR imaging fusion of 3DRA has been previously shown to be a useful adjunct to evaluate complex neurovascular lesions in children.³¹ 3DRA is a volumetric angiographic study with the possibility of CT angiographic reconstruction. The ability to perform 3DRA with low radiation doses while maintaining high spatial and contrast resolution reconstructions has also been demonstrated.³² This allows the use of 3DRA-MR imaging fusion to confidently identify or exclude small vascular nidi or dysplastic structures that are characteristic of bAVM recurrence in children. This is especially relevant for false-positive MR imaging studies because MR imaging enhancement, though highly sensitive for vascular structures, is of questionable significance in the posttreatment setting, as described above. Additionally, a stack of reformatted fused images can conclusively corroborate a negative MR imaging finding. The superior 3D depiction enabled by 3DRA has been used for radiosurgical treatment planning as well as for neuronavigation of bAVMs. The ability to merge the high vascular detail

from 3DRA and anatomic information from MR imaging makes this an ideal tool to depict small recurrences for neuro-navigation. In our series, 3DRA MR imaging fusion was available and used for neuronavigation during resection of 2 bAVM nidi that recurred.

Our study had some limitations. Because the study was retrospective, patient inclusion was not consecutive and data collection was limited to available clinical and radiologic information. To minimize heterogeneity arising from reporting patterns, the study neuroradiologist analyzed all images in a blinded fashion, and another neuroradiologist analyzed 3DRA-MR imaging fusion images, both of whom have several years' experience with neurovascular imaging and angiography. In addition, several patients with treated bAVMs who had not been followed per protocol with posttreatment MR imaging and conventional angiography at our institution were excluded from the study. Therefore, our cohort, selected for the purpose of this study, did not allow reporting of true recurrence rates and resulted in a spuriously high recurrence rate (13/39, 33%) as a result of our study design, with individuals with positive MR imaging findings being more likely to receive close angiographic follow-up. However, it was not the objective of this study to determine recurrence rates for bAVM, which are well-documented in the literature.

We also noted a large variation in the intervals between treatment and imaging, with longer interval times before 2015 (treatment to MR imaging time: before 2015, 555.3 ± 755.8 days; after 2015, 170.3 ± 128.9 days; $P = .08$). This presumably reflects the evolution of practice patterns with time, and a progressively increasing acceptance of MR imaging as a screening tool. Another limitation was that all patients in our cohort had low grade (equal or less than grade 3) bAVMs, not allowing us to draw strong conclusions about the effect of grade on recurrence. This is as much because most pediatric bAVMs are smaller at presentation, as it is due to most larger grade bAVMs being either not amenable to therapeutic interventions or receiving staged treatment with no angiographic "cure." Finally, we did not examine data for long-term recurrence rates or cure, which, though crucial information for bAVM prognostication and follow-up, would have been limited by sample sizes being prohibitively small for this exercise. Further longitudinal studies of long-term recurrence rates are planned to determine these data.

CONCLUSIONS

TOF-MRA and CEMRI sequences provide complementary information for determining bAVM recurrence after angiographic cure in children with bAVMs and, when interpreted together, have an approximately 85% predictive value compared with conventional angiography. Certain MR imaging features can increase accuracy, but MR imaging as a surveillance tool for this population must still be supplemented by conventional angiography. Coregistering 3DRA with MR imaging increases the diagnostic confidence regarding the presence and location of bAVM recurrence and is therefore potentially suited for intraoperative neuronavigation.

ACKNOWLEDGMENTS

We would like to acknowledge all the neuroradiologists and neurosurgeons at our institution and the MR imaging, CT, and Interventional Radiology technologists who played a key role in the acquisition of images used in this study. Furthermore, we acknowledge the support of the Ontasian Imaging Lab.

Disclosures: Afsaneh Amirabadi—UNRELATED: Employment: The Hospital for Sick Children. Manohar M. Shroff—UNRELATED: Expert Testimony: Canadian Medical Protective Association or plaintiff lawyer, Comments: occasional expert testimony in abusive head trauma or neonatal hypoxic ischemic encephalopathy, none so far in the matter of brain AVM and its imaging. Timo Krings—UNRELATED: Consultancy: Stryker, Medtronic; Royalties: Thieme, Comments: principal author of 2 books on neuroradiology.

REFERENCES

1. Stapf C, Mast H, Sciacca RR, et al. **Predictors of hemorrhage in patients with untreated brain arteriovenous malformation.** *Neurology* 2006;66:1350–55 CrossRef Medline
2. Rutledge WC, Ko NU, Lawton MT, et al. **Hemorrhage rates and risk factors in the natural history course of brain arteriovenous malformations.** *Transl Stroke Res* 2014;5:538–42 CrossRef Medline
3. van Beijnum J, van der Worp HB, Buis DR, et al. **Treatment of brain arteriovenous malformations: a systematic review and meta-analysis.** *JAMA* 2011;306:2011–19 CrossRef Medline
4. Blauwblomme T, Bourgeois M, Meyer P, et al. **Long-term outcome of 106 consecutive pediatric ruptured brain arteriovenous malformations after combined treatment.** *Stroke* 2014;45:1664–71 CrossRef Medline
5. Beslow LA, Licht DJ, Smith SE, et al. **Predictors of outcome in childhood intracerebral hemorrhage: a prospective consecutive cohort study.** *Stroke* 2010;41:313–18 CrossRef Medline
6. Gross BA, Du R. **Natural history of cerebral arteriovenous malformations: a meta-analysis.** *J Neurosurg* 2013;118:437–43 CrossRef Medline
7. Caplan JM, Yang W, Garzon-Muvdi T, et al. **120 rates of re-hemorrhage, risk factors, and outcomes of previously ruptured arteriovenous malformations (AVMs).** *Neurosurgery* 2017;64(CN_suppl_1):226–26 CrossRef
8. Mohr JP, Parides MK, Stapf C, et al; international ARUBA investigators. **Medical management with or without interventional therapy for unruptured brain arteriovenous malformations (ARUBA): a multicentre, non-blinded, randomised trial.** *Lancet* 2014;383:614–21 CrossRef Medline
9. Elhammady MS, Heros RC. **Editorial: the ARUBA study—where do we go from here?** *J Neurosurg* 2017;126:481–85 CrossRef Medline
10. Wong J, Slomovic A, Ibrahim G, et al. **Microsurgery for ARUBA trial (A Randomized Trial of Unruptured Brain Arteriovenous Malformation)—eligible unruptured brain arteriovenous malformations.** *Stroke* 2017;48:136–44 CrossRef Medline
11. Mohr JP, Hartmann A, Kim H, et al. **Viewpoints on the ARUBA trial.** *AJNR Am J Neuroradiol* 2015;36:615–17 CrossRef Medline
12. Morgenstern PF, Hoffman CE, Kocharian G, et al. **Postoperative imaging for detection of recurrent arteriovenous malformations in children.** *J Neurosurg Pediatr* 2016;17:134–40 CrossRef Medline
13. Javadpour M, Al-Mahfoudh R, Mitchell PS, et al. **Outcome of microsurgical excision of unruptured brain arteriovenous malformations in ARUBA-eligible patients.** *Br J Neurosurg* 2016;30:619–22 CrossRef Medline
14. Joyce C, Gomez CR. **Reimagining ARUBA: theoretical optimization of the treatment of unruptured brain arteriovenous malformations.** *J Stroke Cerebrovasc Dis* 2018;27:3100–07 CrossRef Medline
15. Jimenez JE, Gersey ZC, Wagner J, et al. **Role of follow-up imaging after resection of brain arteriovenous malformations in pediatric patients: a systematic review of the literature.** *J Neurosurg Pediatr* 2017;19:149–56 CrossRef Medline

16. Geibprasert S, Pongpech S, Jiarakongmun P, et al. **Radiologic assessment of brain arteriovenous malformations: what clinicians need to know.** *Radiographics* 2010;30:483–501 CrossRef Medline
17. Tranvinh E, Heit JJ, Hacein-Bey L, et al. **Contemporary imaging of cerebral arteriovenous malformations.** *AJR Am J Roentgenol* 2017; 208:1320–30 CrossRef Medline
18. Lang SS, Beslow LA, Bailey RL, et al. **Follow-up imaging to detect recurrence of surgically treated pediatric arteriovenous malformations.** *J Neurosurg Pediatr* 2012;9:497–504 CrossRef Medline
19. Gross BA, Frerichs KU, Du R. **Sensitivity of CT angiography, T2-weighted MRI, and magnetic resonance angiography in detecting cerebral arteriovenous malformations and associated aneurysms.** *J Clin Neurosci* 2012;19:1093–35 CrossRef Medline
20. Chowdhury AH, Ghose SK, Mohammad QD, et al. **Digital subtraction angiography is superior to magnetic resonance angiography in diagnosis of cerebral arteriovenous malformation.** *Mymensingh Med J* 2015;24:356–65 Medline
21. Lee CC, Reardon MA, Ball BZ, et al. **The predictive value of magnetic resonance imaging in evaluating intracranial arteriovenous malformation obliteration after stereotactic radiosurgery.** *J Neurosurg* 2015;123:136–44 CrossRef Medline
22. Lescher S, Schniewindt S, Jurcoane A, et al. **Time window for postoperative reactive enhancement after resection of brain tumors: less than 72 hours.** *Neurosurg Focus* 2014;37:E3 CrossRef Medline
23. Bette S, Gempt J, Huber T, et al. **Patterns and time dependence of unspecific enhancement in postoperative magnetic resonance imaging after glioblastoma resection.** *World Neurosurg* 2016;90: 440–47 CrossRef Medline
24. Gulani V, Calamante F, Shellock FG, et al. **Gadolinium deposition in the brain: summary of evidence and recommendations.** *Lancet Neurol* 2017;16:564–70 CrossRef Medline
25. Semelka RC, Ramalho J, Vakharia A, et al. **Gadolinium deposition disease: Initial description of a disease that has been around for a while.** *Magn Reson Imaging* 2016;34:1383–90 CrossRef Medline
26. Guo BJ, Yang ZL, Zhang LJ. **Gadolinium deposition in brain: current scientific evidence and future perspectives.** *Front Mol Neurosci* 2018;11:335 CrossRef Medline
27. Terashima KH, Reich DS. **Gadolinium deposition: practical guidelines in the face of uncertainty.** *Lancet Neurol* 2017;16:495–97 CrossRef Medline
28. Aboukaïs R, Vinchon M, Quidet M, et al. **Reappearance of arteriovenous malformations after complete resection of ruptured arteriovenous malformations: true recurrence or false-negative early postoperative imaging result?** *J Neurosurg* 2017;126:1088–93 CrossRef Medline
29. Freudenstein D, Duffner F, Ernemann U, et al. **Recurrence of a cerebral arteriovenous malformation after surgical excision.** *Cerebrovasc Dis* 2001;11:59–64 CrossRef Medline
30. Sorenson TJ, Brinjikji W, Bortolotti C, et al. **Recurrent brain arteriovenous malformations (AVMs): a systematic review.** *World Neurosurg* 2018;116:e856–66 CrossRef Medline
31. Muthusami P, Shkumat N, Rea V, et al. **CT reconstruction and MRI fusion of 3D rotational angiography in the evaluation of pediatric cerebrovascular lesions.** *Neuroradiology* 2017;59:625–33 CrossRef Medline
32. Shkumat NA, Shroff MM, Muthusami P. **Radiation dosimetry of 3D rotational neuroangiography and 2D-DSA in children.** *AJNR Am J Neuroradiol* 2018;39:727–33 CrossRef Medline

Quantification of DTI in the Pediatric Spinal Cord: Application to Clinical Evaluation in a Healthy Patient Population

¹B.B. Reynolds, ²S. By, ³Q.R. Weinberg, ⁴A.A. Witt, ⁵A.T. Newton, ⁶H.R. Feiler, ⁷B. Ramkorun, ⁸D.B. Clayton, ⁹P. Couture, ¹⁰J.E. Martus, ¹¹M. Adams, ¹²J.C. Wellons III, ¹³S.A. Smith, and ¹⁴A. Bhatia

ABSTRACT

BACKGROUND AND PURPOSE: The purpose of the study is to characterize diffusion tensor imaging indices in the developing spinal cord, evaluating differences based on age and cord region. Describing the progression of DTI indices in the pediatric cord increases our understanding of spinal cord development.

MATERIALS AND METHODS: A retrospective analysis was performed on DTI acquired in 121 pediatric patients (mean, 8.6 years; range, 0.3–18.0 years) at Monroe Carell Jr. Children's Hospital at Vanderbilt from 2017 to 2018. Diffusion-weighted images (15 directions; $b = 750$ s/mm²; slice thickness, 5 mm; in-plane resolution, 1.0×1.0 mm²) were acquired on a 3T scanner in the cervicothoracic and/or thoracolumbar cord. Manual whole-cord segmentation was performed. Images were masked and further segmented into cervical, upper thoracic, thoracolumbar, and conus regions. Analyses of covariance were performed for each DTI-derived index to investigate how age affects diffusion across cord regions, and 95% confidence intervals were calculated across age for each derived index and region. Post hoc testing was performed to analyze regional differences.

RESULTS: Analyses of covariance revealed significant correlations of age with axial diffusivity, mean diffusivity, and fractional anisotropy (all, $P < .001$). There were also significant differences among cord regions for axial diffusivity, radial diffusivity, mean diffusivity, and fractional anisotropy (all, $P < .001$).

CONCLUSIONS: This research demonstrates that diffusion evolves in the pediatric spinal cord during development, dependent on both cord region and the diffusion index of interest. Future research could investigate how diffusion may be affected by common pediatric spinal pathologies.

ABBREVIATIONS: AD = axial diffusivity; ANCOVA = analyses of covariance; DTI = diffusion tensor imaging; EPI = echo planar imaging; FA = fractional anisotropy; FOV = field-of-view; GM = gray matter; MD = mean diffusivity; PMM = population marginal means; RD = radial diffusivity; SNR = signal to noise ratio; WM = white matter

Clinical MR imaging of the pediatric spinal cord lacks sensitivity to tissue microstructural abnormalities; however, DTI provides unique information about tissue microstructure and potentially biomarkers for spinal cord pathology through DTI-de-

rived indices of axial diffusivity (AD), radial diffusivity (RD), mean diffusivity (MD), and fractional anisotropy (FA).^{1–3} DTI is relatively well-studied in the brain, including for developmental effects and regional differences,⁴ DTI has aided in the identification and characterization of microstructural discrepancies, which can result from several pathologic mechanisms.⁵

Spinal cord DTI presents additional challenges compared with brain DTI: 1) the small size of the cord; 2) lower SNR; 3) cardiac, respiratory, and patient motion; and 4) dynamic vascular and CSF flow,⁶ all of which are further exacerbated in the pediatric spinal cord. Consequently, spinal cord DTI has been clinically underused, and developmental changes are poorly understood. However, improvements in the optimization of spinal cord DTI offer increased signal to noise, reduced artifacts, and reliability.^{3,7,8} Before pediatric spinal cord DTI can reach its clinical potential, normal ranges of diffusion indices must be established, including the variation in derived indices across development and cord regions.⁹

Received February 13, 2019; accepted after revision May 16.

From the Department of Radiology and Radiological Sciences (A.T.N., P.C., S.A.S., A.B.), Urology (D.B.C., M.A.), Pediatrics (A.T.N.), and Division of Pediatric Orthopaedics (J.E.M.), Monroe Carell Jr. Children's Hospital at Vanderbilt, Nashville, Tennessee; Department of Biomedical Engineering (S.A.S.) and Institute of Imaging Science (B.B.R., S.B., Q.R.W., A.A.W., A.T.N., H.R.F., B.R., S.A.S., A.B.), Vanderbilt University, Nashville, Tennessee; Department of Ophthalmology (S.A.S., J.C.W. III), Vanderbilt University Medical Center, Nashville, Tennessee.

This research was supported, in part, by the Surgical Outcomes Center for Kids at Monroe Carell Jr. Children's Hospital at Vanderbilt and through the Section for Surgical Sciences at Vanderbilt University Medical Center.

Please address correspondence to Aashim Bhatia, MD, MS, Monroe Carell Jr. Children's Hospital at Vanderbilt, Department of Radiology, 2200 Children's Way, Suite 1422, Nashville, TN 37232; e-mail: aashimbhatia@gmail.com; @draash

<http://dx.doi.org/10.3174/ajnr.A6104>

Previous studies in pediatric patients have shown age- and region-related DTI differences and report positive correlations between age and FA,¹⁰⁻¹² negative correlations between age and AD,¹¹ RD,¹¹ and MD,¹⁰⁻¹² and several regional differences.^{11,12} However, these studies used relatively small sample sizes ($n = 22-41$)¹⁰⁻¹² over an incomplete pediatric age range (6-16 years)^{11,12} and/or used suboptimal DTI sequence parameters.¹⁰

Our aim was to leverage improved, clinically focused DTI acquisitions in a large clinical sample to characterize the range of normal DTI indices over all pediatric ages and measure variation across age and cord regions in DTI-derived indices. We hypothesized that DTI-derived indices would correlate with age, and the effect of age on DTI indices would differ among spinal cord regions.

MATERIALS AND METHODS

Participants

DTI data were retrospectively collected from 247 pediatric patients (mean age, 7.9 years; range, 0.3-18.0 years) at Monroe Carell Jr. Children's Hospital at Vanderbilt from 2017 to 2018. All studies were performed under local institutional review board approval (AAA_171784). Only patients with a normal spinal cord (absence of signal abnormalities or pathology in T1- and T2-weighted spinal cord images reviewed by a licensed pediatric neuroradiologist) were evaluated and analyzed ($n = 121$; mean age, 8.6 years; range, 0.3-18.0 years). The indications for the clinical MRIs ranged from back pain to excluding intraspinal pathology.

Data Acquisition

Imaging was performed using a 3T whole-body MR imaging scanner (Achieva; Philips Healthcare, Best, the Netherlands). A quadrature body coil was used for excitation, and a 16-channel sensitivity encoding neurovascular coil and a 15-channel spine array were used for reception for cervicothoracic and thoracolumbar volumes, respectively. DTI datasets and clinical sequences (sagittal and axial T1- and T2-weighted) were acquired in either the cervicothoracic or thoracolumbar regions or both.

Each DTI acquisition used a reduced-FOV¹³ spin-echo with a single-shot EPI readout in the axial plane.¹⁴ Scans were acquired with 15 uniformly sampled directions ($b = 750 \text{ s/mm}^2$) and a minimally weighted image ($b = 0 \text{ s/mm}^2$) and were cardiac-gated. Additional parameters were the following: anteroposterior phase encoding direction; sensitivity encoding = 1.5; flip angle = 90° ; TR = 5 beats (~ 5 seconds); TE = 50 ms; in-plane resolution = $1 \times 1 \text{ mm}^2$; slice thickness = 5 mm; 14 slices; FOV = $64 \times 48 \text{ mm}$; diffusion gradient times of $\Delta = 24.4 \text{ ms}$ and $\delta = 12.8 \text{ ms}$; and total scan time = ~ 4 minutes and 30 seconds.⁷

Data Processing

The diffusion tensor was estimated with the Camino toolbox (www.camino.org.uk) using a nonlinear fit.¹⁵ AD, RD, MD, and FA maps were calculated from the eigenvalues of the diffusion tensor. Manual segmentation of whole-cord ROIs was performed on the $b=0$ images to maximize cord-containing voxels while minimizing visual partial volume effects of CSF, and ROIs were drawn on AD, RD, MD, and FA maps. Furthermore, for each ROI drawn, we examined the median value to exclude outliers due to

CSF. Images with extensive motion artifacts were not analyzed; however, in many of our younger patients, individuals were scanned under anesthesia, which minimized gross motion. To identify outlier voxels, we calculated the 99.5% value for each DTI-derived index across all voxels and all patients; voxels in each DTI-derived map greater than the 99.5% value were removed ($AD_{99.5} = 4.432$, $RD_{99.5} = 1.200$, $MD_{99.5} = 2.181$, $FA_{99.5} = 0.999$).

For each image set, the vertebral locations of the most rostral and caudal cord-containing slices were identified and assigned. Image slices were labeled as cervical if between vertebral levels C1 and C7, upper thoracic if between T1 and T6, and as thoracolumbar if at T7 or lower. The last 4 cord-containing slices (20 mm) of thoracolumbar images identified as the conus were removed from the thoracolumbar set. A single mean value was calculated across all slices for each region in which a patient had data, resulting in 72 cervical, 33 upper thoracic, 100 thoracolumbar, and 107 conus segments of the spinal cord. Figure 1A presents an 8-year-old patient's sagittal T2-weighted image and the corresponding location of diffusion imaging. However, the exact location of imaging volumes varied from patient to patient. Figure 1B shows sample DTI-derived indices for each cord region from the same 8-year-old patient.

Statistical Analysis

Statistical analyses were performed in Matlab (MathWorks, Natick, Massachusetts). ANCOVA was performed for each DTI-derived index using Matlab's Analysis of Covariance Tool, `aocool`. Patient age served as the predictor variable; spinal cord region, as the categorical variable; and DTI index, as the dependent variable. Separate regression lines were modeled for each cord region. Eta squared (η^2) and partial η^2 were calculated as measures of effect size.¹⁶ As a model for the "normal" range of diffusion values, pointwise 95% confidence bands were calculated for each cord region and DTI index. Post hoc comparisons among slope, intercept, and population means were performed with Matlab's `multcompare` function. The Scheffé procedure was used for multiple-comparison correction.¹⁷ Statistical significance was identified at $P < .05$.

RESULTS

Analyses of Covariance

AD ANCOVA significantly correlated with age ($F = 44.26$, $P < .0001$) and showed significant differences among cord regions ($F = 8.72$, $P < .0001$). There was no significant interaction between the age and region ($F = 1.36$, $P = .26$). Effect size measures, η^2 and partial eta squared (η_p^2) indicated that age accounted for 11.69%-12.71% of the variance in AD ($\eta^2 = 0.1169$, $\eta_p^2 = 0.1271$), whereas region accounted for 6.92%-7.93% of the variance ($\eta^2 = 0.0692$, $\eta_p^2 = 0.0793$). Figure 2A, $-D$ shows trends for AD and age across the cervical, upper thoracic, thoracolumbar, and conus regions of the spinal cord.

RD ANCOVA revealed no correlation with age ($F = 2.24$, $P = .14$) but showed significant differences among cord regions ($F = 5.43$, $P = .001$). There was no significant interaction between age and region ($F = 0.94$, $P = .42$). Effect size measures indicated that region accounted for 5.01%-5.08% of the variance in RD

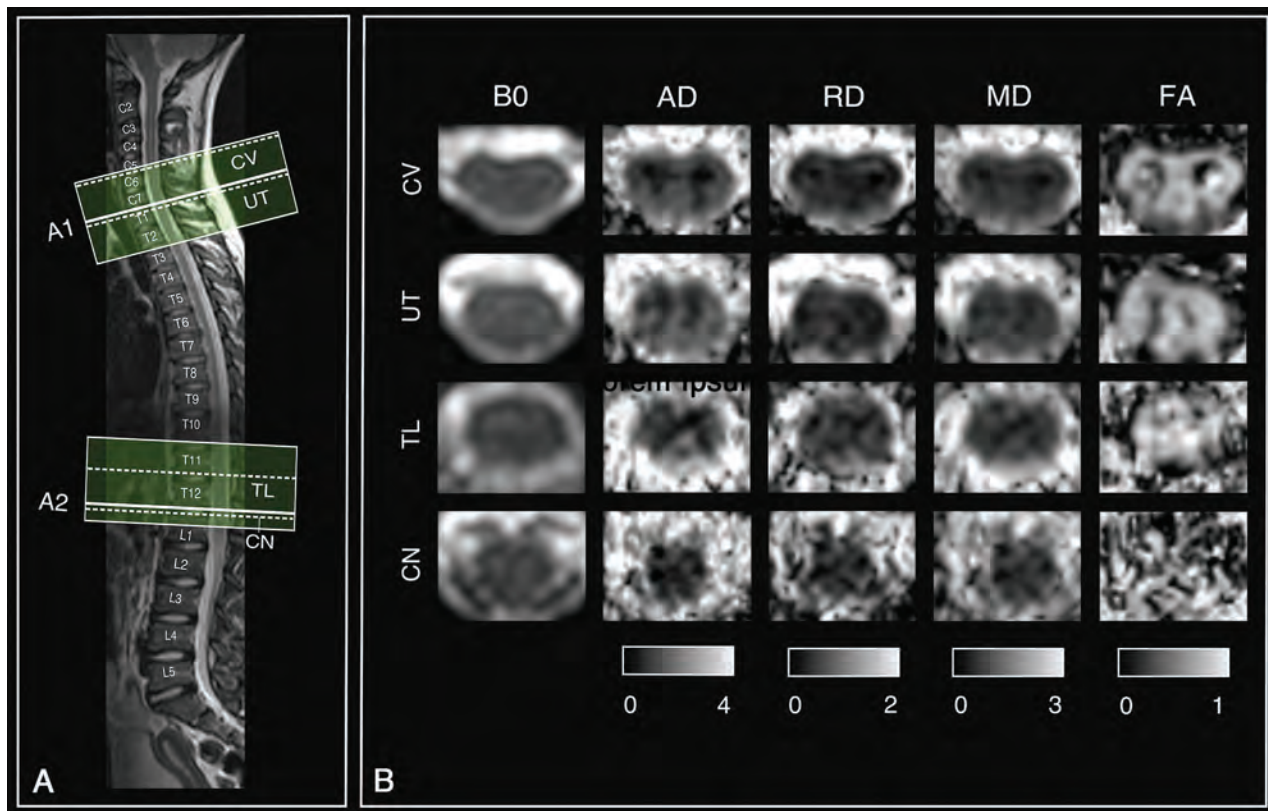


FIG 1. Diffusion images and metrics. *A*, Patient's sagittal T2-weighted image with overlay shows where 2 different diffusion imaging volumes (A1 and A2) were acquired and to which region they were assigned. *B*, Sample DTI-derived maps for each region for the same patients as in *A*. B_0 indicates minimally weighted diffusion image; CV, cervical; UT, upper thoracic; TL, thoracolumbar; CN, conus. Scale bars show the range of visualized values for each metric.

values ($\eta^2 = 0.0501$, $\eta_p^2 = 0.0508$). Figure 2E–H shows trends for RD and age across cord regions.

MD ANCOVA significantly correlated with age ($F = 16.20$, $P = .001$) and showed significant differences among cord regions ($F = 6.93$, $P < 0.001$). There was no significant interaction between age and region ($F = 1.44$, $P = .23$). Effect size measures indicated that age accounted for 4.69%–5.06% of the variance in MD values ($\eta^2 = 0.0469$, $\eta_p^2 = 0.0506$), whereas region accounted for 6.02%–6.40% of the variance ($\eta^2 = 0.0602$, $\eta_p^2 = 0.0640$). Figure 2I–L shows trends for MD and age across cord regions.

FA ANCOVA significantly correlated with age ($F = 96.11$, $P < .001$) and showed significant differences among cord regions ($F = 6.55$, $P < 0.001$). There was no significant interaction between age and region ($F = 1.94$, $P = .12$). Effect size measures indicated that age accounted for 22.58%–24.02% of the variance in MD values ($\eta^2 = 0.2258$, $\eta_p^2 = 0.2402$), whereas region accounted for 4.62%–6.07% of the variance ($\eta^2 = 0.0462$, $\eta_p^2 = 0.0607$). Figure 2M–P shows trends for FA and age across cord regions.

ANCOVA summary statistics and η^2 and η_p^2 are presented in the Table.

Post Hoc Comparisons

AD, RD, MD, and FA post hoc testing revealed no significant differences in age-related slope or intercept for cord regions; however, it did show significant differences in population marginal means for region comparisons.

DISCUSSION

The purpose of the study was to characterize DTI-derived indices across the pediatric spinal cord, evaluating differences in age and cord region, and to expand our understanding of diffusion trends in the normal pediatric cord, potentially benchmarking the clinical utility of DTI. Herein, clinically acquired diffusion MR imaging from 121 patients across the pediatric age spectrum was studied. ANCOVA analyses showed evidence of increasing axial diffusivity, mean diffusivity, and fractional anisotropy in the spinal cord during maturation, with 95% confidence bands identifying the normal variations across each region and age. Post hoc analyses demonstrated that trends were present throughout the spinal cord, yet average diffusion indices differed among cord regions, with higher diffusivities (AD, RD, and MD) in rostral compared with caudal regions and lower FA in the thoracolumbar cord.

In the brain, the trajectory of DTI indices of white matter during maturation are well-described and characterized by increasing FA and decreasing diffusivities (AD, RD, and MD), with higher order cognitive regions developing later than lower order sensorimotor regions.^{18–22} AD exhibits a generally weaker developmental trend and high variability across regions, with AD decreasing with age in cortical white matter,^{19,20} exhibiting no change in the corticospinal tract¹⁹ and increasing in the pons.²⁰ While our observed age-related trends of increasing AD, MD, and FA do not match developmental trends in brain white

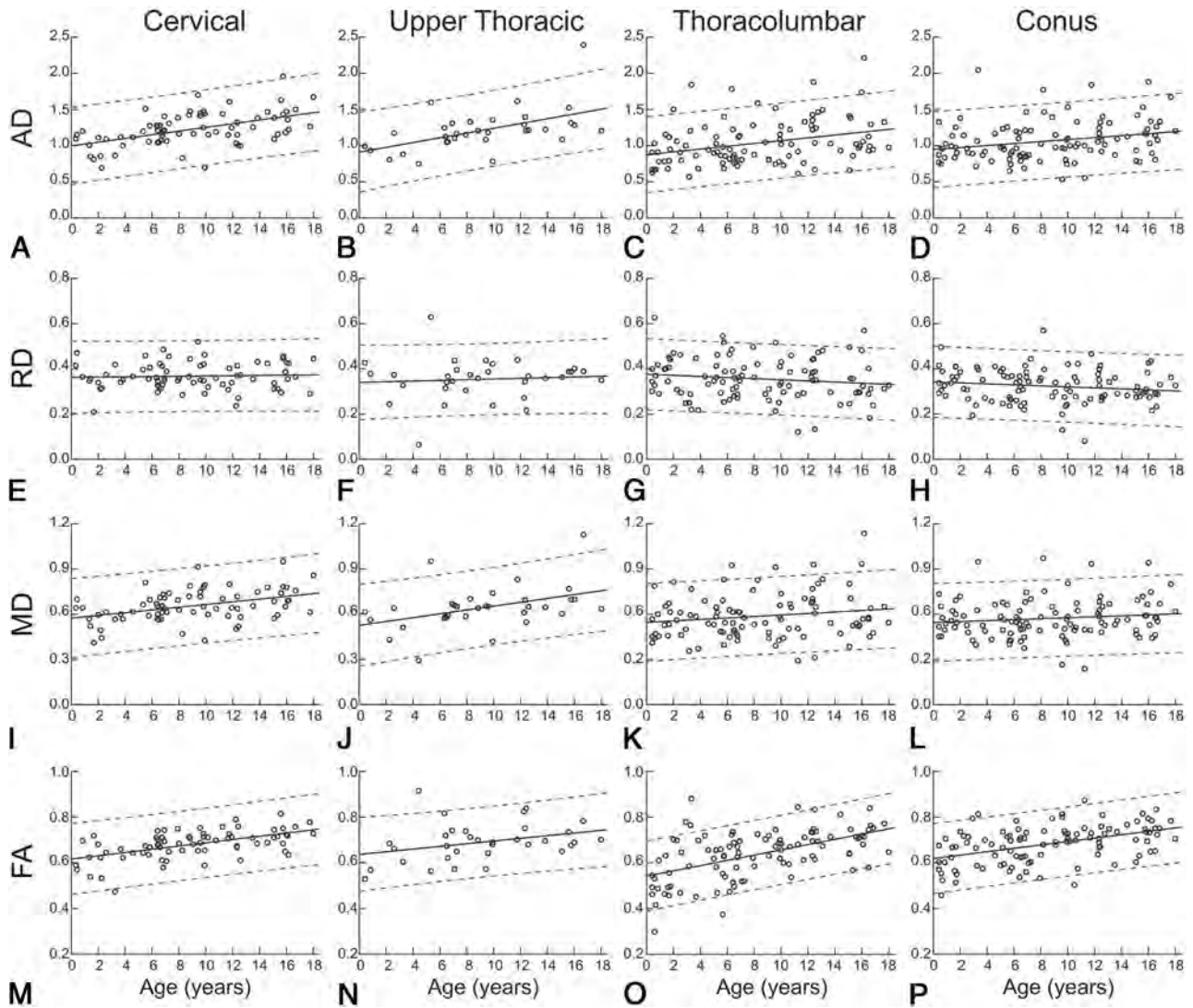


FIG 2. Average regional DTI indices as a function of age. Age-related trends are shown across pediatric development for each spinal cord region and diffusion-derived index. *Circles* show mean DTI-derived index values for individual patients, *solid lines* indicate the age-related trend, and *dashed lines* indicate the 95% confidence interval.

matter (WM), the spinal cord contains both WM and gray matter (GM), which may exhibit different trends. In the brain, the GM/WM ratio decreases during development.^{23,24} While brain growth progresses rapidly from birth until early childhood,^{19,25} development in childhood and beyond occurs primarily through increasing WM volume and decreasing GM volume.^{23,24} If the spinal cord is myelinated early in infancy, then a decreasing GM/WM ratio could be responsible for increased AD. Although the lack of a significant decrease in RD suggests that a decreasing GM/WM ratio may not be the sole process responsible for our findings, it is also likely that the proportion of larger sized axons (compared with smaller axons) within a voxel increases with the growth of the child and contributes positively to the increasing AD in the spinal cord with age. Last, it is well-understood that FA and AD can be biased upward due to low SNR, and the acquisitions we used were optimized for improved speed and concomitantly SNR compared with conventionally acquired DTI of the brain.

Previous pediatric studies comparing DTI-derived indices

across age and cord regions have shown positive correlations between age and FA,¹⁰⁻¹² agreeing with our findings. However, some have reported negative correlations between age and AD,¹¹ RD,¹¹ and MD,¹⁰⁻¹² disagreeing with our findings. However, previous studies used the following: 1) a narrower age range for subjects (6–16 years)^{11,12}; 2) smaller sample sizes ($n = 22-41$)¹⁰⁻¹²; 3) a non-cardiac-gated DTI acquisition,¹⁰⁻¹² which reduces robustness²⁶; and/or 4) manually defined ROIs.¹⁰⁻¹² These differences may account for the discrepancies between our results and previous literature.

We hypothesize that some of the regional (across spinal levels) differences in DTI indices could be partly related to an increasing GM/WM ratio of the caudal cord compared with the rostral levels. We also posit that the myelination within the spinal cord is possibly more mature and uniform at birth in a full-term neonate compared with the brain and less of a factor in regional differences.

To our knowledge, this study investigates the largest dataset of pediatric spinal cord DTI to evaluate variations across age and

ANCOVA and eta statistics

ANCOVA/Factor	Sum Squared	df	Mean Squared	F	P Value	η^2	Partial η^2
Axial diffusivity							
Main effects							
Age	3.045	1	3.045	44.26	<.001	0.1169	0.1271
Region	1.801	3	0.600	8.72	<.001	0.0692	0.0793
Interaction							
Age \times region	0.280	3	0.093	1.36	.26	0.0108	0.0132
Model error	20.917	304	0.069			0.8032	
Model totals	26.044						
Radial diffusivity							
Main effects							
Age	0.014	1	0.014	2.24	.14	0.0069	0.0073
Region	0.101	3	0.034	5.43	.001	0.0501	0.0508
Interaction							
Age \times region	0.018	3	0.006	0.94	.42	0.0087	0.0092
Model error	1.890	304	0.006			0.9344	
Model totals	2.023						
Mean diffusivity							
Main effects							
Age	0.270	1	0.270	16.20	<.001	0.0469	0.0506
Region	0.346	3	0.115	6.93	<.001	0.0602	0.0640
Interaction							
Age \times region	0.072	3	0.024	1.44	.23	0.0125	0.0140
Model error	5.061	304	0.017			0.8804	
Model totals	5.749						
Fractional anisotropy							
Main effects							
Age	0.563	1	0.563	96.11	<.001	0.2258	0.2402
Region	0.115	3	0.038	6.55	<.001	0.0462	0.0607
Interaction							
Age \times region	0.034	3	0.011	1.94	.12	0.0136	0.0187
Model error	1.781	304	0.006			0.7143	
Model totals	2.493						

cord region and represents the most comprehensive coverage of the pediatric age range to date. Also, we further demonstrate the feasibility of acquiring clinical DTI of the pediatric spinal cord with sufficient quality to identify biologically relevant effects. With a greater understanding of the normal variation in pediatric patients, we can leverage these findings to study pathologic processes and increase the clinical use of spinal cord DTI in pediatrics. Damage to spinal cord microstructure in trauma, infection, or congenital spinal dysraphism may result in abnormal DTI-derived indices.²⁷⁻²⁹ Individual pathologies may exhibit distinctive patterns of diffusion changes that could aid in clinical decision-making in combination with clinical signs and symptoms.

There are limitations that should be considered in light of our results. First, the DTIs in this study were collected from pediatric patients who were being evaluated for potential spinal pathology. A licensed pediatric neuroradiologist reviewed T1- and T2-weighted images for each patient to identify patients with a normal-appearing spinal cord, but it is possible that pathology was not detected by conventional imaging in some patients. Second, DTI indices were obtained within a whole-cord ROI, including both GM and WM. With the GM/WM ratio varying across age and cord regions,^{30,31} the change in the GM/WM ratio could contribute to the effects seen. Third, DTI of the pediatric spinal cord is a low-SNR acquisition (small imaging region, motion artifact, and CSF flow), and a low SNR results in bias toward higher FA values but not diffusivities.³² The conus is the small-

est volume of cord tissue in this analysis, and with the decreased cord size, fewer voxels are contained in the ROIs placed. While this region did demonstrate similar trends of age-related changes in the DTI indices, further studies with improved DTI protocols need to be evaluated in a larger sample size. Last, manually selected whole-cord masks are standard practice in spinal cord DTI analysis¹⁰⁻¹² due to the limited resolution of clinically feasible acquisitions, yet they can introduce subjectivity into the analysis and may reduce reproducibility.³³

Progress is being made on the development of objective and automated segmentation of the spinal cord, including differentiation between GM and WM.³⁴ Future work will be focused on confirming these results in age-matched controls. We are currently in the process of differentiating the DTI indices across both GM and WM throughout the spinal cord using high-resolution sequences with increased SNR, such as multiecho fast-field gradient echo, a Philips proprietary sequence, which will be coregistered with the DTI acquisition.

CONCLUSIONS

We demonstrate that microstructure-sensitive DTI-derived indices evolve in the pediatric spinal cord during development and depend on both the DTI index of interest and cord region. Future research will investigate whether GM and WM follow these trends exclusively and whether DTI in the pediatric spinal cord could serve as a clinical biomarker for spinal pathologies.

Disclosures: Samantha By—UNRELATED: Employment: Hyperfine, Philips, Comments: employee of Hyperfine August 27, 2018 to present, employee of Philips, August 2018 to September 2019; Stock/Stock Options: Hyperfine.

REFERENCES

1. Hasan KM, Walimuni IS, Abid H, et al. **A review of diffusion tensor magnetic resonance imaging computational methods and software tools.** *Comput Biol Med* 2011;41:1062–72 CrossRef Medline
2. Le Bihan D, Mangin JF, Poupon C, et al. **Diffusion tensor imaging: concepts and applications.** *J Magn Reson Imaging* 2001;13:534–46 CrossRef Medline
3. Martin AR, De Leener BD, Cohen-Adad J, et al. **Clinically feasible microstructural MRI to quantify cervical spinal cord tissue injury using DTI, MT, and T2*-weighted imaging: assessment of normative data and reliability.** *AJNR Am J Neuroradiol* 2017;38:1257–65 CrossRef Medline
4. Oishi K, Faria AV, Yoshida S, et al. **Quantitative evaluation of brain development using anatomical MRI and diffusion tensor imaging.** *Int J Dev Neurosci* 2013;31:512–24 CrossRef Medline
5. Carney O, Falzon A, MacKinnon AD. **Diffusion-weighted MRI in paediatric neuroimaging.** *Clin Radiol* 2018;73:999–1013 CrossRef Medline
6. Clark CA, Hedehus M, Moseley ME. **In vivo mapping of the fast and slow diffusion tensors in human brain.** *Magn Reson Med* 2002;47:623–28 CrossRef Medline
7. By S, Smith AK, Dethrage LM, et al. **Quantifying the impact of underlying measurement error on cervical spinal cord diffusion tensor imaging at 3T: error in cervical spinal cord DTI at 3T.** *J Magn Reson Imaging* 2016;44:1608–18 CrossRef Medline
8. Smith SA, Jones CK, Gifford A, et al. **Reproducibility of tract-specific magnetization transfer and diffusion tensor imaging in the cervical spinal cord at 3 Tesla.** *NMR Biomed* 2010;23:207–17 CrossRef Medline
9. Taso M, Girard OM, Duhamel G, et al. **Tract-specific and age-related variations of the spinal cord microstructure: a multi-parametric MRI study using diffusion tensor imaging (DTI) and inhomogeneous magnetization transfer (ihMT).** *NMR Biomed* 2016;29:817–32 CrossRef Medline
10. Singhi S, Tekes A, Thurnher M, et al. **Diffusion tensor imaging of the maturing paediatric cervical spinal cord: from the neonate to the young adult.** *J Neuroradiol* 2012;39:142–48 CrossRef Medline
11. Saksena S, Middleton DM, Krisa L, et al. **Diffusion tensor imaging of the normal cervical and thoracic pediatric spinal cord.** *AJNR Am J Neuroradiol* 2016;37:2150–57 CrossRef Medline
12. Alizadeh M, Fisher J, Saksena S, et al. **Age related diffusion and tractography changes in typically developing pediatric cervical and thoracic spinal cord.** *Neuroimage Clin* 2018;18:784–92 CrossRef Medline
13. Wilm BJ, Svensson J, Henning A, et al. **Reduced field-of-view MRI using outer volume suppression for spinal cord diffusion imaging.** *Magn Reson Med* 2007;57:625–30 CrossRef Medline
14. Wheeler-Kingshott CA, Hickman SJ, Parker GJ, et al. **Investigating cervical spinal cord structure using axial diffusion tensor imaging.** *Neuroimage* 2002;16:93–102 CrossRef Medline
15. Cook PA, Bai Y, Nedjati-Gilani S, et al. **Camino: Open-Source Diffusion-MRI Reconstruction and Processing.** In: *Proceedings of the Annual Meeting of the International Society for Magnetic Resonance in Medicine*, Seattle, Washington. May 6–12, 2006;14:1
16. Cohen J. **Eta-squared and partial eta-squared in fixed factor ANOVA designs.** *Educational and Psychological Measurement* 1973;33:107–12 CrossRef
17. Hochberg Y, Tamhane AC. *Multiple Comparison Procedures.* New York: Wiley; 1987
18. Engelbrecht V, Scherer A, Rassek M, et al. **Diffusion-weighted MR imaging in the brain in children: findings in the normal brain and in the brain with white matter diseases.** *Radiology* 2002;222:410–18 CrossRef Medline
19. Faria AV, Zhang J, Oishi K, et al. **Atlas-based analysis of neurodevelopment from infancy to adulthood using diffusion tensor imaging and applications for automated abnormality detection.** *Neuroimage* 2010;52:415–28 CrossRef Medline
20. Löbel U, Sedlacik J, Güllmar D, et al. **Diffusion tensor imaging: the normal evolution of ADC, RA, FA, and eigenvalues studied in multiple anatomical regions of the brain.** *Neuroradiology* 2009;51:253–63 CrossRef Medline
21. Yoshida S, Oishi K, Faria AV, et al. **Diffusion tensor imaging of normal brain development.** *Pediatr Radiol* 2013;43:15–27 CrossRef Medline
22. Qiu A, Mori S, Miller MI. **Diffusion tensor imaging for understanding brain development in early life.** *Annu Rev Psychol* 2015;66:853–76 CrossRef Medline
23. Courchesne E, Chisum HJ, Townsend J, et al. **Normal brain development and aging: quantitative analysis at in vivo MR imaging in healthy volunteers.** *Radiology* 2000;216:672–82 CrossRef Medline
24. Paus T, Collins DL, Evans AC, et al. **Maturation of white matter in the human brain: a review of magnetic resonance studies.** *Brain Res Bull* 2001;54:255–66 CrossRef Medline
25. Dekaban AS, Sadowsky D. **Changes in brain weights during the span of human life: relation of brain weights to body heights and body weights.** *Ann Neurol* 1978;4:345–56 CrossRef Medline
26. Figley CR, Stroman PW. **Investigation of human cervical and upper thoracic spinal cord motion: implications for imaging spinal cord structure and function.** *Magn Reson Med* 2007;58:185–89 CrossRef Medline
27. Grabher P, Mohammadi S, Trachsler A, et al. **Voxel-based analysis of grey and white matter degeneration in cervical spondylotic myelopathy.** *Sci Rep* 2016;6:24636 CrossRef Medline
28. Rajasekaran S, Yerramshetty JS, Chittode VS, et al. **The assessment of neuronal status in normal and cervical spondylotic myelopathy using diffusion tensor imaging.** *Spine* 2014;39:1183–89 CrossRef Medline
29. Cui JL, Li X, Chan TY, et al. **Quantitative assessment of column-specific degeneration in cervical spondylotic myelopathy based on diffusion tensor tractography.** *Eur Spine J* 2015;24:41–47 CrossRef Medline
30. Junghanns H, Schmorl G. *The Human Spine in Health and Disease.* Philadelphia: Grune & Stratton; 1971
31. Fontana PA, Barbeito CG, Goya RG, et al. **Impact of very old age on the expression of cervical spinal cord cell markers in rats.** *J Chem Neuroanat* 2009;37:98–104 CrossRef Medline
32. Farrell JAD, Landman BA, Jones CK, et al. **Effects of signal-to-noise ratio on the accuracy and reproducibility of diffusion tensor imaging-derived fractional anisotropy, mean diffusivity, and principal eigenvector measurements at 1.5T.** *J Magn Reson Imaging* 2007;26:756–67 CrossRef Medline
33. Barakat N, Shah P, Faro SH, et al. **Inter- and intra-rater reliability of diffusion tensor imaging parameters in the normal pediatric spinal cord.** *World J Radiol* 2015;7:279–85 CrossRef Medline
34. Prados F, Ashburner J, Blaiotta C, et al. **Spinal cord grey matter segmentation challenge.** *Neuroimage* 2017;152:312–29 CrossRef Medline

Subject-Specific Studies of CSF Bulk Flow Patterns in the Spinal Canal: Implications for the Dispersion of Solute Particles in Intrathecal Drug Delivery

W. Coenen, C. Gutiérrez-Montes, S. Sincomb, E. Criado-Hidalgo, K. Wei, K. King, V. Houghton, C. Martínez-Bazán, A.L. Sánchez, and J. C. Lasheras

ABSTRACT

BACKGROUND AND PURPOSE: Recent flow dynamics studies have shown that the eccentricity of the spinal cord affects the magnitude and characteristics of the slow bulk motion of CSF in the spinal subarachnoid space, which is an important variable in solute transport along the spinal canal. The goal of this study was to investigate how anatomic differences among subjects affect this bulk flow.

MATERIALS AND METHODS: T2-weighted spinal images were obtained in 4 subjects and repeated in 1 subject after repositioning. CSF velocity was calculated from phase-contrast MR images for 7 equally spaced levels along the length of the spine. This information was input into a 2-time-scale asymptotic analysis of the Navier-Stokes and concentration equations to calculate the short- and long-term CSF flow in the spinal subarachnoid space. Bulk flow streamlines were shown for each subject and position and inspected for differences in patterns.

RESULTS: The 4 subjects had variable degrees of lordosis and kyphosis. Repositioning in 1 subject changed the degree of cervical lordosis and thoracic kyphosis. The streamlines of bulk flow show the existence of distinct regions where the fluid particles flow in circular patterns. The location and interconnectivity of these recirculating regions varied among individuals and different positions.

CONCLUSIONS: Lordosis, kyphosis, and spinal cord eccentricity in the healthy human spine result in subject-specific patterns of bulk flow recirculating regions. The extent of the interconnectivity of the streamlines among these recirculating regions is fundamental in determining the long-term transport of solute particles along the spinal canal.

ABBREVIATION: SSAS = spinal subarachnoid space

A major feature of CSF flow in the spinal subarachnoid space (SSAS) is its periodic oscillation. The volume of oscillations of the blood flowing in and out of the rigid cranial vault causes the intracranial pressure to change in a time-periodic fashion with each heartbeat.¹⁻³ This pressure fluctuation drives CSF periodically in and out of the compliant spinal canal, as needed to ensure that the sum of the volumes of the brain, CSF, and intracranial blood in the rigid cranial vault remains constant (the

so-called Monro-Kellie doctrine).^{4,5} Because of the slenderness of the spinal canal, the CSF flow velocity in the SSAS is aligned with the spinal cord. The limited compression of the venous and fatty tissue in the epidural space that surrounds the dura mater allows the spinal canal to accommodate a stroke volume $\Delta V \sim 1$ mL during each intracranial pressure pulsation, much smaller than the total volume $V \sim 60-90$ mL of CSF contained in the SSAS.

As revealed by imaging studies using radionuclides injected into the SSAS,⁶⁻⁹ in addition to the oscillatory flow, there is a steady bulk flow of CSF with much smaller velocities. Our recent studies^{10,11} combining multiscale asymptotic analyses of the Navier-Stokes equations with controlled experiments in canonical in vitro models of the SSAS have shed light on the physical mechanisms responsible for the establishment of this slow bulk motion. In particular, it has been shown that in addition to the oscillatory flow with a zero time average, the motion of the fluid particles is affected by a small velocity correction resulting from the combined effects of fluid inertia (the so-called “steady streaming”) and spatial gradients of amplitude of the axial pulsation (the so-called “Stokes drift”). Thus, the mean Lagrangian velocity ob-

Received February 22, 2019; accepted after revision May 8.

From the Departments of Mechanical and Aerospace Engineering (W.C., S.S., E.C.-H., A.L.S., J.C.L.) and Bioengineering (J.C.L.), University of California, San Diego, San Diego, California; Department of Mechanical and Mining Engineering (C.G.-M., C.M.-B.), University of Jaén, Jaén, Andalucía, Spain; MRI Center (K.W., K.K.), Huntington Medical Research Institutes, Pasadena, California; and Department of Radiology (V.H.), School of Medicine and Public Health, University of Wisconsin, Madison, Wisconsin.

C.M.-B. acknowledges the financial support provided by the Spanish MINECO (Secretaría de Estado de Investigación, Desarrollo e Innovación) through grant DPI2017-88201-C3-2-R, co-financed by the European Regional Development Fund (ERDF).

Please address correspondence to Wilfried Coenen, PhD, Department of Mechanical and Aerospace Engineering, University of California San Diego, 9500 Gilman Dr, No. 0411, La Jolla, CA 92093; e-mail: wicoenen@ucsd.edu

<http://dx.doi.org/10.3174/ajnr.A6097>

tained by filtering out the high-frequency ebb and flow of periodic oscillations exhibits a small steady component (the sum of the steady streaming velocity and the Stokes drift velocity) that is responsible for the bulk motion observed in previous imaging studies.⁶⁻⁹

Our analyses have shown that the bulk flow in the SSAS depends on the specific geometry (anatomy) of the SSAS, the frequency of the intracranial pressure pulsation, and the compliance of the spinal canal. In particular, it was demonstrated that the eccentricity of the spinal cord plays a major role, with the resulting flow being directed in opposite directions in the narrow and wide parts of the canal.¹⁰ Because the slow bulk motion is responsible for the convective transport of solute molecules,^{10,11} anatomic differences and changes in physiologic parameters are suspected of greatly affecting the rate at which solute particles are transported along the spinal canal. Thus, the main goal of the current study was to use our recently developed mathematical analysis to investigate how subject-specific anatomic differences affect the slow bulk flow of the CSF, providing improved understanding of the mechanisms regulating the transport of molecules and drugs along the spinal canal.

MATERIALS AND METHODS

General Outline

We used our recently developed mathematical formulation^{10,11} to compute the average Lagrangian bulk motion of solute particles in healthy volunteers. To apply the model, we first obtained from MR imaging measurements all of the input parameters: the subject-specific anatomy of the SSAS, the frequency of the intracranial pressure pulsation, and an estimation of the distribution of compliance (elasticity) of the spinal canal. In the following text, we describe the methodology used to obtain these parameters from MR imaging measurements, along with the salient features of the mathematical model. For a detailed description of the mathematical model, the reader is referred to our previous publications.^{10,11} Note that our approach is not that of a traditional computational fluid dynamics simulation in which the Navier-Stokes equations are marched in time. Instead, by leveraging the disparity in time scales between the intracranial pressure oscillations and bulk motion, we obtained a set of time-independent equations to directly compute the velocity field of the bulk motion. These equations and the methods used to solve them are fully accessible by any potential user. Also note that the assumptions and analytic techniques used in the model have been verified by means of measurements in an *in vitro* simplified phantom model.¹⁰ Finally, although our methodology uses patient-specific input, variations in physiologic conditions for the duration of the experiment are not taken into account and might significantly affect the predicted CSF bulk flow, as has recently been shown in the context of numerical simulations of hemodynamic flow.¹²⁻¹⁵

Mathematical Model for CSF Flow in the Spinal Canal

The long-term transport of a solute in the spinal canal results from the competition between advection by the bulk motion of the CSF and the molecular diffusion of the drug. The extent of the latter is limited by the small value of the diffusivity of drugs used in intrathecal therapies, of the order 10^{-10} m²/s. Our recent stud-

ies demonstrate that the concentration of the solute in the SSAS is only a function of the longitudinal and azimuthal position in the canal, $c(x, s)$, whose evolution is governed by the transient convective equation,

$$\frac{\partial c}{\partial t} + U_L \frac{\partial c}{\partial x} + W_L \frac{\partial c}{\partial s} = 0,$$

where $U_L(x, s)$ and $W_L(x, s)$ are the width-averaged Lagrangian velocities in the longitudinal and azimuthal direction, respectively.¹¹

The computation of U_L and W_L in each subject requires as input the spatial distributions of the canal width, $h(x, s)$, the perimeter length of the spinal cord, $\ell(x)$, and the compliance, $\gamma(x, s)$.¹¹ The methodology used to obtain these functions $h(x, s)$, $\ell(x)$, and $\gamma(x, s)$ for each subject on the basis of MR imaging measurements is outlined below.

Acquisition of Anatomic Data and CSF Oscillatory Velocity with MR Imaging

In this institutional review board–approved study conducted at the Huntington Medical Research Institutes, MR imaging data collection and analysis of CSF oscillatory and bulk flow were performed in presumptively healthy subjects. Health Insurance Portability and Accountability Act standards for the management of subjects were followed in the procedure. Volunteers who had good health, normal pulse and respiratory rates, and no spinal disorders were recruited. The MR images obtained in the subjects were reviewed by a neuroradiologist to confirm the absence of spinal pathologies. Cobb angles were measured to determine the degree of cervical lordosis as the angle between the inferior endplate of the C2 vertebra and the inferior endplate of the T4 vertebra, and the degree of thoracic kyphosis, as the angle between the superior endplate of the T4 vertebra and the inferior endplate of the T11 vertebra.

All imaging was performed with a 3T Signa scanner (software Version HD23; GE Healthcare, Milwaukee, Wisconsin) using a 16-channel head/neck/spine receiver coil. No contrast was administered. High-resolution isotropic (0.5 mm) 3D fast spin-echo T2-weighted (TR = 2500 ms, TE = 111 ms, bandwidth = 83.3 kHz, FOV = 25.6 × 25.6, matrix = 256 × 256, NEX = 2, slice thickness = 1 mm) images were obtained using 3 overlapping sets in the sagittal plane to cover brain-to-cervical, thoracic, and lumbar spine regions (Fig 1A). Total scan time was approximately 40 minutes. The image sets were segmented in the axial orientation using the semiautomatic threshold-based segmentation tool of the open-source program ITK-SNAP (Version 3.6.0; www.itksnap.org).¹⁶ Matlab (MathWorks, Natick, Massachusetts) was used to extract the 3D position of the pia and dura mater (Fig 1B, -C). The cord perimeter $\ell(d_{FM})$ was measured as a function of the longitudinal distance from the foramen magnum, d_{FM} . The width h of the SSAS was projected on the spinal cord to obtain a map $h(d_{FM}, d_{MP})$, where d_{MP} is the azimuthal distance from the midline of the posterior spinal cord (Fig 1D). We applied a Gaussian smoothing filter in the cervical region to remove high-frequency noise in h originating from imperfections in the segmentation. In the lumbar region, the cauda equina was represented as a single tapered structure, continuous with the spinal cord, with a cross-section equal to the sum of that of all nerve roots. Dimensionless coordinates (x, s) were

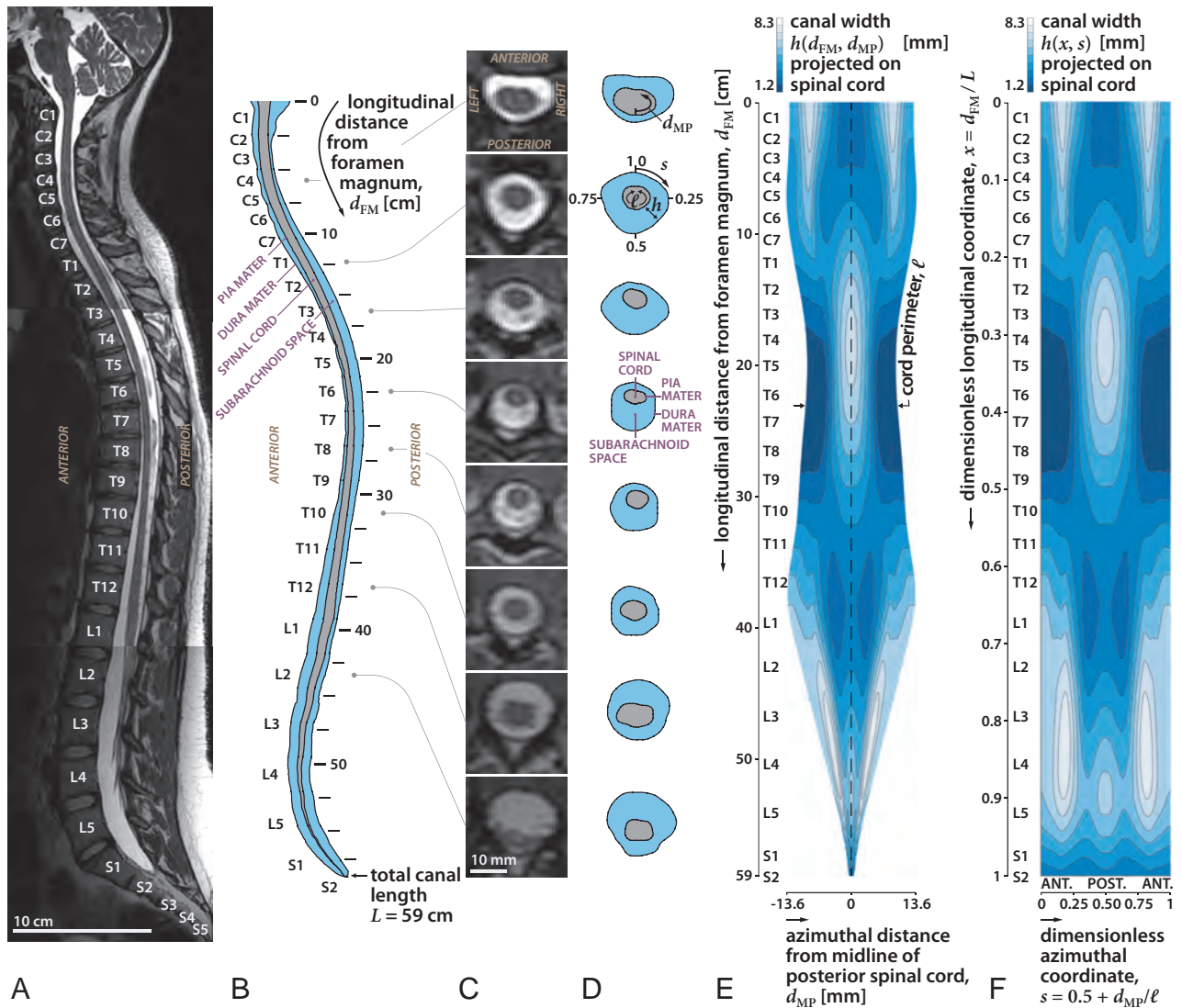


FIG 1. Sagittal T2-weighted MR image of the spine in subject 1 in the supine position (A), diagram of the sagittal images (B) and axial images (C), diagrams of the images at selected locations along the spine (D), width of the SSAS projected onto a 2D plane obtained by unrolling the space (E), and 2D map of the width of the SSAS after converting the length and circumference to dimensionless units (F). Length of the canal (x) is the fraction of the distance between the foramen magnum and the termination of the SSAS. The azimuth location in the canal (s) is the fraction of the rotation clockwise from the anterior midline. ANT and POST refer to the anterior and posterior regions of the SSAS, respectively. The width of the SSAS is greater anteriorly in the cervical region and posteriorly in the thoracic region, consistent with the different degrees of spinal cord eccentricity.

List of characteristic anatomic parameters for each subject

Parameter	Subject 1				
	Subject 1	(Repositioned)	Subject 2	Subject 3	Subject 4
L (cm)	59.5	58.8	63.7	64.0	63.7
ℓ_c (mm)	21.8	20.6	20.6	27.4	21.7
h_c (mm)	3.6	3.9	3.3	2.6	3.8
Cervical lordosis	8.5°	0.5°	1.0°	—	—
Thoracic kyphosis	28.0°	18.0°	22.5°	—	—

Note: —, indicates no data.

introduced to facilitate comparison of the results corresponding to different subjects, with the axial coordinate $x = d_{FM} / L$ defined by scaling the longitudinal distance with the total length of the canal L (measured from the foramen magnum to the end of the dural sac) and the azimuthal coordinate, $s = 0.5 + d_{MP} / \ell$, defined by scaling the azimuthal distance with the local cord perimeter ℓ (Fig 1F).

For illustration, the results of the above-described methodology and the relevant anatomic features will be discussed for subject 1 (Table). An important relevant anatomic feature—common to all subjects—is the change in the eccentricity of the spinal cord along the canal. The position of the spinal cord relative to the dura membrane within the anteroposterior plane varies along the canal (Fig 1). Observe in Fig 1A that the midline diameter of the SSAS on the posterior side ($s = 0.5$) exhibits, at its most cephalic end, a narrow region from C1 to C6, a wider region from C6 to T10, a moderately narrow region from T10 to L4, and, finally, a moderately wider region from L4 to S2 (Fig 1D, -E). Conversely, the anterior SSAS ($s = 0$ or, equivalently, $s = 1$) exhibits moderate

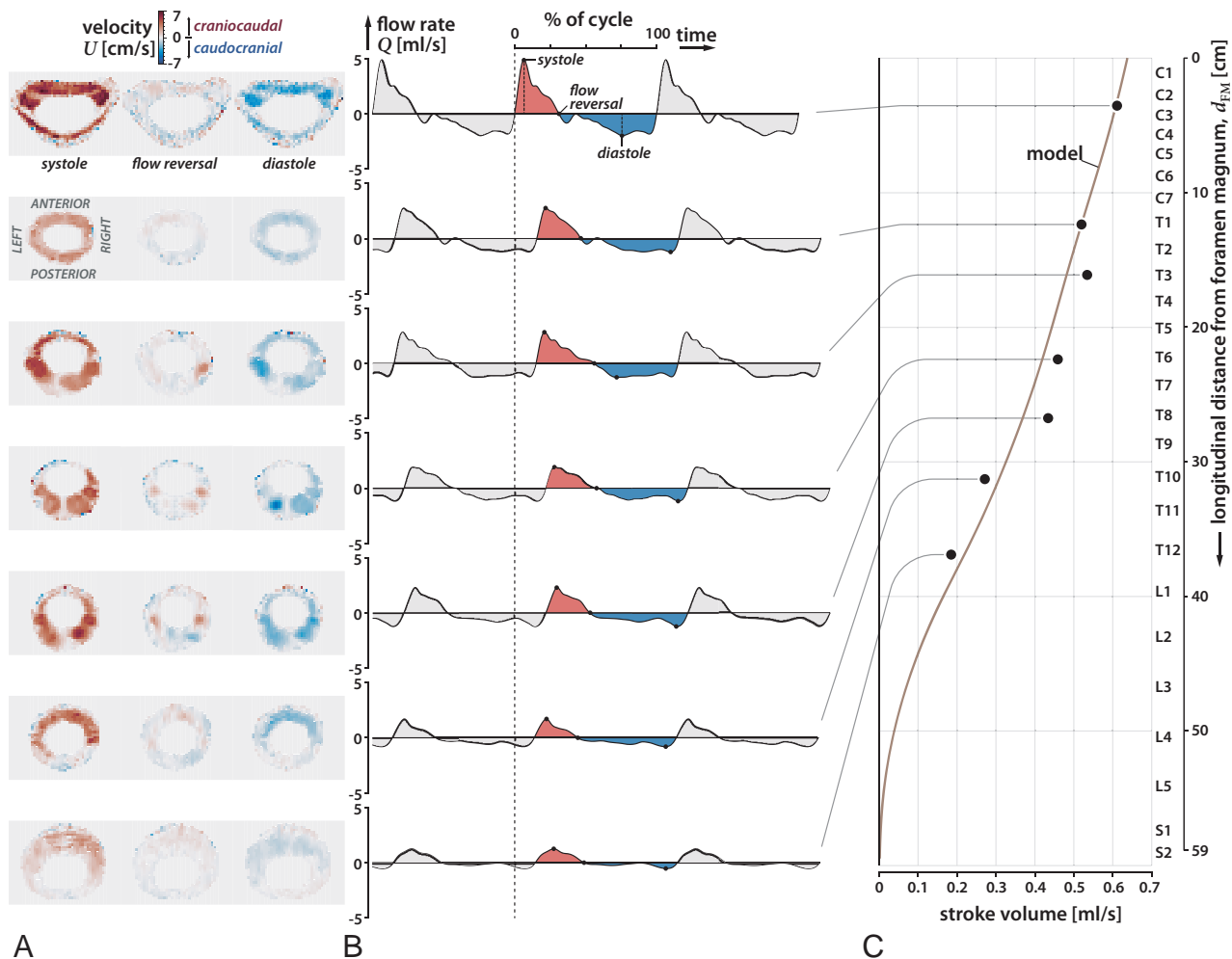


FIG 2. Axial MR images of oscillatory flow velocity in 7 locations in the spine (C3, T1, T3, T6, T8, T10, T12) at systole, reversal of flow, and diastole for subject 1 (A), plot of CSF flow rate over 3 cardiac cycles at the 7 locations, using as a reference time the beginning of systole at the C3 level (dashed line) (B), and plot of the variation of the stroke volume of the oscillations of the CSF over the length of the spinal canal (C). During the cardiac cycle, systolic flow (shaded red) has greater velocity and shorter duration than diastolic flow (shaded blue). Oscillatory CSF flow rates diminish in the craniocaudal direction along the spine with the stroke volume diminishing to zero at the sacral end of the spine. CSF flow oscillatory velocities are greater in the anterior ($s = 0$) and anterolateral regions of the cervical subarachnoid space ($s = 0.25$ and $s = 0.75$) than in the posterior subarachnoid space ($s = 0.5$).

widening in the cervical region (C1 to C7), it narrows from C7 to T11, and finally enlarges gradually toward the caudal end. Although all subjects share this common feature, they exhibit small-but-important changes in the locations where the cord eccentricity changes from posterior to anterior, and these will be shown in the following text to greatly affect the pattern of bulk CSF flow in each patient.

CSF flow velocity data were acquired at 7 vertebral levels (C3, T1, T3, T6, T8, T10, T12) (Fig 2) using phase-contrast MR imaging with respiratory and cardiac gating, and with a slice orientation perpendicular to the CSF flow direction. The imaging protocol consisted of a 2D single-shot gradient recalled-echo sequence with a slice thickness of 5 mm and an in-plane resolution of 0.5469×0.5469 mm. The specific imaging parameters include TR/TE = 18/6.66 ms, flip angle = 20° , and velocity encoding = 10, 4, 5, 6, 6, 6, 3 cm/s for the respective vertebral levels. At each level, 30 cardiac phases were obtained.¹⁷ During the acquisition, the heart rate of the subjects was 54–66 bpm. The MR phase and magnitude data were processed with in-house Matlab code to

obtain the 2D distribution of longitudinal velocity U_0 in the SSAS for 30 cardiac phases at the 7 x -locations (Fig 2A). These velocity fields were then numerically integrated over the area of the SSAS to obtain the flow rate that passes through each section x as a function of time t , $Q(x, t) = \int U_0 dA$ (Fig 2B). Finally, numerically integrating $Q(x, t)$ over the complete cardiac cycle yields the craniocaudal decay of the stroke volume $\Delta V(x) = (1/2) \int |Q(x, t)| dt$ (Fig 2C).

The measured velocity fields for subject 1 at each location are plotted in Fig 2A at the instance in time corresponding to the peak systolic velocity, peak diastolic velocity, and first flow reversal. The temporal evolution of the CSF flow rates at these locations is plotted in-phase in Fig 2B, where we used as a reference time the beginning of systole at the C3 vertebral level (indicated by the dashed line). These measurements allow estimation of the speed of the elastic wave propagating along the spinal canal and consequently the mean value of the canal compliance. The stroke volume $\Delta V(x)$ at each measurement plane computed by integrating the flow rate during 1 cardiac cycle is shown in Fig 2C. Note that

the stroke volume decreases monotonically in the craniocaudal direction, with smaller slopes in the cervical and upper thoracic regions, indicating a more compliant canal in the thoracic and lumbar regions compared with the cervical region, which is consistent with an increased presence of fatty and soft tissues.¹⁸ Because of the strong coupling of the oscillatory flow at all levels—the wavelength of the elastic wave being comparable with the length of the spinal canal—accurate flow predictions can be obtained even without the use of velocity measurements at the lumbar level, which generally have a low signal-to-noise ratio.

Once the anatomic functions $h(x, s)$ and $\ell(x)$ are determined, one still needs to determine the compliance of the canal $\gamma(x, s)$. As previously mentioned, its mean value, which determines the effective wave speed of the elastic wave that propagates craniocaudally along the canal, is inferred from the phase shift in $Q(x, t)$ between different vertebral levels (Fig 2B). The spatial variation can be obtained in an iterative fashion by comparison with the model computations. The computational procedure was started by using a presumed distribution $\gamma(x, s)$ in computing from the mathematical model,¹⁰ the leading-order oscillatory flow, and the craniocaudal decay of the stroke volume, $\Delta V(x)$. The comparison of the latter with the craniocaudal decay of the measured stroke volume led to an updated guess for $\gamma(x, s)$, which was iteratively adjusted to minimize departures between experimental measurements and theoretic predictions. In the case of subject 1, the final compliance distribution was found to be accurately represented by a slowly varying function, $\gamma(x, s) = 14.3 [0.8 + 0.3 \tanh(4x - 0.2)]$ m/MPa, which leads to predictions in excellent agreement with the measurements, as shown in Fig 2C. This function $\gamma(x, s)$, along with the anatomic functions $h(x, s)$ and $\ell(x)$, constitute the subject-specific information needed as input to the mathematical model.

Subjects of Study

We studied 4 healthy subjects without known anomalies of the spinal canal. Subject 1 was a 25-year-old woman who was first examined in the supine position and then again with cushions under her shoulders with an extended hip to change the degree of cervical and lumbar lordosis. Subject 2 was a 36-year-old man; subject 3, a 38-year-old man; and subject 4, a 23-year-old woman. The input data for subject 1 (in both body positions) and subject 2 were fully acquired in our study: The subjects underwent MR imaging in the supine position to obtain the spinal canal anatomy, and the primary oscillatory CSF flow was measured with MR phase contrast, using the aforementioned techniques. For subject 3, we obtained the anatomic image set from Ackerman, 1998,¹⁹ and proceeded with the segmentation to obtain the spinal anatomy. Subject 4 corresponds to the subject in Khani et al, 2018,²⁰ whose segmented spinal geometry and the craniocaudal decay of the stroke volume, $\Delta V(x)$, were already available. Because no velocity measurements were available for subject 3, to be able to apply our model, we used for this subject the compliance distribution $\gamma(x, s)$ obtained for subject 1, together with a nominal heart rate of 60 bpm. The Table shows a list of characteristic anatomic parameters for each subject: namely, the total canal length L , the average characteristic cord perimeter ℓ_c , and canal width h_c over the thoracic region, and the Cobb angles corresponding to cervical lordosis and thoracic kyphosis.

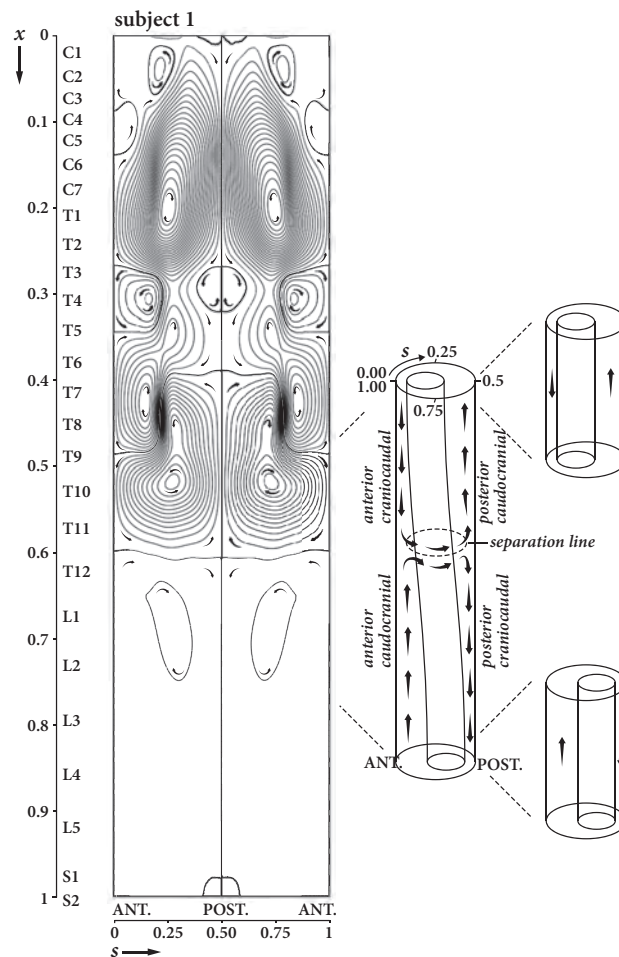


FIG 3. Streamlines and direction for bulk (mean Lagrangian) flow of the CSF in the SSAS in subject 1 in the supine position projected onto the 2D dimensionless plane with anterior midline SSAS at $s = 0$ and the posterior one at $s = 0.5$. Higher densities of streamlines near the posterior and anterior regions of the subarachnoid space indicate greater local bulk flow velocity. Bulk flow has multiple regions of patterns of circular flow where the fluid particles get trapped for long periods of time (Lagrangian vortices). Flow longitudinally in the SSAS occurs in the anterior and posterior subarachnoid space. In the lateral subarachnoid space ($s = 0.25$ and $s = 0.75$), flow is horizontally oriented where streamlines are present or essentially stagnant where streamlines are sparse. Subject 1 has 3 major pairs of Lagrangian vortices, 1 pair anatomically centered on C7, the second on T10, and the third on L1. Smaller Lagrangian vortices are also present. Where vortices contact each other, the mean Lagrangian flow in the adjacent vortices is in the same direction. Direction of flow along the spinal axis depends on cord eccentricity (sketch to the reader's right). In the cervical region, bulk flow occurs in a cephalad direction in the anterior subarachnoid space and in the caudal direction in the posterior subarachnoid space. In the thoracic region, bulk flow occurs in a cranial direction in the anterior subarachnoid space and in the cephalad direction in the posterior subarachnoid space. These flow directions are reversed again in the third lumbar vortex pair, with the CSF flowing caudocranially in the anterior wider space and craniocaudally in the posterior space.

RESULTS

CSF Bulk Lagrangian Motion

Figure 3 shows the streamlines and direction of the width-averaged mean Lagrangian velocity field (U_L, W_L) for subject 1, obtained from the mathematical model. These streamlines are also the paths followed by the solute particles in the SSAS, with decreasing spacing between streamlines corresponding to increasing

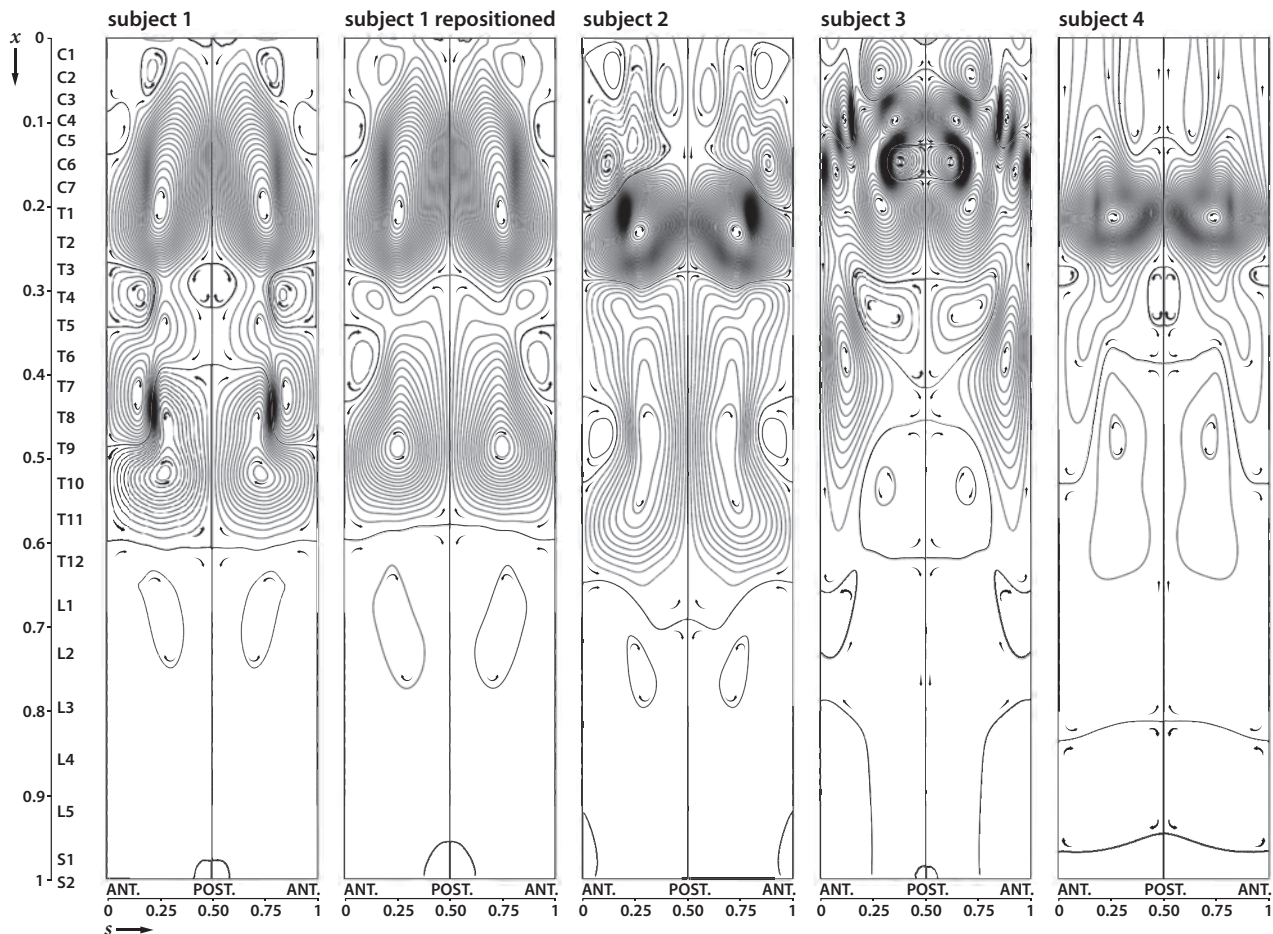


FIG 4. Streamlines and direction for bulk (mean Lagrangian) flow in subject 1 in the first and second positions and in 3 other subjects. In subject 1, bulk flow patterns change with the change in spine position. The other subjects illustrate variations of the pattern of bulk vortices, which generally have greater numbers of streamlines (higher magnitude of the bulk flow velocity) in the cervical and upper thoracic region and the least in the lumbar region (lower magnitude of the bulk flow velocity). Generally, different vortex rotations are present in the cervical, thoracic, and lumbar regions though the patterns differ.

speeds. The resulting flow patterns show the existence of 3 distinct regions of recirculating flow where the fluid particles may remain trapped for long periods. Hereafter, we will refer to these regions as “Lagrangian vortices.” The 3 vortices, separated by streamlines that are nearly horizontal, are approximately located from C1 to T4, T4 to T11, and T11 to the caudal end of the SSAS. The lowest speed is found in the near-core regions of the vortical patterns of closed streamlines. In the upper cervical Lagrangian vortex, the bulk flow is caudocranial in the wider anterior subarachnoid space and craniocaudal in the narrower posterior space. On the other hand, in the intermediate thoracic region, the flow is craniocaudal in the anterior narrow space and caudocranial in the posterior wider space. These flow directions are reversed again in the third lumbar vortex with the CSF flowing caudocranial in the anterior wider space and craniocaudal in the posterior space.

As indicated in the sketch of Fig 3, the directions of the bulk flow along the spinal axis are correlated with cord eccentricity. In the cervical region, the Lagrangian vortex rotates clockwise to the reader’s left and counterclockwise to the reader’s right. The direction of rotation of these vortices is reversed in the thoracic region and once again in the lumbar region. The velocity of the bulk flow varies between vortices, being 2–3 orders of magnitude (100–

1000 times) smaller in the lumbar than in the cervical region. The formation of these closed recirculating Lagrangian vortices can be understood in view of our recent modeling studies and experiments conducted in phantom models,^{10,11} in which we analyzed the bulk motion of the CSF in a simplified geometry consisting of 2 long cylinders with nonzero constant eccentricity along its length. The resulting bulk Lagrangian motion was seen to be directed in opposite directions in the narrow and wide parts of the SSAS. In the human SSAS, the eccentricity is not constant, exhibiting 2 changes along the spinal axis (Fig 1B, -D). At the location where the eccentricity changes from posterior to anterior and vice versa, the craniocaudal CSF flow in the narrow anterior part collides with the caudocranial flow from the wide anterior part, deviating the flow in the azimuthal direction toward the posterior section and forming the Lagrangian vortices, as indicated schematically in Fig 3.

Differences in Bulk Flow between Subjects

Although the existence of closed recirculation regions is a common feature for all subjects (Fig 4), there are important differences in the topology of these regions between different subjects and body positions. In subject 1, small variations in the body

position, which reduced cervical lordosis by 8° and reduced thoracic kyphosis by 10°, resulted in a decrease in the number of Lagrangian vortices in the thoracic part of the SSAS. Subject 2 exhibits a large thoracic vortex that extends from T3 to L2, together with an intense region of bulk recirculating flow from C7 to T3. In subject 3, a complicated pattern of multiple Lagrangian vortices extends from C1 to T8, whereas caudally from T8, only a very weak bulk motion is observed. This metameric distribution of bulk flow velocity is even more emphasized in subject 4, for which the region of intense bulk flow is limited to a single vortex extending between C6 and T3.

Our results indicate that the long-term transport of solute particles, which occurs along the streamlines shown in Fig 4 with a velocity proportional to the local streamline interspacing, changes drastically between different subjects and subject postures. In all cases, the location and spatial extent of these Lagrangian vortices are strongly correlated with the location where the eccentricity of the spinal cord changes from posterior to anterior and vice versa.

DISCUSSION

Our analysis shows that CSF bulk flow in the SSAS, responsible for the convective transport of solute particles, exhibits distinct patterns (Lagrangian vortices) in the cervical, thoracic, and lumbar regions. The location and interconnectivity of these zones strongly depend on cord eccentricity. The bulk flow velocity varies from region to region along the spinal canal, being higher in the Lagrangian vortices closer to the foramen magnum and progressively lower in the thoracic and lumbar regions, where velocity is 2–3 orders of magnitude (~100–1000 times) smaller than in the cervical region. Bulk flow patterns and velocities vary from individual to individual and with posture, suggesting that these differences may be the most important factor in the variability of the movement of solutes and drugs in the SSAS.

Our study has a small number of subjects exhibiting anatomic variations that are probably within the normal range. The analysis needs to be extended to a larger number of subjects to investigate reproducibility and to determine how specific variations in spine curvature and spine pathology affect flow. Future studies should also consider modulation of the intracranial pressure by the respiratory cycle, resulting in a smaller additional component of the oscillation of the CSF in the spinal canal at a lower frequency (12–18 cycles per minute in adults).^{21–23} In our analysis, we have assumed that the compliance of the canal varies only with the longitudinal distance along the canal. There might be an additional azimuthal dependency associated with the nonuniform distribution of fatty tissue along the perimeter of the canal. Our mathematical model also does not account for the effects associated with the presence of microanatomic features, such as nerve roots and denticulate ligaments, which may contribute to additional local mixing, especially in the cervical region where velocities are greatest,^{20, 24–26} thereby promoting interaction between adjacent Lagrangian vortices.

Our flow analysis, showing peaking of oscillatory flow in the midline anterior to anterolateral subarachnoid space in the mid and upper cervical spine, is in agreement with previous observations.^{4,27} Previous reports have illustrated a craniocaudal flow of CSF in the anterior subarachnoid space and in a caudocranial

direction in the posterior subarachnoid space.⁶ Some previous publications have illustrated more complex bulk CSF flow such as a sinuous caudocranial current.⁸ The mechanism by which CSF has a net bulk flow in both craniocaudal and caudocranial directions and the presence of Lagrangian vortices have not, to our knowledge, been reported previously.

CONCLUSIONS

Bulk flow is key to the normal functioning of the CNS and to the transport of drugs, anesthetics, and chemotherapeutic agents in the SSAS. The existence of Lagrangian vortices, in which fluid particles may be retained for long periods, can have important implications for intrathecal drug delivery.^{28,29} Studies of flow patterns in a subject can potentially benefit intrathecal drug-delivery protocols, for example, through the identification of optimal injection sites to place a drug centrally into a Lagrangian vortex or into a cephalad- or caudal-oriented bulk stream. Patient posture has also been shown to affect the motion of the CSF and the dispersion of the drug in the spinal canal.^{30,31} It is clear that the knowledge acquired through patient-specific analyses of bulk CSF motion on the grounds of rigorous mathematical theory and subject-specific anatomic measurements can help improve the effectiveness and predictability of intrathecal drug delivery treatments in the future.

REFERENCES

1. du Boulay GH. **Pulsatile movements in the CSF pathways.** *Br J Radiol* 1966;39:255–62 CrossRef Medline
2. Bhadelia RA, Bogdan AR, Kaplan RF, et al. **Cerebrospinal fluid pulsation amplitude and its quantitative relationship to cerebral blood flow pulsations: a phase-contrast MR flow imaging study.** *Neuroradiology* 1997;39:258–64 CrossRef Medline
3. Wagshul ME, Chen JJ, Egnor MR, et al. **Amplitude and phase of cerebrospinal fluid pulsations: experimental studies and review of the literature.** *J Neurosurg* 2006;104:810–19 CrossRef Medline
4. Loth F, Yardimci MA, Alperin N. **Hydrodynamic modeling of cerebrospinal fluid motion within the spinal cavity.** *J Biomech Eng* 2001; 123:71–79 Medline
5. Mokri B. **The Monro-Kellie hypothesis: applications in CSF volume depletion.** *Neurology* 2001;56:1746–48 CrossRef Medline
6. Di Chiro G. **Observations on the circulation of the cerebrospinal fluid.** *Acta Radiol Diagn (Stockh)* 1966;5:988–1002 CrossRef
7. Di Chiro G, Hammock MK, Bleyer WA. **Spinal descent of cerebrospinal fluid in man.** *Neurology* 1976;26:1–8 CrossRef Medline
8. Greitz D, Hannerz J. **A proposed model of cerebrospinal fluid circulation: observations with radionuclide cisternography.** *AJNR Am J Neuroradiol* 1996;17:431–38 Medline
9. Hesterman JY, Kost SD, Holt RW, et al. **Three-dimensional dosimetry for radiation safety estimates from intrathecal administration.** *J Nucl Med* 2017;58:1672–78 CrossRef Medline
10. Sanchez AL, Martinez-Bazan C, Gutierrez-Montes C, et al. **On the bulk motion of the cerebrospinal fluid in the spinal canal.** *J Fluid Mech* 2018;841:203–27 CrossRef
11. Lawrence JJ, Coenen W, Sanchez AL, et al. **On the dispersion of a drug delivered intrathecally in the spinal canal.** *J Fluid Mech* 2019; 861:679–720 CrossRef
12. Jansen IG, Schneiders JJ, Potters WV, et al. **Generalized versus patient-specific inflow boundary conditions in computational fluid dynamics simulations of cerebral aneurysmal hemodynamics.** *AJNR Am J Neuroradiol* 2014;35:1543–48 CrossRef Medline
13. Karmonik C. **Toward improving fidelity of computational fluid dynamics simulations: boundary conditions matter.** *AJNR Am J Neuroradiol* 2014;35:1549–50 CrossRef Medline

14. Karmonik C, Müller-Eschner M, Partovi S, et al. **Computational fluid dynamics investigation of chronic aortic dissection hemodynamics versus normal aorta.** *Vasc Endovascular Surg* 2013;47:625–31 CrossRef Medline
15. Karmonik C, Partovi S, Loebe M, et al. **Computational fluid dynamics in patients with continuous-flow left ventricular assist device support show hemodynamic alterations in the ascending aorta.** *J Thorac Cardiovasc Surg* 2014;147:1326–33.e1 CrossRef Medline
16. Yushkevich PA, Piven J, Hazlett HC, et al. **User-guided 3D active contour segmentation of anatomical structures: significantly improved efficiency and reliability.** *Neuroimage* 2006;31:1116–28 CrossRef Medline
17. Haughton V, Mardal KA. **Spinal fluid biomechanics and imaging: an update for neuroradiologists.** *AJNR Am J Neuroradiol* 2014;35:1864–69 CrossRef Medline
18. Reina MA, Franco CD, López A, et al. **Clinical implications of epidural fat in the spinal canal: a scanning electron microscopic study.** *Acta Anaesthesiol Belg* 2009;60:7–17 Medline
19. Ackerman MJ. **The Visible Human Project: a resource for anatomical visualization.** *Stud Health Technol Inform* 1998;52(Pt 2):1030–32 Medline
20. Khani M, Sass LR, Xing T, et al. **Anthropomorphic model of intrathecal cerebrospinal fluid dynamics within the spinal subarachnoid space: spinal cord nerve roots increase steady-streaming.** *J Biomech Eng* 2018;140:081012 CrossRef
21. Kao YH, Guo WY, Liou AJ, et al. **The respiratory modulation of intracranial cerebrospinal fluid pulsation observed on dynamic echo planar images.** *Magn Reson Imaging* 2008;26:198–205 CrossRef Medline
22. Hettiarachchi HD, Hsu Y, Harris TJ Jr, et al. **The effect of pulsatile flow on intrathecal drug delivery in the spinal canal.** *Ann Biomed Eng* 2011;39:2592–602 CrossRef Medline
23. Dreha-Kulaczewski S, Konopka M, Joseph AA, et al. **Respiration and the watershed of spinal CSF flow in humans.** *Sci Rep* 2018;8:5594 CrossRef Medline
24. Drøsdal IN, Mardal KA, Stoverud K, et al. **Effect of the central canal in the spinal cord on fluid movement within the cord.** *Neuroradiol J* 2013;26:585–90 CrossRef Medline
25. Mardal KA, Rutkowska G, Linge S, et al. **Estimation of CSF flow resistance in the upper cervical spine.** *Neuroradiol J* 2013;26:106–10 CrossRef Medline
26. Linge SO, Haughton V, Løvgren AE, et al. **CSF flow dynamics at the craniovertebral junction studied with an idealized model of the subarachnoid space and computational flow analysis.** *AJNR Am J Neuroradiol* 2010;31:185–92 CrossRef Medline
27. Quigley AM, Buscombe JR, Shah T, et al. **Intertumoural variability in functional imaging within patients suffering from neuroendocrine tumours: an observational, cross-sectional study.** *Neuroendocrinology* 2005;82:215–20 CrossRef Medline
28. Kamran S, Wright BD. **Complications of intrathecal drug delivery systems.** *Neuromodulation* 2001;4:111–15 CrossRef Medline
29. Pardridge WM. **Drug transport in brain via the cerebrospinal fluid.** *Fluids Barriers CNS* 2011;8:7 CrossRef Medline
30. Shafer SL, Eisenach JC, Hood DD, et al. **Cerebrospinal fluid pharmacokinetics and pharmacodynamics of intrathecal neostigmine methylsulfate in humans.** *Anesthesiology* 1998;89:1074–88 CrossRef Medline
31. Ranger MR, Irwin GJ, Bunbury KM, et al. **Changing body position alters the location of the spinal cord within the vertebral canal: a magnetic resonance imaging study.** *Br J Anaesth* 2008;101:804–09 CrossRef Medline

Celebrating 35 Years of the AJNR

July 1984 edition

Computed Tomography of Orbital Myositis

Steven C. Dresner¹
William E. Rothfus²
Thomas S. Sliemers^{1,3}
John S. Kainerd^{1,3}
Hugh D. Curtin²

The computed tomographic (CT) scans of 11 consecutive patients with orbital myositis were reviewed to better characterize the CT appearance of this condition. The findings in this series differed from those of previous reports in several ways. Multiple muscle involvement predominated. Bilateral involvement was more frequent than previously reported. Enlargement of the tendon as well as the muscle was a frequent finding, but a normal tendinous insertion did not preclude the diagnosis of orbital myositis. Although the CT appearance of orbital myositis is often helpful, the findings are not pathognomonic; correlation with history, clinical findings, and therapeutic response must be considered in making the diagnosis.

Orbital myositis is a recognized subgroup of the nonspecific orbital inflammatory syndrome or orbital pseudotumor [1-3]. Early-generation computed tomography (CT) characterized orbital pseudotumor as a diffuse process; however, with improved resolution, specific target organs in the orbit have been identified [3]. For example, when the inflammatory process is localized to the lacrimal gland, sclera, nerve sheath, or extraocular muscle, a diagnosis of dacryoadenitis, periorbititis, perineuritis, or orbital myositis can be made.

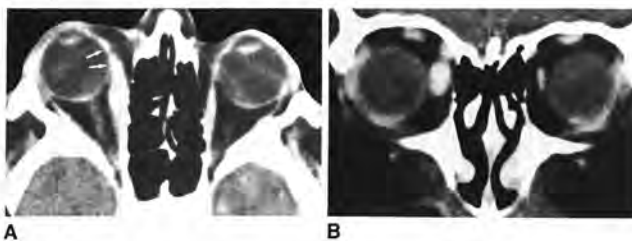
Previous reports characterized orbital myositis as a predominantly unilateral inflammatory process causing irregular enlargement of a single isolated extraocular muscle and its tendinous insertion [3]. It was suggested that this appearance on CT could serve to distinguish orbital myositis from dysthyroid orbitopathy and other orbital conditions causing enlarged extraocular muscles. The present study was undertaken to better characterize the CT appearance of orbital myositis with high-resolution axial and coronal scans.

Materials and Methods

We reviewed the CT scans of 11 consecutive patients with a diagnosis of orbital myositis based on their history, clinical course, and response to steroids. Patients with diffuse orbital pseudotumor were excluded. Eight of the 11 studies were performed on a GE 8800 scanner. Three studies were performed on an AS & E 5500 scanner. All patients had axial and coronal scans with 5-mm sections. Contrast material was used in nine of the 11 studies. No patients had a history of thyroid dysfunction or signs or symptoms of dysthyroid orbitopathy. Laboratory evaluation (done in six patients) was negative for thyroid abnormalities.

Results

Twenty-nine muscles in 11 patients were identified as enlarged on CT: the medial rectus muscle(s) in eight patients, the lateral rectus in five, the superior rectus, levator palpebrae superioris complex in four, and the inferior rectus and superior oblique in two each. Five of 11 cases had bilateral involvement. Of the six with unilateral involvement, five had a single isolated enlarged extraocular muscle or muscle complex.



This article appears in the July/August 1984 issue of AJNR and the September 1984 issue of AJR.

Received August 4, 1983; accepted after revision December 3, 1983.

¹Department of Ophthalmology, University Health Center of Pittsburgh, Pittsburgh, PA 15261.

²Department of Radiology, University Health Center of Pittsburgh, Pittsburgh, PA 15261. Address reprint requests to W. E. Rothfus, Division of Neurology, Presbyterian-University Hospital, Delkno at O'Hara St., Pittsburgh, PA 15213.

³Department of Neurology, University Health Center of Pittsburgh, Pittsburgh, PA 15261.

AJNR 5:351-354, July/August 1984
0195-9584/84/0504-0351\$2.00
© American Thoracic Society

Intravenous Contrast-Enhanced CT of the Postoperative Lumbar Spine: Improved Identification of Recurrent Disk Herniation, Scar, Arachnoiditis, and Diskitis

J. George Teplick¹
Marvin E. Haskin¹

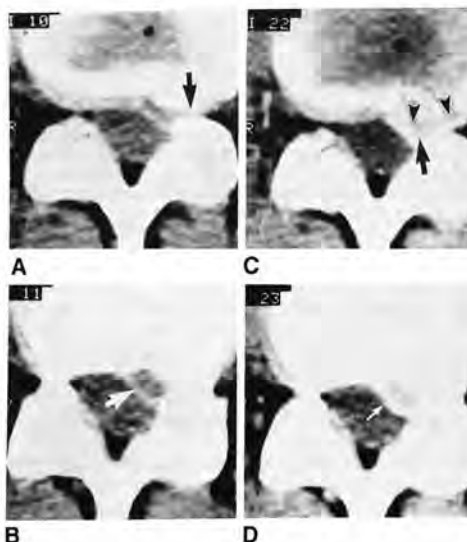
Unsuccessful relief of symptoms after back surgery is usually attributable to hypertrophic extradural scar or recurrent herniated disk. Their clinical and myelographic differentiation is difficult, yet important because reoperation is not always beneficial for scar removal. This article examines the usefulness of intravenous contrast-enhanced computed tomography for this problem. Forty-five postoperative patients were studied; eight had subsequent surgery, to the four with hypertrophic scars, intravenous contrast enhancement of the scar allowed its recognition in each case; in the four with recurrent disk herniation, nonenhancement of the extruded disk allowed its recognition in three. In the other 37 patients who were not reoperated, 33 were believed to have scar on the basis of contrast enhancement. Continuous contrast infusion during scanning, avoidance of patient movement, and careful consideration of other structures in the spinal canal are important in interpretation. The method seems promising for more accurate evaluation of failed back surgery, including the recognition of diskitis.

High-resolution computed tomography (CT) has proven to be the most accurate method for evaluating the causes of failure of relief or later recurrence of symptoms after back surgery [1-6]. Two of the most common causes are hypertrophic extradural scar and recurrent herniated disk [1, 2, 5, 7]. The distinction of one from the other is of considerable importance, since extradural scar removal often leads to further scar formation [1, 2, 5, 8], while removal of a recurrent herniated disk is generally beneficial. Until recently the distinction usually could not be made conclusively before reoperation, and too often the surgeon was disappointed in finding a scar and not a recurrent herniated disk.

Both recurrent herniated disk and symptomatic hypertrophic scar can produce similar low-back symptoms and radiculopathy. Gradually increasing symptoms beginning a year or more after discectomy are considered more likely due to scar radiculopathy, while a more abrupt onset at any interval after surgery is more likely due to recurrent herniated disk [1, 2]. Myelography, unfortunately, cannot make a reliable distinction in most cases [3, 8-10], since both lesions can create a clear-cut myelographic defect at or near the interspace.

In most CT scans of the postoperative lumbar spine, fairly confident recognition of fibrosis (scar) is possible using recently published criteria [4-6]. However, when the postoperative lesion resembles a typical herniated disk on CT, it may still prove to be a hypertrophic scar mass (figs. 1 and 2). Sometimes repeat postoperative CT scans are helpful. If, over a period of months or years, there is a definite increase of extradural soft tissues, it is highly probable that a recurrent herniated disk has developed. The postoperative extradural tissue, which generally begins as a postoperative hematoma [2, 4-6], tends to diminish slightly as fibrosis develops and matures, but does not usually enlarge. Consequently, an enlarging extradural soft-tissue mass on follow-up CT will mean that a recurrent disk herniation has developed (fig. 3).

To make the distinction with greater certainty, some suggest a CT scan with



Polymer Embolism from Bioactive and Hydrogel Coil Embolization Technology: Considerations for Product Development

Modified (bioactive and hydrogel) coil embolization technologies were introduced to reduce aneurysm recurrence rates. The addition of bioactive polymers to bare platinum coils is designed to induce a tissue response and promote neoendothelialization. Hydrogel polymers on platinum coils swell in contact with the physiologic environment, filling the aneurysmal sac, and possibly increasing occlusion rates.

Reinges et al¹ animal study reported on rates of vessel wall reconstruction over the aneurysm neck with modified coil technologies. After 12 months, the study determined a minimal neointimal or neoendothelial layer for bioactive coils and complete aneurysm obliteration and neoendothelialization for hydrogel coils at the aneurysm neck. For aneurysms treated with hybrid bare platinum–hydrogel coils, a postmortem study of 13 human aneurysms retrieved between 1 and 74 days postembolization reported that neointima formation had begun at 5 days and a new vessel wall supported by smooth-muscle cells (at the margins) had traversed the aneurysm neck at 74 days.²

Notably, until the clot-coil complex is formed and the aneurysm neck is bridged, bioactive and hydrogel polymers on platinum coils are exposed to continuous pulsatile blood flow. Polymers on intravascular devices exposed to aqueous environments are known to avulse in a relatively short time. For example, an *in vitro* test highlights shedding of polymer from the distal end of a guide catheter immersed in 0.9% saline in as little as 60 minutes.³ Of relevance, the average time it takes for the aforementioned physiologic processes to occur (a few days) far exceeds the time it takes for polymers to detach from the modified coils when exposed to an aqueous environment. For embolization coils, polymer separation begins when coil loops form and interact with each other on deployment within the aneurysmal sac, resulting in shedding and possible displacement of the polymer material. Stent-assisted coiling and coil-supported flow diversion may further facilitate mechanical abrasion and subsequent polymer detachment. Polymer embolism from coil embolization procedures has been associated with the formation of round enhancing lesions and surrounding vasogenic edema, resulting in neurologic decline between 1 and 270 days from the coiling procedure (average, 1–2

months).³ In reported events, even though the edema was effectively treated with corticosteroids, some patients were dependent on medications with remnant brain lesions years after the initial procedure.³

The 2015 US FDA safety communication sheds light on this iatrogenic complication of polymer embolism and states that it will work with stakeholders to close gaps in standards related to polymer coating integrity.⁴ Currently particulate testing—determining the count and size of polymer particulates separated from a device when tested in a clinically representative environment—is the standard for evaluating coating integrity on an intravascular device.⁵ Given the ubiquitous use of hydrophilic coatings on neurovascular devices, mitigating particulates may be the preferred method of addressing this complication, especially from permanently implantable devices. Improvements in coil embolization technology with the addition of bioactive and hydrogel polymers emphasize the importance of particulate testing to determine, mitigate, and possibly eliminate the impact of this potential iatrogenic complication from these important neurovascular technologies. This information is relevant to physicians, regulators, design engineers, and manufacturers for product development as newer generations of embolization coils become available for use.

Disclosures: Juan Pablo Cruz—UNRELATED: Payment for lectures including service on speakers bureaus: Roche, Comments: a talk regarding the role of MR imaging in the pharmacovigilance for progressive multifocal leukoencephalopathy (PML) in MS for a national congress.

REFERENCES

1. Reinges MH, Krings T, Drexler AY, et al. **Bare, bio-active and hydrogel-coated coils for endovascular treatment of experimentally induced aneurysms: long-term histological and scanning electron microscopy results.** *Interv Neuroradiol* 2010;16:139–50 [CrossRef](#) [Medline](#)
2. Killer M, Arthur AS, Barr JD, et al. **Histomorphology of thrombus organization, neointima formation, and foreign body response in retrieved human aneurysms treated with hydrocoil devices.** *J Biomed Mater Res B Appl Biomater* 2010;94:486–92 [CrossRef](#) [Medline](#)
3. Chopra AM, Mehta M, Bismuth J, et al. **Polymer coating embolism from intravascular medical devices: a clinical literature review.** *Cardiovasc Pathol* 2017;30:45–54 [CrossRef](#) [Medline](#)
4. U.S. Food and Drug Administration Safety Communications. **Lubricious Coating Separation from Intravascular Medical Devices:**

FDA Safety Communication. November 23, 2015. <http://wayback.archive-it.org/7993/20170404182155/https://www.fda.gov/MedicalDevices/Safety/AlertsandNotices/ucm473794.htm>. Accessed January 13, 2019

5. U.S. Food and Drug Administration. Recognized Consensus Standards. Recognition number 3–99, AAMI TIR42:2010. Evaluation of Particulates Associated with Vascular Medical Devices. Updated September 17, 2018. https://www.accessdata.fda.gov/scripts/cdrh/cfdocs/cfStandards/detail.cfm?standard__identification_no=38909. Accessed January 13, 2019

 **A.M. Chopra**

Chemical Engineer/Medical Researcher
Camarillo, California

 **J.P. Cruz**

Department of Radiology
Hospital Clínico de la Pontificia Universidad Católica de Chile
Santiago, Chile

 **Y.C. Hu**

Department of Neurosurgery
University Hospitals Cleveland Medical Center
Cleveland, Ohio

Optic Nerve Evaluation in Idiopathic Intracranial Hypertension

We read with great interest the article by Golden et al¹ concerning the use of MR imaging with contrast-enhanced 3D-FLAIR imaging in patients with idiopathic intracranial hypertension (IIH). We would like to congratulate the authors for their fascinating study but would like to make some comments on the methodology used to conduct the research.

The authors used MR imaging in patients with IIH and control subjects to study the optic nerve and the optic nerve head and correlated their findings to the Frisén scale, an ophthalmologic scale for grading papilledema severity.

We have some concerns about the method used because Hayreh,² in 2016, showed that the appearance of the optic nerve head does not simultaneously correlate with the measurement of intracranial pressure (ICP). In fact, as the authors correctly stated in the discussion, the appearance of papilledema is related to the elevated ICP that expresses itself with axoplasmic stasis and ischemia, with subsequent neurotoxicity. Thus, in the case of IIH, the optic disc could still appear edematous when the ICP is normalized or, to the contrary, could even be normal in the early phase of ICP increase.

Thus, recently, several articles have suggested using sonography to safely and noninvasively detect ICP and follow patients with high ICP, but unfortunately most of the authors used the B-scan technique, which, in our opinion, is not very reliable for this purpose.^{3,4}

In our opinion, a standardized A-scan, first introduced by K.C.⁵ Ossoinig in late 1970s is much more sensitive for this purpose because it can immediately detect the presence of high ICP or

even differentiate papilledema from pseudopapilledema (eg, in case of optic nerve drusen).

Furthermore, MR imaging is mandatory to exclude or determine the reason for the high ICP, but when a diagnosis of benign intracranial hypertension is entertained, we see no reason to use MR imaging to follow these patients when a cheaper and less invasive technique such as sonography can be used.

REFERENCES

1. Golden E, Krivochenitser R, Mathews N, et al. **Contrast-enhanced 3D-FLAIR imaging of the optic nerve and optic nerve head: novel neuroimaging findings of idiopathic intracranial hypertension.** *AJNR Am J Neuroradiol* 2019;40:334–39 CrossRef Medline
2. Hayreh SS. **Pathogenesis of optic disc edema in raised intracranial pressure.** *Prog Retin Eye Res* 2016;50:108–44 CrossRef Medline
3. Iaconetta G, De Bernardo M, Rosa N. **Coronal axis measurement of the optic nerve sheath diameter.** *J Ultrasound Med* 2017;36:1073 CrossRef Medline
4. De Bernardo M, Rosa N. **Clarification on using ultrasonography to detect intracranial pressure.** *JAMA Ophthalmol* 2017;135:1004–05 CrossRef Medline
5. Ossoinig KC. **Standardized echography of the optic nerve.** In: Till P, ed. *Documenta Ophthalmologica Proceedings Series vol 55, Ophthalmic echography 13.* Dordrecht: Springer Netherlands; 1990, 3–99

● M. De Bernardo

● L. Vitiello

● N. Rosa

Department of Medicine, Surgery, and Dentistry
Scuola Medica Salernitana
University of Salerno
Salerno, Italy

<http://dx.doi.org/10.3174/ajnr.A6091>

REPLY:

We appreciate the thoughtful comments shared by De Bernardo et al regarding our recent publication exploring the use of contrast-enhanced 3D-FLAIR imaging in the evaluation of patients with idiopathic intracranial hypertension (IIH).¹ In their comments, the authors of the response wished to raise awareness of how patients with IIH could be serially monitored with sonography as a more sensitive and cost-effective technique to evaluate optic nerve edema compared with contrast-enhanced MR imaging.

We would like to highlight, however, that the overarching objective of our report was to evaluate the sensitivity of contrast-enhanced 3D-FLAIR imaging in patients for the initial (and sometimes opportunistic) diagnosis of IIH, as opposed to serial and longitudinal imaging of these patients. In patients presenting a priori with headaches and blurred vision, it is important to

evaluate the brain to rule out other causes of elevated intracranial pressure, and a head MR imaging without and with contrast remains the standard of care to evaluate this patient population.² Our investigation identified a moderate correlation between the Frisén Scale and findings seen on contrast-enhanced 3D-FLAIR, particularly in patients with higher grades of papilledema. Once a diagnosis of IIH has been clinically established, sonography may play a role in follow-up as the authors suggest.

REFERENCES

1. Golden E, Krivochenitser R, Mathews N, et al. **Contrast-enhanced 3D-FLAIR imaging of the optic nerve and optic nerve head: novel neuroimaging findings of idiopathic intracranial hypertension.** *AJNR Am J Neuroradiol* 2019;40:334–39 CrossRef Medline
2. American College of Radiology. ACR Appropriateness: Headache. (<https://acsearch.acr.org/docs/69482/Narrative/>). Accessed May 10, 2019

● T.A. Kennedy

Department of Radiology, Division of Neuroradiology
University of Wisconsin School of Medicine and Public Health
Madison, Wisconsin

<http://dx.doi.org/10.3174/ajnr.A6094>

Automated Segmentation of Hippocampal Volume: The Next Step in Neuroradiologic Diagnosis of Mesial Temporal Sclerosis

I have read with great interest the article titled “Improved Detection of Subtle Mesial Temporal Sclerosis: Validation of a Commercially Available Software for Automated Segmentation of Hippocampal Volume” by Mettenburg et al.¹ Mesial temporal sclerosis (MTS) is one of the most common operable causes of drug-resistant epilepsy. As rightly noted by the authors, clinical, electrophysiologic, and radiologic concordance is essential for selecting a patient for epilepsy surgery. With a good sensitivity (89%), Neuroreader software (<https://brainreader.net/p/product/neuroreader>) would definitely improve the pickup rate of mesial temporal sclerosis. Further improvement in the sensitivity to >95% would make Neuroreader a reliable tool to aid the radiologist.

Although this was a retrospective study, it would be useful to see the probable clinical impact of Neuroreader in those patients in whom Neuroreader identified the MTS correctly and MTS was missed by the neuroradiologist. The authors could have assessed whether invasive monitoring was performed in those misdiagnosed patients and whether it could have been avoided by the use of Neuroreader.

The burden of drug-resistant epilepsy is large in developing countries. In these countries, temporal lobe seizure operations are performed on the basis of 1.5T MR imaging of the brain. Ahdidan et al² have shown significant correlation between hippocampal volume quantification by Neuroreader in 1.5T and 3T MR images. Neuroreader would be useful in developing countries if a 1.5T volumetric acquisition could be used for identifying MTS. This may require a clinical study to determine the validity of Neuroreader on a population different from that in its training data.

The cost of Neuroreader would be an important consideration

for widespread use in developing countries. Desikan et al³ have reported the cost of Neuroreader per study at \$80, which would cost more than MR imaging of the brain in developing countries. Publicly available software like JFL/CL (<https://www.nitrc.org/projects/ashs/>; <https://sites.google.com/site/hipposubfields/>)⁴ and HIPPOSEG (<http://niftyweb.cs.ucl.ac.uk/program.php?p=BRAIN-STEPS>),⁵ though not FDA-approved, would aid in MTS identification and aid the neuroradiologist.

Although there were only 26 patients positive for MTS, the authors have done a commendable statistical analysis and this study plays a vital role in emphasizing the importance of automated segmentation software in aiding neuroradiology reporting and operative decision-making.

REFERENCES

1. Mettenburg JM, Branstetter BF, Wiley CA, et al. **Improved detection of subtle mesial temporal sclerosis: validation of a commercially available software for automated segmentation of hippocampal volume.** *AJNR Am J Neuroradiol* 2019;40:440–45 CrossRef Medline
2. Ahdidan J, Raji CA, DeYoe EA, et al. **Quantitative neuroimaging software for clinical assessment of hippocampal volumes on MR imaging.** *J Alzheimers Dis* 2016;49:723–32 CrossRef Medline
3. Desikan RS, Rafii MS, Brewer JB, et al. **An expanded role for neuroimaging in the evaluation of memory impairment.** *AJNR Am J Neuroradiol* 2013;34:2075–82 CrossRef Medline
4. Hadar PN, Kini LG, Coto C, et al. **Clinical validation of automated hippocampal segmentation in temporal lobe epilepsy.** *Neuroimage Clin* 2018;20:1139–47 CrossRef Medline
5. Winston GP, Cardoso MJ, Williams EJ, et al. **Automated hippocampal segmentation in patients with epilepsy: available free online.** *Epilepsia* 2013;54:2166–73 CrossRef Medline

 N. Damodaran

Department of Neurosurgery
Mahatma Gandhi Medical College and Research Institute
Pondicherry, India

<http://dx.doi.org/10.3174/ajnr.A6092>

In the article “Prevalence of Superior Semicircular Canal Dehiscence on High-Resolution CT Imaging in Patients without Vestibular or Auditory Abnormalities” by A.W. Berning, K. Arani, and B.F. Branstetter, IV (*AJNR Am J Neuroradiol* 2019;40:709–12), the images and legends for Figs 3 and 4 were incorrectly matched. They should appear as shown below. The authors regret the error.

<http://dx.doi.org/10.3174/ajnr.A6082>



FIG 3. A thin-but-intact superior semicircular canal. Coronally reformatted CT of the temporal bone demonstrates very thin bone overlying the superior semicircular canal (*arrow*). This quantity of bone should be classified as intact in patients with and without suggestive symptoms.

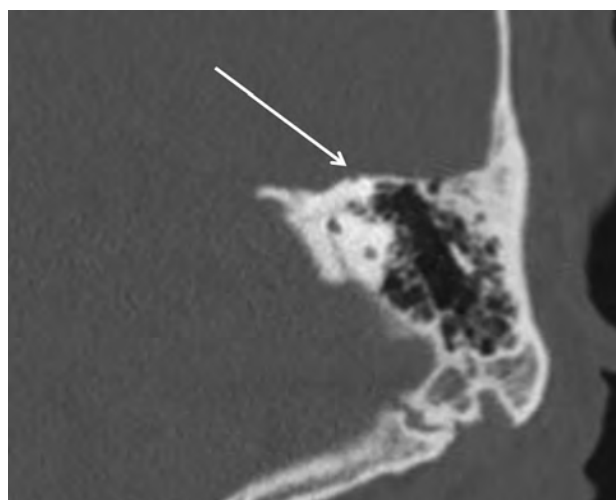


FIG 4. Dehiscent superior semicircular canal. Coronally reformatted CT of the temporal bone demonstrates dehiscence of the roof of the superior semicircular canal (*arrow*).